



# Tracing back the cosmic history of galaxy formation with the large ALMA interferometer

Maximilien Franco

## ► To cite this version:

Maximilien Franco. Tracing back the cosmic history of galaxy formation with the large ALMA interferometer. Galactic Astrophysics [astro-ph.GA]. Université Paris Cité, 2019. English. NNT : 2019UNIP7012 . tel-02975612

**HAL Id: tel-02975612**

**<https://theses.hal.science/tel-02975612>**

Submitted on 22 Oct 2020

**HAL** is a multi-disciplinary open access archive for the deposit and dissemination of scientific research documents, whether they are published or not. The documents may come from teaching and research institutions in France or abroad, or from public or private research centers.

L'archive ouverte pluridisciplinaire **HAL**, est destinée au dépôt et à la diffusion de documents scientifiques de niveau recherche, publiés ou non, émanant des établissements d'enseignement et de recherche français ou étrangers, des laboratoires publics ou privés.

# UNIVERSITÉ DE PARIS

ECOLE DOCTORALE D'ASTRONOMIE ET D'ASTROPHYSIQUE D'ÎLE-DE-FRANCE ED127

## THÈSE DE DOCTORAT

préparée au département d'astrophysique du CEA-Saclay

présentée pour obtenir le grade de

docteur de l'Université de Paris

Spécialité : Astronomie et Astrophysique

par

**MAXIMILIEN FRANCO**

---

# Tracing back the cosmic history of galaxy formation with the large ALMA interferometer

---

Thèse dirigée par

DAVID ELBAZ

Présentée et soutenue publiquement le 19 septembre 2019 devant un jury composé de :

ISABELLE GRENIER	PROFESSEUR	UNIVERSITÉ DE PARIS	PRÉSIDENTE DU JURY
RAFFAELLA SCHNEIDER	PROFESSEUR	SAPIENZA UNIVERSITÀ DI ROMA	RAPPORTRICE
AMÉLIE SAINTONGE	PROFESSEUR ASSOCIÉE	UNIVERSITY COLLEGE LONDON	RAPPORTRICE
FRANÇOISE COMBES	PROFESSEUR	OBSERVATOIRE DE PARIS	EXAMINATRICE
DAVE ALEXANDER	PROFESSEUR	UNIVERSITY OF DURHAM	EXAMINATEUR
DAVID ELBAZ	DIRECTEUR DE RECHERCHE	UMR AIM - CEA PARIS SACLAY	DIRECTEUR DE THÈSE



Except where otherwise noted, this is work licensed under  
<https://creativecommons.org/licenses/by-nc-nd/3.0/fr/>





*“The woods are lovely dark and deep.  
But I have promises to keep,  
And miles to go before I sleep,  
And miles to go before I sleep.”*

*Robert Frost*



## Resumé

Comprendre l'évolution des galaxies avec le temps cosmique est l'un des enjeux clés de l'astrophysique. Plusieurs questions se posent lorsque nous observons les galaxies distantes dans l'univers lointain : les galaxies à décalage vers le rouge élevé sont-elles plus riches en gaz ou leur efficacité de formation d'étoiles est-elle plus importante ? Les galaxies à flambée d'étoiles à décalage vers le rouge élevé sont-elles les analogues des LIRG et ULIRG locales, c'est-à-dire des galaxies en interaction ? Les galaxies lointaines massives, compactes, à forte formation d'étoiles, sont-elles les ancêtres des galaxies elliptiques ? Quelle est la fraction de la formation des étoiles qui est masquée par la poussière à  $z > 2$  (c.-a-d. au-delà du midi cosmique de la formation stellaire) ? Quelle est la fraction de galaxies trop obscurcies pour être détectées par les relevés existants dans les domaines optiques et proche infrarouge ? La présence d'un noyau actif affecte-t-elle les propriétés physiques d'une galaxie ?

Le plus grand sondage cosmologique à 1.1mm réalisé avec l'interféromètre ALMA sur lequel j'ai travaillé lors de ma thèse de doctorat offre une occasion unique d'aborder ces questions. Cette observation a été réalisée dans une région du ciel, le champ GOODS-Sud, qui bénéficie des observations les plus profondes du télescope spatial *Hubble*, des observatoires infrarouges *Spitzer* et *Herschel*, ainsi que des données de l'observatoire X *Chandra* et l'interféromètre radio VLA. Ces observations à 1.1mm avec ALMA complètent donc ce panorama multi-longueurs d'onde, et font de cette région du ciel un laboratoire de premier plan pour l'étude de l'évolution des galaxies.

L'observation avec ALMA nous permet d'observer cette région du ciel sans être affecté par la limite de confusion qui affectait les observations du satellite *Herschel*, et de chercher des galaxies plus éloignées. Pour la première fois, nous pouvons étudier la formation d'étoiles obscurcie par la poussière à  $z > 2$  sur une surface assez grande pour réduire les différents biais d'observation.

Une grande partie de cette thèse a été consacrée à l'exploitation scientifique de cette image cosmologique à 1.1 mm. Pour ce faire, nous avons analysé les données interférométriques, caractérisé précisément le sondage, défini des seuils de détectabilité et des indicateurs permettant de quantifier la crédibilité des détections, et effectué des simulations. Nous avons ensuite extrait et identifié les galaxies présentes sur l'image. Cette analyse montre que les relevés ALMA peuvent révéler de nouvelles galaxies qui ne sont pas détectées par les relevés les plus profonds effectués avec le télescope spatial *Hubble*. Ces galaxies "sombres" comptent parmi les galaxies les plus massives et les plus distantes de cette région du ciel. La découverte de ces nouvelles galaxies sombres, qui représentent de l'ordre de 10 à 20% des détections ALMA, suggère que le nombre de galaxies massives formant des étoiles dans l'univers lointain pourrait être beaucoup plus important que prévu. Ces travaux ont également permis de déterminer les propriétés des galaxies détectées par ALMA, à travers la modélisation de leurs distributions d'énergie spectrale : le taux de formation d'étoiles, les masses de gaz et de poussières, la température des poussières, le temps nécessaire à une galaxie pour consommer son gaz, la relation entre la luminosité infrarouge et la luminosité radio, l'excès de la composante infrarouge dans le spectre d'une galaxie. L'analyse de ces résultats suggère que les galaxies massives à fort décalage vers le rouge épuisent leur gaz par la formation d'étoiles.

De plus, la caractérisation précise de ce grand relevé ALMA a permis d'estimer le nombre de galaxies dans le ciel par unité de surface et de densité de flux. Cette étude montre également que les galaxies détectées avec ALMA hébergent une fraction beaucoup plus élevée de noyaux actifs que les galaxies massives équivalentes à des décalages vers le rouge similaires. Cependant,

l'origine de cette propriété reste à déterminer. Il n'est notamment pas possible de dire à ce stade s'il existe une relation de causalité ou si la formation d'étoiles poussiéreuse et l'activité des noyaux actifs sont toutes deux activées par la même cause, par exemple une fusion galactique.

Enfin, nous avons mesuré la taille de ces galaxies détectées par ALMA à 1.1 mm, en utilisant plusieurs méthodes. Bien qu'elles aient des dimensions dans le proche infrarouge comparables à celles de la majorité des galaxies ayant les mêmes masses et les mêmes décalages vers le rouge, leur zone d'émission de poussière, c'est-à-dire la région traçant la partie obscure de la formation des étoiles, est relativement compacte et a une taille comparable aux galaxies passives à  $z \sim 2$ . De plus, un nombre significatif de ces galaxies ont une faible fraction de gaz, tout en maintenant un taux élevé de formation d'étoiles. Cela signifie que si elles continuent à former des étoiles à ce rythme sans réapprovisionnement en gaz, elles épuiseront leurs réservoirs de gaz sur des échelles de temps cosmiques relativement courtes ( $\sim 100$  Myr). Tous ces différents indicateurs conduisent à penser que ces galaxies sont les ancêtres idéales des galaxies passives à  $z \sim 2$ .

## Abstract

Understanding the evolution of galaxies with cosmic time is one of the key issues in astrophysics. Several questions arise when we look deep into the Universe, at the high redshift galaxies: are high redshift galaxies richer in gas or is star formation efficiency more important at high redshift? Are starburst galaxies at high redshift the analogues of local LIRGs and ULIRGs, i.e. interacting galaxies? Are distant massive, compact, highly star-forming galaxies the progenitors of elliptical galaxies? What is the fraction of star formation at  $z > 2$  that is dust-obscured (i.e., beyond the cosmic noon of star formation)? What is the fraction of galaxies too obscured to be detected by existing optical and near-infrared surveys? Does the presence of an active nucleus affect the physical properties of a galaxy?

The largest cosmological survey with the large ALMA interferometer at 1.1mm that I have worked on during my PhD thesis offers a unique opportunity to tackle these questions. This observation was performed in a region of the sky, the GOODS-South field, which benefits from the deepest observations of the Hubble Space Telescope, the *Spitzer* and *Herschel* infrared space observatories, as well as data from the *Chandra* X-ray telescope and the VLA Radio Interferometer. These observations at 1.1mm with ALMA therefore complete this multi-wavelength panorama, and make this region of the sky a leading laboratory for the study of the evolution of galaxies. The observation with ALMA allows us to observe this region of the sky without being affected by the confusion limit that affected *Herschel*, and to search for more distant galaxies. For the first time, we can study dust-obscured star formation at  $z > 2$  over a large enough area to reduce different observational biases.

A large part of this thesis was devoted to the scientific exploitation of this 1.1mm cosmological image. This was done by analysing the image from the interferometric data, precisely characterising the survey, defining detectability thresholds and indicators that can quantify the credibility of detections, and carrying out simulations on these images. We then extracted and identified the galaxies present in the image.

This analysis shows that ALMA surveys can reveal new galaxies that are not detected by the deepest surveys conducted with the Hubble Space Telescope. These “dark” galaxies are among the most massive and distant galaxies in this region of the sky. The discovery of these new dark galaxies, which represent of the order of 10 – 20% of the ALMA detections, suggests that the number of massive star-forming galaxies in the distant universe may be much larger than previously expected.

This work has also made it possible to determine properties of the galaxies detected by ALMA, through the modelling of their spectral energy distributions: the star formation rate, the masses of gas and dust, the dust temperature, the time required for a galaxy to consume its gas, the relationship between the infrared luminosity and the radio luminosity, and the excess of the infrared component in the spectrum of a galaxy. Analysis of these findings suggests that massive galaxies at high redshift consume their gas in a secular fashion to form stars.

Additionally, the precise characterization of this large ALMA survey has led to the number counts, i.e., the estimation of the number of galaxies in the sky per unit area and flux density. This study also shows that galaxies detected with ALMA host a much higher fraction of active nuclei (AGN) than equivalently massive galaxies at similar redshifts. However the origin of this property remains to be investigated. It is, in particular, not possible to say at this stage whether there is

a causality relation or whether both dusty star-formation and AGN activity are activated by the same cause, such as a galaxy merger.

Finally, we have measured the size of these ALMA-detected galaxies at 1.1mm, using several methods. Although they have near-infrared sizes comparable to the majority of the galaxies with the same masses and redshifts, their dust emission area, i.e., the region tracing the obscured part of the star formation, is relatively compact and has a size comparable to passive galaxies at  $z \sim 2$ . In addition, a significant number of these galaxies have a low gas fraction, whilst maintaining a high star formation rate. This means that if they continue to form stars at this rate without gas replenishment, they will exhaust their gas reservoirs on relatively short cosmic time scales ( $\sim 100$  Myrs). All of these different pieces of evidence indicate that these galaxies are the ideal progenitors of passive galaxies at  $z \sim 2$ .

## Remerciements

Je souhaiterais tout d'abord remercier David qui m'a accompagné et soutenu pendant ces trois années de thèse. Merci de m'avoir fait confiance en me confiant ces projets et de m'avoir fait progresser en étant à la fois conciliant et exigeant. Merci pour les décisions importantes que tu m'as aidé à prendre. Je reste impressionné par tes intuitions, ta capacité à repérer facilement les erreurs dans mes raisonnements et dans mes codes, ton envie de partager tes connaissances, et de trouver le bon angle pour les présenter. Merci pour tes conseils et toutes ces discussions qu'on a eues ensemble pendant cette thèse. Je n'aurais sûrement pas pu mieux tomber.

Merci au CEA et à l'IRFU pour leur accueil, pour leur réactivité et pour m'avoir donné tous les outils nécessaires à un travail dans un environnement optimal.

Je remercie ceux qui m'ont fait choisir cette voie, Julie, Aldo et Patrice avec qui j'ai mis pour la première fois un œil derrière un télescope et qui m'ont initié à l'astronomie; Nicolas, Eric et l'association française d'astronomie, avec qui j'ai pu pratiquer pendant quelques années avant de me décider à sauter le pas, recommencer un nouveau cursus et m'engager dans un parcours difficile mais passionnant.

Merci Emeric, Emanuele et Anaëlle qui n'ont jamais hésité à me donner de leur temps lorsque j'en avais besoin et qui m'ont prodigué de nombreux conseils pour aborder des problématiques sous un angle original.

J'ai été très touché par les rapports de mes deux rapportrices, Amélie Saintonge et Raffaella Schneider. Merci d'avoir pris le temps de lire attentivement cette thèse et de m'avoir fait des retours aussi précieux. Merci aux membres du jury, à la présidente, Isabelle Grenier ainsi qu'à Françoise Combes et Dave Alexander d'avoir fait le déplacement et de m'avoir écouté avec une oreille aussi critique que bienveillante.

Un grand merci à Mark Dickinson et Adriano Fontana de m'avoir écrit une quantité astronomique de lettres de recommandation. Je leur en suis infiniment reconnaissant. J'ai particulièrement apprécié toutes les discussions que l'on a pu avoir ensemble et tous les commentaires que vous m'avez envoyés sur les projets de recherche, articles et les propositions de temps de télescope. Sans vous et sans David, je n'aurais sûrement pas pu trouver mon post-doc.

Merci à Kristen Coppin, qui elle aussi m'a fait confiance pour continuer à travailler sur les galaxies lointaines et qui va m'aider à développer mon domaine d'expertise.

Je remercie ceux avec qui j'ai partagé ces trois ans, ceux qui ont partagé mon bureau, Tao, Laure, Wenjia et Antonello que je regrette déjà pour leur gentillesse et le temps passé à discuter. Ceux qui ont partagé mon couloir et bien plus, Chiara, Anna, Baptiste, Solène, Boris, Ivan, Lorenzo, Carlos, Shuo-Wen, Anita, Francesco, Antoine, Raphaël, Maryam, Hamza, Jeremy, Bilal, et tout ceux avec qui j'ai partagé un café.

Merci Mélissa, la meilleure colocataire possible, pour avoir partagé tristesse et joie pendant ces années et sans qui je n'aurais sûrement pas fait cette thèse.

Merci Rose de m'avoir supporté, de m'avoir si souvent aidé dans mon travail, fait progresser en anglais et pour tout le temps que tu m'as donné lorsque j'en avais besoin.



Et pour finir, je remercie mes parents et mes sœurs de m'avoir encouragé dans ce projet, aidé, et à être resté jusqu'au bout de la présentation de thèse. Merci Héloïse pour la préparation du pot de thèse et de cette journée qui restera inoubliable, et merci Charlotte pour toutes les relectures et les corrections de dernière minute que tu as toujours faites en un temps record.

<b>Résumé en français</b>	<b>v</b>
<b>Abstract</b>	<b>vii</b>
<b>Remerciements</b>	<b>ix</b>
<b>Sommaire</b>	<b>xi</b>
<b>1 Introduction</b>	<b>1</b>
1.1 Global context . . . . .	1
1.2 Problematic . . . . .	4
1.3 On the origin of elliptical galaxies . . . . .	6
1.4 The hidden star-formation at high redshift . . . . .	16
1.5 Probing galaxy properties using a multiwavelength approach . . . . .	21
<b>2 Summary of the work done in this thesis</b>	<b>29</b>
<b>3 GOODS-ALMA</b>	<b>35</b>
3.1 Historical context . . . . .	35
3.2 CANDELS . . . . .	37
3.3 Multi-wavelength coverage . . . . .	37
3.4 Survey presentation . . . . .	43
3.5 Mosaic . . . . .	47
3.6 Noise map . . . . .	49
<b>4 Creation of the ALMA source catalog</b>	<b>57</b>
4.1 Source Detection . . . . .	57
4.2 Threshold determination . . . . .	58
4.3 Creation of the catalog . . . . .	60
4.4 Supplementary catalog . . . . .	63
4.5 Astrometric correction . . . . .	65
4.6 Identification of counterparts . . . . .	66
4.7 Mass and redshift . . . . .	74
4.8 AGN . . . . .	78
4.9 Conclusion . . . . .	79
<b>5 Number counts</b>	<b>81</b>
5.1 Motivation of the number counts . . . . .	81
5.2 The different forms of number counts . . . . .	82
5.3 Number counts in a static Euclidean universe . . . . .	83
5.4 (Sub)millimeter surveys over contiguous areas of the sky . . . . .	84
5.5 Bias estimation . . . . .	87
5.6 Comparison with other surveys . . . . .	96
5.7 Estimation of number counts . . . . .	96
5.8 Parametrizing number counts . . . . .	99
5.9 Comparison with models . . . . .	100
5.10 Contribution to the cosmic infrared background . . . . .	100

5.11 Conclusion . . . . .	101
<b>6 Using IRAC priors to probe fainter millimeter galaxies</b>	<b>103</b>
6.1 Introduction . . . . .	103
6.2 Data . . . . .	104
6.3 Astrometric correction of the HST image of GOODS-South . . . . .	105
6.4 ALMA Main and Supplementary catalogs . . . . .	107
6.5 Catalog . . . . .	115
6.6 Comparison of the properties of the ALMA galaxies from the Main and Supplementary catalogs . . . . .	120
6.7 Conclusion . . . . .	123
<b>7 HST-dark galaxies</b>	<b>129</b>
7.1 Outline of the problem . . . . .	129
7.2 History . . . . .	129
7.3 HST-dark galaxies in GOODS-ALMA . . . . .	131
7.4 Spitzer/IRAC a loyal ally for HST-dark galaxies identification . . . . .	141
7.5 The HST-dark galaxy as an overdensity tracer . . . . .	144
7.6 Implications of HST-dark galaxies in cosmic density of star-formation . . . . .	147
7.7 Conclusion . . . . .	148
<b>8 The slow downfall of star-formation in <math>z = 2-3</math> massive galaxies</b>	<b>151</b>
8.1 SED-fitting . . . . .	151
8.2 Derived parameters . . . . .	154
8.3 The slow downfall of star-formation in $z = 2-3$ massive galaxies . . . . .	164
8.4 Conclusions . . . . .	172
<b>9 Conclusion</b>	<b>177</b>
<b>10 Perspectives</b>	<b>181</b>
10.1 Lower resolution image . . . . .	181
10.2 Combined GOODS-South ALMA surveys . . . . .	183
10.3 Resolving the dust emission in a clumpy galaxy . . . . .	184
10.4 Complete census in mass . . . . .	188
10.5 Preparing the next generation of survey . . . . .	190
<b>Bibliography</b>	<b>192</b>
<b>11 List of publications</b>	<b>245</b>
11.1 First author publications . . . . .	245
11.2 Other publications . . . . .	245
11.3 Non-refereed publications . . . . .	246
<b>12 Proposals</b>	<b>247</b>
12.1 Approved proposals . . . . .	247
12.2 Pending proposals . . . . .	247
<b>13 Published paper</b>	<b>255</b>

## 1.1 Global context

### 1.1.1 An expanding universe

#### The Great Debate

It will soon be a century ago, on April 26, 1920, that what every astronomer knows as the Great Debate took place at the Smithsonian Museum of Natural History. At the beginning of the last century, a particularly hot subject agitated the world of astronomy: what was the real nature of nebulae. The term nebulae referred to any diffuse object of the sky. Many of these diffuse objects were known since antiquity, but it was the astronomer Charles Messier who, at the end of the 18th century, attempted to make an exhaustive list of them by drawing up a catalog of 110 objects. This great debate saw two astronomers confront each other: Harlow Shapley and Heber Curtis. While the latter thought that nebulae were extragalactic objects, that is, distant objects located beyond our galaxy, Shapley argued in favor of the Milky Way being the entire Universe, and put forward arguments suggesting that these nebulae were close objects located within our galaxy<sup>1</sup>.

No definite conclusion emerged from this great debate at the time, but it had the merit of focusing attention on this crucial issue, and inspiring generations of astronomers. These astronomers, a few years later, will accredit Curtis' thesis thanks to the observation of a category of standard candles, the Cepheids<sup>2</sup>. The characterization of the relationship between the period and luminosity (thus making Cepheids excellent tools for distance measurements) made by Henrietta Swan Leavitt in 1908 ([Leavitt and Pickering, 1912](#)), and then by Ejnar Hertzsprung ([Hertzsprung, 1913](#)), [Shapley \(1914\)](#), and [Hubble \(1925\)](#), demonstrated that the distance to the Cepheids inside the Andromeda nebula was incompatible with the dimensions of our Milky Way.

This opening of the boundaries of the Universe, from our galaxy to a Universe with billions of galaxies moving relative to each other, is undoubtedly one of the greatest paradigm shifts that the Universe has ever known, similar to the passage from a geocentric world in which we occupy the predominant place, to a heliocentric world in which the sun has the place of choice. The subtlety of a Universe that is not centered on us is that it most likely does not have a center, or centers

1. Shapley relied on false observations of star motions within the Pinwheel Galaxy. If star rotations were visible inside this galaxy, it meant that the galaxy was nearby.

2. The name Cepheid comes from one of the very first measures of the period of this type of variable star in the constellation of Cepheus in 1785, by an English amateur astronomer, John Goodricke ([Goodricke and Englefield, 1785](#)).

everywhere, as Blaise Pascal famously summarizes it: the universe “is a sphere whose center is everywhere, the circumference is nowhere”<sup>3</sup> (*Les Pensées* (1670), II, 72 by Blaise Pascal).

### The first pieces of evidence

In 1913, with the Brashear spectrograph on the 24-inch refractor telescope at the Lowell Observatory in Flagstaff, Arizona (Thompson, 2011), Vesto Slipher brought the first observational evidence of a universe whose limit exceeds that of our Milky Way, and also that the Universe seemed to be expanding. After measuring the radial velocity of Andromeda’s (M31) cloud cover in 1913 (Slipher, 1913), Vesto Slipher expanded his sample to 15 nebulae in 1915 (Slipher, 1915), and then to 25 two years later (Slipher, 1917). Of these 25 clouds, 21 have positive radial velocities - that is, they move away from us. If the velocity distributions of the nebulae were randomly distributed, if they were equally likely to move away from or towards the Earth, the probability of finding such an imbalance in the results is less than 1 in 2000<sup>4</sup>. The average velocity of the 21 nebulae moving away from us<sup>5</sup> is 640 km.s<sup>-1</sup>, which is much faster than the speed of the stars inside the Milky Way.

### The confirmation

Georges Lemaître, priest and professor of physics at the Catholic University of Louvain understood the importance of these measurements, using Vesto Slipher’s observations. In 1927, he wrote a paper “A homogeneous Universe of constant mass and increasing radius accounting for the radial velocity of extragalactic nebulae” (Lemaître, 1927) in which he explains: “Using 42 nebulae from the Hubble and Strömberg lists [lists that used Vesto Slipher’s radial velocity measurements, Stromberg 1925, N.D.A.], and taking into account the proper speed of the sun [...], we find an average distance of 0.95 million parsecs and a radial velocity of 600Km./sec, or 625Km./sec at 10<sup>6</sup> parsecs. We will therefore adopt”:

$$R'/R = v/rc \quad (1.1)$$

Lemaître, therefore, states a law of proportionality between the speed of galaxies and their distance from the observer, and proposes a constant value of the proportionality. This is what every astronomy student knows as Hubble’s Law. However, this predates the publication of Edwin Hubble’s famous paper by two years. Unfortunately, as it is written in French in *Les Annales de la Société Scientifique de Bruxelles*, which did not have an international reputation, this paper did not have the impact it should have had. It was translated in 1931 Lemaître (1931a), but Eq. 1.1 (Eq. 24 in Lemaître’s original paper) does not appear in the translation. Many theories have circulated about this mysterious disappearance (e.g., van den Bergh, 2011) but the mystery seems to have been solved by the discovery of an original letter addressed to the publisher Livio (2011) in which Georges Lemaître explains his choice not to reproduce his equation: “I did not find advisable to reprint the provisional discussion of radial velocities which is clearly of no actual interest”. Lemaître’s paper, unlike Hubble’s, does not simply give a relationship between the speed of distance of galaxies and their distance, he explains this phenomenon by the expansion of the Universe (Lemaître, 1931a) and evokes the beginning of the universe (Lemaître, 1931b)

3. The origin of this quotation is regularly debated. This sentence exists in a similar form in the pen Nicholas of Cusa or Giordano Bruno.

4.  $\Pr\{X \geq 21\} = 1 - \sum_{k=0}^{21} C_{25}^k p^k \times 0.5^{(25-k)} = 0.0005$  with  $C_{25}^k$  the coefficient of the pair.

5. The four nebulae with negative radial velocities (M31, M32, M33, and M8) are nebulae of the local group (Baade, 1935). They are linked together by the force of gravity that dominates in relation to the expansion of the Universe.

by its theory of the primitive atom, the real anchor of the big bang. This law is now known as the "Hubble-Lemaître law". This decision was taken after a recommendation dated August 30, 2018, during the 30th meeting of the International Astronomical Union<sup>6</sup>, which was then decided on October 29, 2018. It can be expressed as explained in the following.

As shown in Fig. 1.1 of Hubble's original article (Hubble, 1929)<sup>7</sup>, if  $v_r$  is the recession rate of distant nebulae and  $d$  their distance from us, there is a linear relationship between  $v_r$  and  $d$ :

$$v_r = H_0 \times d \quad (1.2)$$

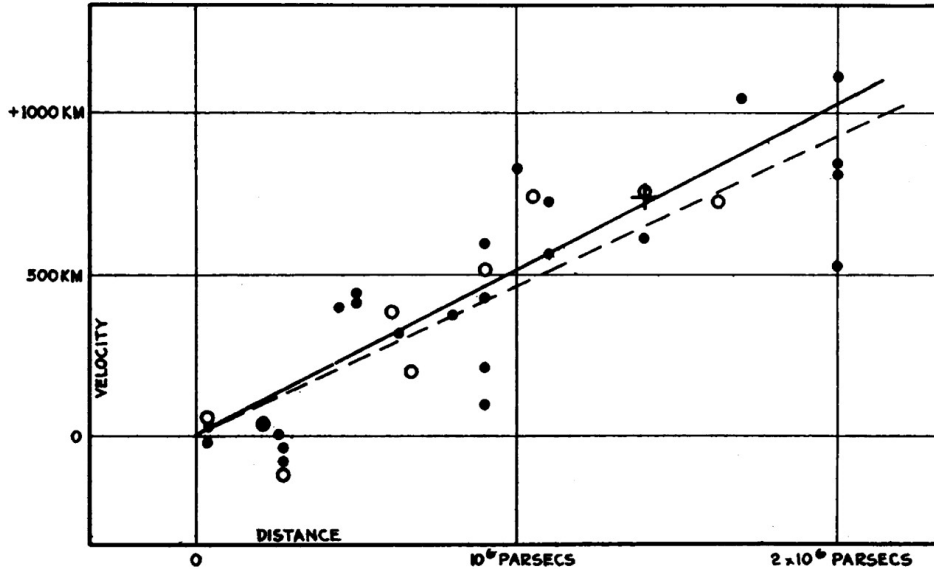


FIGURE 1.1: "Radial velocities, corrected for solar motion, are plotted against distances estimated from involved stars and mean luminosities of nebulae in a cluster. The black discs and full line represent the solution for solar motion using the nebulae individually; the circles and broken line represent the solution combining the nebulae into groups; the cross represents the mean velocity corresponding to the mean distance of 22 nebulae whose distances could not be estimated individually". Figure and citation from Hubble (1929).

However, this Hubble-Lemaître law cannot be applied to all distances. If  $z \ll 1$ :

$$z \simeq \frac{v_r}{c} \quad (1.3)$$

$$v_r \simeq cz \simeq H_0 \times d. \quad (1.4)$$

For galaxies with high redshifts ( $z > 1$ ), this law is no longer valid, and the distance of the galaxies follows the equations of general relativity.

### 1.1.2 The Relativist Revolution

The real revolutions concerning our vision of the Universe took place in 1905 (Einstein, 1905) and 1915 (Einstein, 1915), with the publication of Albert Einstein's two famous papers presenting the theories of special and general relativity, respectively. These theories lay the foundations

6. <https://www.iau.org/static/archives/announcements/pdf/ann18029e.pdf>

7. We would like to point out that in this article, Edwin Hubble uses the determination of galaxy velocities performed by V. Slipher without ever mentioning it.

of modern astrophysics. General relativity is based on the cosmological principle, discussed below.

### Cosmological principle

There are two parts to the cosmological principle:

- Generalized Copernican principle (we do not occupy a particular place in space)
- Isotropy and homogeneity (the general appearance of the Universe does not depend on the position of the observer)

Several pieces of observational proof statistically validate this cosmological principle. One of the most convincing proofs is the prediction in 1948 of the Cosmic Microwave Background (CMB)<sup>8</sup> by Ralph Alpher and Robert Herman (Alpher and Herman, 1948a,b) then its discovery<sup>9</sup> sixteen years later, in 1964 by A. Penzias and Wilson (Penzias and Wilson, 1965) with the 20-foot horn-reflector antenna (Crawford et al., 1961) at the Crawford Hill Laboratory, Holmdel, New Jersey. The discovery of the CMB not only supports the hypothesis of an expanding universe, and by extension the Big-Bang hypothesis, but also, through the observation of near-perfect isotropy, measured with great precision by Cosmic Background Explorer (COBE), the Wilkinson Microwave Anisotropy Probe (WMAP), and the Planck satellite. Another observation confirms the hypothesis of an isotropic and homogeneous universe - the distribution of radio sources. The number density and brightness of distant radio galaxies show that the Universe is globally isotropic<sup>10</sup>.

The vision of space and time is also transformed by linking these two entities into a single equation describing the structure of the space around us. The notion of distances is transformed, and paradoxes can appear. For example, the angular size of an object may, after a certain distance, increase (see Fig. 1.2). In addition, in this paradigm, by the distortion of space-time, the light from a distant galaxy could be bend around a massive object and magnify it, allowing us to see it as if it were under a lens.

## 1.2 Problematic

An essential question at the forefront of astronomy is to understand how galaxies assemble their baryonic mass into stars and supermassive black holes (SMBHs), and how this assembly depends on internal factors (e.g., gravitational instabilities, feedback from a supernova or AGNs) and external (dark matter halo, mergers) factors. Deep field surveys like GOODS have gathered exceptional multiwavelength data from X-ray through to radio wavelengths to allow astronomers to attack these questions in many ways. They provide thousands of galaxies with spectroscopic and photometric redshifts back to  $z = 8$  and beyond, stellar population properties and masses, galaxy structure from HST, star formation rates (SFRs) from UV and FIR data, and pinpoint AGN

8. It is challenging to give an exact date for the prediction of the Cosmic Microwave Background (CMB). Ralph Alpher and Robert Herman estimate a temperature of the CMB close to 5K. A few years earlier, Robert Dicke carried out work on the radiation of cosmic matter and predicted a temperature of  $\sim 20$ K.

9. To be more precise, the link between the observation of an excess of 3.5K isotropic, unpolarized emission, free from seasonal variations, and the theoretical explanation of the cosmological diffuse background was given by Dicke et al. (1965).

10. This statement actually depends on the scale. Some observations would tend to show that the distribution of radio sources is not homogeneous at large scales (e.g., Jackson, 2012).

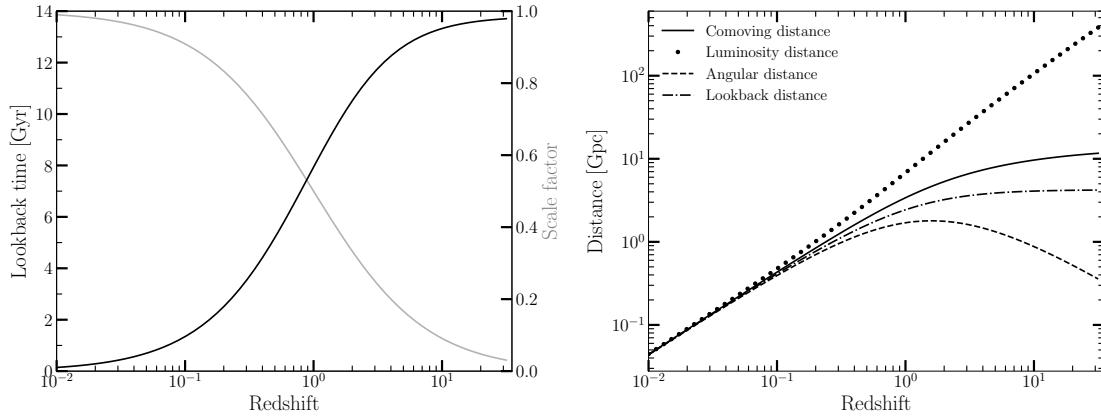


FIGURE 1.2: Left panel: Lookback time as a function of the redshift, black curve as well as the cosmic scale factor  $a(t)$ , gray curve. Right panel: different distances used in cosmology (comoving distance with the solid line, luminosity distance with the dotted line, angular distance with the dashed line, lookback distance with the dot-dashed line) as a function of the redshift.

accretion in different modes (i.e., radiative, obscured and unobscured) over a wide dynamic range of luminosity and Eddington ratio. A broad picture has emerged portraying the rise and fall of cosmic star formation and SMBH growth, and the organization of star formation into an evolving  $\text{SFR-M}_*$  "main sequence" for the majority of galaxies (e.g., [Schreiber et al., 2015](#), and references therein).

Several questions then arise: Are high redshift galaxies rich in gas, or is star formation efficiency more important at high redshift? Are starburst galaxies at high redshift analogues of LIRG or ULIRG galaxies, i.e., mainly interacting galaxies? Are massive, compact, highly star-forming galaxies the progenitors of elliptical galaxies at  $z = 2$ ? What is the rate of galaxy formation at  $z > 2$  (i.e., beyond the cosmic noon of star formation)? Which part of the formation of high redshift galaxies is too obscured to have been detected by the surveys that have been carried out so far? Does the presence of an AGN modify the physical properties of a galaxy?

To answer these questions, a large, contiguous region was observed with ALMA during the autumn of 2016 in one of the most observed region in the sky, the deep part of the GOODS-South field. This region benefits from some of the deepest observations of the Hubble Space Telescope and the Spitzer and Herschel infrared observation satellites, as well as X-ray data from the Chandra Telescope and the Very Large Array (VLA) radio interferometer. The observations at 1.1mm from ALMA, therefore, complete this multiwavelength panorama and make this region of the sky a leading laboratory for the study and evolution of galaxies. The observation with ALMA will allow us to observe this region of the sky without being affected by the confusion limit of *Herschel*, and to search for deeper regions of the sky. For the first time, with ALMA, we can observe the sky over a large enough surface to reduce cosmic variance and observe galaxy star formation at  $z > 2$ .

During the three years of this PhD., I have had the great opportunity to play a central role in the processing and data analysis of this largest ever ALMA survey. An overview of the history of the formation and evolution of massive, dusty, high redshift galaxies is beginning to emerge of the fog little by little thanks to these observations. It is this vision that I will explain in this thesis manuscript.



In the introduction, we will see that galaxies, whose extragalactic nature we have known for less than a century, can, thanks to the formalism of general relativity and to multiwavelength observations, tell us a part of the history of the Universe. We will also take the time to explain the origin of these questions and place this work in a more general context to identify and characterize precisely the issues we are trying to answer.

In the second chapter, we will present the framework of these observations, the GOODS-South field and the specificity of millimeter observations with a large interferometer. In the next chapter, we will explain how we constructed scientifically exploitable images from ALMA data, and how we were able to acquire a sufficiently precise knowledge of these images to detect galaxies and extract fluxes from them.

We will then explain, in the following chapter, that this flux-limited sample has allowed us, after many simulations and after the correction of several biases, to carry out counts, i.e., to know the number of sources per unit area at different fluxes that are present in our visible and accessible Universe.

We will then see that the search for these sources could be completed, using previous optical observations using HST data, and near-infrared using both the IRAC filters of the Spitzer space telescope and the Magellan telescope, in order to have the most unbiased galaxy sample possible. We present a method, which can be used for other blind surveys, to detect galaxies above the threshold imposed by a purity criterion.

In the following chapter, we will show that this blind survey has allowed us to detect galaxies that had previously been missed by HST observations. These galaxies, optically dark, represent about 20% of our blind detections. These galaxies are interesting because they are particularly dusty, massive, and distant. Taking these galaxies into account could change our vision of star formation in massive high redshift galaxies and change our understanding of the star formation density in the first billions of years after the Big Bang. We will also see that these optically dark galaxies could turn out to be excellent tracers of overdensities at high redshift.

The galaxies detected in this work will be analyzed using a multiwavelength approach. We will see that these massive and compact galaxies, with high star formation rates and gas deficiencies, are the ideal progenitors of compact elliptical galaxies at  $z > 2$ . This population of progenitors of distant elliptical galaxies is still poorly constrained, and escapes most of the current observations made with the Hubble Space Telescope.

## 1.3 On the origin of elliptical galaxies

### 1.3.1 Galaxy classification

#### Before the Hubble tuning fork

Historically, the first work on the classification of galaxies according to their morphologies was done by Max Wolf in 1908 (Wolf, 1908). This classification was only made possible by advances in astrophotography techniques that have been developed a few years earlier. Indeed, to the naked eye, it is impossible to identify the smallest detail of a galaxy. Less than 50 years after the first astrophotography (daguerreotype of the Moon taken on March 23, 1840, by John William

Draper from the roof of New York University), Isaac Roberts made for the first time, in 1887, using a 20 inch aperture reflecting telescope, a photograph<sup>11</sup> with high enough quality to be able to distinguish the spiral arms of the nearest spiral galaxy to ours, the Andromeda galaxy. This work was published 6 years later in *A Selection of Photographs of Stars, Star-clusters and Nebulae* (Roberts, 1893). Wolf (1908) was the first study to differentiate, in a linear sequence, galaxies that do not have structures (type d to k), spirals (types r to w).

### The Hubble tuning fork

In *Extragalactic nebulae*, based on 400 extragalactic nebulae for which Holetschek determined the magnitudes (Hubble, 1926), Edwin Hubble proposes a classification of galaxies according to their morphology in a diagram that is now known as the Hubble tuning fork, or the Hubble sequence.

”The classification of these nebulae is based on structure, the individual members of a class differing only in apparent size and luminosity” (Hubble, 1926).

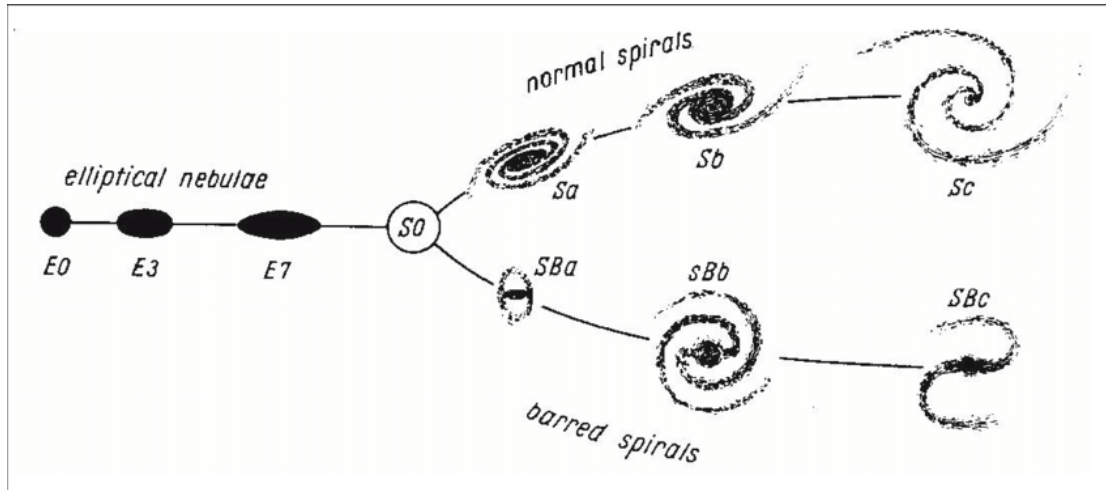


FIGURE 1.3: Classification of galaxies made by Edwin Hubble commonly known as the Hubble tuning fork. From: (Hubble, 1936b).

This classification was illustrated 10 years later with the famous Hubble tuning fork diagram (see Fig. 1.3) in *The Realm of the nebulae* (Hubble, 1936b). This diagram is divided into two parts: elliptical and spiral galaxies. On the left side of Fig. 1.3, we can see the elliptical galaxies without defined structures. Within these elliptical galaxies, stars are dominated by random motions. These elliptical galaxies are classified from E0 to E7. The number characterizes the degree of ellipticity of the galaxy, where the higher this number is, the more elliptical the galaxy is, and the smaller this number is, the more spherical the galaxy is. The ellipticity of a galaxy can be defined by:

$$e = 1 - \frac{a}{b} \quad (1.5)$$

where  $a$  and  $b$  are the length of the galaxy's major and minor axis respectively.

The number next to the E corresponds to the number of the decimal of Eq. 1.5. The E0 galaxies

11. It is not really a photograph as we understand it, it was made using a "stellar pantograver" (Roberts, 1888) which engraves the image of a glass plate directly onto copper plate (James, 1993).

will therefore be spherical, while the E7 labeled galaxies will be very elongated. No galaxy with an ellipticity greater than 0.7 has been found by Edwin Hubble. *"The structural transition is so smooth and continuous that the selection of division points for further classification is rather arbitrary."* (Hubble, 1926)

On the right side of the Hubble tuning fork are the spiral galaxies. Spiral galaxies are themselves subdivided into two parts, "normal" spiral galaxies (from Sa to Sc) and barred spiral galaxies (from SBa to SBc). The lowercase letters correspond to the compactness of the galaxies. The most compact spiral galaxies are designated with the letter *a* while the more aerial, larger galaxies inherit the letter *c*.

The "node" of this tuning fork is composed of a rather particular family of nebulae, the lenticular galaxies (S0). These galaxies make the connection between elliptical and spiral galaxies.

In addition to elliptical and spiral nebulae, Hubble introduces the notion of irregular galaxies. There are two types of irregular galaxies (Irr I and Irr II). The purpose of this classification was to be complete, so that each galaxy could fall into a category. Although the Hubble tuning fork classification is still used today, many attempts at improvement or substitution have been proposed (e.g., de Vaucouleurs, 1959; Sandage, 1961, 1975; Sandage and Tammann, 1981).

Although the division between elliptical and spiral galaxies is still in effect today, the interpretation of the tuning fork has evolved. Hubble thought that galaxies evolved from left to right in his diagram. He thought that young galaxies were elliptical (early-type galaxies) and gradually evolve towards more complexity by forming spiral arms (late-type galaxies). These temporal terms between the "early", "middle" and "late" were central to Edwin Hubble's vision of the evolution of nebulae. Subsequent observations, notably Toomre and Toomre (1972) and the future of infrared astronomy, seem to contradict this initial interpretation. Spiral galaxies seem to be young, intermediate-mass galaxies, rich in gas and forming stars. Elliptical galaxies seem more compact, more massive and almost without gas. One of the possible origins of elliptical galaxies could be the merging of two spiral galaxies. This merging could be followed by an intense episode of star formation (a starburst) and then a transformation of their morphology. The morphology of a galaxy could, therefore, be an indicator of the environment of a galaxy. The more galaxies evolving in a dense environment, the more likely it is that galaxies will merge and that a galaxy will become elliptical. This also explains why elliptical galaxies are more often in dense environments.

This transformation in the morphology of a galaxy, as well as the timescale and mechanisms causing the transformation of a spiral to an elliptical galaxy, are still poorly known phenomena, and observations of a large region of the sky with ALMA could give crucial information to understand the death of a galaxy, and understand how a galaxy forming stars in a secular way stops (or at least significantly reduces) its star formation rate (SFR).

### 1.3.2 The quest for progenitors of elliptical galaxies at high redshift

The primary progenitors of passive compact galaxies at  $z \sim 2$  are largely unknown (e.g., Williams et al., 2014; Straatman et al., 2015; Wang et al., 2019). Current observations are ineffective in finding this galaxy population, which is paradoxically very massive. As the most massive galaxies are also the dustiest (see Chapter 7), UV observations are not efficient to detect them (see Sect. 1.4). Only (sub)millimeter observations have the capacity to constrain this galaxy population.

The mechanisms causing the drop in star formation in galaxies are largely unknown. This is one of the main questions in the study of galaxy evolution: why and how do galaxies stop forming stars?

The study of distant and massive galaxies is crucial to understand our models of galaxy formation and evolution, as they are the ideal candidate progenitors of compact quiescent galaxies at  $z \sim 2$  (Barro et al. 2013; Williams et al. 2014; van der Wel et al. 2014; Kocevski et al. 2017, see also Elbaz et al. 2018). Massive star-forming galaxies at  $z > 2$  are rare; to be able to detect them, it is essential to cover the largest possible area of the sky. It is for this region that it was decided to carry out the largest survey with ALMA to discover very massive galaxies forming large quantities of stars. These galaxies cannot continue to form stars for long periods. If this was the case, they would become much more massive than the most massive galaxies we have observed at  $z = 1$ , or in the local universe.

Unlike many studies that have been carried out with ALMA in recent years, the galaxies we will study in this thesis have not been selected as compact galaxies in the  $H$ -band. They are flux-selected at 1.1mm. Due to the low dispersion of the main sequence (MS; e.g., Noeske et al., 2007; Elbaz et al., 2007; Daddi et al., 2007; Pannella et al., 2009; Schreiber et al., 2015), this selection is equivalent to a mass selection. We will see how these galaxies detected by ALMA, not selected for their compact size in  $H$ -band, can give us indications on the end-of-life scenarios of a galaxy at  $z > 2$ . Before getting to the heart of the matter, we will introduce, in the next paragraph, the notion of bimodality of galaxies, to reveal the life and death scenarios of galaxies.

### 1.3.3 The galaxy bimodality

In the same way that it is possible to differentiate galaxies through their morphology (which can be seen as a proxy for the angular momentum of the galaxy), it is also possible to differentiate galaxies according to their stellar populations. Massive stars, with a short lifetime ( $< 100$  Myr) and are therefore tracers of star formation, will typically have a blue color, while low mass, long lifetime stars ( $> 10$  Gyr) will have a red color. This color distinction therefore makes it possible to differentiate star-forming galaxies from galaxies that are no longer forming stars (passive galaxies)<sup>12</sup>.

When galaxies are placed on a color-magnitude diagram (or a color-stellar mass diagram), we note that they can be separated into two distinct populations, a blue cloud and a red sequence (e.g., Visvanathan and Sandage, 1977; Visvanathan, 1981; Strateva et al., 2001; Baldry et al., 2004; Dekel and Birnboim, 2006; Schawinski et al., 2014). This transition between the two galaxy populations is visible in Fig. 1.4. The vast majority of star-forming spiral galaxies are located in the blue cloud, while passive elliptical galaxies are located on the red sequence. This boundary is not always strict, recent studies have shown that elliptical galaxies can be on the blue side (e.g., Yi et al., 2005; Kannappan et al., 2009; Schawinski et al., 2009) or spiral galaxies on the red side (van den Bergh, 1976; Masters et al., 2010). The low presence of gas is also not a sufficient criterion for the high reduction of star formation in elliptical galaxies (e.g., Gobat et al., 2018). These observations are not anecdotal; this shows that there are mechanisms that

12. It is not entirely accurate to say that galaxies no longer form stars, passive galaxies are defined as galaxies forming  $10\times$  fewer stars than galaxies of comparable mass and redshift Noeske et al. (2007).

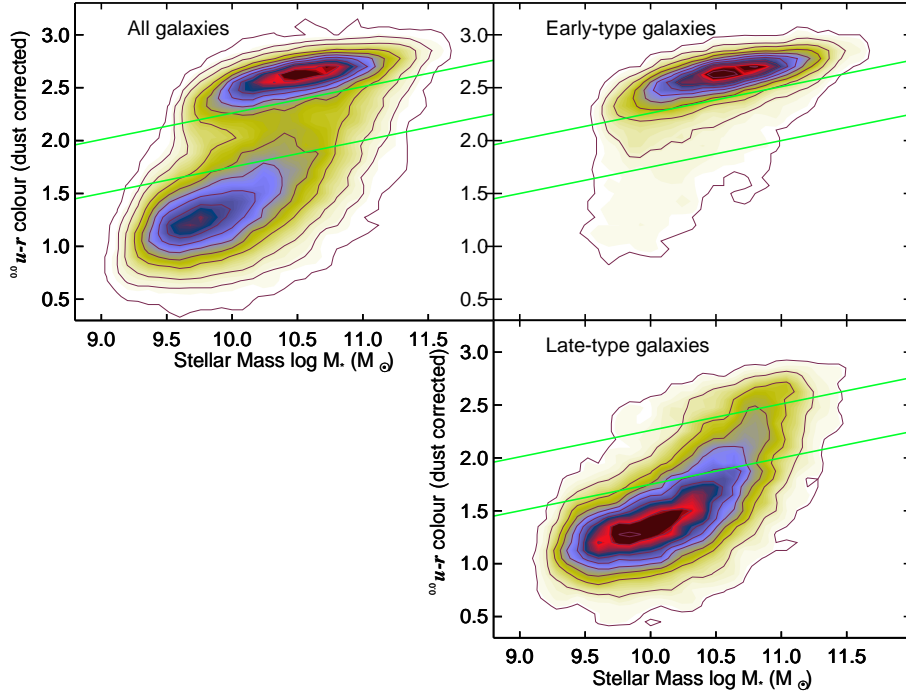


FIGURE 1.4:  $u-r$  color-mass diagram corrected for reddening using the Sloan Digital Sky Survey (SDSS; York et al. 2000; Abazajian et al. 2009), the Galaxy Evolution Explorer (GALEX; Martin et al. 2005) and the Galaxy Zoo project (Lintott et al. 2008, 2011). The two peaks of the galaxy distribution according to their colors and masses are visible on the top left panel. The division is made into Early-type galaxies (top right panel) and Late-type galaxies (bottom right panel). The scatter of the dispersion in Early-type galaxies is smaller than that of Late-type galaxies. This is why these two populations are called the red sequence and blue cloud respectively. Green lines show the green valley. Figure from Schawinski et al. (2014).

stop star formation that are not necessarily induced by (or dependent on) the morphological transformation of galaxies or the complete absence of cold gas.

To differentiate star-forming galaxies from passive galaxies in this thesis we will use a separation based on two colors, to break the age-dust degeneracy (e.g., Wuyts et al., 2007; Williams et al., 2009; Whitaker et al., 2011). We will use the rest-frame color criterion given by Williams et al. (2009) applied at all redshifts and stellar masses, as suggested by Schreiber et al. (2015):

$$\begin{aligned}
 U - V &< 1.3 \\
 V - J &> 1.6 \\
 U - V &< 0.88 \times (V - J) + 0.49
 \end{aligned} \tag{1.6}$$

The characteristic stellar mass that separates these two populations of galaxies  $M_* \simeq 3 \times 10^{10} M_\odot$  (Dekel and Birnboim, 2006). We will see in the rest of this thesis that this critical stellar mass also defines the lower mass limit of our detections and makes the galaxies studied in this thesis a unique laboratory to understand the transition mechanisms between active and passive

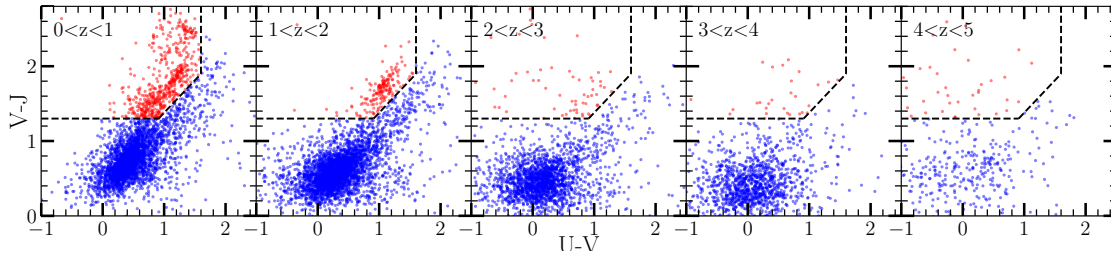


FIGURE 1.5: Rest-frame  $U-V$  vs.  $V-J$  with the boundaries presented in Eq. 1.6 for five redshift bins performed with ZFOURGE (Straatman et al., 2016) data. Star-forming galaxies are represented in blue while quiescent galaxies are represented in red.

galaxies. This sample will investigate the physical origin of the critical mass where the separation between passive and active galaxies occurs.

This bimodality can be expressed in different ways. We have seen the division in color and magnitude (or stellar mass, e.g., Baldry et al., 2004; Hogg et al., 2004; Blanton et al., 2005), but it can also be expressed in other ways, for example by looking at color in relation to the environment (e.g., Balogh et al., 2004; Kauffmann et al., 2004; Blanton et al., 2006), star formation rate in relation to the age of the stellar population (e.g., Kauffmann et al., 2003; Madgwick et al., 2003), the gas to-stellar mass ratio (e.g., Kannappan, 2004), the bulge-to disc ratio (e.g., Blanton et al., 2005), the luminosity/mass functions (e.g., Baldry et al., 2004; Bell et al., 2003), the excess of X-ray flux (e.g., Mathews and Brighenti, 2003; Osmond and Ponman, 2004), and the size as a function of stellar mass (e.g., van der Wel et al., 2014, see Dekel and Birnboim 2006; Cattaneo et al. 2006 for a review).

Passive galaxies constitute only a minority of the number of galaxies ( $\sim 30\%$  at  $z = 0$ ), but are dominant in mass, with stellar masses contributing  $\sim 70\%$  to the total mass of the galaxies (e.g., Hogg et al., 2002; Bell et al., 2003; Baldry et al., 2004). These passive galaxies have been detected at all redshifts up to  $z \sim 4$  (e.g., Glazebrook et al., 2004; Straatman et al., 2014; Spitler et al., 2014; Glazebrook et al., 2017; Schreiber et al., 2018b) which means that star formation may be faster and more efficient than most models predict.

This bimodality of galaxies raises several questions. One of them is the origin of such high masses in passive galaxies. There is a mass transition between active and passive galaxies (e.g., Dekel and Cox, 2006; Faber et al., 2007). One of the explanations given for this is a slow evolution of the mass of passive galaxies through a series of gas-poor, or "dry" mergers (Faber et al., 2007). Another origin that will be discussed in this manuscript is the rapid mass growth of massive galaxies at high redshift.

One of the questions underlying galaxy bimodality is also to know which scenarios trigger star formation in galaxies, and why at some point this star formation stops. In particular, we are interested in whether this cessation of star formation is due to internal mechanisms (supernova, AGN) or if the environment plays an important role (e.g., Dressler, 1980; Kauffmann et al., 2004; Balogh et al., 2004; Hogg et al., 2005). It is important to tracing back the star-formation in the galaxy to understand this bimodality.



### 1.3.4 Star formation in galaxies

Star forming galaxies follow a tight correlation (scatter of  $\sigma = 0.2\text{-}0.3$  dex, [Speagle et al. 2014](#), [Whitaker et al. 2015](#)) between their star formation rate and stellar mass. This so-called 'Main Sequence' ([Noeske et al. \(2007\)](#)) represents  $\sim 70\%$  of the total galaxy population. This main sequence, which extends over at least 4 orders of magnitudes in mass ([Santini et al., 2009](#)) was first characterized for local galaxies ( $z \approx 0$ ; [Brinchmann et al. 2004](#); [Salim et al. 2007](#)) then extended to more distant galaxies ( $z \approx 1$ ; [Noeske et al. \(2007\)](#); [Elbaz et al. \(2007\)](#),  $z = 2$  ([Pannella et al., 2009](#); [Rodighiero et al., 2011](#); [Whitaker et al., 2012](#)),  $z = 3$  ([Magdis et al., 2010](#); [Kurczynski et al., 2016](#)),  $z = 4$  ([Schreiber et al., 2015](#); [Pannella et al., 2015](#); [Tomczak et al., 2016](#)),  $z = 5$  ([Tasca et al., 2015](#)), and  $z = 6$  ([Salmon et al., 2015](#)).

This relationship evolves with redshift (see Fig. 1.6). While a galaxy with a stellar mass of  $10^{11} M_{\odot}$  located on the main sequence forms on average  $\sim 25 M_{\odot}$  per year at a redshift  $\sim 0.5$ , a galaxy of the same mass will produce on average 10 times more stars at  $z = 3$ . However, the scatter in the MS remains constant over both cosmic time and the stellar mass of the galaxies ([Tomczak et al., 2016](#)). This suggests that the main mode of growth in a galaxy is secular. On the other hand, the mechanism of slow and secular formation of galaxies involves a gas refill process. Indeed, if a galaxy only has its own gas reserves ( $M_{\text{gas,mol}}/M_{*} \sim 1$  for a galaxy of  $\sim 10^{11} M_{\odot}$  at  $z \sim 2$ ; [Tacconi et al. 2018](#)), this galaxy would exhaust these reserves in only  $\sim 650$  million years. If we observe this galaxy, and all those in this configuration, it would mean that we live in a privileged time, which would tend to violate the generalized Copernican principle. About 90% of star formation occurs on the main sequence in the universe, essentially in disk-like galaxies (e.g., [Wuyts et al., 2011](#); [Combes, 2016](#)), with only about 10% in starburst galaxies.

In the rest of this thesis, we will use the equation parameterized by [Schreiber et al. \(2015\)](#) to calculate the star formation rate of a galaxy on the main sequence:

$$\log_{10}(SFR_{ms}) = m - m_0 + a_0 r - a_1 [\max(0, m - m_1 - a_2 r)]^2 \quad (1.7)$$

where  $m_0 = 0.5 \pm 0.07$ ,  $a_0 = 1.5 \pm 0.15$ ,  $a_1 = 0.3 \pm 0.08$ ,  $m_1 = 0.36 \pm 0.3$  and  $a_2 = 2.5 \pm 0.6$  the  $SFR_{ms}$  is given in units of  $M_{\odot}\text{yr}^{-1}$  (see Fig. 1.6).

Recently, several studies have suggested that this relationship does not follow a power-law but seems to flatten for the most massive galaxies (e.g., [Whitaker et al., 2015](#); [Schreiber et al., 2015](#); [Lee et al., 2015](#); [Tomczak et al., 2016](#); [Popesso et al., 2019](#))<sup>13</sup>. This flattening could bring into question the fast transition between the star-forming galaxies and the quenched galaxy population, as strongly suggested by the apparent dichotomy with few galaxies between these two populations (in the green valley).

The star formation main sequence seems to be the consequence of a proportionality between star formation density ( $\Sigma_{SFR}$ ) and gas density ( $\Sigma_{gas}$ ). The beginnings of this proportionality were set out in [van den Bergh \(1957\)](#), before [Schmidt \(1959\)](#) made it explicit:

$$\Sigma_{SFR} \propto (\Sigma_{gas})^n \quad (1.8)$$

---

13. However, we note that some studies (e.g., [Speagle et al., 2014](#); [Rodighiero et al., 2014](#)) do not find this flattening

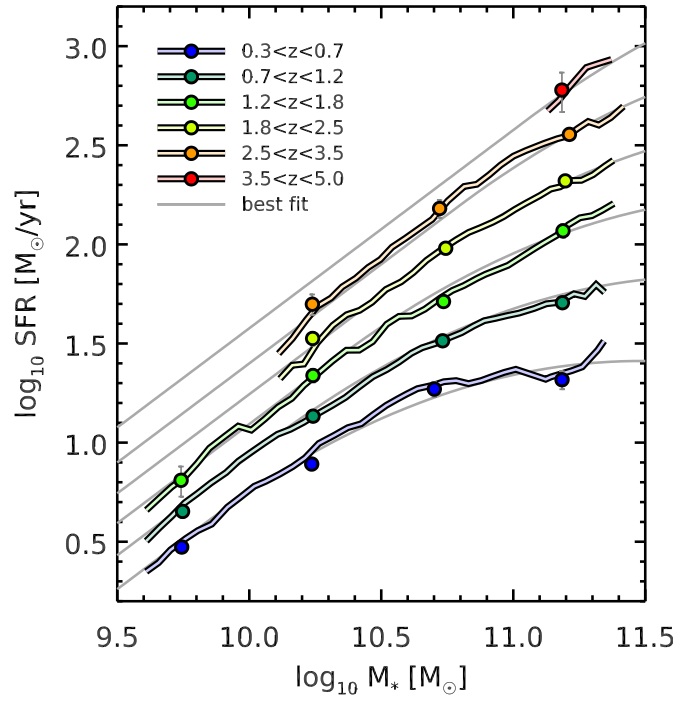


FIGURE 1.6: Evolution of the average SFR of star-forming galaxies as a function of stellar mass and redshift. The filled colored circles are the result of stacking analysis, while the gray curves show the best-fit relation for the main sequence. Figure from [Schreiber et al. \(2015\)](#).

This relationship was later refined through measurements of  $H_\alpha$ ,  $H_I$  and CO in a sample of normal spiral galaxies combined with starburst galaxies: [Kennicutt \(1998\)](#):

$$\Sigma_{SFR} = (2.5 \pm 0.7) \times 10^{-4} \left( \frac{\Sigma_{gas}}{1 M_\odot pc^{-2}} \right)^{1.4 \pm 0.15} M_\odot yr^{-1} kpc^{-2} \quad (1.9)$$

where the gas refers to the the sum of both the atomic and molecular gas content.

This law which is now known as Schmidt-Kennicutt law (SK; [Schmidt 1959](#); [Kennicutt 1983, 1998](#)), and tells us that the star formation is proportional to the density of the gas content (see Fig. 1.7). This law also tells us that the denser a region of a galaxy is in gas, the more intense the star formation is<sup>14</sup>. The SK law is not linear (see Fig. 1.7); it can be divided into three distinct regimes:

- $\Sigma_{gas} < 9 M_\odot pc^{-2}$  : The efficiency of gas in producing stars drops drastically (e.g., [Kennicutt, 1989](#); [Martin and Kennicutt, 2001](#); [Schaye, 2004](#); [Bigiel et al., 2008](#)). There is a threshold below which Schmidt-Kennicutt law no longer works.
- $15 < \Sigma_{gas} < 200 M_\odot pc^{-2}$ . Normal regime of SK law
- $\Sigma_{gas} > 200 M_\odot pc^{-2}$  : molecular surface density is higher.  $\Sigma_{SFR}$  is more important than for SK law. This regime corresponds to starburst galaxies and could reflect real changes in the ISM of these galaxies.

<sup>14</sup>. In this thesis, we will try to parameterize a relationship that similarly links the  $(\Sigma_{IR})$  to the star formation efficiency of a galaxy.



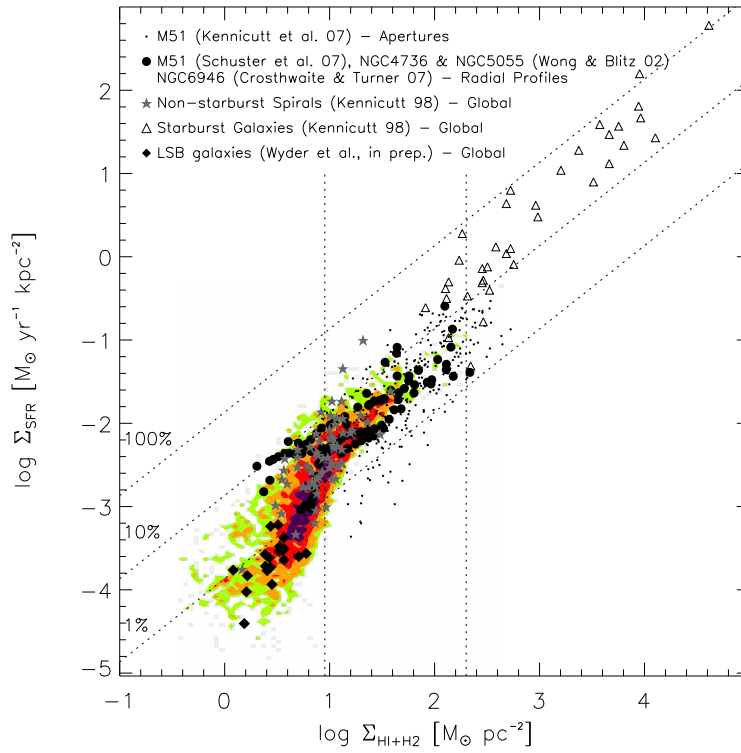


FIGURE 1.7: Illustration of the Schmidt-Kennicutt law by Bigiel et al. (2008) showing the evolution of the SFR density as a function of the total gas surface density. In addition, the three distinctly different regimes (indicated by the vertical lines) of the star-formation law are also shown. Figure from Bigiel et al. (2008).

### Starburst galaxies

In contrast to quenched galaxies, there is a galaxy population with much higher star formation rates than normal, for a galaxy of given stellar mass and redshift (see Fig. 1.7). Although there are several definitions for starburst galaxies, based on the SFR or the birth-rate parameter ( $b = \text{SFR}(t_{\text{now}})/\langle \text{SFR}(t) \rangle$ , Kennicutt 1983; Heckman et al. 1990), the definition we have adopted in this thesis is to consider that a galaxy is starburst if the SFR is 4 or higher than the main sequence (e.g., Rodighiero et al., 2011). This definition is not completely satisfactory. In the two-star-formation-mode (2SFM) formalism introduced by Sargent et al. (2012), see Fig. 1.8, star-forming galaxies can be separated, depending on their distance from the main sequence ( $\text{RSB} = \text{sSFR}/\langle \text{sSFR} \rangle_{\text{MS}}$ , where  $\text{sSFR} = \text{SFR}/M_*$  is the specific star formation rate, i.e., the SFR per unit stellar mass), into two galaxy populations that can be modelled by a double Gaussian. This would mean that there are a number of starburst galaxies belonging to the starburst Gaussian distribution but having an RSB close to 1. This population of starburst galaxies on the main sequence has been studied by Elbaz et al., (2018), who show that gas depletion time ( $t_{\text{dep}} = M_{\text{gas}}/\text{SFR}$ , i.e. the characteristic time a galaxy needs to empty its gas reserves by assuming a constant SFR and no replenishment of gas) is a key parameter for distinguishing these galaxies. We will see that we have also identified this type of galaxy population in this study.

Starburst galaxies represent only 2% of the stellar mass but 10% of the SFRD at  $z = 2$  and  $M_* > 10^{10} M_\odot$ . Rodighiero et al. (2011) showed that starburst galaxies were not just an extension of MS galaxies, but that there was a dichotomy between these two populations of galaxies.

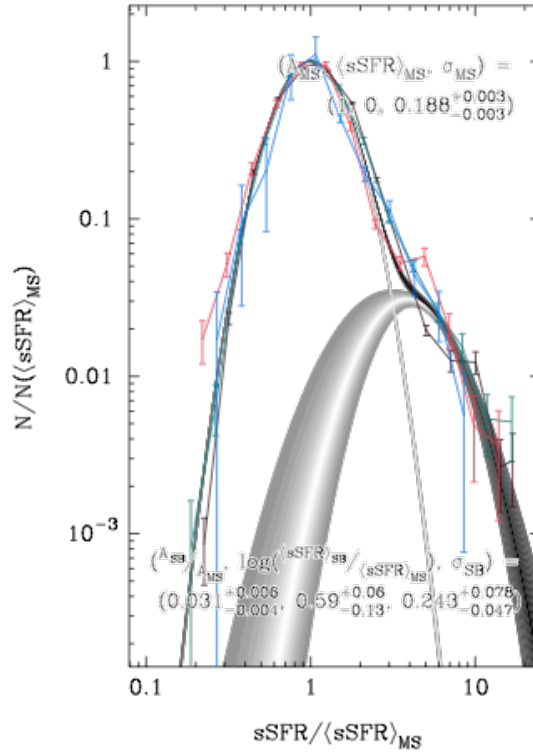


FIGURE 1.8: Double-Gaussian decomposition (main-sequence, MS, and starburst, SB, activity) of the sSFR distribution at fixed  $M_* > 10^{10} M_\odot$  for galaxies at  $z \sim 2$ . Figure from [Sargent et al. \(2012\)](#).

The spectra of the MS and SB galaxies also differ (e.g., [Kinney et al., 1996](#); [Lançon and Rocca-Volmerange, 1996](#)). The distribution of stars is not identical between these two galaxy populations - we can see an increase in the IR8 ratio ( $L_{IR}/L_8$ ), corresponding to the total infrared brightness over the brightness at  $8\mu\text{m}$  ([Elbaz et al., 2011](#)), in the starburst galaxies. In other words, it is the relationship between dust emission and PAH emission (see Sect. 1.4). PAHs are more easily destroyed than dust in photo-dissociation regions near stars. A PAH deficit means that starburst galaxies are more compact and could result from the merging of galaxies that is known to make galaxies more compact in the near universe. The dust temperature also follows two distinct trends for MS and SB galaxies (e.g., [Schreiber et al., 2018c](#); [Donevski et al., 2018](#); [Jin et al., 2019](#)), with higher dust temperatures in starburst galaxies.

Several questions arise from these observation. Do all galaxies experience a starburst phase in their existence? Is it a unique phenomenon in the history of the galaxy, or on the contrary, is it repeated periodically? What are the causes of these star formation outbreaks?

Many studies have attempted to link the post-starburst phase of galaxies with quenching (e.g., [Whitaker et al., 2012](#); [Yesuf et al., 2014](#); [Maltby et al., 2018](#)). There are similarities and continuities between the growth of the bulge due to a starburst phase and the quenching of galaxies ([Tran et al., 2004](#)), which leads to a change in morphology between disk-dominated and elliptical. This morphological change can be characterized by a change in the Sérsic index ([Sérsic, 1963](#), see Fig. 1.9), which is equal to 1 for disk galaxies, and at least 4 for elliptical galaxies. Galaxies in the starburst phase often have a Sérsic index between these values (e.g., [Goto, 2005](#); [Mendel et al., 2013](#)).

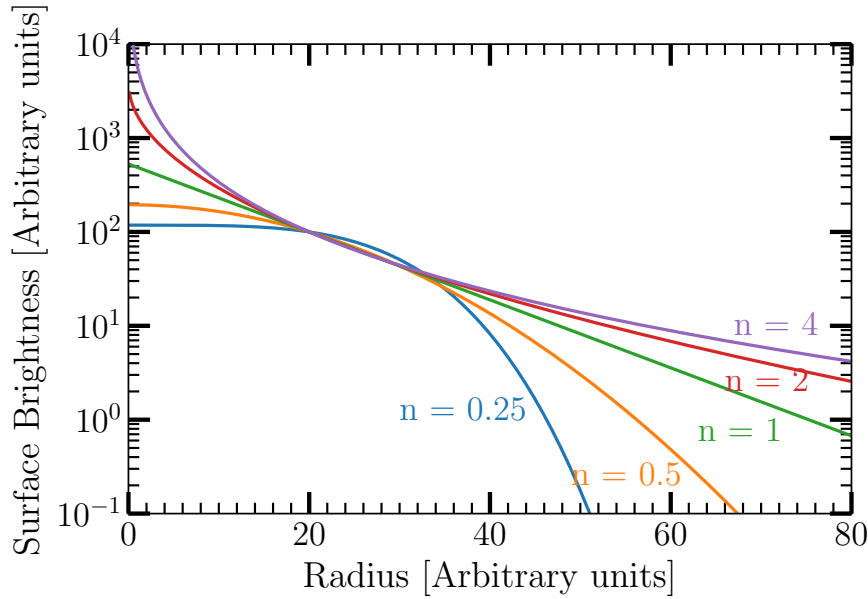


FIGURE 1.9: Evolution of the surface brightness as a function of the Sérsic index (from 0.25 to 4).  $n = 0.5$  corresponds to a Gaussian profile while  $n = 1$  and  $n = 4$  correspond to exponential and de Vaucouleurs profiles respectively. The surface brightness and the radius are given in arbitrary units.

In this thesis we will attempt to uncover which mechanisms may be at the origin of the increase in the surface brightness at the center of a galaxy, and we will study the hypothesis of a violent episode of compact star formation in the center of the galaxy, as the origin of the increase in the Sérsic index (Toft et al., 2014).

In addition, we will also focus on galaxy sizes as an indicator of quenching (van der Wel et al., 2014). Indeed, as we will show in Chapter 8, finding massive, star-forming galaxies with very compact star formation sizes may be a sign that they will soon become quenched. On average, the size of early-type galaxies evolves rapidly (e.g., Toft et al., 2007; van Dokkum et al., 2008; Newman et al., 2012; Cassata et al., 2013; Morishita et al., 2014; van der Wel et al., 2014). We will also discuss the different mechanisms that can drive the evolution of a galaxy, such as the negative feedback of an AGN, ram pressure, morphological quenching, and major mergers.

## 1.4 The hidden star-formation at high redshift

Over the last 8 billion years, the cosmic star formation density has decreased by a factor  $\sim 10$  (e.g., Madau and Dickinson, 2014). One of the major enigmas in astrophysics is to understand why the Universe reaches a peak around  $z = 2$  and why it is now so ineffective at generating stars.

The study of cosmic star formation is crucial to validate cosmological models. To be able to estimate the star formation rate density (SFRD), it is necessary to observe a large enough field of view, deep enough and with multiwavelength coverage to be able to derive both redshifts and star formation rates. Among the first estimates of the SFRD, we can cite the work of Lilly et al. (1996) who used the 4-m Canada-France-Hawaii Telescope, the Canada-France Redshift Survey

(CFRS), and Madau et al. (1996) who use the *Hubble* Ultra Deep Field. These two studies, which were carried out almost simultaneously, used galaxy UV emission to derive the star formation rate. Although the work of Lilly et al. (1996) focused mainly on galaxies with redshifts less than 1; one of the most striking results of this survey was to show that the star formation rate has declined drastically from  $z = 1$  until now (see Fig. 1.10).

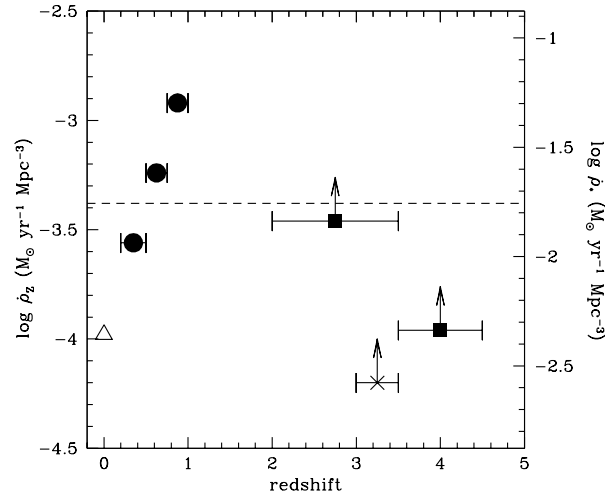


FIGURE 1.10: Cosmic star formation history of the Universe from UV observation in the Hubble Deep Field. The filled dots come from Lilly et al. (1996) while the diagonal crosses come from Steidel et al. (1996), and the squares from Madau et al. (1996). Figure from Madau et al. (1996).

Since then, several other surveys have explored the sky in order to build the star formation history (SFH) and trace the stellar mass build-up in galaxies to higher redshift (e.g., Steidel et al., 2003; Giavalisco et al., 2004; Bouwens et al., 2014). However, the evolution of star formation rate density is only currently constrained by infrared observations from the local Universe until the cosmic peak around  $z \sim 2$  (see Fig. 1.11). Due to the lack of infrared surveys able to detect normal star-forming galaxies at  $z > 2$ , the actual contribution of dust-obscured galaxies to the cosmic star formation history at these redshifts remains largely unknown, especially at high masses where galaxies are known to be metal (e.g., Garnett, 2002; Tremonti et al., 2004; Gallazzi et al., 2005; Mannucci et al., 2010; Yates et al., 2012; Foster et al., 2012; Kirby et al., 2013; Dayal et al., 2013) and dust-rich (e.g., Heckman et al., 1998; Boissier et al., 2004; Reddy et al., 2010). Evidence already exists that the Lyman break galaxy (LBG) technique is missing a dominant population of massive dusty galaxies above a stellar mass of typically  $5 \times 10^{10} M_{\odot}$ , because of their faintness and the redness of the UV slope (e.g., van Dokkum et al., 2006; Bian et al., 2013; Wang et al., 2016). The star-formation rates (SFRs) of these high redshift galaxies are mostly estimated from UV measurements emitted by short-lived massive stars (e.g., Kennicutt and Evans, 2012). This UV emission is strongly affected by the presence of dust in the interstellar medium (ISM). In order to correctly estimate the SFR, a dust correction needs to be applied using an extinction law (e.g., Meurer et al., 1999; Calzetti et al., 2000; Reddy, 2006), a  $\beta$  slope (see Chapter 8, and the UV luminosity. This approach has proved effective for distant galaxies (e.g., Oesch et al., 2015; Bouwens et al., 2015; McLeod et al., 2015) but suffers from caveats due to the large number of parameters that are poorly constrained (e.g., Cowie et al., 1996; Pannella et al., 2009). In particular, the extinction law could be different in the distant Universe, especially for galaxies with high star-formation rates (e.g., Rodighiero et al., 2011). For this reason, constraining galaxy infrared re-emission is essential to obtain a robust star formation tracer.

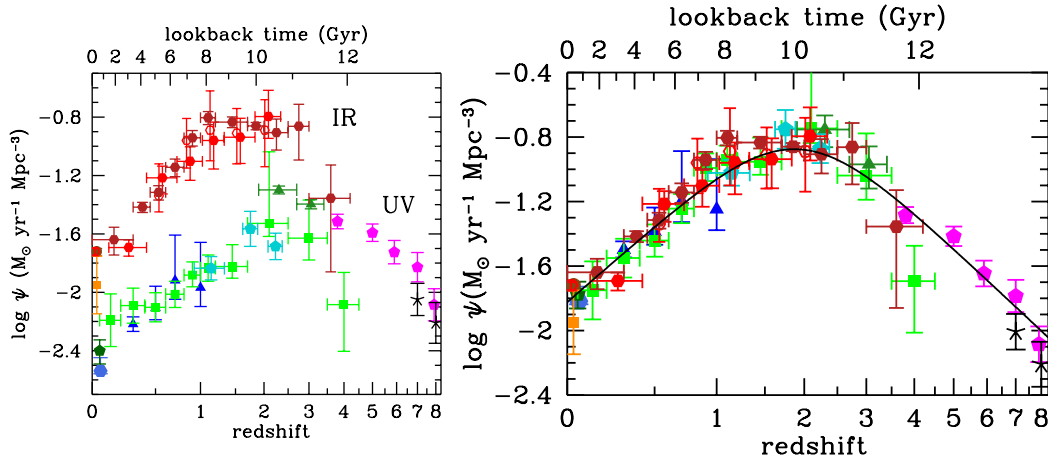


FIGURE 1.11: Left panel: Evolution of the star formation rate density in UV (uncorrected for dust attenuation) and in IR. Left panel: combination of the UV and IR to derive the SFRD. The solid curve is the best-fit. Figures from (Madau and Dickinson, 2014).

This is really one of the main goals of the survey in this study. Several scenarios can be imagined when we look back at the cosmic history of galaxy formation. Some authors suggest the possibility of a relatively constant star formation density when the Universe was young (Rowan-Robinson et al., 2017), then a decline of star formation after the cosmic noon. Others on the contrary lean towards the hypothesis of a progressive increase in star formation density to the cosmic noon and then a progressive decline beyond. To be able to settle this debate and constrain the cosmic history of galaxy formation, one of the only ways is to carry out a broad survey exploring the infrared emission of galaxies. Until the advent of ALMA, infrared observations suffered from poor resolution or were much less efficient than optical observations, which generally meant that only galaxies biased towards the extremes could be analyzed. Thanks to this new domain of sensitivity, ALMA is able to unveil less extreme objects, bridging the gap between massive starbursts and more ‘normal’ galaxies. However, many previous ALMA studies have been based on biased samples, with prior selection (pointing) or a posteriori selection (e.g., based on HST detections) of galaxies, or in a relatively limited region of the sky. In this study, we present an unbiased view of a large (69 arcmin<sup>2</sup>) region of the sky, without prior or a posteriori selection based on already known galaxies, in order to improve our understanding of dust-obscured star formation, and to investigate the main properties of these objects. We take advantage of one of the most potentially transformational outputs of ALMA - its ability to reveal a new class of galaxies through serendipitous detections. This is one of the main reasons for performing blind extragalactic surveys.

Dust only represents about 1% of the mass of the interstellar medium (for local galaxies, Draine 2003), yet it considerably modifies the emission of a galaxy. Fig. 1.12 shows the part of the galaxy spectrum affected by dust absorption. The term dust incorporates several categories of chemical element, with a typical grain size of less than micron<sup>15</sup>.

In general, we can distinguish large grains (BG for Big Grains), very small grains (VSG for Very Small Grains) and aromatic molecules (PAH for Polycyclic Aromatic Hydrocarbon). This grain size issue is essential, because absorption is highest for wavelengths at the order of magnitude

15. the size distribution of dust grains can be represented by the following formula:  $dn = a^{-3.5} da$ , where  $dn$  is the number of grains with a radius between  $a$  and  $a + da$  (Mathis et al., 1977).

of the size of the dust grains. For this reason, dust obscuration primarily affects UV and visible light.

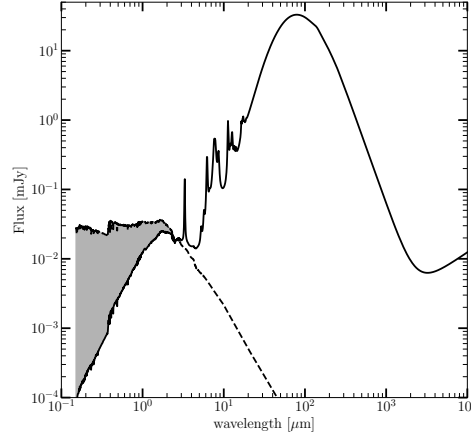


FIGURE 1.12: Spectral energy distribution of one galaxy selected from the galaxies detected in GOODS-ALMA. The difference between the solid and dotted curves (grey area) represents the part of the stellar emission that is absorbed by the dust. We have assumed an exponentially declining star formation history and a dust attenuation law as described by Calzetti et al. (2000).

In order to reach galaxies at high redshift, and to constrain the emission of dust from a galaxy, it is necessary to observe it in (sub)millimeter wavelengths. The rest-frame peak of a galaxy spectral energy distribution (SED) can vary between 72 and 125  $\mu\text{m}$  for a dust temperature between 30 and 50 K (e.g., Casey et al., 2014), corresponding to an observed peak between 288 and 500  $\mu\text{m}$  at redshift 3. To constrain the shape of the SED, at least one measurement has to be made beyond this peak. This is why (sub)millimeter observations are necessary to constrain the IR luminosity of a galaxy. Thanks to the strong negative K-correction at submillimeter wavelengths (see Sect. 1.4.1), infrared emission does not suffer from distance attenuation, making submillimeter observations insensitive to redshift across a wide redshift range  $2 < z < 10$  (Blain et al., 2002). The *Herschel* Space Observatory (Pilbratt et al., 2010) was limited by a poor angular resolution (36'' at 500 $\mu$ ). To overcome the difficulty caused by this angular resolution, it is necessary to deblend the sources based on deep observations made at shorter wavelengths. This has been done for the SPIRE filter Griffin et al. (2010) of *Herschel* (e.g., Roseboom et al., 2012; Merlin et al., 2015; Wright et al., 2016; Pearson et al., 2018; Wang et al., 2019) as well as for PACS (Poglitsch et al., 2010). Unfortunately, these techniques may, in some cases, prove to be imprecise for galaxies with low fluxes.

Other techniques such as stacking allow us to recover information on these weak sources Pannella et al. (2015); Schreiber et al. (2015); Álvarez-Márquez et al. (2016). This technique is very efficient but only allows us to measure the statistical properties (average or median) of the galaxies studied. Any particularly interesting properties of an individual faint galaxy are therefore lost in the galaxy stack.

With ALMA, it is now possible to overcome the confusion limit and to detect galaxies with continuum emission below 1 mJy and a resolution lower than 1 arcsec, which enables more secure counterpart association. Some recent studies have measured (sub-)millimeter fluxes down to 0.2 mJy (e.g., Hatsukade et al., 2013; Carniani et al., 2015; Fujimoto et al., 2016; Aravena et al., 2016; Muñoz Arancibia et al., 2018).

### 1.4.1 K-correction

Following [Kinney et al. \(1996\)](#), the word k-correction comes from the expression K-term introduced in [Wirtz \(1918\)](#). The letter K comes from the German word for constant: "konstante". [Hubble \(1936a\)](#) popularized the use of the letter  $K$  to introduce the notion of magnitude correction due to redshift. The K-correction is the correction that must be applied to a distant object to adjust its absolute magnitude from observed-frame to rest-frame. In other words, it is the ratio between the rest-frame luminosity of a galaxy and its observed-frame luminosity:

$$K(\nu, z) = \frac{L_{\nu(1+z)}}{L_{\nu}} \quad (1.10)$$

What makes (sub)millimeter observations powerful is that in this wavelength domain, the k-correction becomes particularly strong and negative. By convention, and in relation to the relative magnitudes that decrease when the observed flux increases, K-correction is designated negative when the density flux increases with increasing redshift, and is positive when the density flux decreases with increasing redshift.

At these wavelengths, the emission of dust is described by a Rayleigh-Jeans spectrum with the following shape:

$$S_{\nu} \propto \nu^{2+\beta} \quad (1.11)$$

with  $\beta \sim [1.5-2]$  (e.g., [Chapman et al., 2005](#); [Gordon et al., 2010](#); [Greve et al., 2012](#); [Magnelli et al., 2012](#); [Boselli et al., 2012](#); [Bianchi, 2013](#); [Rémy-Ruyer et al., 2013](#)). This dust emissivity index may vary depending on the metallicity of the galaxy, the size distribution of dust grains and the location in the galaxy. For a "classic" galaxy, the Rayleigh-Jeans tail dominates at rest-frame wavelengths between  $200\mu\text{m}$  and  $1\text{mm}$  (see Sect. 1.5 for more details).

The evolution of the flux density for a galaxy is given according to the following equation:

$$S_{\nu} = \frac{L_{\nu}}{4\pi D_L^2} \quad (1.12)$$

where  $D_L$  is the luminosity distance. This formula shows that the luminosity of a galaxy is uniformly diluted in a sphere with a radius  $D_L$ . In Fig. 1.13, we show the luminosity distance as a function of redshift. We compare this luminosity distance with the function  $f(z) = A \times (1+z)^{\alpha}$  with  $\alpha = 1.5, 2$  and  $3$ . We can see that the luminosity distance evolves as  $(1+z)^{2.5}$  for  $0.25 < z < 1.25$ ,  $(1+z)^2$  for  $1.25 < z < 2.25$ , and  $(1+z)^{1.5}$  for  $2.25 < z < 7$ .

By combining Eq. 1.11 and Eq. 1.12, we find that  $S_{\nu}(z) \propto \nu^{2+\beta}/4\pi D_L^2 \propto \nu^{2+\beta}/(1+z)^{2\alpha} \propto \nu_{rest}^{2+\beta} (1+z)^{2+\beta}/(1+z)^{2\alpha} \propto (1+z)^{2+\beta-2\alpha}$ . To have a flux density that does not change,  $2+\beta - 2\alpha$  must be equal to 0. This is the case when  $1.25 < z < 2.25$  assuming  $\beta = 1.5$ . For higher redshifts, this factor becomes negative and the observed flux increases with redshift. This correction is highly dependent on the value of  $\beta$ , which in turn depends on the galaxy.

In this sense, submillimeter observations are unique in making dusty star-forming galaxies accessible from the peak of the star formation rate density ( $z \sim 2$ , [Madau and Dickinson 2014](#)) up to  $z \sim 5$  ([Blain and Longair, 1993](#)). In Fig. 1.14, we show the evolution of the flux density as a function of the redshift for one of our detected galaxies, which we will present in detail in this study (AGS1), through different filters from the mid infrared ( $24\mu\text{m}$ ) to the radio ( $5\text{cm}$ ). We can clearly see the drop in the mid-IR and radio flux density as a function of the redshift, while the



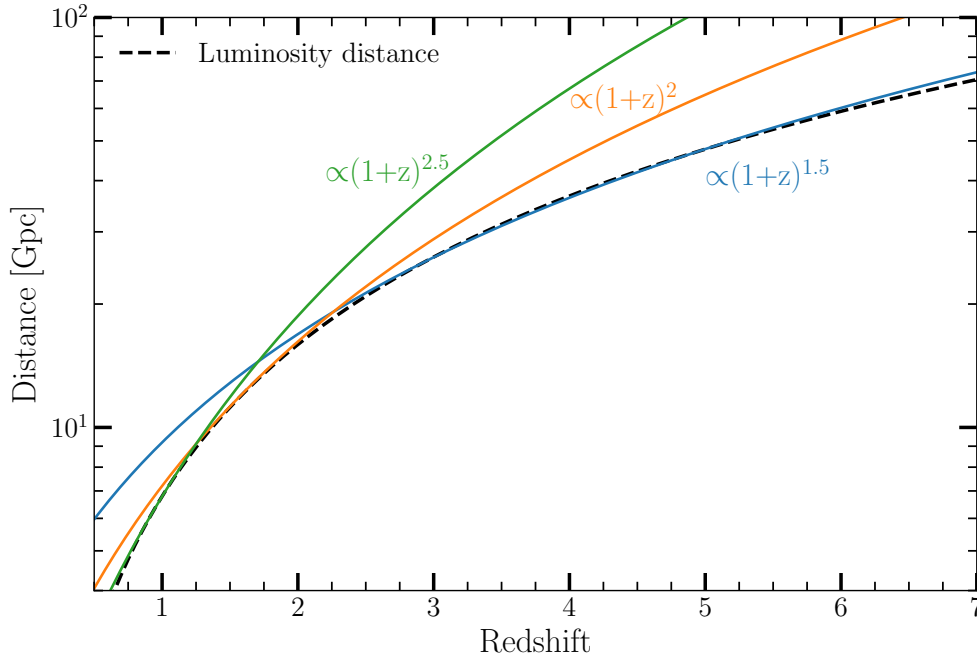


FIGURE 1.13: Luminosity distance as a function of redshift adopting a spatially flat  $\Lambda$ CDM cosmological model with  $H_0 = 70 \text{ km s}^{-1} \text{ Mpc}^{-1}$ ,  $\Omega_m = 0.7$  and  $\Omega_\Lambda = 0.3$ . For comparison, the function  $f(z) = A \times (1+z)^\alpha$  with  $\alpha = 1.5, 2$  and  $3$  has been scaled to fit the luminosity distance.

millimeter flux remains roughly constant, and has a tendency to increase slightly for redshifts higher than  $z = 2$  (see Fig. 1.14 and 1.15).

## 1.5 Probing galaxy properties using a multiwavelength approach

In the late 1990s a population of galaxies was discovered at submillimeter wavelengths using the Submillimeter Common-User Bolometer Array (SCUBA; [Holland et al. 1999](#)) on the James Clerk Maxwell Telescope (see e.g., [Smail et al. 1997](#); [Hughes et al. 1998](#); [Barger et al. 1998](#); [Blain et al. 2002](#)). These "submillimeter galaxies" or SMGs, are highly obscured by dust, typically located around  $z \sim 2\text{--}2.5$  (e.g., [Chapman et al., 2003](#); [Wardlow et al., 2011](#); [Yun et al., 2012](#)), massive ( $M_\star > 7 \times 10^{10} M_\odot$ ; e.g., [Chapman et al., 2005](#); [Hainline et al., 2011](#); [Simpson et al., 2014](#)), gas-rich ( $f_{\text{gas}} > 50\%$ ; e.g., [Daddi et al., 2010](#)), and have high star formation rates (SFR) - often greater than  $100 M_\odot \text{ year}^{-1}$  (e.g., [Magnelli et al., 2012](#); [Swinbank et al., 2014](#)). This makes them significant contributors to cosmic star formation (e.g., [Casey et al., 2013](#)), often driven by mergers (e.g., [Tacconi et al., 2008](#); [Narayanan et al., 2010](#)) and often hosting an active galactic nucleus (AGN; e.g., [Alexander et al. 2008](#); [Pope et al. 2008](#); [Wang et al. 2013](#)). With ALMA, we can now bridge the gap between massive starbursts and more normal galaxies: SMGs no longer stand apart from the general galaxy population.

Thanks to the survey presented in this thesis, and after the identification of galaxy counterparts, we will use a multiwavelength approach to better understand the evolution of distant galaxies. We will estimate key properties of galaxies to probe the evolution of the gas fraction, star formation rate, and depletion time of galaxies detected by ALMA.



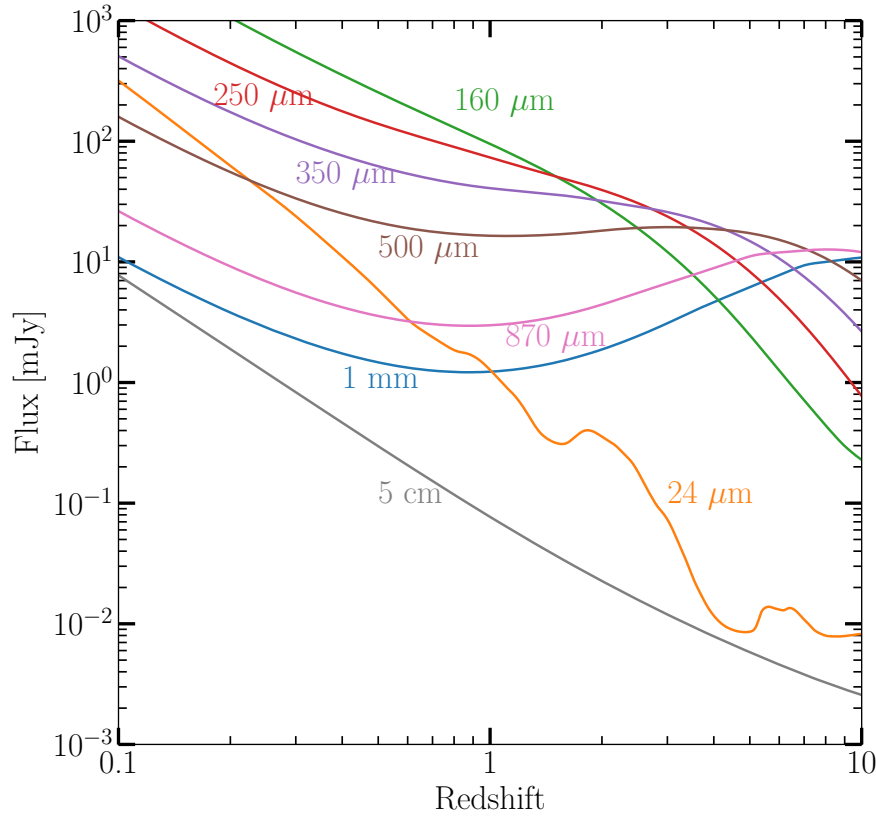


FIGURE 1.14: Evolution of the flux of a galaxy (given in arbitrary units) as a function of the redshift, through different filters, *Spitzer*-MIPS at  $24\ \mu\text{m}$ , *Herschel*-PACS, at  $160\ \mu\text{m}$ , *Herschel*-SPIRE at  $250$ ,  $350$ , and  $500\ \mu\text{m}$ , ALMA band 6 and band 7 at  $870\ \mu\text{m}$  and  $1\text{mm}$  and VLA at  $5\text{cm}$ . The effect of the strong negative  $k$ -correction, which is clearly visible at (sub)millimeter wavelengths, disappears at radio wavelengths.

### 1.5.1 Multiwavelength emission of a galaxy

Each element of a galaxy emits at a specific wavelength. A multiwavelength approach is, therefore, necessary to have a full overview of the galaxy, understand the different emission mechanisms, and derive its redshift. In this section, we will explain the different processes contributing to the emission of a galaxy for each wavelength domain, and present the techniques used to derive galaxy parameters. We will then discuss the techniques used to fit the SEDs.

#### Radio emission

In the absence of AGN, radio emission has two primary origins: synchrotron radiation from relativistic electrons and free-free emission from HII regions (e.g., [Condon, 1992](#)).

**Synchrotron emission** Synchrotron radiation (magneto-bremsstrahlung) arises mainly from the end of life of massive stars. Stars with a mass higher than  $8M_{\odot}$  ([Condon, 1992](#)), but less than  $40$  or  $50M_{\odot}$  ([Gilmore, 2004](#)), will rapidly collapse and explode, resulting in Type II or Type Ib supernova. In the remains of the supernova (supernova remnant; SNR) the two fundamental ingredients of the synchrotron emission process coexist - high-energy electrons and a magnetic field (e.g., [Urošević, 2014](#)). Relativistic electrons rotating around the magnetic field

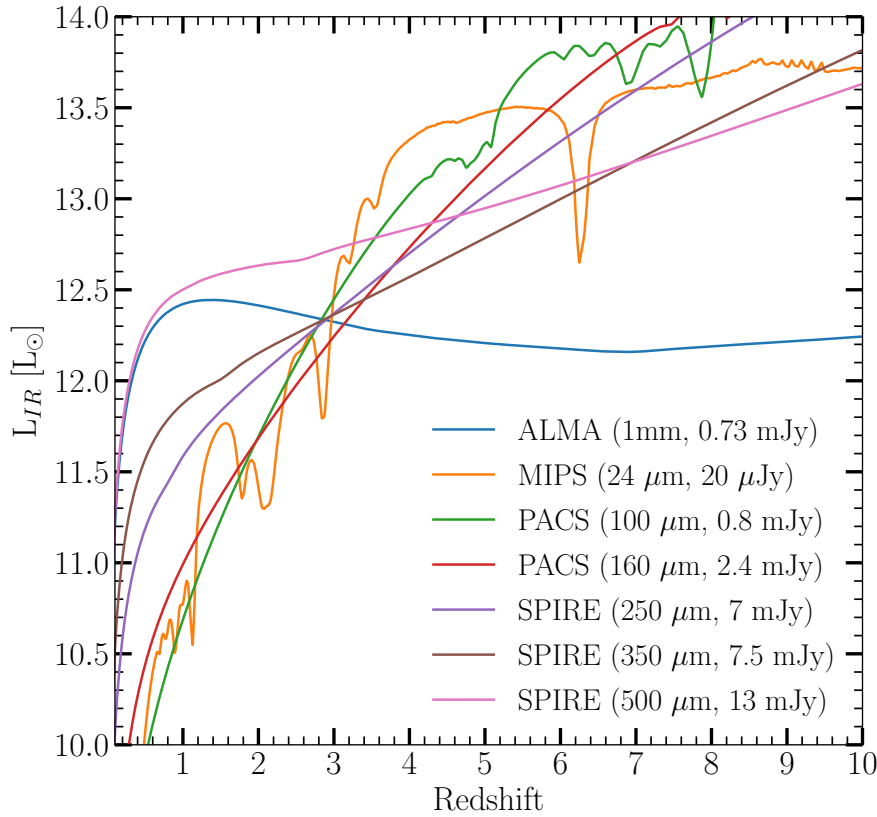


FIGURE 1.15: Infrared luminosity limit in the GOODS-ALMA field, from the infrared at  $24\mu\text{m}$  to millimeter wavelengths at 1mm. Detection limits (given in parentheses for each filter) correspond to the detection limit in the GOODS-South field (Elbaz et al., 2011; Schreiber et al., 2015).

lines will generate synchrotron radiation. Synchrotron emission, which is non-thermal emission, is generated when the acceleration of the electron is in a plane perpendicular to its velocity. The emission is directed in the direction of velocity vectors. The acceleration of electrons is generally due to multiple interactions of an electron on either side of the supernova shock wave (Niklas et al., 1997).

$$I_\nu \propto \frac{\nu^{-\alpha_0}}{1 + (\nu/\nu_b)^{\Delta_\alpha}} \quad (1.13)$$

**free-free emission** "Free-free" emission (Thermal bremsstrahlung) is produced directly in HII regions, i.e. clouds of ionized hydrogen. The intensity of the free-free emission is proportional to the production rate of Lyman continuum photons. Free-free emission is produced when an electron scatters off another charged particle, such as a proton in a HII star-forming region. It is called free-free because the electron is free both before and after the interaction. HII regions are the regions around stellar formation sites, where atomic hydrogen has been ionized. It is the massive and young stars (typically OB stars) that ionize this interstellar environment. As these stars have a short life expectancy, HII and free-free emission regions trace the recent stellar formation.

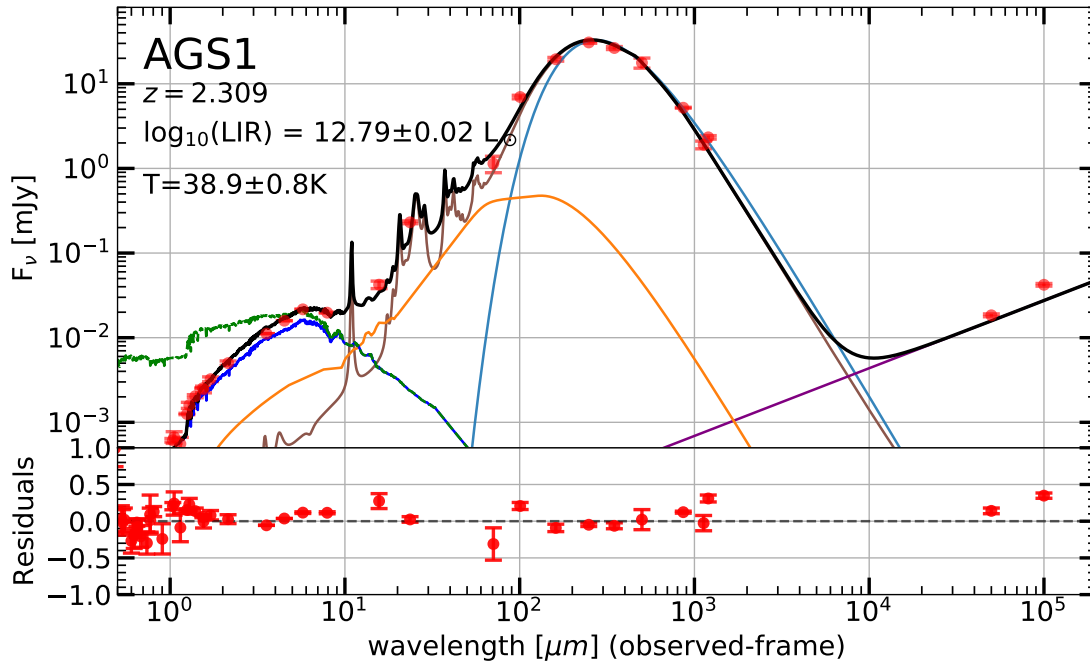


FIGURE 1.16: Example of the spectral energy distribution for AGS1. The solid black line represents the best fit which can be decomposed by the IR dust contribution (brown line), a stellar component uncorrected for dust attenuation (dark blue line), synchrotron emission (brown line) and the AGN contribution (orange line). In addition, we show the best fit of a modified black body, with  $\beta = 1.5$  (light blue line). The corrected UV emission is also shown in green. The bottom panel shows the residuals: (observation - model)/observation.

For the majority of galaxies, synchrotron emission is dominant at rest-frame frequencies below 30GHz, while the dust is dominant at frequencies higher than 200 GHz. Between these two frequencies, the free-free emission is greater than the other two other components (see Fig. 1.17).

It is massive stars ( $M \geq 10^8 M_{\odot}$ ) that contribute to the heating of dust in the interstellar medium (and are therefore responsible for the infrared part of a galaxy's spectrum), and that also produce radio emission in HII regions (thermal free-free emission) and from supernova explosions (synchrotron emission). There is therefore a correlation between the radio and infrared emission of a galaxy.

### Infrared emission

In the infrared, we can differentiate between 3 main domains: the near infrared ( $0.8\mu\text{m} - 5\mu\text{m}$ ), the mid infrared ( $5\mu\text{m} - 25\mu\text{m}$ ) and the far infrared ( $25\mu\text{m} - 500\mu\text{m}$ ).

Near-infrared emission is dominated by stars on the stellar main sequence, which are old, relatively small and cold (3000 - 8000 K, see Fig. 1.18). These low mass stars ( $\leq 1M_{\odot}$ ) are the most numerous stars in a galaxy, and dominate the total mass of the galaxy<sup>16</sup> Near-infrared emission therefore makes it possible to trace the stellar mass of a galaxy directly. However, these not very massive stars are not the only contributors to the near IR emission - the presence of an active

16. A star of 10 solar masses will produce light equivalent to 4000 solar luminosities. Massive stars therefore dominate in brightness, while low mass stars dominate the total mass of a galaxy.

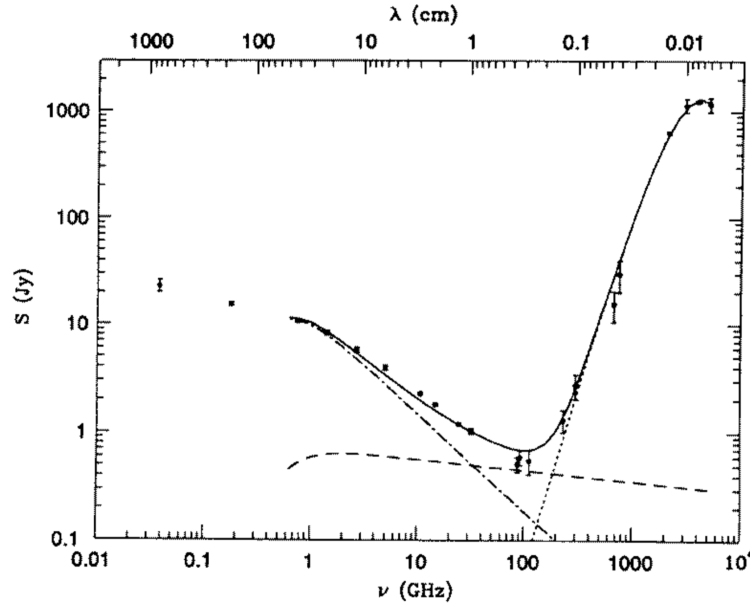


FIGURE 1.17: Observed radio-far infrared spectrum of M82. The measurements (black dots) were made by Klein et al. (1988) and Carlstrom and Kronberg (1991). The synchrotron emission (dot-dashed line), the free-free emission (dashed line), the dust component (dotted line) and the sum of the SED (solid line) are shown as a function of the frequency. For M82, the synchrotron emission is dominant for frequencies below 30GHz, while the dust is dominant for frequencies higher than 200 GHz. Between these two frequencies, the free-free emission is higher than the two other components. Figure from: Condon (1992).

galactic nucleus may also contribute<sup>17</sup>. For this reason, the presence of an AGN can artificially overestimate the stellar mass derived for a galaxy. Indeed, as we will see in Chapter 8, it is not always straightforward to (i) know if the galaxy is hosting an AGN; (ii) subtract the AGN's contribution to the spectrum of the galaxy, and this subtraction is a source of great uncertainty. We will also see that, in the same way, AGN can introduce biases on the measurement of galaxy mass, and the measurement of infrared luminosity and therefore star formation rate in the far-infrared part of the galaxy SED.

PAHs and small dust grains dominate the mid-IR emission. The polycyclic aromatic hydrocarbons (PAHs) have their emission bands around  $10\mu\text{m}$ . The brightest bands are located at  $\sim 3.3, 6.2, 7.7, 8.6, 11.3$  and  $12.7\mu\text{m}$  and are associated with the vibration, elongation and bending modes of the C-H and C-C bonds (e.g., Leger and Puget, 1984; Allamandola et al., 1985; Li and Draine, 2012; Galliano et al., 2008). For wavelengths greater than  $10\mu\text{m}$ , mid-infrared emission is associated with small grains. PAHs and small dust particles are not in thermal equilibrium (and cannot be modeled by a modified blackbody law (e.g., Boselli et al., 2011); this is why they have strong emission bands (see Fig. 1.16).

At greater than  $\sim 50\mu\text{m}$ , large grains are responsible for the majority of a galaxy's emission. In the far-infrared, the SED can be approximated by a simple modified black body. If we consider a single blackbody temperature for grains of dust, the SED can be modeled by the following formula Blain et al. (2002):

$$L_\nu = \Omega \epsilon_\nu B_\nu(T_d) \quad (1.14)$$

17. The near-infrared emission of an AGN is most often associated with type I AGN (Burtscher et al., 2015).

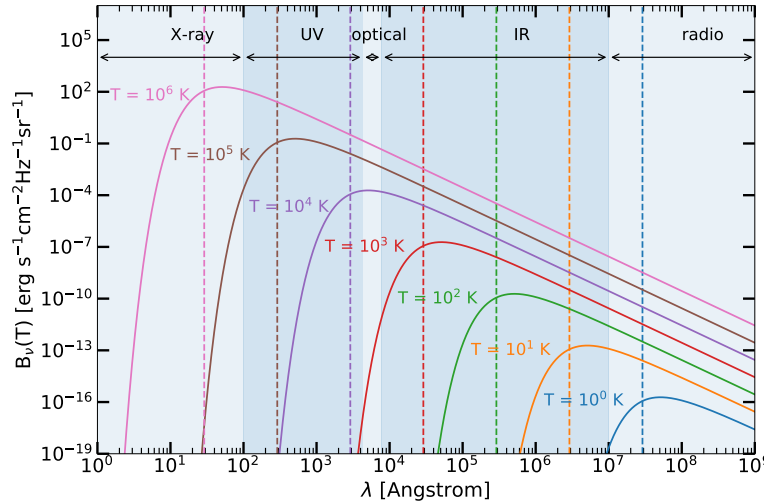


FIGURE 1.18: Blackbody emission spectrum, according to Planck's law as a function of wavelength at different temperatures. According to Wien's Law, the peak emission wavelength of a body depends on its temperature. The warmer the body is, the more it will emit at higher frequencies, and the colder it is, the lower wavelength its peak emission will be. That is why "cold" stars with temperatures  $\sim 3000\text{--}5000\text{ K}$  emit in the near-infrared, and why we use millimeter wavelengths to study  $20 - 50\text{ K}$  dust emission.

where  $\Omega$  is the solid emission angle,  $\epsilon_\nu$  the emissivity coefficient and  $B_\nu(T_d)$  is the Planck function which has the following form:

$$B_\nu(T_d) = \frac{2h}{c^2} \frac{\nu^3}{\exp(\frac{h\nu}{k_B T_d}) - 1} [\text{erg s}^{-1} \text{Hz}^{-1} \text{m}^{-2} \text{sr}^{-1}]. \quad (1.15)$$

We can also rewrite this equation according to the wavelength<sup>18</sup>  $\lambda$ , and we will preferably use this notation in the rest of this thesis:

$$B_\nu(T_d) = \frac{2hc}{\lambda^3} \frac{1}{\exp(\frac{hc}{\lambda k_B T_d}) - 1}. \quad (1.16)$$

The emissivity coefficient can be approximated by:

$$\epsilon_\nu \sim \kappa_\nu M_{\text{dust}} [m^2 \text{kg}^{-1}] \quad (1.17)$$

where  $\kappa_\nu$  is the dust mass absorption coefficient at a given frequency. By injecting this term into Eq. (1.14), we obtain the following formula:

$$M_{\text{dust}} = \frac{L_\nu}{4\pi\kappa_\nu B_\nu(T_d)} \quad (1.18)$$

with:

$$L_\nu = S_\nu \frac{4\pi D_L^2}{(1+z)}. \quad (1.19)$$

Here,  $S_\nu$  is the observed flux density and  $D_L$  is the luminosity distance.

18. We express  $B_\nu$  according to  $\lambda$ . However, we must be careful with the unit with which the emissivity of the black body is expressed because  $B_\nu(T)d\nu = B_\lambda(T)d\lambda$ , and hence  $B_\nu(T) = B_\lambda(T) \frac{\lambda^2}{c}$ .

By combining Eq. 1.18 and Eq. 1.19, we obtain:

$$M_{dust} = \frac{S_\nu D_L^2}{(1+z)\kappa_\nu B_\nu(T_d)} \quad (1.20)$$

where  $\kappa_\nu$  is defined as follows:

$$\kappa_\nu = \kappa_0 \left( \frac{\nu}{\nu_0} \right)^\beta. \quad (1.21)$$

as the absorption coefficient of the dust mass at the given rest frame wavelength, with  $\beta = 1.5$  [Gordon et al. \(2010\)](#).

To be consistent with the model of [Draine and Li \(2007\)](#) (DL07) we adopt a value of  $\kappa_{250} = 5.1 \text{ cm}^2 \text{g}^{-1}$  obtained by [Li and Draine \(2001\)](#). We calculate the uncertainties on  $M_{dust}$  in the same way as DL07, using a Monte-Carlo simulation. Using Eq. 1.18:

$$L_\nu = 4\pi M_{dust} \kappa_\nu B_\nu(T_d) = M_{dust} \frac{8\pi h \kappa_0}{\nu_0^\beta c^2} \frac{\nu^{3+\beta}}{\exp(\frac{h\nu}{k_B T_d}) - 1} \quad (1.22)$$

so that:

$$L_\nu \propto \frac{\nu^{3+\beta}}{\exp(\frac{h\nu}{k_B T_d}) - 1} \quad (1.23)$$

which is the simplified form of the modified black body.

Wien's law gives us the dust temperature from the fit of the modified black body:

$$T = \frac{h \times c}{4.9651 k_B \times \lambda_{pic}} = \frac{2.898 \times 10^{-3}}{\lambda_{pic}} \quad (1.24)$$

where  $h$  is the Planck constant,  $k_B$  is the Boltzmann constant and  $c$  is the speed of light.

## Optical and UV

UV emission is associated with the emission of young and massive stars. Young stars radiate predominantly in the ultraviolet and optical domains, and the youngest and most massive of them (OB type stars) will contribute primarily to far-ultraviolet emission. This is why UV brightness is a good indicator of massive star formation (e.g., [Kennicutt, 1983](#); [Meurer et al., 1995](#)). However, these young and massive stars are also mainly located in regions that are rich in gas and dust. They are therefore significantly affected by dust obscuration (e.g., [Buat and Burgarella, 1998](#); [Kong et al., 2004](#); [Cortese et al., 2008](#)). We also see many emission lines produced in HII regions at UV wavelengths.

## X-ray emission

The X-ray emission of a galaxy has several origins. It can come from diffuse hot gas, point source objects such as X-ray binaries or neutron stars, supernova, or the AGN accretion disk of galaxies, which is heated by viscous friction at temperatures  $\sim 10^5 \text{ K}$ . The X-ray emission can be divided into soft X-rays (0.1-2keV) and hard X-rays (2-100 keV).

### 1.5.2 SED fitting

There are several types of models and techniques to fit the spectral energy distribution of a galaxy, whether it is with radiative transfer models (e.g., [Siebenmorgen and Krügel, 2007](#)), empirical templates (e.g., [Chary and Elbaz, 2001](#); [Dale et al., 2001](#); [Dale and Helou, 2002](#); [Draine and Li, 2007](#); [Draine et al., 2014](#); [Rieke et al., 2009](#)), or energy balance techniques (e.g., [da Cunha et al., 2008](#); [Nonino et al., 2009](#); [Burgarella et al., 2005](#)), for example.

In this thesis, we chose to model the spectral energy distributions mainly using CIGALE<sup>19</sup> ([Noll et al., 2009](#); [Nonino et al., 2009](#); [Burgarella et al., 2005](#)). When IR information is not available to fit a SED with CIGALE, we will match to the millimeter flux with the dust spectral energy distribution library<sup>20</sup> presented in [Schreiber et al. \(2018a\)](#). The calculation of the star formation rate is done by adding  $\text{SFR}_{UV}$  (uncorrected for dust attenuation) to the  $\text{SFR}_{IR}$ , with the method described in Chapter 8. We will also see that  $\text{SFR}_{total} \sim \text{SFR}_{IR}$  in this chapter, but to be more accurate in our derivation of SFRs, we also include the contribution from  $\text{SFR}_{UV}$ .

Throughout this thesis, we adopt a spatially flat  $\Lambda$ CDM cosmological model with  $H_0 = 70 \text{ km s}^{-1} \text{ Mpc}^{-1}$ ,  $\Omega_m = 0.7$  and  $\Omega_\Lambda = 0.3$ . We assume a Salpeter ([Salpeter, 1955](#)) Initial Mass Function (IMF). We use the conversion factor of  $M_\star$  ([Salpeter 1955 IMF](#)) =  $1.7 \times M_\star$  ([Chabrier 2003 IMF](#)). All magnitudes are quoted in the AB system ([Oke and Gunn, 1983](#)).

19. For more specific needs, we also used LePhare, Eazy, FAST, etc.

20. Publicly available at <http://cschreib.github.io/s17-irlib/>

During the three years of my Ph.D., I had the opportunity to work on several different projects. In particular, I was in charge of the scientific exploitation of the largest deep survey on the sky with ALMA. I will explain these projects in detail in this manuscript. I have had the chance to work on all of the stages of conducting a research project, both upstream and downstream, by writing telescope proposals (for ALMA and VLA), by going directly to observe (VLT), by reducing and analyzing data (CASA, Gildas), by publishing and presenting my research at international conferences and being active in the international community preparing for future projects (TolTEC/LMT). I have also had the opportunity to collaborate, throughout my Ph.D., within major international collaborations (VANDELS, CANDELS and LMT) and have visited regularly colleagues in different institutes in order to exchange and compare viewpoints, and to work on joint projects.

## Characterization of the survey and creation of a catalog

The precise characterization of an ALMA survey in the GOODS-South field, the identification of the galaxies present in this survey, the definition of detectability thresholds and indicators that can define the reliability of these detections. The objective was to find the best compromise between the number of sources detected, i.e., to have the most complete sample possible and to have as high reliability as possible, i.e., to ensure that detections are not due to noise. We chose to produce a blind catalog, without using other wavelengths for the selection process, which allowed us to detect sources without optical counterparts. By choosing to create a blind catalog, we allowed a small proportion of spurious sources to be included in our catalog. We quantified this proportion and found criteria for segregation between spurious and "real" sources.

I also created noise maps, using a sigma clipping technique, for our images at different resolutions. We compared several softwares both for source detection (Blobcat, AEGEAN, PyBDSM, SExtractor) and flux extraction (CASA, Blobcat, Galfit). An important part of my work has been to accurately measure the emitted fluxes of these galaxies, and through simulations to determine precisely which fraction of the galaxies could be detected in our maps.

I compared the number of detections, flux, etc., between clean and dirty images and chose to work with the dirty images in order to have better control of our data. To measure the fluxes correctly, we needed to know if the sources were resolved or point-like. This is an important point to be able to quantify the reliability of flux measurements. To measure the size of our detections, we combined several techniques. We stacked all of our detections together and compared them to the PSF size. We also used flux extraction tools to compare the residuals between a point source model (PSF) or a Gaussian or Sérsic profile. We used CASA and Gildas to perform the size analyses in the UV-plane.



I also note an astrometry difference between ALMA and HST images. One systematic offset had already been found. After subtracting this offset, we unveil the presence of a non-negligible local offset, with a structured pattern, resulting from the way the HST maps were built. The precise knowledge of the astronomy of the GOODS-South field has enabled us to confirm in a robust way, the optical counterparts of our ALMA detections.

## Number Counts

I computed the completeness of our observations using Monte Carlo simulations performed on a tapered image. I injected artificial sources in each slice to quantify the differences between the fluxes and sizes of the sources injected into the image and the fluxes and sizes measured. I also quantify and model the relation between the number of sources injected and the number of sources found, as a function of the flux and size. This knowledge of the completeness allows us to estimate, from the number of sources detected, and after correcting several observational biases which we will describe in detail in Chapter 5, the theoretical number of sources present, per unit area and per bin of flux, in the GOODS-South field. This work also led to the compilation of data from literature and the creation of a parametrization of the submillimeter number counts. This compilation and the computed fit has since been reused in scientific publications.

## Using IRAC priors to probe fainter millimeter galaxies

I took advantage of three other wavelengths in addition to our ALMA data (HST/WFC3 H-band, Spitzer/IRAC channel 1 and an ultra-deep  $K_s$ -band image) to lower the detection threshold from  $4.8$  to  $3.5 \sigma$ , and thus increase our number of detections. In order to validate the robustness of these prior-based detections, we used statistical tests such as the Kolmogorov-Smirnov test. The creation of an additional supplementary catalog, based on priors, has two advantages. The first is to increase the number of sources detected with ALMA and therefore have a more robust statistics on our derived properties. The second advantage is to be able to make a comparative study of the galaxies detected at higher flux, without priors and those detected with priors. This study revealed that detection with priors allows us to detect larger, less massive sources that span over a wider redshift range than the galaxies of the main catalog.

## HST-dark galaxies

During the creation of our catalogs, blind and with priors, we detected several sources without optical counterparts. The advantage of a blind survey is that they can reveal the presence of sources missed by the HST, that we believe may represent the missing candidates responsible for the formation of massive elliptical galaxies. As these sources are rare, they highlight the importance of a survey over a larger area than other studies, as we have done here, despite the ALMA limited field of view.

I used several spectral energy distribution (SED) fitting tools, such as Le PHARE and EAZY, to estimate the stellar masses and redshifts of our sample. I investigated whether the flux of HST-galaxies arose from neighboring galaxies by using SED models to also measure the redshifts and

stellar masses of nearby galaxies, and estimated the dust temperature that nearby galaxies would need to have if they were responsible for generating the ALMA flux.

We found that all of the sources without an optical counterpart had an infrared counterpart, visible in deep Spitzer/IRAC images. I quantified the probability that these are chance alignments as a function of distance to the infrared counterpart, and we calculate for each HST-dark galaxy a percentage of random false associations through Monte Carlo simulations.

## Properties of detected sources

I fit the multiwavelength SED with CIGALE to derive several properties of these galaxies. I also used the IDL routine DeconvIR to split the IR-SED into AGN and host-galaxy components. These fits allowed us to calculate the dust masses of the galaxies. Based on these dust masses and an assessment of the metallicity of the galaxies, we were able to derive the gas mass. I compared the amount of gas found by this technique with other methods used in the literature. I also calculated the dust temperature using a modified blackbody model and compared the dust temperature of the ALMA detected galaxies to all of the galaxies lying in the GOODS-ALMA field. We aimed to confirm that the detection of ALMA sources was not biased due to a lower dust temperature therefore making it easier to detect these galaxies.

I was able, from the IR and UV luminosities, to determine the star formation rate of the galaxies detected with ALMA, and estimate the proportion of galaxies on the main sequence compared with the starburst galaxies.

I compared the size of galaxies calculated in the  $H$ -band, which are on the relation of  $uvj$  active galaxies (at the same mass and redshift), with the millimeter sizes, which are particularly compact. I also note that a significant part of our galaxy sample has abnormally low gas fractions while having a star formation rate higher than the main sequence.. The underlying question in the study is to understand whether these distant, dusty, massive, high star-forming galaxies can be the progenitors of passive galaxies that are known to be compact at  $z = 2$ . Thanks to radio observations of the GOODS-South field, we also studied the evolution of the ratio between infrared and radio luminosity as a function of redshift.

I also calculated the star formation efficiency of galaxies as a function of IR brightness density, confirmed that there is a strong relationship between these two quantities and parameterized it. The more concentrated a galaxy's brightness surface is, the greater its star formation efficiency.

## Contribution as a co-author

I was pleased to be able to collaborate with other researchers during my Ph.D., and to be involved in several papers as a co-author. The list of papers for which I contributed can be found in Chapter 11.

In particular, I contributed to D. Elbaz's paper on starbursts in and out of the star-formation main sequence. For this paper, I fit IR SEDs and AGN SEDs to derive the star formation rate, as well as the contribution to IR luminosity due to an AGN, for a sample of 7 galaxies.

I also participated in the VANDELS collaboration, in particular by observing high redshift galaxies within the Chandra Deep Field South and UKIDSS Ultra Deep Survey survey field, using the multi-object spectrograph VIMOS on the VLT. I am a co-author of two papers, by R. McLure and L. Pentericci respectively, presenting this project and the first results.

I am a co-author of a paper by W. Rujopakarn, who observed at high resolution (200-parsec resolution) with ALMA to reveal the morphology of the dust distribution in galaxies. I contributed to this paper by correcting the astrometry between ALMA and HST observations.

I am also co-author of a paper by T. Wang on the proportion of optically-dark galaxies among massive galaxies in the early Universe. My primary contribution to this paper was to perform a compared analysis of the fluxes ratio between IRAC and ALMA for the optically dark galaxies detected in the GOODS-ALMA survey and the  $H$ -dropout sample from T. Wang.

I also reduced data from the combination of the NOEMA interferometer and the 30m IRAM antenna, to be able to measure the CO transition (6-5) for a highly lensed galaxy. This study will be presented in Rujopakarn et al., in prep.

In addition, I collaborated in the study of an optically dark galaxy, detected in GOODS-ALMA. This galaxy has the intriguing behavior of being located in the center of an overdensity of several galaxies at  $z \sim 3.5$  and being the most massive galaxy at  $z > 3$  without an AGN in this part of the sky. This work will be presented in detail in Zhou et al. in prep.

And finally, I provided a literature compilation of number counts for G. Popping and discussed with him about the redshift distribution. These results will be presented in Popping et al. in prep.

## Observations and proposals

I observed during seven nights at the VLT on the wide field imager and multi-object spectrograph VIMOS for the VANDELS survey. VANDELS is an ESO spectroscopic survey targeting galaxies at  $z > 2.5$  within the Chandra Deep Field South (CDFS) and UKIDSS Ultra Deep Survey (UDS) survey fields. The goal of this survey is to constrain the metallicity, dust content and star-formation rates of more than two thousand  $2.5 < z < 5.5$  galaxies with a high signal-to-noise ratio (minimum of 20 hours per source to a maximum of 80 hours per source). I had an active role in these observations, identifying the guide stars and adjusting the instrumental offset to be applied to the telescope to center the guide stars. I regularly measured the diffraction spot caused by these guide stars to control the quality of the observations and change the observed field when necessary.

During this Ph.D., I apply for several observation with ALMA and VLA as principal investigator. The complete list of proposals (accepted and pending) is given in Chapter 12. The ALMA data of one of this proposal have just been delivered.

## Teaching and outreach

I have devoted a significant part of my Ph.D. to science outreach and teaching activities. At university, during these last three years, I was a teaching assistant in Physics (mechanics, fluid mechanics, electrostatics, acoustics, imaging), and informatics. In addition to astronomy outreach and teaching activities that I regularly carry out in different associations, I have participated in several occasional events such as science cafés, debates in museums, observation evenings, thesis presentation contest or radio broadcast<sup>1</sup>.

I have also written outreach scientific articles for CEA's communication, through a "Highlight"<sup>2</sup> on the HST-dark galaxies detected by ALMA, an article for the Fundamental Research Division<sup>3</sup>, as well as an article in the monthly journal of CEA "Défis du CEA".

---

1. <https://www.franceculture.fr/emissions/la-methode-scientifique/galaxies-noires-cest-pas-si-clair>  
2. [http://irfu.cea.fr/dap/en/Phoce/Vie\\_des\\_labos/Ast/ast.php?t=actu&id\\_ast=4567](http://irfu.cea.fr/dap/en/Phoce/Vie_des_labos/Ast/ast.php?t=actu&id_ast=4567)  
3. <http://www.cea.fr/drf/Pages/Actualites/En-direct-des-labos/2019/il-etait-une-fois-deux-galaxies-tres-sombres-et-tres-l.aspx>



In this chapter, we will discuss the deep fields in astronomy, explain why the GOODS-*South* field was chosen and observed by ALMA, and then detail the exceptional multiwavelength coverage of this part of the sky. We then explain in detail how ALMA images and noise maps were created and give the characteristics of these images.

### 3.1 Historical context

The history of deep contiguous fields in astronomy is closely linked to Robert Williams' pioneering choices. Director of the Space Telescope Science Institute (StSci), he decided, against the opinion of many of his collaborators, to dedicate a large part of his Director's Discretionary time to pointing the Hubble Space Telescope towards nothing. He chose a region of the sky ( $\sim 4$  square arcminutes, RA = 12h 36m 49s, Dec. =  $+62^\circ 12' 58''$ ; J2000), close to the seven brightest stars of the Big Dipper constellation, in which there were a low density of nearby bright stars, and which has a low Galactic extinction. This observation, which lasted 10 consecutive days (about 150 orbits) from December 18 to 30, 1995, of the region now known as the Hubble Deep Field (Williams et al., 1996) revealed thousands of galaxies (e.g., Abraham et al., 1996; van den Bergh et al., 1996). *"The image provides both a new source of inspiration for those interested in the wonders of the universe, and the latest and greatest source of data in a long line of surveys that push the limits of technology to attempt to see what galaxies like our own looked like in their early stages of evolution"* (Ferguson, 1998). This image, which has become one of the most famous in astronomy, has made it possible, by extrapolation, to have a first idea of the number of galaxies in our universe and trace back the cosmic history of star formation (see Sect. 1.4). This region was subsequently observed at many different wavelengths by several telescopes as we will detail in Sect. 3.3.

To test the isotropy and homogeneity of the Universe, another region of the sky was observed in 1998 October, this time in the southern hemisphere, the Hubble Deep Field-South (HDF-S; RA = 22h 32m 56.22s and declination of  $-60^\circ 33' 02.69''$ ), in a program similar to the northern Hubble Deep Field (Williams et al., 2000; Ferguson et al., 2000). One of the many results of this comparative analysis was to show that these two fields are qualitatively similar (Casertano et al., 2000).

The GOODS fields (GOODS-North and GOODS-*South*) are successors and extensions of the Hubble Deep Field (HDF). The launch of the Spitzer space telescope in 2003 allowed us to observe much larger fields. While the GOODS-North field is a direct extension of the HDF, the GOODS-*South* field was chosen to be part of the Chandra Deep Field South (CDF-S). This field was observed by the Chandra X-ray observatory (Weisskopf et al., 1996), centered at RA 3h 32m 28.0s DEC  $-27^\circ 48' 30''$  (J2000.0) (Giacconi et al., 2000, 2001, 2002) and was chosen for its low

Galactic extinction, containing no stars brighter than  $m_v \sim 14$  and being well located, such that this field is accessible to observations with 8 m class telescopes such as the VLT and Gemini (Gi-acconi et al., 2002). Because Milky Way gas did not make ideal observations in HDF-S for both VLT and X-observations with Chandra, another field was chosen, the GOODS-South field. The GOODS-South field is therefore centered on the Chandra Deep Field South.

This corresponds to the period of the Great Observatories four telescopes that were launched between 1990 and 2003 to observe the sky at four different wavelengths (see Fig. 3.1). The Hubble Space Telescope (HST) observes at optical, near ultraviolet and (since 1997 with the installation of the new WFC3 camera), in near infrared. The Compton Gamma Ray Observatory (CGRO) captured gamma-ray (and later, hard x-ray) emission. We can observe the infrared with the Spitzer Space Telescope (SST), and X-ray emission with the Chandra X-ray Observatory (CXO).

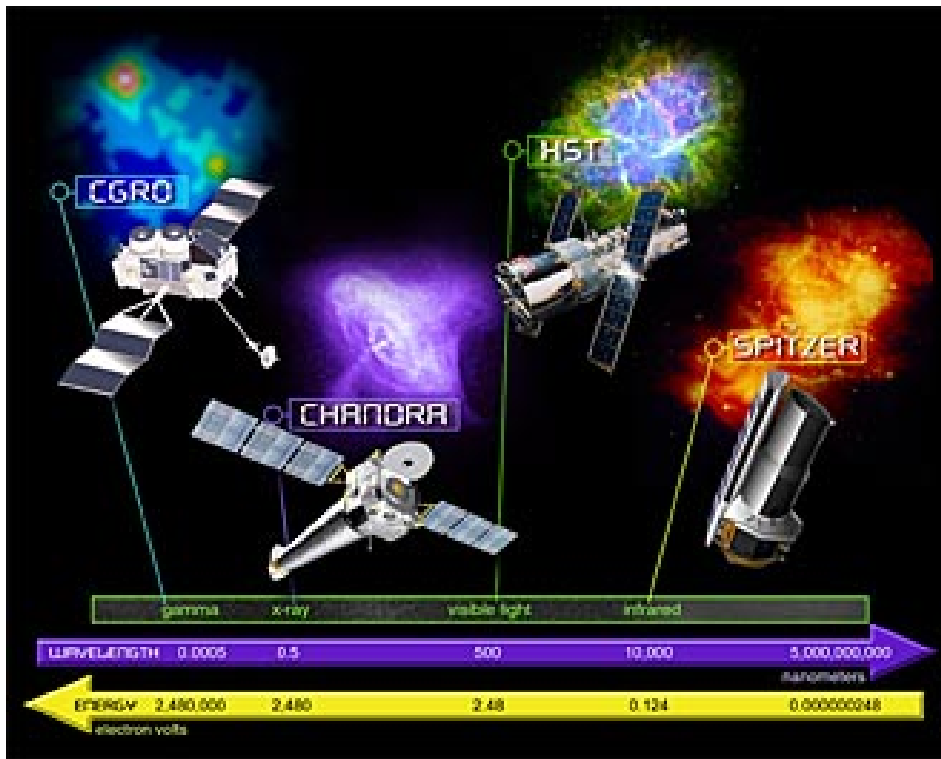


FIGURE 3.1: Representation of the four great observatories. These space-based telescopes were launched by NASA to observe the sky at different wavelengths (visible, gamma-ray, X-ray, and infrared). From left to right, the Compton Gamma Ray Observatory (CGRO) the Chandra X-ray Observatory, the Hubble Space Telescope (HST) and the Spitzer Space Telescope. Credit: NASA ([http://www.nasa.gov/images/content/90950main\\_Observatories.jpg](http://www.nasa.gov/images/content/90950main_Observatories.jpg))

The GOODS-South field is also part of a larger program, The Cosmic Assembly Near-infrared Deep Extragalactic Legacy Survey (CANDELS, Koekemoer et al. (2011); Grogin et al. (2011)). This program was presented at an August 2013 press conference<sup>1</sup> as "the largest project in the history of Hubble". The CANDELS program, which includes five deep fields (GOODS-South, GOODS-North, COSMOS, EGS and UDS), will be briefly presented in the next section.

1. <https://www.spacetelescope.org/news/heic1315/>

## 3.2 CANDELS

This large survey, 902-orbit Multi-Cycle Treasury (MCT) was designed, among other things, to probe the evolution of galaxies and black holes at  $z \sim 1.5\text{--}8$ , to have several observations of galaxies in the reionization era (“cosmic dawn”), study the growth and morphological transformation of galaxies, measure supernova rate evolution and test Type Ia supernovae to determine if they can be used as standard candles for cosmological use, to investigate the role and transformation induced by active galactic nucleus (AGN) activity and understand how star formation proceeds and how galaxies quench at  $z > 2$  (Grogin et al., 2011). The focus of the observation of the five CANDELS fields was to use the brand new HST/WFC3 camera that was installed on Hubble in May 2009. This new camera, which allows us to reach extremely distant objects, is associated with HST/ACS in order to benefit from multi-wavelength coverage from optical to near infrared, covering a surface of about 800 arcmin<sup>2</sup> (Guo et al., 2013). The five CANDELS fields that are located in both the southern and northern celestial hemisphere include:

- The central part of the Cosmic Evolution Survey (COSMOS, Scoville et al. 2007) centered at RA=150.116321°, DEC +2.200973.
- UKIDSS-Ultra Deep Survey (UDS; Lawrence et al. 2007; Cirasuolo et al. 2007), centered at RA = 4.406250°, DEC = -5.2000000°
- The Extended Groth Strip (EGS; Davis et al. 2007, centered at RA = 214.825000°, DEC = +52.825000°
- The Great Observatories Origins Deep Survey (GOODS; Dickinson and GOODS Legacy Team 2001; Giavalisco et al. 2004). The GOODS program is divided into two fields, one in the northern part of the sky (GOODS–North) centered at RA = 189.228621°, DEC = +62.238572°, the other in the southern part (GOODS–South), centered at RA = 53.122751°, DEC = -27.805089°.

To summarize, the CANDELS survey can be divided in two parts, ordered by depth in  $H$ -band: deep regions (CANDELS/Deep;  $5\sigma$  point-source limit  $H = 27.7$  mag) within a part of the GOODS-North and GOODS-South ( $\sim 125$  arcmin<sup>2</sup>), and wider regions (CANDELS/Wide;  $5\sigma$  point-source limit  $H > 27$  mag) within the other part of the GOODS fields, COSMOS, UDS and EGS ( $\sim 675$  arcmin<sup>2</sup>). The details are a little more complex, with some of these fields themselves being split into wide and deep regions.

In total, more than 250 000 galaxies (Grogin et al., 2011) were detected in the CANDELS program. In the following, we will focus in detail on one of these five fields, the GOODS–South field, that was chosen to be observed by ALMA. We will first describe the multi-wavelength coverage, the characteristics of this field and then finish by presenting the GOODS-ALMA survey, its purpose and how the ALMA observations were made.

## 3.3 Multi-wavelength coverage

The area covered by the GOODS-ALMA survey is ideally located, in that it profits from ancillary data from some of the deepest sky surveys at infrared (IR), optical and X-ray wavelengths including the *Spitzer* Extended Deep Survey (Ashby et al., 2013), the GOODS–*Herschel* Survey (Elbaz et al., 2011), the *Chandra* Deep Field–South (Luo et al., 2017) and ultra-deep radio imaging with the VLA (Rujopakarn et al., 2016). In addition, the region covered by ALMA in this survey



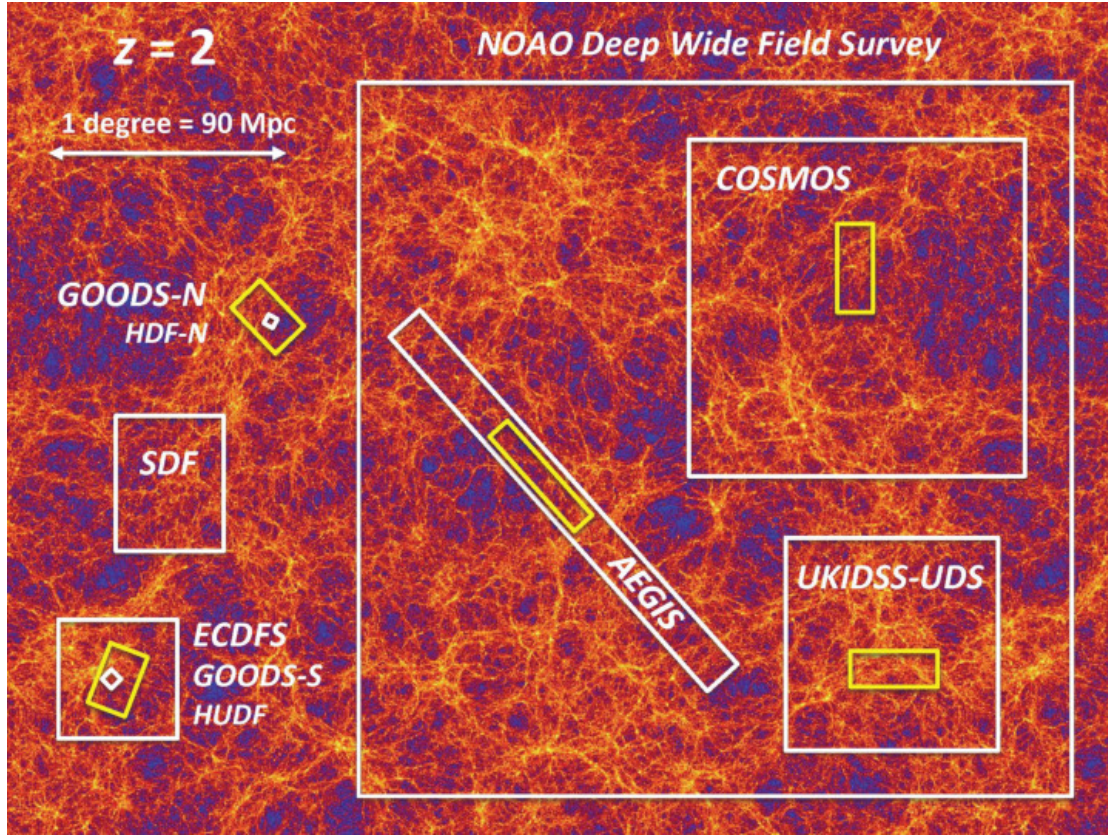


FIGURE 3.2: Relative sizes of some of the main large surveys. The yellow rectangles indicate the five CANDELS fields overlaid on a cosmological N-body simulation performed within the MultiDark project (see <http://www.multidark.org/MultiDark/>) viewed at  $z = 2$ . Figure from Madau and Dickinson (2014).

corresponds to the region with the deepest HST-WFC3 coverage, and has also been chosen for a guaranteed time observation (GTO) program with the James Webb Space Telescope (JWST).

In this section, we describe all of the data that were used in the analysis of the ALMA data.

### Optical/near-infrared imaging

We have supporting data from CANDELS; Grogan et al. 2011) with images obtained with the Wide Field Camera 3/infrared channel (WFC3/IR) and UVIS channel, along with the Advanced Camera for Surveys (ACS; Koekemoer et al. 2011). The area covered by this survey lies in the deep region of the CANDELS program (central one-third of the field). The  $5\text{-}\sigma$  detection depth for a point-source reaches a magnitude of 28.16 for the  $H_{160}$  filter (measured within a fixed aperture of  $0.17''$ ; Guo et al. 2013). The CANDELS/Deep program also provides images in 7 other bands: the  $Y_{125}$ ,  $J_{125}$ ,  $B_{435}$ ,  $V_{606}$ ,  $i_{775}$ ,  $i_{814}$  and  $z_{850}$  filters, reaching  $5\text{-}\sigma$  detection depths of 28.45, 28.35, 28.95, 29.35, 28.55, 28.84, and 28.77 mag respectively.

The Guo et al. (2013) catalog also includes galaxy magnitudes from the VLT, taken in the  $U$ -band with VIMOS (Nonino et al., 2009), and in the  $K_s$ -band with ISAAC (Retzlaff et al., 2010) and HAWK-I (Fontana et al., 2014).

In addition, we use data coming from the FourStar Galaxy Evolution Survey (ZFOURGE, PI: I. Labbé) on the 6.5 m Magellan Baade Telescope. The FourStar instrument (Persson et al., 2013) observed the CDFS (encompassing the GOODS–*South* Field) through 5 near-IR medium-bandwidth filters ( $J_1$ ,  $J_2$ ,  $J_3$ ,  $H_s$ ,  $H_l$ ) as well as broad-band  $K_s$ . By combination of the FourStar observations in the  $K_s$ -band and previous deep and ultra-deep surveys in the  $K$ -band, VLT/ISAAC/ $K$  (v2.0) from GOODS (Retzlaff et al., 2010), VLT/HAWK-I/ $K$  from HUGS (Fontana et al., 2014), CFHST/WIRCAM/ $K$  from TENIS (Hsieh et al., 2012) and Magellan/PANIC/ $K$  in HUDF (PI: I. Labbé), a super-deep detection image has been produced. The ZFOURGE catalog reaches a completeness greater than 80% to  $K_s < 25.3 - 25.9$  (Straatman et al., 2016).

We use the stellar masses and redshifts from the ZFOURGE catalog, except when spectroscopic redshifts are available. Stellar masses have been derived from Bruzual and Charlot (2003) models (Straatman et al., 2016) assuming exponentially declining star formation histories and a dust attenuation law as described by Calzetti et al. (2000).

### Mid/far-infrared imaging

Data in the mid and far-IR are provided by the Infrared Array Camera (IRAC; Fazio et al. 2004) at 3.6, 4.5, 5.8, and 8  $\mu\text{m}$ , *Spitzer* Multiband Imaging Photometer (MIPS; Rieke et al. 2004) at 24  $\mu\text{m}$ , *Herschel* Photodetector Array Camera and Spectrometer (PACS, Poglitsch et al. 2010) at 70, 100 and 160  $\mu\text{m}$ , and *Herschel* Spectral and Photometric Imaging REceiver (SPIRE, Griffin et al. 2010) at 250, 350, and 500  $\mu\text{m}$ .

The IRAC observations in the GOODS–*South* field were taken in February 2004 and August 2004 by the GOODS *Spitzer* Legacy project (PI: M. Dickinson). These data have been supplemented by the *Spitzer* Extended Deep Survey (SEDS; PI: G. Fazio) at 3.6 and 4.5  $\mu\text{m}$  (Ashby et al., 2013) as well as the *Spitzer*-Cosmic Assembly Near-Infrared Deep Extragalactic Survey (S-CANDELS; Ashby et al. 2015) and recently by the ultra-deep IRAC imaging at 3.6 and 4.5  $\mu\text{m}$  (Labbé et al., 2015).

The flux extraction and deblending in 24  $\mu\text{m}$  imaging have been provided by Magnelli et al. (2009) to reach a depth of  $S_{24} \sim 30 \mu\text{Jy}$ . *Herschel* images come from a 206.3 h GOODS–*South* observational program (Elbaz et al., 2011) and combined by Magnelli et al. (2013) with the PACS Evolutionary Probe (PEP) observations (Lutz et al., 2011). Because the SPIRE confusion limit is very high, we use the catalog of T. Wang et al. (in prep), which is built with a state-of-the-art de-blending method using optimal prior sources positions from 24  $\mu\text{m}$  and *Herschel* PACS detections.

### Complementary ALMA data

As the GOODS–*South* Field encompasses the Hubble Ultra Deep Field (HUDF), we take advantage of deep 1.3-mm ALMA data of the HUDF. The ALMA image of the full HUDF reaches a  $\sigma_{1.3\text{mm}} = 35 \mu\text{Jy}$  (Dunlop et al., 2017), over an area of 4.5 arcmin<sup>2</sup> that was observed using a 45-pointing mosaic at a tapered resolution of 0.7". These observations were taken in two separate periods from July to September 2014. In this region, 16 galaxies were detected by Dunlop et al. (2017), 3 of them with a high SNR (SNR > 14), the other 13 with lower SNRs ( $3.51 < \text{SNR} < 6.63$ ).

We also take advantage of the recent ALMA twenty-six arcmin<sup>2</sup> survey of GOODS-S at one-millimeter (ASAGAO). This survey reaches a depth of  $61 \mu\text{Jy beam}^{-1}$  in a tapered map with a beam of  $0''.51 \times 0''.45$ . The observations were made during the month of September 2016 (Project code: 2015.1.00098.S, PI: K. Kohno) at 1.2mm. This survey is composed of 9 sub-surveys, each one was covered by 90-pointing mosaic in a C40-6 array configuration. In total, 45 sources were detected in this survey (combined with the HUDF-ALMA survey described above) with an SNR  $> 4.5$ .

### Radio imaging

We also use radio imaging at 5 cm from the Karl G. Jansky Very Large Array (VLA). These data were observed during 2014 March - 2015 September for a total of 177 hours in the A, B, and C configurations (PI: W. Rujopakarn). The images have a  $0''.31 \times 0''.61$  synthesized beam and an rms noise at the pointing centre of  $0.32 \mu\text{Jy.beam}^{-1}$  (Rujopakarn et al., 2016). Here, 179 galaxies were detected with a significance greater than  $3\sigma$  over an area of 61 arcmin<sup>2</sup> around the HUDF field, with a rms sensitivity better than  $1 \mu\text{Jy.beam}^{-1}$ . However, this radio survey does not cover the entire ALMA area presented in this paper. We also use an other radio imaging at 10cm, also from the Karl G. Jansky Very Large Array (VLA; PI: W. Rujopakarn, private communication). This radio image, centered on the Hubble Ultra Deep Field (HUDF) encompasses the entire GOODS-ALMA field and was observed for a total of 177 hours (configurations A, B, & C) to reach a depth of  $\sigma_{rms} = 0.32 \mu\text{Jy/beam}$  with a resolution of  $\sim 0.3''$ .

### X-ray

The *Chandra* Deep Field-South (CDF-S) was observed for 7 Msec between 2014 June and 2016 March. These observations cover a total area of 484.2 arcmin<sup>2</sup>, offset by just  $32''$  from the centre of our survey, in three X-ray bands: 0.5-7.0 keV, 0.5-2.0 keV, and 2-7 keV (Luo et al., 2017). The average flux limits over the central region are  $1.9 \times 10^{-17}$ ,  $6.4 \times 10^{-18}$ , and  $2.7 \times 10^{-17}$  erg cm<sup>-2</sup> s<sup>-1</sup> respectively. This survey enhances the previous X-ray catalogs in this field, the 4 Msec *Chandra* exposure (Xue et al., 2011) and the 3 Msec XMM-Newton exposure (Ranalli et al., 2013). We will use this X-ray catalog to identify candidate X-ray active galactic nuclei (AGN) among our ALMA detections.

### 3.3.1 Spectroscopic-survey

In addition, the GOODS-South field, or in some cases its deepest region, the HUDF, has been the target of several spectroscopic observations (e.g., Le Fèvre et al., 2004; Szokoly et al., 2004; Mignoli et al., 2005; Ravikumar et al., 2007; Cimatti et al., 2008; Vanzella et al., 2008; Popesso et al., 2009; Wuyts et al., 2009; Balestra et al., 2010; Silverman et al., 2010; Le Fèvre et al., 2013; Morris et al., 2015; Kriek et al., 2015; Momcheva et al., 2016; McLure et al., 2018; Urrutia et al., 2019). In total, there are more than 20,000 galaxies for which spectroscopic redshifts have been determined in the GOODS-South field, including about 7750 in the GOODS-ALMA field.

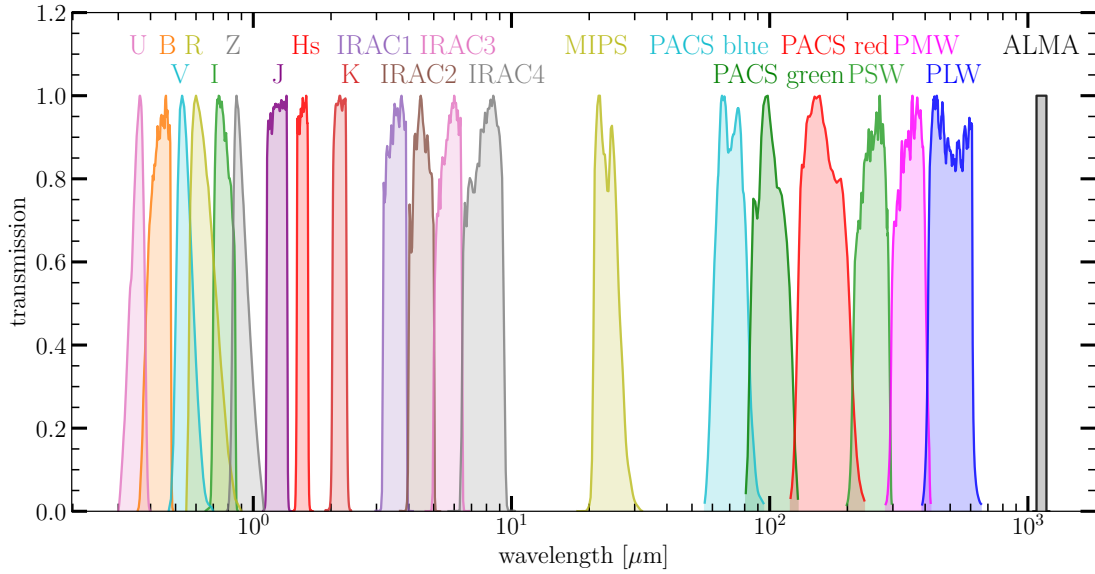


FIGURE 3.3: Transmission of UV to millimeter of some of the filters used in our study. All transmissions are normalized to 1.

z	0.5	1.0	1.5	2.2	3.0	4.0
$\log_{10}(M_*) [M_\odot]$	8.3	8.7	9.0	9.4	9.9	10.3

TABLE 3.1: Stellar mass above which the GOODS-South field is at least 90% complete (Schreiber et al., 2015).

catalog	# galaxies within GOODS-ALMA	filter	reference
CANDELS	16049	$H$	Guo et al. (2013)
ZFOURGE	11615	$K_s$	Straatman et al. (2016)
S-CANDELS	5572	IRAC ( $3.6\mu\text{m}$ )	Ashby et al. (2015)
GOODS-Herschel	764	PACS blue ( $70\mu\text{m}$ )	Elbaz et al. (2011)

TABLE 3.2: Main catalogs used. The number of galaxies listed in these catalogs, as well as the selection band and references used are also indicated.

### 3.3.2 Completeness

The mass completeness of the GOODS-South field with *Herschel* was studied by Schreiber et al. (2015). The results obtained in this study are reported in the Table 3.1. Completeness was obtained by generating a mock population with a given stellar mass, associating a brightness function with these galaxies and adding a Gaussian error. These results are on average 0.3 dex lower than the results of Pannella et al. (2015), who estimated the completeness using a stellar population model from Rodighiero et al. (2010).

Over the range of redshifts and stellar masses of our ALMA detections, the CANDELS catalog is 90% complete. We give the number of galaxies in some of the main catalogs in Table 3.2.





### 3.4 Survey presentation

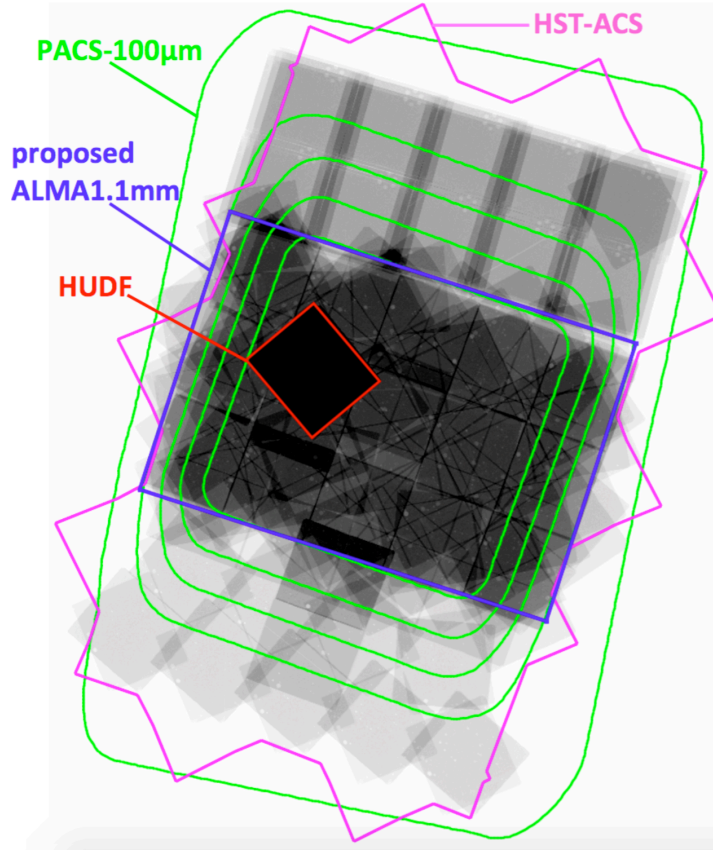


FIGURE 3.5:  $10' \times 6.8'$  ALMA 1.1mm survey (0.128 mJy-rms; blue rectangle) overlaid on HST-WFC3 coverage (greyscale) and matching the deep CANDELS WFC3 region. Green contours: GOODS-Herschel ultra deep survey spaced with 40% intervals starting from a  $100 \mu\text{m}$  rms of 0.17 mJy in the center. Red square :  $4 \text{ arcmin}^2$  ALMA HUDF 1.3mm survey (PI Dunlop). Pink polygon: HST-ACS borders.

Our ALMA coverage extends over an effective area of  $69 \text{ arcmin}^2$  within the GOODS-South field (Fig. 4.3), centred at  $\alpha = 3^{\text{h}} 32^{\text{m}} 30.0^{\text{s}}$ ,  $\delta = -27^\circ 48' 00''$  (J2000; 2015.1.00543.S; PI: D. Elbaz). To cover this  $\sim 10' \times 7'$  region (comoving scale of  $15.1 \text{ Mpc} \times 10.5 \text{ Mpc}$  at  $z = 2$ ), we designed a 846-pointing mosaic, each pointing being separated by 0.8 times the antenna Half Power Beam Width (i.e. HPBW  $\sim 23''3$ ).

To accommodate such a large number of pointings within the ALMA Cycle 3 observing mode restrictions, we divided this mosaic into six parallel, slightly overlapping, sub-mosaics of 141 pointing each. To get a homogeneous pattern over the 846 pointings, we computed the offsets between the sub-mosaics so that they connect with each other without breaking the hexagonal pattern of the ALMA mosaics.

Each sub-mosaic (or slice) has a length of 6.8 arcmin, a width of 1.5 arcmin and an inclination (PA) of 70 deg (see Fig. 4.3). This required three execution blocks (EBs), yielding a total on-source integration time of  $\sim 60$  seconds per pointing (Table 3.6). We determined that the highest frequencies of the band 6 is the optimal setup for a continuum survey and we thus set the ALMA correlator to Time Division Multiplexing (TDM) mode and optimised the setup for continuum detection at 264.9 GHz ( $\lambda = 1.13 \text{ mm}$ ) using four 1875 MHz-wide spectral windows centered at

Name	Effective wavelength ( $\mu\text{m}$ )	$5\sigma$ limiting depth (AB)	PSF FWHM (arcsec)	Instrument
$U_{VIMOS}$	0.3722	27.97	0.8	VLT/VIMOS
$WFI_{U38}$	0.373	26	1	ESODepPublicSurvey
IA427	0.427	25.01	1.01	Subaru/Suprime-Cam
F435W	0.4317	28.95	0.08	HST/ACS
IA445	0.445	25.18	1.23	Subaru/Suprime-Cam
IA464	0.464	24.38	1.79	Subaru/Suprime-Cam
IA484	0.484	26.22	0.76	Subaru/Suprime-Cam
IA505	0.505	25.29	0.94	Subaru/Suprime-Cam
IA527	0.5259	26.18	0.83	Subaru/Suprime-Cam
IA550	0.55	25.45	1.13	Subaru/Suprime-Cam
IA574	0.5763	25.16	0.95	Subaru/Suprime-Cam
F606W	0.5918	29.35	0.08	HST/ACS
IA598	0.6007	26.05	0.63	Subaru/Suprime-Cam
IA624	0.6231	25.91	0.61	Subaru/Suprime-Cam
$R_{VIMOS}$	0.6443	27.5	0.65	VLT/VIMOS
IA651	0.6498	26.14	0.6	Subaru/Suprime-Cam
IA679	0.6782	26.02	0.8	Subaru/Suprime-Cam
IA709	0.709	24.52	1.6	Subaru/Suprime-Cam
IA738	0.7359	25.93	0.77	Subaru/Suprime-Cam
IA767	0.7682	24.92	0.7	Subaru/Suprime-Cam
F775W	0.7693	28.55	0.08	HST/ACS
$WFI_V$	0.793	26	1	ESODepPublicSurvey
IA797	0.7966	24.69	0.68	Subaru/Suprime-Cam
F814W	0.8047	28.84	0.09	HST/ACS
IA827	0.827	23.6	1.69	Subaru/Suprime-Cam
IA856	0.8565	24.41	0.67	Subaru/Suprime-Cam
$WFI_B$	0.871	26.1	1	ESODepPublicSurvey
F850LP	0.9055	28.55	0.09	HST/ACS
F098M	0.9851	28.77	0.13	HST/WFC3
J1	1.054	25.6	0.59	Fourstar/ZFOURGE
F105W	1.055	28.45	0.15	HST/WFC3
J2	1.1448	25.5	0.62	Fourstar/ZFOURGE
NB118	1.18	25.2	0.55	Fourstar
F125W	1.2486	28.34	0.16	HST/WFC3
J3	1.2802	25.5	0.56	Fourstar/ZFOURGE
$WFI_R$	1.502	26.1	1	ESODepPublicSurvey
F160W	1.537	28.16	0.17	HST/WFC3
Hs	1.5544	24.9	0.6	Fourstar/ZFOURGE
Hl	1.702	25	0.5	Fourstar/ZFOURGE
NB209	2.09	24.8	0.55	Fourstar
$K_s$	2.1538	24.8	0.46	Fourstar/ZFOURGE
IRAC1	3.5569	26.5	1.66	Spitzer/IRAC
IRAC2	4.502	26.5	1.72	Spitzer/IRAC
IRAC3	5.745	23.75	1.88	Spitzer/IRAC
IRAC4	7.9158	23.72	1.98	Spitzer/IRAC
MIPS	24	16.514	0.02	Spitzer/MIPS
PACS blue	70	16.514	1	Herschel/PACS
PACS green	100	16.642	6.7	Herschel/PACS
PACS red	160	15.449	11	Herschel/PACS
PSW	250	14.287	18.1	Herschel/SPIRE
PMW	350	14.212	24.9	Herschel/SPIRE
PLW	500	13.615	36.6	Herschel/SPIRE
ALMA	1130	16.547	0.6	ALMA/Band6

TABLE 3.3: Details of the filter characteristics used in this survey from UV to millimeter wave-length. The PSF FWHM of ALMA corresponds to the tapered image used in this work. The effective wavelength is computed as  $\sqrt{(\int S(\lambda)\lambda d\lambda)/(\int S(\lambda)\lambda^{-1}d\lambda)}$  (Tokunaga and Vacca, 2005).

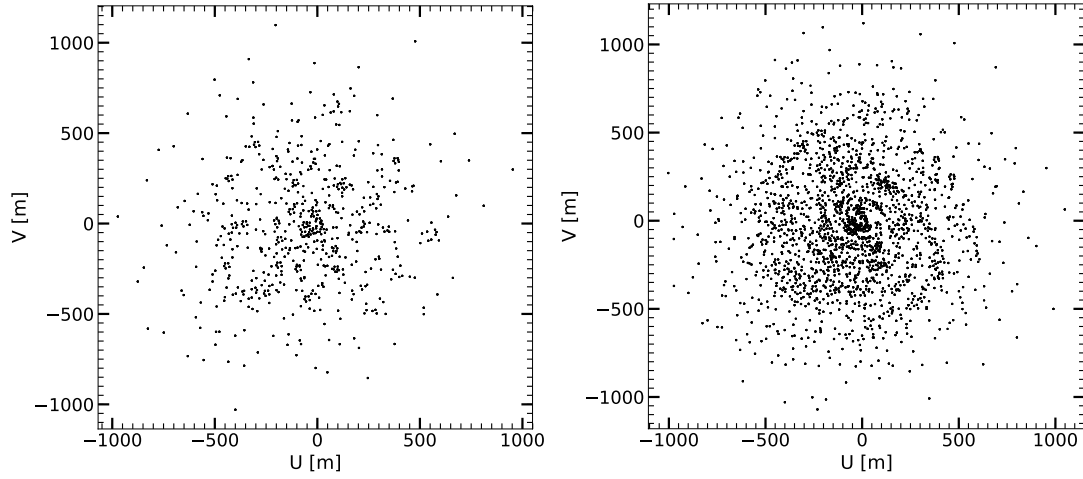


FIGURE 3.6: uv-coverage of one of the 846 ALMA pointings constituting this survey. We show the uv-coverage for one pointing, left panel as well as for all 846 pointings, right panel. This uv-coverage allows us to perform the source detection in the dirty map.

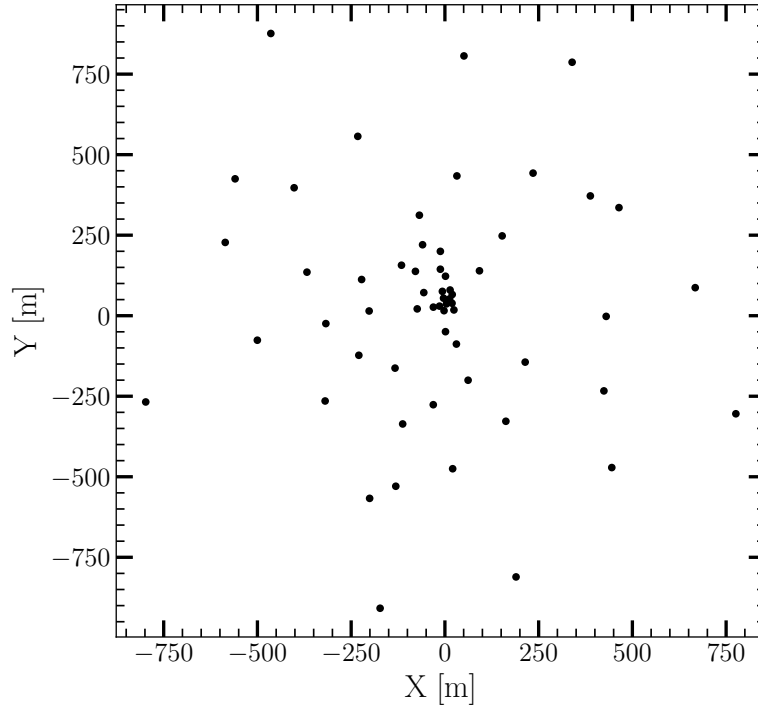


FIGURE 3.7: Antenna position during our survey. ALMA was in C40-5 configuration with a minimum baseline of 16.7 m and a maximum baseline of  $\sim 1200$  m.



255.9 GHz, 257.9 GHz, 271.9 GHz and 273.9 GHz, covering a total bandwidth of 7.5 GHz (see Fig. 3.8).

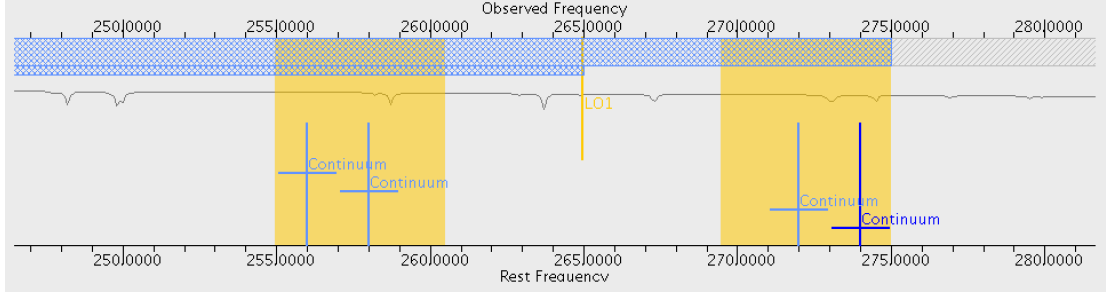


FIGURE 3.8: Spectral visualizer set with the parameters of our survey. The Local Oscillator (LO1) frequency is shown with a yellow line at the middle of the image at a frequency of 264.9 GHz. The bandwidth of the four spectral windows at 255.9 GHz, 257.9 GHz, 271.9 GHz and 273.9 GHz are represented with blue line within the sideband in yellow. The atmospheric transmission curve is also display in gray.

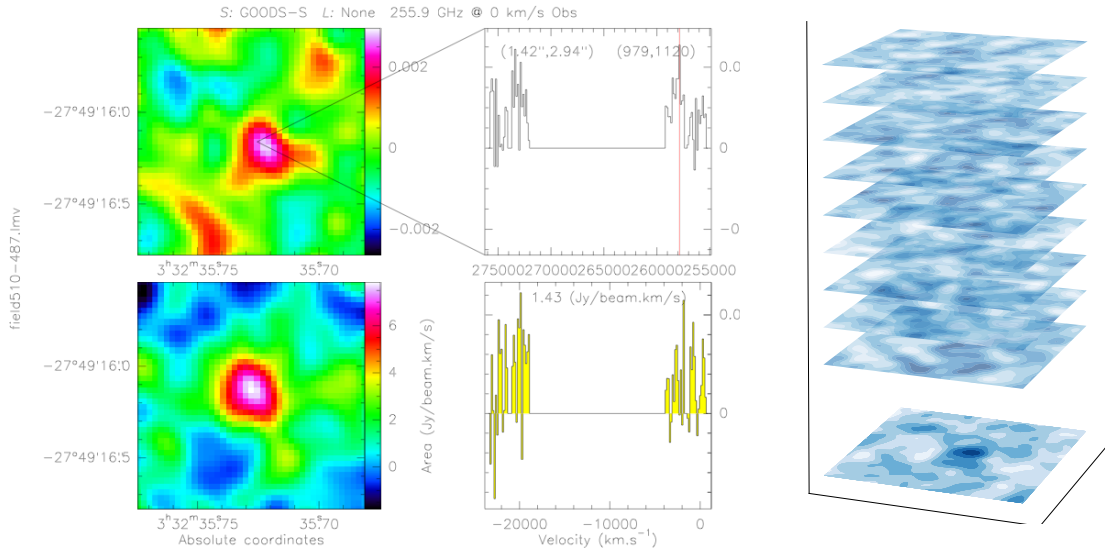


FIGURE 3.9: Left panel: illustration of a detection in the stacked continuum map, bottom part while the detection is displayed in a random channel in the top part. Middle panel: visualization of the spectrum of the detection. Right panel: illustration of the stacking process, to produce the image in the continuum. All the individual channels are summed together to produce the continuum map.

The TDM mode has 128 channels per spectral window, providing us with  $\sim 37$  km/s velocity channels. We illustrate, in Fig. 3.9 a source in the continuum image (bottom left image) as well as in a random channel (top left image). The spectrum of this detection is given on the central panel while an illustration of the stacking process, to produce the image in the continuum, is presented in Fig. 3.9, right panel. We also used these channels to investigate whether we could detect an emission line. This search did not reveal the presence of an emission line among our detections.

Observations were taken between the 1<sup>st</sup> of August and the 2<sup>nd</sup> of September 2016, using  $\sim 40$  antennae (see Table 3.6) in configuration C40-5 with a maximum baseline of  $\sim 1500$  m. J0334-4008 and J0348-2749 (VLBA calibrator and hence has a highly precise position) were systematically used as flux and phase calibrators, respectively. In 14 EBs, J0522-3627 was used as

bandpass calibrator, while in the remaining 4 EBs J0238+1636 was used. Observations were taken under nominal weather conditions with a typical precipitable water vapour of  $\sim 1$  mm.

### 3.4.1 Data reduction

All EBs were calibrated with CASA (McMullin et al., 2007) using the scripts provided by the ALMA project. Calibrated visibilities were systematically inspected and few additional flaggings were added to the original calibration scripts. Flux calibrations were validated by verifying the accuracy of our phase and bandpass calibrator flux density estimations.

Finally, to reduce computational time for the forthcoming continuum imaging, we time- and frequency-averaged our calibrated EBs over 120 seconds and 8 channels, respectively. Imaging was done in CASA using the multi-frequency synthesis algorithm implemented within the task CLEAN. Sub-mosaics were produced separately and combined subsequently using a weighted mean based on their noise maps. As each sub-mosaic was observed at different epochs and under different weather conditions, they exhibit different synthesized beams and sensitivities (Table 3.6). Sub-mosaics were produced and primary beam corrected separately, to finally be combined using a weighted mean based on their noise maps.

To obtain a relatively homogeneous and circular synthesized beam across our final mosaic, we applied different  $u$ ,  $v$  tapers to each sub-mosaic. The best balance between spatial resolution and sensitivity was found with a homogeneous and circular synthesized beam of  $0''.29$  Full Width Half Maximum (FWHM; hereafter  $0''.29$ -mosaic; Table 3.6). This resolution corresponds to the highest resolution for which a circular beam can be synthesized for the full mosaic.

We also applied this tapering method to create a second mosaic with an homogeneous and circular synthesized beam of  $0''.60$  FWHM (hereafter  $0''.60$ -mosaic; Table 3.6), i.e., optimised for the detection of extended sources. Mosaics with even coarser spatial resolution could not be created because of drastic sensitivity and synthesized beam shape degradations.

Due to the good coverage in the  $uv$ -plane (see Fig. 3.6) and because the sources present in our image do not cover a large dynamic range in flux densities (see Sect. 4.3), the lobes of our dirty beams do not carry significant amounts of flux (see Fig. 4.8). To prevent any bias generated by the CLEAN process, we decided to work with the dirty map. We have cleaned all maps imaged at the original beam size to test the possible gain that would result from the cleaning process. The noise in these clean maps is not significantly better ( $< 1\%$ ), suggesting that indeed it is not necessary to clean these maps. In Fig. 3.10, we show the clean (left panel) as well as the dirty beam (right panel).

## 3.5 Mosaic

The GOODS-ALMA field was observed by ALMA over a continuous area of  $\sim 70$  arcmin<sup>2</sup> via a mosaic of 846 pointings (see Fig. 3.13). The antenna half power beam width (HPBW) is:

$$\theta_{PB} = A \times \frac{\lambda}{D} \quad (3.1)$$

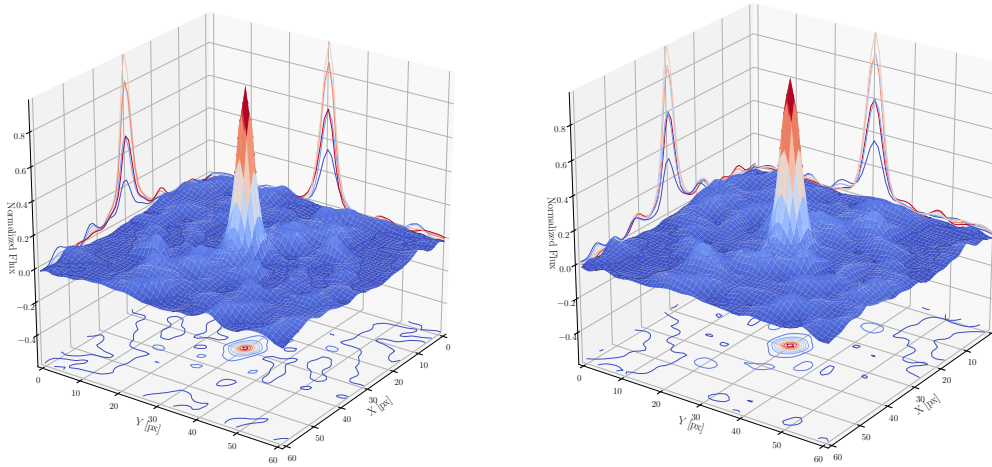


FIGURE 3.10: 3D representation of the clean beam (left panel) and dirty beam (right panel). The projection of these beams according to each of the dimensions is also represented. Because the clean and the dirty beam are very similar and in order to prevent any bias generated by the CLEAN process, we decided to work with the dirty map.

with  $\lambda$  the observed wavelength and  $D$  the diameter of a single antenna. This field of view is therefore independent of the interferometer configuration. The factor  $A$  depends on the morphology of the observation instrument.  $A = 1.22$  for a single dish and less than 1.22 for an interferometer. In our configuration, with a wavelength of 1.13 mm and an antenna diameter of 12 m, the HPBW is  $\sim 23.3''$ .

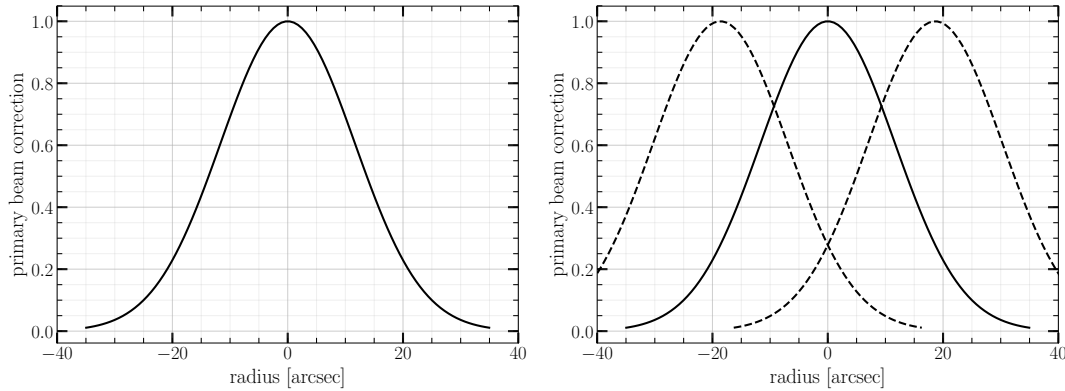


FIGURE 3.11

The [Ekers and Rots \(1979\)](#) theorem tell us that an interferometer does not just measure the angular scale

$$\theta = \lambda/b \quad (3.2)$$

with  $b$  the length of a baseline (distance between 2 antennas); but the interferometer can also measures all the angular scales

$$\lambda/(b + D) < \theta < \lambda/(b - D) \quad (3.3)$$

with  $D$  the diameter of an antenna. A few years later, [Cornwell \(1988\)](#) understands that the Ekers theorem allows an interferometer to perform wide-field imaging ([Pety and Rodríguez-Fernández, 2010](#)). There is a decrease in sensitivity when you move away from the centre of the pointing (see Fig. 3.11). A primary beam correction was applied after the mosaic was created to compensate for this decrease in sensitivity and make the sensitivity uniform over the entire surface. The sensitivity of a mosaic also depends on the position and spacing of the different pointings. There are different patterns to form a mosaic. The most commonly used are the organization of pointings in rectangular grid or hexagonal grid (see Fig. 3.12).

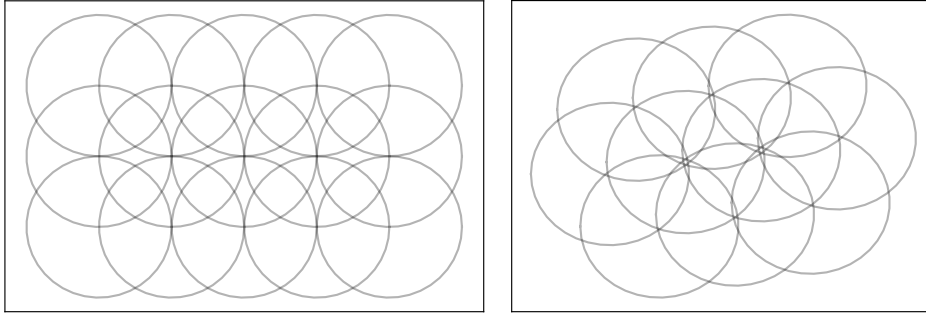


FIGURE 3.12: Example of different patterns to create a mosaic. Left panel: rectangular grid. The separation between the center of two pointings is  $\lambda/2D$  to meet the Nyquist sampling criteria. Right panel: Hexagonal grid. In this configuration the distance between 2 pointings is  $\lambda/(\sqrt{3}D)$ . This last configuration requires more pointings to cover the same area as a rectangular grid but ensures a sensitivity close to the uniform universe.

For rectangular paving, the distance between the center of two pointings is  $\lambda/2D$  to meet the sampling criterion of [Nyquist \(1928\)](#). For hexagonal paving, the distance between the center and two pointings is  $\lambda/(\sqrt{3}D)$ . The pointings are therefore closer to each other, so more pointings are needed to cover the same area as for a rectangular grid. A hexagonal grid ensures a sensitivity close to the uniform with a minimum number of pointings ([ALMA Partnership et al., 2016](#)). According to [Cornwell \(1988\)](#), it is theoretically the optimal sampling of a field.

ALMA imposes a limitation on the number of pointings per observation block. The total number of pointings must be less than or equal to 150. 846 pointing is required to fully map the deepest part of the CANDELS program in GOODS-South, so this region has been divided into 6 slices containing 141 pointings (see Fig. 3.13).

The next generation of telescopes and (sub)millimeter survey will make it possible to get rid of these combinations of pointings by allowing continuous observations to be made directly by the On-The-Fly observing mode.

## 3.6 Noise map

### 3.6.1 Building of the noise map

We build the RMS-map of the ALMA survey by a  $k\text{-}\sigma$  clipping method. This method can be applied when the pixel distribution is Gaussian (or almost Gaussian), centered on zeros and when the sources are relatively punctual. It is also a very effective method to remove all outliers from an image such as cosmic rays [Akhlaghi and Ichikawa \(2015\)](#). This method is iterative, for each

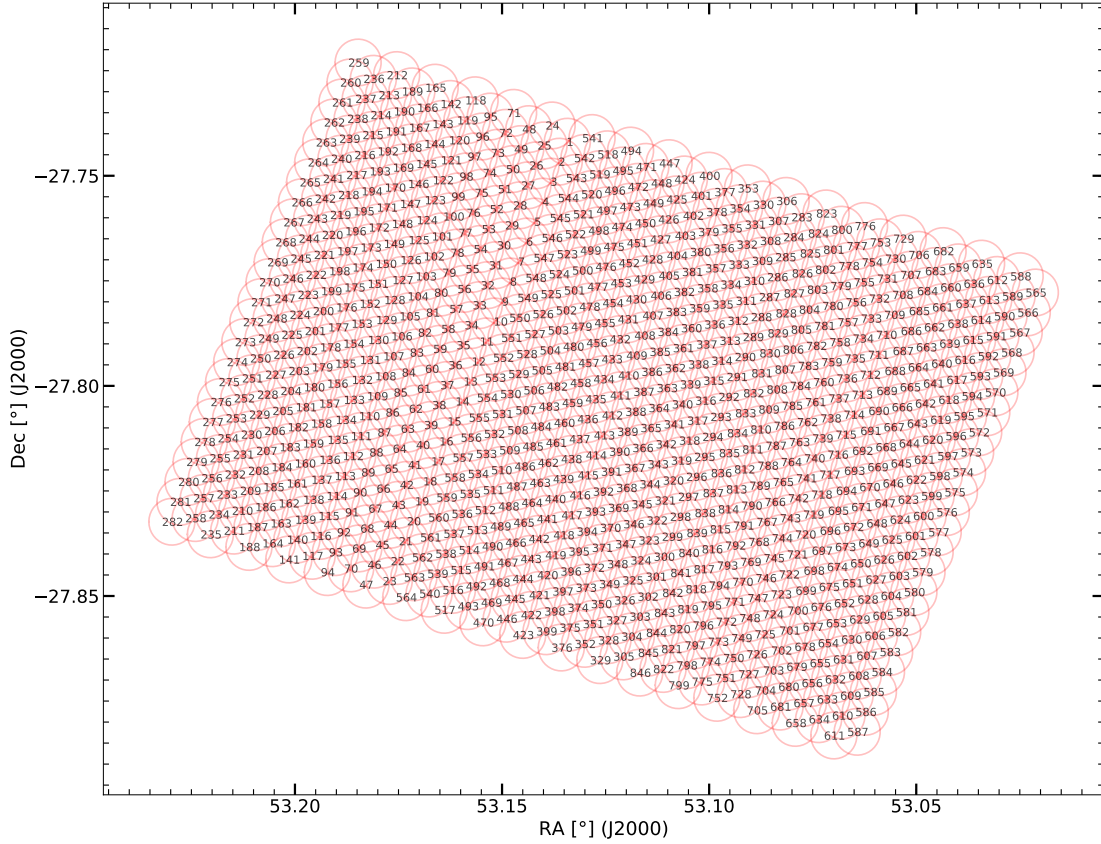


FIGURE 3.13: Distribution of the 846 pointings composing the GOODS-ALMA image according to a hexagon configuration. Each pointing has an antenna Half Power Beam width  $\sim 23.3''$  and are separated by 0.8 times the HPBW.

pixel of our image, we calculate the standard deviation ( $\sigma$ ) and median ( $m$ ) of all pixels contained in a square centered on the central pixel. The size of the region to be taken into account was determined by performing a series of tests. We calculated the median of the standard deviations as a function of the size of the region considered (see Fig. 3.14 and Table 3.4). We wanted to find the smallest region to best respect local variations in image sensitivity and be as accurate as possible, large enough that this region would not be affected by sources that might be present. In the end a size of  $100 \times 100$  pixels was chosen from the map tapered at  $0.60''$  (the pixel size is  $0.1''$ ).

The pixels, inside this box, with values greater than 3 times the standard deviation ( $\sigma$ ) from the median value were masked. This procedure was repeated 3 times unless the exit criteria is reached before then. One of the classic criteria used is to set a threshold beyond which the iterative process stops. We did not use this exit criterion but another one: if the standard deviation in step  $n+1$  is greater than or equal to the standard deviation in step  $n$ , the process stops.

In steps of 4 pixels on the image map, the standard deviation was computed in a square of  $100 \times 100$  pixels around the central pixel. The pixels, inside this box, with values greater than 3 times the standard deviation ( $\sigma$ ) from the median value were masked. This procedure was repeated 3 times. Finally, we assign the value of the standard deviation of the non-masked pixels to the central pixel. The step of 4 pixels corresponds to a sub-sampling of the beam so, the noise should not vary significantly on this scale. The median value of the standard deviation is

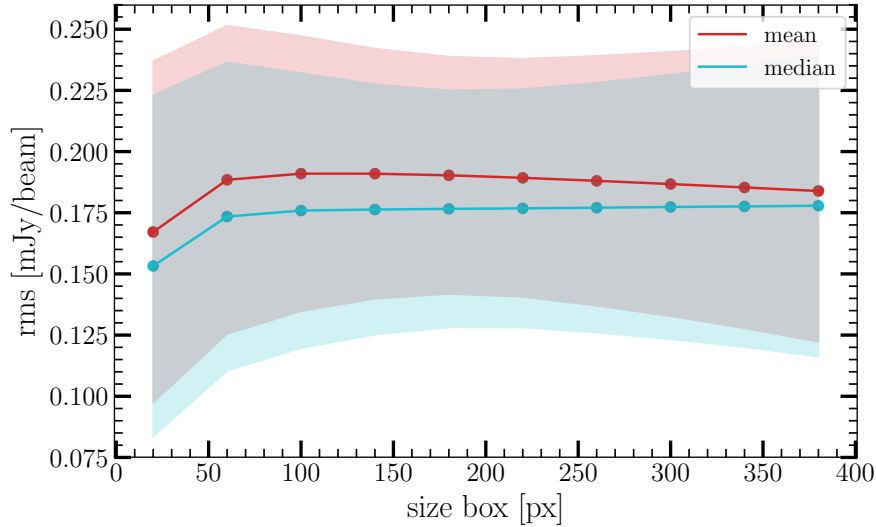


FIGURE 3.14: Measurement of the average of the rms (red line) and the median of the rms (blue line) according to the size of the measured area. The grey areas represent the standard deviation of the measurement. The size of the chosen area is 100 pixels. This corresponds to the smallest possible area (which takes better into account the spatial variations of the noise map) for which the rms stops increasing. The rms map converges to the typical value of the noise in the ALMA map while taking into account the local variation of noise

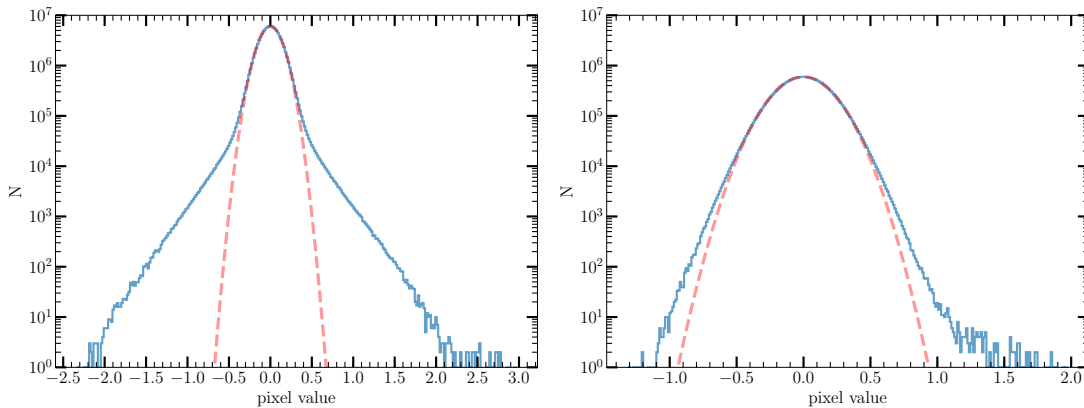


FIGURE 3.15: Distribution of flux density of the signal map at two different resolution 0.29'' in the left panel and 0.60'' in the right panel. While the S/N distribution is practically Gaussian, except at high SN, for detections (see Fig. 4.1, the pixel distribution is not Gaussian at low or high signal.

$0.176 \text{ mJy.beam}^{-1}$ . In comparison, the Gaussian fit of the unclipped map gives a standard deviation of  $0.182 \text{ mJy.beam}^{-1}$ . We adopt a general value of rms sensitivity  $\sigma = 0.18 \text{ mJy.beam}^{-1}$ . The average values for the  $0''.29$ -mosaic and the untapered mosaic are given in Table 3.6.

### 3.6.2 Sampling Theorem

To ensure that the information contained in the uv plane is not lost when the image is created, the pixel size has been carefully chosen. The pixel size must satisfy the Nyquist criteria (Nyquist, 1928) demonstrated a few years later by Shannon (Shannon, 1949)<sup>2</sup>

2. The sampling theorem is often called Nyquist–Shannon sampling theorem but similar results had been demonstrated independently by Whittaker (1915); Kotelnikov (1933); Raabe (1939); Gabor (1946); Someya (1949).



size box	mean	median
20	$0.167 \pm 0.070$	$0.153 \pm 0.070$
60	$0.188 \pm 0.063$	$0.173 \pm 0.063$
100	$0.191 \pm 0.056$	$0.176 \pm 0.056$
140	$0.191 \pm 0.051$	$0.176 \pm 0.051$
180	$0.190 \pm 0.048$	$0.177 \pm 0.048$
220	$0.189 \pm 0.049$	$0.177 \pm 0.049$
260	$0.188 \pm 0.051$	$0.177 \pm 0.051$
300	$0.187 \pm 0.054$	$0.177 \pm 0.054$
340	$0.185 \pm 0.058$	$0.178 \pm 0.058$
380	$0.184 \pm 0.062$	$0.178 \pm 0.062$

TABLE 3.4: Quantification of the effect of the change the size of the selected area on the average and median noise when creating the noise map.

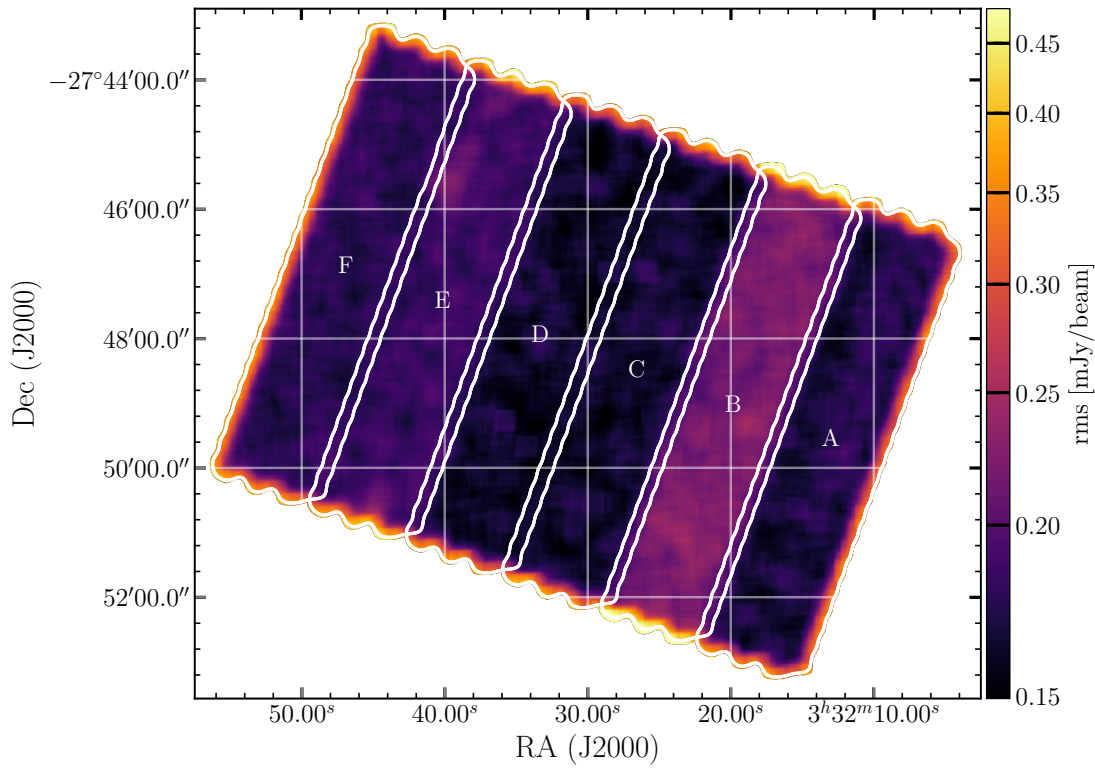


FIGURE 3.16: Noise map for the image tapered at  $0.6''$ , created by  $\sigma$  clipping method. With the exception of slice B, which has a higher average noise than the others ( $224 \mu\text{Jy}$ ), the average noise of the other slices is between  $164$  and  $186 \mu\text{Jy}$  (see Table 3.6). The edge of the noise map does not benefit from the overlapping of several pointings and has a higher noise level than the rest of the map. In the analysis of the image tapered at  $0.6''$ , areas located on the edge and having a noise greater than  $0.3 \text{ mJy.beam}^{-1}$  will not be taken into account.

The pixel size in the image plane must therefore be at most half of the synthesized beam size and satisfy the following equation:

$$\Delta l < \frac{1}{2u_{\max}} \quad \Delta m < \frac{1}{2v_{\max}} \quad (3.4)$$

In practice, to ease deconvolution the image must be created with a sampling greater than the

resolution	native	0"25	0"29	0"60
number of independent beams	14 154 380	9 027 437	6 692 225	1 536 162
statistical spurious detections ( $3\sigma$ )	19 107	12 186	9 034	2 074
statistical spurious detections ( $4\sigma$ )	448	286	212	49
statistical spurious detections ( $5\sigma$ )	4	3	2	0

TABLE 3.5: Number of statistical spurious as a function of the depth for different resolutions. The results have been rounded to the nearest unit.

Nyquist's criteria. [Felli and Spencer \(1989\)](#) for example, recommend choosing a pixel size so that there is 3 to 5 pixels across the FWHM. The pixel size chosen was therefore 0"1 for the 0"60 mosaic and 0"05 for the 0"29 mosaic and 0"05 for the untapered image.

### 3.6.3 Tapering

We have produced maps with different levels of tapering, in other words, apodize the  $(u,v)$  sampling by a Gaussian:

$$W(u, v) = \exp \left\{ -\frac{(u^2 + v^2)}{t^2} \right\} \quad (3.5)$$

with  $t$  the tapering parameter.

The use of tapering will considerably increase the detectability of an extended source. On the other hand, the spatial resolution is also degraded.

The tapering in our survey will allow both: (i) to reduce the number of independent beams; (ii) to prevent the resolution of extended sources.

The reduction in the number of beams induced by a purely statistical effect reduces the number of spurious detections. This is what we illustrated in the Table 3.5. If we set our detection threshold at  $4\sigma$ , we expect 39 false detections in the image tapered at 0.60" while we can have 170 in the map at 0.60". However, by tapering our map, we also degrade the sensitivity of our detections:  $4\sigma$  corresponds on average to 0.47mJy in the map at 0.29", while it corresponds to 0.73mJy in the map at 0.60". We will discuss in detail, in the Sect. 4.3 the delicate balance to be found between reducing the number of spurious sources and the desire to have as complete a catalog as possible.

The tapering also allows to reveal extended sources that would have been missing in the map at 0.29". In Fig. 3.17, we show the example of two sources, the top line shows AGS18. This is the most extended source of our main catalog (see Sect. 4.3), it is neither detected in the untapered image nor in the mosaic at 0.29". On the other hand, the AGS3 source, which is a compact source, is detected at all resolutions. The size of this source in the image will be very similar to the size of the beam.



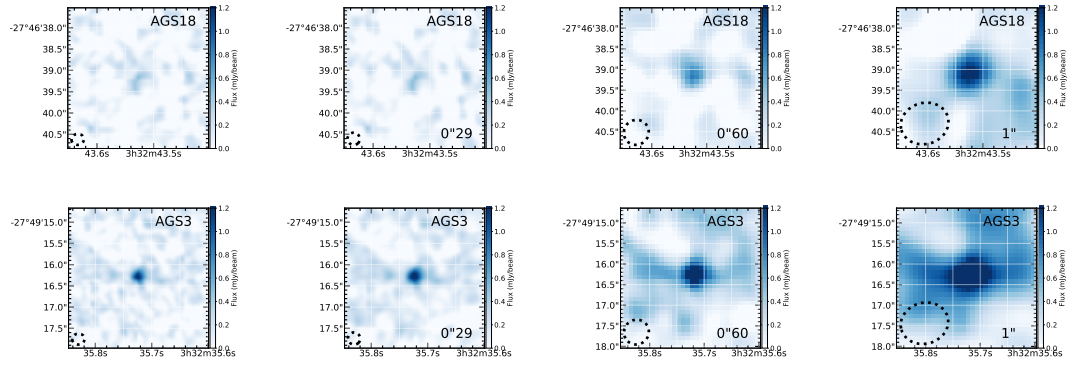


FIGURE 3.17: Example of two sources AGS18 on the top line and AGS3 on the bottom line at different resolutions. From left to right, untapered image, image tapered at 0.29'', 0.60'' and 1''. The color scale has been fixed to better visualize the effects of tapering. The beam size is indicated for each resolution with a dotted black line. AGS18 is the most extended source of our main catalog (see Sect. 4.3) while AGS3 is the most compact source.

Slice	Date	#	t on target min	total t min	Original Mosaic		0''29-Mosaic		0''60-Mosaic	
					Beam mas $\times$ mas	$\sigma$ $\mu\text{Jybeam}^{-1}$	Beam mas $\times$ mas	$\sigma$ $\mu\text{Jybeam}^{-1}$	Beam mas $\times$ mas	$\sigma$ $\mu\text{Jybeam}^{-1}$
A	August 17	42	46.52	72.12						
	August 31	39	50.36	86.76	240 $\times$ 200	98	297 $\times$ 281	108	618 $\times$ 583	171
	August 31	39	46.61	72.54						
B	September 1	38	46.87	72.08						
	September 1	38	48.16	72.48	206 $\times$ 184	113	296 $\times$ 285	134	614 $\times$ 591	224
	September 2	39	46.66	75.06						
C	August 16	37	46.54	73.94						
	August 16	37	46.54	71.58	243 $\times$ 231	102	295 $\times$ 288	107	608 $\times$ 593	166
	August 27	42	46.52	74.19						
D	August 16	37	46.54	71.69						
	August 27	44	46.52	72.00	257 $\times$ 231	107	292 $\times$ 289	111	612 $\times$ 582	164
	August 27	44	46.52	72.08						
E	August 01	39	46.54	71.84						
	August 01	39	46.53	72.20	285 $\times$ 259	123	292 $\times$ 286	124	619 $\times$ 588	186
	August 02	40	46.53	74.46						
F	August 02	40	46.53	72.04						
	August 02	41	46.53	71.61	293 $\times$ 256	118	292 $\times$ 284	120	613 $\times$ 582	178
	August 02	39	46.53	71.55						
Mean		40	46.86	73.35	254 $\times$ 227	110	294 $\times$ 286	117	614 $\times$ 587	182
Total			843.55	1320.22						

TABLE 3.6: Summary of the observations. The slice ID, the date, the number of antennae, the time on target, the total time (time on target + calibration time), the resolution and the 1- $\sigma$  noise of the slice are given.



# CHAPTER 4

## CREATION OF THE ALMA SOURCE CATALOG

### Contents

3.1 Historical context . . . . .	35
3.2 CANDELS . . . . .	37
3.3 Multi-wavelength coverage . . . . .	37
3.4 Survey presentation . . . . .	43
3.5 Mosaic . . . . .	47
3.6 Noise map . . . . .	49

From the mosaic and noise map, described in the previous chapter, we will present in this chapter the way we have proceeded to detect sources. We wanted to create a blind catalog, i.e., without being biased by information from other wavelengths in order to be able to include sources that would have been missed during previous surveys, for example with the HST.

In this Chapter, we will explain how we determined the threshold of detectability that allowed us to obtain the best compromise between the number of detections and the lowest possible number of spurious sources. We will then present the methods used to calculate the flux of galaxies. Finally, from the counterparts to which we have associated these sources, we will investigate some properties of our galaxies such as redshift and mass distributions. We will see that some of these galaxies do not have optical counterparts and devote Chapter 7 to these HST-dark galaxies.

### 4.1 Source Detection

The search for faint sources in high-resolution images with moderate source densities faces a major limitation. At the native resolution ( $0''.25 \times 0''.23$ ), the untapered ALMA mosaic encompasses almost four million independent beams, where the beam area is  $A_{beam} = \pi \times \text{FWHM}^2 / (4 \ln(2))$ <sup>1</sup>. It results that a search for sources above a detection threshold of  $4\sigma$  would include as many as 130 spurious sources assuming a Gaussian statistics. Identifying the real sources from such catalog is not possible knowing that the total number of sources is  $\sim 200$ . In order to increase the detection quality to a level that ensures a purity greater than 80% – in other words, the excess of sources in the original mosaic needs to be five times greater than the number of detections in the mosaic multiplied by (-1) – we have decided to use a tapered image and adapt the detection threshold accordingly.

By reducing the weight of the signal originating from the most peripheral ALMA antennae, the tapering reduces the angular resolution hence the number of independent beams. The lower

1. The Beam Area is given by  $A_{beam} = 2 \times \pi \times \sigma^2$ . For a 2-D gaussian,  $\text{FWHM} = 2\sigma \sqrt{2 \ln(2)}$ . By combining these two equations, we obtain the formula set out above.

angular resolution presents the advantage of optimizing the sensitivity to point sources – we recall that  $0''.24$  corresponds to a proper size of only 2 kpc at  $z \sim 1-3$  – and therefore will result in an enhancement of the signal-to-noise ratio for the sources larger than the resolution.

We chose to taper the image with a homogeneous and circular synthesized beam of  $0''.60$  FWHM – corresponding to a proper size of 5 kpc at  $z \sim 1-3$  – having tested various kernels and finding that this beam was optimized for our mosaic, avoiding both a beam degradation and a too heavy loss of sensitivity. This tapering reduces by nearly an order of magnitude the number of spurious sources expected at a  $4\text{-}\sigma$  level down to about 19 out of 600 000 independent beams. However, we will check in a second step whether we may have missed in the process some compact sources by also analyzing the  $0''.29$  tapered map.

We also excluded the edges of the mosaic, where the standard deviation is larger than  $0.30 \text{ mJy.beam}^{-1}$  in the  $0''.60$ -mosaic. The effective area was thus reduced by 4.9% as compared to the full mosaic ( $69.46 \text{ arcmin}^2$  out of  $72.83 \text{ arcmin}^2$ ).

To identify the galaxies present on the image, we used BLOBCAT (Hales et al., 2012). BLOBCAT is a source extraction software using a "flood fill" algorithm to detect and catalog blobs (see Hales et al. 2012). A blob is defined by two criteria:

- at least one pixel has to be above a threshold ( $\sigma_p$ )
- all the adjacent surrounding pixels must be above a floodclip threshold ( $\sigma_f$ )

where  $\sigma_p$  and  $\sigma_f$  are defined in number of  $\sigma$ , the local RMS of the mosaic.

A first guess to determine the detection threshold  $\sigma_p$  is provided by the examination of the pixel distribution of the signal to noise map (S/N-map). The S/N-map has been created by dividing the  $0''.60$  tapered map by the noise map. Fig. 4.1 shows that the S/N-map follows an almost perfect Gaussian below  $S/N = 4.2$ . Above this threshold, a significant difference can be observed that is characteristic of the excess of positive signal expected in the presence of real sources in the image. However, this histogram alone cannot be used to estimate a number of sources because the pixels inside one beam are not independent of one another. Hence although the non-Gaussian behavior appears around  $S/N = 4.2$  we performed simulations to determine the optimal values of  $\sigma_p$  and  $\sigma_f$ .

## 4.2 Threshold determination

We first conducted positive and negative – on the continuum map multiplied by (-1) – detection analysis for a range of  $\sigma_p$  and  $\sigma_f$  values ranging from  $\sigma_p = 4$  to 6 and  $\sigma_f = 2.5$  to 4 with intervals of 0.05 and imposing each time  $\sigma_p \geq \sigma_f$ . The difference between positive and negative detections for each pair of  $(\sigma_p, \sigma_f)$  values provides the expected number of real sources.

We then searched for the pair of threshold parameters offering the best compromise between (i) providing the maximum number of detections, and (ii) minimizing the number of spurious sources. The later purity criterion,  $p_c$ , is defined as:

$$p_c = \frac{N_p - N_n}{N_p} \quad (4.1)$$

where  $N_p$  and  $N_n$  are the numbers of positive and negative detections respectively. To ensure a purity of 80% as discussed above, we enforced  $p_c \geq 0.8$ . This led to  $\sigma_p = 4.8 \sigma$  when fixing

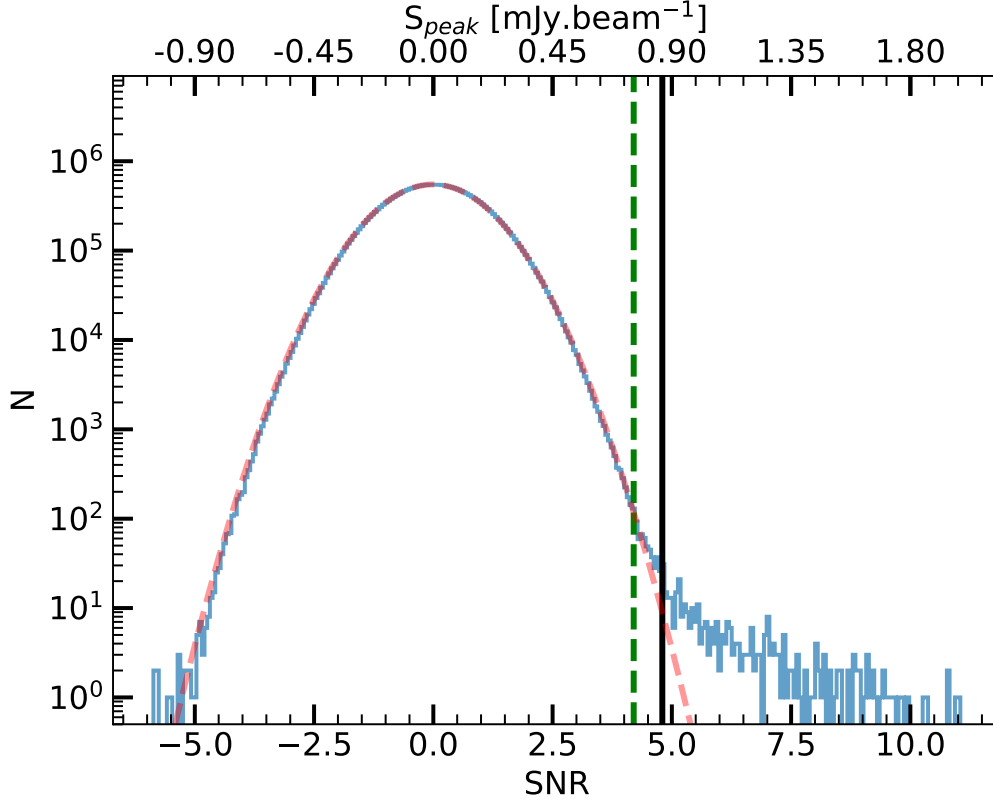


FIGURE 4.1: Histogram of pixels of the signal to noise map, where pixels with noise  $> 0.3 \text{ mJy.beam}^{-1}$  have been removed. The red dashed line is the best Gaussian fit. The green dashed line is indicative and shows where the pixel brightness distribution moves away from the Gaussian fit. This is also the  $4.2\sigma$  level corresponding to a peak flux of  $0.76 \text{ mJy}$  for a typical noise per beam of  $0.18 \text{ mJy}$ . The solid black line corresponds to our peak threshold of  $4.8\sigma$  ( $0.86 \text{ mJy}$ ).

the value of  $\sigma_f = 2.7\sigma$  (see Fig. 4.2-left). Below  $\sigma_p = 4.8\sigma$ , the purity criterion rapidly drops below 80% whereas above this value it only mildly rises. Fixing  $\sigma_p = 4.8\sigma$ , the purity remains roughly constant at  $\sim 80 \pm 5\%$  when varying  $\sigma_f$ . We did see an increase in the difference between the number of positive and negative detections with increasing  $\sigma_f$ . However, the size of the sources above  $\sigma_f = 2.7\sigma$  drops below the  $0''.60$  FWHM and tends to become pixel-like, hence non physical. This is because an increase of  $\sigma_f$  results in a reduction of the number of pixels above the floodclip threshold ( $\sigma_f$ ) that will be associated with a given source. This parameter can be seen as a percolation criterion that sets the size of the sources in a number of pixels. Reversely reducing  $\sigma_f$  below  $2.7\sigma$  results in adding more noise than signal and a reduction in the number of detections. We therefore decided to set  $\sigma_f$  to  $2.7\sigma$ .

While we did not wish to impose a criterion on the existence of optical counterparts to define our ALMA catalog, we found that high values of  $\sigma_f$  not only generate the problem discussed above, but also generate a rapid drop of the fraction of ALMA detections with an HST counterpart in the Guo et al. (2013) catalog,  $p_{HST} = N_{HST}/N_p$ .  $N_{HST}$  is the number of ALMA sources with an HST counterpart within  $0''.60$  (corresponding to the size of the beam). The fraction falls rapidly from around  $\sim 80\%$  to  $\sim 60\%$ , which we interpreted as being due to a rise of the proportion of spurious sources, since the faintest optical sources, for example, detected by HST-WFC3, are not necessarily associated with the faintest ALMA sources due to the negative K-correction at  $1.1 \text{ mm}$ . This rapid drop can be seen in the dashed green and dotted pink lines of Fig. 4.2-right.

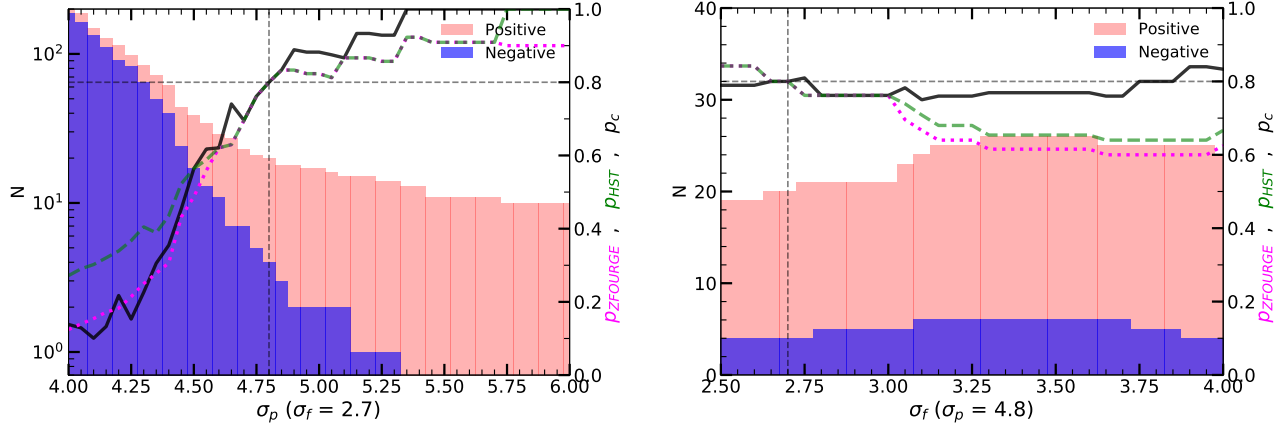


FIGURE 4.2: Cumulative number of positive (red histogram) and negative (blue histogram) detections as a function of the  $\sigma_p$  (at a fixed  $\sigma_f$ , left panel) and  $\sigma_f$  (at a fixed  $\sigma_p$ , right panel) in units of  $\sigma$ . Solid black line represents the purity criterion  $p_c$  define by Eq. 6.1, green dashed-line represents the percentage of positive detection with HST-WFC3 counterpart  $p_{HST}$  and magenta dashed-line represents the percentage of positive detection with ZFOURGE counterpart  $p_{ZFOURGE}$ . Gray dashed-lines show the thresholds  $\sigma_p = 4.8 \sigma$  and  $\sigma_f = 2.7 \sigma$  and the 80% purity limit.

This confirms that the sources that are added to our catalog with a floodclip threshold greater than  $2.7 \sigma$  are most probably spurious. Similarly, we can see in Fig. 4.2-left that increasing the number of ALMA detections to fainter flux densities by reducing  $\sigma_p$  below  $4.8 \sigma$  leads to a rapid drop of the fraction of ALMA detections with an HST counterpart. Again there is no well-established physical reason to expect the number of ALMA detections with an optical counterpart to decrease with decreasing S/N ratio in the ALMA catalog.

As a result, we decided to set  $\sigma_p = 4.8 \sigma$  and  $\sigma_f = 2.7 \sigma$  to produce our catalog of ALMA detections. We note that we only discussed the existence of HST counterparts as a complementary test on the definition of the detection thresholds but our approach is not set to limit in any way our ALMA detections to galaxies with HST counterparts.

Indeed, evidence for the existence of ALMA detections with no HST-WFC3 counterparts already exist in the literature. Wang et al. (2016) identified *H*-dropouts galaxies, that is galaxies detected above the *H*-band with *Spitzer*-IRAC at  $4.5 \mu\text{m}$  but undetected in the *H*-band and in the optical. The median flux density of these galaxies is  $F_{870\mu\text{m}} \simeq 1.6 \text{ mJy}$  (Wang et al., in prep.). By scaling this median value to our wavelength of  $1.1 \text{ mm}$  (the details of this computation are given in Sect. 5.7), we obtain a flux density of  $0.9 \text{ mJy}$ , close to the typical flux of our detections (median flux  $\sim 1 \text{ mJy}$ , see Table 4.2).

### 4.3 Creation of the catalog

Using the optimal parameters of  $\sigma_p = 4.8 \sigma$  and  $\sigma_f = 2.7 \sigma$  described in Sect. 4.1 & 4.2, we obtained a total of 20 detections down to a flux density limit of  $S_{1.1\text{mm}} \approx 880 \mu\text{Jy}$  that constitute our main catalog. These detections are listed in Fig. 4.3, sorted by decreasing S/N. The comparison of negative and positive detections suggests the presence of  $4 \pm 2$  (assuming a Poissonian uncertainty on the difference between the number of positive and negative detections) spurious sources in this sample.

In the following, we assume that the galaxies detected in the  $0''.60$ -mosaic are point-like. This hypothesis will later be discussed and justified in Sect. 4.6.1. In order to check the robustness of our flux density measurements, we compared different flux extraction methods and softwares: PyBDSM (Mohan and Rafferty, 2015); Galfit (Peng et al., 2010); Blobcat (Hales et al., 2012). The peak flux value determined by Blobcat refers to the peak of the surface brightness corrected for peak bias (see Hales et al. 2012). The different results were consistent, with a median ratio of  $F_{peak}^{Blobcat}/F_{peak}^{PyBDSM} = 1.04 \pm 0.20$  and  $F_{peak}^{Blobcat}/F_{PSF}^{Galfit} = 0.93 \pm 0.20$ . The fluxes measured using psf-fitting (Galfit) and peak flux measurement (Blobcat) for each galaxy are listed in Table 4.2. We also ran CASA *fitsky* and a simple aperture photometry corrected for the ALMA PSF and also found consistent results. The psf-fitting with Galfit was performed inside a box of  $5 \times 5''$  centered on the source.

The main characteristics of these detections (redshift, flux, S/N, stellar mass, counterpart) are given in Table 4.2. We used redshifts and stellar masses from the ZFOURGE catalog (see Sect. 3.3).

We compared the presence of galaxies between the  $0''.60$ -mosaic and the  $0''.29$ -mosaic. Of the 20 detections found in the  $0''.60$  map, 14 of them are also detected in the  $0''.29$  map. The presence of a detection in both maps reinforces the plausibility of a detection. However, a detection in only one of these two maps may be a consequence of the intrinsic source size. An extended source is more likely to be detected with a larger beam, whereas a more compact source is more likely to be missed in the maps with larger tapered sizes and reduced point source sensitivity.

A first method to identify potential false detections was to compare our results with a deeper survey overlapping with our area of the sky. We compared the positions of our catalog sources with the positions of sources found by Dunlop et al. (2017) in the HUDF. This 1.3-mm image is deeper than our survey and reaches a  $\sigma \simeq 35 \mu\text{Jy}$  (corresponding to  $\sigma = 52 \mu\text{Jy}$  at 1.1mm) but overlaps with only  $\sim 6.5\%$  of our survey area. The final sample of Dunlop et al. (2017) was compiled by selecting sources with  $S_{1.3} > 120 \mu\text{Jy}$  to avoid including spurious sources due to the large number of beams in the mosaics and due to their choice of including only ALMA detections with optical counterparts seen with HST.

With our flux density limit of  $S_{1.1mm} \approx 880 \mu\text{Jy}$  any non-spurious detection should be associated with a source seen at 1.3mm in the HUDF, the impact of the wavelength difference being much smaller than this ratio. We detected three galaxies in the HUDF, that were also detected by Dunlop et al. (2017), UDF1, UDF2 and UDF3, all of which have  $S_{1.3mm} > 0.8 \text{ mJy}$ . The other galaxies detected by Dunlop et al. (2017) have a flux density at 1.3 mm lower than  $320 \mu\text{Jy}$ , which makes them undetectable with our sensitivity.

We note however that we did not impose as a strict criterion the existence of an optical counterpart to our detections, whereas Dunlop et al. (2017) did. Hence if we had detected a source with no optical counterpart within the HUDF, this source may not be included in the Dunlop et al. (2017) catalog. However, as we will see, the projected density of such sources is small and none of our candidate optically dark sources fall within the limited area of the HUDF. We also note that the presence of an HST-WFC3 source within a radius of  $0''.6$  does not necessarily imply that is the correct counterpart. As we will discuss in detail in Sect. 4.6, due to the depth of the HST-WFC3 observations and the large number of galaxies listed in the CANDELS catalog, a match between the HST and ALMA positions may be possible by chance alignment alone (see Sect. 4.6).



ID	ID <sub>CLS</sub>	ID <sub>ZF</sub>	RA <sub>ALMA</sub> deg	Dec <sub>ALMA</sub> deg	RA <sub>HST</sub> deg	Dec <sub>HST</sub> deg	$\Delta_{HST_1}$ arcsec	$\Delta_{HST_2}$ arcsec	$(\Delta\alpha)_{HST}$ arcsec	$(\Delta\delta)_{HST}$ arcsec	$\Delta_{IRAC}$ arcsec
(1)	(2)	(3)	(4)	(5)	(6)	(7)	(8)	(9)	(10)	(11)	(12)
AGS1	14876	17856	53.118815	-27.782889	53.118790	-27.782818	0.27	0.03	0.091	-0.278	0.16
AGS2	7139	10316	53.063867	-27.843792	53.063831	-27.843655	0.51	0.23	0.163	-0.269	0.04
AGS3	9834	13086	53.148839	-27.821192	53.148827	-27.821121	0.26	0.06	0.099	-0.262	0.10
AGS4	8923b	12333	53.142778	-27.827888	53.142844	-27.827890	0.21	0.40	0.087	-0.264	0.09
AGS5	20765	23898	53.158392	-27.733607	53.158345	-27.733485	0.46	0.13	0.087	-0.329	0.26
AGS6	15669	-	53.183458	-27.776654	53.183449	-27.776584	0.26	0.03	0.054	-0.267	0.40
AGS7	4854	7867	53.082738	-27.866577	53.082705	-27.866567	0.11	0.19	0.124	-0.225	0.03
AGS8	15261	18282	53.020356	-27.779905	53.020297	-27.779829	0.33	0.03	0.159	-0.275	0.20
AGS9	12016	15639	53.092844	-27.801330	53.092807	-27.801208	0.45	0.16	0.100	-0.276	0.18
AGS10	16972	19833	53.082118	-27.767299	53.081957	-27.767202	0.62	0.39	0.128	-0.300	0.40
AGS11	-	7589	53.108818	-27.869055	-	-	-	-	-	-	0.12
AGS12	15876	18701	53.160634	-27.776273	53.160594	-27.776129	0.53	0.28	0.076	-0.242	0.51
AGS13	16274	19033	53.131122	-27.773194	53.131080	-27.773108	0.34	0.05	0.087	-0.291	0.14
AGS14	-	-	53.223156	-27.826771	-	-	-	-	-	-	-
AGS15	3818b	6755	53.074847	-27.875880	53.074755	-27.875976	0.45	0.57	0.125	-0.195	0.12 <sup>1</sup>
AGS16	-	-	53.039724	-27.784557	-	-	-	-	-	-	-
AGS17	4414b	6964	53.079374	-27.870770	53.079327	-27.870781	0.16	0.27	0.122	-0.231	0.06
AGS18	15639	18645	53.181355	-27.777544	53.181364	-27.777501	0.16	0.12	0.043	-0.256	0.10
AGS19	-	-	53.108041	-27.813610	-	-	-	-	-	-	-
AGS20	9089	12416	53.092365	-27.826829	53.092381	-27.826828	0.05	0.29	0.116	-0.247	0.18
AGS21	6905	10152	53.070274	-27.845586	53.070230	-27.845533	0.24	0.06	0.143	-0.249	0.07
AGS22	28952	-	53.108695	-27.848332	53.108576	-27.848242	0.50	0.29	0.106	-0.226	-
AGS23	10954	14543	53.086623	-27.810272	53.086532	-27.810217	0.35	0.19	0.111	-0.263	0.16

TABLE 4.1: Details of the positional differences between ALMA and HST-WFC3 for our catalog of galaxies identified in the 1.1mm-continuum map. Columns: (1) Source ID; (2),(3) IDs of the HST-WFC3 (from the CANDELS catalog) and ZFOURGE counterparts of these detections (the cross correlations between ALMA and HST-WFC3 and between ALMA and ZFOURGE are discussed in Sect. 4.6). b indicates HST-WFC3 galaxies located in a radius of 0''/6 around the ALMA detection, although strong evidence presented in Sect. 7.3 suggests they are not the optical counterparts of our detections; (4), (5) RA and Dec of the sources in the ALMA image (J2000); (6), (7) Positions of HST-WFC3 *H*-band counterparts when applicable from Guo et al. (2013), (8), (9) Distances between the ALMA and HST source positions *before* ( $\Delta_{HST_1}$ ) and *after* ( $\Delta_{HST_2}$ ) applying the offset correction derived from the comparison with Pan-STARRS and GAIA; (10), (11) Offset to be applied to the HST source positions, which includes both the global systematic offset and the local offset; (12) Distance from the closest IRAC galaxy. <sup>1</sup> For AGS15 we used the distance given in the ZFOURGE catalog (see Sect. 7.3).

## 4.4 Supplementary catalog

After the completion of the main catalog, three sources that did not satisfy the criteria of the main catalog presented strong evidence of being robust detections. We therefore enlarged our catalog, in order to incorporate these sources into a supplementary catalog. These three sources are each detected using a combination of  $\sigma_p$  and  $\sigma_f$  giving a purity factor greater than 80%, whilst also ensuring the existence of an HST counterpart.

The galaxy AGS21 has a  $S/N = 5.83$  in the  $0''.29$  tapered map, but is not detected in the  $0''.60$  tapered map. The non-detection of this source is most likely caused by its size. Due to its dilution in the  $0''.60$ -mosaic, a very compact galaxy detected at  $5\sigma$  in the  $0''.29$ -mosaic map could be below the detection limit in the  $0''.60$ -mosaic. The ratio of the mean RMS of the two tapered maps is 1.56, meaning that for a point source of certain flux, a  $5.83\sigma$  measurement in the  $0''.29$ -mosaic becomes  $3.74\sigma$  in the  $0''.60$ -map.

The galaxy AGS22 has been detected with an  $S/N = 4.9$  in the  $0''.60$  tapered map ( $\sigma_p = 4.9$  and  $\sigma_f = 3.1$ ). With  $\sigma_p$  and  $\sigma_f$  values more stringent than the thresholds chosen for the main catalog, it may seem paradoxical that this source does not appear in the main catalog. With a floodclip criterion of  $2.7\sigma$ , this source would have an  $S/N$  just below 4.8, excluding it from the main catalog. This source is associated with a faint galaxy that has been detected by HST-WFC3 ( $ID_{CANDELS} = 28952$ ) at  $1.6\mu\text{m}$  ( $6.6\sigma$ ) at a position close to the ALMA detection ( $0''.28$ ). Significant flux has also been measured at  $1.25\mu\text{m}$  ( $3.6\sigma$ ) for this galaxy. In all of the other filters, the flux measurement is not significant ( $< 3\sigma$ ). Due to this lack of information, it has not been possible to compute its redshift. AGS22 is not detected in the  $0''.29$ -mosaic map with  $p_c > 0.8$ . The optical counterpart of this source has a low  $H$ -band magnitude ( $26.8 \pm 0.2$  AB), which corresponds to a range for which the [Guo et al. \(2013\)](#) catalog is no longer complete. This is the only galaxy (except the three galaxies most likely to be spurious: AGS14, AGS16 and AGS19) that has not been detected by IRAC (which could possibly be explained by a low stellar mass). The probability of the ALMA detection being spurious, within the association radius  $0''.6$  of a  $H$ -band source of this magnitude or brighter, is 5.5%. For these reasons, we did not consider it as spurious.

The galaxy AGS23 was detected in the  $0''.60$  map just below our threshold at  $4.8\sigma$ , with a combination  $\sigma_p = 4.6$  and  $\sigma_f = 2.9$  giving a purity criterion greater than 0.9. This detection is associated with an HST-WFC3 counterpart. It is for these two reasons that we include this galaxy in the supplementary catalog. The photometric redshift ( $z = 2.36$ ) and stellar mass ( $10^{11.26} M_\odot$ ) both reinforce the plausibility of this detection.

ID	z	S/N	$S_{\text{Blobcat}}^{\text{peak}}$ mJy	$f_{\text{deboost}}$	$S_{\text{PSF}}^{\text{GaFit}}$ mJy	$\log_{10} M_{\star}$ $M_{\odot}$	0'60	0'29	$S_{6\text{GHz}}$ $\mu\text{Jy}$	$L_X/10^{42}$ $\text{erg.s}^{-1}$	ID <sub>sub(mm)</sub>
(1)	(2)	(3)	(4)	(5)	(6)	(7)	(8)	(9)	(10)	(11)	(12)
AGS1	2.309	11.26	$1.90 \pm 0.20$	1.03	$1.99 \pm 0.15$	11.05	1	1	$18.38 \pm 0.71$	1.93	GS6, ASA1
AGS2	2.918	10.47	$1.99 \pm 0.22$	1.03	$2.13 \pm 0.15$	10.90	1	1	-	51.31	
AGS3	2.582	9.68	$1.84 \pm 0.21$	1.03	$2.19 \pm 0.15$	11.33	1	1	$19.84 \pm 0.93$	34.54	GS5, ASA2
AGS4	4.32	9.66	$1.72 \pm 0.20$	1.03	$1.69 \pm 0.18$	11.45	1	1	$8.64 \pm 0.77$	10.39	
AGS5	3.46	8.95	$1.56 \pm 0.19$	1.03	$1.40 \pm 0.18$	11.13	1	1	$14.32 \pm 1.05$	37.40	
AGS6	3.00	7.63	$1.27 \pm 0.18$	1.05	$1.26 \pm 0.16$	10.93	1	1	$9.02 \pm 0.57$	83.30	UDF1, ASA3
AGS7	3.29	7.26	$1.15 \pm 0.17$	1.05	$1.20 \pm 0.13$	11.43	1	1	-	24.00	
AGS8	1.95	7.10	$1.43 \pm 0.22$	1.05	$1.98 \pm 0.20$	11.53	1	1	-	3.46	LESS18
AGS9	3.847	6.19	$1.25 \pm 0.21$	1.05	$1.39 \pm 0.17$	10.70	1	1	$14.65 \pm 1.12$	-	
AGS10	2.41	6.10	$0.88 \pm 0.15$	1.06	$1.04 \pm 0.13$	11.32	1	1	-	2.80	
AGS11	4.82	5.71	$1.34 \pm 0.25$	1.08	$1.58 \pm 0.22$	10.55	1	1	-	-	
AGS12	2.543	5.42	$0.93 \pm 0.18$	1.10	$1.13 \pm 0.15$	10.72	1	1	$12.65 \pm 0.55$	4.53	UDF3, C1, ASA8
AGS13	2.225	5.41	$0.78 \pm 0.15$	1.10	$0.47 \pm 0.14$	11.40	1	0	$22.52 \pm 0.81$	13.88	ASA12
AGS14*	-	5.30	$0.86 \pm 0.17$	1.10	$1.17 \pm 0.15$	-	1	0	-	-	
AGS15	-	5.22	$0.80 \pm 0.16$	1.11	$0.64 \pm 0.15$	-	1	1	-	-	LESS34
AGS16*	-	5.05	$0.82 \pm 0.17$	1.12	$0.99 \pm 0.17$	-	1	0	-	-	
AGS17	-	5.01	$0.93 \pm 0.19^{\dagger}$	1.14	$1.37 \pm 0.18$	-	1	0	-	-	LESS10
AGS18	2.794	4.93	$0.85 \pm 0.18^{\dagger}$	1.15	$0.79 \pm 0.15$	11.01	1	0	$6.21 \pm 0.57$	-	UDF2, ASA6
AGS19*	-	4.83	$0.69 \pm 0.15$	1.16	$0.72 \pm 0.13$	-	1	0	-	-	
AGS20	2.73	4.81	$1.11 \pm 0.24$	1.16	$1.18 \pm 0.23$	10.76	1	1	$12.79 \pm 1.40$	4.02	
AGS21	3.76	5.83	$0.64 \pm 0.11$	1.07	$0.88 \pm 0.19$	10.63	0	1	-	19.68	
AGS22	-	4.90	$1.05 \pm 0.22$	1.15	$1.26 \pm 0.22$	-	1	0	-	-	
AGS23	2.36	4.68	$0.98 \pm 0.21$	1.19	$1.05 \pm 0.20$	11.26	1	0	-	-	

TABLE 4. 2: Details of the final sample of sources detected in the ALMA GOODS–South continuum map, from the primary catalog in the main part of the table and from the supplementary catalog below the solid line (see Sect. 4.3 and Sect. 4.4). Columns: (1) IDs of the sources as shown in Fig. 4.3. The sources are sorted by S/N. \* indicates galaxies that are most likely spurious (not detected at any other wavelength); (2) Redshifts from the ZFOURGE catalog. Spectroscopic redshifts are shown with three decimal places. As AGS6 is not listed in the ZFOURGE catalog, we used the redshift computed by Dunlop et al. (2017); (3) Signal to noise ratio of the detections in the 0'60 mosaic (except for AGS21). This S/N is computed using the flux from Blobcat and is corrected for peak bias; (4) Peak fluxes measured using Blobcat in the 0'60-mosaic image before de-boosting correction; (5) Deboosting factor; (6) Fluxes measured by PSF-fitting with GaFit in the 0'60-mosaic image before de-boosting correction; (7) Stellar masses from the ZFOURGE catalog; (8); (9) Flags for detection by Blobcat in the 0'60-mosaic and 0'29-mosaic images, where at least one combination of  $\sigma_p$  and  $\sigma_f$  gives a purity factor (Eq. 6.1) greater than 80%; (10) Flux for detection greater than  $3\sigma$  by VLA (5 cm). Some of these sources are visible in the VLA image but not detected with a threshold  $> 3\sigma$ . AGS8 and AGS16 are not in the field of the VLA survey; (11) Absorption-corrected intrinsic 0.5–7.0 keV luminosities. The X-ray luminosities have been corrected to account for the redshift difference between the redshifts provided in the catalog of Luo et al. (2017) and those used in the present table, when necessary. For this correction we used Eq. 1 from Alexander et al. (2003), and assuming a photon index of  $\Gamma = 2$ ; (12) Corresponding IDs for detections of the sources in previous (sub)millimeter ancillary data. UDF is for Hubble Ultra Deep Field survey (Dunlop et al., 2017) at 1.3 mm, C indicates the ALMA Spectroscopic Survey in the Hubble Ultra Deep Field (ASPECS) at 1.2 mm (Aravena et al., 2016), LESS indicates data at 870  $\mu\text{m}$  presented in Hodge et al. (2013), GS indicates data at 870  $\mu\text{m}$  presented in Elbaz et al. (2018), ASA indicates the ALMA 26 arcmin<sup>2</sup> Survey of GOODS-S at One-millimeter (ASAGAO). We also note the pointed observations of AGS1 presented in Barro et al. (2017), and those of AGS13 by Talia et al. (2018). For the two sources marked by a †, the hypothesis of a point-like source is no longer valid. We therefore apply correction factors of 2.3 and 1.7 to the peak flux values of AGS17 and AGS18 respectively, to take into account the extended flux emission of these sources.

## 4.5 Astrometric correction

The comparison of our ALMA detections with HST (Sect. 4.3) in the previous section was carried out after correcting for an astrometric offset, which we outline here. In order to perform the most rigorous counterpart identification and take advantage of the accuracy of ALMA, we carefully investigated the astrometry of our images. Before correction, the galaxy positions viewed by HST were systematically offset from the ALMA positions. This offset has already been identified in previous studies (e.g., [Maiolino et al., 2015](#); [Rujopakarn et al., 2016](#); [Dunlop et al., 2017](#)).

In order to quantify this effect, we compared the HST source positions with detections from the Panoramic Survey Telescope and Rapid Response System (Pan-STARRS). This survey has the double advantage to cover a large portion of the sky, notably the GOODS–*South* field, and to observe the sky at a wavelength similar to HST-WFC3. We used the Pan-STARRS DR1 catalog provided by [Flewelling et al. \(2016\)](#) and also included the corresponding regions issued from the GAIA DR1 ([Gaia Collaboration et al., 2016](#)). Cross-matching was done within a radius of  $0''.5$ . In order to minimize the number of false identifications, we subtracted the median offset between the two catalogs from the [Guo et al. \(2013\)](#) catalog positions, after the first round of matching. We iterated this process three times. In this way, 629 pairs were found over the GOODS–*South* field.

To correct for the median offset between the HST and ALMA images, the HST image coordinates needed to be corrected by  $-96 \pm 113$  mas in right ascension,  $\alpha$ , and  $261 \pm 125$  mas in declination,  $\delta$ , where the uncertainties correspond to the standard deviation of the 629 offset measurements. This offset is consistent with that found by [Rujopakarn et al. \(2016\)](#) of  $\Delta\alpha = -80 \pm 110$  mas and  $\Delta\delta = 260 \pm 130$  mas. The latter offsets were calculated by comparing the HST source positions with 2MASS and VLA positions. In all cases, it is the HST image that presents an offset, whereas ALMA, Pan-STARRS, GAIA, 2MASS and VLA are all in agreement. We therefore deduced that it is the astrometric solution used to build the HST mosaic that introduced this offset. We will discuss this offset in more detail Sect. 6.3. These local offsets are larger in the periphery of GOODS–*South* than in the center, and close to zero in the HUDF field. The local offsets can be considered as a distortion effect. The offsets listed in Table 4.1 include both effects, the global and local offsets. The separation between HST and ALMA detections before and after offset correction, and the individual offsets applied for each of the galaxies are indicated in Table 4.1 and can be visualized in Fig. 4.4. We applied the same offset corrections to the galaxies listed in the ZFOURGE catalog.

This accurate subtraction of the global systematic offset, as well as the local offset, does not however guarantee a perfect overlap between ALMA and HST emission. The location of the dust emission may not align perfectly with the starlight from a galaxy, due to the difference in ALMA and HST resolutions, as well as the physical offsets between dust and stellar emission that may exist. In Fig. 4.5, we show the ALMA contours ( $4$  to  $10\sigma$ ) overlaid on the F160W HST-WFC3 images after astrometric correction. In some cases (AGS1, AGS3, AGS6, AGS13, AGS21 for example), the position of the dust radiation matches that of the stellar emission; in other cases, (AGS4, AGS17 for example), a displacement appears between both two wavelengths. Finally, in some cases (AGS11, AGS14, AGS16, and AGS19) there are no optical counterparts. We will discuss the possible explanations for this in Sect. 7.3.

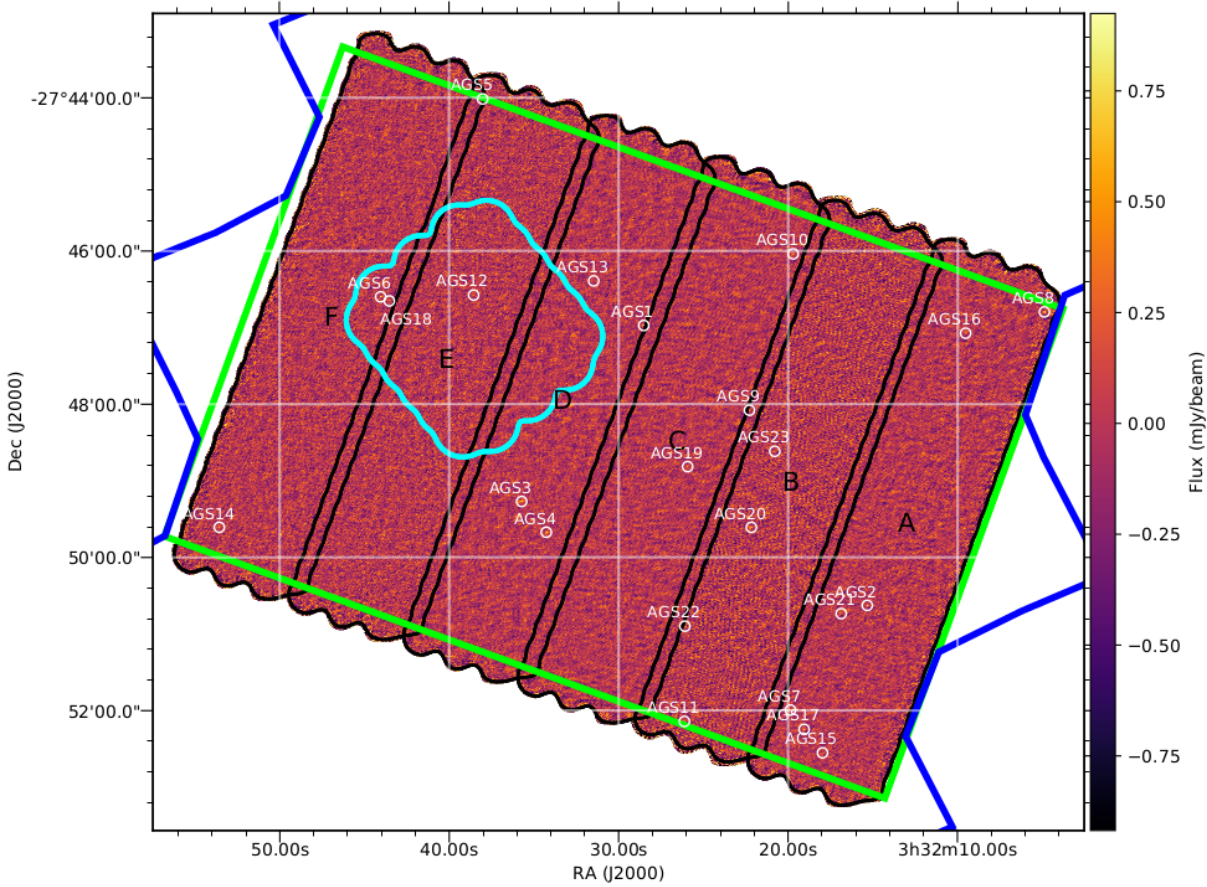


FIGURE 4.3: ALMA 1.1 mm image tapered at  $0''.60$ . The white circles have a diameter of 4 arcseconds and indicate the positions of the galaxies listed in Table 4.1. Black contours show the different slices (labelled A to F) used to compose the homogeneous 1.1 mm coverage, with a median RMS-noise of 0.18 mJy per beam. Blue lines show the limits of the HST/ACS field and green lines indicate the HST-WFC3 deep region. The cyan contour represents the limit of the [Dunlop et al. \(2017\)](#) survey covering all the Hubble Ultra Deep Field region. All of the ALMA-survey field is encompassed by the *Chandra Deep Field-South*.

## 4.6 Identification of counterparts

We searched for optical counterparts in the CANDELS/GOODS–*South* catalog, within a radius of  $0''.6$  from the millimeter position after applying the astrometric corrections to the source positions described in Sect. 4.5. The radius of the cross-matching has been chosen to correspond to the synthesized beam ( $0''.60$ ) of the tapered ALMA map used for galaxy detection. Following [Condon \(1997\)](#); [Condon et al. \(1998\)](#), the maximal positional accuracy of the detection in the 1.1mm map is given by  $\theta_{\text{beam}}/(2 \times S/N)$ . In the  $0''.60$ -mosaic, the positional accuracy therefore ranges between 26.5 mas and 62.5 mas for our range of S/N (4.8–11.3), corresponding to physical sizes between 200 and 480 pc at  $z = 3$ .

Despite the high angular resolution of ALMA, the chance of an ALMA-HST coincidence is not negligible, because of the large projected source density of the CANDELS/GOODS–*South* catalog. Fig. 4.6 shows a Monte Carlo simulation performed to estimate this probability. We separate here the deeper Hubble Ultra Deep Field (blue histogram) from the rest of the CANDELS-deep area (orange histogram). We randomly defined a position within GOODS–*South* and then measured



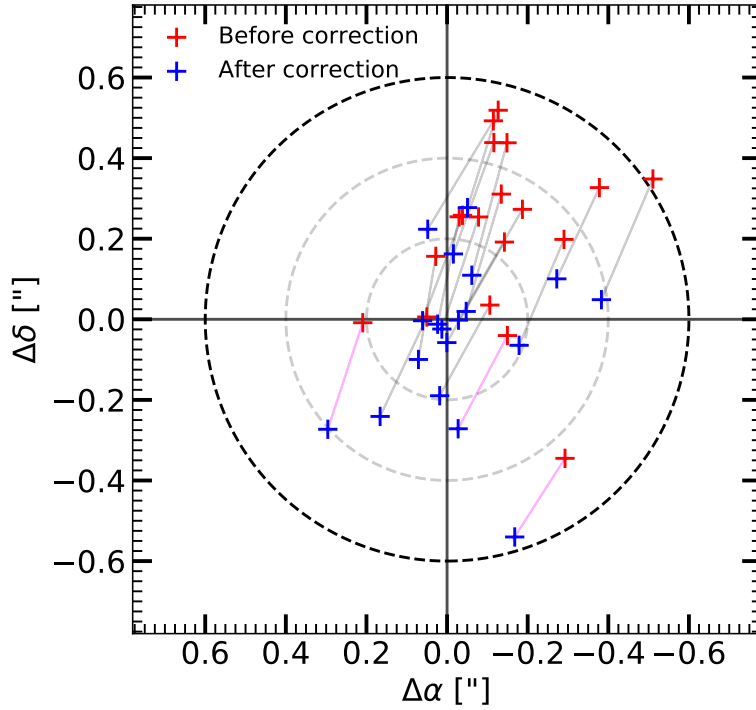


FIGURE 4.4: Positional offset ( $\text{RA}_{\text{HST}} - \text{RA}_{\text{ALMA}}$ ,  $\text{DEC}_{\text{HST}} - \text{DEC}_{\text{ALMA}}$ ) between HST and ALMA before (red crosses) and after (blue crosses) the correction of both a global systematic offset and a local offset. The black dashed circle corresponds to the cross-matching limit radius of  $0''.6$ . The gray dashed circles show a positional offset of  $0''.2$  and  $0''.4$  respectively. The magenta lines indicate the HST galaxies previously falsely associated with ALMA detections.

the distance to its closest HST neighbor using the source positions listed in Guo et al. (2013). We repeated this procedure 100 000 times inside and outside the HUDF. The probability for a position randomly selected in the GOODS–*South* field to fall within 0.6 arcsec of an HST source is 9.2% outside the HUDF, and 15.8% inside the HUDF. We repeated this exercise to test the presence of an IRAC counterpart with the Ashby et al. (2015) catalog (green histogram). The probability to randomly fall on an IRAC source is only 2.1%. With the detection threshold determined in Sect. 4.1, 80% of the millimeter galaxies detected have an HST-WFC3 counterpart, and four galaxies remain without an optical counterpart. We cross-matched our detections with the ZFOURGE catalog.

Fig. 4.7 shows  $3''.5 \times 3''.5$  postage stamps of the ALMA-detected galaxies, overlaid with the positions of galaxies from the CANDELS/GOODS–*South* catalog (magenta double crosses), ZFOURGE catalog (white circles) or both catalogs (sources with an angular separation lower than  $0''.4$ , blue circles). These are all shown after astrometric correction. Based on the ZFOURGE catalog, we found optical counterparts for one galaxy that did not have an HST counterpart: AGS11, a photometric redshift has been computed in the ZFOURGE catalog for this galaxy. The redshifts of AGS4 and AGS17 as given in the CANDELS catalog are unexpectedly low ( $z = 0.24$  and  $z = 0.03$ , respectively), but the redshifts for these galaxies given in the ZFOURGE catalog ( $z = 3.76$  and  $z = 1.85$ , respectively) are more compatible with the expected redshifts for galaxies detected with ALMA. These galaxies, missed by the HST or incorrectly listed as local galaxies are particularly interesting galaxies (see Sect. 7.3). AGS6 is not listed in the ZFOURGE catalog, most likely because it is close ( $< 0''.7$ ) to another bright galaxy ( $\text{ID}_{\text{CANDELS}} = 15768$ ). These galaxies are blended in the ZFOURGE ground-based  $K_s$ -band images. AGS6 has previously been

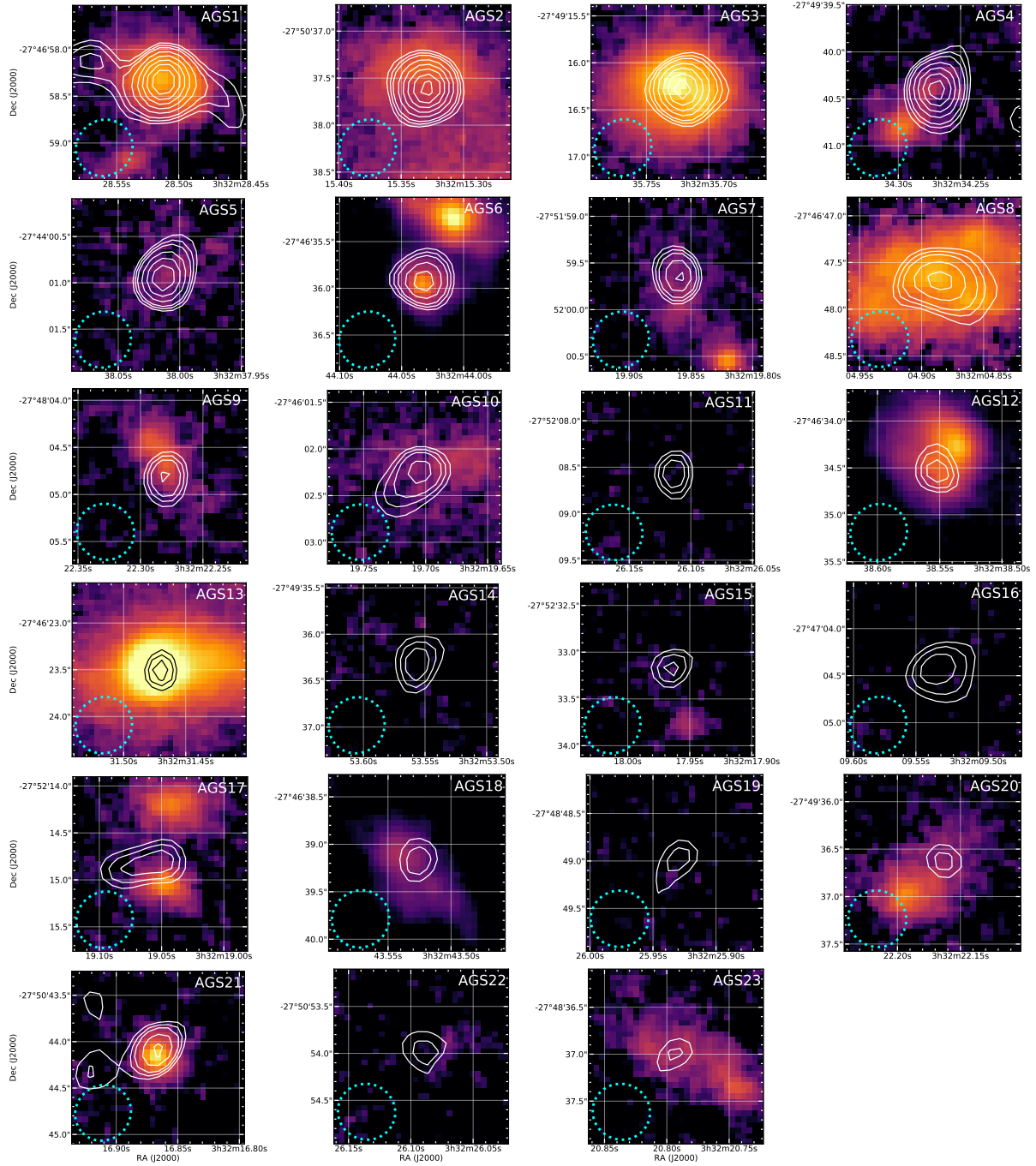


FIGURE 4.5: Postage stamps of  $1.8 \times 1.8$  arcsec. ALMA contours (4, 4.5 then 5 to 10- $\sigma$  with a step of 1- $\sigma$ ) at 1.1mm (white lines) are overlaid on F160W HST/WFC3 images. The images are centered on the ALMA detections. The shape of the synthesized beam is given in the bottom left corner. Astrometry corrections described in Sect. 4.5 have been applied to the HST images. In some cases (AGS1, AGS3, AGS6, AGS13, AGS21 for example), the position of the dust radiation matches that of the stellar emission; in other cases, (AGS4, AGS17 for example), a displacement appears between both two wavelengths. Finally, in some cases (AGS11, AGS14, AGS16, and AGS19) there are no optical counterparts. We will discuss the possible explanations for this in Sect. 7.3.

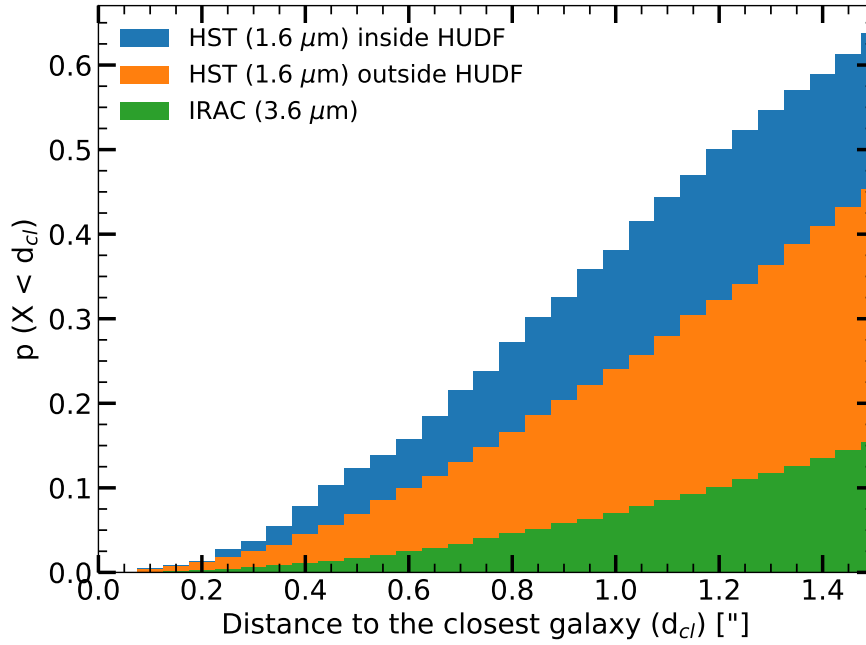


FIGURE 4.6: Probability of a randomly selected position in the area defined by this survey to have at least one HST (blue, orange) or *IRAC* (green) neighbor as a function of distance. We computed this probability by Monte Carlo simulation using the distribution of galaxies listed in the CANDELS/GOODS-South catalog. Due to the presence of the HUDF within the GOODS-South field, we cannot consider that the density of HST galaxies is uniform, and we consider these two fields separately (blue inside and orange outside the HUDF).

detected at 1.3 mm in the HUDF, so we adopt the redshift and stellar mass found by [Dunlop et al. \(2017\)](#). The consensus CANDELS zphot from [Santini et al. \(2015\)](#) is  $z = 3.06$  (95% confidence:  $2.92 < z < 3.40$ ), consistent with the value in [Dunlop et al. \(2017\)](#).

#### 4.6.1 Galaxy sizes

Correctly estimating the size of a source is an essential ingredient for measuring its flux. As a first step, it is imperative to know if the detections are resolved or unresolved. In this section, we discuss our considerations regarding the sizes of our galaxies. The low number of galaxies with measured ALMA sizes in the literature makes it difficult to constrain the size distribution of dust emission in galaxies. Recent studies (e.g., [Barro et al., 2016](#); [Rujopakarn et al., 2016](#); [Elbaz et al., 2018](#); [Ikarashi et al., 2017](#); [Fujimoto et al., 2017](#)) with sufficient resolution to measure ALMA sizes of galaxies suggest that dust emission takes place within compact regions of the galaxy. Two of our galaxies (AGS1 and AGS3) have been observed in individual pointings (ALMA Cycle 1; P.I. R. Leiton, presented in [Elbaz et al. 2018](#)) at  $870 \mu\text{m}$  with a long integration time (40-50 min on source). These deeper observations give more information on the nature of the galaxies, in particular on their morphology. Due to their high S/N ( $\sim 100$ ) the sizes of the dust emission could be measured accurately:  $R_{1/2\text{maj}} = 120 \pm 4$  and  $139 \pm 6$  mas for AGS1 and AGS3 respectively, revealing extremely compact star-forming regions corresponding to circularized effective radii of  $\sim 1$  kpc at redshift  $z \sim 2$ . The Sérsic indices are  $1.27 \pm 0.22$  and  $1.15 \pm 0.22$  for AGS1 and AGS3 respectively: the dusty star-forming regions therefore seem to be disk-like. Based on their sizes, their stellar masses ( $> 10^{11} M_{\odot}$ ), their SFRs ( $> 10^3 M_{\odot} \text{yr}^{-1}$ ) and their redshifts ( $z \sim 2$ ), these very compact galaxies are ideal candidate progenitors of compact quiescent galaxies at



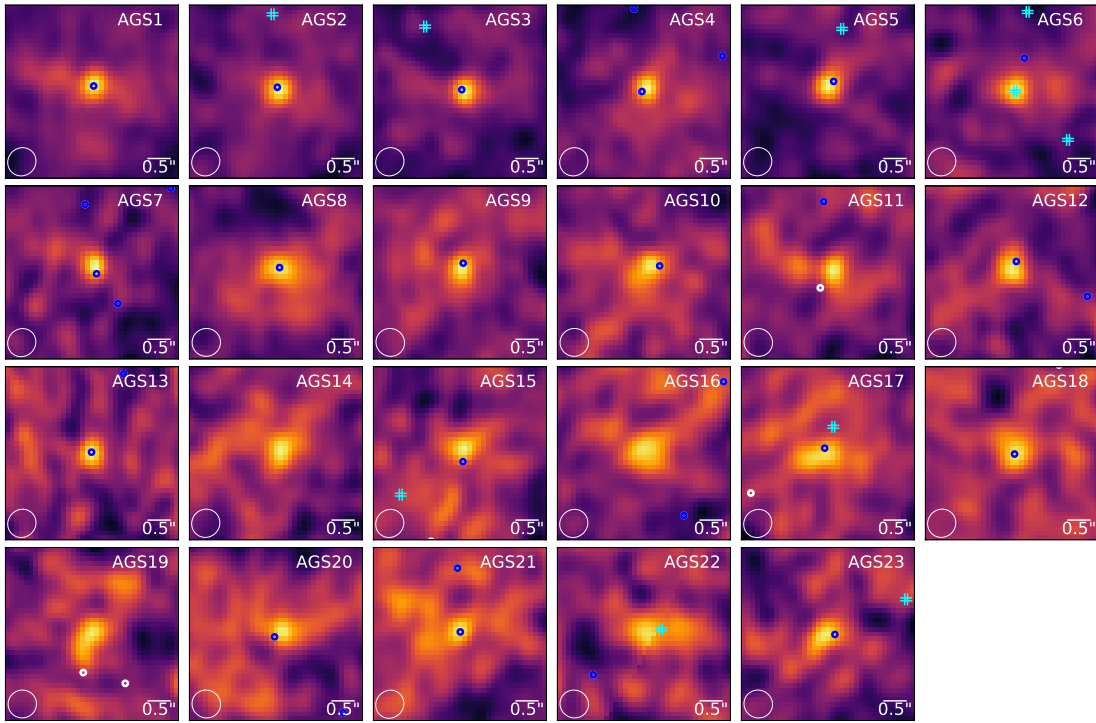


FIGURE 4.7: ALMA 1.1 mm continuum maps for the 23 detections tapered at 0.60 arcsec. Each  $3''.5 \times 3''.5$  image is centered on the position of the ALMA detection. Cyan double crosses show sources from the GOODS-S CANDELS catalog. White circles show sources from the ZFOURGE catalog. Blue circles show common sources from both optical catalogs (sources with an angular separation lower than  $0''.4$ ). The shape of the synthesized beam is given in the bottom left corner.

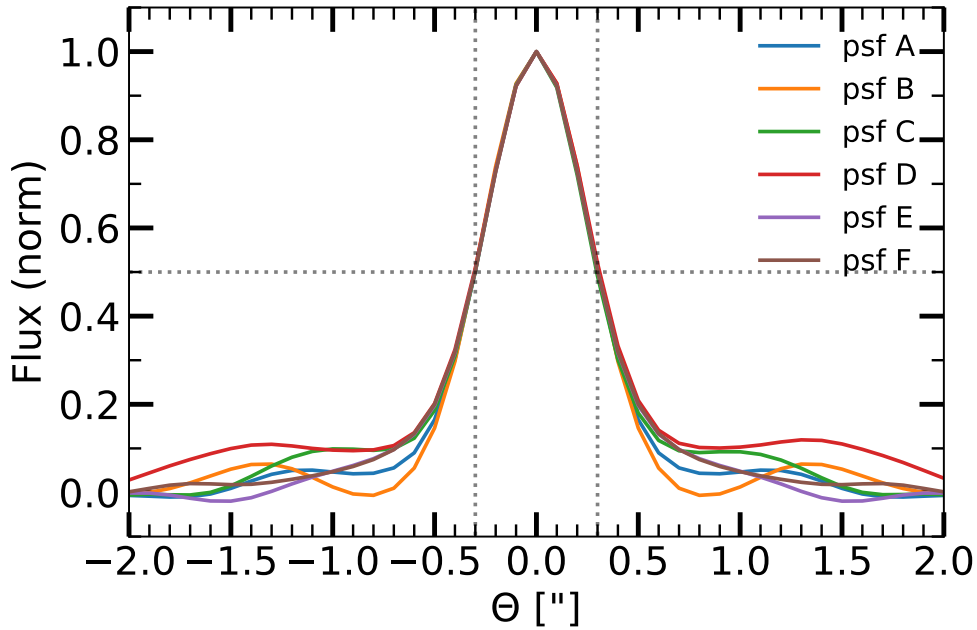


FIGURE 4.8: East-west profile of the PSFs corresponding to the six different parallel slices composing the ALMA image in the  $0''.60$ -mosaic (see Fig. 4.3).

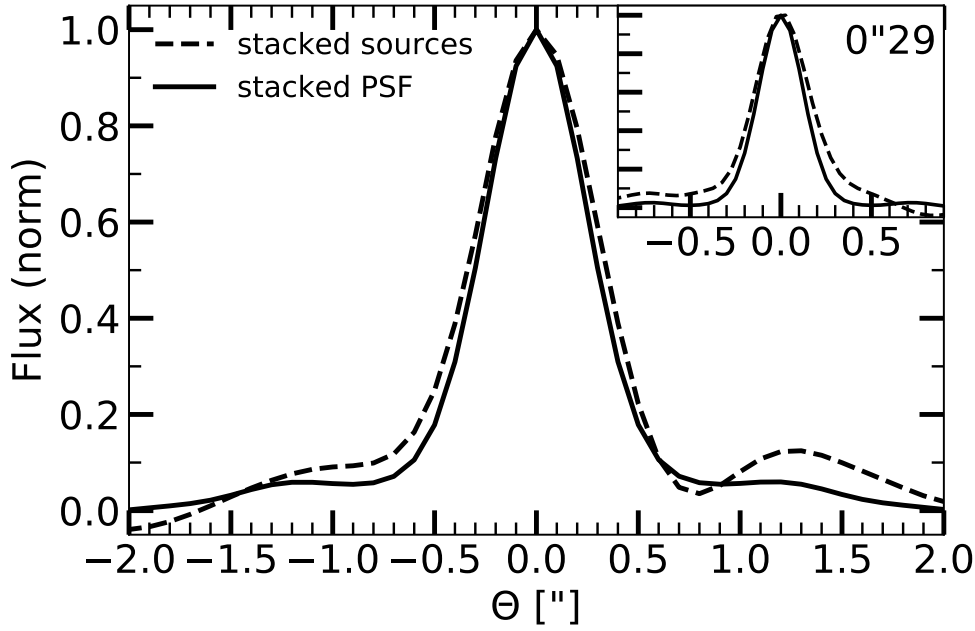


FIGURE 4.9: Comparison between the stacked PSF (black solid line) and the stack of the 23 ALMA-detections (black dashed line) in the  $0''.60$ -mosaic. As each slice has a specific PSF, we stack the PSF corresponding to the position of each detection. The fluxes of each detection have been normalized, so that the brightest sources do not skew the results. Fluxes of the PSF and ALMA detections are normalized to 1. Flux profiles are taken across the East-west direction. The result is consistent with unresolved or marginally resolved sources at this resolution. The insert in the top-right corner shows the same procedure for the 15 sources detected in the  $0''.29$ -mosaic (see Table 4.2).

$z \sim 2$  (Barro et al. 2013; Williams et al. 2014; van der Wel et al. 2014; Kocevski et al. 2017, see also Elbaz et al. 2018).

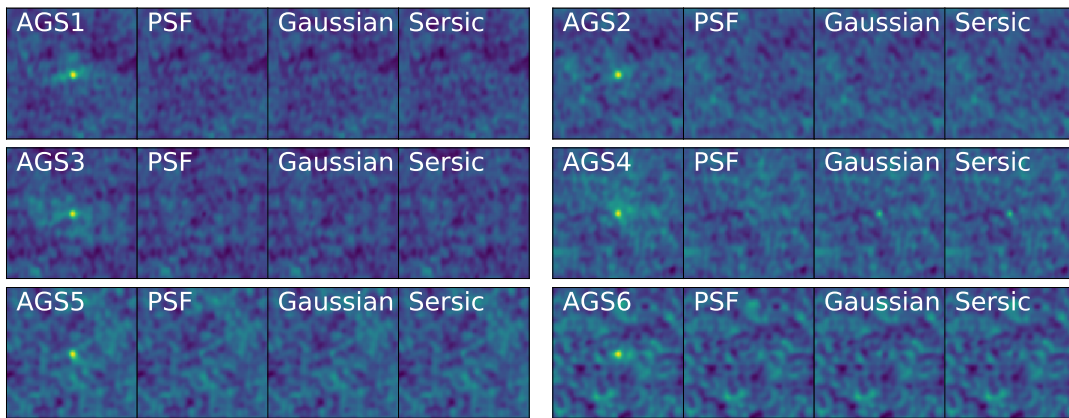


FIGURE 4.10:  $10'' \times 10''$  postage stamps, centered on the galaxy detections. Left to right: the source in the  $0''.60$ -mosaic map, and the residuals obtained after PSF, Gaussian and Sérsic flux fitting. The residuals are very similar between the three different extraction methods. Only the 6 brightest galaxies are shown.

Size measurements of galaxies at (sub)millimeter wavelengths have previously been made as part of several different studies. Ikarashi et al. (2015) measured sizes for 13 AzTEC-selected SMGs. The Gaussian FWHM range between  $0''.10$  and  $0''.38$  with a median of  $0''.20^{+0''.03}_{-0''.05}$  at 1.1 mm. Simpson et al. (2015a) derived a median intrinsic angular size of  $\text{FWHM} = 0''.30 \pm 0''.04$

for their 23 detections with a  $S/N > 10$  in the Ultra Deep Survey (UDS) for a resolution of  $0''.3$  at  $870 \mu\text{m}$ . [Tadaki et al. \(2017\)](#) found a median FWHM of  $0''.11 \pm 0.02$  for 12 sources in a  $0''.2$ -resolution survey at  $870 \mu\text{m}$ . [Barro et al. \(2016\)](#) use a high spatial resolution (FWHM  $\sim 0''.14$ ) to measure a median Gaussian FWHM of  $0''.12$  at  $870 \mu\text{m}$ , with an average Sérsic index of 1.28. For [Hodge et al. \(2016\)](#), the median major axis size of the Gaussian fit is  $\text{FWHM} = 0''.42 \pm 0''.04$  with a median axis ratio  $b/a = 0.53 \pm 0.03$  for 16 luminous ALESS SMGs, using high-resolution ( $\sim 0''.16$ ) data at  $870 \mu\text{m}$ . [Rujopakarn et al. \(2016\)](#) found a median circular FWHM at  $1.3 \text{ mm}$  of  $0''.46$  from the ALMA image of the HUDF ([Dunlop et al., 2017](#)). [González-López et al. \(2017\)](#) studied 12 galaxies at  $S/N \geq 5$ , using 3 different beam sizes ( $0''.63 \times 0''.49$ ), ( $1''.52 \times 0''.85$ ) and ( $1''.22 \times 1''.08$ ). They found effective radii spanning  $< 0''.05$  to  $0''.37 \pm 0''.21$  in the ALMA Frontier Fields survey at  $1.1 \text{ mm}$ . [Ikarashi et al. \(2017\)](#) obtained ALMA millimeter-sizes of  $0''.08 - 0''.68$  (FWHM) for 69 ALMA-identified AzTEC SMGs with an  $S/N$  greater than 10. These galaxies have a median size of  $0''.31$ . These studies are all broadly in agreement, revealing compact galaxy sizes in the sub(millimeter) regime of typically  $0''.3 \pm 0''.1$ . Size measurements require a high  $S/N$  detection to ensure a reliable result. The  $S/N$  range of our detections is 4.8-11.3. Following [Martí-Vidal et al. \(2012\)](#), the reliable size measurement limit for an interferometer is:

$$\theta_{min} = \beta \left( \frac{\lambda_c}{2 S/N^2} \right)^{1/4} \times \theta_{beam} \simeq 0.88 \frac{\theta_{beam}}{\sqrt{S/N}} \quad (4.2)$$

where  $\lambda_c$  is the value of the log-likelihood, corresponding to the cutoff of a Gaussian distribution to have a false detection and  $\beta$  is a coefficient related to the intensity profile of the source model and the density of the visibilities in Fourier space. This coefficient usually takes values in the range 0.5-1. We assumed  $\lambda_c = 3.84$  corresponding to a  $2\sigma$  cut-off, and  $\beta = 0.75$ . For  $\theta_{beam} = 0''.60$  and a range of  $S/N$  between 4.8 and 11.3, the minimum detectable size (FWHM) therefore varies between  $0''.16$  and  $0''.24$ . Using the  $0''.60$ -mosaic map, the sizes of a large number of detections found in previous studies could therefore not be reliably measured.

To quantitatively test if the millimeter galaxies are resolved in our survey we performed several tests. The first test was to stack the 23 ALMA-detections and compare the obtained flux profile with the profile of the PSF. However, in the mosaic map, each slice has its own PSF. We therefore also needed to stack the PSFs at these 23 positions in order to obtain a global PSF for comparison. Fig. 4.8 shows the different PSFs used in this survey in the  $0''.60$ -mosaic. The FWHM of each PSF is identical, the differences are only in the wings. The stack of the 23 PSFs for the 23 detections and the result of the source stacking in the  $0''.60$ -mosaic is shown in Fig. 4.9. The flux of each detection is normalized so that all sources have the same weight, and the stacking is not skewed by the brightest sources.

Size stacking to measure the structural parameters of galaxies is at present a relatively unexplored area. This measurement could suffer from several sources of bias. The uncertainties on the individual ALMA peak positions could increase the measured size in the stacked image, for example. On the other hand, due to the different inclination of each galaxy, the stacked galaxy could appear more compact than the individual galaxies (e.g., [Hao et al., 2006](#); [Padilla and Strauss, 2008](#); [Li et al., 2016](#)). Alternatively, some studies (e.g., [van Dokkum et al., 2010](#)) indicate that size stacking gives reasonably accurate mean galaxy radii. In our case, the result of the size stacking is consistent with unresolved sources or marginally resolved at this resolution which corresponds to a physical diameter of 4.6 kpc at  $z = 3$ .

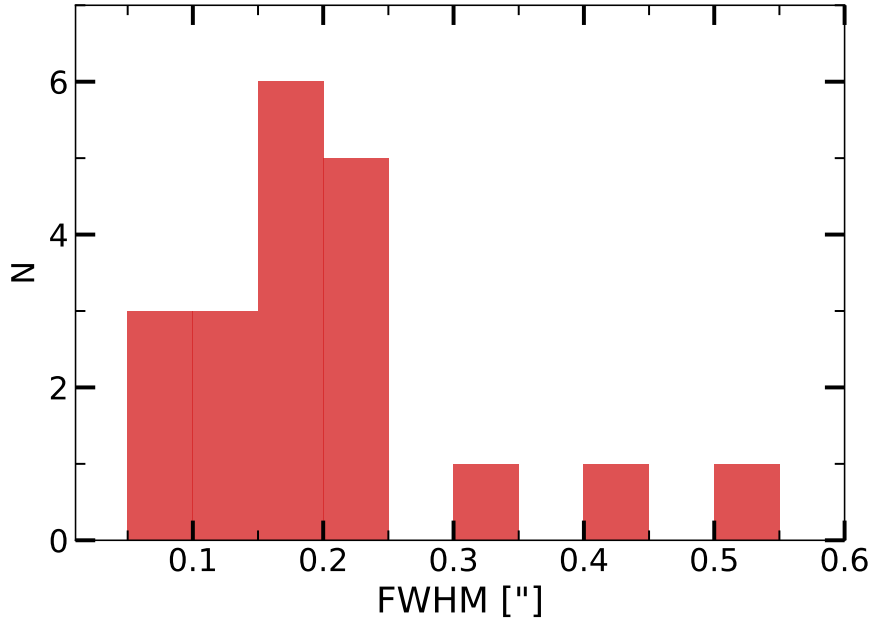


FIGURE 4.11: Size distribution histogram for the 20 robust detections. These sizes are computed by fitting the ALMA detections with a circular Gaussian in the  $uv$ -plane using `uvmodelfit` in CASA. 85% of the sources exhibit a FWHM smaller than  $0''.25$ .

The second test was to extract the flux for each galaxy using PSF-fitting. We used `Galfit` (Peng et al., 2010) on the  $0''.60$ -mosaic. The residuals of this PSF-extraction are shown for the 6 brightest galaxies in Fig. 4.10. The residuals of 21/23 detections do not have a peak greater than  $3\sigma$  in a radius of  $1''$  around the source. Only sources AGS10 and AGS21 present a maximum in the residual map at  $\sim 3.1\sigma$ .

We compared the PSF flux extraction method with Gaussian and Sérsic shapes. As our sources are not detected with a particularly high S/N, and in order to limit the number of degrees of freedom, the Sérsic index was frozen to  $n = 1$  (exponential disk profile, in good agreement with Hodge et al. 2016 and Elbaz et al. 2018 for example), assuming that the dust emission is disk-like. Fig. 4.10 shows the residuals for the three different extraction profiles. The residuals are very similar between the point source, Gaussian and Sérsic profiles, suggesting that the approximation that the sources are not resolved is appropriate, and does not result in significant flux loss. We also note that, for several galaxies, due to large size uncertainties, the Gaussian and Sérsic fits give worse residuals than the PSF fit (AGS4 for example).

For the third test, we took advantage of the different tapered maps. We compared the peak flux for each detection between the  $0''.60$ -mosaic map and the  $0''.29$ -mosaic map. The median ratio is  $S_{peak}^{0''.29}/S_{peak}^{0''.60} = 0.87 \pm 0.16$ . This small decrease, of only 10% in the peak flux density between the two tapered maps suggests that the flux of the galaxies is only slightly more resolved in the  $0''.29$ -mosaic map.

In order to test the impact of our hypothesis that the sources can be considered as point-like in the mosaic tapered at  $0''.60$ , we fit their light profiles with a circular Gaussian in the  $uv$ -plane using `uvmodelfit` in CASA (we also tested the use of an asymmetric Gaussian but the results remained similar although with a lower precision due to the larger number of free parameters in the fit). The sizes that we obtained confirmed our hypothesis that our galaxies are particularly compact since 85% of the sources (17 out of 20 robust detections) exhibit a FWHM smaller than

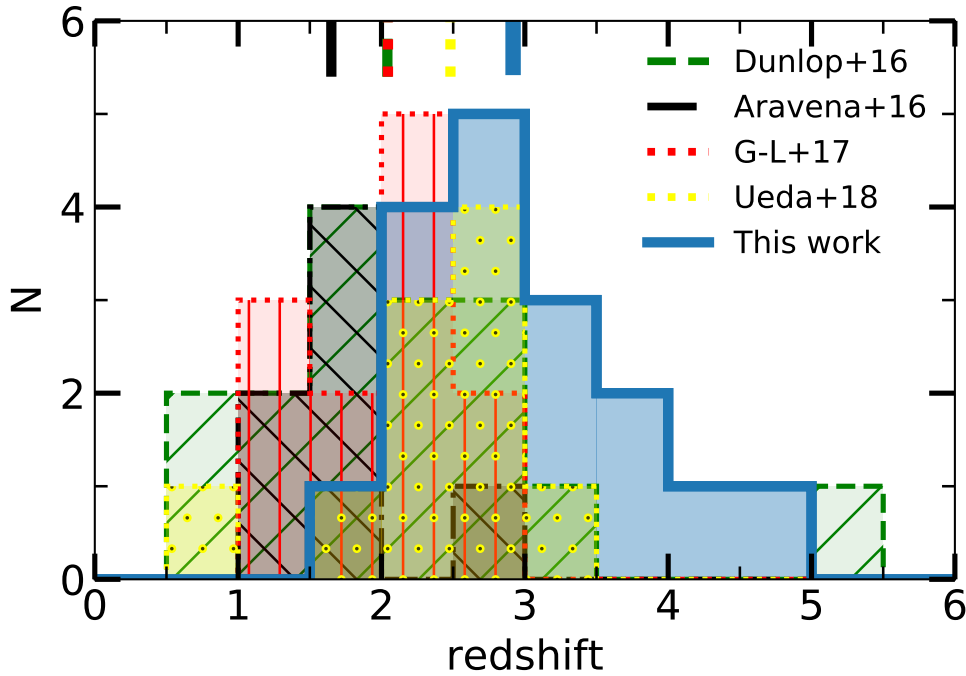


FIGURE 4.12: Redshift distributions (photometric or spectroscopic) for millimetre-selected galaxies. The blue solid line shows the redshift distribution of our ALMA GOODS–*South* blind survey. The green dashed line shows the Hubble Ultra Deep Field Survey redshift distribution (Dunlop et al., 2017), the black dash-dotted line shows the ASPECS sample (Aravena et al., 2016), the red dotted line shows the ALMA Frontier Fields Survey (González-López et al., 2017) and the yellow dotted line shows the ASAGAO survey (Ueda et al., 2018). Short coloured lines at the top of the figure indicate the median redshifts for these four studies.

$0''.25$  (in other words the half-light radius is twice smaller than this value). The median size of our sample of 20 galaxies is  $0''.18$  (see the distribution of sizes in Fig. 4.11). This analysis shows that two sources are outliers with sizes of  $0''.41 \pm 0''.03$  and  $0''.50 \pm 0''.08$ , for AGS17 and AGS18 respectively. For these two sources, the assumption of point-like sources is not valid and leads to an underestimate of the actual flux densities by a factor of 2.3 and 1.7 respectively. This correction has been applied to the list of peak flux densities provided in Table 4.2.

Having performed these tests, we concluded that for all of the detections, except AGS17 and AGS18, the approximation that these sources appear point-like in the  $0''.60$ -mosaic map is justified. For the two remaining sources, we applied a correction given above. Our photometry was therefore performed under this assumption.

## 4.7 Mass and redshift

We now study the physical properties of the ALMA detected sources, taking advantage of the wealth of ancillary data available for the GOODS–*South* field.

### 4.7.1 Redshift distribution

Among the 17 ALMA-detected sources for which redshifts have been computed, six have a spectroscopic redshift (AGS1, AGS2, AGS3, AGS9, AGS12, AGS13 and AGS18) determined by [Kurk et al. \(2013\)](#), and recently confirmed by [Barro et al. \(2017\)](#), [Momcheva et al. \(2016\)](#), [Vanzella et al. \(2008\)](#), Mobasher (private communication), [Inami et al. \(2017\)](#), [Kriek et al. \(2008\)](#) and [Dunlop et al. 2017](#) – from a private communication of Brammer – respectively. The redshift distribution of these 17 ALMA sources is presented in Fig. 4.12, compared to the distributions of four other deep ALMA blind surveys ([Dunlop et al., 2017](#); [Aravena et al., 2016](#); [González-López et al., 2017](#); [Ueda et al., 2018](#)). Of the 17 sources, 15 are in the redshift range  $z = 1.9 - 3.8$ . Only two galaxies (AGS4 and AGS11) have a redshift greater than 4 ( $z_{\text{phot}} = 4.32$  and  $4.82$  respectively). We discuss these galaxies further in Sect. 7.3. The mean redshift of the sample is  $z = 3.03 \pm 0.17$ , where the error is computed by bootstrapping. This mean redshift is significantly higher than those found by [Dunlop et al. \(2017\)](#), [Aravena et al. \(2016\)](#), [González-López et al. \(2017\)](#) and [Ueda et al. \(2018\)](#) who find distributions peaking at 2.13, 1.67, 1.99 and 2.28 respectively. The median redshift of our sample is  $2.92 \pm 0.20$ , which is a little higher than the value expected from the models of [Béthermin et al. \(2015\)](#), which predict a median redshift of 2.5 at 1.1 mm, considering our flux density limit of  $\sim 874 \mu\text{Jy}$  ( $4.8\sigma$ ). Our limiting sensitivity is shallower than that of previous blind surveys: 0.184 mJy here compared with  $13 \mu\text{Jy}$  in [Aravena et al. \(2016\)](#),  $35 \mu\text{Jy}$  in [Dunlop et al. \(2017\)](#),  $(55-71) \mu\text{Jy}$  in [González-López et al. \(2017\)](#) and  $89 \mu\text{Jy}$  in [Ueda et al. \(2018\)](#). However our survey covers a larger region on the sky:  $69 \text{ arcmin}^2$  here, compared to  $1 \text{ arcmin}^2$ ,  $4.5 \text{ arcmin}^2$ ,  $13.8 \text{ arcmin}^2$  and  $26 \text{ arcmin}^2$  for these four surveys respectively. The area covered by our survey is therefore a key parameter in the detection of high redshift galaxies due to a tight link between 1.1mm luminosity and stellar mass, as we will show in the next section. The combination of two effects: a shallower survey allowing us to detect only brighter SMGs, which are more biased toward higher redshifts (e.g., [Pope et al., 2005](#)), as well as a larger survey allowing us to reach more massive galaxies, enables us to open the parameter space at redshifts greater than 3, as shown in Fig. 4.12. This redshift space is partly or totally missed in smaller blind surveys. We show in Fig. 4.13 the size of the recent ALMA survey as a function of their depth. We represented the surveys of [Aravena et al. \(2016\)](#); [González-López et al. \(2017\)](#); [Dunlop et al. \(2017\)](#); [Hatsukade et al. \(2018\)](#), as well as this work, color-coded as a function of the median redshift.

We can see in this figure a clear trend between the depth of the survey and the median redshift. The more the survey will be shallow, the higher the average redshift will be. This trend is parameterized in [Béthermin et al. \(2015\)](#). According to this study, a 1.1 mm survey with a flux density cut of 1 mJy would have a median redshift  $z = 2.5$  while a survey with a flux density cut of 0.3 mJy would have a median redshift  $z = 2$ .

Another factor that greatly influences the average redshift of a survey is the observed wavelength. For example, [Béthermin et al. \(2015\)](#); [Casey et al. \(2018\)](#); [Magnelli et al. \(2019\)](#) have shown that the longer the observed wavelength, the higher the average redshift would be. For example, a survey at 2 mm is efficient to isolate the dusty star-forming galaxies with the highest redshift by excluding the majority of lower redshift galaxies due to the negative K-correction ([Casey et al., 2019](#)). In the survey conducted by [Magnelli et al. \(2019\)](#) with Goddard IRAM Superconducting Millimeter Observer (GISMO) at the IRAM 30m-telescope ([Staguhn et al., 2014](#)) in the COSMOS field, all the detection but one lie above  $z \sim 3$ . Finally, we can also note that lensed fields have on average higher  $z$  than non-lensed fields (e.g., [Hezaveh and Holder, 2011](#)).

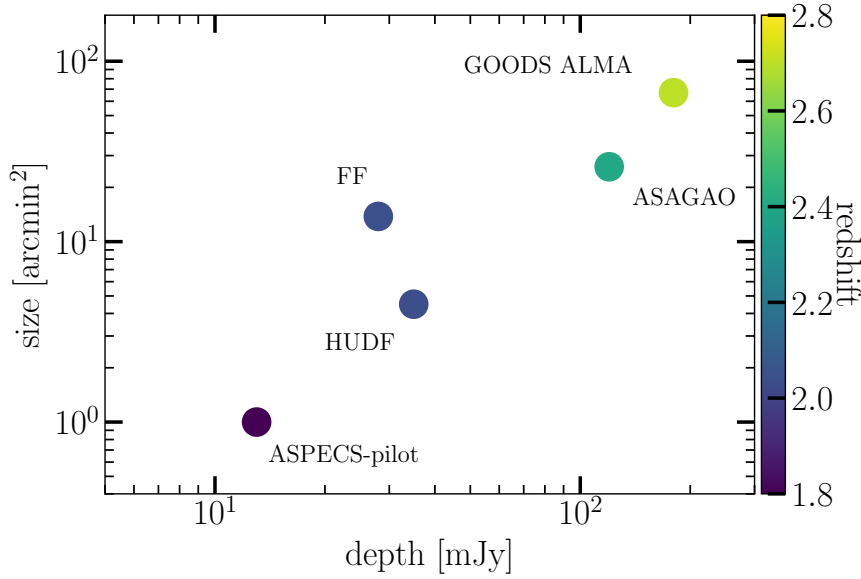


FIGURE 4.13: Size-depth plan for the contiguous ALMA surveys color-coded by the median redshift. We represented the Hubble Ultra Deep Field Survey (Dunlop et al., 2017), the pilot-ASPECS sample (Aravena et al., 2016), the ALMA Frontier Fields Survey (González-López et al., 2017), the ASAGAO survey (Hatsukade et al., 2018) and this work. For this work, we also include the sample of galaxies describes in Chapter 6 (which has a lower median redshift than the sample presented in this chapter).

We emphasize that the two HST-dark galaxies (see Chapter 7.3) for which the mass and redshift could be determined (AGS4 and AGS11) are the two most distant galaxies in our sample, with redshifts greater than 4.

#### 4.7.2 Stellar Masses

Over half (10/17 of galaxies for which a stellar mass has been determined) of our galaxies have a stellar mass greater than  $10^{11} M_{\odot}$  (median mass of  $M_{\star} = 1.1 \times 10^{11} M_{\odot}$ ). The population of massive and compact star-forming galaxies at  $z \sim 2$  has been documented at length (e.g., Daddi et al., 2005; van Dokkum et al., 2015), but their high redshift progenitors are to-date poorly detected in the UV. Our massive galaxies at redshifts greater than 3 might therefore give us an insight into these progenitors. Fig. 4.14 shows the stellar mass as a function of redshift for all of the UVJ active galaxies, listed in the ZFOURGE catalog, in our ALMA survey field of view. Star forming galaxies (SFGs) have been selected by a UVJ colour-colour criterion as given by Williams et al. (2009) and applied at all redshifts and stellar masses as suggested by Schreiber et al. (2015):

$$SFG = \begin{cases} U - V < 1.3, \text{ or} \\ V - J > 1.6, \text{ or} \\ U - V < 0.88 \times (V - J) + 0.49 \end{cases} \quad (4.3)$$

We will call them "UVJ active" and the complementary population of passive galaxies "UVJ passive". All galaxies not fulfilling these colour criteria (Eq. 4.3) are considered as quiescent galaxies and are excluded from our comparison sample (9.3% of the original sample). The ALMA detected galaxies in our survey are massive compared to typical SFGs detected in deep



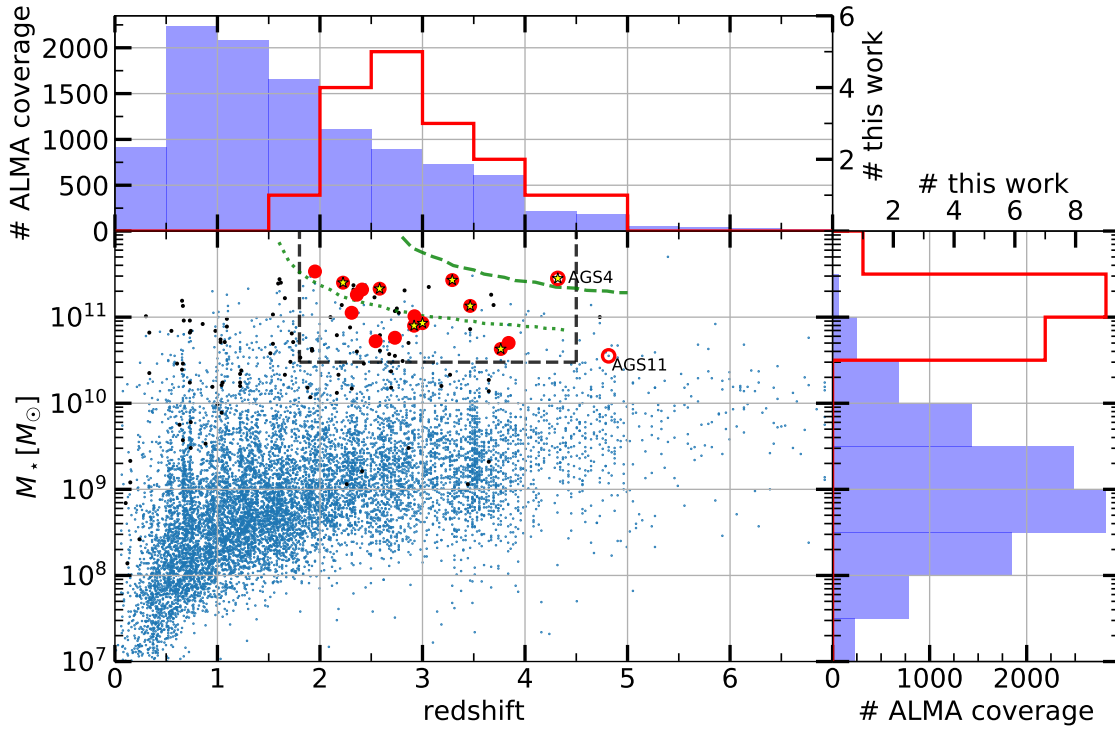


FIGURE 4.14: Stellar mass versus redshift for the galaxies detected in our ALMA GOODS–*South* blind survey (red points). For comparison, the distribution of all of the galaxies, listed in the ZFOURGE catalog, in the same field of view is given in blue. Only UVJ active galaxies are shown. The two HST–dark galaxies for which we have estimated a photometric redshift (AGS4 and AGS11) are represented by open circles. The redshift of AGS11 is however uncertain. The green dashed line shows the position that would be occupied by a typical star-forming galaxy – lying on the median of the SFR– $M_*$  star-formation main sequence (MS) – that would produce a 1.1mm flux density equal to our average detection limit of 0.88 mJy ( $4.8\sigma$ ) using the Spectral Energy Distribution (SED) library of Schreiber et al. (2018a). The dotted line illustrates the position of galaxies 3 times above the MS using the appropriate SEDs from the same library. Galaxies hosting an AGN that are undetected or detected by ALMA are identified with black dots and yellow stars respectively. Inside the black dashed rectangle, 50% of the galaxies detected by ALMA host an AGN, while only 14% of the UVJ active galaxies undetected by ALMA host an AGN.

optical and near-IR surveys like CANDELS, in the same redshift range ( $2 < z < 4$ ), as shown in Fig. 4.14.

The high proportion of massive galaxies among the ALMA detected sources suggests that stellar mass can be a strong driver for a source to be detected by ALMA at high redshift (Dunlop et al., 2017). The strong link between detection and stellar mass is related to the underlying relation between stellar mass and star formation rate of SFGs (e.g., Noeske et al., 2007; Elbaz et al., 2011). Almost one third (7/24) of the galaxies previously cataloged in the field of view of this study with  $M_* > 10^{11} M_\odot$  and  $2 < z < 3$  are also detected with ALMA. The position of our galaxies along the main sequence of star formation (MS) will be studied Chapter 8.

We observe a lack of detections at redshift  $z < 2$ , driven by both a strong positive K-correction favouring higher redshifts and a decrease in the star formation activity at low redshift. Indeed, the specific star formation rate (sSFR), defined as the ratio of galaxy SFR to stellar mass, drops quickly at lower redshifts ( $z < 2$ ), whereas this rate increases continuously at greater redshifts (e.g., Schreiber et al., 2015). In addition, very massive galaxies (stellar mass greater than  $10^{11} M_\odot$ ) are relatively rare objects in the smaller co-moving volumes enclosed by our survey at lower



redshift. To detect galaxies with these masses, a survey has to be sufficiently large. The covered area is therefore a critical parameter for blind surveys to find massive high redshift galaxies.

In order to estimate the selection bias relative to the position of our galaxies on the main sequence, we show in Fig. 4.14 the minimum stellar mass as a function of redshift that our survey can detect, for galaxies on the MS of star formation (green dashed line), and for those with a SFR three times above the MS (green dotted line). To determine this limit, we calculate the SFR of a given MS galaxy, based on the galaxy stellar mass and redshift as defined in Schreiber et al. (2015). From this SFR and stellar mass, the galaxy SED can also be calculated using the Schreiber et al. (2018a) library. We then integrate the flux of this SED around 1.1mm.

It can be seen that the stellar mass detection limit corresponding to MS galaxies lies at higher stellar mass than all of the galaxies detected by our ALMA survey (as well as all but one of the other star-forming galaxies present in the same region). This means that our survey is unable to detect star-forming galaxies below the main sequence. We can quantify the offset of a galaxy from the main sequence, the so-called "starburstiness" (Elbaz et al., 2011), by the ratio  $\text{SFR}/\text{SFR}_{MS}$ , where  $\text{SFR}_{MS}$  is the average SFR of "main sequence" galaxies computed from Schreiber et al. (2015). We also indicate our detection limit for galaxies with  $\text{SFR}/\text{SFR}_{MS} = 3$ . In this case, 7 of the 17 galaxies shown lie above the limit. To have been detected, these galaxies must therefore have SFRs at least larger than the  $\text{SFR}_{MS}$ , the other ten galaxies must have a SFR at least three times above the MS. This highlights that our survey is biased towards galaxies with high SFRs.

## 4.8 AGN

In this Section, we discuss the presence of AGN within the 20 most robust ALMA detections, i.e., rejecting the 3 spurious detections with no IRAC counterpart (AGS14, AGS16 and AGS19 marked with a star in Table 4.2) but including 3 of the supplementary sources (AGS21, AGS22 and AGS23). We find an X-ray counterpart for 65% of them (13/20) in the 7 Msec X-ray survey of GOODS–South with *Chandra* (Luo et al., 2017). Most of these galaxies were classified as AGN in the catalog of Luo et al. (2017) that identifies as AGN all galaxies with an intrinsic 0.5-7.0 keV luminosity higher than  $L_{X,int} = 3 \times 10^{42} \text{ erg.s}^{-1}$ , among other criteria. However, our ALMA galaxies being biased towards highly star-forming galaxies, we decided to increase the minimum X-ray luminosity to a three times stronger X-ray luminosity threshold to avoid any contamination by star-formation. We also consider as AGN the galaxies exhibiting a hard X-ray spectrum. Hence, we adopt here the following criteria to identify AGN: either (i)  $L_{X,int} > 10^{43} \text{ erg.s}^{-1}$  (luminous X-ray sources) or (ii)  $\Gamma < 1.0$  (hard X-ray sources). As the redshifts adopted by Luo et al. (2017) are not always the same as ours, when necessary we scaled the X-luminosities to our redshifts using Eq. 1 from Alexander et al. (2003), and assuming a photon index of  $\Gamma = 2$ . Using these conservative criteria, we find that 8 ALMA galaxies host an X-ray AGN (marked with a yellow star in Fig. 4.14). In order to compare the AGN fraction among ALMA detections with galaxies undetected by ALMA with similar masses and redshifts, we restrict our comparison to galaxies with  $M_* > 3 \times 10^{10} M_\odot$  and  $1.8 < z < 4.5$  (rectangle in black dotted lines in Fig. 4.14). In this area encompassing 16 ALMA detections, we find that 50% of the ALMA sources host an AGN (8/16) as compared to only 14% (23/160) of the star-forming galaxies undetected by ALMA located in this same area (selected using the UVJ criteria recalled in Eq. 4.3 in the ZFOURGE catalog). The presence of a large fraction of AGN among the galaxies detected by

ALMA may reflect the fact that the ALMA sources are experiencing a starburst (well above the MS marked with a green dashed line in Fig. 4.14), possibly triggered by a merger that may dramatically reduce the angular momentum of the gas and drive it towards the centre of the galaxies (e.g., [Rovilos et al., 2012](#); [Gatti et al., 2015](#); [Lamastra et al., 2013](#)) or violent disk instabilities ([Bournaud et al., 2012](#)). In addition, the high AGN fraction may be driven by the link between the presence of an AGN and the compactness of their host galaxy. [Elbaz et al. \(2018\)](#), [Chang et al. \(2017\)](#) and [Ueda et al. \(2018\)](#) suggest that the proportion of galaxies hosting an AGN increases with IR luminosity surface density. As discussed in Sect. 5.5.5, the size, and therefore the compactness of a galaxy, increases the likelihood of an ALMA detection at our angular resolution. Alternatively ALMA might preferentially detect galaxies with a high gas, hence also dust, content, more prone to efficiently fuel the central black hole and trigger an AGN. This fraction of galaxies with a high X-ray luminosity ( $L_{X,int} > 10^{43} \text{ erg.s}^{-1}$ ) seems to be significantly higher than that found in some other ALMA surveys, in particular in [Dunlop et al. \(2017\)](#) (2/16) or [Ueda et al. \(2018\)](#) (4/12).

## 4.9 Conclusion

The GOODS–ALMA survey covers an area of  $69 \text{ arcmin}^2$  matching the deepest HST–WFC3 coverage of the GOODS–*South* field at 1.1 mm and at a native resolution of  $\sim 0''.24$ . We used a  $0''.60$  tapered mosaic due to the large number of independent beams at the native resolution. A comparison of the HST source positions with existing catalogs such as Pan-STARRS allowed us to correct the HST astrometry of the GOODS–*South* field from both a global and local offset (equivalent to a distortion map, see also Dickinson et al. in prep.). We find a median offset between the HST and ALMA images of  $-94 \pm 42 \text{ mas}$  in right ascension,  $\alpha$ , and  $262 \pm 50 \text{ mas}$  in declination,  $\delta$ . The main conclusions from our study are listed below.

- 20 galaxies brighter than 0.7 mJy at 1.1mm. We detect in total 20 sources above a detection threshold that guarantees an 80% purity (less than 20% chance to be spurious). Among these 20 galaxies (with an  $\text{SNR} > 4.8$ ), we expect  $4 \pm 2$  spurious galaxies from the analysis of the inverted map and we identify 3 probably spurious detections with no HST nor *Spitzer*–IRAC counterpart, consistent with the expected number of spurious galaxies. An additional three sources with HST counterparts are detected either at high significance in the higher resolution map, or with different detection-algorithm parameters ensuring a purity greater than 80%. Hence we identify in total 20 robust detections.
- Pushing further in redshift the blind detection of massive galaxies with ALMA. The sources exhibit flux densities ranging from 0.6 to 2 mJy, have a median redshift (and rms) of  $z = 2.92 \pm 0.20$  and stellar mass of  $M_* = (1.1 \pm 0.4) \times 10^{11} M_\odot$ . By comparison with deeper but smaller ALMA extragalactic surveys ([Aravena et al. 2016](#); [Dunlop et al. 2017](#); [González-López et al. 2017](#); [Ueda et al. \(2018\)](#)), our redshift distribution is shifted to higher values even though our survey is shallower. This is due to the low surface density of massive, metal hence dust-rich, galaxies at high redshifts. The size of the ALMA survey is therefore a key parameter to detect high redshift galaxies.
- Exceptionally high AGN fraction. We find a high proportion of AGNs in our ALMA 1.1mm sample with 40% (8 out of 20 robust detections) detected in the 7Msec *Chandra* X-ray survey of GOODS–*South* in the 0.5–7.0 keV band with a X-luminosity greater than  $10^{43} \text{ erg.sec}^{-1}$ . Limiting our analysis to the ALMA sources with a redshift and stellar mass

determination, we find that 50% of the ALMA sources located in a well-defined stellar mass ( $M_{\star} > 3 \times 10^{10} M_{\odot}$ ) - redshift ( $z \sim 1.8-4.5$ ) range host an AGN as compared to 14% only for the galaxies located within the same zone but undetected by ALMA. This excess AGN contribution may be due to the fact that the ALMA galaxies are preferentially in a starburst mode due to our detection limit – hence possibly experiencing a merger – or/and that the high-resolution of ALMA favours unresolved, hence compact, sources knowing that the mechanism that leads to such compact star-formation may also trigger an AGN.

## Contents

4.1	Source Detection	57
4.2	Threshold determination	58
4.3	Creation of the catalog	60
4.4	Supplementary catalog	63
4.5	Astrometric correction	65
4.6	Identification of counterparts	66
4.7	Mass and redshift	74
4.8	AGN	78
4.9	Conclusion	79

## 5.1 Motivation of the number counts

Number counts make it possible to model the flux distribution of sources in the sky. The great strength of this modelling approach is that it is done without any a priori knowledge, and therefore is not biased on the nature of the galaxies observed. It is, for example, not necessary to know the redshift or the mass of the galaxies. In addition to that, they set key constraints on galaxy evolution models using only one single filter or frequency band. However, detailed analysis of the observations and characterization and correction of observational biases must be carried out in order to obtain an accurate model of the evolution of galaxy density as a function of fluxes.

In this section, we will briefly present the reasons for conducting these number counts and explain the two types of number counts we have conducted. We will then explain the different biases to which we have been exposed and the tests and simulations we have performed to correct these biases. We will then compare the results we have obtained with those obtained in other surveys or models. Finally, we will use the parameterization of our number counts to estimate the contribution of the resolved sources detected in this survey to the Cosmic Infrared Background.

The observation in 1964 of the Cosmic Microwave Background (CMB) by Penzias and Wilson ([Penzias and Wilson, 1965](#)) opened a new era in the history of astronomy and the understanding of the evolution of the universe. Thirty years later, another discovery, less well known to the general public, also had a profound impact on our understanding of the evolution of galaxies: a significant part of the Extragalactic Background Light (EBL) is detected at infrared or millimetre wavelengths (see [Fig. 5.1](#); [Puget et al. 1996](#); [Fixsen et al. 1998](#); [Dole et al. 2006](#)). We will discuss

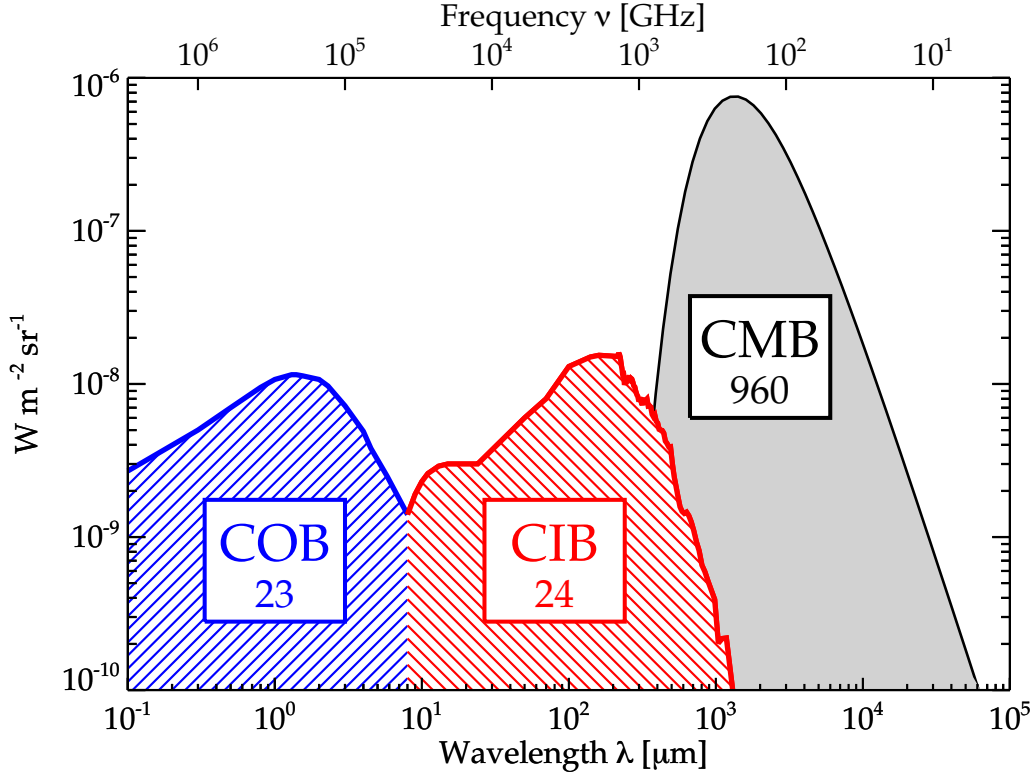


FIGURE 5.1: Schematic Spectral Energy Distributions for the Cosmic Microwave Background (CMB), the Cosmic Infrared Background (CIB) and the Cosmic Optical Background (COB). For each panel, the brightness is given in units of  $\text{nW m}^{-2} \text{sr}^{-1}$ . Figure from [Dole et al. \(2006\)](#).

the contribution of the Cosmic Infrared Background (CIB) to the EBL in detail in Sect 5.10. The first survey carried out with single-dish telescopes at submillimeter wavelengths, which detected only galaxies with a flux greater than a few mJy (e.g., [Barger et al., 1998](#); [Eales et al., 1999](#); [Smail et al., 2002](#)), showed that only a small part of this Cosmic Infrared Background was resolved into galaxies. Herschel studies have now shown that the CIB can be resolved ([Lagache et al., 2000](#); [Dole et al., 2006](#); [Berta et al., 2010](#)). One of the key questions that motivates (sub)millimetre surveys and galaxy number counts is to know what proportion of the CIB is coming from dust re-processed stellar emission of high redshift galaxies.

## 5.2 The different forms of number counts

### 5.2.1 Cumulative number counts

The aim of cumulative number counts is to model the number of galaxies per unit area with a flux greater than  $S_\nu$ . The interpretation of the cumulative number counts is straightforward. On the y-axis is the number of sources with a flux greater than a given flux per unit area. On the other hand, since these are cumulative number counts, the number of low-flux sources is dependent on the number of high-flux sources. The slightest error or uncertainty is propagated to all the number counts.

### 5.2.2 Differential number counts

The aim of differential number counts is to model the number of galaxies per unit area with a flux between  $S_\nu$  and  $S_\nu + dS_\nu$ . One of the advantages of using differential number counts compared to cumulative number counts is the absence of correlation of the counts between the different bins. However, the differential number counts are sensitive to the lower number of detections per flux density bin.

## 5.3 Number counts in a static Euclidean universe

If we lived in a static Euclidean universe, then the number counts would be a breeze to predict. Inside a sphere of radius  $R$ , the number of sources would not evolve in this sphere. The relationship between flux density and luminosity would simply be given by:

$$S_\nu = \frac{L_\nu}{4\pi R^2} \quad (5.1)$$

The number of sources can be expressed within a sphere of radius  $R$  by:

$$N = \frac{\Omega}{4\pi} \int_0^R N_0 4\pi r^2 dr = \frac{\Omega}{3} N_0 R^3 \quad (5.2)$$

with  $N_0$  the number of sources per unit volume. The number of sources is therefore proportional to the cube of the radius of this sphere ( $N \propto R^3$ ). Moreover, Eq. 5.1 tells us that the flux of a source is inversely proportional to the radius of the sphere squared ( $S_\nu \propto R^{-2}$ ). By combining these two proportionality relationships, we see that  $N \propto S_\nu^{-3/2}$  for cumulative number counts.

$$N = \frac{\Omega}{3} N_0 \left( \frac{L_\nu}{4\pi} \right)^{3/2} S_\nu^{-3/2} \quad (5.3)$$

For differential counts, we find that  $N \propto S_\nu^{-5/2}$ .

$$\frac{dN}{dS_\nu} = \frac{\Omega}{2} N_0 \left( \frac{L_\nu}{4\pi} \right)^{3/2} S_\nu^{-5/2} \quad (5.4)$$

It is common to represent number counts normalized to the Euclidean trend, i.e., by multiplying them by flux to the power of 2.5 (units of  $\text{mJy}^{1.5} \text{deg}^{-2}$ , see Fig. 5.2). However, in the rest of our study, we do not represent the counts in Euclidean-normalized units, in order to be consistent with the latest published studies.

Unfortunately (for the implicit interpretation of the number counts), we do not live in a Euclidean universe, so the flux of galaxies varies with redshift. We therefore have to consider the K-correction (see Sect. 1.4.1). Moreover, the spectrum of a galaxy evolves according to the redshift, meaning that a distant galaxy will not have, for example the same stellar population, nor the same size, nor the same dust temperature, and thus does not have the same SED as a nearby galaxy. It is also important to note that in a non-Euclidean universe, the radius of the sphere is no longer constant, and evolves with cosmic time. It is therefore no longer the radius that must

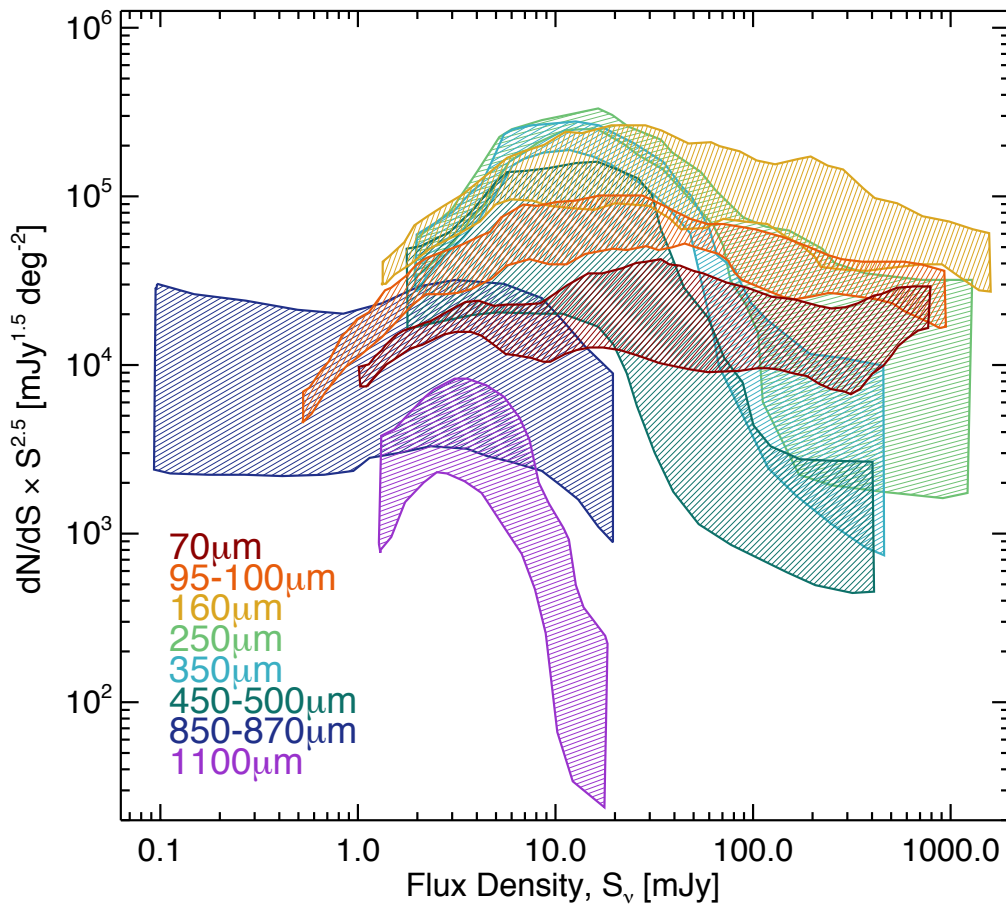


FIGURE 5.2: Differential number counts at  $70\mu\text{m}$ ,  $100\mu\text{m}$ ,  $160\mu\text{m}$ ,  $250\mu\text{m}$ ,  $350\mu\text{m}$ ,  $500\mu\text{m}$ ,  $850\mu\text{m}$ , and  $1.1\text{ mm}$  plotted with Euclidean-normalized units. The shaded regions represent the  $1\sigma$  uncertainties. Figure from Casey et al. (2014).

be taken into account, but the luminosity distance. This luminosity distance varies as  $(1+z)^\alpha$ , with  $\alpha$  evolving with the redshift (see Fig. 1.13).

In a non-Euclidean universe, the flux of a galaxy evolves as:

$$S_\nu(z) = \frac{L_{\nu(1+z)}(z)}{4\pi D_l^2} \quad (5.5)$$

## 5.4 (Sub)millimeter surveys over contiguous areas of the sky

In this section we discuss the surveys performed with  $850\mu\text{m} < \lambda < 3\text{ mm}$ . During the last decades, many (sub)millimetre surveys have been carried out by many instruments, for example, the Submillimetre Common-User Bolometer Array (SCUBA; Holland et al. 1999) on the James Clerk Maxwell Telescope, the Large APEX Bolometer Camera (LABOCA; Siringo et al. 2009) on the Atacama Pathfinder Experiment (APEX; Güsten et al. 2006); the Max Planck Millimeter Bolometer Array (MAMBO; Kreysa et al. 1998) on 30 meter telescope at the Institut de Radio Astronomie Millimetrique (IRAM); the AzTEC camera (Wilson et al., 2008) and the the Atacama

Submillimeter Telescope Experiment (ASTE; [Ezawa et al. 2004](#)) and Bolocam ([Glenn et al., 1998](#)) on the Caltech Submillimeter Observatory (CSO), the Goddard IRAM Superconducting Millimeter Observer (GISMO) at the IRAM 30m-telescope ([Staguhn et al., 2014](#); [Magnelli et al., 2019](#)) as well as with interferometer such as ALMA.

In order to be able to constrain the number counts, surveys have been carried out at different depths (see Fig. 5.3). This allows both the faint and bright ends of the number counts to be constrained. The first surveys carried out by SCUBA at the end of the 1990s covered small areas. The development of more efficient instruments, such as SCUBA-2, has made it possible to carry out surveys covering a larger area but the depth remains limited by the confusion noise (see Sect. 5.5.7). Recently, thanks to the advent of the Atacama Large Millimeter/submillimeter Array (ALMA) and its capabilities to perform both high-resolution and high-sensitivity observations, our view of galaxies detected in (sub)millimeter wavelengths has become increasingly refined. The high angular resolution compared to single-dish observations reduces drastically the uncertainties of source confusion and blending, and provides new opportunities for robust galaxy identification and flux measurement. The ALMA sensitivity permits the detection of sources down to 0.1 mJy (e.g., [Carniani et al., 2015](#)), the analysis of populations of dust-poor high- $z$  galaxies ([Fujimoto et al., 2016](#)) or main sequence (MS; see Sect. 1.3.4) galaxies (e.g., [Papovich et al., 2016](#); [Dunlop et al., 2017](#); [Schreiber et al., 2017](#)), and also demonstrates that the extragalactic background light (EBL) can be resolved partially or totally by faint galaxies ( $S < 1$  mJy; e.g., [Hatsukade et al. 2013](#); [Ono et al. 2014](#); [Carniani et al. 2015](#); [Fujimoto et al. 2016](#)). Thanks to this new domain of sensitivity, ALMA is able to unveil less extreme objects, bridging the gap between massive starbursts and more normal galaxies: SMGs no longer stand apart from the general galaxy population (e.g. [Dunlop et al., 2017](#); [Elbaz et al., 2018](#)).

Soon, large millimeter surveys are planned to cover unparalleled areas of the sky, whether in the short term with the TolTEC at the Large Millimeter Telescope (LMT; [Bryan 2018](#)), the SPT3G at the SPT, NIKA-2 camera ([Adam et al., 2018](#)) at the IRAM 30m-telescope, the Chajnantor Sub/Millimeter Survey Telescope (CSST; [Golwala 2018](#)) or in the longer term with the Origins Space Telescope (OST; [Battersby et al. 2018](#)).



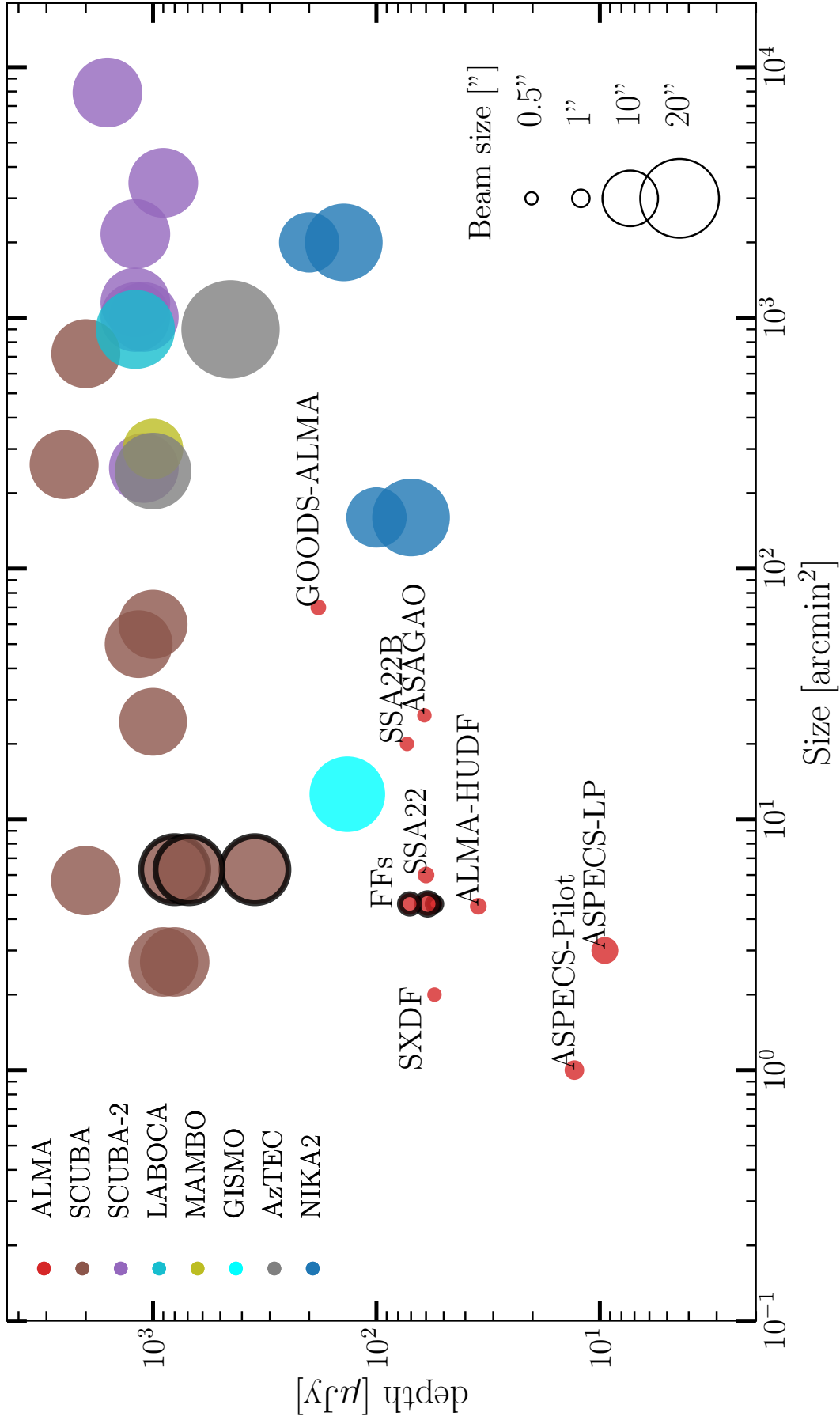


FIGURE 5.3: Size-depth plan for some of the main (sub)millimeter surveys with  $850\mu\text{m} \lambda < 3\text{ mm}$ . The dots represent the following surveys: Hughes et al. (1998); Barger et al. (1998); Eales et al. (1999, 2000); Bertoldi et al. (2000); Scott et al. (2002); Cowie et al. (2002); Webb et al. (2003); Mortier et al. (2005); Coppin et al. (2006); Perera et al. (2008); Weiß et al. (2009); Hatsu et al. (2011); Staghun et al. (2014); Hatsu et al. (2016); Dunlop et al. (2017); Umehata et al. (2017); González-López et al. (2017); Geach et al. (2017); Umehata et al. (2018); Hatsu et al. (2018); Franco et al. (2018); González-López et al. (2019a) as well as the future NIKA2 Cosmological Legacy Survey (NIKA2 GT-LP - N2CLS, PI : G. Lagache, A. Beelen, N. Ponthieu). The dots color-coded following the instruments used. The size of the dots correspond to the size of the beam. The black outer line means that the survey covers a lensed area. This list of surveys is not exhaustive. We point out that to date, the GOODS-ALMA survey is the largest (sub)millimeter survey without confusion issues.

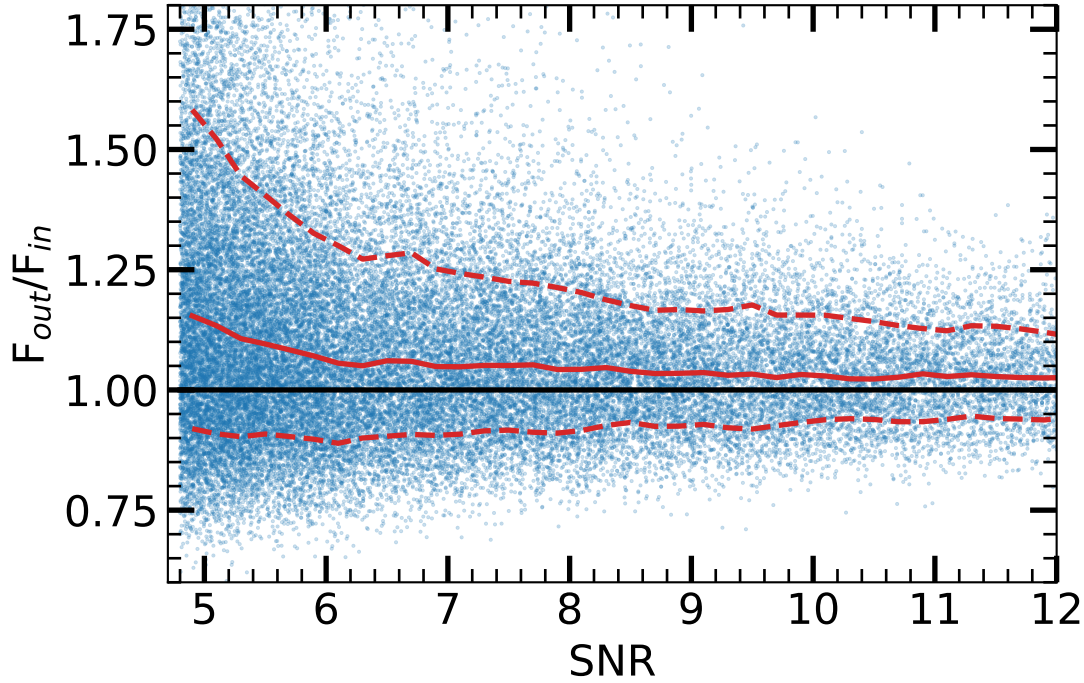


FIGURE 5.4: Flux boosting as a function of measured S/N estimated from simulations. The median of the boosting is shown by a solid red line. The  $1\sigma$  confidence intervals (dashed red lines) are overplotted. The solid black horizontal line corresponds to  $F_{\text{out}} = F_{\text{in}}$  (see text for details). We have used the same set of simulations that we used for the completeness analysis.

## 5.5 Bias estimation

In this section, we will discuss the different biases that we have estimated and corrected in order, from our observations, to be able to trace back the number of galaxies present in the sky per unit of surface area.

### 5.5.1 Deboosting fluxes

In this section, we evaluate the effect of flux boosting. Galaxies detected with a relatively low S/N tend to be boosted by noise fluctuations (see [Hogg and Turner 1998](#); [Coppin et al. 2005](#); [Scott et al. 2002](#)). To estimate the effect of flux boosting, we used the same set of simulations that we used for completeness estimations (see Sect. 5.5.5).

The results of our simulations are shown in Fig. 5.4. The boosting effect is shown as the ratio between the input and output flux densities as a function of the measured S/N. For point sources, we observed the well-known flux boosting effect for the lowest S/Ns. This effect is not negligible for the faintest sources in our survey. At  $4.8\sigma$ , the flux boosting is  $\sim 15\%$ , and drops below 10% for an S/N greater than 5.2. We estimated the de-boosted flux by dividing the measured flux by the median value of the boosting effect as a function of S/N (red line in Fig. 5.4).

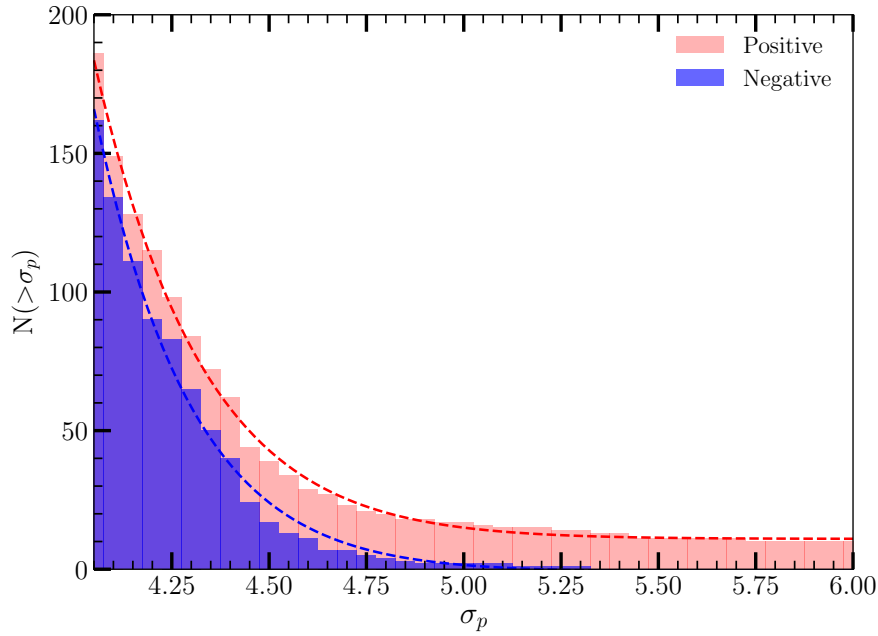


FIGURE 5.5: Cumulative number of positive (red histogram) and negative (blue histogram) detections as a function of the  $\sigma_p$ . The red and blue dashed lines use the best fit parameters of the Eq. 5.6 for the positive and negative distribution respectively.

### 5.5.2 Purity

We parameterize the purity criterion (see Eq. 6.1 and Fig. 4.2) according to the following equation:

$$\text{purity}(S/N) = A \left( 1 - \text{erf}\left(\frac{S/N}{B}\right) \right) + C \quad (5.6)$$

where  $A = (-7.58 \pm 1.31) \times 10^5$ ,  $B = -1.55 \pm 0.02$ ,  $C = (1.51 \pm 0.25) \times 10^6$  for the positive histogram and  $A = (-1.9 \pm 0.5) \times 10^6$ ,  $B = -1.46 \pm 0.02$ ,  $C = 3.80 \pm 0.91 \times 10^6$  for the negative histogram.

The histogram showing the number of positive and negative sources (see Fig. 5.5) is not intuitive to read. At  $\sigma_p = 4.8$ , we have 20 positive sources for 4 negative ones, which is a purity rate of 80%. That does not mean that it is strictly each one of the 20 sources that has an 80 percent chance of being false. With a detection threshold of  $4.8\sigma$ , the S/N range of our detections is  $\sim 4.8$ -11. Each source has a probability of being false equal to its purity estimated at the S/N of its detection.

### 5.5.3 Eddington Bias

As sources with lower luminosities are more numerous than sources with higher luminosities, assuming that the noise is Gaussian distributed gives rise to an overestimation of the number counts in the lowest flux bins. Sir Arthur Stanley Eddington, in 1913, proposed a formula to correct the statistical effects of magnitude distribution between the observed magnitude distribution

and the "true" magnitude distribution (Eddington, 1913). After Dyson (1926) had studied in detail a particular form of Eddington bias in the distribution of stellar parallaxes, Sir Arthur Stanley Eddington proposed a literal form of this bias (Eddington, 1940).

We also corrected for the effects of the Eddington bias (Eddington, 1913). We simulated a realistic number of sources (the slope of the number counts were computed using the coefficients given in Table 5.2) and added Gaussian noise to each simulated source. The correction factor for each flux bin was therefore the ratio between the flux distribution before and after adding the noise. The bias is that when Gaussian noise is added to the flux density  $F_\nu + \delta F_\nu$ , since the number of low flux density galaxies is much higher than the number of high flux sources, the number of sources artificially entering the counts because of the noise fluctuations at low flux density is higher than the number of galaxies artificially leaving the number counts at higher flux density. This creates a bias between the "real" source number per flux density interval and the observed number (see Fig. 5.6). In order to correct this effect, we simulated a realistic number of sources (the slope of the number counts is computed using the coefficients given in Table 5.2) and add Gaussian noise to each simulated source. The correction factor for each flux bin is therefore the ratio between the flux distribution before and after adding the noise.

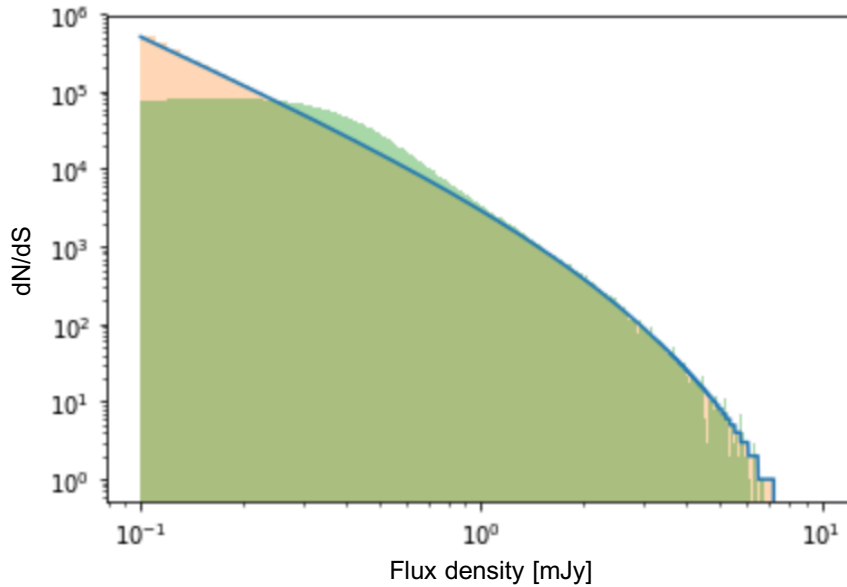


FIGURE 5.6: Distribution of the number of galaxies calculated according to the set of parameters given in Table 5.2 ; blue curve) as a function of flux density, and when a Gaussian noise is added (green distribution). The difference between the two curves represents the Eddington bias.

### 5.5.4 Effective Area

As the sensitivity of our 1.1mm ALMA map is not uniform, we defined an effective area where a source with a given flux can be detected with an  $S/N > 4.8\sigma$ , as shown in Fig. 5.7. Our map is composed of six different slices - one of them, slice B, presents a noise 30% greater than the mean of the other five, whose noise levels are comparable. The total survey area is  $69.46 \text{ arcmin}^2$ , with 90% of the survey area reaching a sensitivity of at least  $1.06 \text{ mJy.beam}^{-1}$ . We considered the relevant effective area for each flux density in order to compute the number counts. We considered the total effective area over all slices in the number counts computation.

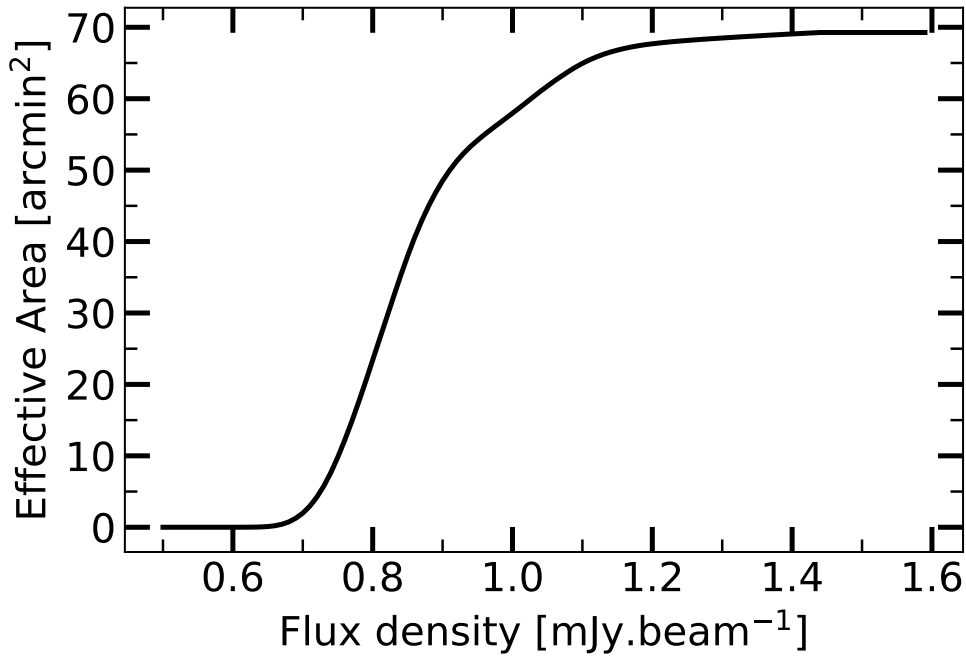


FIGURE 5.7: Effective area as a function of flux density, where a source with a given flux can be detected with an  $\text{SN} > 4.8\sigma$ . 90 percent of the survey area reaches a sensitivity of at least  $1.06 \text{ mJy.beam}^{-1}$ .

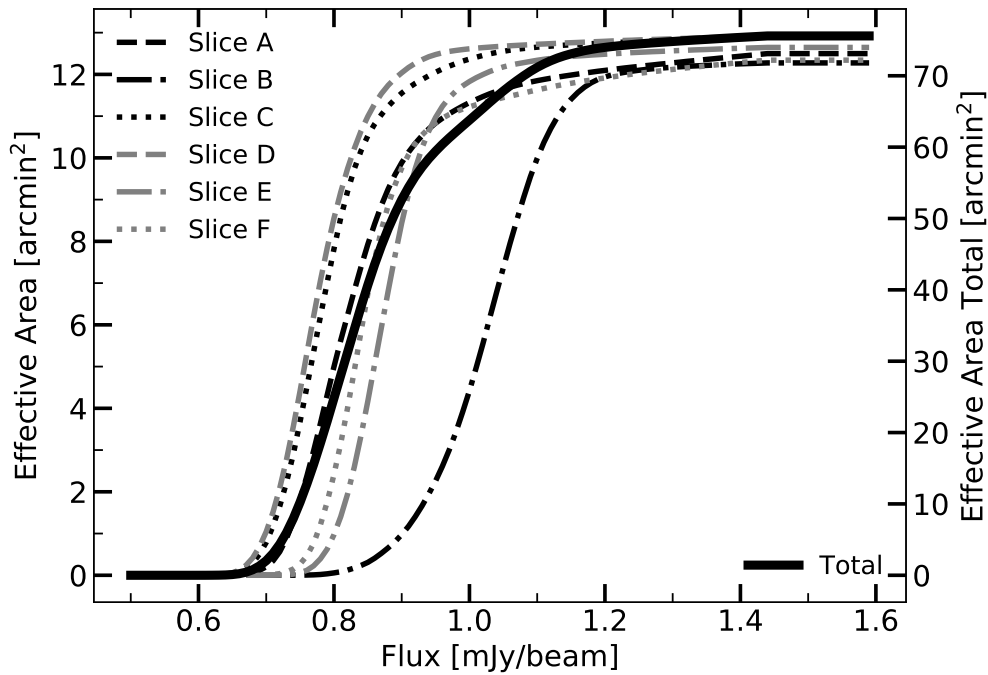


FIGURE 5.8: As the noise map is not uniform (see Table 3.6 and Fig. 3.16), we have split the effective area according to the slices (different dashed lines for each slices) in addition to the total area shown by the solid line. For each slice, excluding slice B, 50% of the effective area is reached between 0.7-0.9 mJy, or 1.1mJy for slice B.

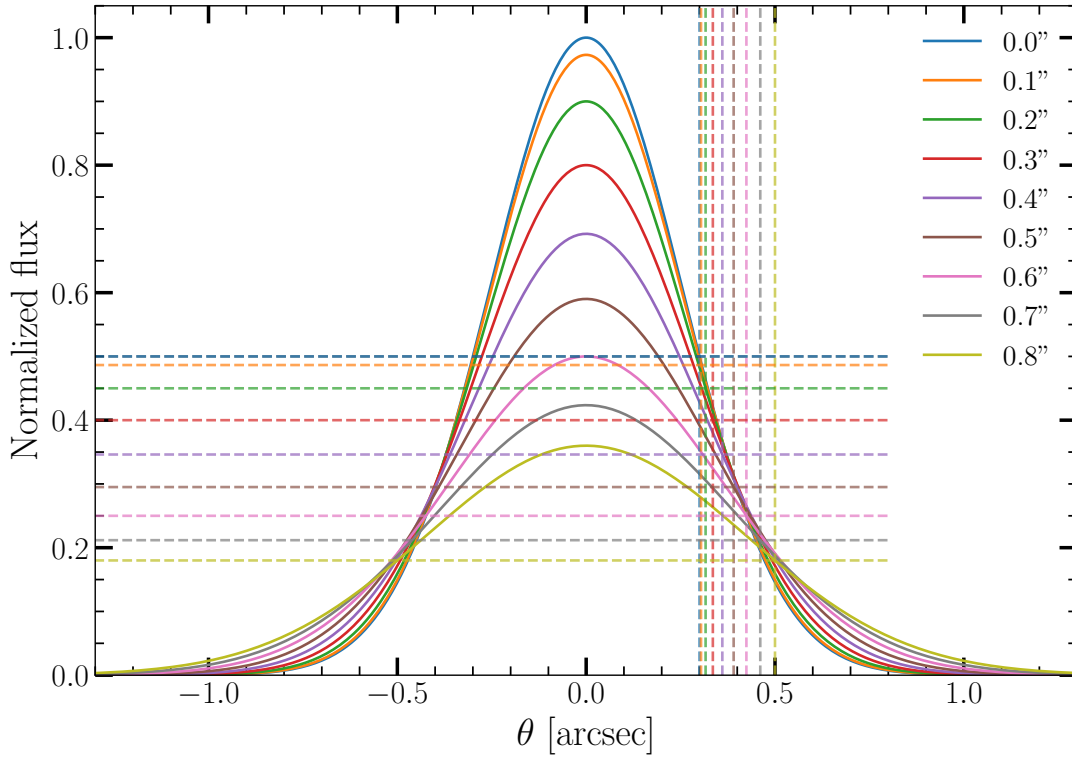


FIGURE 5.9: Convolution of a source (Gaussian form) of different sizes with a Gaussian of  $0.6''$  (representing the PSF). Half of the FWHM of this convolution is given by the dotted lines. The integrated flux is the same for all convolutions.

### 5.5.5 Completeness

For the same integrated flux, the more compact a source will be, the easier its detection will be (see Fig. 5.9). Basically, if we consider that the shape of the source is Gaussian and that the PSF is Gaussian too:

$$f(x) = \frac{1}{\sqrt{2\pi}\sigma_f} e^{-\frac{(x-\mu_f)^2}{2\sigma_f^2}} \quad \text{and} \quad g(x) = \frac{1}{\sqrt{2\pi}\sigma_g} e^{-\frac{(x-\mu_g)^2}{2\sigma_g^2}} \quad (5.7)$$

The convolution of these two Gaussians will be given by<sup>1</sup>:

$$\int_0^x f(x-\tau)g(\tau)d\tau = f \otimes g \quad (5.8)$$

$$F^{-1}[F(f(x))F(g(x))] = f(x) \otimes g(x) \quad (5.9)$$

$$F(f(x)) = \frac{1}{\sqrt{2\pi}\sigma_f} \int_{-\infty}^{\infty} e^{-\frac{x'^2}{2\sigma_f^2}} e^{-2\pi i k(x'+\mu_f)} dx' = \frac{e^{-2\pi i k\mu_f}}{\sqrt{2\pi}\sigma_f} \int_{-\infty}^{\infty} e^{-\frac{x'^2}{2\sigma_f^2}} e^{-2\pi i kx'} dx' \quad (5.10)$$

$$P_{f \otimes g}(x) = F^{-1}[F(f(x))F(g(x))] = \frac{1}{\sqrt{2\pi(\sigma_f^2 + \sigma_g^2)}} e^{-\frac{(x-(\mu_f+\mu_g))^2}{2(\sigma_f^2 + \sigma_g^2)}} \quad (5.11)$$

1. this calculation is inspired by <http://www.tina-vision.net/docs/memos/2003-003.pdf>

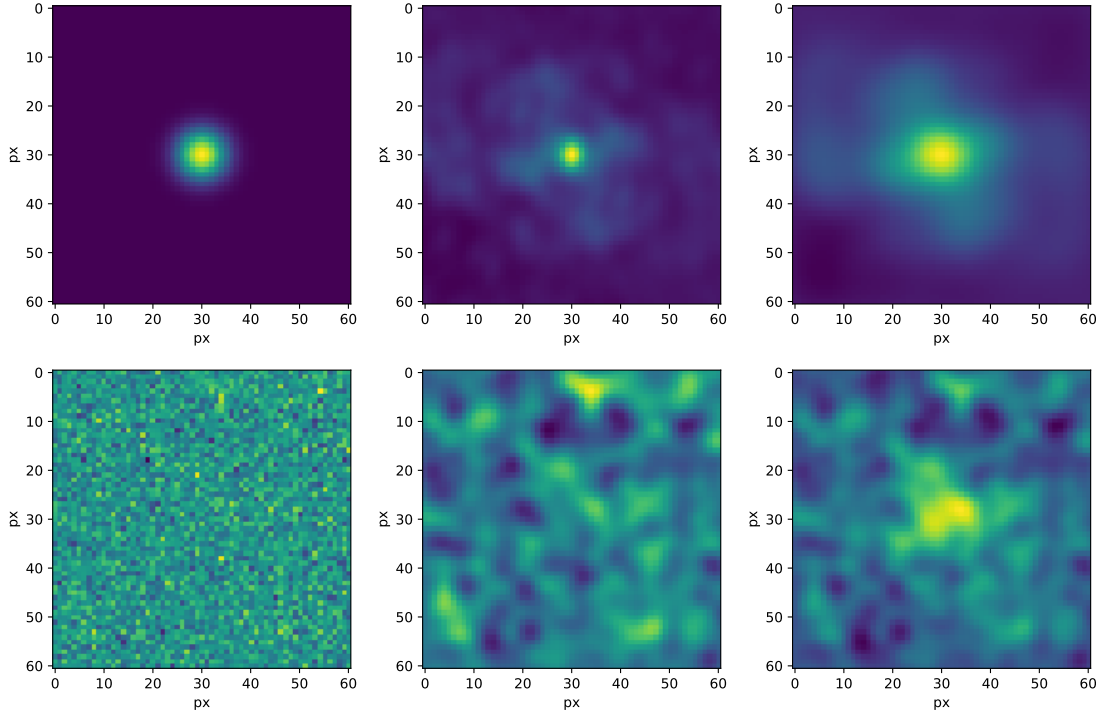


FIGURE 5.10: Process of creation and injection of artificial sources. Top left: Gaussian shape sampled accounting to pixel size; Top middle: PSF of the slice considered; Top right: convolution of the Gaussian by the PSF. Bottom left: Gaussian noise; Bottom middle: the flux is smoothened by a Gaussian kernel so that it is no longer random pixel by pixel but correlated as in our image. Bottom right: addition of the source (Gaussian shape) convolved with the PSF and the correlated noise. The integrated flux of the injected source is 1mJy, i.e.,  $S/N = 5.5$  (the cuts of the image are normalized to the source).

We assessed the accuracy of our catalog by performing completeness tests. The completeness is the probability of a source to be detected in the map. We computed the completeness of our observations using Monte Carlo simulations performed on the  $0''.60$ -mosaic map. We injected 50 artificial sources in each slice. Each source was convolved with the PSF and randomly injected on the dirty map tapered at  $0''.60$  (see Fig. 5.10). In total, for each simulation run, 300 sources with the same flux were injected into the total map (see Fig. 5.11). In view of the size of the map, the number of independent beams and the few number of sources detected in our survey, we can consider, to first order, that our dirty map can be used as a blank map containing only noise, and that the probability to inject a source exactly at the same place as a detected galaxy is negligible.

The probability that at least two point sources, randomly injected, are located closer than FWHM ( $p_b$ ) is:

$$p_b = 1 - \prod_{k=0}^{n-1} \frac{N_b - k}{N_b} \quad (5.12)$$

where  $N_b$  is the number of beams in the full mosaic and  $n$  is the number of injected sources. For each one of the six slices of the survey, we have  $\sim 100\,000$  independent beams at the resolution of  $0''.60$ . The probability of having source blending for 50 simulated sources in one map is therefore  $\sim 1\%$ .



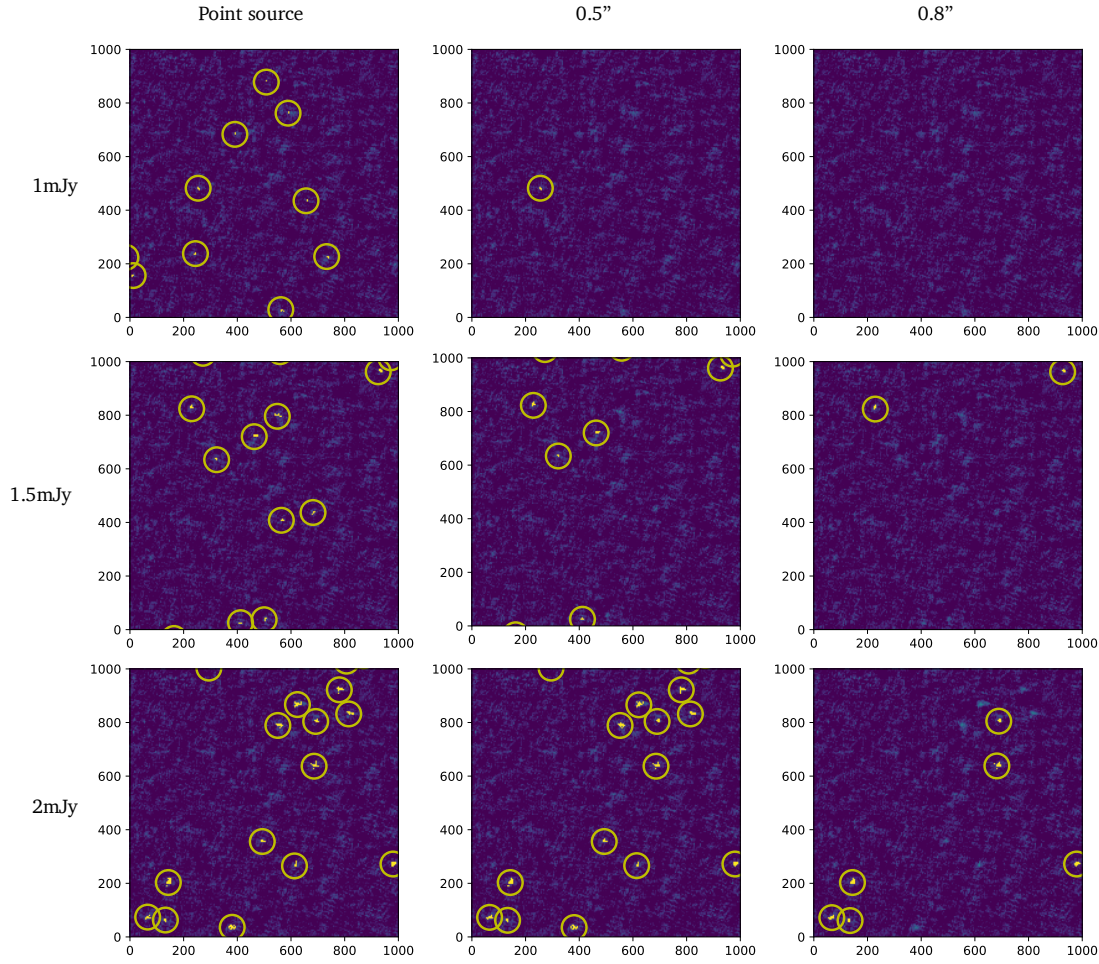


FIGURE 5.11: Example of detection test according to the intrinsic size of the injected source and its integrated flux, for the left column, for a point-like source, for the middle column for a source with an FWHM of  $0.5''$  and for the right column for an FWHM of  $0.8''$ . To better analyze the effects of size on detection, for a run, at each given flux, the sources were injected at the same positions when we vary the size. Detections at a threshold of  $4.8\sigma$ , corresponding to the detection threshold of our survey are indicated by a yellow circle. To ensure that these completion tests are done in exactly the same way as for the creation of our catalog, we used the same code, `Blobcat` for the source detection.

We then counted the number of injected sources detected with  $\sigma_p = 4.8\sigma$  and  $\sigma_f = 2.7\sigma$ , corresponding to the thresholds of our main catalog. We injected 300 artificial sources of a given flux, and repeated this procedure 100 times for each flux density. Our simulations cover the range  $S_\nu = 0.5\text{--}2.4\text{ mJy}$  in steps of  $0.1\text{ mJy}$ . Considering the resolution of the survey, it would be reasonable to expect that a non-negligible number of galaxies are not seen as point sources but extended sources (see Sect. 4.6.1). We simulated different sizes of galaxies with Gaussian FWHM between  $0''.2$  and  $0''.9$  in steps of  $0''.1$ , as well as point-source galaxies, to better understand the importance of the galaxy size in the detectability process. We matched the recovered source with the input position within a radius of  $0''.6$ .

Fig. 5.12 shows the resulting completeness as a function of input flux, for different FWHM Gaussian sizes convolved by the PSF and injected into the map.

As a result of our simulations, we determined that at  $1.2\text{ mJy}$ , our sample is  $94 \pm 1\%$  complete for point sources. This percentage drastically decreases for larger galaxy sizes. For the same



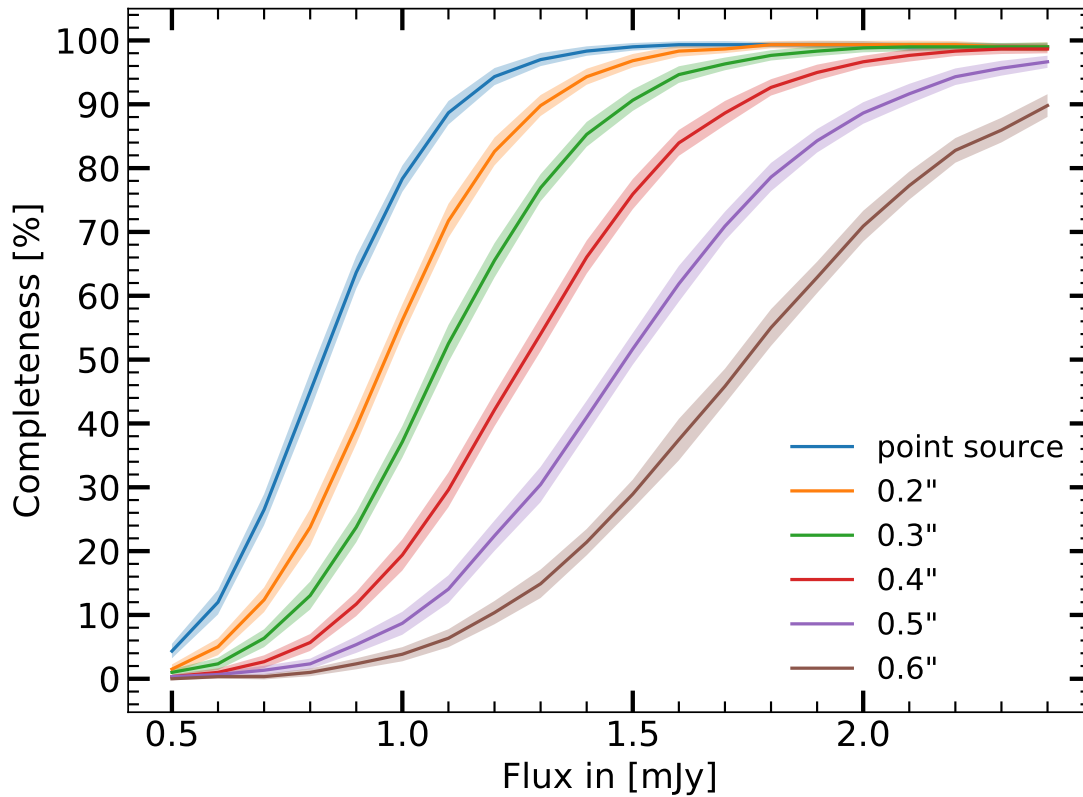


FIGURE 5.12: Median source detection completeness for simulated point-like and Gaussian galaxies as a function of integrated flux, for different FWHMs (see figure’s legend). The shaded regions correspond to the standard deviation of 100 runs, each containing 300 simulated sources.

flux density, the median detection rate drops to  $61 \pm 3\%$  for a galaxy with  $\text{FWHM} \sim 0''.3$ , and to  $9 \pm 1\%$  for a  $\text{FWHM} \sim 0''.6$  galaxy. This means, that for a galaxy with an intrinsic flux density of  $1.2 \text{ mJy}$ , we are more than ten times more likely to detect a point source galaxy than a galaxy with  $\text{FWHM} \sim 0''.6$ .

The size of the millimeter emission area plays an essential role in the flux measurement and completeness evaluation. In order to roughly estimate this effect, we assumed that ALMA sizes are 1.4 times smaller than the size measured in HST  $H$ -band (as derived by [Fujimoto et al. 2017](#) using 1034 ALMA galaxies). We are aware that this size ratio is poorly constrained at the present time, but such relations have been observed in several studies (see Sect. 4.6.1). For example, of the 12 galaxies presented by [Laporte et al. \(2017\)](#), with fluxes measured using ALMA at  $1.1 \text{ mm}$  ([González-López et al., 2017](#)), seven of them have a size measured by HST F140W/WFC3 similar to the size measured in the ALMA map. On the other hand, for the remaining five galaxies, their sizes are approximately two times more compact at millimeter wavelengths than at optical wavelengths. This illustrates the dispersion of this ratio.

### 5.5.6 Cosmic variance

When studying relatively small fields and wanting to extend this result to the whole sky, there is an observational uncertainty, based on the variation in density of large scale structures. Indeed, it is not always clear whether the part of the sky we are observing is representative of the

whole sky, or whether we are looking at a region that is particularly rich or poor in galaxies. This variation, which depends on the size of the area studied, as well as the masses and redshifts of the observed galaxies, is called the cosmic variance. This cosmic variance is particularly important when the studied area is small, the galaxies are massive, and the redshifts high. Unfortunately, it is precisely these characteristics that define the field and the galaxies that we study in GOODS-ALMA. The relative cosmic variance can be defined by:

$$\sigma_v^2 = \frac{\langle N^2 \rangle - \langle N \rangle^2}{\langle N \rangle^2} - \frac{1}{\langle N \rangle} \quad (5.13)$$

where  $\langle N^2 \rangle$  and  $\langle N \rangle^2$  are the mean and the variance of the probability to have  $N$  objects within a volume  $V$ . The last term in this equation corresponds to the Poissonian uncertainty.

Following [Peebles \(1980\)](#) and [Moster et al. \(2011\)](#):

$$\sigma_v^2 = \frac{1}{V^2} \int_V dV_a dV_b \xi(|r_a - r_b|) \quad (5.14)$$

where  $\xi$  is the two-point correlation function of the sample .

The cosmic variance is therefore dependent on the galaxy population studied. For example, extremely red objects (EROs) at  $z \sim 1.2$  in the GOODS fields will have a relatively high cosmic variance ( $\sim 0.4-0.6$ ), much higher than the LBG population at  $z \sim 3$ , because the LBG population is much less clustered than the ERO population ([Somerville et al., 2004](#)).

Cosmic variance was not taken into account in the calculation of the errors. Above  $z = 1.8$  and up to the redshift of the farthest galaxy in our catalog at  $z = 4.8$ , the strong negative K-correction at this wavelength ensures that the selection of galaxies is not redshift-biased. The cosmic variance, although significant for massive galaxies in a small solid angle, is counterbalanced by the negative K-correction, which makes the redshift interval of our sources ( $\Delta z = 3$  in Eq. 12 in [Moster et al. 2011](#)) relatively large, spanning a comoving volume of  $1400 \text{ Gpc}^3$ . Based on [Moster et al. \(2011\)](#), the cosmic variance for our sources is  $\sim 15\%$ , which does not significantly affect the calculation of the errors on our number counts.

There are also other types of bias, such as cosmic bias (e.g., [Szapudi et al., 1999](#)), but this is negligible in our case in relation to cosmic variance ([Colombi and et al., 1999](#)), and is therefore not taken into account.

### 5.5.7 Confusion limit

This becomes the limiting factor when the observation is deep. As the number of low flux sources is greater than the number of bright sources, the deeper the observation is, the more the distance between two galaxies decreases. For SCUBA-2 for example, the confusion limit at  $850 \mu\text{m}$  is approximately  $1.7 \text{ mJy}$  ( $4\sigma$ ; [Cowie et al. \(2018\)](#)). This limit corresponds to a SFR of  $\sim 220 \text{ M}_\odot \text{yr}^{-1}$  (Kroupa IMF). For ALMA, the beam size is considerably smaller than for single dish-telescopes. If we assume a Poissonian distribution of sources, the probability that two sources brighter than  $S_{lim}$  are closer than the size of the beam is given by:

$$P(< \theta_{min}) = 1 - e^{-\pi N \theta^2} \quad (5.15)$$

In practice, this probability is even lower, and current extraction techniques allow us to detect two sources that are separated by a distance up to  $0.8\theta$  (Dole et al., 2003).

$$N = -\frac{\ln(1 - P(< \theta_{\min}))}{\pi\theta^2} \quad (5.16)$$

In the end with ALMA, in the case of this study, we are not limited by the confusion limit and the noise confusion is negligible and will not be taken into consideration.

## 5.6 Comparison with other surveys

We were able to extend the range of fluxes studied in the number counts by integrating previous (sub)millimetre number counts studies: Lindner et al. (2011); Scott et al. (2012); Karim et al. (2013); Hatsukade et al. (2013); Ono et al. (2014); Simpson et al. (2015b); Oteo et al. (2016); Carniani et al. (2015); Hatsukade et al. (2016); Aravena et al. (2016); Fujimoto et al. (2016); Umehata et al. (2017); Geach et al. (2017); Dunlop et al. (2017). We took advantage of our ALMA survey to open the parameter space in terms of surface-flux and to limit the cosmic variance due to the small size of previous ALMA surveys, which tends to strongly bias the number counts. In addition, the large size of our survey allows us to detect massive galaxies with high redshift that have been missed by smaller ALMA surveys.

There is a gap in the compilation of the (sub)millimetre number counts (see Fig. 5.13) at the level of our flux range, i.e. between 0.8 and 1.5 mJy. Our study will therefore help to fill this gap. In addition, there is a tension in the literature for fluxes  $> 1.5$  mJy. Some studies such as Geach et al. (2017) or Scott et al. (2012) that have been carried out on single dish telescopes show systematically higher counts than those carried out with ALMA for these flux ranges. There could be a blending phenomenon for galaxies with the highest fluxes when observing with a single dish telescope. These counts with ALMA (e.g., Karim et al., 2013; Simpson et al., 2015b) were done with a shorter wavelength ( $\lambda = 870 \mu\text{m}$ ). The conversion factor between  $870 \mu\text{m}$  and 1.1 mm described in detail Sect. 5.7 can suffer from great uncertainties. This ALMA survey is therefore ideal for fixing this tension.

At low flux, we can note that the deepest counts were carried out in small and lensed regions (e.g., Fujimoto et al., 2016). Here again, great uncertainties regarding number counts may appear in this for these regions of the sky. We will discuss in detail these sensitive surveys in the conclusion of this chapter.

## 5.7 Estimation of number counts

We use sources with an S/N greater than 4.8 from the main catalog to create cumulative and differential number counts. We need to take into account the contamination by spurious sources, completeness effects, and flux boosting in order to compute these number counts.

The contribution of a source with flux density  $S_i \pm dS_i$  to the cumulative number counts is given by:

$$\frac{dN(S_i)}{dS_i} = \frac{p_c(S_i)}{A_{eff}(S_i)C(S_i, R_{\text{ALMA}}^{\text{circ}})} \times \frac{dN_{\text{obs}}(S_i)}{dS_i} \quad (5.17)$$

$S_\nu$ mJy (1)	$N(> S_\nu)$ deg <sup>-2</sup> (2)	$N_{\text{cum}}$ (3)	$S_\nu$ mJy (4)	$dN/dS_\nu$ mJy <sup>-1</sup> deg <sup>-2</sup> (5)	$N_{\text{diff}}$ (6)
0.70	$2772^{+1776}_{-2641}$	19	0.80	$8257^{+26121}_{-8023}$	7
0.88	$950^{+575}_{-775}$	13	1.27	$1028^{+6547}_{-638}$	6
1.11	$524^{+530}_{-188}$	11	2.01	$327^{+148}_{-160}$	6
1.40	$327^{+277}_{-124}$	7			
1.76	$209^{+178}_{-119}$	4			

TABLE 5.1: Number counts at 1.1mm derived from  $> 4.8\sigma$  detections (main catalog). Columns: (1) Flux Density; (2) Cumulative number counts; (3) Number of entries per bin for cumulative number counts; (4) Centre of the flux density bin; (5) Differential number counts; (6) Number of entries per bin for differential number counts. Flux density bins,  $\Delta\log S_\nu = 0.20$  dex wide for differential number counts. The uncertainties are computed by Monte-Carlo simulations, added in quadrature to the Poisson uncertainties.

where  $p_c(S_i)$  is the purity criterion as defined in Eq. 6.1 at the flux density  $S_i$ ,  $A_{\text{eff}}(S_i)$  and  $C(S_i, R_{\text{ALMA}}^{\text{circ}})$  are the effective area and the completeness for the flux interval  $dS_i$ , as shown in Fig. 5.12 and Fig. 5.7. The completeness is strongly correlated with the sizes of the galaxies. To estimate the completeness, galaxies that do not have measured sizes in the  $H$ -band (van der Wel et al., 2012) are considered as point sources otherwise we use  $R_{\text{ALMA}}^{\text{circ}} = R_{\text{H}}^{\text{circ}}/1.4$  (see Sect. 5.5.5).

The cumulative number counts are given by the sum over all of the galaxies with a flux density higher than  $S$ :

$$N(> S) = \sum_{S_i > S} \frac{p_c(S_i)}{A_{\text{eff}}(S_i)C(S_i, R_{\text{ALMA}}^{\text{circ}})} \times \frac{dN_{\text{obs}}(S_i)}{dS_i} \times dS_i \quad (5.18)$$

Errors are computed by Monte-Carlo simulations, added in quadrature to the Poisson uncertainties. The derived number counts are provided in Tab. 5.1. AGS19 is located at a position where the noise is artificially low, and has therefore not been taken into account

In Fig. 5.13, we compare our results with previous studies (Lindner et al., 2011; Scott et al., 2012; Karim et al., 2013; Hatsukade et al., 2013; Simpson et al., 2015b; Oteo et al., 2016; Hatsukade et al., 2016; Aravena et al., 2016; Fujimoto et al., 2016; Umehata et al., 2017; Geach et al., 2017; Dunlop et al., 2017). To standardize these previous studies, the different flux densities are scaled to 1.1 mm using a Modified Black Body (MBB) model, assuming a dust emissivity index  $\beta = 1.5$  (e.g., Gordon et al., 2010), a dust temperature  $T_d = 35$  K (eg. Chapman et al., 2005; Kovács et al., 2006; Coppin et al., 2008), and a redshift of  $z = 2.5$  (e.g., Wardlow et al., 2011; Yun et al., 2012). These values have also been chosen to be consistent with Hatsukade et al. (2016). The different flux densities were therefore scaled to 1.1 mm using the relations  $S_{1.1\text{mm}}/S_{1.2\text{mm}} = 1.29$ ,  $S_{1.1\text{mm}}/S_{1.3\text{mm}} = 1.48$  and  $S_{1.1\text{mm}}/S_{870\mu\text{m}} = 0.56$ . It is a real challenge to standardize these previous studies because instruments, observational techniques or resolution often vary between studies. Some of these counts have been computed from individual pointings, by brightness selection, or by serendipitous detections. Observations with a single dish or a low resolution can also overestimate the number counts for the brightest fluxes, because of blending effects (see Ono et al. 2014). Another non-negligible source of error can come from an inhomogeneous distribution of bright galaxies. An underdensity by a factor of two of submillimeter galaxies with far infrared luminosities greater than  $2 \times 10^{12}L_\odot$  in the extended *Chandra* deep field south (ECDFS) compared to other deep fields has been revealed by Weiß et al. (2009).

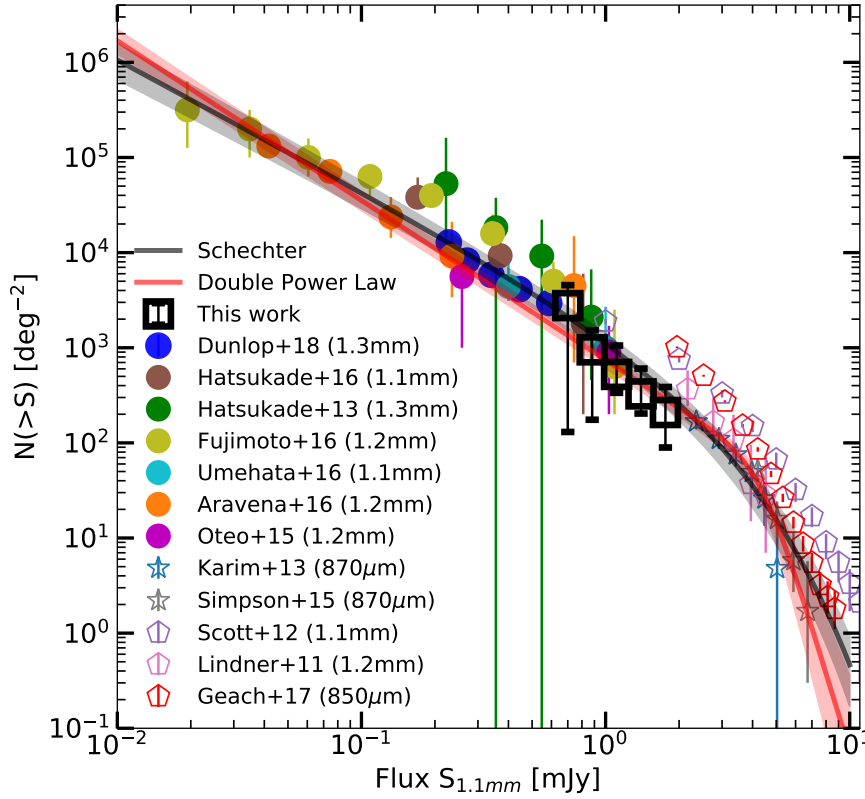


FIGURE 5.13: 1.1-mm cumulative number counts derived using the corrections described in Sect. 5.7, for the sources detected at  $> 4.8\sigma$  in the main catalog. AGS19 is located at a position where the noise is artificially low, and has therefore not been taken into account. Previous (sub)millimetre cumulative number counts are also shown (Lindner et al., 2011; Scott et al., 2012; Karim et al., 2013; Hatsukade et al., 2013; Ono et al., 2014; Simpson et al., 2015b; Oteo et al., 2016; Carniani et al., 2015; Hatsukade et al., 2016; Aravena et al., 2016; Fujimoto et al., 2016; Umehata et al., 2017; Geach et al., 2017; Dunlop et al., 2017). The different fluxes are scaled to 1.1 mm flux densities using  $S_{1.1\text{mm}}/S_{1.2\text{mm}} = 1.29$ ,  $S_{1.1\text{mm}}/S_{1.3\text{mm}} = 1.48$ ,  $S_{1.1\text{mm}}/S_{870\mu\text{m}} = 0.56$ . From the study of Umehata et al. (2017), we use only sources which do not have  $z = 3.09$ , (i.e. we are excluding the protocluster members). Results from single-dish surveys are shown with unfilled pentagon markers and are only indicative, they are not considered for model fitting. The grey curve shows the best-fit Schechter function (with  $1\text{-}\sigma$  uncertainties, and the red curve shows the best-fit DPL function (with  $1\text{-}\sigma$ ).

Despite those potential caveats, the results from our ALMA survey in the GOODS-South field are in good agreement with previous studies for flux densities below 1 mJy. For values above this flux density, two different trends coexist as illustrated in Fig. 5.13: our counts are similar to those found by Karim et al. (2013), but below the trend characterized by Scott et al. (2012). These two previous studies have been realized under different conditions. The effects of blending, induced by the low resolution of a single dish observation, as with Scott et al. (2012), tend to overestimate the number counts at the bright-end (Ono et al., 2014; Karim et al., 2013; Béthermin et al., 2017). We indicate these points on the Fig. 5.13 on an indicative basis only.

The differences in wavelength between the different surveys, even after applying the scaling corrections above, can also induce scatter in the results, especially for wavelengths far from 1.1mm.

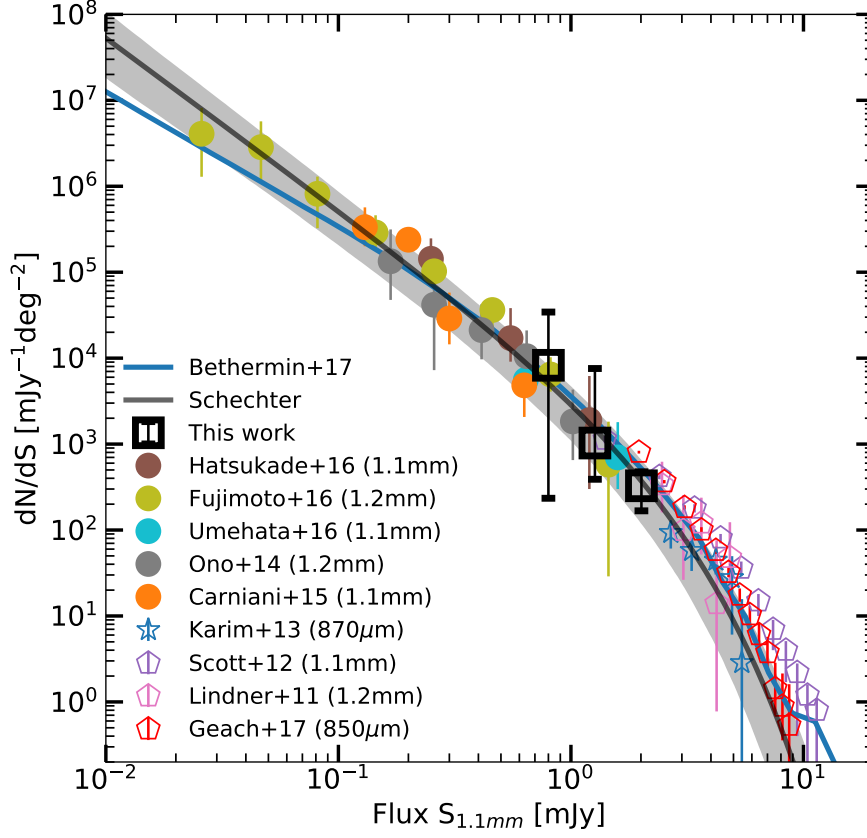


FIGURE 5.14: 1.1-mm differential number counts derived using the corrections described in Sect. 5.7, for the sources detected at  $> 4.8\sigma$  in the main catalog. AGS19 is located at a position where the noise is artificially low, and has therefore not been taken into account. Previous (sub)millimetre differential number counts are also shown (Lindner et al., 2011; Scott et al., 2012; Karim et al., 2013; Ono et al., 2014; Carniani et al., 2015; Hatsukade et al., 2016; Fujimoto et al., 2016; Umehata et al., 2017; Geach et al., 2017). The different fluxes are scaled to 1.1 mm flux densities using  $S_{1.1\text{mm}}/S_{1.2\text{mm}} = 1.29$ ,  $S_{1.1\text{mm}}/S_{1.3\text{mm}} = 1.48$ ,  $S_{1.1\text{mm}}/S_{870\mu\text{m}} = 0.56$ . From the study of Umehata et al. (2017), we use only sources which do not have  $z = 3.09$ , (i.e. we are excluding the protocluster members). Results from single-dish surveys are shown with unfilled pentagon markers and are only indicative, they are not considered for model fitting. The grey curve shows the best-fit Schechter function (with  $1-\sigma$  uncertainties), the blue curve shows the model of Béthermin et al. (2017).

## 5.8 Parametrizing number counts

The cumulative source counts from the 20 detections in this study and the results from other interferometric blank surveys are fitted with a Double Power Law (DPL) function (e.g., Scott et al., 2002) given by:

$$N(> S) = \frac{N_0}{S_0} \left[ \left( \frac{S}{S_0} \right)^\alpha + \left( \frac{S}{S_0} \right)^\beta \right]^{-1} \quad (5.19)$$

and a modified Schechter (Schechter, 1976) function (e.g., Knudsen et al., 2008):

$$N(> S) = \frac{N_0}{S_0} \left( \frac{S}{S_0} \right)^\alpha \exp \left( -\frac{S}{S_0} \right) d \left( \frac{S}{S_0} \right) \quad (5.20)$$

where  $N_0$  is the normalization,  $S_0$  the characteristic flux density and  $\alpha$  is the faint-end slope.  $\beta$  is the bright-end slope of the number of counts in Eq. 5.19. We use a least squares method with

	$N_0$ $10^2 \text{deg}^{-2}$	$S_0$ mJy	$\alpha$	$\beta$
Cumulative number counts				
DPL	$2.8 \pm 0.2$	$4.4^{+0.3}_{-0.5}$	$8.45^{+0.28}_{-1.07}$	$1.68 \pm 0.02$
Schechter	$14.3^{+1.4}_{-2.3}$	$2.0 \pm 0.3$	$-1.38 \pm 0.05$	
Differential number counts				
Schechter	$35.2^{+4.6}_{-10.8}$	$1.6^{+0.3}_{-0.4}$	$-1.99 \pm 0.07$	

TABLE 5.2: Best-fit parameters for the cumulative and differential number counts for a double power law function (Eq. 5.19) and a Schechter function (Eq. 5.20).

the Trust Region Reflective algorithm for these two fitted-functions. The best-fit parameters are given in Table 5.2.

## 5.9 Comparison with models

We compare our results with an empirical model that predicts the number counts at far-IR and millimeter wavelengths, developed by Béthermin et al. (2017). This simulation, called SIDES (Simulated Infrared Dusty Extragalactic Sky), updates the Béthermin et al. (2012) model. These predictions are based on the redshift evolution of the galaxy properties, using a two star-formation mode galaxy evolution model (see also Sargent et al. 2012).

The Béthermin et al. (2017) prediction is in good agreement with the number counts derived in this study, for the two bins with the lowest flux densities (see Fig. 5.14). For the highest-flux density bin, the model is slightly above the data ( $\sim 1\sigma$  above the best Schechter fit for flux densities greater than 1 mJy). However, both the Béthermin et al. (2017) model and our data points are below the single-dish measurements for flux densities greater than 1 mJy. This disagreement between interferometric and single-dish counts is expected, because the boosting of the flux densities of single-dish sources by their neighbor in the beam (Karim et al., 2013; Hodge et al., 2013; Scudder et al., 2016). Béthermin et al. (2017) derived numbers counts from a simulated single-dish map based on their model and found a nice agreement with single-dish data, while the intrinsic number counts in the simulation are much lower and compatible with our interferometric study.

## 5.10 Contribution to the cosmic infrared background

The contribution of our ALMA sources to the extragalactic background light (EBL) is derived by integrating the derived number counts down to a certain flux density limit. Using the 20 ( $>4.8\sigma$ ) sources detected, we computed the fraction of the 1.1 mm EBL resolved into discrete sources. The integrated flux density is given by:

$$I(S > S_{lim}) = \int_{S_{lim}}^{\infty} \frac{dN(S)}{dS} S dS \quad (5.21)$$

We used the set of parameters given in Table 5.2 on the differential number counts. We compared our results with observations from the far infrared absolute spectrophotometer (FIRAS)



on the cosmic background explorer (COBE), knowing that uncertainties exist on the COBE measurements (e.g., Yamaguchi et al., 2016). We used the equation given in Fixsen et al. (1998) to compute the total energy of the EBL:

$$I_\nu = (1.3 \pm 0.4) \times 10^{-5} \left( \frac{\nu}{\nu_0} \right)^{0.64 \pm 0.12} P_\nu(18.5 + 1.2K) \quad (5.22)$$

where  $\nu_0 = 100 \text{ cm}^{-1}$ , and  $P_\nu$  is the familiar Planck function with  $I_\nu$  in  $\text{erg.s}^{-1}\text{cm}^{-1}\text{Hz}^{-1}\text{sr}^{-1}$ . From this equation, we find that at 1.1 mm, the energy of the EBL is  $2.87 \text{ nW.m}^{-2}\text{sr}^{-1}$ .

As surface brightness is expressed in units of  $\text{nW m}^{-2} \text{sr}^{-1}$ , we use the following conversion:

$$1 \text{ nW.m}^{-2} \text{sr}^{-1} = 3000 \text{ mJy/sr}. \quad (5.23)$$

From Eq. 5.21 we can estimate the integrated EBL. For our data, the lowest flux density bin for differential counts  $S_{lim}$  is 0.7 mJy, and we extrapolate to lower flux densities. We have resolved only  $13.7^{+9.6}_{-5.3}\%$  of the EBL into individual galaxies at 0.7 mJy. This result is in good agreement with studies such as Fujimoto et al. (2016). In order to have the majority of the EBL resolved (e.g., Hatsukade et al. 2013; Ono et al. 2014; Carniani et al. 2015; Fujimoto et al. 2016), we would need to detect galaxies down to 0.1 mJy (about 50 % of the EBL is expected to be resolved at this value).

The extrapolation following the model of the differential number counts (see the coefficients in the Table 5.2) of the integrated flux density below  $S_{lim}$  suggests a flattening of the number counts. The population of galaxies that dominate this background is composed of the galaxies undetected in our survey, with a flux density below our detection limit.

## 5.11 Conclusion

The derived differential and cumulative number counts of our 20 primary detections have allowed us to partly alleviate the degeneracy observed above  $1 \text{ mJy.beam}^{-1}$  in previous (sub)millimetre studies. However, we can note that due to our low detection rate, our uncertainties on the number counts are relatively high.

This work allowed us to set the number counts to 1.1mm using our survey and the main surveys carried out in (sub)-millimetres. We have configured them with a Schechter function and a double power law. We can note the faint-end of the number counts was done through a cluster by taking advantage of a lensing. Fujimoto et al. (2016) with an ALMA survey at 1.2mm reached sources Down to  $\sim 0.02 \text{ mJy}$ . More recently, Muñoz Arancibia et al. (2018) has reached the same depths here too with lensed galaxies. There is a real doubt about the evolution of faint-end of the number counts compaction (i.e. one of the two models is not physical). Semi-analytical models such as Popping et al. in prep, coupling the UniverseMachine (Behroozi et al., 2019) with empirical and theoretical relations on the dust emission are in good agreement with the trends found for galaxies with fluxes of  $> 0.1 \text{ mJy}$  but present flattening for lower flux. This may mean that the faint-end of the number counts over small and lensed regions may not be extrapolated to all number counts.



We also showed that  $\sim 14\%$  of the extragalactic background light is resolved into individual sources at 0.7 mJy. By extrapolation,  $\sim 50\%$  of the EBL is resolved at 0.1 mJy.

# CHAPTER 6

## USING IRAC PRIORS TO PROBE FAINTER MILLIMETER GALAXIES

### Contents

5.1 Motivation of the number counts . . . . .	81
5.2 The different forms of number counts . . . . .	82
5.3 Number counts in a static Euclidean universe . . . . .	83
5.4 (Sub)millimeter surveys over contiguous areas of the sky . . . . .	84
5.5 Bias estimation . . . . .	87
5.6 Comparison with other surveys . . . . .	96
5.7 Estimation of number counts . . . . .	96
5.8 Parametrizing number counts . . . . .	99
5.9 Comparison with models . . . . .	100
5.10 Contribution to the cosmic infrared background . . . . .	100
5.11 Conclusion . . . . .	101

### 6.1 Introduction

The formation and evolution of the most massive galaxies ( $M_{\star} > 5 \times 10^{10} M_{\odot}$ ) at redshifts  $z > 2$  is still largely debated. Their observed number density exceeds theoretical expectations assuming typical dark matter to stellar mass ratios (Steinhardt et al., 2016). The downsizing of galaxy formation challenges theoretical models which match either the low or high mass end but are unable to match both ends (e.g., Fontanot et al., 2009). The presence of a population of massive passive galaxies at  $z \sim 2$  with compact stellar surface densities challenges searches for their progenitors (?).

Since infrared (IR) wavelengths contribute to approximately half of the total Extragalactic Background Light (EBL; e.g., Dole et al. 2006), the study of dust-enshrouded star-formation in distant galaxies is an important tool to progress in our understanding of the evolution of massive galaxies. The first submillimeter extragalactic surveys (Smail et al., 1997; Barger et al., 1998; Hughes et al., 1998) performed with the Submillimetre Common-User Bolometer Array (SCUBA; Holland et al. 1999) on the James Clerk Maxwell Telescope (JCMT) have revealed a population of high redshift galaxies that are massive, highly obscured and have high star formation rates (SFRs). Recent observations using the Atacama Large Millimetre/submillimetre Array (ALMA), which provides a resolution more than an order of magnitude higher than SCUBA, has since refined our understanding of galaxy evolution by securing the identification of optical counterparts and allowing us to detect not only extreme galaxies (galaxies with particularly high star

formation rates, e.g., starburst or lensed galaxies), but also "normal" galaxies that are secularly forming stars.

This chapter extends our previous analysis (see Chapter 4) of a deep continuum 1.1mm survey with ALMA over an area of  $69'^2$ . This survey is located in the Great Observatories Origins Deep Survey–*South* (GOODS–*South*) at a location covered with the deepest integrations in the H-band with the HST-WFC3 camera. Chapter 4, we limited our analysis to the blind detection of ALMA sources without considering prior information at other wavelengths. Due to the large number of independent beams in the high-resolution ALMA image, we were limited to the  $4.8\text{-}\sigma$  detection limit. Here we extend the detection limit to  $3.5\text{-}\sigma$  by cross-matching the ALMA detections with catalogs in the near and mid-infrared. The need for a good astrometric calibration led us to introduce an improved correction for the astrometry of the HST image of the GOODS–*South* field (hereafter GOODS-S).

## 6.2 Data

### 6.2.1 Additional data

#### IRAC catalog

We use the *Spitzer*-Cosmic Assembly Near-Infrared Deep Extragalactic Survey (S-CANDELS; Ashby et al. 2015) catalog of galaxies detected at  $3.6$  and  $4.5\text{ }\mu\text{m}$  with the Infrared Array Camera (IRAC; Fazio et al. 2004) aboard the *Spitzer* Space Telescope (Werner et al., 2004). The catalog (Ashby et al., 2015) – hereafter S-CANDELS catalog – that reaches a  $5\text{-}\sigma$  depth of  $26.5$  mag (AB) includes 2627 galaxies in the GOODS-ALMA field, i.e. about  $38\text{ sources.arcmin}^{-2}$ .

#### HST H-band catalog

The GOODS-ALMA area covers the deepest H-band part of the Cosmic Assembly Near-IR Deep Extragalactic Legacy Survey (CANDELS; Grogin et al. 2011) field (central one-third of the field). The point source catalog reaches a  $5\text{-}\sigma$  depth of  $28.16$  mag (AB) in the  $H_{160}$  filter (measured within a fixed aperture of  $0.17''$ ; Guo et al. 2013). The surface density of galaxies detected at  $1.6\text{ }\mu\text{m}$  with the Wide Field Camera 3 / infrared channel (WFC3/IR) within the GOODS-ALMA field is about  $233\text{ sources.arcmin}^{-2}$ .

#### Near-infrared $K_s$ -band catalog

We use the  $2.2\text{ }\mu\text{m}$  catalog described in Straatman et al. (2016) that uses an ultradeep image resulting from the combination of multiple observations in the  $K$  and  $K_s$  bands from: (i) the very large telescope (VLT), which combines the images of GOODS-S done with the Infrared Spectrometer and array camera (ISAAC; Moorwood et al. (1999)) in the  $K_s$ -band (Retzlaff et al., 2010) with the High Acuity Wide field /  $K$ -band imager (Hawk-I; Kissler-Patig et al. 2008) image in the  $K$ -band (Fontana et al., 2014), (ii) the 6.5m Magellan Baade Telescope combining the  $K_s$ -band image from the FourStar Galaxy Evolution Survey (ZFOURGE, PI: I. Labbé) using the FourStar near-infrared Camera (Persson et al., 2013) with the  $K$ -band image using the Persson's

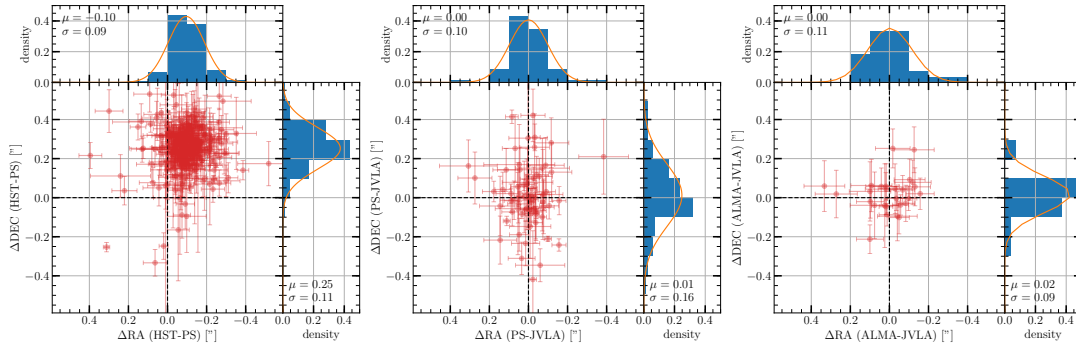


FIGURE 6.1: Left: offset between Pan-STARRS and HST; Middle: offset between JVLA and Pan-STARRS; Right: offset between JVLA and ALMA. For each panel, the histogram of the offsets in RA and DEC is shown as well as a fit with a Gaussian function (orange curve). The position of the peak and the standard deviation of the Gaussian is indicated for each curve. The middle and the right panels show that there are no significant astrometric differences between ALMA and JVLA nor between JVLA and PS1, while the left panel shows the clear shift in both RA and DEC between the positions of 375 sources in common between the Pan-STARRS (PS) and HST images. We measure a systematic offset of  $\Delta\text{RA} = -96 \pm 83$  mas and  $\Delta\text{Dec} = 252 \pm 107$  mas. In addition, a local offset is presented in Fig. 6.2.

Auxillary Nasmyth infrared camera (PANIC; Martini et al. 2004) in the HUDF (PI: I. Labbé), (iii) the Canada-France-Hawaii Telescope (CFHT), with the  $K$  band image done with the wide-field infrared camera (WIRCam; Puget et al. (2004) as part of the Taiwan ECDFS near Infrared survey (TENIS; Hsieh et al. 2012).

The  $5\text{-}\sigma$  point-source detection threshold in this ultra-deep  $K_s$  image reaches a magnitude between 26.2 and 26.5, which leads to an average galaxy surface density of about  $168 \text{ sources.arcmin}^{-2}$ .

### Radio catalog

A radio image that encompasses the GOODS-ALMA field was observed with the Karl G. Jansky Very Large Array (VLA) at a frequency of 3 GHz (10 cm) and an angular resolution of  $\sim 0''.3$  for a total of 177 hours (configurations A, B, & C; PI: W. Rujopakarn). Down to the average depth of the radio catalog within the GOODS-ALMA region of  $\text{RMS} = 2.1 \mu\text{Jy.beam}^{-1}$ , the average surface density of radio sources is about  $5 \text{ sources.arcmin}^{-2}$ .

## 6.3 Astrometric correction of the HST image of GOODS-South

We describe in Chapter 4 the presence of a systematic offset of  $\Delta\text{RA} = -96 \pm 113$  mas in right ascension, and  $\Delta\text{Dec} = 261 \pm 25$  mas in declination between the ALMA and HST images. This offset, interpreted as a positional shift of the HST image with respect to all other reference frames, is in good agreement with the offset previously discussed in Dunlop et al. (2017) and Rujopakarn et al. (2016). For the GOODS-North field, the coordinates were shifted by approximately 0.3 arcsec, primarily in declination, compared to those of other astrometric reference datasets (Dunlop et al., 2017). However, this correction has not been made to the v2.0 release for GOODS-South, in part because no external astrometric reference data with both suitable absolute accuracy and faint source density (such as the SDSS) were available<sup>1</sup>.

1. [https://archive.stsci.edu/pub/hlsp/goods/v2/h\\_goods\\_v2.0\\_rdm.html](https://archive.stsci.edu/pub/hlsp/goods/v2/h_goods_v2.0_rdm.html)

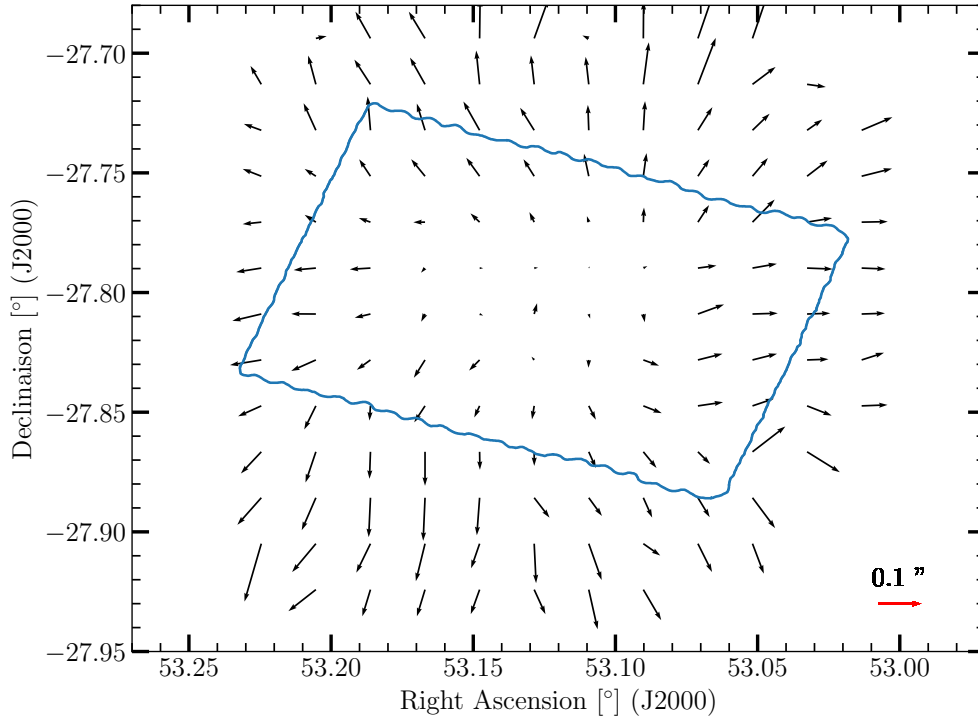


FIGURE 6.2: Difference between HST and Pan-STARRS position after subtraction of the median offset value. Each arrow represents a sliding median including in average 15 points, with an overlap of 60 percent between neighboring arrows. The blue line defines the area encompassing the GOODS-ALMA survey.

The offset used until now only corrects for the bulk global shift in astrometry but it does not account for the relative error in the astrometric calibration that was introduced in the building of the HST mosaic. In the following, we propose to determine this local correction that behaves like a distortion correction. This correction is important in the present study since we aim at using prior knowledge of existing sources from other wavelengths in order to push the ALMA detection limit to deeper levels.

We take advantage of the Panoramic Survey Telescope and Rapid Response System (Pan-STARRS) Data Release 2 (Flewelling et al., 2016). The offset between HST and Pan-STARRS images computed using an ensemble of 375 common detections (see Fig. 6.1 left panel) is comparable to the one presented chapter 4:  $\Delta RA = -96 \pm 83$  mas and  $\Delta Dec = 252 \pm 107$  mas.

The comparison of the positions of 69 sources in common between our 3 GHz VLA catalog ( $5\sigma$  detections; Rujopakarn et al., in prep.) and Pan-STARRS within a radius of  $0.6''$  shows that there is no offset between both images (Fig. 6.1 middle panel). To reduce the risk of misidentification, in all the astrometric analysis, we only retained galaxies that had been observed at least twice in the same filter during the Pan-STARRS survey. The average deviations are found to be  $\Delta RA = 0 \pm 98$  mas and  $\Delta Dec = 12 \pm 160$  mas.

Similarly, we find no offset between our ALMA sources (both the Main catalog presented chapter 4 and the supplementary catalog presented in the following) and their VLA counterparts for the 27 galaxies in common between both catalogs (Fig. 6.1, right panel). The average offset is  $\Delta RA = 3 \pm 113$  mas and  $\Delta Dec = 16 \pm 93$  mas well within the expected uncertainties for  $S/N \sim 4$  sources (Ivison et al., 2007; Hatsukade et al., 2018). Some of these sources come from the

supplementary list discussed in the following of the paper, but since we applied this astrometric correction to the HST sources used as priors in the catalog production, we decided to present the astrometric correction upfront and to illustrate the positions of all our ALMA galaxies in this section.

The excellent agreement in the astrometry of VLA, ALMA, and Pan-STARRS implies that it is most likely the HST coordinate system that needs to be corrected.

After subtracting this systematic and global offset from the HST data, the residuals offsets present spatially coherent patterns (see Fig. 6.2). Each arrow represents the median offset between Pan-STARRS and HST positions, for a sliding median containing in average 30 points. This local offset varies with position in the GOODS-South field, and we refer to this as a distortion offset artificially introduced in the mosaicing of the HST data. The absolute value of the distortion offset is lower than the systematic offset, but it is not negligible, and can reach values higher than  $0''.15$  at the edge of our GOODS-ALMA survey. A possible explanation for this local distortion may come from the process of making the HST maps themselves. Before the projection of the HST image onto the reference grid according to the World Coordinate System (WCS), a geometric distortion was applied using the WFC3 SMOV F606W data alone<sup>2</sup> (Windhorst et al., 2011). This *wavelength-independent* geometric solution becomes greater for regions near the field edge (Windhorst et al., 2011), where the error on the correction itself also becomes very large. The combined effect of the global offset and distortion offset between the ALMA and HST positions is illustrated in Fig. 6.3 and listed in Table 6.1 both before and after applying the global offset of  $\Delta\text{RA} = -96 \pm 83$  mas and  $\Delta\text{Dec} = 252 \pm 107$  mas and the distortion offset. With the exception of two galaxies for which the offset between the ALMA detected position and that of HST is  $\sim 0.4''$  (after correction of both the global offset and the distortion offsets, AGS27 and AGS35), all other galaxies have a difference in the two positions of  $< 0.27''$ . The average deviation after correction is  $-35$  mas in RA and  $47$  mas in DEC for the sample of galaxies selected in this study. (indicated by a magenta cross in Fig. 6.3). The updated RA and Dec positions derived for all galaxies in the Guo et al. (2013) catalog after the correction of both systematic and local offset are given at <https://github.com/maximilienfranco/astrometry/>.

## 6.4 ALMA Main and Supplementary catalogs

### 6.4.1 ALMA Main Catalog

The main ALMA catalog consists of 20 sources detected above  $4.8\sigma$  (see Chapter 4). This catalog was built without any prior assumption from a blind source extraction down to the  $4.8\sigma$ -limit using BLOBCAT (Hales et al., 2012).

The detection limit was set to  $S/N \geq 4.8$  due to the large number of independent beams that leads to spurious detections that become rapidly more numerous than the number of robust detections below this threshold despite the tapering at  $0''.60$ . Here the  $4.8\sigma$ -limit concerns the central pixel detection threshold ( $\sigma_p = 4.8$ ) and is associated with a constraint on the adjacent surrounding pixels that are included in the source if they pass a detection threshold of  $\sigma_f = 2.7$ .

2. <http://www.stsci.edu/hst/wfc3/idctab.lbn>

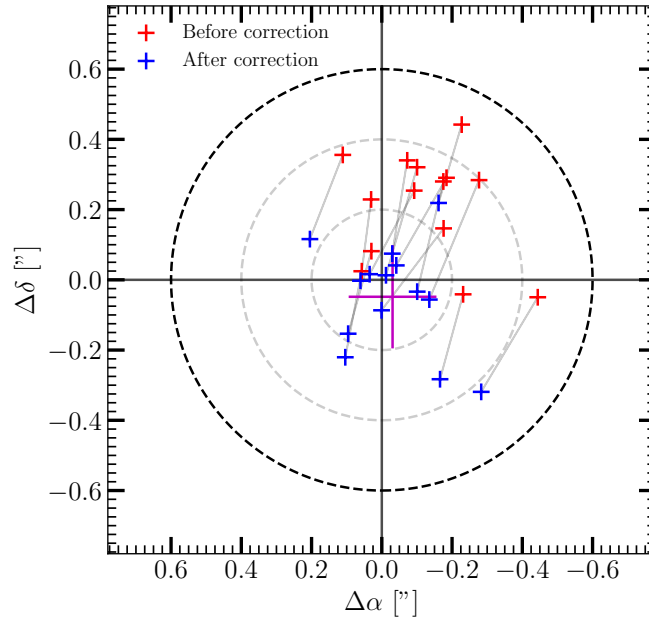


FIGURE 6.3: Positional offset ( $RA_{HST} - RA_{ALMA}$ ,  $DEC_{HST} - DEC_{ALMA}$ ) between *HST* and ALMA, before (red crosses) and after (blue crosses) the correction of both a global systematic offset and a local distortion offset. The black dashed circle corresponds to the cross-matching limit radius of  $0''.6$ . The grey dashed circles show positional offsets of  $0''.2$  and  $0''.4$  respectively. The mean offset and the standard deviation are shown by the magenta cross.

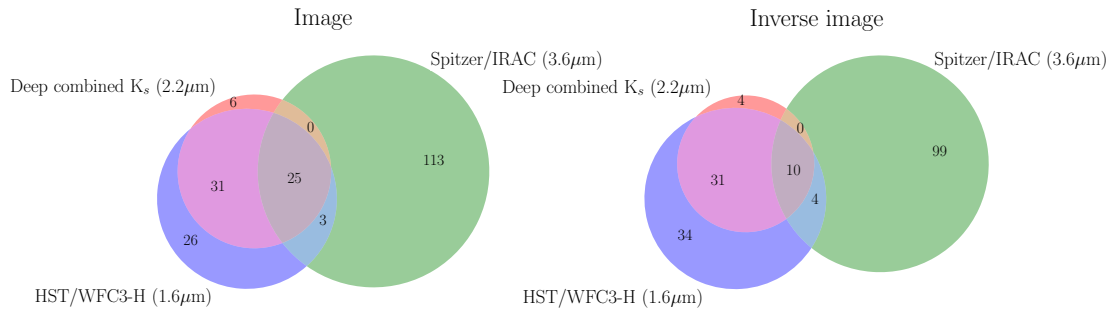


FIGURE 6.4: Number of sources cross-matched between the ALMA  $3.5\sigma$  detection and the ZFOURGE (Straatman et al., 2016), CANDELS (Guo et al., 2013) and S-CANDELS (Ashby et al., 2015) catalog in the image (left panel) and in the inverse image (right panel), within a radius of  $0.6''$  for the ZFOURGE and CANDELS catalogs and  $1.95''$  with the S-CANDELS catalog Ashby et al. (2015). Beforehand, we previously removed from the image the sources that had been detected Chapter 4. For example, in the “direct” image, 6 galaxies are only detected in  $K_s$ -band, 26 only in  $H$ -band, 113 only with IRAC. 31 are detected in the ultra-deep  $K_s$  and  $H$ -band but are not present the S-CANDELS catalog, 3 source are in common between  $H$ -band image and *Spitzer*/IRAC channel 1 image but are not detected in the ultra-deep  $K_s$  image and 25, in addition to being detected at  $3.5\sigma$  with ALMA, are detected in the 3 other wavelengths.

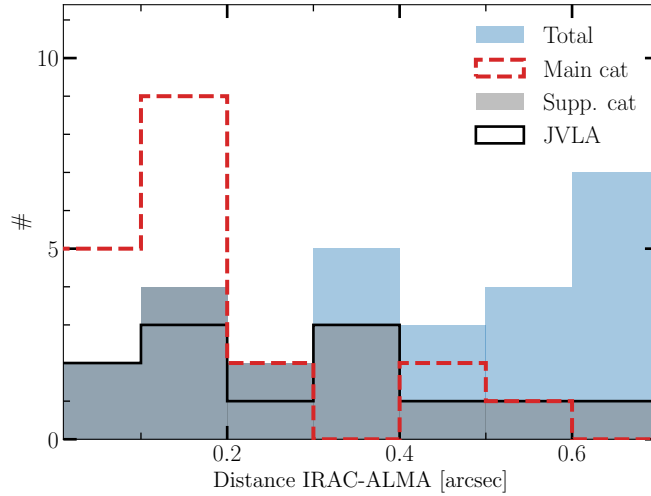


FIGURE 6.5: Distance between ALMA detection and the closest IRAC galaxy listed in the S-CANDELS catalog for the sources presented Chapter 4, red-dashed line, for the supplementary catalog, gray and for the all the  $3.5\sigma$  detection. We also represented the JVLA counterparts (at 3GHz) with a black solid line. All the ALMA  $3.5\sigma$  detections with both IRAC and JVLA counterpart between 0.3 and 0.7'' from the ALMA detection have been selected.

This combination of parameters ensures an 80 % purity where the purity criterion  $p_f$  defined as:

$$p_f = \frac{N_p - N_n}{N_p} > 0.8 \quad (6.1)$$

where  $N_p$  and  $N_n$  are the number of positive and negative detections. The negative detections refer to the detections in the inverse map (in other words detections in the continuum map multiplied by -1).

The initial catalog coming out of the blind source extraction contains 23 detections including 3 detections that we flagged as spurious Chapter 4 (marked with an asterisk in the Table 4.3). Finding three spurious detections out of 23 detections matches the expected number of spurious sources obtained from the difference between positive and negative peaks above the  $4.8\sigma$  level of 4 with a Poissonian uncertainty of  $\pm 2$ . These three sources are the only ALMA detections in the list without any sign of an IRAC counterpart at  $\lambda = 3.6$  or  $4.5 \mu\text{m}$  (Spitzer/IRAC channels 1 and 2) despite the availability of ultra-deep IRAC data in this field (26.5 AB mag, Ashby et al. 2015). The possibility that these sources are most likely spurious was later on confirmed by Cowie et al. (2018) using a 100 arcmin<sup>2</sup> survey of the field down to an RMS  $\sim 0.56$  mJy at 850  $\mu\text{m}$  with SCUBA-2. While none of the three detections that we listed as spurious were detected by SCUBA-2, 17 out of our 20 brightest ALMA sources were detected by Cowie et al. (2018). The remaining 3 sources were either confirmed with ALMA by Cowie et al. (2018) – AGS21 and AGS23 – or lie outside of the SCUBA-2 field of view – AGS22. We note however, that AGS22 is both at the very limit of our detection threshold and that it is the only galaxy of our list that does not show any IRAC counterpart. In view of the very large number of expected spurious detections at the  $3.5\sigma$  limit that we plan to reach in the present paper, we will adopt the strategy to limit ourselves to the most secure ALMA detections, which exhibit a clear IRAC counterpart. As a result, we will limit the original main sample to 19 galaxies only, leaving aside AGS22 for consistency.



### 6.4.2 ALMA Supplementary Catalog

#### Using IRAC counterparts to identify robust ALMA sources down to $3.5\text{-}\sigma$

In the present paper, we propose to use counterparts at other wavelengths to identify robust ALMA detections below the  $4.8\text{-}\sigma$  limit of the Main Catalog described in Sect. 6.4.1. This approach is similar in the philosophy to a prior source extraction approach, except that we start from the ALMA blind source extraction at a lower threshold and then only keep sources with counterparts already identified in the near and mid infrared.

We start with the list of sources detected with the same algorithm than the Main Catalog but push it down to the  $\sigma_p=3.5$  limit. A total of 1077 sources are detected down to this threshold, most of which are spurious simply due to the large number of independent beams (more than one million in the  $0''60$  tapered map). Indeed the inverse map exhibits an equivalently large, even larger, number of detections of 1157. The number of detections at this level obviously depends on noise fluctuations but does not preclude the existence of real positive sources. Hence we cannot rely on Eq. 6.1 to calculate the probability that a source is real from a purely blind detection approach.

We observed Chapter 4 that all the ALMA robust detections of the Main Catalog present an IRAC counterpart, hence we start by imposing the requirement that all candidate detections exhibit an IRAC counterpart. We note that this criterion may lead us to reject real ALMA sources without any IRAC counterpart with the possible consequence to bias our sample towards the most massive galaxies, but this is for the sake of the robustness of the sources. ALMA sources without any IRAC counterpart may well exist (see e.g. Williams et al. 2019) and would be particularly interesting to analyse, but this is out of the scope of the present paper, since including sources without IRAC counterparts would imply including a significant number of hazardous sources in the sample.

In the process of cross-matching the ALMA and IRAC images, we identified several cases of IRAC sources that were present in the IRAC image but were not listed in the S-CANDELS catalog (see Sect. 6.2.1). These sources were systematically located close to one or several brighter IRAC sources. We therefore implemented a new source extraction for those sources taking care of modeling the neighboring sources to proceed to a clean de-blending of the IRAC sources. This allowed us to determine the S/N ratio of those sources and only keep real detections. In most cases, those sources exhibited a counterpart in either the H and  $K_s$  band catalogs (described in Sect. 6.2.1, 6.2.1). This led us to extend our counterpart search to the H and  $K_s$  bands that we will use as priors to identify candidate IRAC sources that may have been missed in the original S-CANDELS catalog.

We choose the cross-matching radius between the positions of the ALMA detections and the IRAC, H and K band catalogs to be equal to the value of the largest FWHM. It is equal to  $0''60$ , the FWHM of the tapered 1.1mm ALMA image, for the cross-match with the CANDELS H-band and ZFOURGE K-band catalogs, and it is equal to  $1''95$  for the cross-match with the IRAC channel 1 ( $3.6\text{ }\mu\text{m}$ ) catalog ( $FWHM_{IRAC} = 1.95''$  at  $3.6\text{ }\mu\text{m}$ ,  $FWHM_{IRAC} = 2.05''$  at  $4.5\text{ }\mu\text{m}$ ). Before performing this cross-matching, we apply the astrometric correction to the CANDELS and ZFOURGE catalogs which use the HST reference frame, as described in Sect. 6.3.

A total of 204 sources detected with ALMA above  $3.5\sigma$  at 1.1 mm have a counterpart in at least one of the three catalogs (see Fig. 6.4). In comparison, there are 182 detections above  $3.5\sigma$  that also fulfill these criteria in the inverse image. We recall that we used the H and K-band counterparts as priors to search for IRAC sources that may have been missed in the S-CANDELS catalog due to the presence of a bright neighbor.

We note that 84% (16 out of 19 sources) of the ALMA sources in the Main Catalog described Chapter 4 have an IRAC counterpart closer than  $0''.3$  (red dashed line in Fig. 6.5). Since our goal is not here to include all possible ALMA sources but to limit the Supplementary Catalog to the most robust candidates, we decided to impose a more stringent constraint on the association with IRAC counterparts by keeping as robust candidates those within a distance of  $0''.3$ . In total, 8 ALMA sources detected between  $3.5\sigma$  and  $4.8\sigma$  fulfill this criterion. This close association between ALMA and IRAC may be due in part to the fact that the FWHM of the IRAC images is limited by the pixel size rather than the diffraction limit, hence position accuracies may actually be better determined than the  $1''.95$  FWHM of IRAC.

Looking at the remaining three sources in the Main Catalog, we noticed another interesting characteristics. They are all closer than  $0''.7$  from their IRAC counterpart and nearly all exhibit a radio counterpart as well (2 out of 3). In fact, out of the 19 sources in the Main Catalog, 16 hence again 84% exhibit a radio counterpart. We therefore chose to list in the Supplementary Catalog the sources that have both an IRAC and a radio counterpart closer than  $0''.7$ . This extra condition adds up an extra 6 ALMA sources detected between  $3.5\sigma$  and  $4.8\sigma$ .

In total, we end up with a list of 14 sources which fulfill the criteria of having an IRAC counterpart either (i) closer than  $0''.3$  or (ii) closer than  $0''.7$  but associated with a radio counterpart in the 3 GHz catalog.

It is possible that using these criteria does not allow us to detect all "real" ALMA detections with a  $S/N > 3.5$  but these conservative criteria ensure a high purity rate. We performed Monte Carlo simulation to estimate the probability that an ALMA detection lies randomly close to a galaxy listed in the S-CANDELS catalog. We randomly define a position within GOODS-South and then measure the distance to its closest IRAC neighbour using the source positions listed in Ashby et al. (2015) for IRAC sources with  $S/N > 5$ . We repeat this procedure 100 000 times. The distance from the nearest IRAC galaxies, within a radius of  $1.95''$  is given Table 6.1. In our supplementary catalog, for the farthest source of an IRAC source ( $0.64''$ ), the percentage of a random IRAC association is 2.85%. With the exception of one other source, the other detections have a probability of random IRAC association  $\leq 1\%$ .

We checked whether deeper surveys covering parts of the GOODS-S field could be used to validate or invalidate those ALMA Supplementary Catalog sources. The HUDF (Dunlop et al., 2017) and ASAGAO (Hatsukade et al., 2018) surveys reach a depth of  $RMS \simeq 35 \mu Jy$  at 1.3mm and  $RMS \simeq 6 \mu Jy$  at 1.2 mm respectively. Using the same scaling factors as those presented Chapter 4, these depths convert to  $RMS \simeq 52 \mu Jy$  and  $RMS \simeq 79 \mu Jy$  respectively at the wavelength of 1.1mm of the present GOODS-ALMA survey. Only three ALMA 1.1mm sources from the Supplementary Catalog fall in the area covered by these deeper surveys and all of them were detected and listed in the associated catalogs (see Fig. 6.8). The sources AGS29 and AGS35 from our Supplementary Catalog were both detected within the ASAGAO survey and listed as the sources 18 and 26 respectively (Hatsukade et al., 2018). The source AGS38 falls within the HUDF survey and is listed as UDF16 (Dunlop et al., 2017). Hence our independent identification of sources

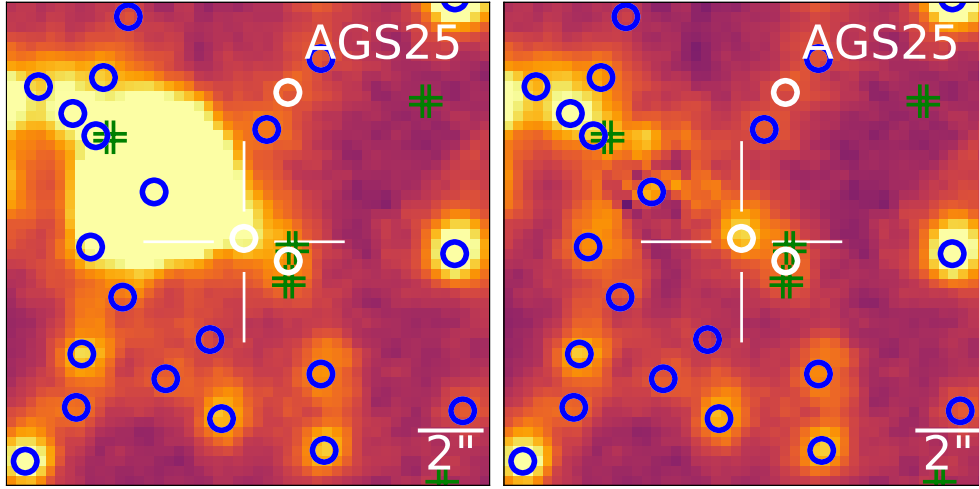


FIGURE 6.6: IRAC  $3.6\mu\text{m}$  map ( $17'' \times 17''$ ) image is centred on the position of the ALMA detection. We show the image before (left panel) and after (right panel) the subtraction with GALFIT of the source  $\text{ID}_{\text{ZFOURGE}} = 11024$  located to the Northeast of the detection and which masks the emission of the source located at the ALMA position. After subtraction we can see an emission located in the central position which suggest that the source is not present in [Ashby et al. \(2015\)](#) only because of blending. Cyan double crosses show sources from the GOODS-S CANDELS catalog. White circles show sources from the ZFOURGE catalog. Blue circles show common sources from both optical catalogs (i.e. sources with an angular separation lower than  $0''.4$ ).

down to the  $3.5\text{-}\sigma$  level did not bring any spurious source without any counterpart in deeper ALMA surveys, instead all 3 sources in these deeper images are confirmed.

### Supplementary catalog: optically dark galaxies

As discussed above, we searched for potential IRAC sources that were present in the IRAC images but missed in the S-CANDELS catalog because of the presence of a bright IRAC neighbor. Starting from the H and K-band images and catalogs, we identified two such sources, AGS24 and AGS25. Both are detected in the K-band, but neither of these two sources has been detected by the HST even in the  $1.6\mu\text{m}$  H-band (down to the  $5\sigma$  limiting depth of  $H = 28$  AB), hence they are HST-dark like 4 sources listed Chapter 4 and as also discussed in [Wang et al. e.g., 2016](#); [Elbaz et al. e.g., 2018](#); [Schreiber et al. e.g., 2018c](#); [Yamaguchi et al. e.g., 2019a](#).

The source AGS24 exhibits extended IRAC emission that is  $0''.36$  away from the ALMA position. This is slightly larger than the  $0''.3$  criterion but the source is also detected in the radio at 6 GHz ( $3.7\sigma$ ) and 3 GHz ( $5.7\sigma$ ). The S/N of this source is higher in the  $0''.29$  mosaic than in the  $0''.60$  tapered image, which suggests that it is particularly compact at 1.1 mm. This galaxy will be presented in detail in Zhou et al. (in prep), where a mass and photometric redshift are estimated to be  $z \sim 3.5$  and  $M_\star = 1.82^{+0.27}_{-0.50} \times 10^{11}$ .

The source AGS25 is  $0''.1$  away from its K-band counterpart in the ZFOURGE catalog (after applying the astrometric correction to the position of the ZFOURGE source), the source  $\text{ID}_{\text{ZFOURGE}} = 11353$  with a magnitude  $K = 25.9$  AB shown by a circle in Fig. 7.10. This source is not listed in the CANDELS catalog [Guo et al. \(2013\)](#), nor in the S-CANDELS catalog [Ashby et al. \(2015\)](#). It is marginally detected in radio at 5 and 10 cm with a S/N ratio close to 3. AGS25 is close ( $3''$ ) to a massive galaxy listed in CANDELS,  $\text{ID}_{\text{CANDELS}} = 8067$  with a stellar mass of  $M_\star = 5.6 \times 10^{10} M_\odot$ .

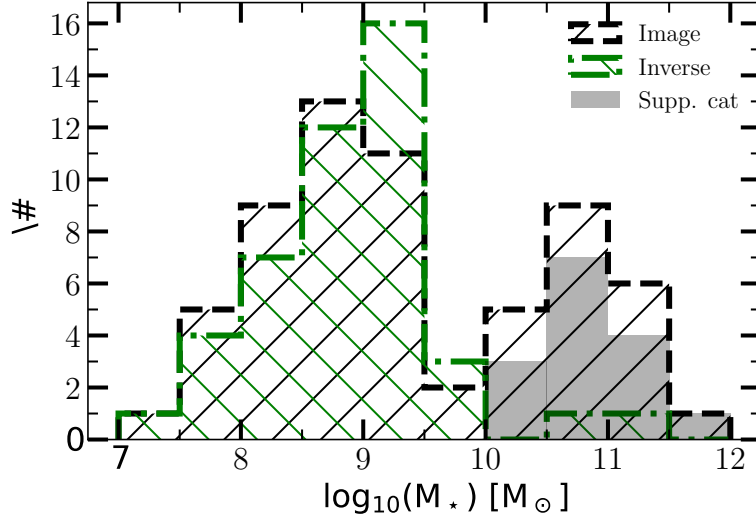


FIGURE 6.7: Stellar mass distribution for the sources that were cross-matched between the ZFOURGE catalog and the image (black contours) or the inverse image (green contours). The sample galaxies selected in this study are shown in grey.

at a redshift of  $z_{\text{spec}} = 1.038$ ). ID<sub>CANDELS</sub> = 8067 is the bright neighbor that explains the absence of AGS25 in S-CANDELS. We subtracted it from the IRAC image by modeling a Sérsic profile with GALFIT Peng et al. (2010) and measured an IRAC flux density of  $0.81 \pm 0.19$  mJy (see Fig. 7.10). The IRAC source is  $0''.28$  away from the ALMA position of AGS25.

Since the ALMA source is only  $0''.1$  away from the ZFOURGE source ID<sub>ZFOURGE</sub> = 11353, we use the stellar mass and redshift from the ZFOURGE catalog for this source. The characteristics of this galaxy make it particularly interesting, with  $z_{\text{AGS25}} = 4.66^{+0.25}_{-0.26}$  and  $M_{*,\text{AGS25}} = 2.0 \times 10^{10} M_{\odot}$ . These properties are similar to those of the Main Catalog source AGS11, which is also an HST-dark galaxy, with  $z_{\text{AGS11}} = 4.83^{+0.82}_{-0.76}$  and  $M_{*,\text{AGS11}} = 2.8 \times 10^{10} M_{\odot}$ .

We note that among the 4 HST-dark galaxies for which we were able to determine a stellar mass and redshift, there appear to be two distinct trends. Galaxies (AGS4 and AGS24) are among the most massive of all active uvj galaxies detected in the region covered by the ALMA survey. AGS4 has a stellar mass  $M_{*} = 2.81^{+1.65}_{-1.03} \times 10^{11} M_{\odot}$ . In other words, it is the most massive galaxy at  $4 < z < 5$  in our catalogs. AGS24 has a stellar mass  $M_{*} = 1.82^{+0.27}_{-0.50} \times 10^{11} M_{\odot}$ . The other two HST-dark galaxies are of intermediate mass, but with a redshift higher than 4.5.

In total, we end up with a list of 16 sources in the Supplementary Catalog including the two HST-dark sources AGS24 and AGS25 which exhibit the strongest S/N ratio of the catalog. Their properties are listed in Table 6.1 and Table 6.2 .

### 6.4.3 Consistency test of the Supplementary Catalog: stellar mass distribution

If we compare the nature of the counterparts of ALMA detections above  $3.5\text{-}\sigma$  in the image and the inverse image, we can see a difference that strengthens the solidity of the 16 sources of the Supplementary Catalog. There are 62 and 45 detections above  $3.5\text{-}\sigma$  in the ALMA image that have a counterpart in the K-band in the ZFOURGE catalog in the image and inverse image

ID	RA <sub>ALMA</sub> deg	Dec <sub>ALMA</sub> deg	RA <sub>HST</sub> deg	Dec <sub>HST</sub> deg	$\Delta_{HST_1}$ arcsec	$\Delta_{HST_2}$ arcsec	$(\Delta\alpha)_{HST}$ arcsec	$(\Delta\delta)_{HST}$ arcsec	$\Delta_{IRAC}$ arcsec	%RAa %
(1)	(2)	(3)	(4)	(5)	(6)	(7)	(8)	(9)	(10)	(11)
AGS24	53.087178	-27.840217	...	...	...	...	...	...	...	...
AGS25	53.183710	-27.836515	...	...	...	...	...	...	...	...
AGS26	53.157229	-27.833468	53.157238	-27.833446	0.09	0.18	0.066	-0.235	0.305	0.65
AGS27	53.069132	-27.807155	53.068992	-27.807169	0.45	0.43	0.161	-0.269	0.643	2.85
AGS28	53.224467	-27.817214	53.224476	-27.817151	0.23	0.06	0.030	-0.231	0.086	0.06
AGS29	53.202362	-27.826284	53.202340	-27.826190	0.35	0.08	0.043	-0.266	0.585	2.39
AGS30	53.168097	-27.832632	53.168025	-27.832509	0.50	0.27	0.066	-0.223	0.261	0.43
AGS31	53.068906	-27.879739	53.068851	-27.879698	0.23	0.09	0.177	-0.233	0.133	0.11
AGS32	53.111595	-27.767860	53.111564	-27.767771	0.34	0.02	0.089	-0.308	0.136	0.11
AGS33	53.049749	-27.771007	53.049662	-27.770929	0.40	0.15	0.142	-0.340	0.206	0.26
AGS34	53.093099	-27.786607	53.092938	-27.786582	0.52	0.44	0.104	-0.269	0.357	0.92
AGS35	53.181971	-27.814127	53.181989	-27.814120	0.06	0.24	0.047	-0.245	0.118	0.09
AGS36	53.153025	-27.735192	53.152971	-27.735114	0.33	0.11	0.074	-0.314	0.370	0.96
AGS37	53.071752	-27.843712	53.071694	-27.843631	0.34	0.06	0.143	-0.249	0.009	0.01
AGS38	53.176650	-27.785435	53.176577	-27.785446	0.24	0.33	0.066	-0.242	0.371	...
AGS39	53.091634	-27.853413	53.091606	-27.853342	0.27	0.04	0.127	-0.238	0.114	0.09

TABLE 6.1: Details of the positional differences between ALMA and *HST*-WFC3 for our catalog of galaxies identified in the 1.1mm-continuum map. Columns: (1) Source ID; (2), (3) Coordinates of the detections in the ALMA image (J2000); (4), (5) Positions of *HST*-WFC3 *H*-band counterparts when applicable from Guo et al. (2013), (6), (7) Distances between the ALMA and *HST* source positions *before* ( $Dec\Delta_{HST_1}$ ) and *after* ( $\Delta_{HST_2}$ ) applying both the systematic and local offset correction presented in Sect. 6.3; (8), (9) Offset to be applied to the *HST* source positions, which includes both the global systematic offset and the local offset; (10) Distance from the closest IRAC galaxy; (11) IRAC random association (RaA) between the ALMA detection and the closest and IRAC galaxy.

respectively. The stellar mass distributions of both samples are represented by dashed black and green lines for the image and inverse image respectively in Fig. 6.7. Both histograms show the same behavior at masses below  $10^{10}M_{\odot}$  but there are nearly no galaxies above this mass threshold in the inverse image while there is a second bump in the histogram of the sources in the real image. Massive galaxies being rarer than low mass ones, the probability to get an association with such galaxy is lower and the fact that there is a second bump at high masses in the real image suggests that these may be real. The Supplementary Catalog histogram shown in filled grey matches very nicely this second bump of massive galaxies. We recall that we did not impose any criterion of brightness or mass in the selection of the Supplementary Catalog but only distances to IRAC, K-band and radio sources. If we limit ourselves to the galaxies above a stellar mass of  $10^{10}M_{\odot}$ , we can see that the number of sources in the Supplementary Catalog is close to the difference between the image and inverse image.

In the sample of cross-matched galaxies from the positive image, 21/62 galaxies ( $\sim 34\%$ ) have a stellar mass greater than  $10 \times 10^{10}M_{\odot}$ , compared with only 2/45 galaxies ( $\sim 4\%$ ) in the inverse image (see Fig. 6.7). A Kolmogorov-Smirnov (KS) test on these data gives a p-value of  $3.9 \times 10^{-3}$  between these two samples, meaning that the likelihood that the two samples were drawn from the same distribution is extremely low. When we remove the sample of 16 galaxies listed in Table 6.1, the two samples become more similar. The p-value from a KS test then reaches 0.71. This means that once the galaxies in our study have been removed, the detections that remain have as high a probability of originating from the same parent sample as the inverse image detections, so that they are no longer statistically different from noise.

This suggests that not only the Supplementary Catalog is robust but also that there is little margin for an extra population of real sources that we would have missed.

ID ALMA	ID <sub>CLS</sub>	ID <sub>ZF</sub>	ID <sub>S-CLS</sub>	z <sub>CLS</sub>	z <sub>ZF</sub>	z <sub>sp</sub>	S/N	Flux mJy	log <sub>10</sub> (M <sub>*</sub> ) M <sub>⊙</sub>	S <sub>3GHz</sub> μJy
(1)	(2)	(3)	(4)	(5)	(6)	(7)	(8)	(9)	(10)	(11)
AGS24	...	...	...	...	...	...	3.9	0.88 ± 0.22	11.26†	12.43 ± 2.19
AGS25	...	11353	...	...	4.644	...	4.36	0.81 ± 0.19	10.39	...
AGS26	8409	11442	J033237.75-275000.8	1.711	1.592	1.619 <sup>sp</sup>	4.31	0.97 ± 0.15	10.89	85.09 ± 2.55
AGS27	11287	14926	J033216.54-274825.7	4.931	4.729	...	3.76	1.43 ± 0.28	10.93	5.95 ± 1.86
AGS28	10286	13388	J033253.87-274901.9	2.021	2.149	...	4.10	1.56 ± 0.21	11.17	17.19 ± 1.85
AGS29	9242	12438	J033248.53-274934.8	1.346	1.071	1.117 <sup>sp</sup>	3.56	0.61 ± 0.18	10.71	65.01 ± 2.38
AGS30	8557	11581	J033240.33-274957.3	0.646	0.672	0.65 <sup>sp</sup>	4.00	0.67 ± 0.17	10.30	...
AGS31	3584	6153	J033216.53-275247.0	2.686	2.445	...	3.93	0.72 ± 0.19	11.38	...
AGS32	16822	19964	J033226.78-274604.2	4.526	4.729	...	3.92	1.23 ± 0.16	11.00	4.47 ± 1.38
AGS33	16558	19463	J033211.93-274615.5	2.571	2.676	...	3.85	1.77 ± 0.27	10.71	21.20 ± 2.84
AGS34	14035	17374	J033222.32-274711.9	2.866	2.750	...	3.72	0.55 ± 0.15	10.82	15.55 ± 1.98
AGS35	10497	14146	J033243.67-274851.0	2.986	9.476	...	3.71	1.16 ± 0.21	10.83	31.49 ± 1.42
AGS36	20859	23463	J033236.70-274406.6	0.646	0.663	0.665 <sup>sp</sup>	3.66	0.74 ± 0.21	10.46	11.71 ± 1.60
AGS37	7184	10241	J033217.22-275037.3	1.971	1.864	1.956 <sup>sp</sup>	3.64	1.10 ± 0.16	11.22	22.61 ± 4.39
AGS38	14638	17465	J033242.37-274707.8	1.346	1.323	1.314 <sup>sp</sup>	3.62	... ± ...	11.080	9.92 ± 2.28
AGS39	6131	9248	J033222.00-275112.3	2.906	2.360	...	3.62	0.80 ± 0.23	10.60	17.24 ± 2.29

TABLE 6.2: Columns: (1) Source ID; (2),(3),(4) IDs of the HST-WFC3 (from the CANDELS catalog), ZFOURGE and IRAC (SEDs catalog) counterparts of these detections; (5),(6) Photometric redshifts from the CANDELS catalog (Guo et al., 2013), z<sub>CLS</sub>, and ZFOURGE catalog (Straatman et al., 2016), z<sub>ZF</sub> (note that AGS24 has a photometric redshift of  $z \simeq 3.5$  determined by Zhou et al. (in prep., see Sect. 6.4.2) ; (7) Spectroscopic redshift when available (see Sect. 6.5.1), flagged with a "sp" exponent to avoid confusion; (8) S/N of the detections in the 0''60 mosaic. This S/N is given for the peak flux; (9) Flux and error on the flux as explained in Sect. 6.5.2; (10) Stellar mass from the ZFOURGE catalog with the exception of AGS24, marked with a †, the determination of the stellar mass of this galaxy will be presented in Zhou et al. (in prep.) ; (11) 3GHz flux density from VLA (PI W.Rujopakarn.)

## 6.5 Catalog

The positions of the ALMA sources listed in the Main and Supplementary catalogs are shown in Fig. 6.8 where they can be compared to the locations of other ALMA surveys. The postage-stamp images of the sources are shown in Appendix 6.14.

### 6.5.1 Redshifts and stellar masses

Except for the two HST-dark galaxies, AGS24 and AGS25 (discussed in Sect. 6.4.2), all sources listed in the ALMA Supplementary Catalog have been attributed a photometric redshift by the CANDELS (Guo et al., 2013) and ZFOURGE (Straatman et al., 2016) teams. The two sources of photometric redshifts listed in the Col.(5) and Col.(6) of Table 6.2 are in excellent agreement (see Fig. 6.9-left). Excluding AGS35 (whose redshift given in the ZFOURGE catalog,  $z = 9.48$  is much higher than that given by the CANDELS catalog,  $z = 2.99$ ), the average of  $|z_{\text{HST}} - z_{\text{ZFOURGE}}| / (1 + (z_{\text{HST}} + z_{\text{ZFOURGE}})/2)$  for the galaxies that have redshifts in both catalogs is 0.03.

A total of 38 % of the galaxies in the Supplementary Catalog (6/16) have been attributed a spectroscopic redshift:

- AGS26:  $z_{\text{spec}} = 1.619$  determined with VLT/FORS2 (Vanzella et al., 2008).
- AGS29:  $z_{\text{spec}} = 1.117$  from the VIMOS VLT Deep Survey (Le Fèvre et al., 2013).
- AGS30:  $z_{\text{spec}} = 0.65$  from the HST/ACS slitless grism spectroscopy of the PEARS program (Ferreras et al., 2009).



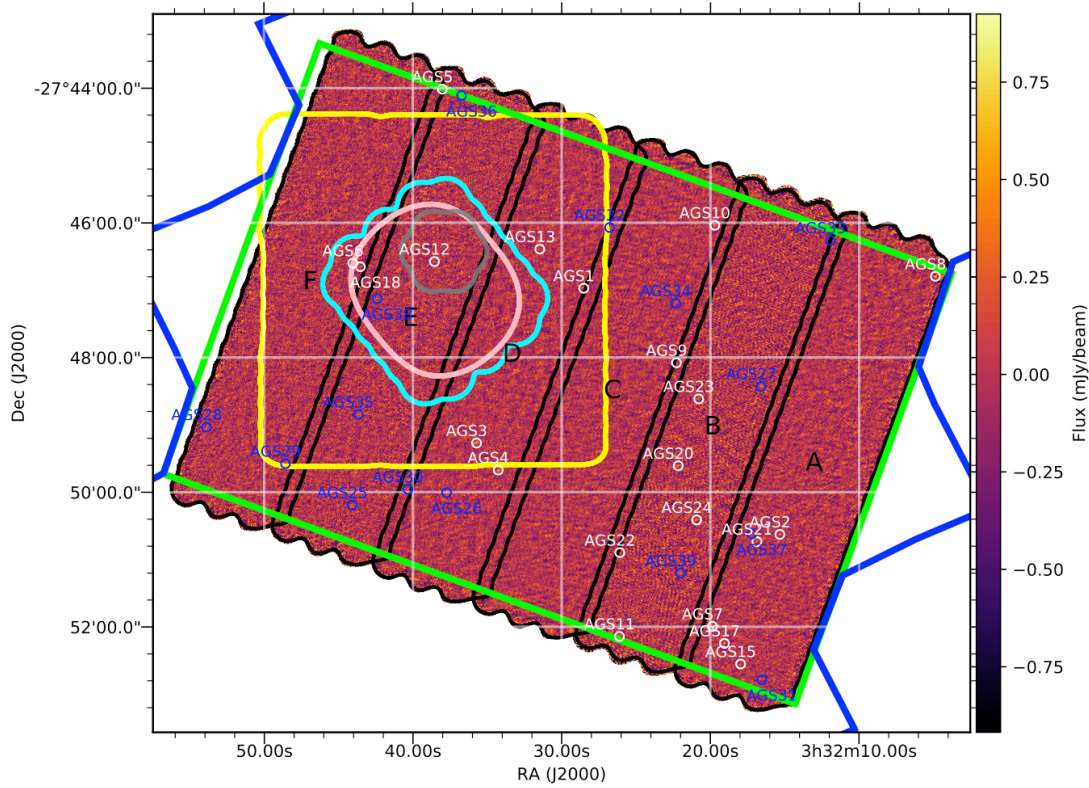


FIGURE 6.8: ALMA 1.1 mm image tapered at  $0''.60$ . The white circles have a diameter of 4 arcseconds and indicate the positions of the galaxies listed in Table 6.1. Black contours show the different slices (labeled A to F) used to construct the homogeneous 1.1 mm coverage, with a median RMS =  $0.18 \text{ mJy.beam}^{-1}$ . Blue lines show the limits of the HST/ACS field and green lines indicate the HST-WFC3 deep region. The cyan contours represent the limit of the [Dunlop et al. \(2017\)](#) survey covering all of the Hubble Ultra Deep Field region, the yellow contours show the ASAGAO survey ([Hatsukade et al., 2018](#)), while the purple contours show the ASPECS Pilot survey ([Walter et al., 2016](#)), the pink contours show the ASPECS Large Program ([Decarli et al., 2019](#)). The *Chandra Deep Field-South* encompasses all of the ALMA-survey field.

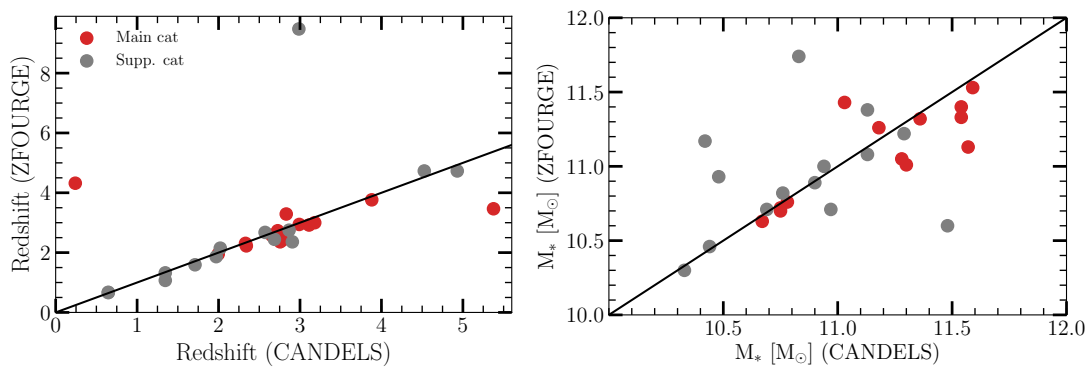


FIGURE 6.9: Comparison of redshift (left panel) and stellar mass (right panel) from the CANDELS and the ZFOURGE catalog. Solid black lines represents  $z_{\text{ZFOURGE}} = z_{\text{CANDELS}}$ . The galaxies presented in Chapter 4 (main catalog) are shown in red, while the galaxies presented in this paper are shown in gray. Black squares indicate spectroscopic redshifts. The stellar mass has been scaled from a Chabrier IMF to a Salpeter IMF by applying a factor of 1.7 in the ZFOURGE catalog. In this paper, we will take, with the exception of AGS36 which has an inconsistent redshift ( $z_{\text{AGS36,ZFOURGE}} = 9.47$  and for which we will take the data from the CANDELS catalog), the redshifts and stellar masses are given from the ZFOURGE catalog.

- AGS36:  $z_{spec} = 0.646$  from the Arizona CDFS Environment Survey (ACES), spectroscopic redshift survey of the Chandra Deep Field South (CDFS) using IMACS on the Magellan-Baade telescope (Cooper et al., 2012) and confirmed by the VIMOS VLT Deep Survey (Le Fèvre et al., 2013).
- AGS37:  $z_{spec} = 1.956$  determined using the *Spitzer* Infrared Spectrograph (Wuyts et al., 2009; Fadda et al., 2010) and confirmed with the 3D-HST survey (Momcheva et al., 2016).
- AGS38:  $z_{spec} = 1.314$  determined with VLT/FORS2 (Vanzella et al., 2008).

We note that two additional spectroscopic redshifts have been determined for galaxies in the Main Catalog since the publication of F18.

- AGS6, previously reported at  $z = 3.00$ , has been observed by the ALMA Spectroscopic Survey Large Program (ASPECS-LP; Decarli et al. 2019) in the Hubble Ultra-Deep Field, giving a  $z_{spec} = 2.698$  from the transition of CO(3-2) at 93.51 GHz. This spectroscopic redshift confirms the redshift also found by MUSE, at the same position (Boogaard et al., 2019).
- AGS18, previously reported at  $z = 2.794$ , has also been observed in the ASPECS-LP survey, giving a  $z_{spec} = 2.696$  from the transition of CO(3-2) at 93.51 GHz. This spectroscopic redshift again confirms the one found by MUSE at the same position Boogaard et al. (2019).

In the following, we will adopt for each source (*i*) the spectroscopic redshift when available, otherwise (*ii*) the photometric redshift from the ZFOURGE catalog (except for AGS35 for which we use the CANDELS redshift). These redshifts are given in Table 6.2.

We note that the redshift range of the Supplementary Catalog covers a wider dynamic range than the sources of the Main Catalog including two low redshift sources ( $z \sim 0.6$ ), with no equivalent in the Main Catalog. These two sources will be discussed in detail in a following Chapter.

The stellar masses of the Main and Supplementary catalogs have been chosen from the ZFOURGE catalog (except AGS35, for the reasons mentioned above). They were multiplied by a factor 1.7 to scale them from the Chabrier IMF to a Salpeter IMF. Both catalogs provide globally consistent stellar masses with no systematic offset, the median of the ratio  $M_{\star, \text{CANDELS}}/M_{\star, \text{ZFOURGE}} = 1.06$  (see Fig. 6.9-right).

## 6.5.2 Flux and size measurements

Flux densities of the Supplementary Catalog sources were measured by fitting the light profiles with a circular Gaussian in the uv-plane using `uvmodelfit` in CASA (McMullin et al., 2007). Due to the low S/N ( $3.5 < S/N < 4.8$ ), we have opted for a circular Gaussian rather than an asymmetric Gaussian, in order to limit the number of free parameters. We use the formula given by Martí-Vidal et al. (2012) as in Chapter 4 to determine the minimum size that can be reliably measured in the uv-plane as a function of the S/N ratio of the source for an interferometer :

$$\theta_{beam} \simeq 0.88 \frac{\theta_{beam}}{\sqrt{S/N}} \quad (6.2)$$

We use the S/N of the tapered map at  $0''60$  and  $\theta_{beam} = 0''60$ . Galaxies for which the circular Gaussian fit in the uv-plane give a size (FWHM) smaller than  $\theta_{beam}$ , the size limit given by



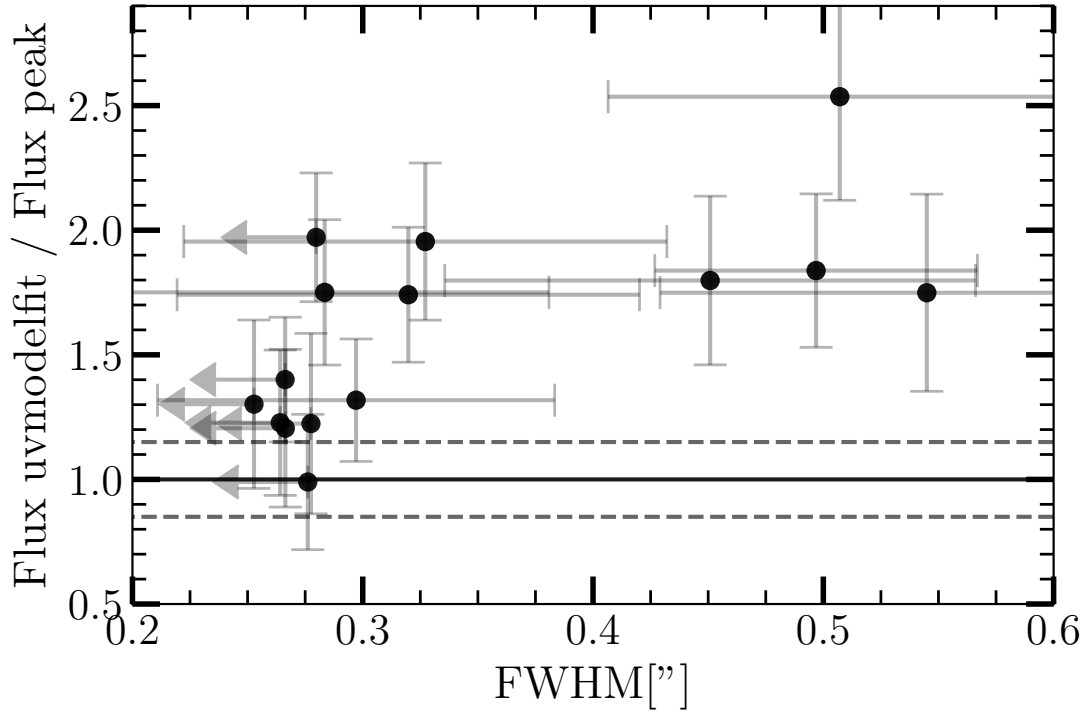


FIGURE 6.10: Ratio between the flux extracted using `uvmodelfit` in CASA and the peak flux as a function of the size of the galaxy for the supplementary catalog. When the measured size is below the reliable size measurement limit (see Eq. 6.2), we consider the size given by Eq. 6.2 as an upper limit. The horizontal solid line indicates  $\text{flux uvmodelfit} = \text{peak flux}$ . The dotted lines show a 15 percent deviation from this equality. For galaxies larger than  $0.25''$  (vertical dotted line), the approximation of a point source is no longer valid, and we assume the flux value derived from `uvmodelfit` for these galaxies.

Eq. 6.2, we set the size of the galaxy to  $\theta_{beam}$  and use the peak flux density measured on the direct image. This choice is expected to lead to slightly underestimated flux densities since it implies that sources are assumed to be point-like while the typical size measured for distant ALMA galaxies is on average close to  $0''.3$  (Simpson et al. 2015a; Ikarashi et al. 2017; Elbaz et al. 2018). Assuming a point-like source for a real size extension of  $0''.3$  FWHM would lead to an underestimation of the real flux density by a factor  $F_{real}/F_{peak}=1.2$  (see Fig. 6.11) but in the absence of a robust size measurement, we decided to keep the peak flux values having in mind that they may be lower by about 20%. Using the measurements coming out of `uvmodelfit` would lead to larger uncertainties for those sources with no reliable size measurement.

For galaxies whose sizes measured using `uvmodelfit` are larger than this limit (see Fig. 6.10), we keep the size given by `uvmodelfit`. For these galaxies, the peak flux approximation is no longer valid and we keep the integrated flux given by `uvmodelfit`. The flux density of each galaxy, as well as its uncertainty, are listed in Table 6.2. The sizes measured by `uvmodelfit`, the detection limit derived from the Eq. 6.2 and the size of the galaxies are given Table 6.3.

In order to check whether our flux density measurements were underestimated by a large factor, we computed the expected ALMA flux density that those sources would have if they had been located on the star-formation main sequence (MS; Noeske et al. 2007; Rodighiero et al. 2011; Elbaz et al. 2011). Since a large fraction of the ALMA sources are actually starbursting and above the MS, this assumption only provides a rough estimate of a lower-limit to the ALMA

ID	$\theta_{\text{uvmodelfit}}$	$\theta_{\text{lim}}$	$\theta_{\text{final}}$
AGS24	0.06	0.27	0.27
AGS25	0.12	0.25	0.25
AGS26	0.30	0.25	0.30
AGS27	0.54	0.27	0.54
AGS28	0.50	0.26	0.50
AGS29	...	0.28	0.28
AGS30	...	0.26	0.26
AGS31	...	0.27	0.27
AGS32	0.33	0.27	0.33
AGS33	0.51	0.27	0.51
AGS34	...	0.27	0.27
AGS35	0.45	0.27	0.45
AGS36	0.23	0.28	0.28
AGS37	0.28	0.28	0.28
AGS38	0.32	0.28	0.32
AGS39	0.25	0.28	0.28

TABLE 6.3: Table of sizes measured with `uvmodelfit` and reliable size measurement limit given [Martí-Vidal et al. \(2012\)](#). The last column gives the adopted size:  $\theta_{\text{uvmodelfit}}$  if  $\theta_{\text{uvmodelfit}} > \theta_{\text{lim}}$ ,  $\theta_{\text{lim}}$  if  $\theta_{\text{uvmodelfit}} < \theta_{\text{lim}}$ .

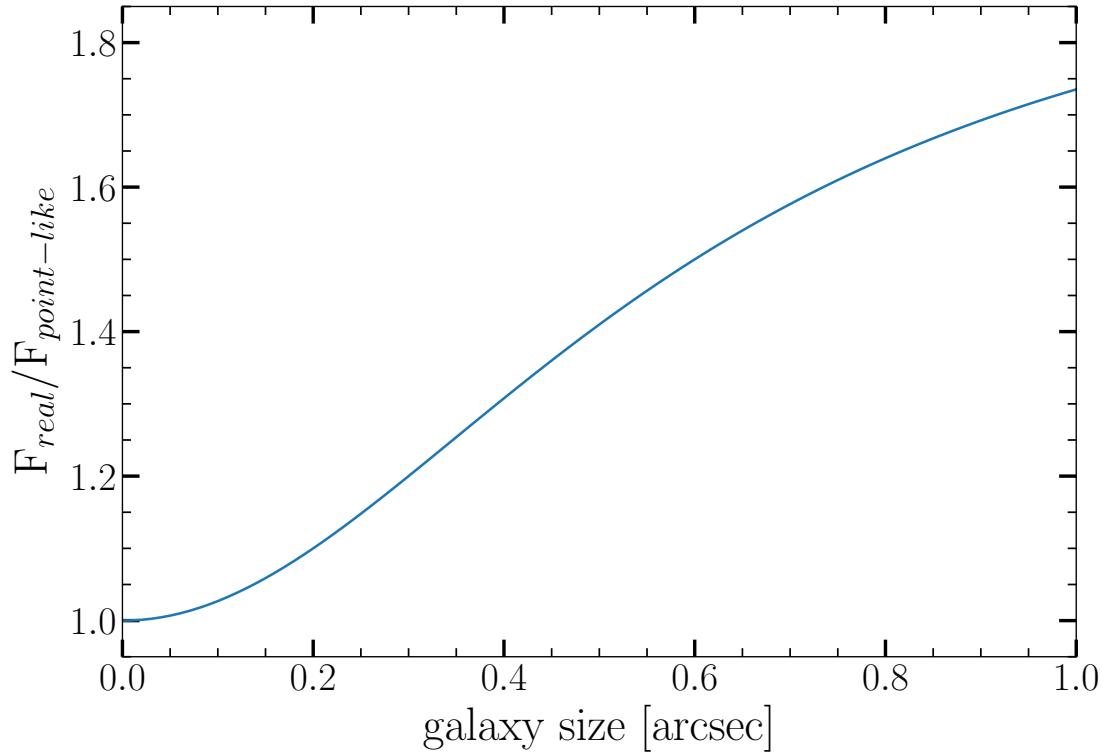


FIGURE 6.11: Underestimation of the flux when assuming a point-like source instead of the real size of the galaxy. For example, a source with an intrinsic FWHM of  $0''.3$  will be underestimated of 20%.

flux densities. We used the infrared spectral energy distributions (IR SED) from the library presented in [Schreiber et al. \(2018c\)](#), with the stellar masses and redshifts listed in Table 6.1 as input parameters. The measured,  $F_{ALMA}$ , and predicted,  $F_{SED}$ , flux densities exhibit a ratio  $F_{ALMA}/F_{SED}$  ranging from 0.73 to 5.2 with a median (average) of 2.4 (2.7) suggesting that about 50 % of the galaxies of the Supplementary Catalog fall within the factor 2 dispersion of the MS, the remaining half being in a starburst phase. None of the measured flux densities fall more than 25 % below the predicted MS ALMA flux density, which suggests that our flux density measurements are probably not largely underestimated.

## 6.6 Comparison of the properties of the ALMA galaxies from the Main and Supplementary catalogs

### 6.6.1 Redshifts

The redshifts of the Supplementary Catalog covers a wider range ( $z = 0.65 - 5.36$ ) than the sources of the Main Catalog ( $z = 1.95 - 4.82$ ). Galaxies with a redshift greater than  $z=4.5$  represented 5 % of the Main Catalog (1/19), they make 19 % of the Supplementary Catalog (3/16, see Fig. 6.12). On the other extreme, none of the Main Catalog sources were detected below  $z=1.9$  whereas 38 % (6/16) of the sources in the Supplementary Catalog are found in this lower redshift range. Despite these differences, the median redshifts of both catalogs are similar,  $z = 2.70$  and  $2.56$  for the Main and Supplementary catalogs, showing that there is no systematic shift in redshift between both catalogs but a wider dynamic range for the Supplementary Catalog. This median redshift is also similar to [Stach et al. \(2019\)](#), who derive a median redshift of  $2.61 \pm 0.09$ . We found no correlation between redshift and flux density of the Supplementary Catalog sources.

### 6.6.2 Stellar Masses

All galaxies detected in GOODS-ALMA have a stellar mass greater than  $M_* = 2 \times 10^{10} M_\odot$ . The median stellar mass of galaxies from the Supplementary Catalog,  $M_*^{\text{Supp}} = 6.6 \times 10^{10} M_\odot$ , is twice lower than that from galaxies in the Main Catalog,  $M_*^{\text{Main}} = 1.1 \times 10^{11} M_\odot$ . Hence by pushing down the ALMA detection limit using IRAC priors, we have reached more normal galaxies, with less extreme stellar masses, and extended the redshift range of the ALMA sources.

We can now compare the galaxies detected by GOODS-ALMA, combining the Main and Supplementary catalogs, to their parent sample of distant star-forming galaxies taken from the ZFOURGE catalog after selecting only the UVJ active galaxies ([Williams et al. 2009](#), using the same definition as in Chapter 4, see Fig. 6.12).

GOODS-ALMA detects nearly half (46%, 6/13) of the most massive star-forming galaxies with  $\log_{10} (M_*/M_\odot) = 11-12$  in the range  $2 < z < 2.5$ . Pushing further in redshift to  $2.5 < z < 3$ , GOODS-ALMA also sees nearly half of the star-forming galaxies with  $\log_{10} (M_*/M_\odot) = 10.7-11$  (44%, 7/16). At even further redshifts of  $3 < z < 4$ , GOODS-ALMA detects 38% (3/8) of the most massive galaxies ( $\log_{10} (M_*/M_\odot) = 11-12$ ).

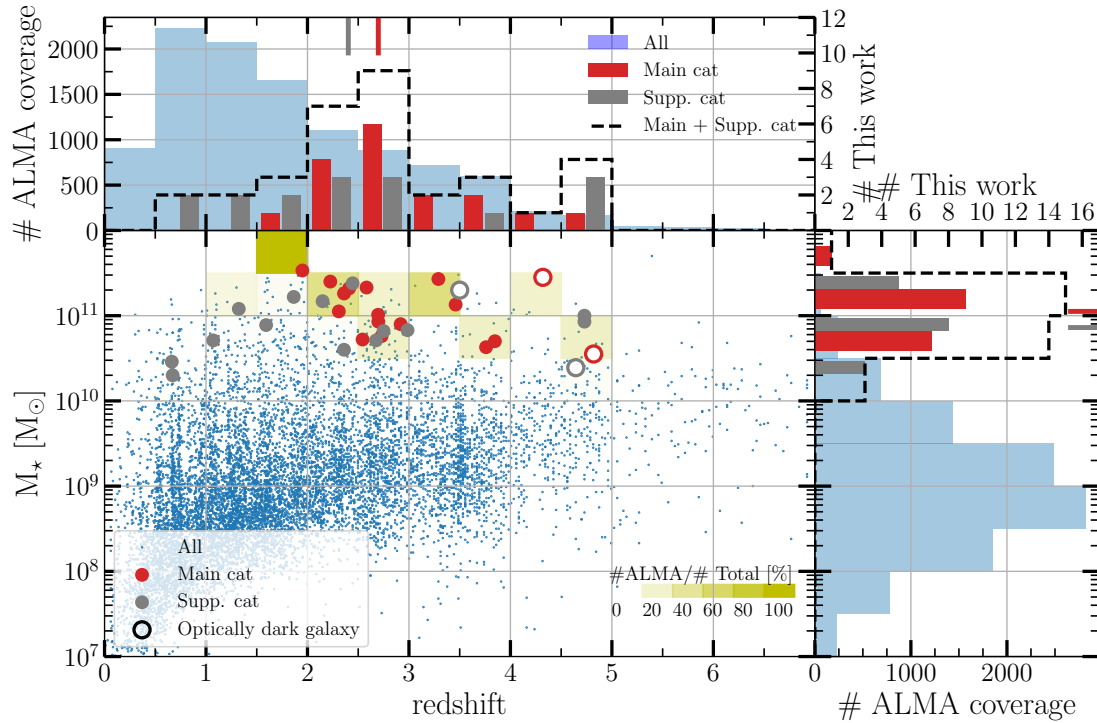


FIGURE 6.12: Stellar mass as a function of redshift for the galaxies detected in Chapter 4 (red points) and in this work (gray points). For comparison, the distribution of all of the galaxies, listed in the ZFOURGE catalog, in the same field of view is given in blue. Only UVJ active galaxies are shown. For each bins of redshift ( $z = 0.5$ ) and stellar mass ( $\log_{10}(M_*) = 0.5$ ), with a yellow shade, the fraction of sources detected by ALMA compare to the uvj active galaxies in GOODS-ALMA. The optically dark galaxies for which redshifts and masses have been derived are represented by open circles. The upper panel shows the compared distribution of redshift between all the UVJ active galaxies in GOODS-ALMA and the ALMA-detected galaxies while the right panel shows the stellar mass distribution. The median of the redshift and of the stellar mass are shown in these two panels. The median redshift is 2.56 for the galaxies presented in this paper, compared to 2.70 in Chapter 4, while the median stellar mass is  $6.7 \times 10^{10} M_{\odot}$  in this study, compared to  $1.1 \times 10^{11} M_{\odot}$  in Chapter 4.

In total, GOODS-ALMA detects about 30 % (11/37) of the most massive star-forming galaxies with a redshift  $2 < z < 4$  ( $\log_{10}(M_*/M_{\odot}) = 11 - 12$ ).

### 6.6.3 Sizes

The sizes of the sources of the Main and Supplementary catalogs were derived by fitting a circular Gaussian in the uv-plane using `uvmodelfit` in CASA. We find that by pushing down the detection limit to  $3.5\text{-}\sigma$  using IRAC priors, we have been able to identify galaxies with nearly twice larger ALMA sizes. The median ALMA 1.1mm FWHM of the galaxies in the Supplementary Catalog is indeed  $0''.32$  as compared to  $0''.18$  for the galaxies in the Main Catalog. When accounting for the redshift of the sources, we find that the physical circularized half-light radius of the new sources in the present Supplementary Catalog ( $R_{1/2} = \text{FWHM}/2$ ) is 1.3 kpc as compared to only 0.65 kpc for the Main Catalog. If we take into account the fact that the Supplementary sources exhibit twice lower stellar masses, this implies that pushing down the ALMA detection limit using priors, we were able to identify lower mass galaxies in which dust-enshrouded star-formation extends over twice larger sizes.

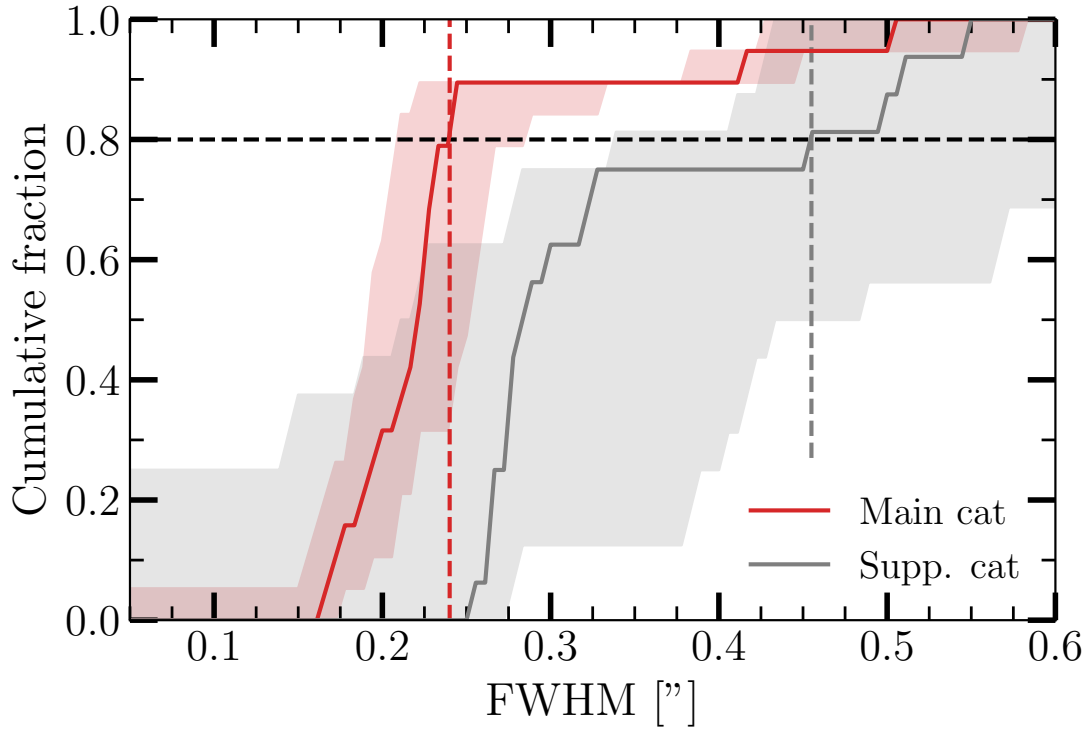


FIGURE 6.13: Cumulative fraction of sources with a FWHM below a given size for the main (red) and the supplementary catalog (gray). These sizes are computed by fitting the ALMA detections with a circular Gaussian in the uv-plane using `uvmodelfit` in CASA. The shaded areas correspond to the integration of the individual uncertainties of the sizes of each detection.

In Fig. 6.13, we show the cumulative fraction of sources with a major axis below a given size for the Main (red) and Supplementary (grey) catalogs. This figure clearly shows that the galaxies detected in the main catalog are generally more compact than the supplementary catalog: 80% of the galaxies in the Main Catalog have a FWHM below  $0''.24$ , whereas in the Supplementary Catalog, 80% the sources have a size above  $0''.27$  arcsec. The size below which 80% of the galaxies in the Supplementary Catalog are found is twice larger with a FWHM of  $0''.49$ .

This shows that while the projected sizes of dust-enshrouded star-formation probed by ALMA are globally small for massive and distant galaxies, the new sources that we present here in the Supplementary Catalog do not extend the sample to much lower flux densities but to sources with a wider extension of the dust emission. This explains in part why these sources were not detected in the Main Catalog. Although their integrated flux densities may be equal (and sometimes higher) than sources in the Main Catalog, this flux is diluted into several beams and therefore drops below the detection limit for the central beam.

We recall that this increase in the ALMA sizes measured in the Supplementary Catalog remains such that globally the ALMA emission extends over much smaller sizes than their H-band sizes, confirming that the ALMA sources are particularly compact at 1.1 mm (e.g., [Chen et al., 2015](#); [Simpson et al., 2015b](#); [Rujopakarn et al., 2016](#); [Elbaz et al., 2018](#); [Calistro Rivera et al., 2018](#), see also [Franco et al., in prep](#)).

### 6.6.4 How complete is the Main plus Supplementary catalog ?

The average noise in the GOODS-ALMA image is  $\text{RMS}=0.182$  mJy, hence the  $3.5\text{-}\sigma$  limit of the Supplementary Catalog converts into a detection limit of about 0.64 mJy. We note that since the RMS of the noise varies across the image, because it is subdivided in 6 slices taken at different epochs, sources may be detected below 0.64mJy (a source was detected at 0.55mJy).

The various studies that have carried out millimetric counts (e.g., [Hatsukade et al., 2013](#); [Oteo et al., 2016](#); [Aravena et al., 2016](#); [Umeshata et al., 2017](#); [Fujimoto et al., 2017](#); [Dunlop et al., 2017](#); [Franco et al., 2018](#); [Hatsukade et al., 2018](#)) allow us to estimate an expected galaxy surface density that varies between 2000 and 3500 galaxies.deg<sup>2</sup> above 0.65 mJy at 1.1 mm. Over the size of 69.5 arcmin<sup>2</sup> of the GOODS-ALMA survey, this amounts to an estimated number of sources ranging between 39 and 48. In comparison, we have now extended the number of detections in GOODS-ALMA to 35 galaxies. This number is not far from the expected one, especially when one accounts for cosmic variance, and suggests that the present sample may be more than 70 % complete above 0.65 mJy.

## 6.7 Conclusion

Using prior information at 3.6 and 4.5  $\mu\text{m}$  from IRAC (combined with deep HST *H*-band and ground-based *Ks*-images), we were able to explore the presence of galaxies detected at 1.1mm with ALMA down to the  $3.5\text{-}\sigma$  limit. This was done despite the extremely large number of independent beams in the ALMA image even after tapering from 0''29 to 0''6.

In order to avoid introducing spurious associations, we restricted the new sample to ALMA detections with either an IRAC counterpart closer than 0''3 or closer than 0''6 but with a radio counterpart as well. In two cases, we used the K-band image to deconvolve IRAC sources that were missed by previous studies because of their close proximity to bright IRAC neighbors. These two galaxies do not exhibit any counterpart in the HST images, hence they are HST-dark, but both present a radio counterpart. In total we find 16 galaxies in the Supplementary Catalog that bring the total sample of GOODS-ALMA 1.1mm sources to 35 galaxies. This number is between 70 and 90 % of the predicted number of galaxies expected to be detected at 1.1 mm above 0.65 mJy as derived from existing millimeter number counts. We now detect in GOODS-ALMA between a third and half of the most massive star-forming galaxies ( $\log_{10}(M_{\star}/M_{\odot}) = 11 - 12$ ) depending on the redshift range within  $2 < z < 4$ .

The redshift range of the Supplementary Catalog covers a wider dynamic range ( $z = 0.65 - 5.36$ ) than the sources of the Main Catalog ( $z = 1.95 - 4.82$ ), with no systematic shift in the median redshift of  $z \simeq 2.6$ . The typical physical size of the new sources in the present Supplementary Catalog (1.3 kpc) is twice larger than that of the Main Catalog sources (0.65 kpc). The lower surface brightness of these sources explains partly why they were not detected in the Main Catalog. Hence, pushing down the ALMA detection limit using IRAC priors allowed us to reach twice less massive galaxies (median stellar mass  $M_{\star} = 6.6 \times 10^{10} M_{\odot}$ ) in which dust-enshrouded star-formation extends over twice larger sizes. However, this increase in the ALMA sizes is not large enough to question the fact that the ALMA emission globally extends over much smaller sizes than the H-band light, confirming that the ALMA sources are particularly compact at 1.1 mm.

Finally, we used a comparison of nearly 400 galaxies in common between HST and Pan-STARRS in the GOODS-ALMA field to show that the astrometry of the HST image does not only suffer from a global astrometric shift, as already discussed in previous papers, but also from local shifts that draw the equivalent of a distortion map that was artificially introduced in the process of building the mosaic of the GOODS-South HST image. We present a solution to correct for this distortion and use this correction in our identification of counterparts. We note that in some cases, the absence of this correction led previous studies to attribute the wrong counterpart to ALMA detections. This will be discussed in more detail in a paper in preparation.

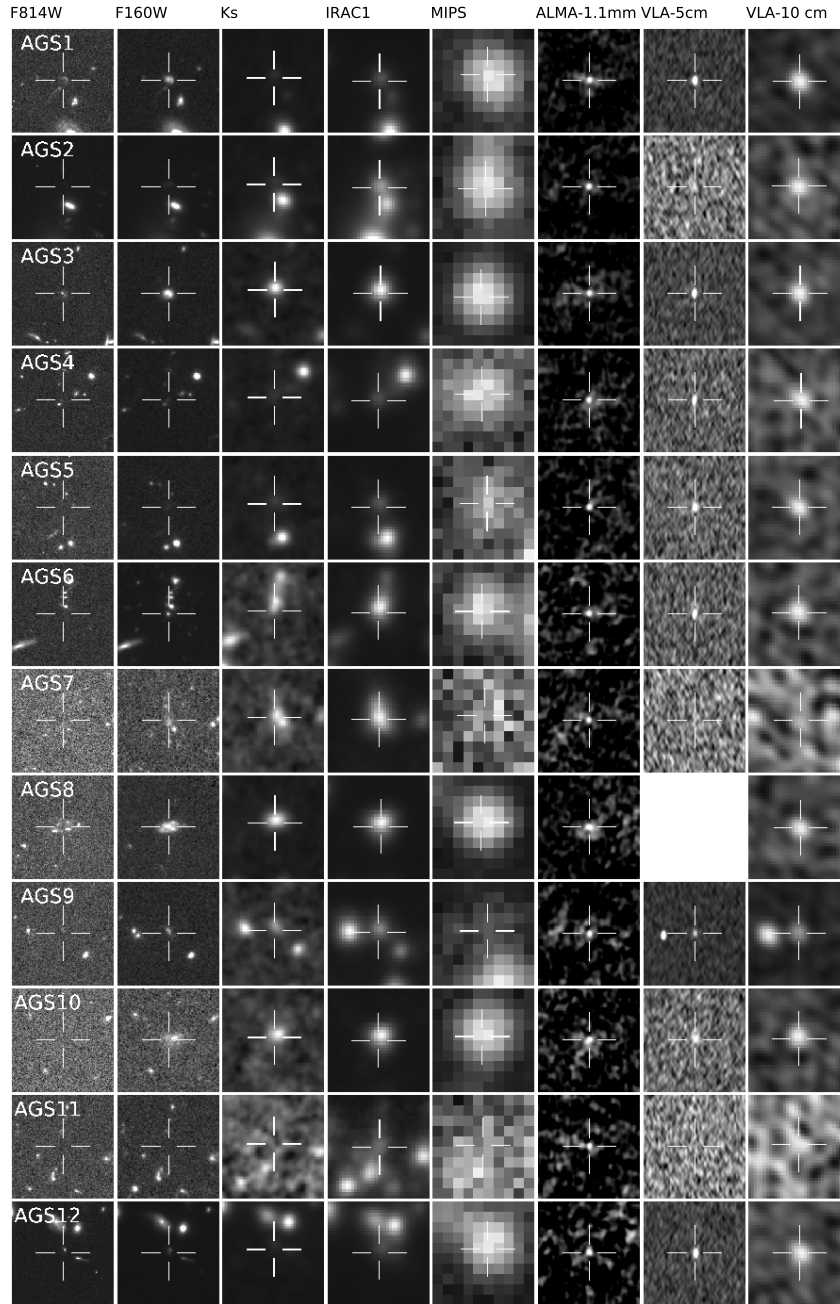


FIGURE 6.14: Postage-stamp ( $10 \times 10$  arcseconds), centred on the position of the ALMA detection at different wavelengths. From left to right : HST-WFC3 (a verifier (F814W, F160W), ZFOURGE ( $K_s$ ), *Spitzer*-IRAC channel 1 ( $3.6 \mu\text{m}$ ), *Spitzer*-MIPS ( $24 \mu\text{m}$ ), ALMA band 6 (1.1mm), VLA (5 and 10 cm). Blank images mean that the source is out of the field of view of the instrument. The white cross indicates the position of the ALMA detection.



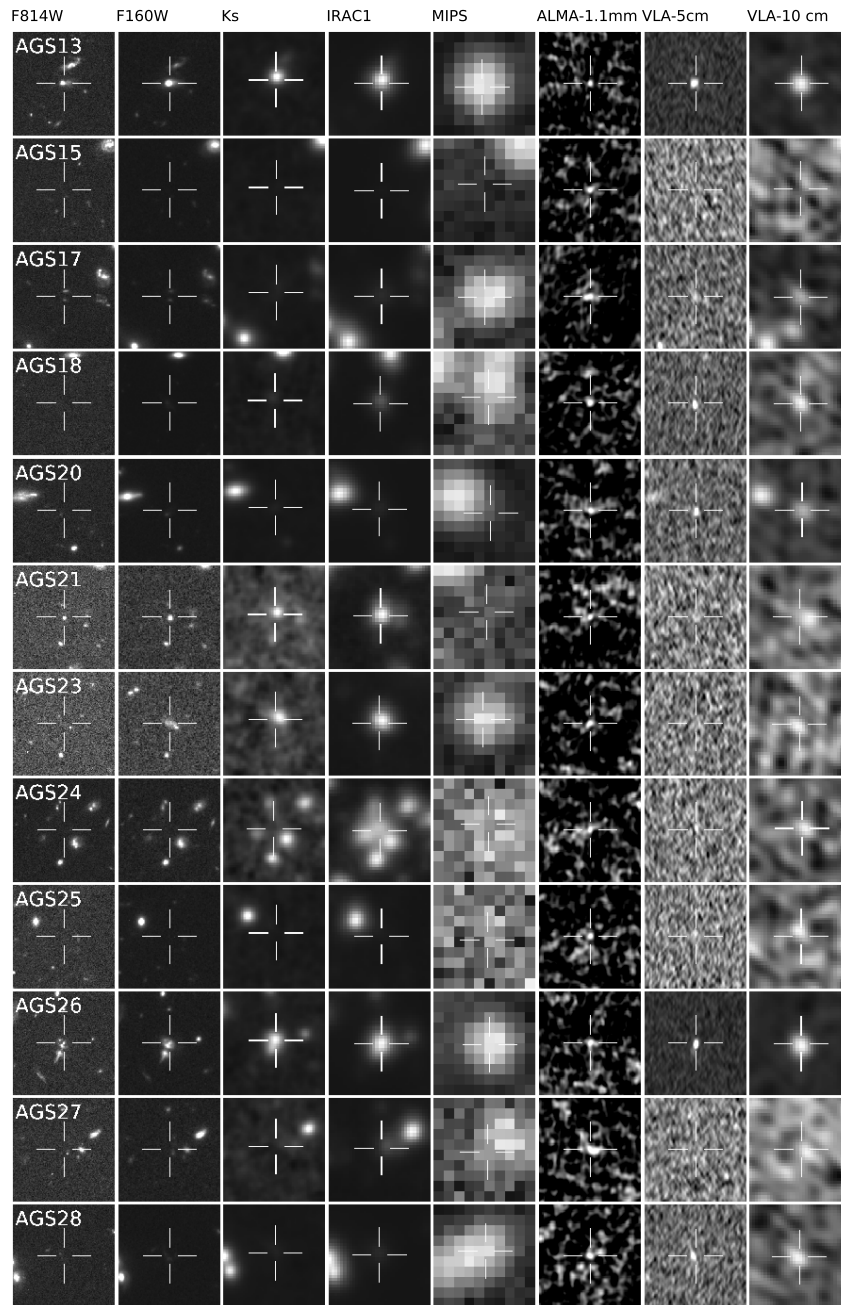


FIGURE 6.15: (continued)

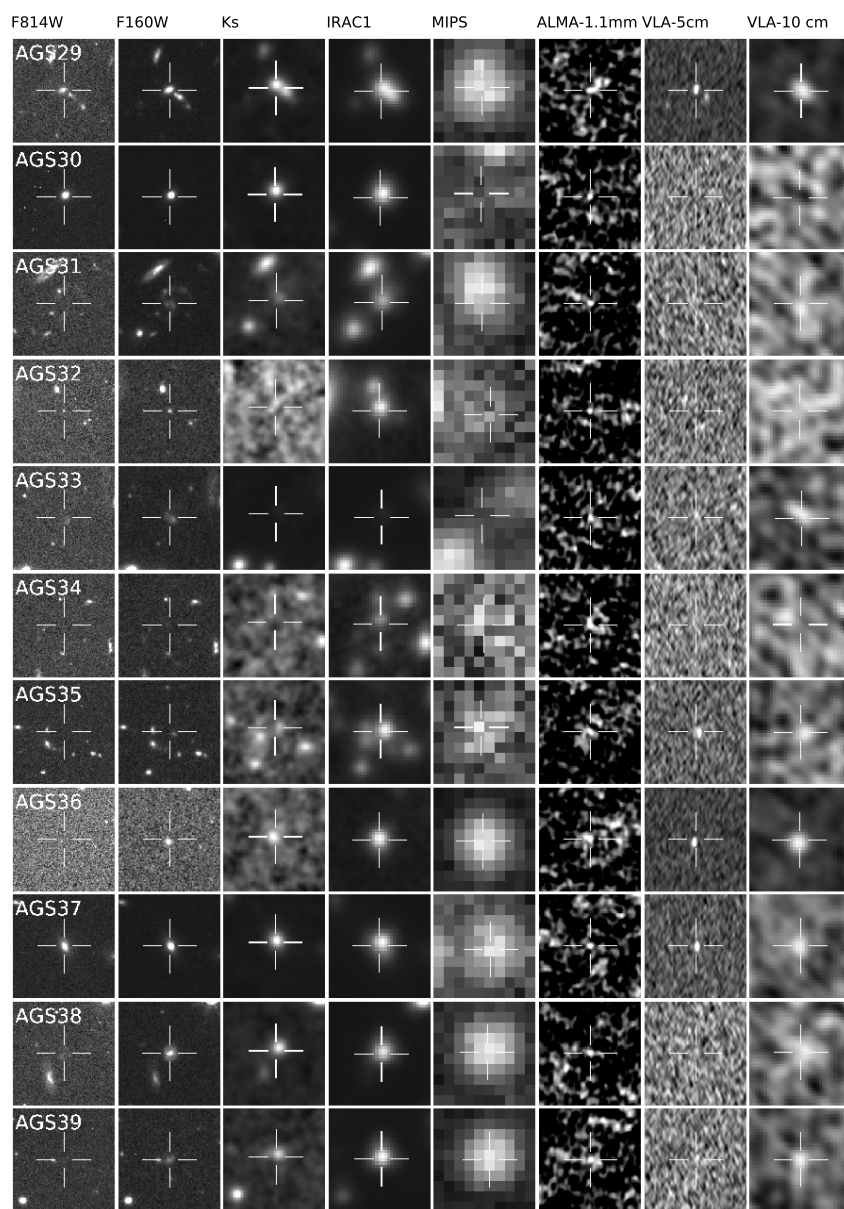


FIGURE 6.16: (continued)



## Contents

6.1	Introduction . . . . .	103
6.2	Data . . . . .	104
6.3	Astrometric correction of the HST image of GOODS-South . . . . .	105
6.4	ALMA Main and Supplementary catalogs . . . . .	107
6.5	Catalog . . . . .	115
6.6	Comparison of the properties of the ALMA galaxies from the Main and Supplementary catalogs . . . . .	120
6.7	Conclusion . . . . .	123

## 7.1 Outline of the problem

The primary progenitors at  $z \sim 2$  of massive galaxies are largely unknown from the current state of our observations (e.g., [Williams et al., 2014](#); [Straatman et al., 2015](#); [Wang et al., 2019](#)). Understanding this missing element is essential in order to constrain the star formation density beyond the peak of cosmic star formation ( $z \sim 2$ ; [Madau and Dickinson 2014](#)), to understand the massive end of the main sequence at high redshift, and more generally the evolution of massive galaxies at these high redshifts.

We will see in this chapter that the galaxies detected by ALMA in this survey, particularly the optically dark galaxies, are ideal candidates to be the progenitors of the massive, compact, passive galaxies at  $z \sim 2$ . We will first present a brief history of previous discoveries of HST-dark galaxies, and then define this term more specifically. We will then present the 6 HST-dark galaxies that we find in the GOODS-ALMA field, which are missed by the HST but unveiled by ALMA. Then, we will discuss the hypothesis that these galaxies are tracers of overdensities, and the implications of HST-dark galaxies on the cosmic density of star-formation.

## 7.2 History

The history of optically dark galaxies is closely linked to the history of (sub)-millimetre surveys. This begins with [Smail et al. \(1997\)](#), one of the first submillimeter surveys “of the distant universe” of two lensing clusters (lensed galaxies at  $z = 0.37$  and  $z = 0.33$ ) observed at two submillimeter wavelengths with SCUBA ( $450\mu\text{m}$  and  $850\mu\text{m}$ ; see Fig. 7.1).

Two years later, [Smail et al. \(1999\)](#) used ground-based near-IR ( $2\mu\text{m}$ ) images of these two lensing clusters to find the counterparts to the luminous submillimeter galaxies they had previously

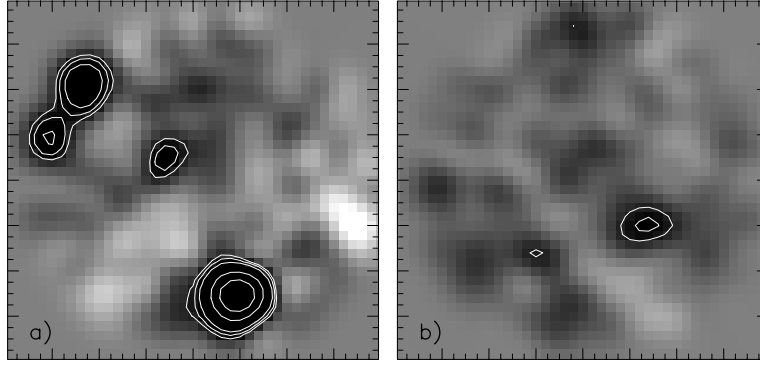


FIGURE 7.1: Figure from [Smail et al. \(1997\)](#). Observation at  $850\ \mu\text{m}$  of the fields A370, left panel and Cl 2244–02, right panel.

found. These near-IR observations did not show apparent optical counterparts corresponding to the SCUBA sources. Color constraints implied that these two galaxies with no optical counterparts had a redshift greater than 2, that therefore did not belong to the lensing clusters themselves.

However, the findings we present in this section are significantly different from these first cases of submillimeter galaxies with no optical counterparts. Indeed, it is rather different to discuss the absence of a counterpart of a (sub)millimeter source when the size of the (sub)millimeter beam is greater than  $15''$ , compared with  $0.25''$ , as with our survey. In the former case, the counterpart is not necessarily easy to identify, and it is often only possible to give the probability of association with a submillimeter source. The advent of interferometers allowing subarcsecond resolution has changed this picture. Since the commissioning of the Submillimeter Array (SMA, [Ho et al. 2004](#)) several high redshift galaxies without optical counterparts have been discovered. For example, [Tamura et al. \(2010\)](#) present the discovery of a galaxy undetected at wavelengths  $< 3\ \mu\text{m}$ , which is located in a protocluster at  $z = 3.09$  in SSA2 ([Steidel et al., 1998](#)). This observation is particularly interesting because, in our field, ALMA unveils several HST-dark galaxies which could be part of an overdensity. We will discuss the implications of these observations in Sect. 7.6.

The advent of ALMA marked the beginning of a new era. ALMA allows deep resolved surveys to be carried out (e.g., [Walter et al., 2016](#); [Dunlop et al., 2017](#); [González-López et al., 2019b](#)), reaching rms levels down to  $30\ \mu\text{Jy}$ .

Unfortunately, obtaining deep observations in small areas is not very efficient in finding optically-dark galaxies. These sources are, for those currently known, particularly massive and distant galaxies, hence rather rare, with surface densities that suffer from strong cosmic variance ([Wang et al., 2016](#)). The more massive a galaxy is, the more metal-rich (e.g. [Garnett, 2002](#); [Tremonti et al., 2004](#); [Gallazzi et al., 2005](#); [Mannucci et al., 2010](#); [Yates et al., 2012](#); [Foster et al., 2012](#); [Kirby et al., 2013](#); [Dayal et al., 2013](#)) and dust-rich (e.g. [Heckman et al., 1998](#); [Boissier et al., 2004](#); [Reddy et al., 2010](#)) it will be. The gravitational potential of the galaxy will prevent dust and metal from escaping from the galaxy ([Pannella et al., 2015](#); [Barone et al., 2018](#)) and prevents the metal-rich gas from being ejected from the galaxy, as it requires a higher escape velocity. There is a strong correlation between the stellar mass of a star-forming galaxy and its dust attenuation (e.g., [Buat et al., 2012](#); [Heinis et al., 2014](#); [Oteo et al., 2014](#); [Pannella et al., 2015](#)). The density of galaxies with stellar masses greater than  $10^{11}\ M_{\odot}$  at redshift greater

than 3.5 is lower than  $0.1 \text{ arcmin}^{-2}$  (Davidzon et al., 2017; Williams et al., 2019). We would therefore expect no sources with these characteristics to reside in fields such as the HUDF. In addition, these massive and distant galaxies are mostly clustered (Chiang et al., 2017), which increases the effects of cosmic variance and enhances the randomness of finding them in small areas.

To detect this type of sources, it is therefore essential to extend the search area by carrying out large surveys. This search can be performed by single-dish telescopes that have a large half power beam width (HPBW) antenna. For example, the JCMT and SCUBA-2 can cover large areas (e.g. Geach et al., 2017), but the angular resolution is low ( $\theta \sim 15''$  at  $850 \mu\text{m}$ ). Future large surveys are planned with the NIKA2 camera ( $\theta \sim 11''$  at  $1.2 \text{ mm}$ ) on the 30m of IRAM (PIs: A.Beelen, G.Lagache & N.Ponthieu), for example, and with the TolTEC Camera (Bryan 2018,  $\theta \sim 5''$  at  $1.1 \text{ mm}$ ) at the 50-meter Large Millimeter-wave Telescope (LMT, e.g., Pope et al., 2019).

Another solution is to multiply the pointings with an interferometer. The ALMA HPBW, with the configuration used in our analysis, is  $\sim 23''/3$ . This requires a significant number of pointings to cover a large surface area (846 to cover a surface of  $69 \text{ arcmin}^2$ ). However, the advantage of the interferometer, despite the complexity of mapping large surfaces, is to benefit from an unprecedented angular resolution and thus to identify the counterparts of detected galaxies with high precision. Intermediate size surveys (ASAGAO,  $26 \text{ arcmin}^2$ ), have subsequently allow the detection of some optically-dark galaxies Yamaguchi et al. (2019a), but larger surveys such as the one presented in this work are the ideal method to detect this type of object.

This notion of a HST-dark galaxy is obviously relative. In this work, we will use this term to refer to a galaxy that has not been detected in a catalog based on HST observations. This definition is somewhat problematic because it depends on the depth of HST observations. Indeed, if the HST detection limit of our survey had been shallower, we would have found many more HST-dark sources. In our survey, the detection at  $5\sigma$  in  $H$ -band reaches a magnitude limit of 28.2 AB. The detection limit in  $H$ -band is also not uniform in the GOODS-ALMA field - for example, in HUDF9 (Bouwens et al., 2010) the detection limit reaches 29.74 AB. Definitions can, therefore, disagree on this notion of HST-dark: those “absolute” definitions that are based only on the HST detection limit, and the more relative definitions based on a color difference, for example.

### 7.3 HST-dark galaxies in GOODS-ALMA

We have discovered a number of galaxies without  $H$ -band HST-WFC3 ( $1.6 \mu\text{m}$ ) counterparts. We discuss below the possibility that these detections are real HST-dark galaxies. Some ALMA detections that were previously attributed to an HST counterpart seem in fact to be either more distant galaxies, extremely close on the line of sight to another galaxy, hidden by a foreground galaxy, or too faint at optical rest-frame wavelengths to be detected by HST. It is already known that some of the most luminous millimeter or submillimeter galaxies can be completely missed at optical wavelengths (e.g., Huang et al., 2011; Caputi et al., 2012; Ono et al., 2014; Fujimoto et al., 2016; Wang et al., 2016; Schreiber et al., 2018b; Yamaguchi et al., 2019b; Williams et al., 2019), even in the deepest optical surveys, due to dust extinction.

Among the sources that do not have detections in the  $H$ -band of HST-WFC3, we distinguish between sources not detected by HST but detected by other instruments (we will discuss the

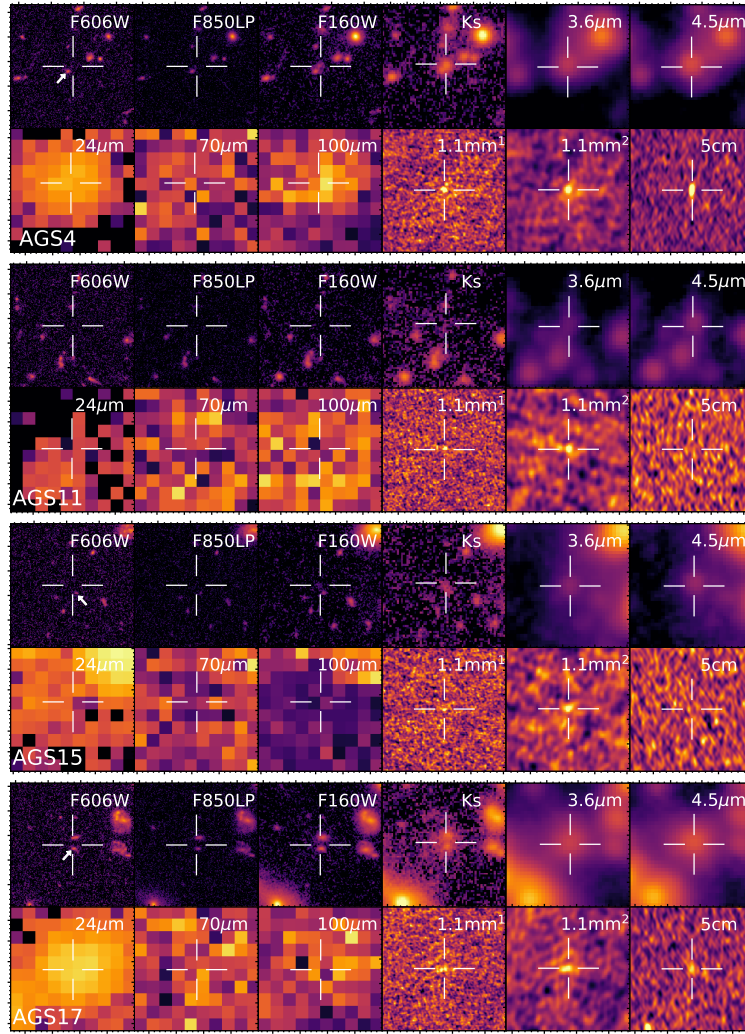


FIGURE 7.2: Postage stamps of  $10 \times 10$  arcsec from HST-WFC3 at  $0.606 \mu\text{m}$  to VLA at 5cm, for the four optically-dark galaxies discussed in Sect. 7.3. For the two ALMA images at 1.1 mm, those marked by <sup>1</sup> correspond to the non-tapered images, those marked by <sup>2</sup> correspond to the  $0''.60$ -mosaic images. The  $K_s$ -band thumbnail comes from the super-deep detection image described in Sect. 3.3. All images are centered on the ALMA detection. We indicate with white arrows the position of the previously associated HST counterpart.

particular importance of the IRAC filters), and sources undetected by HST as well as all of the other available instruments in the GOODS-South field (described in the Sect. 4.4). Of the 20 galaxies detected in our main catalog, seven (35%) do not present an obvious HST counterpart. This number is slightly higher than the expected number of spurious sources ( $4 \pm 2$ ), predicted by the statistical analysis of our survey. To be more accurate, for three of these seven galaxies (AGS4, AGS15 and AGS17), an HST galaxy is in fact relatively close to the ALMA detection on the line of sight. However, strong evidence, presented below, suggest that these HST galaxies are not the counterparts of the ALMA detections, and without the resolution of ALMA we would falsely associate the counterparts. For the four other ALMA detections without HST-WFC3 counterparts within a radius of  $0''.60$ , one of them (AGS11) has also been detected at other wavelengths. In this section, we will discuss four particularly interesting cases of HST-dark galaxies (AGS4, AGS11, AGS15, and AGS17), and discuss our reasons for classifying the other three as spurious sources (see Fig. 7.2).



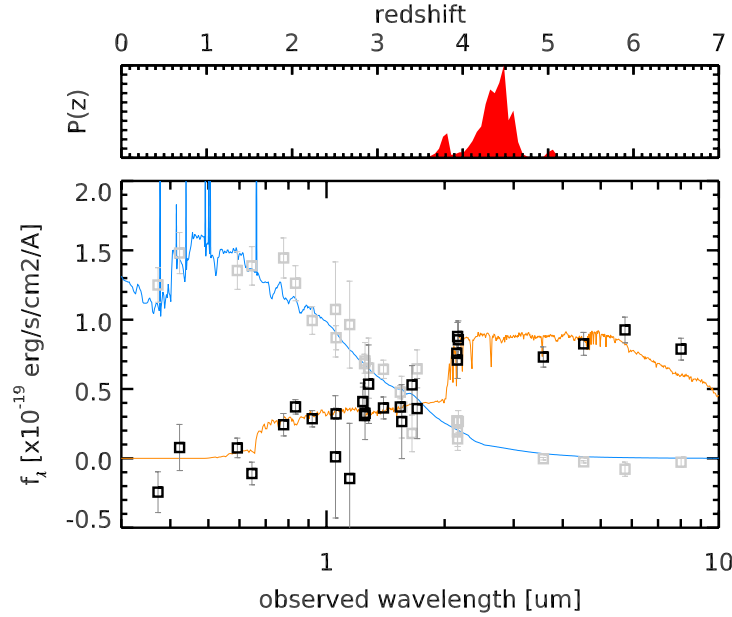


FIGURE 7.3: Spectral energy distributions of AGS4 and ID<sub>CANDELS</sub> 8923. Aperture photometry allows the separation between the local galaxy detected by HST (blue, and indicated by a white arrow in Fig. 7.2, ID<sub>CANDELS</sub> 8923) and the distant galaxy detected by ALMA (orange). The top panel shows the photometric redshift probability distribution of AGS4. As the Balmer break is well established in the *K*-band, we consider that this redshift determination is robust, and we adopt the derived redshift  $z_{\text{AGS4}} = 4.32^{+0.25}_{-0.21}$  and stellar mass ( $10^{11.45 \pm 0.2} M_{\odot}$ ) values for AGS4.

### 7.3.1 AGS4

AGS4 is a close neighbor of ID<sub>CANDELS</sub> 8923. AGS4 is the fourth brightest detection in our survey, with a S/N greater than 9. The center of the ALMA detection is located at only 0''38 from ID<sub>CANDELS</sub> 8923, its closest neighboring galaxy. Before the astrometric correction (see Sect. 4.5), this distance was only 0''21. This is, therefore, an example where the astrometric correction moves the ALMA galaxy away from the supposed counterpart. In Fig. 7.2, we can clearly see that the ALMA emission is offset from the observed *H*-band galaxy shown by the white arrow. This offset could be explained physically, for example, as a region extremely obscured by dust, within the same galaxy, greatly extinguishing the optical rest-frame emission, but still visible with ALMA. However, for AGS4, a series of clues suggest another explanation.

The first piece of evidence is the comparison between the IR SED at the position of the ALMA detection and the redshift of the optical galaxy. The redshift of the optical galaxy is  $z = 0.241$ , whereas the far IR SED peaks around 350  $\mu\text{m}$  (see Fig. 7.5). If AGS4 was a dusty star-forming region in the outskirts of 8923, this infrared SED would suggest an abnormally cold dust temperature. It is, therefore, more probable that AGS4 is not part of ID<sub>CANDELS</sub> 8923, and is a dusty distant galaxy. The fuzzy emission in the *H*-band HST image, exactly centered at the position of the ALMA detection (see Fig. 7.2) has not led to any detection in the CANDELS catalog. In the *V*-band HST images, only ID<sub>CANDELS</sub> 8923 is present, seen to the South-East of the position of the ALMA detection (indicated by a white cross). No emission is visible at the exact position of the ALMA detection. In the *z*-band, a barely visible detection appears extremely close to the center of the image.



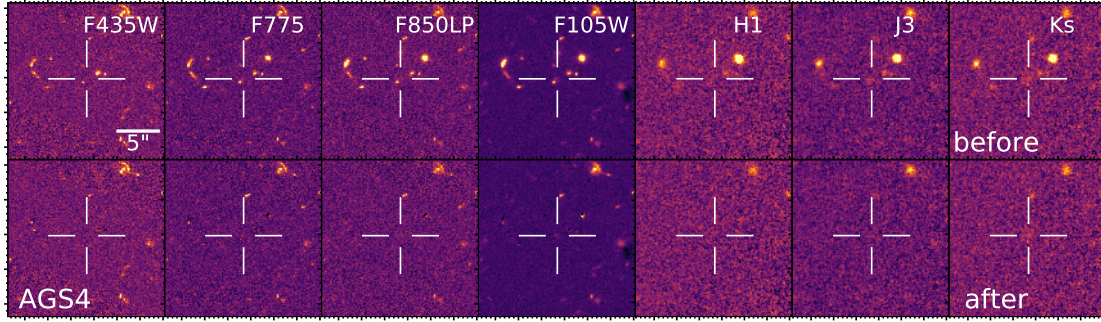


FIGURE 7.4: Postage stamps ( $18'' \times 18''$ ) centered at the position of AGS4 (white cross). The top line shows the original image while the bottom line shows the image after the sources located near AGS4 have been removed using Galfit. The extracted fluxes were used to fit the spectral energy distributions of Fig. 7.3

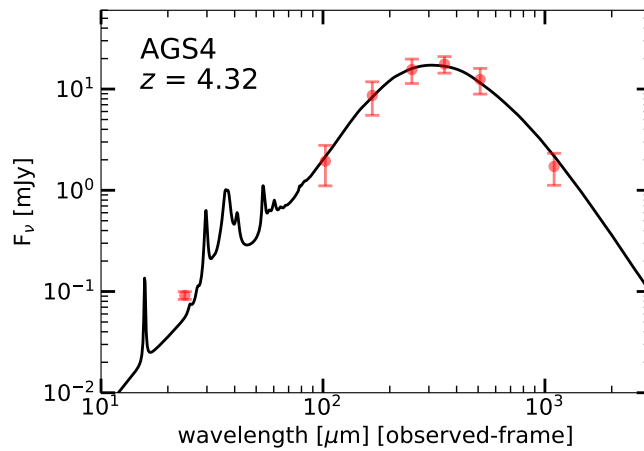


FIGURE 7.5: Spectral energy distribution (SED) of AGS4. The flux densities from 100 to 500  $\mu\text{m}$  are from GOODS-Herschel (Elbaz et al., 2011). AGS4 ( $z = 4.32$ , see Sect. 7.3) is fitted with the model of Schreiber et al. (2018a).

The second clue is the detection of a galaxy with redshift  $z = 3.76$  in the FourStar galaxy evolution survey,  $0''.16$  from the ALMA detection. This redshift is much more consistent with the peak of the IR SED. The ZFOURGE survey is efficient in detecting galaxies with redshifts between 1 and 4 by using a  $K_s$ -band detection image (instead of  $H$ -band as used for the CANDELS survey), and also due to the high spectral resolution ( $\lambda/\Delta\lambda \approx 10$ ) of the medium-bandwidth filters which provide fine sampling of the Balmer/4000  $\text{\AA}$  spectral break at these redshifts (Tomczak et al., 2016). Furthermore, the stellar mass derived in the ZFOURGE catalog ( $10^{10.50} M_\odot$ <sup>1</sup> compared with  $10^{7.64} M_\odot$  in the CANDELS catalog) is more consistent with the expected mass of galaxies detected by ALMA. Indeed as shown in this paper, and as already shown by Dunlop et al. (2017), ALMA tends to reveal the most massive dusty galaxies.

The third piece of evidence is the presence, in the *Spitzer*-CANDELS catalog (Ashby et al., 2015), of a galaxy detected with the IRAC filters only  $0''.1$  from our ALMA detection. This IRAC galaxy has a magnitude of 22.51 at 3.6  $\mu\text{m}$ , measured within an aperture of  $2''.4$  radius.

We also note that Rujopakarn et al. (2016) detect a radio galaxy at  $S/N \approx 17$  only 55 mas from the center of the ALMA detection shown in Fig. 7.2 (the positional accuracy of this VLA image

1. As a reminder, all the stellar masses given in this manuscript have been converted into a Salpeter (1955) IMF.

is 40 mas). Additionally, AGS4 is detected in two of the three *Chandra* bands: 0.5-7.0 keV (full band; FB) and 0.5-2.0 keV (soft band; SB), but not at 2-7 keV (hard band; HB) from the 7 Ms *Chandra* observations of the GOODS-South field. The integrated X-ray flux is only  $6.86 \times 10^{40} \text{ erg.s}^{-1}$ , but this galaxy is classified as an AGN in the 7 Ms catalog.

The detection of a local galaxy at this position has been largely documented (e.g., [Hsu et al., 2014](#); [Skelton et al., 2014](#); [Santini et al., 2015](#)). In contrast, some studies present the galaxy located at this location as a distant galaxy. [Cardamone et al. \(2010\)](#) take advantage of the 18-medium-band photometry from the Subaru telescope and the photometric redshift code EAZY ([Brammer et al., 2008](#)) to derive a redshift  $z = 3.60$ . [Wuyts et al. \(2008\)](#) find a redshift of  $z = 3.52$  also using EAZY. We can also add a redshift determination by [Rafferty et al. \(2011\)](#) using the Zurich extragalactic Bayesian redshift analyzer (ZEBRA, [Feldmann et al. 2006](#)), at  $z = 2.92$ . These determinations of a high redshift by independent studies support the existence of a distant galaxy at this position.

Although close to one another, the two sources (ID<sub>CANDELS</sub> 8923 and 8923b) were successfully de-blended using two light-profile models, determined by fitting the HST *H*-band image with Galfit. The two sources were then fit simultaneously using these two models on all of the available images, fixing the profiles to those observed in the *H* band. The SEDs of these two galaxies are shown in Fig. 7.3, in blue for the HST galaxy and in orange for the ALMA galaxy, together with the photometric redshift probability distribution for AGS4. The redshifts were estimated using EAZY. For the blue HST galaxy we found  $z = 0.09^{+0.06}_{-0.07}$ , in good agreement with that found by [Skelton et al. \(2014\)](#). On the other hand, the redshift found for AGS4 is slightly higher than in ZFOURGE, with  $z_{\text{AGS4}} = 4.32^{+0.25}_{-0.21}$ . However, we can also see a secondary peak in the redshift probability distribution, at the position of the ZFOURGE redshift. As the Balmer break is well established in the *K*-band, we consider that the redshift determination ( $z_{\text{AGS4}} = 4.32^{+0.25}_{-0.21}$ ) is robust and we adopt this redshift for AGS4. The stellar mass of the ALMA galaxy was then computed with FAST ([Kriek et al., 2009](#)), and we found  $10^{11.45 \pm 0.2} M_{\odot}$  (probably slightly overestimated due to the presence of an AGN, suggested by a flux excess in the IRAC bands). The IR SED of this galaxy is shown in Fig. 7.5. For the first time, thanks to ALMA, we can argue that there exists, at this position, not one but two galaxies, close to each other on the line of sight.

### 7.3.2 AGS11

AGS11 is detected at 1.1 mm with a flux of 1.4 mJy (S/N~8) without any counterpart in the deep HST image. However, the galaxy is also detected by IRAC, confirming the existence of a galaxy at this position (see Fig. 7.6). A galaxy was recently found, for the first time, in the ZFOURGE catalog at 0".18 from the center of the ALMA position. This galaxy was not detected directly in the Magellan image but in a super-deep combined *K<sub>s</sub>*-band image at  $4.5 \sigma$ . From this position, the flux in the IRAC-bands has been extracted with S/Ns of 26, 34, 8 and 8 at 3.6  $\mu\text{m}$ , 4.5  $\mu\text{m}$ , 5.8  $\mu\text{m}$  and 8.0  $\mu\text{m}$  respectively.

This HST-dark galaxy falls in a projected overdensity on the sky, consisting of sources in the redshift range  $3.42 \leq z \leq 3.56$  and brighter than  $K_s < 24.9$  ([Forrest et al., 2017](#)). This density has been computed by [Forrest et al. \(2017\)](#) using the 7<sup>th</sup> nearest-neighbor technique ([Papovich et al., 2010](#)). This overdensity, centered at RA = 53.08, DEC = -27.85, extends beyond approximately 1.8 Mpc.

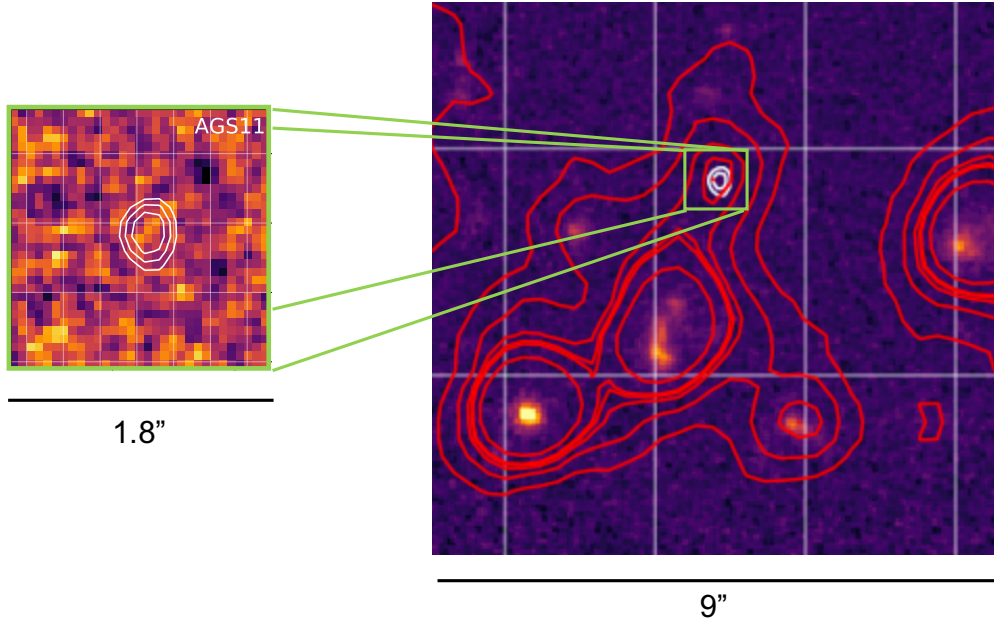


FIGURE 7.6: Left panel: Postage stamp of  $1.8 \times 1.8$  arcsec centered at the position of AGS11. ALMA contours (4, 4.5, 5  $\sigma$ ) at 1.1mm (white lines) are overlaid on F160W HST/WFC3 images. Right panel: Postage stamp of  $9 \times 9$  arcsec showing the ALMA contours (white), IRAC  $3.6\mu\text{m}$  contours (red) overlaid on IRAC channel 1 image.

The redshift derived in the ZFOURGE catalog is  $z = 4.82$ , making it the farthest galaxy detected in this blind survey. However, we remain cautious regarding this redshift, as this entry has been flagged in the ZFOURGE catalog ( $\text{use} = 0$ ) due to the S/N of this galaxy (4.7) being below the limit defining galaxies with good photometry ( $\text{S/N} \geq 5$ ). This galaxy is the only galaxy in our catalog flagged in the ZFOURGE catalog. AGS11 has not been detected in the 7 Ms *Chandra* survey.

The stellar mass, derived in the ZFOURGE catalog,  $3.55 \times 10^{10} M_{\odot}$ , is consistent with the masses of all of the other ALMA galaxies found in this survey. What is particularly interesting in the multiwavelength images of this galaxy is that AGS11 is detectable only by ALMA and in the IRAC-bands (in non-stacked images). Outside of these wavelengths, no emission is detectable.

### 7.3.3 AGS15

AGS15 is at a distance of  $0''.59$  from its possible HST counterpart ( $\text{ID}_{\text{CANDELS}} 3818$ ) after astrometric correction, corresponding to a physical distance of 4.33 kpc. This is the largest HST-ALMA offset in our entire catalog. The IRAC position, in contrast, matches much more closely with the ALMA position, with an offset of only  $0''.14$ . The stellar mass of the optical galaxy, given by the ZFOURGE catalog ( $7.24 \times 10^9 M_{\star}$ ) would have made AGS15 a galaxy lying far from the median stellar mass ( $1.1 \times 10^{11} M_{\odot}$ ) of our survey. The redshift of  $\text{ID}_{\text{CANDELS}} 3818$  ( $z = 3.46$ ) is nevertheless consistent with the other redshifts found in this study. Moreover, we will see later in this chapter that this redshift is particularly interesting. It could correspond to the redshift of other HST-dark galaxies and a redshift of an overdensity in GOODS-ALMA (we will discuss this in detail when we discuss AGS24).

### 7.3.4 AGS17

AGS17 is a close neighbor ( $0''.27$ ) of ID<sub>CANDELS</sub> 4414 ( $z = 1.85$ ). AGS17 is one of the three galaxies detected by Hodge et al. (2013) at  $870\mu\text{m}$  in the ALMA field of view (along with AGS8 and AGS15 previously discussed). The counterpart of AGS17 was attributed to ID<sub>CANDELS</sub> 4414 by Wiklind et al. (2014) with an offset between the ALMA detection and the corresponding F160W object of  $0''.32$ . Again, there are indications that the identification may be false: the peak of the IR SED is  $\sim 400\mu\text{m}$  (see Fig. 7.7), suggesting a more distant galaxy. To be detected with the flux densities reported in Table 4.2, a galaxy at  $z = 1.85$  would have an extraordinarily high star formation rate ( $\sim 820 \pm 240 \text{ M}_\odot \text{yr}^{-1}$ ), using the IR SEDs of Schreiber et al. (2018a). If truly associated with the CANDELS counterpart, this galaxy would be an extreme starburst with an SFR  $59 \pm 17$  times greater than the SFR<sub>MS</sub>. Galaxies with these properties cannot be ruled out, as galaxies with much higher star formation rates (and offsets from the main sequence) have already been observed (e.g., Pope et al., 2005; Fu et al., 2013). However, such objects are relatively rare. In addition, the stellar mass of ID<sub>CANDELS</sub> 4414 ( $10^{10} \text{ M}_\odot$ ) is inconsistent with the trend of the other detections (more than one order of magnitude below the median stellar mass of our catalog).

Another galaxy (ID<sub>CANDELS</sub> 4436) is relatively close ( $0''.57$ ) to the ALMA detection. The position of the ALMA detection, which is between ID<sub>CANDELS</sub> 4414 and ID<sub>CANDELS</sub> 4436, could be the signature of a major merger occurring between these two galaxies. The emission observed by ALMA could result in this case from the heating of the dust caused by the interaction of these two galaxies, but the redshift determination of  $0.92^{+0.04}_{-0.18}$  by Le PHARE (Arnouts et al., 1999; Ilbert et al., 2006) dismisses this hypothesis.

After subtraction of the two galaxies close on the line of sight (ID<sub>CANDELS</sub> 4414 and 4436) in the HAWK-I image, a diffuse source is revealed (half-light radius =  $1''.55 \pm 0''.12$ , Sérsic index = 1.0). Lower resolution ALMA observations would be needed in order to correctly measure the total submm flux of this extended source.

We also note the position of the IRAC source, which is located only  $0''.06$  from the ALMA detection.

### 7.3.5 AGS24

This galaxy will be presented in detail in Zhou et al., in prep. This galaxy is the only galaxy added to the supplementary catalog (see Chapter 6) that was not detected using prior information, but instead, by slightly lowering the threshold ( $S/N = 3.9$ ) in the tapered map to  $0''.60$ . The  $S/N$  of this source is higher in the  $0''.29$  mosaic which suggests that this source is particularly compact. This galaxy has been detected in the radio band at 6 GHz ( $3.7\sigma$ ) and 3 GHz ( $5.7\sigma$ ). In Fig. 7.8, we show the emission of this galaxy at different wavelengths, from the  $H$  band, at  $1.6\mu\text{m}$  to the 10cm radio. While for all wavelengths below the IRAC filter, the galaxy is invisible, it appears, at the position of the ALMA detections, from the IRAC filters. It was possible, by the same method as that used to determine the AGS4 redshift, to determine the AGS24 redshift ( $z = 3.5$ , see Fig. 7.9). The fact that this galaxy is located at  $z \simeq 3.5$  is particularly interesting, this galaxy could be at the center of an overdensity at  $z \simeq 3.5$ . We will discuss this hypothesis in detail in Sect. 7.5.

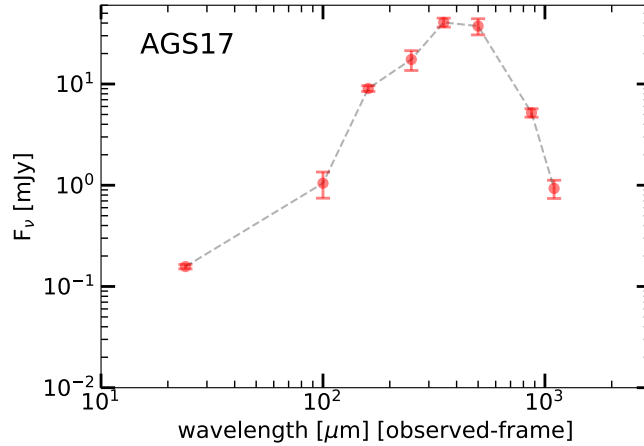


FIGURE 7.7: Spectral energy distribution of AGS17. The flux densities from 100 to 500  $\mu\text{m}$  are from GOODS-*Herschel* (Elbaz et al., 2011). The SED of AGS17 (bottom), which has no known redshift, is simply presented with an interpolation between the observed flux densities to illustrate that it peaks around 400  $\mu\text{m}$ . This peak is inconsistent with the redshifts of the two optical sources with ID<sub>CANDELS</sub> 4414 ( $z = 1.85$ ) and 4436 ( $z = 0.92$ ).

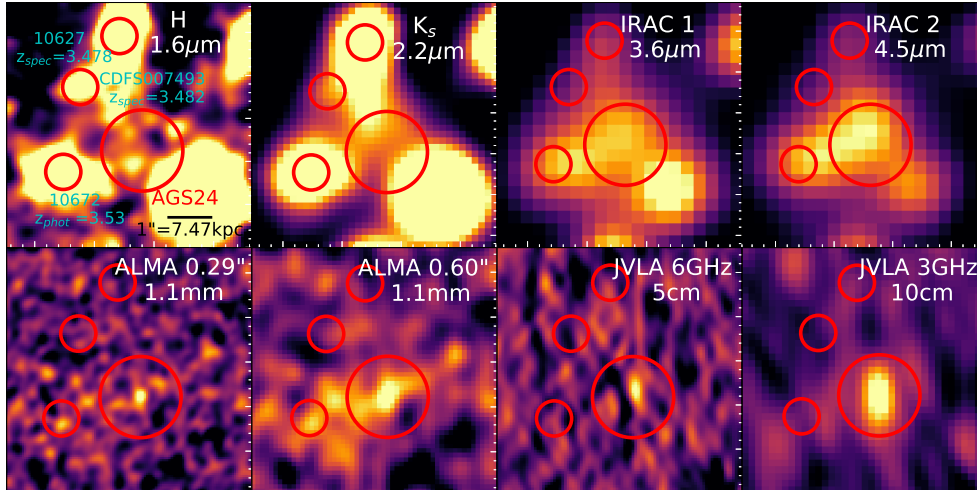


FIGURE 7.8: Postage stamps of  $5 \times 5$  arcsec from HSTWFC3 at  $0.606 \mu\text{m}$  to VLA at 5 cm, for AGS24. The biggest red circle shows the position of AGS24. Figure from Zhou et al., in prep.

### 7.3.6 AGS25

This detection is not listed in the CANDELS catalog (Guo et al., 2013), nor the S-CANDELS catalog (Ashby et al., 2015), nor is it detected in X-ray (Luo et al., 2017). This galaxy is marginally detected in radio at 5 and 10 cm.

In Chapter 4, we showed that the presence of ALMA detection alone was not sufficient to qualify a galaxy as HST-dark. The four HST-dark galaxies presented in Chapter 4 (AGS4, AGS11, AGS15, and AGS17) have at least one feature in common - the presence of an IRAC detection. The presence of an IRAC detection was until now the element that validated the blind HST-dark detection. We do not exclude that there may be HST-dark galaxies detected by ALMA, and without IRAC counterparts, but these galaxies will have to be tested further before they can be considered as robust. The case of AGS25 is rather special. AGS25 is close ( $3''$ ) to one of the galaxies



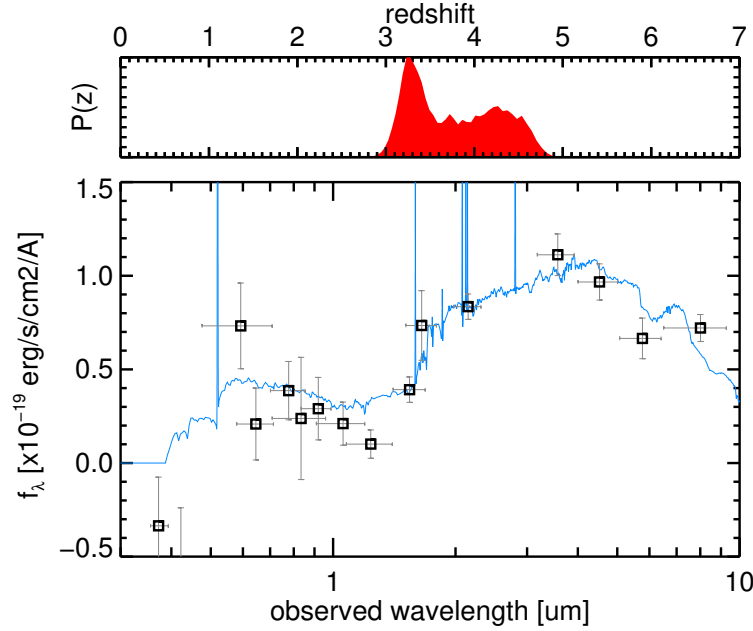


FIGURE 7.9: Top: Photometric redshift probability distribution function derived by EAZY (Brammer et al., 2008). Below: SED fitting using the technique described in Sect. 7.3.1. Figure from Zhou et al., in prep.

ID<sub>CANDELS</sub> = 8067, which is very ( $M_* = 5.6 \times 10^{10} M_\odot$ ) for its redshift ( $z_{\text{spec}} = 1.038$ ). The IRAC emission of this galaxy is large and extends to the position of AGS25. It is therefore probable that the emission of AGS25 in IRAC filters is blended with the emission of ID<sub>CANDELS</sub> = 8067. We see in Fig. 7.12 that the IRAC contours around the galaxies extend to the side of the ALMA detection. We performed deblending (source subtraction) to see if we could detect emission in the IRAC filter at the position of the ALMA detection. We did this by modeling a Sérsic profile with GALFIT (Peng et al., 2010).

After subtraction of the Sérsic model (see Fig. 7.10), we found IRAC emission. Moreover at less than 0".1 from the ALMA position (after astrometric correction, see Sect. 6.3), a galaxy is listed in the ZFOURGE catalog (ID<sub>ZFOURGE</sub> = 11353, shown by a circle in Fig. 7.10), with a magnitude in K band = 25.9 AB. The subtraction with GALFIT suggests that the source is not present in Ashby et al. (2015) only because of blending. In this study, we will use this mass and redshift, derived from the ZFOURGE catalog.

The characteristics of this galaxy make it particularly interesting, with  $z_{\text{AGS25}} = 4.66^{+0.25}_{-0.26}$  and  $M_{*,\text{AGS25}} = 2.0 \times 10^{10} M_\odot$ . These properties are similar to those of AGS11,  $z_{\text{AGS11}} = 4.83^{+0.82}_{-0.76}$ ,  $M_{*,\text{AGS11}} = 2.8 \times 10^{10} M_\odot$ .

Among the 6 HST-dark galaxies for which we were able to determine a mass and redshift, there appear to be two distinct trends. Galaxies AGS4 and AGS24 are among the most massive of all active uvj galaxies detected in the region covered by the ALMA survey. AGS4 has a mass  $M_* = 2.81^{+1.65}_{-1.03} \times 10^{11}$ . In other words, it is the most massive galaxy at  $4 < z < 5$  in our catalogs. AGS24 has a stellar mass  $M_* = 1.82^{+0.27}_{-0.50} \times 10^{11}$ . Two HST-dark galaxies are of intermediate mass, but with a redshift higher than 4.5 (see Fig. 6.12) and for the two remaining galaxies, neither the mass nor the redshift have been estimated for the moment. The HST-dark galaxies could therefore be very massive galaxies ( $M_* > 10^{11} M_\odot$ ) at  $z > 3.5$ . These massive galaxies are

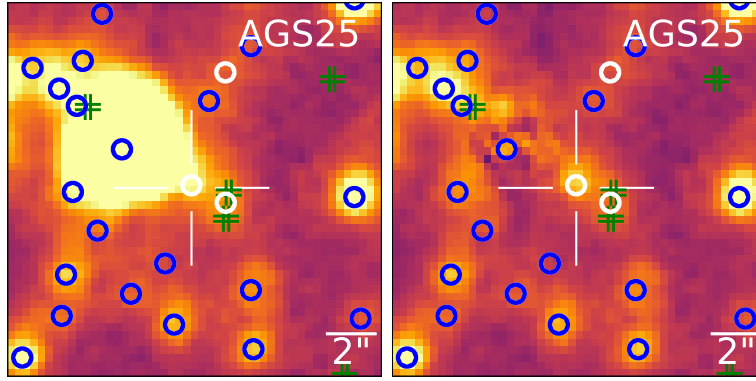


FIGURE 7.10: IRAC  $3.6\mu\text{m}$  ( $18'' \times 18''$ ) image centred on the position of the ALMA detection. We show the image before (left panel) and after (right panel) the subtraction with GALFIT of the source  $\text{ID}_{\text{ZFOURGE}} = 11024$  located to the Northeast of the detection and which masks the emission of the source located at the ALMA position. After subtraction we can see an emission located in the central position which suggest that the source is not present in Ashby et al. (2015) only because of blending. Cyan double crosses show sources from the GOODS-S CANDELS catalog. White circles show sources from the ZFOURGE catalog. Blue circles show common sources from both optical catalogs (i.e. sources with an angular separation lower than  $0''.4$ ).

almost non-existent at  $z > 4.5$  (in the volume defined by GOODS-ALMA), so we find HST-dark galaxies at these redshift with smaller stellar masses.

### 7.3.7 Verification of dubious galaxies

For several sources, there was a relatively large offset between the position of the ALMA detection and the position of the HST counterpart (see Table 4.1 and Table 6.1). This is the case, for example for AGS20 (see Fig. 7.11; left panel) which displays an offset of  $\sim 0.3''$  between optical and infrared detections. We can ask ourselves for this source if ALMA detects an obscured part of the galaxy, not visible in optics or if it is two separate galaxies. In the rest of this paragraph, we will call the part "ALMA" the one that is in the center of Fig. 7.11; left panel) and we will call the HST part, the part clearly visible in this image. We will try to determine the characteristics of these two emissions separately to determine if we can find the signature of a distant galaxy at the ALMA emission level, which would show that they are two different galaxies. If the determined redshifts are comparable, this study will not allow us to decide between the fusion of two galaxies, one highly dust-obscured or if the dusty star formation region of this galaxy is offset of the stellar light visible in  $H$ -band. As for AGS4, the two possible sources (optical and submillimeter) were then fit simultaneously using these two light-profile models (using GALFIT) on all of the available images, fixing the profile to that observed in the  $H$ -band (see Fig. 7.11; right panel). The blue curve represents the spectral energy distribution for the galaxy clearly visible in optics, while the orange curve represents the spectral energy distribution at the ALMA position and which becomes dominant from the K band. The characteristics of these two parts taken separately are given in Table 7.1.

The spectral energy distribution of the ALMA galaxy is very attenuated, while the other is virtually dust-free and has little star formation. The redshifts of the ALMA part and the optical part are coherent (see Table 7.1). The probability density of the redshift of the HST part gives a single peak and is well constrained to  $z = 2.47$ . For the ALMA part, the probability density allows a redshift to  $z=2.4$  or  $z=2.8$ . This last value corresponds to the redshift determined in the ZFOURGE

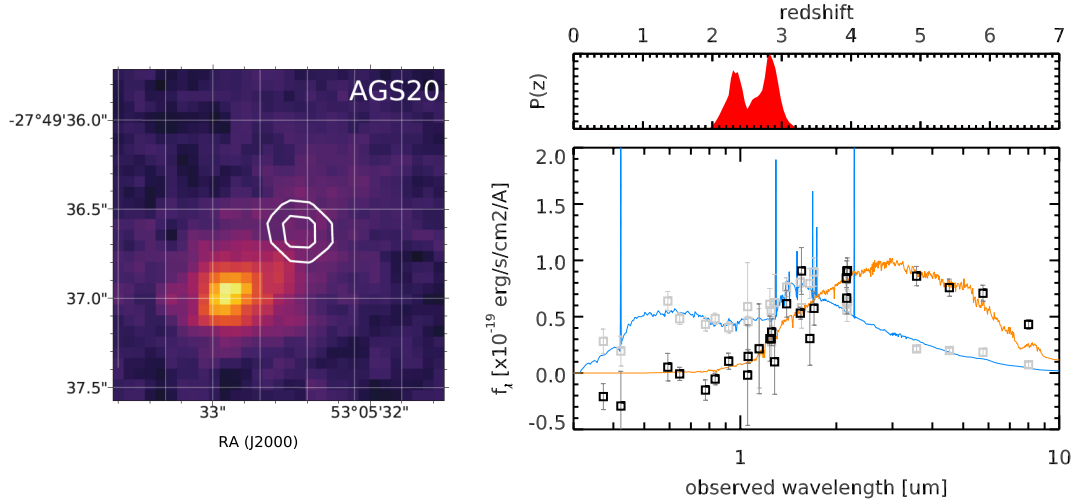


FIGURE 7.11: Right panel:  $1.8 \times 1.8$  arcsec postage stamps centered at the position of the ALMA detection. The ALMA contour ( $4$  and  $4.5\sigma$ ), in white are superimposed to an HST  $H$ -band image. Left panel: The two possible source, at the position of the HST detection and at the position of the ALMA detection were then fit simultaneously using these two light-profile models (using *Galfit*) on all of the available images, fixing the profile to that observed in the  $H$ -band. The redshift probability density of the "ALMA" galaxy is represented at the top of the panel.

	ALMA	HST
redshift	$2.61^{+0.32}_{-0.34}$	$2.47^{+0.07}_{-0.08}$
$\log_{10}(M_*)$	$10.85^{+0.09}_{-0.04}$	$10.05^{+0.04}_{-0.09}$
$A_v$	$2.4^{+0.3}_{-0.5}$	$0.6^{+0.0}_{-0.4}$

TABLE 7.1: Redshift, stellar mass and dust attenuation for the ALMA detection as well as for the HST-detection.

catalog. On the other hand,  $z=2.4$  is better compatible with the redshift of the other galaxy, which is much better constrained. We will therefore tend to favour  $z=2.4$ . With the information we have, it is difficult to decide whether it is a galaxy merger or a dark part within the galaxy. The determination of the redshift around  $z=2.5$  would require a spectroscopic validation. In any case, we think we can eliminate the hypothesis of a distant galaxy masked by a bright HST galaxy, as it was the case for AGS4.

## 7.4 Spitzer/IRAC a loyal ally for HST-dark galaxies identification

Our four HST-dark galaxies (AGS4, AGS11, AGS15, and AGS17) have at least one feature in common, the presence of an IRAC detection and the fact that this IRAC detection is closer on the sky than the unrelated HST detection (see Table 4.1). The IRAC detections come from the [Ashby et al. \(2015\)](#) catalog, except for AGS15 where the position comes from the ZFOURGE catalog, using the [Labbé et al. \(2015\)](#) survey. The offset between the IRAC and HST sources might suggest that they are different sources. Fig. 7.12 shows the IRAC contours at  $3.6 \mu\text{m}$  centered on the ALMA detection, superimposed over the HST  $H$ -band image. The presence of IRAC detections at these distances from the ALMA galaxies is a very strong driver for the identification of sources. The probability of random IRAC association is between one and two



ID	AGS4	AGS11	AGS15	AGS17
HST RaA [%]	4.52	-	9.14	2.12
IRAC RaA [%]	0.06	0.18	0.12	0.05

TABLE 7.2: The probability of an HST or IRAC random association (RaA) between the ALMA detection and the closest HST and IRAC galaxies (see Fig. 4.6) for the 4 HST-Dark galaxies discussed in Sect. 7.3.

orders of magnitude less likely than random HST association for this range of distances, as shown in Fig. 4.6 and Table 7.2. The selection of ALMA candidates from galaxies detected in IRAC channels 1 and 2 but missed by HST-WFC3 at  $1.6\ \mu\text{m}$  has already been experimented successfully by T. Wang et al. (in prep.), and seems to be a good indicator to detect HST-dark ALMA galaxies.

As each of our HST-dark galaxies has different features, we will discuss each galaxy individually.

Of the total 23 detections in this survey, 7 do not show an HST  $H$ -band counterpart. This lack of counterpart could arise from an occultation of the optical counterpart by a foreground galaxy, faint emission at optical wavelengths, or a spurious ALMA detection.

For the four galaxies previously discussed (AGS4, AGS11, AGS15 and AGS17), we observe a signal with IRAC at  $3.6\ \mu\text{m}$  and  $4.5\ \mu\text{m}$ , despite the limiting sensitivity of IRAC (26 AB mag at  $3\sigma$  for both  $3.6$  and  $4.5\ \mu\text{m}$ ; Ashby et al. 2015) being lower than HST-WFC3 (28.16 AB mag at  $5\sigma$  for F160W; Guo et al. 2013) in the respective images. Furthermore, two of the galaxies (AGS15 and AGS17) have already been detected at submillimetre wavelengths ( $870\ \mu\text{m}$ ) by Hodge et al. (2013).

The other three galaxies (AGS14, AGS16 and AGS19) are not detected at any other wavelength hence there is a high probability that they are spurious. This number is in good agreement with the expected number of spurious sources for our sample ( $4\pm 2$ ).

Fig. 4.4 gives us a glimpse into how sources can be falsely associated with an HST galaxy. When the offset correction is applied, the three galaxies shown with magenta lines move further away from the center position ( $\Delta\delta = 0$ ,  $\Delta\alpha = 0$ ), rather than closer to it

The IRAC detections seem to be particularly useful to confirm the existence of a source. In the main catalog, except for the three galaxies that we consider as spurious, all others are also detected in the IRAC filters.

In conclusion, we have detected 20% HST-dark galaxies (4 out of 20 robust detections) with a counterpart confirmed at least by IRAC. This proportion may depend in a manner that we cannot address here on the depth of the optical and millimeter images. Knowing that these HST-dark galaxies are dust, hence metal, rich they are likely progenitors of the most massive galaxies seen at  $z = 0$ , hence potentially hosted by massive groups or clusters of galaxies. Two of these HST-dark galaxies have a tentative redshift of  $z = 4.82$  and  $z = 3.76$ , we, therefore, expect these galaxies to be located at  $z > 3$  (Wang et al., 2019). These two galaxies are already massive ( $10^{10.55}\ M_\odot$  and  $10^{10.50}\ M_\odot$  respectively), suggesting that this population of galaxies is particularly interesting for understanding massive galaxy formation during the first billion years after the Big Bang. Spectroscopy with the JWST NIRSpec instrument will permit very sensitive spectroscopic detection of  $H\alpha$  emission at  $z < 6.6$ , and hence an important new tool to measure redshifts of these HST-dark galaxies. GOODS-South will undoubtedly be a venue for extensive

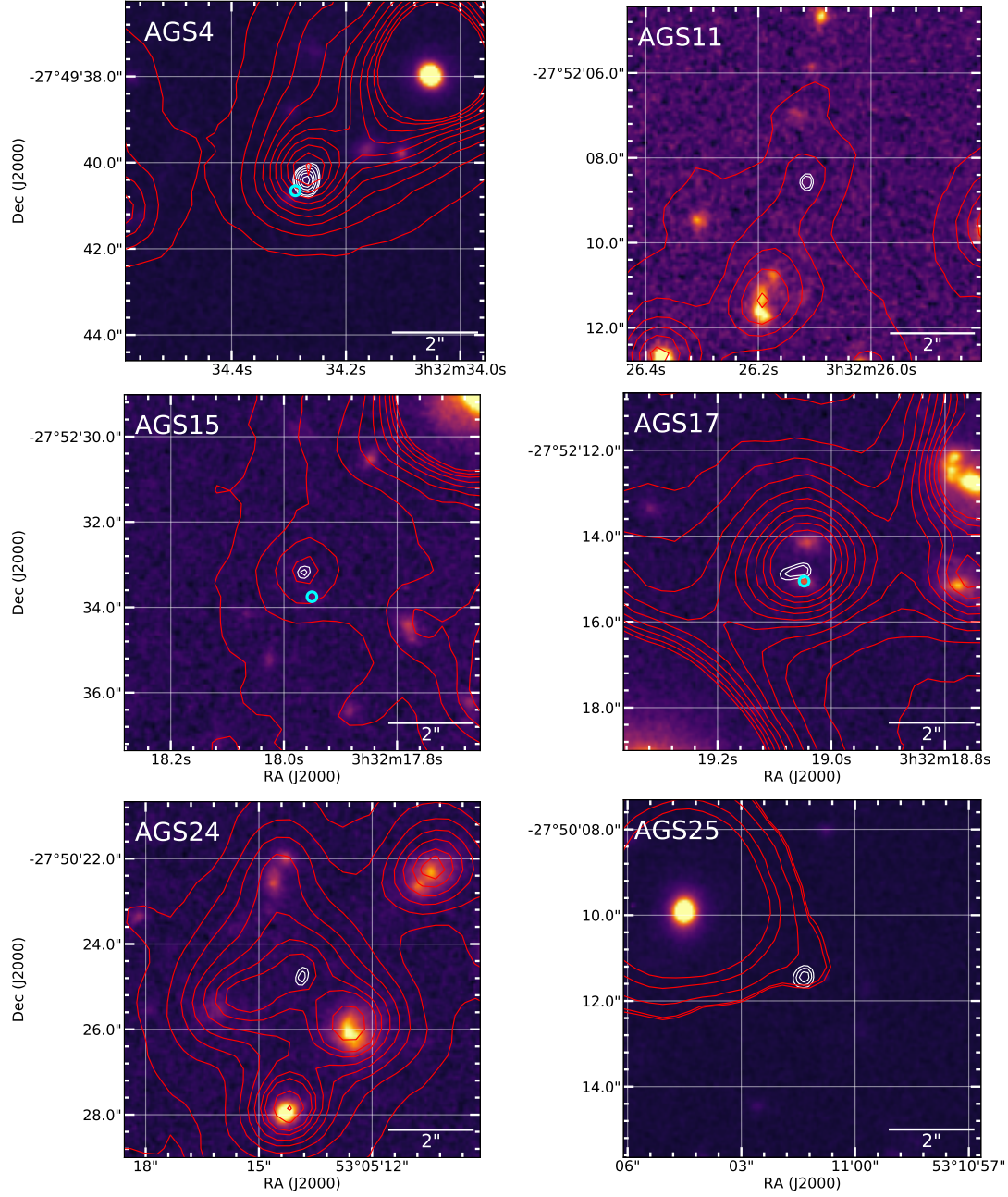


FIGURE 7.12: IRAC 3.6  $\mu\text{m}$  (red contours, 3.0  $\mu\text{Jy}$  to 30.0  $\mu\text{Jy}$  in steps of 3.0  $\mu\text{Jy}$ ) and ALMA 1.1mm (white contours, 4, 4.5 then 5 to 10- $\sigma$  in steps of 1- $\sigma$ ) overlaid on  $8'' \times 8''$  HST  $H$ -band images. The position of the previously associated HST counterpart is shown by a cyan circle.

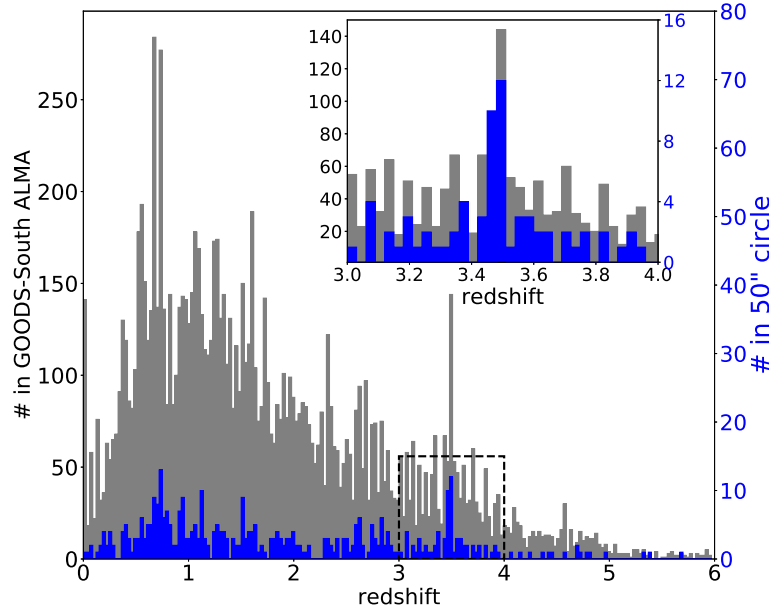


FIGURE 7.13: Redshift distribution for galaxies listed in the ZFOURGE catalog encompassing the GOODS-ALMA (grey distribution) while the galaxies within 50'' of AGS24 are shown in blue. Figure from Zhou et al., in prep.

JWST spectroscopy, including Guaranteed Time Observations. Spectral scan observations with ALMA can also be a powerful tool to determine the distances, and hence physical properties, of this intriguing population of HST-dark galaxies.

## 7.5 The HST-dark galaxy as an overdensity tracer

The presence of several overdensities in the South GOODS field has been established for several years. For example, [Salimbeni et al. \(2009\)](#) describe the presence of several overdensities at  $z \sim 0.7$ , at  $z \sim 0.96$ ,  $z \sim 1.05$ , and at  $z \sim 2.3$ . These different  $z$  peaks can be visualized in Fig. 7.13 (Zhou et al., in prep) which shows in grey, the redshift distribution of galaxies in the GOODS-ALMA field.

These overdensities underline high-density structures. The analysis of these large scale structures is essential to understand the evolution of galaxies. These structures can link the primordial fluctuations of the cosmic diffuse background with the current galaxies (e.g., [White and Scott, 1996](#); [Boughn and Crittenden, 2004](#); [Efstathiou et al., 2010](#)), they can also probe the distribution of the dark matter halo around the galaxies (e.g., [Springel et al., 2008](#); [Taylor, 2011](#); [Piras et al., 2018](#)) and can be used to study the environmental effects on galaxies (e.g., [Treu et al., 2003](#); [Mei et al., 2006](#); [Rettura et al., 2009](#)). [Castellano et al. \(2007\)](#), analyses an overdensity at  $z \sim 1.6$  while [Forrest et al. \(2017\)](#) focuses on an overdensity at  $z = 3.47$ . It is this last overdensity that will interest us here. [Forrest et al. \(2017\)](#) characterize a population of extreme [OIII] + H $\beta$  emitting galaxies tracing an overdensity with  $3.42 < z_{\text{spec}} < 3.478$  at RA = 53.08°, Dec = -27.85° covering approximately 1.8 Mpc in size.

The overdensity described in [Forrest et al. \(2017\)](#), therefore, corresponds spatially to the region in which AGS24 was discovered but also corresponds with the redshift determined by SED fitting.

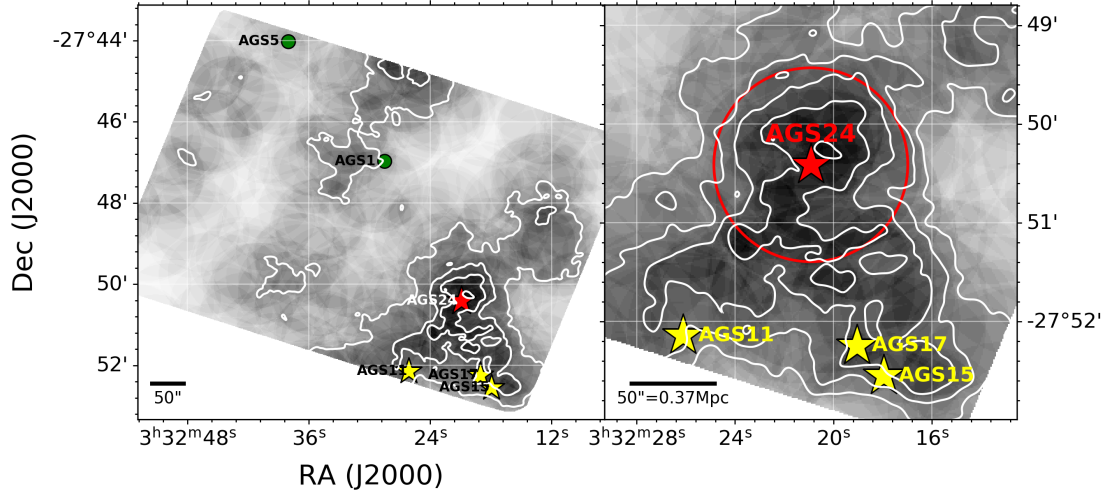


FIGURE 7.14: Projected density map of the 366 galaxies with  $3.42 \leq z \leq 3.57$  with the GOODS-ALMA field. The red star shows AGS24 while the yellow stars indicate three other optically dark galaxies, AGS11, AGS15, and AGS17. Two other galaxies, listed in the main catalog, AGS1, and AGS5 with the same redshift range are shown with the green dots. The red circle has a radius of  $50''$  corresponding to a physical radius of  $400 kpc$  at  $z = 3.5$ . Figure from Zhou et al., in prep.

In Fig. 7.14, we show the ratio between the density within 2 Mpc comoving distance ( $\rho$ ) to the average number density over this field with  $3.42 \leq z \leq 3.57$  within the GOODS-ALMA field as well as the position of AGS24 in red, and the positions of AGS11, AGS15 and AGS17 (Zhou et al., in prep).

In addition, from the redshift, it was possible to estimate a mass for AGS24 using FAST++<sup>1</sup>. The stellar mass determined in this way is  $M_* = 1.82^{+0.27}_{-0.50} \times 10^{11} M_\odot$ . This would make this galaxy the most massive galaxy of this overdensity with a mass of  $\sim 10$  times more massive than the second most massive galaxy with  $z \sim 3-4$  within this region (Ginolfi et al., 2017).

We will discuss in Sect. 7.6 the possible implications of these HST-dark galaxies in understanding the evolution of galaxies and their possible contribution to the cosmic density of star formation among the most massive galaxies at high redshift. The position of AGS24 at the center of this overdensity and especially its mass makes this galaxy a candidate of a future bright cluster galaxy (BCG) or central dominant (cD) galaxy (Zhou et al., in prep).

In addition, the other HST-dark galaxies, i.e., AGS11, AGS15, AGS17, seem to be positioned in the overdensity region (see Fig. 7.14). Although the AGS11 redshift that we have taken from the CANDELS catalog ( $z_{AGS11} = 4.82$ ) is higher than the redshift of this overdensity, the SED of AGS11 could be fit with  $z \sim 3.5$ . In Fig. 7.15, which was taken from the ZFOURGE database ([http://zfourge.tamu.edu/DR2017/CDFS/object\\_pages/7500/7589.html](http://zfourge.tamu.edu/DR2017/CDFS/object_pages/7500/7589.html)), we can see that the Balmer break could fall between the  $H$ -band and the  $K$ -band which could possibly lead to a redshift  $z \sim 3.5$ . It is therefore not excluded that AGS11 may be part of this overdensity.

Finally, we calculated the probability that AGS11, AGS15, AGS17, and AGS24 would be located randomly so close to each other. To do this, we randomly injected 4 points into the area covered by the GOODS-ALMA survey and calculated the minimum area covered by a circle, including these four positions (see Fig. 7.16). We repeated this operation 10,000 times and compared the distribution of these surfaces to the area covered by the HST-dark sources AGS11, AGS15,

1. FAST++: <https://github.com/cschreib/fastpp>

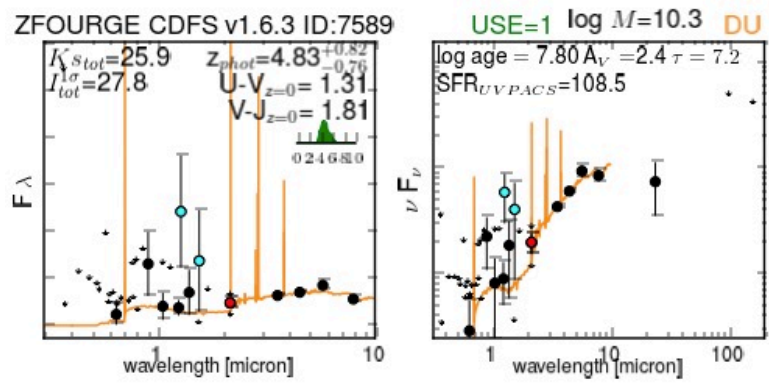


FIGURE 7.15: Spectral energy distribution of AGS11 in units of  $F_\lambda$ , left panel and  $\nu F_\nu$ , right panel. The balmer break may have been misidentified which would allow a redshift  $z \sim 3.5$ . (Figure from: <http://zfourge.tamu.edu/>).

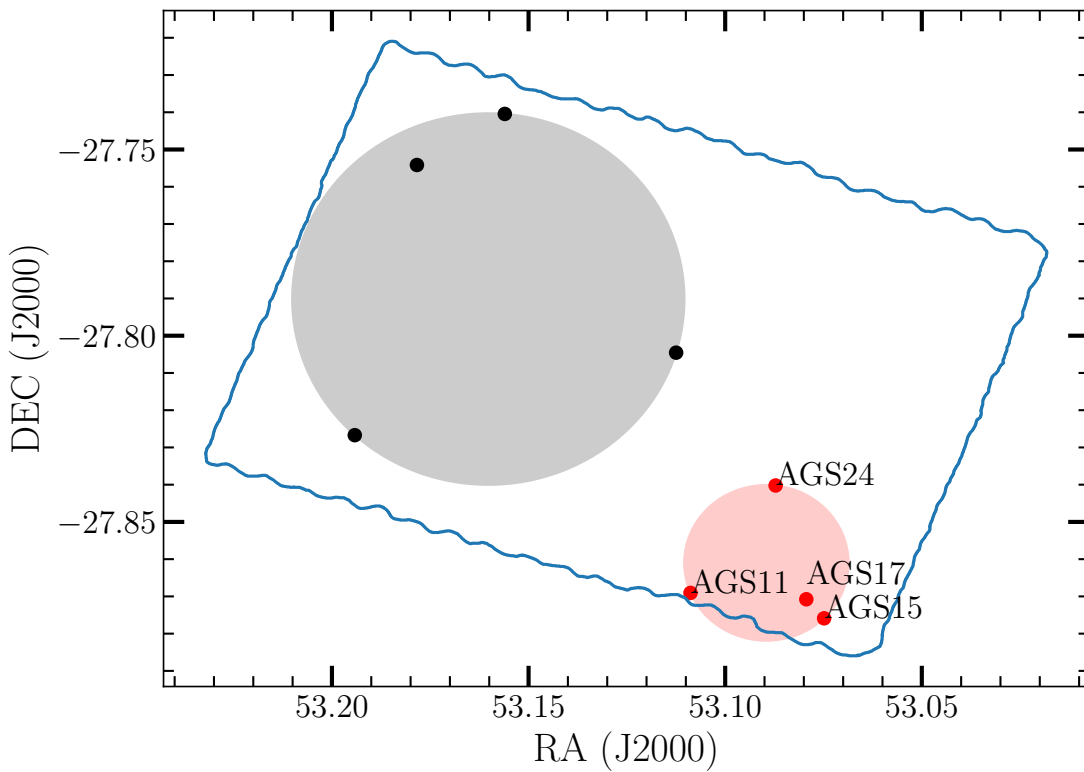


FIGURE 7.16: Smallest area covered (gray area) by a circle including the four randomly thrown sources (black dots) in the GOODS-ALMA field (indicated by blue edges) compared to the area covered by the HST-dark sources AGS11, AGS15, AGS17 and AGS24 shown in red.

AGS17, and AGS24. The surface area of the points thrown at random is higher than the surface area covered by the HST-dark galaxies in 99.6% of cases (see Fig. 7.16).

This means that despite the fact these sources have a low projected surface density, they seem to be clustered. A two-point correlation function will be presented in detail in Zhou et al., in prep to accurately estimate the clustering of massive galaxies at these redshifts.



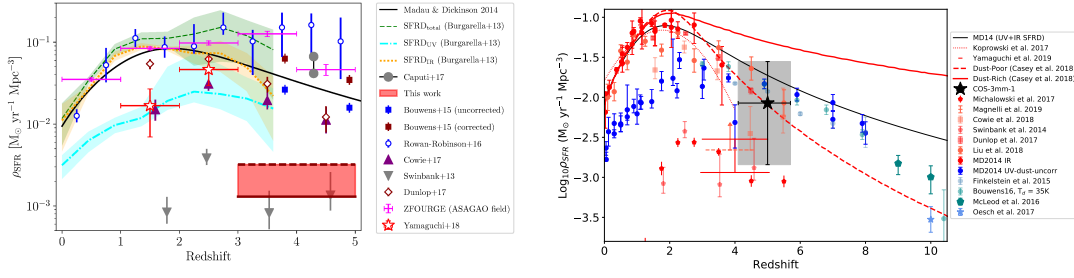


FIGURE 7.17: Left panel: Contribution of the ASAGAO sources to the cosmic star-formation rate density. The contribution of the two secure optically dark galaxies is shown with the red solid line while the additional contribution of the three less secure sources are shown with the red dashed-line. Figures from [Yamaguchi et al. \(2019a\)](#), left panel and [Williams et al. \(2019\)](#), right panel

## 7.6 Implications of HST-dark galaxies in cosmic density of star-formation

It is difficult with such fragmented information to constrain the physical properties of these optically dark galaxies or to determine their implication in the evolution of the galaxies. The redshift determination for the few galaxies for which a determination can be attempted is highly uncertain.

The precise quantification of this type of object, according to their mass and redshift interval is necessary to understand the involvement of HST-dark galaxies in the evolution of galaxies, to know if their density is compatible with massive, compact and passive galaxies at  $z \sim 2$ .

We were recently able to serendipitously detect an HST-dark galaxy using data from only 8 ALMA pointings ([Elbaz et al., 2018](#)). This serendipitously-detected HST-dark galaxy suggests a blind detection rate of 1 galaxy per 8 pointings, similar to the 20% of HST-dark galaxies found among the galaxies detected by ALMA in this work. These optically dark galaxies are therefore probably not marginal among the most massive galaxies. However, it is necessary to have a larger statistics to be able to have robust estimations of the proportion of these galaxies among massive galaxies.

Recently, with some serendipitous detections found (2 + 3 less secure for [Yamaguchi et al. 2019a](#)) in the ASAGAO field, 1 for [Williams et al. \(2019\)](#) in the cosmos field, these two authors have tried to estimate the contribution of optically-dark sources to the cosmic star formation density (see Fig. 7.17). The underlying idea is to know if the density of star formation increases continuously from the observation of distant galaxies to the cosmic noon as for example in the models of [Madau and Dickinson \(2014\)](#) or if this density of stellar formation is relatively constant, before decreasing as in the models of [Rowan-Robinson et al. \(2016\)](#).

For our survey, an analysis of both the sources detected and by stacking sources too weak to have been individually detected to probe to fainter levels is underway to determine the cosmic SFRD of the GOODS-ALMA field.

Another method, not requiring broad survey analysis, was used by [Wang et al. \(2019\)](#). I have participated to this study and am a co-author of the paper just accepted in *Nature* (publication August 7). Based on a selection of color-selection technique ( $[4.5] < 24$  mag and  $H - [4.5] > 2.5$  mag similar to the method presented in [Wang et al. \(2016\)](#), [Wang et al. \(2019\)](#) identified 63

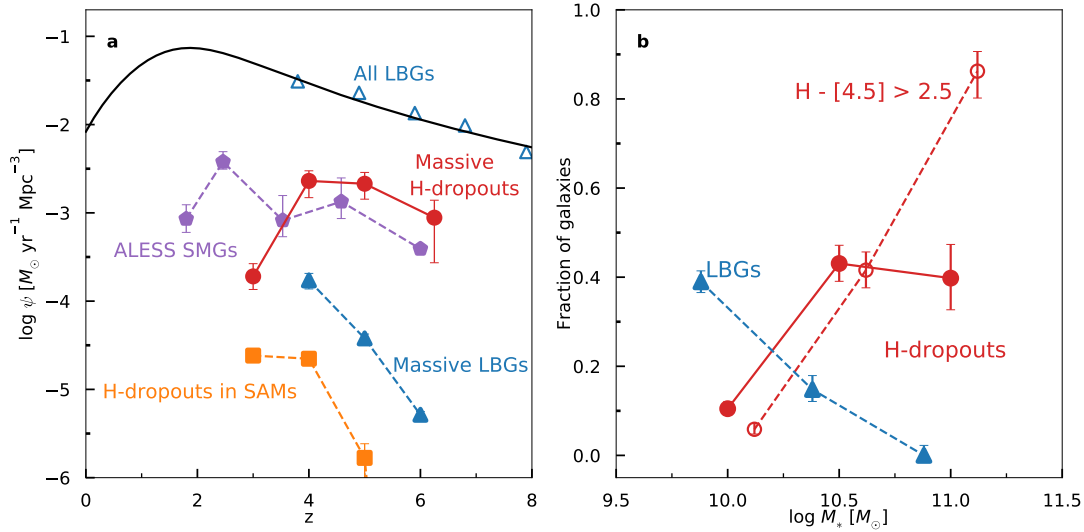


FIGURE 7.18: Left panel: Current cosmic star formation rate density based on LBGs at  $z > 4$  (black solid line and blue triangle). The contribution of the massive  $H$ -dropout (red dots), ALESS SMGs (purple pentagons),  $H$ -dropout in semi-analytical models (orange squares) as well as the massive LBGs ( $M_{*} > 10^{10.3} M_{\odot}$ ; based on dust-corrected UV) are shown in this image. Right panel: Fraction of massive galaxies, in number, that are either detected as LBGs or  $H$ -dropouts for galaxies with  $3.5 < z < 6.5$ . Figures from: Wang et al. (2019)

interesting targets across the GOODS-South, COSMOS and UDS fields. An observation of 1.8 min for each of these targets allowed the detection of 62% of this sample, i.e., 39 detected with a signal on noise  $S/N > 4\sigma$ . The SED fitting allowed to derive a median redshift of 4 and an average stellar mass of  $M_{*} \sim 10^{10.8} M_{\odot}$  confirming that these objects are for the most part very massive and distant. The analysis of the contribution of massive UV-bright galaxies and  $H$ -equivalent mass dropout showed that the latter contributed 10 times more to the cosmic star formation rate density for  $z > 3$  (see Fig. 7.18; left panel). In addition, a numerical analysis showed that at high redshifts, the  $H$ -dropout population became dominant from a stellar mass of  $M_{*} \sim 10^{10.25} M_{\odot}$  (see Fig. 7.18; right panel).

## 7.7 Conclusion

Although there may be pure ALMA detection (e.g., Williams et al., 2019), we validated in this study that Spitzer/IRAC is an extremely powerful tool to confirm the existence of an ALMA source.

The complementarity of these two instruments can remove ambiguity about the identification of a counterpart, as has been the case for several HST-dark galaxies presented in this section. By using the color difference between  $H$  and IRAC bands, it is possible to find solid candidates for the counterparts of (sub)millimetric detections done with single dish telescopes. This counterpart association expertise will be particularly useful for surveys as for example with the Nika2 camera (Adam et al., 2018) and especially for the NIKA2 Cosmological Legacy Survey (NIKA2 GT-LP-N2CLS, PI : G. Lagache, A. Beelen, N. Ponthieu). This identification will only be possible in regions of the sky for which there are deep IRAC data.



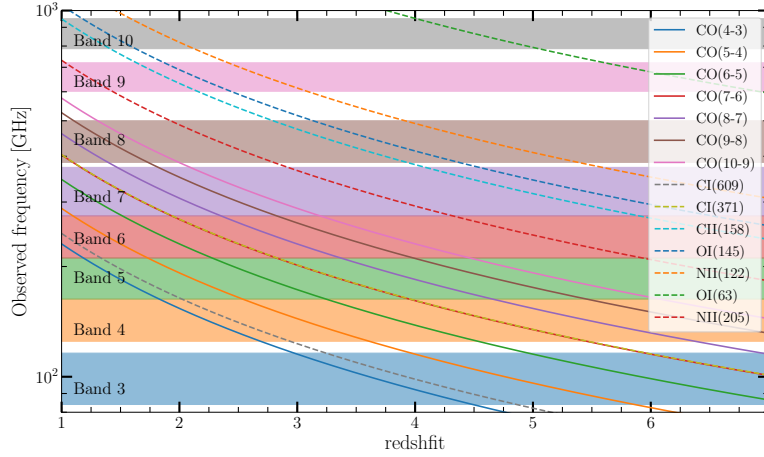


FIGURE 7.19: Position of CO transitions and CI lines as a function of  $z$  and observed frequency for the 10 ALMA band, used here for the spectral  $z$  search for the HST-dark galaxies.

These HST-dark galaxies do not seem to be a marginal population of galaxies when considering massive, star-forming galaxies with high redshift. Their contribution to the SFRD even seems to be major for galaxies with a  $\log_{10}(M_*/M_\odot) > 10.5$  at  $z > 3.5$ .

For the moment these galaxies are very strong candidates to be the progenitors of elliptical galaxies at  $z \sim 2$ . We will discuss this possibility in Chapter 8.

To know precisely the redshift and the characteristics of these galaxies, we have written proposals with ALMA (accepted see appendix) and VLA (rejected). With ALMA we proposed to observe in band 4 to detect possible emission line of CO (CO(7-6), CO(6-5), CO(5-4) or CO(4-3)), depending on the redshift of the considered source (see Fig. 7.19). To be able to determine the redshift of these sources in the most secure way possible, we will use the technique explained and used in Jin et al. (2019) to confirm detection with a secondary emission line ( $H_2O$ , CI, etc.). The data of part of the  $\nu$  range ([136 - 163 GHz]) has just been delivered.



# CHAPTER 8

## THE SLOW DOWNFALL OF STAR-FORMATION IN $z = 2-3$ MASSIVE GALAXIES

### Contents

7.1 Outline of the problem . . . . .	129
7.2 History . . . . .	129
7.3 HST-dark galaxies in GOODS-ALMA . . . . .	131
7.4 Spitzer/IRAC a loyal ally for HST-dark galaxies identification . . . . .	141
7.5 The HST-dark galaxy as an overdensity tracer . . . . .	144
7.6 Implications of HST-dark galaxies in cosmic density of star-formation . . . . .	147
7.7 Conclusion . . . . .	148

In this Chapter, we take advantage of the broad ALMA coverage as well as the large multiwavelength coverage in GOODS-South, to constrain the properties of galaxies detected by ALMA in GOODS-ALMA. We will explore the possibility that these galaxies detected by ALMA are the progenitors of passive elliptical galaxies at  $z \sim 2$ .

To do this, we will first describe how we took advantage of our large multiwavelength coverage to fit both the spectral energy distributions (SEDs), and modified blackbody models (MBB) to the galaxies detected in GOODS-ALMA. We will explain how we derived the main physical parameters of the galaxies ( $M_{\text{dust}}$ ,  $M_{\text{gas}}$ , SFR, depletion time), before showing that the galaxies detected by ALMA are among the most massive galaxies in the GOODS-ALMA field. The majority of these galaxies are starbursts, or are located in the upper part of the Main Sequence. A significant part of the population, located around  $z = 2.5-3$  has an abnormally low gas fraction. The size of these galaxies, although located on the trend of star-forming galaxies in  $H$ -band, have sizes measured with ALMA that are compatible with the sizes of passive galaxies (in  $H$ -band). These results suggest that we are observing progenitors of passive elliptical galaxies at  $z \sim 2$ .

## 8.1 SED-fitting

### 8.1.1 Method

We fit the spectral energy distributions using two different methods, depending on whether or not the galaxy has an *Herschel* counterpart.

For galaxies that have a far-IR fluxes density measured by the *Herschel* space observatory, we employ the SED-fitting code CIGALE<sup>1</sup> (Code Investigating Galaxies Emission: (Noll et al., 2009)).

1. Publicly available at <http://cigale.lam.fr>

Parameter	Value
	Delayed SFH
age [Gyr]	500, 1000, 2000, 3000, 5000, 6000, 8000, 9000, 10000
$\tau_{\text{main}}$ [Gyr]	100, 500, 1000, 3000, 4000, 6000, 8000, 10000
	Dust attenuation
$E(B-V)_*$	0.01, 0.1, 0.3, 0.4, 0.6, 0.7, 0.9, 1., 1.3
	Dust emission
$U_{\text{min}}$	0.1, 0.5, 1., 2.5, 10.
$\alpha$	1., 1.2, 1.4, 1.6, 1.8, 2., 2.2, 2.4, 2.6, 2.8, 3.
$\gamma$	1.e-04, 1.e-03, 1.e- 02, 1.e-01, 5.e-01, 1.
Number of parameters	100000

TABLE 8.1: Parameters used in the SED fitting procedures by CIGALE.

We use the stellar population models of [Bruzual and Charlot \(2003\)](#) and the attenuation law of [Calzetti et al. \(2000\)](#). The IR SED fitting was performed using the dust infrared emission model given by [Draine and Li \(2007\)](#). The galaxy data are fit from the UV to millimeter observations. We independently fit the wavelengths from UV up to  $16 \mu\text{m}$ , and  $24 \mu\text{m}$  up to the millimeter wavelengths respectively (see Fig. 8.11). The radio portion has been added after the fitting process, using the FIR/radio correlation, with a constant ratio between FIR and radio luminosity of 2.34 [Yun et al. \(2001\)](#). The parameters used in CIGALE were given by [Ciesla et al. \(2018\)](#) and are shown in Table 8.1.

In contrast, if the galaxy has no *Herschel* infrared counterpart, we fit the data with the dust spectral energy distribution library<sup>2</sup> presented in [Schreiber et al. 2018a](#), and normalized to the ALMA flux density at 1.13 mm in the SED. We proceed iteratively. After fitting the galaxy with a MS SED, we compute the distance to the main sequence ( $R_{SB} = \text{SFR}/\text{SFR}_{MS}$ ) using the output IR luminosity (8-1000  $\mu\text{m}$ ) and the redshift. The  $R_{SB}$  and the redshift of the galaxy can be used to calculate the dust temperature ( $T_{\text{dust}}$ ) and the IR8 ( $L_{\text{IR}}/L_8$ ) from Eq. 18 and 19 of [Schreiber et al. \(2018c\)](#). IR8 can be used as an indication of the compactness of distant galaxies [Elbaz et al. \(2011\)](#).  $T_{\text{dust}}$  and IR8 are therefore set to these newly calculated values in the SED-fitting process, and an updated SED is generated.

### 8.1.2 AGN subtraction

To fit an SED with an AGN component, we used the code *decompIR* by [Mullaney et al. \(2011\)](#). This code proposes to fit an AGN according to the spectrum of a sample of host galaxies representative of galaxies with an AGN. The contribution of the AGN to the IR luminosity can lead to an overestimation of the dust infrared emission and therefore an overestimation of the SFR.

2. Publicly available at <http://cschreib.github.io/s17-irlib/>

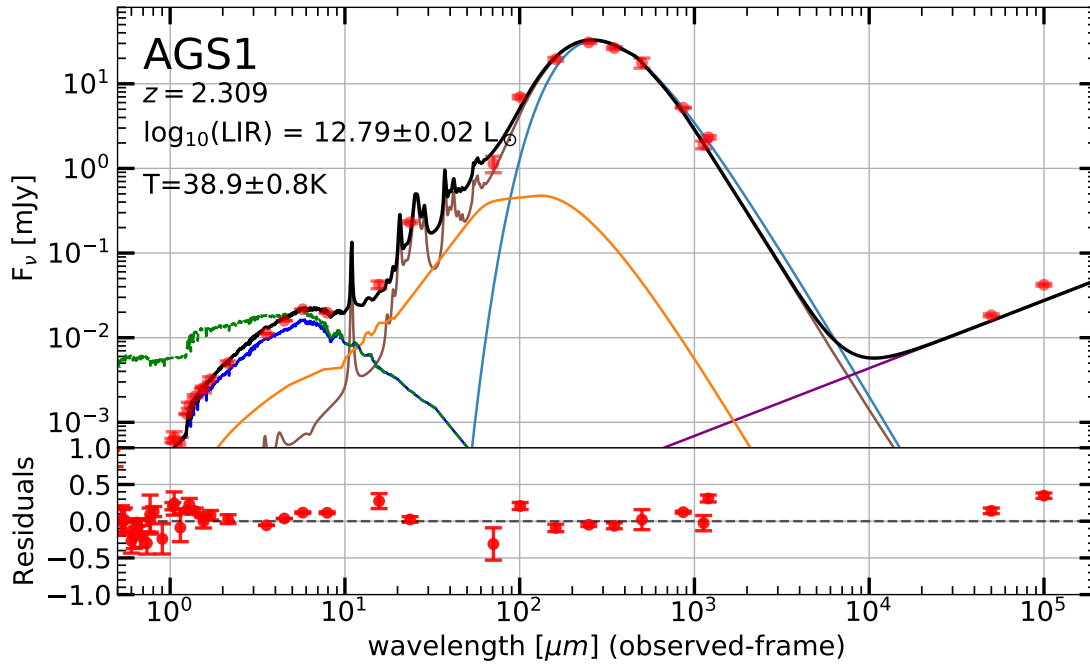


FIGURE 8.1: Example of spectral energy distribution for AGS1. The solid black line represents the best fit, which can be decomposed into the IR dust contribution (brown line), a stellar component uncorrected for dust attenuation (dark blue line), synchrotron emission (brown line) and the AGN contribution (orange line). In addition, we show the best fit of a modified black body, with  $\beta = 1.5$  (light blue line). The corrected UV emission is also shown in green. The bottom panel shows the residuals: (observation - model)/observation. The 34 other SEDs are given at the end of this chapter.

The AGN SED, used in `decompIR` do not include the wavelength below  $6\mu\text{m}$ .

To better characterize the contribution of AGNs to the total infrared luminosity of galaxies, we need to know their behavior at rest-frame wavelengths lower than  $6\mu\text{m}$ , corresponding to the domain where the contribution of AGN is most important. Since this AGN model is only defined for wavelengths  $> 6\mu\text{m}$ , we, therefore, used another AGN model for wavelengths shorter than  $6\mu\text{m}$ .

We therefore use `DecompIR` to extrapolate AGN emission to shorter wavelengths, using an AGN model from [Kirkpatrick et al. \(2015\)](#). We combine the two models according to the recommendation of [Mullaney et al. \(2011\)](#):

$$\nu F_\nu(5\mu\text{m}(\text{AGN})) = \nu F_\nu(0.4\mu\text{m}(\text{QSO})) \quad (8.1)$$

### 8.1.3 Dust Temperature

For the sake of simplicity and comparison with previous studies, we measure the dust temperature by fitting an MBB model, following:

$$S_\nu \propto \frac{\nu^{3+\beta}}{\exp(\frac{h\nu}{k_B T_d}) - 1} \quad (8.2)$$

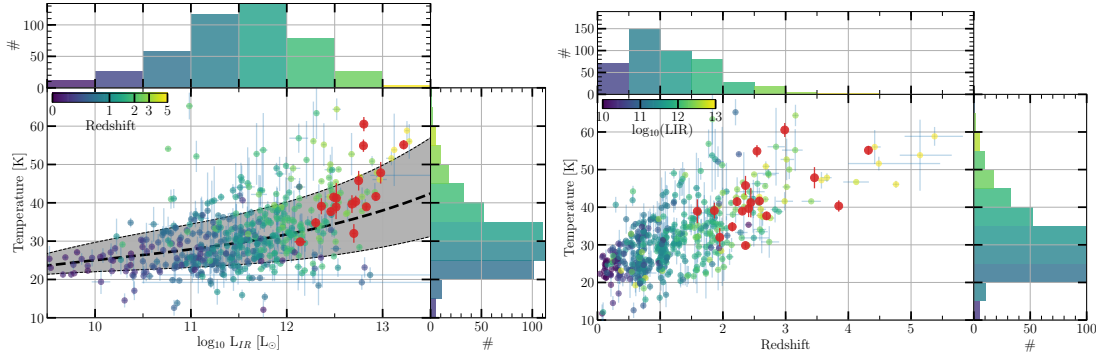


FIGURE 8.2: Evolution of the dust temperature as a function of IR luminosity (left panel) and redshift (right panel). The ALMA detections are shown in red. By comparison, we also plot the temperatures of all the galaxies within GOODS-ALMA, color-coded by redshift (left panel) or IR luminosity (right panel). We show the sliding median (and the  $1\sigma$  error) in black.

where  $k_B$  is Boltzmann's constant,  $h$  is the Planck constant,  $\beta$  is the dust emissivity spectral index,  $T_{dust}$  is the dust temperature and  $L_{\nu}$  is the flux density. We have assumed a spectral index  $\beta = 1.5$  (e.g., Kovács et al., 2006; Gordon et al., 2010). We fit the flux densities at  $\lambda_{rest} \geq 0.55\lambda_{peak}$  using the MBB model as suggested by Hwang et al. (2010), and exclude the synchrotron contribution ( $\lambda_{obs} < 5$  mm). The criteria we have defined to select the points to be modelled with a MBB are as follows:

- at least one data point between  $0.55 \times \lambda_{peak}$  and  $\lambda_{peak}$ .
- at least one data point beyond the submillimeter peak, with a wavelength lower than or equal to 1.1 mm.

Galaxies selected in (sub)millimeter flux density are expected to be biased towards low dust temperatures (e.g. Magdis et al., 2010; McAlpine et al., 2019). Indeed, for the same redshift and infrared brightness, the (sub)millimeter flux of a colder galaxy will be higher than that of a warmer galaxy. We investigated where the galaxies detected in the GOODS-ALMA survey are located in the IR Luminosity-Temperature plane (Fig. 8.2, left panel) and in the Redshift-Temperature plane (Fig. 8.2, right panel). For comparison, we also plot the temperature of all the galaxies located in GOODS-ALMA. We find that the galaxies detected by ALMA do not exhibit a systematic offset compared to those undetected by ALMA.

For an SMG, the dust temperature is correlated with the FIR luminosity (e.g. Wardlow et al., 2011). We have found a median dust temperature of 39.7 K for our sample. However, we see that setting the spectral index  $\beta = 1.5$  has an influence on the temperature. We chose to fix it, in order to have fewer free parameters in our fit and to compare all galaxies consistently. If we had taken  $\beta = 2$ , the modified blackbody temperatures would have been slightly lower (1 - 4 K lower). Note that we do not use this  $T_d$  temperature to determine dust masses (see Sect. 8.2.1).

## 8.2 Derived parameters

### 8.2.1 Dust mass

Following Draine et al. (2007), we adopt the maximum starlight intensity relative to the local interstellar radiation field  $U_{max} = 10^6 U_{\odot}$ , and the power-law index  $\alpha = 2$  in Eq. 8.3. The dust

mass is implemented in the CIGALE code using the formula of [Draine et al. \(2007\)](#):

$$\frac{dM_{dust}}{dU} = (1 - \gamma)\delta(U - U_{min}) + \gamma M_{dust} \frac{\alpha - 1}{U_{min}^{1-\alpha} - U_{max}^{1-\alpha}} U^{-\alpha} \quad (8.3)$$

with  $U_{min} \leq U_{max}$ ,  $\alpha \neq 1$  and is the exponent of the power law describing the intensity distribution of the interstellar radiation field, and  $\gamma$  is the relative fraction of dust heated by each source. [\(Draine et al., 2007\)](#) showed that  $\alpha = 2$  and  $U_{max} = 10^6$  gave a good fit to a large sample of nearby galaxies from the *Spitzer* SINGS program.

### 8.2.2 Gas mass

One of the fundamental questions to understand these ALMA galaxies (which are SB or in the upper part of the MS, see Fig. 8.8) if they have an increased SFE ( $SFR/M_{gas}$ ) compared with MS galaxies, or because they have larger gas reservoirs. For each galaxy, we calculated the gas mass  $M_{gas}$  as well as the gas fraction  $f_{gas}$ , defined by:

$$f_{gas} = \frac{M_{gas}}{M_{gas} + M_{\star}}, \quad (8.4)$$

To compute the gas mass, we assume a ratio between dust mass and gas mass depending only on metallicity. The ratio ( $\delta_{GDR}$ ) was directly derived by [Leroy et al. \(2011\)](#) in the local Universe, and can be applied to our sample, assuming that this relation is valid at all redshifts:

$$\delta_{GDR} = \frac{M_{gas}}{M_{dust}} = (9.4 \pm 1.1) - (0.85 \pm 0.13)[12 + \log(O/H)] \quad (8.5)$$

where  $M_{gas} = M(H_2) + M(H_I)$ . At the redshifts of this study, the atomic hydrogen can be considered negligible compared to the molecular form (e.g. [Leroy et al., 2008](#); [Obreschkow and Rawlings, 2009](#); [Daddi et al., 2010](#)).

We note that recent studies have found evidence for a steep increase in the gas to dust ratio of sub-solar metallicity galaxies at  $z \sim 2$  compared with this local relation ([Coogan et al., 2019](#)), but we do not expect this effect to be significant for our more massive, enriched galaxies. As we do not have direct metallicity measurements for our galaxies, we use the equation given by [Genzel et al. \(2012\)](#) to compute the metallicity:

$$12 + \log(O/H) = -4.51 + 2.18 \log_{10}(M_{\star}/1.7) - 0.0896 [\log_{10}(M_{\star}/1.7)]^2 \quad (8.6)$$

In this equation, we include a conversion factor (1/1.7) to transform the original formula from a Chabrier IMF to a Salpeter IMF. However, the metallicity can be underestimated for galaxies above the main sequence (e.g. [Silverman et al., 2015](#)), which could artificially increase the proportion of gas and conversely underestimate the gas depletion time ([Elbaz et al., 2018](#)). We compared our calculated metallicities to the metallicities obtained using the fundamental metallicity relation (FMR) of [Mannucci et al. \(2010\)](#):

$$12 + \log_{10}(O/H) = 8.90 + 0.37m - 0.14s - 0.19m^2 + 0.12ms - 0.054s^2 \quad (8.7)$$



with  $m = \log_{10}(M_*/1.7) - 10$ , and  $s = \log_{10}(\text{SFR}/1.7)$ . The median metallicity ratio between these two methods is  $1.00 \pm 0.01$ , where the uncertainty corresponds to the standard deviation. For our galaxy sample, both methods are therefore, in good agreement. The metallicities of these ALMA detected galaxies are however somewhat uncertain. The metallicity evolution is poorly constrained for galaxies at high redshift, as well as for starburst galaxies and galaxies with AGNs (e.g., Tan et al., 2013; Kewley et al., 2013).

We also verified that the mass of gas derived by the method described above was in agreement with that derived using the method of Scoville et al. (2016). The Scoville et al. (2016) method is based on the assumption that continuum measurements of the Rayleigh-Jeans tail can be used to estimate the mass of dust and therefore, the mass of gas. Since this method is based on the Rayleigh-Jeans tail, it can only be used at long wavelengths ( $\lambda > 250 \mu\text{m}$ ). However, if the dust emission is optically thin, the Scoville et al. (2016) method may underestimate the gas mass (Miettinen et al., 2017). At 1.13mm, the estimate of the gas mass can be written, according to equations Eq. 6 and Eq. 16 of Scoville et al. (2016), as:

$$M_{\text{mol}} = S_\nu \times 5.12 \times 10^{10} \times (1+z)^{-4.8} \times (d_l)^2 \frac{\Gamma_{RJ}^0}{\Gamma_{RJ}^z} \quad (8.8)$$

with  $S_\nu$  the flux at 1.13 mm in mJy and  $\Gamma_{RJ}^z$  is the correction for departure in the rest frame of the Planck function from Rayleigh-Jeans (Scoville et al., 2016):

$$\Gamma_{RJ}(T_{\text{dust}}, \nu_{\text{obs}}, z) = \frac{h\nu_{\text{obs}} \times (1+z)/(k_b T_{\text{dust}})}{e^{(h\nu_{\text{obs}} \times (1+z)/k_b T_{\text{dust}})} - 1} \quad (8.9)$$

where  $h$  is the Planck constant and  $k_b$  is the Boltzmann constant.

Using a fixed dust temperature (25K), we find a difference between the calculated gas mass ( $M_{(\text{gas}, \text{this work})}$ ) and that derived following Scoville et al. (2016):  $M_{(\text{gas}, \text{Scoville})}/M_{(\text{gas}, \text{this work})} = 1.1 \pm 0.5$ .

The gas mass is directly related to the depletion time by:

$$\tau_{\text{dep}} = \frac{M_{\text{gas}}}{\text{SFR}} \quad (8.10)$$

## 8.2.3 SFR

### SFR<sub>IR</sub>

The infrared luminosity of each galaxy has been converted to SFR using the Kennicutt relation (Kennicutt, 1998) below:

$$\text{SFR} [M_\odot \text{yr}^{-1}] = 1.72 \times 10^{-10} L_{IR} \quad (8.11)$$

with  $L_{IR}$  in  $L_\odot$ , and

$$L_{IR} [L_\odot] = 4\pi d_l^2 \int_{8\mu\text{m}}^{1000\mu\text{m}} F_\nu(\lambda) \times \frac{c}{\lambda^2} d\lambda, \quad (8.12)$$

where  $d_l$  is the luminosity distance.

In Fig. 8.3, we illustrate the distribution of SFRs as a function of redshift for the ALMA-detected galaxies. We also represent the theoretical detection limit of the galaxies present in the survey

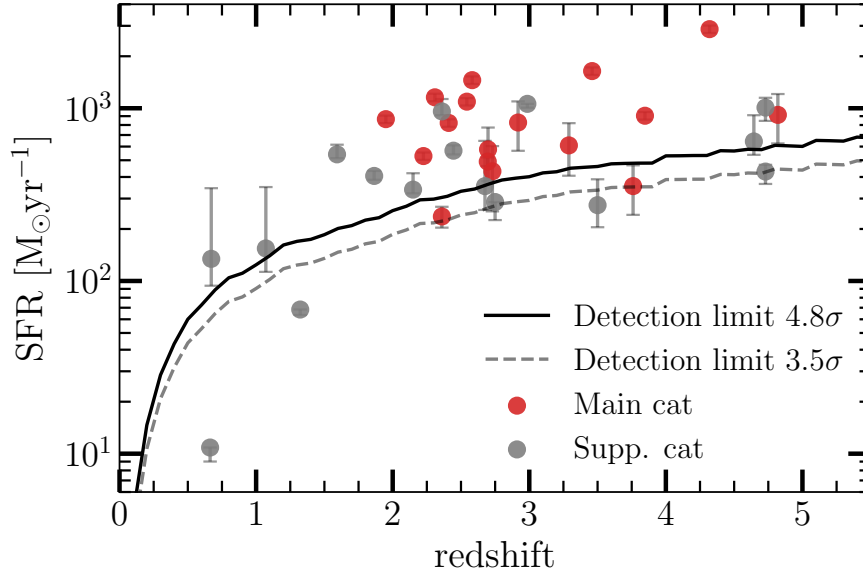


FIGURE 8.3: Star formation rate as a function of redshift, for galaxies from the main (red dots) and supplementary (gray dots) catalogs respectively. The SFR has been computed from the IR luminosity following Eq. 8.11. The detection limits at  $4.8\sigma$  (solid black line) and  $3.5\sigma$  (dashed black line) have also been computed from the IR library of Schreiber et al. (2018c), with a temperature evolving with redshift taking into account the average value of the rms at 0.182 mJy.

at the limit of  $4.8\sigma$  (solid black line) used to create the main catalog, assuming a constant rms (rms = 0.182 mJy) over the whole map, as well as the  $3.5\sigma$  (dashed black line) limit used to build the supplementary catalog. However, as the rms is not constant, and therefore may be lower at some points in the map, some galaxies (AGS21, for example) appear below this line.

We note that there is a galaxy (AGS37) that is clearly offset from the detection limit, with a  $\text{SFR} \sim 10 \text{ M}_\odot \text{yr}^{-1}$ . This galaxy is atypical, as it has the lowest redshift in our sample ( $z = 0.66$ , the same redshift as AGS30) and it also hosts a strong AGN with an X-ray luminosity =  $1.39 \times 10^{43} \text{ erg} \cdot \text{sec}^{-1}$ . It is most likely because of this AGN emission that this galaxy was detected in our survey.

The SFR limit has been computed taking into account the main sequence SED from Schreiber et al. (2018a), with the temperature and the fraction of polycyclic aromatic hydrocarbon (PAH) emission evolving as a function of redshift. The IR luminosity was calculated by integrating the flux from the SED using Eq. 8.12, and was then converted into SFR using Eq. 8.11.

This IR luminosity limit allows us to detect galaxies down to an IR luminosity of  $10^{12} L_\odot$  at redshift  $z = 1.5$ , and down to  $3 \times 10^{12} L_\odot$  at redshift  $z = 4$ . In other words, for an MS galaxy, this allows us to detect galaxies with a minimum stellar mass of  $2.5 \times 10^{11} M_\odot$ ,  $1.8 \times 10^{11} M_\odot$  and  $1.5 \times 10^{11} M_\odot$  for redshifts  $z = 2$ ,  $z = 3$  and  $z = 4$  respectively, using Eq. 9 of Schreiber et al. (2015).

Not surprisingly, the most IR luminous galaxies have been listed in the main catalog. However, we note the presence of a portion of galaxies from the supplementary catalog that are also among the most IR luminous galaxies. The size of the galaxies explains this behavior. The galaxies detected in the supplementary catalog generally have larger sizes than those in the main catalog

(?). Even though the peak flux is fainter on average, the integrated flux can reach values close to those of the main catalog.

All galaxies except one can be classified as ultraluminous infrared galaxies (ULIRGs), with  $\log_{10}(L_{IR}/L_{\odot}) \geq 11.9$ . Among these ULIRGs, one (AGS4) can be classified as a hyper-luminous infrared galaxy (HyLIRG). This galaxy has a high estimated redshift ( $z_{AGS} = 4.32$ , but this estimation is highly uncertain because this source is optically dark (see F18). Its SFR is particularly high at  $SFR_{AGS} = 2870^{+146}_{-142}$ , and this galaxy is probably also a particularly massive galaxy ( $M_{*AGS4} \sim 10^{11.5} M_{\odot}$ , although there are also large uncertainties on its stellar mass). This galaxy is located above the main sequence, with an  $R_{SB}$  of 2.77.

### SFR<sub>UV</sub>

Massive galaxies are known to be heavily dust-obscured at  $z > 2$  (e.g., [Magnelli et al., 2009](#); [Murphy et al., 2011](#)). While the  $SFR_{IR}$  is derived from the dust emission, we also consider the unobscured contribution to the total SFR, observed through UV emission. For the most massive galaxies ( $M_{*} > 10^{10.5} M_{\odot}$ ), the fraction of obscured to unobscured star formation ( $SFR_{IR}/SFR_{IR+UV}$ ) is greater than 90% ([Whitaker et al., 2017](#)).

We derive  $L_{UV}$  from the observed magnitude as follows:

$$L_{UV} = \frac{4\pi d_L^2 \nu_{1600} 10^{-0.4(48.6+m)}}{1+z} \quad (8.13)$$

where  $d_L$  is the luminosity distance and  $m$  is the observed magnitude.

The  $SFR_{UV}$ , uncorrected for dust attenuation, is in turn derived from the  $L_{UV}$ , following ([Daddi et al., 2004](#)):

$$SFR_{UV} = 2.17 \times 10^{-10} \times L_{UV} \quad (8.14)$$

The total SFR ( $SFR_{tot} = SFR_{UV} + SFR_{IR}$ ) is given in Table 8.2. The median contribution from  $SFR_{UV}$  to  $SFR_{tot}$  is only 1.3%.

### 8.2.4 AGN

Of the 1008 sources detected in [Luo et al. \(2017\)](#), 397 lie in the GOODS-ALMA field. We adopted a cross-matching radius of 0.6", after applying the offset correction (see Sect. 6.3). We found that 13/23 (6/20) of our main (supplementary) catalog galaxies had matches with the [Luo et al. \(2017\)](#) catalog. However, the detection in X-ray is not definitive proof that a galaxy hosts an AGN. We corrected the [Luo et al. \(2017\)](#) catalog X-luminosity when redshift deviations were observed, using the following formula:

$$L_X = 4\pi d_L^2 (1+z)^{\Gamma-2} f_X. \quad (8.15)$$

and assuming a fixed  $\Gamma = 2$ . In the following paragraphs, a galaxy will be considered as hosting an AGN if the galaxy has an X-Luminosity  $L_{X,int} > 10^{43} \text{ erg.s}^{-1}$  (luminous X-ray sources).

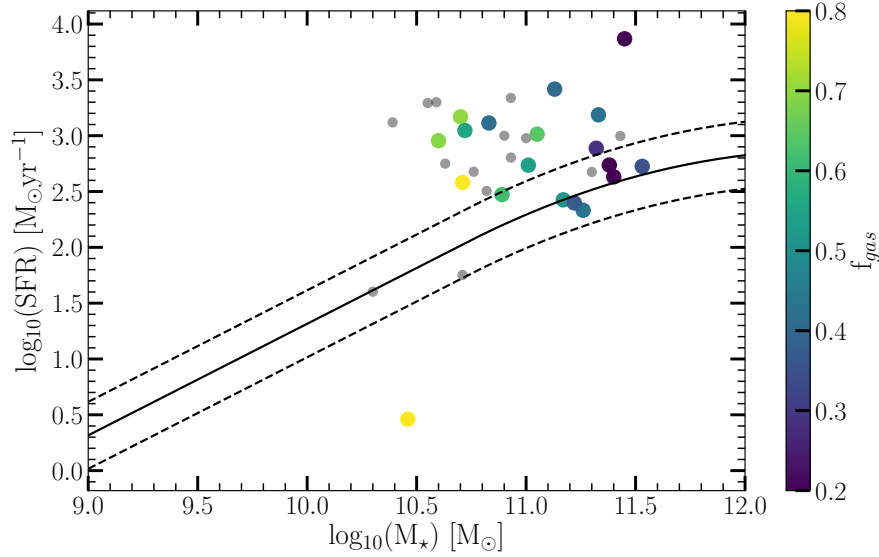


FIGURE 8.4: Location of our ALMA detected galaxies in the SFR- $M_*$  plane. The  $\text{SFR}_{IR}$  of these galaxies have been used. Galaxies with *Herschel* counterparts are color-coded as a function of the  $f_{\text{gas}}$ . The other galaxies are represented by grey dots. We measured the distance to the MS using Eq. 9 from Schreiber et al. (2015) and its dispersion is 0.3 dex. We have rescaled all of the SFRs by multiplying by  $\text{SFR}_{MS}(z)/\text{SFR}_{MS}(z=2.6)$ , in order to maintain their relative positions with respect to the main sequence.

### 8.2.5 IRX- $\beta$ relation

The rest-frame UV slope,  $\beta$ , is defined following the equation (e.g. Calzetti et al., 1994; Meurer et al., 1999):

$$F(\lambda) = \lambda^\beta \quad (8.16)$$

where  $F(\lambda)$  is in  $\text{erg s}^{-1} \text{cm}^{-2} \text{\AA}^{-1}$ . We fit this power law relation between 1200 and 3000  $\text{\AA}$ . Of the 27947 UVJ active galaxies (in the ZFOURGE catalog) encompassed by the GOODS-ALMA field, 520 have coverage in at least two photometric bands, as is needed to constrain  $\beta$  and a far IR counterpart. As the 2175  $\text{\AA}$  bump (existing both at low and high redshift, Conroy et al. (2010); Buat et al. (2012)) can bias the slope measurement in the case of sparse photometric sampling, we excluded the filter(s) that cover this wavelength (Popping et al., 2017; Tress et al., 2018).

Using  $L_{UV}$  and the UV slope, we can define the so-called 'infrared excess', defined as:

$$\text{IRX} = \frac{L_{IR}}{L_{UV}} \quad (8.17)$$

The IRX- $\beta$ , calibrated on local galaxies, has been an important tool for estimating total SFRs when IR data are not available Overzier et al. (2011). Indeed  $\beta$  is measured from UV filters, and can be used as a proxy to measure dust obscuration in galaxies (e.g., Adelberger and Steidel, 2000; Daddi et al., 2007). The dust attenuation ( $A_{UV}$ ) is directly linked to IRX (e.g., Meurer et al., 1999; Calzetti et al., 2000; Buat et al., 2012). For Meurer et al. (1999), for example, the relation between IRX and the dust attenuation at 1600 $\text{\AA}$  is defined by:

$$\log_{10}(\text{IRX}_{1600}) = \log_{10}(10^{0.4A_{1600}} - 1) + 0.076 \pm 0.044 \quad (8.18)$$

ID	$L_{IR}$ $L_{\odot}$	$SFR_{tot}$ $M_{\odot} yr^{-1}$	$SFR/SFR_{MS}$	$M_{dust}$ $M_{\odot}$	$M_{gas}$ $M_{\odot}$	$f_{gas}$	$T_{dust}$ K
AGS1	$12.83 \pm 0.02$	$1166^{+56}_{-58}$	$6.02^{+0.30}_{-0.31}$	$9.2 \pm 0.1$	$11.30 \pm 0.05$	$0.64^{+0.10}_{-0.09}$	$38.95 \pm 0.79$
AGS2†	$12.68 \pm 0.14$	$836^{+268}_{-259}$	$4.25^{+1.38}_{-1.33}$	$8.7 \pm 0.1$	$11.24 \pm 0.14$	$0.68^{+0.31}_{-0.24}$	$37.12 \pm 2.38$
AGS3	$12.93 \pm 0.02$	$1464^{+74}_{-72}$	$4.02^{+0.21}_{-0.20}$	$9.2 \pm 0.1$	$11.21 \pm 0.05$	$0.43^{+0.06}_{-0.06}$	$41.65 \pm 0.98$
AGS4	$13.22 \pm 0.02$	$2880^{+141}_{-142}$	$2.77^{+0.14}_{-0.14}$	$8.8 \pm 0.1$	$10.84 \pm 0.05$	$0.20^{+0.02}_{-0.03}$	$55.13 \pm 1.18$
AGS5	$12.98 \pm 0.02$	$1650^{+82}_{-81}$	$4.14^{+0.21}_{-0.21}$	$8.9 \pm 0.1$	$10.96 \pm 0.06$	$0.40^{+0.06}_{-0.06}$	$47.84 \pm 2.82$
AGS6†	$12.53 \pm 0.15$	$587^{+195}_{-199}$	$3.06^{+1.04}_{-1.06}$	$8.5 \pm 0.2$	$11.05 \pm 0.15$	$0.57^{+0.25}_{-0.21}$	$37.50 \pm 2.39$
AGS7	$12.55 \pm 0.15$	$618^{+210}_{-202}$	$0.95^{+0.33}_{-0.32}$	$8.3 \pm 0.1$	$10.83 \pm 0.15$	$0.20^{+0.07}_{-0.07}$	$38.83 \pm 2.42$
AGS8	$12.70 \pm 0.02$	$873^{+41}_{-44}$	$3.16^{+0.15}_{-0.16}$	$9.2 \pm 0.0$	$11.27 \pm 0.04$	$0.35^{+0.04}_{-0.04}$	$32.01 \pm 2.43$
AGS9	$12.72 \pm 0.02$	$914^{+45}_{-45}$	$5.34^{+0.27}_{-0.27}$	$8.9 \pm 0.1$	$11.07 \pm 0.14$	$0.70^{+0.32}_{-0.25}$	$40.33 \pm 1.51$
AGS10	$12.68 \pm 0.02$	$832^{+40}_{-41}$	$2.59^{+0.13}_{-0.13}$	$8.9 \pm 0.1$	$10.93 \pm 0.06$	$0.29^{+0.04}_{-0.04}$	$39.67 \pm 2.31$
AGS11†	$12.73 \pm 0.14$	$926^{+293}_{-289}$	$5.80^{+1.86}_{-1.84}$	$8.1 \pm 0.1$	$10.81 \pm 0.14$	$0.65^{+0.28}_{-0.22}$	$45.87 \pm 2.66$
AGS12	$12.80 \pm 0.02$	$1101^{+52}_{-54}$	$9.86^{+0.48}_{-0.50}$	$8.6 \pm 0.0$	$10.81 \pm 0.03$	$0.55^{+0.05}_{-0.05}$	$54.90 \pm 1.61$
AGS13	$12.49 \pm 0.02$	$537^{+25}_{-26}$	$1.73^{+0.08}_{-0.09}$	$8.8 \pm 0.1$	$10.80 \pm 0.07$	$0.20^{+0.03}_{-0.03}$	$41.48 \pm 1.13$
AGS18	$12.46 \pm 0.03$	$501^{+27}_{-28}$	$2.21^{+0.13}_{-0.13}$	$9.0 \pm 0.1$	$11.09 \pm 0.10$	$0.54^{+0.15}_{-0.13}$	$37.70 \pm 1.09$
AGS20	$12.40 \pm 0.18$	$440^{+172}_{-178}$	$3.29^{+1.31}_{-1.36}$	$8.4 \pm 0.2$	$11.05 \pm 0.18$	$0.66^{+0.39}_{-0.30}$	$36.26 \pm 2.46$
AGS21†	$12.31 \pm 0.14$	$364^{+113}_{-112}$	$2.53^{+0.81}_{-0.80}$	$8.1 \pm 0.1$	$10.70 \pm 0.14$	$0.54^{+0.22}_{-0.18}$	$41.00 \pm 2.54$
AGS23	$12.14 \pm 0.06$	$245^{+32}_{-32}$	$0.84^{+0.12}_{-0.12}$	$9.1 \pm 0.2$	$11.13 \pm 0.22$	$0.43^{+0.26}_{-0.22}$	$29.82 \pm 0.67$
AGS24	$12.20 \pm 0.11$	$289^{+71}_{-70}$	$0.49^{+0.13}_{-0.12}$	$8.1 \pm 0.1$	$10.64 \pm 0.14$	$0.18^{+0.06}_{-0.06}$	$39.69 \pm 2.44$
AGS25†	$12.57 \pm 0.07$	$654^{+105}_{-105}$	$6.17^{+1.01}_{-1.01}$	$8.2 \pm 0.1$	$10.91 \pm 0.14$	$0.77^{+0.37}_{-0.28}$	$45.06 \pm 2.52$
AGS26	$12.50 \pm 0.02$	$547^{+27}_{-26}$	$6.26^{+0.32}_{-0.31}$	$9.0 \pm 0.0$	$11.10 \pm 0.04$	$0.62^{+0.07}_{-0.07}$	$38.82 \pm 2.79$
AGS27†	$12.77 \pm 0.07$	$1012^{+166}_{-163}$	$2.73^{+0.45}_{-0.44}$	$7.6 \pm 0.1$	$10.17 \pm 0.05$	$0.15^{+0.02}_{-0.02}$	$45.92 \pm 2.62$
AGS28	$12.29 \pm 0.02$	$339^{+16}_{-16}$	$1.61^{+0.08}_{-0.08}$	$9.1 \pm 0.1$	$11.20 \pm 0.13$	$0.52^{+0.19}_{-0.16}$	$32.23 \pm 0.19$
AGS29†	$11.95 \pm 0.12$	$172^{+41}_{-41}$	$3.96^{+1.06}_{-1.06}$	$7.5 \pm 0.1$	$10.09 \pm 0.15$	$0.19^{+0.07}_{-0.07}$	$28.74 \pm 2.46$
AGS30†	$11.89 \pm 0.13$	$136^{+40}_{-40}$	$10.90^{+3.27}_{-3.28}$	$9.0 \pm 0.1$	$11.73 \pm 0.15$	$0.96^{+0.61}_{-0.38}$	$26.73 \pm 2.36$
AGS31	$12.52 \pm 0.02$	$570^{+27}_{-27}$	$1.61^{+0.08}_{-0.08}$	$8.7 \pm 0.1$	$10.76 \pm 0.06$	$0.19^{+0.03}_{-0.03}$	$41.19 \pm 3.12$
AGS32†	$12.40 \pm 0.07$	$441^{+63}_{-65}$	$0.99^{+0.15}_{-0.15}$	$8.0 \pm 0.1$	$10.59 \pm 0.06$	$0.28^{+0.04}_{-0.04}$	$44.99 \pm 2.55$
AGS33	$12.31 \pm 0.12$	$477^{+98}_{-96}$	$3.10^{+0.86}_{-0.84}$	$9.1 \pm 0.4$	$11.31 \pm 0.39$	$0.80^{+1.09}_{-0.92}$	$45.94 \pm inf$
AGS34†	$12.22 \pm 0.09$	$286^{+60}_{-61}$	$1.89^{+0.40}_{-0.40}$	$8.8 \pm 0.1$	$10.95 \pm 0.43$	$0.57^{+0.88}_{-0.63}$	$36.62 \pm 2.38$
AGS35	$12.79 \pm 0.02$	$1060^{+52}_{-53}$	$6.23^{+0.31}_{-0.31}$	$8.5 \pm 0.1$	$10.69 \pm 0.13$	$0.42^{+0.14}_{-0.13}$	$58.70 \pm 3.50$
AGS36	$10.80 \pm 0.07$	$15^{+1}_{-1}$	$0.68^{+0.11}_{-0.12}$	$9.1 \pm 0.2$	$11.38 \pm 0.20$	$0.89^{+0.79}_{-0.44}$	$16.15 \pm inf$
AGS37	$12.37 \pm 0.02$	$415^{+19}_{-20}$	$2.28^{+0.11}_{-0.11}$	$8.9 \pm 0.0$	$10.99 \pm 0.03$	$0.37^{+0.03}_{-0.03}$	$38.48 \pm 2.26$
AGS38	$11.60 \pm 0.03$	$69^{+4}_{-4}$	$0.79^{+0.05}_{-0.06}$	$8.9 \pm 0.4$	$10.97 \pm 0.43$	$0.43^{+0.63}_{-0.44}$	$22.32 \pm inf$
AGS39	$12.75 \pm 0.02$	$960^{+47}_{-47}$	$12.37^{+0.62}_{-0.61}$	$8.7 \pm 0.1$	$10.95 \pm 0.06$	$0.69^{+0.11}_{-0.10}$	$46.41 \pm 1.81$

TABLE 8.2: Derived properties of the GOODS-ALMA sources. Columns: (1) Source name; (2)  $L_{IR}$  derived from SED fitting (3),  $SFR_{tot} = SFR_{IR} + SFR_{UV}$ , (4)  $R_{SB} = SFR/SFR_{MS}$ , where  $SFR_{MS}$  is the average SFR of MS galaxies following [Schreiber et al. \(2015\)](#), (5) Gas mass derived from Eq. 8.5, (6) Gas fraction defined by  $f_{gas} = M_{gas}/(M_{gas} + M_{*})$ , (7) Dust temperature derived from a MBB model assuming  $\beta=1.5$ . † indicates galaxies without *Herschel* counterpart and whose  $L_{IR}$  is determined only by the ALMA contribution. For these galaxies, we show the mass of gas as an indication but we do not use it in the rest of this paper.

This relationship, first defined at low redshift (e.g., [Meurer et al., 1999](#); [Calzetti et al., 2000](#)) was refined using Galaxy Evolution Explorer (GALEX) data ([Overzier et al., 2011](#); [Takeuchi et al., 2012](#)). At high redshift, this relationship is still poorly constrained and the results are contradictory. While some studies show that galaxies at high redshift follow this local relationship (e.g. [Fudamoto et al., 2017](#); [Bourne et al., 2017](#); [McLure et al., 2018](#); [Koprowski et al., 2018](#)), others claim that the results differ at high redshift. The most surprising aspect to note is that when results differ from the relationship, they can be located either under that relationship ([Capak et al., 2015](#); [Álvarez-Márquez et al., 2016](#); [Pope et al., 2017](#); [Bouwens et al., 2016](#); [Barisic et al., 2017](#)) or above this relationship (e.g. [Oteo et al., 2013](#)).

We investigated how the galaxies detected by ALMA are positioned in the IRX- $\beta$  plane. In Fig. 8.4 we compare the position of the ALMA detected galaxies with the [Meurer et al. \(1999\)](#); [Calzetti et al. \(2000\)](#); [Reddy et al. \(2015\)](#) relation.

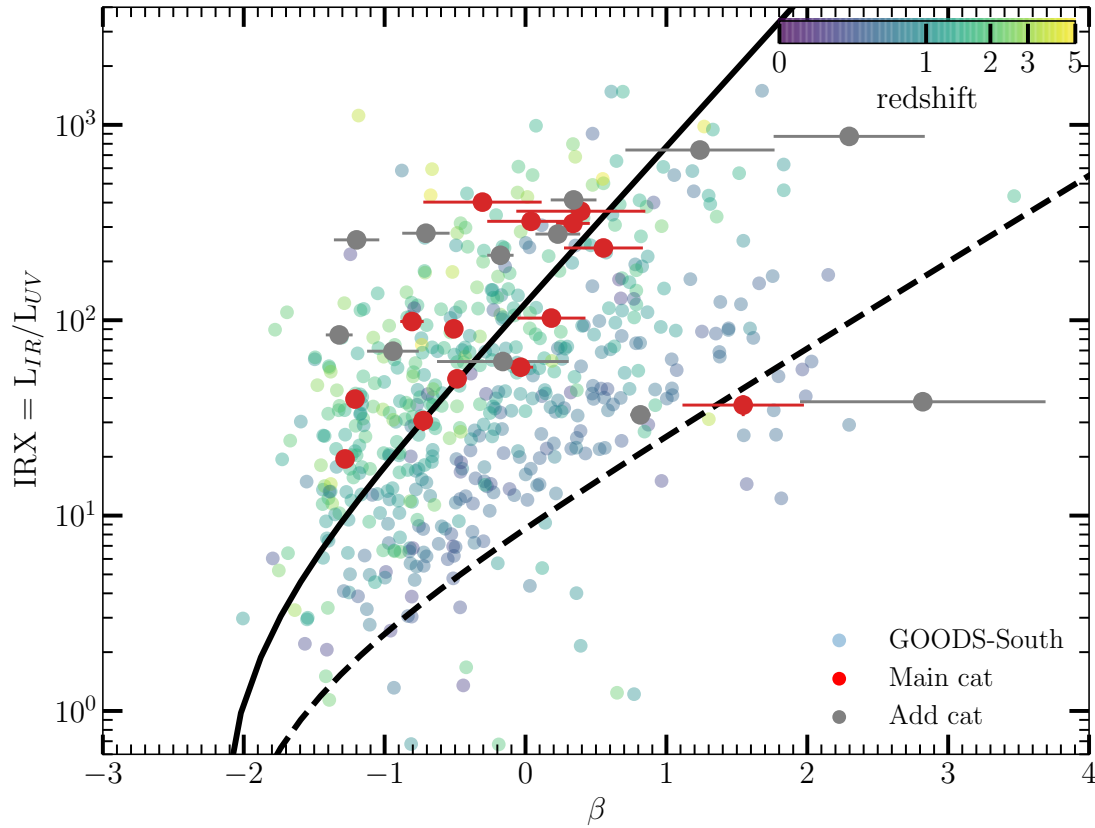


FIGURE 8.5: IRX- $\beta$  relation for the ALMA detected galaxies. The black solid and dashed lines represent the SMC extinction curves from Calzetti et al. (2000) and Pettini et al. (1998) respectively. For comparison, all of the galaxies in the GOODS-South field for which this value has been derived are also shown, color-coded by redshift.

The Galactic extinction correction for each filter (Schlafly and Finkbeiner, 2011) wasn't taken into consideration in the fit process. This correction alters the final values of  $\beta$  by approximately 0.025 for the GOODS-South field (Wang et al., 2018), which is negligible compared to the median error on  $\beta$ .

For comparison with our sample, we have indicated the relationship derived by Meurer et al. (1999):

$$IRX_{Meurer} = 1.75 \times (10^{0.4 \cdot (1.99 \cdot (\beta + 4.43))} - 1) \quad (8.19)$$

The factor 1.75 in Eq. 8.19 comes from the conversion between the FIR brightness used by Meurer et al. (1999) (40 to 120  $\mu\text{m}$ ) and IR luminosity (8 to 1000  $\mu\text{m}$ ) (Calzetti et al., 2000; Reddy, 2006; Bouwens et al., 2016).

We also give the relationship derived by (e.g. Prevot et al., 1984; Pettini et al., 1998; Smit et al., 2016; Bouwens et al., 2016) for SMC-type dust correction:

$$IRX_{SMC} = 10^{0.4 \cdot (1.1 \cdot (\beta + 2.23))} - 1 \quad (8.20)$$

Except for some rare outliers, we find that the galaxies detected by ALMA, whether in the blind catalog or the prior-based catalog, are consistent with the local relationship of Meurer et al. (1999). Fig. 8.4 does not indicate a mass dependence for this relationship. On the other hand,

some studies (e.g. Coppin et al., 2015; Pannella et al., 2015; Fudamoto et al., 2017; Álvarez-Márquez et al., 2016; McLure et al., 2018; Koprowski et al., 2018) show a mass dependence of the IRX values for massive galaxies, where the dust attenuation is more significant for the most massive galaxies.

### 8.2.6 Infrared-radio correlation

The FIR/radio correlation (FRC; de Jong et al. e.g., 1984; Helou et al. e.g., 1985), first defined for local galaxies by the Infrared Astronomical Satellite (IRAS; Neugebauer et al. 1984), was later extended to intermediate redshifts ( $z \sim 0.1-1.5$ , (e.g. Yun et al., 2001; Garrett, 2002; Appleton et al., 2004; Sargent et al., 2010b)) and then to even high redshift galaxies (e.g. Sargent et al., 2010a; Magnelli et al., 2015; Delhaize et al., 2017). One of the major outstanding questions is whether this relationship is evolving with redshift. Recent studies (e.g. Ivison et al., 2010; Sargent et al., 2010a; Magnelli et al., 2015; Delhaize et al., 2017) support a dependence of this relationship on redshift. The capabilities of ALMA now allow for IR detections at high redshift, while having sufficient resolution to give increased confidence in optical counterparts. This infrared-radio correlation arises from the fact that massive stars ( $M \geq 8 M_{\odot}$ ) contribute to the heating of dust in the interstellar medium (and are therefore responsible for the infrared part of the galaxy's spectrum), as well as producing radio emission in HII regions (thermal free-free emission), and from supernova explosions (synchrotron emission). Other phenomena could also come into play, such as the inverse Compton cooling (e.g. Condon, 1992; Lacki et al., 2010) (which depends on the ratio  $RSB = SFR/SFR_{MS}$  or ionization parameter (e.g. Murphy, 2009; Schleicher and Beck, 2013)). This correlation is quantified by the parameter  $q_{FIR}$  :

$$q_{FIR} = \log_{10} \left( \frac{L_{FIR} [W]}{3.75 \times 10^{12}} \right) - \log_{10} (L_{1.4GHz} [W.Hz^{-1}]) \quad (8.21)$$

where  $L_{FIR}$  is the FIR luminosity integrated from rest-frame 42 to  $122 \mu m$ , and  $L_{1.4GHz}$  is the rest frame 1.4-GHz radio luminosity. The 1.4 GHz luminosities of our galaxies have been computed from 6 GHz radio observations (Rujopakarn et al. in prep.), following:

$$L_{1.4GHz} = \frac{4\pi d_L^2}{(1+z)^{1-\alpha}} S_{3GHz} \times \left( \frac{1.4}{3} \right)^{-\alpha} \quad (8.22)$$

where  $d_L$  is the luminosity distance. We have assumed that the radio flux is k-corrected following  $S_{\nu} \propto \nu^{-\alpha}$ , with a synchrotron spectral index  $\alpha = 0.8$  Condon (1992); Ivison et al. (2010) between 1.4 and 3 GHz. According to Magnelli et al. (2012), the radio spectral index does not evolve significantly with redshift or distance from the MS. We therefore take a value of  $\alpha = 0.8$  for all of the galaxies in our sample.

The correlation between radio and FIR luminosity is tight (scatter of 0.26 dex, Yun et al. 2001) spanning over five orders of magnitude (Price and Duric, 1992). This correlation can be used to segregate radio-loud AGNs from SFGs: the presence of an AGN may cause an excess of radio compared to IR luminosity. We compared our derived  $q_{FIR}$  values with the relationship found by Magnelli et al. (2015), who studied the FRC across four extragalactic fields (GOODS-N, GOODS-S, ECDFS, and COSMOS). This study, shows an evolution of  $q_{FIR}$  with redshift, with an increase in relative radio contribution as redshift increases:



$$q_{FIR} = (2.35 \pm 0.08) \times (1 + z)_M^{\alpha_M} \quad (8.23)$$

with  $\alpha_M = -0.12 \pm 0.04$

On the other hand, this relationship does not evolve significantly with the offset from the main sequence (Magnelli et al., 2015). Due to the larger number of sources in common with our catalogs in the 3 GHz radio image than in the 6 GHz image (26 compared to 17), and because no source present at 6GHz is missing from the 3 GHz image, we have chosen the 3 GHz radio image to calculate our radio luminosities. The average ratio  $q_{FIR,3GHz}/q_{FIR,6GHz}$  for the 17 galaxies present in the two radio images is  $1.02 \pm 0.06$ , where the uncertainty corresponds to the standard deviation.

In Fig. 8.5, we compare the  $q_{FIR}$  of our galaxies with the relationship from Delhaize et al. (2017), as well as a local relationship (Yun et al., 2001). Among the 20 galaxies in the main catalog (F18), 15 are detected ( $S/N > 4.5$ ) at 10 cm. Of the five that are not detected, three correspond to the galaxies that we have classified as spurious in F18 and that we have not analyzed in this thesis. More interestingly, the other two galaxies, not detected in radio and not classified as spurious, are HST-dark galaxies (AGS11 and AGS15), supporting the hypothesis that this population of galaxies is particularly distant. While the redshift of AGS11 has been estimated at  $z_{AGS11} = 4.8$ , making it the most distant galaxy of the blindly detected galaxies, the redshift of AGS15 could not be estimated. The strong negative  $K$ -correction applied to the Rayleigh-Jeans tail of the galaxy's SED keeps the observed millimeter flux constant over a wide range of redshifts ( $2 < z < 10$ ; Blain et al. 2002). However, this correction applies less significantly to the radio continuum emission.

In the prior-based catalog, the proportion of galaxies detected by both ALMA and VLA is less significant, with only 11/17 (65%) having a detection with the VLA ( $SN > 3$ ).

Overall, galaxies appear to follow the relationship defined by Magnelli et al. (2015). Of the 24 galaxies for which we have both IR luminosity and robust VLA detections, only five galaxies are significantly offset from this relationship ( $q_{fir} > 2\sigma$  lower than the Magnelli et al. (2015) relation at a given redshift). Of these five galaxies, four have an X-ray detection  $> 10^{43}$  erg.sec $^{-1}$  and are classified as AGN in this study. A single galaxy, (AGS9) has a particularly low value of  $q_{FIR}$  without an X-ray detection and is an excellent candidate to be a radio-loud AGN. Among the galaxies with a particularly low  $q_{FIR}$ , we note that the largest difference with the relationship of Magnelli et al. (2015) is for the two galaxies in our sample that have a low redshift ( $z = 0.66$  and  $1.10$ ). These galaxies are very compact galaxies in the observed  $H$ -band ( $r_e = 0.65$  and  $0.57$  kpc respectively). They are the two galaxies that are below the size-mass relationship of the passive UVJ galaxies in Fig. 8.9, and have typical quasar characteristics.

On the other hand, and more interestingly, some galaxies lie above this trend. The majority of these outliers also host an AGN (AGS3, AGS4, AGS5, green stars in Fig. 8.5). These galaxies have particularly high star formation rates ( $SFR > 1000 M_{\odot} \text{yr}^{-1}$ ). We will discuss the relevance of classifying these galaxies as AGNs in this section.

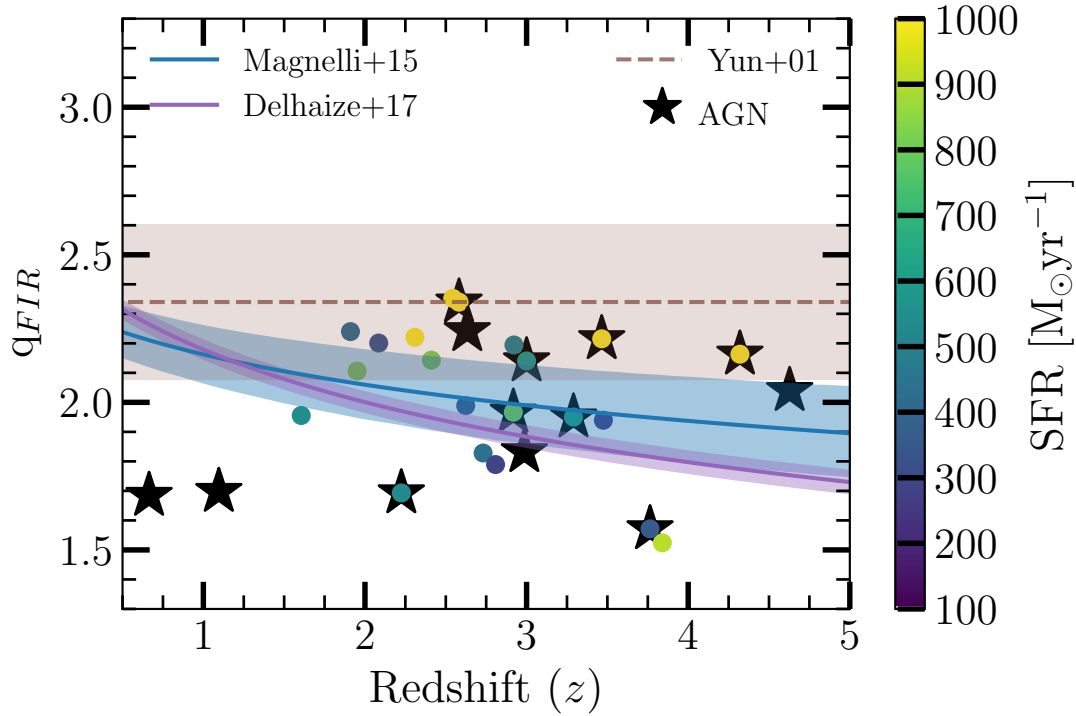


FIGURE 8.6:  $q_{FIR}$  as a function of redshift for the galaxies detected in GOODS-ALMA by both ALMA (at 1.1mm) and the VLA (at 3 GHz). The ALMA-detected galaxies are color-coded as a function of SFR. The Magnelli et al. (2015) and Delhaize et al. (2017) evolutionary trends and the local relation from Yun et al. (2001) are also shown for comparison. The shaded areas represent the  $\pm 1\sigma$  uncertainty on  $q_{FIR}$ .

## 8.3 The slow downfall of star-formation in $z = 2-3$ massive galaxies

### 8.3.1 Large fraction of our sample with low gas fractions

In this survey, we have detected particularly massive galaxies, the majority of which are beyond the cosmic noon at  $z \sim 1-2$ . The study of the gas mass reservoirs is essential to understand how the galaxies will evolve with redshift and whether these galaxies could be the progenitors of passive galaxies at  $z \sim 2$ . To obtain the most robust results possible, we have considered in the following section only galaxies with a *Herschel* counterpart. These are the galaxies marked by † in Table 8.2. In Fig. 8.6 (left panel), we compare the gas fraction of our galaxies as a function of their deviation from the MS, with the relationship presented in Tacconi et al. (2018):

$$M_{\text{gas}}/M_{*} = [0.66^{+0.22}_{-0.23}] \times R_{SB}^{0.53}. \quad (8.24)$$

In the same way, we compare the depletion time with the relationship presented in Tacconi et al. (2018):

$$\tau_{\text{dep}} = [322^{+43}_{-38}] \times R_{SB}^{-0.44} [\text{Myr}]. \quad (8.25)$$

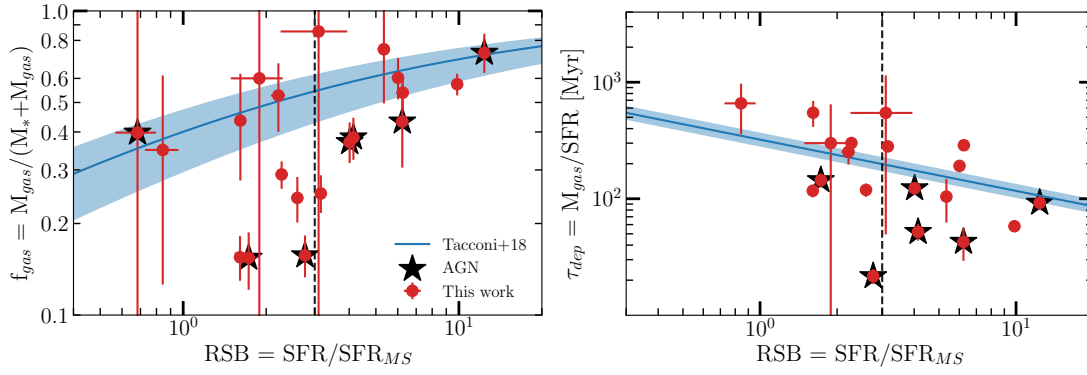


FIGURE 8.7: Evolution of the molecular gas fraction ( $f_{\text{gas}}$ ) and the gas depletion timescale ( $\tau_{\text{dep}}$ ) as a function of the distance to the main sequence of star-forming galaxies ( $R_{SB} = \text{SFR}/\text{SFR}_{MS}$ ), for the main and supplementary catalog of galaxies detected by ALMA in the GOODS-ALMA field. The solid blue line shows the relation obtained by Tacconi et al. (2018) for the median redshift and stellar mass of our sample ( $z_{\text{med}} = 2.69$ ,  $M_{*,\text{med}} = 8.52 \times 10^{10} M_{\odot}$ ). The dispersion is obtained by Monte-Carlo simulations. In order to compare the gas fractions of all of the galaxies in our sample, we have rescaled our gas fractions according to the median redshift and the stellar mass of our sample.

We have rescaled this relationship to correspond to the median redshift ( $z_{\text{med}} = 2.69$ ) and the median stellar mass of our sample ( $M_{*,\text{med}} = 8.23 \times 10^{10} M_{\odot}$ ). To be able to directly compare the gas fraction of our galaxies to the relationship of Tacconi et al. (2018), we have also scaled our gas fractions according to the median redshift and stellar mass of our sample. The gas fractions, before rescaling, are presented in Table 8.2.

The depletion times span a large range, between 20 and 600 Myr. The galaxies studied here show dependence between depletion time and distance to the main sequence, although very scattered.

About half of the GOODS-ALMA galaxies follow the  $f_{\text{gas}}-R_{SB}$  relation from (Tacconi et al. 2018, Eq. 20). However, we find a surprisingly large fraction (47%) of galaxies lying well below this relation, i.e., with excessively short depletion times. Interestingly, this fraction is not correlated with the starburstiness  $R_{SB}$ , as defined by the distance to the MS. The galaxies with the shortest depletion times are also those with the lowest gas fraction. This is because despite exhibiting lower gas masses, these galaxies keep forming stars with a high SFR.

We note that all the ALMA galaxies experiencing a strong AGN episode with  $L_X > 10^{43} \text{ erg.s}^{-1}$  lie below the  $\tau_{\text{dep}}-R_{SB}$  relation and  $f_{\text{gas}}$ . This suggests that the low gas content and associated short depletion time of the galaxies may be due to the offset of the AGN feedback heating the surrounding extragalactic medium and preventing further the infall of gas. In other words, about half of the galaxies at these flux densities and redshift appear to suffer from starvation and constitute excellent candidate progenitors of  $z = 2$  elliptical galaxies. To further investigate this possibility, we show in Sect. 8.3.2 that the ALMA sizes, i.e., where the stars are formed, are consistent with the compact cores of  $z = 2$  elliptical galaxies.

Although there is a trend between the  $R_{SB}$  and the stellar mass of the galaxies, in that the less massive galaxies in our sample have a larger average  $R_{SB}$ . We also investigate the evolution of depletion time as a function of the stellar mass. We found no correlation. This means that the star-formation efficiency ( $\text{SFE} = M_{\text{gas}}/\text{SFR} = 1/\tau_{\text{dep}}$ ) does not change according to the mass of

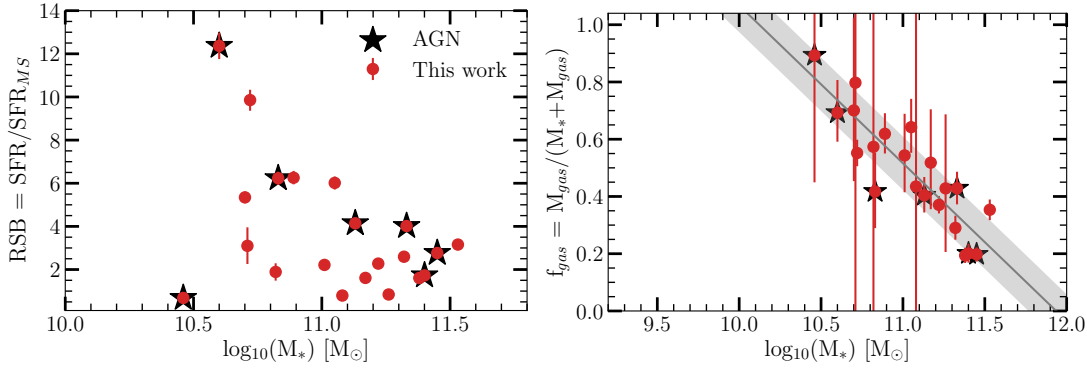


FIGURE 8.8: Evolution of the distance to the main sequence of star-forming galaxies ( $RSB = SFR/SFR_{MS}$ , left panel) and the molecular gas fraction ( $f_{gas}$ , right panel) as a function of the stellar mass. The best fit, given by Eq. 8.26, is shown by the gray shaded region

the galaxy. Galaxies transform their gas into stars at a rate independent of the stellar mass of the galaxy.

The gas fractions cover a significant range of values, between 0.2 and 0.9, with a median of 0.43 (mean = 0.48). We can see in Fig. 8.6 (left panel) that approximately half of the galaxies for which we have gas measurements are on the relationship of Tacconi et al. (2018), taking into account the uncertainties on the gas measurement, and half of our sample are below. For galaxies below the relationship, we can see that this difference is even more pronounced when the galaxy is close to the main sequence.

These values are consistent with other studies, such as Wiklind et al. (2014). We do, however remark that for the two common galaxies between this work and Wiklind et al. (2014), there is a significant difference in the calculated gas fraction. These two common galaxies are outliers from the rest of the Wiklind et al. (2014) sample as they have gas fractions close to unity, and in fact, correspond to two HST-dark galaxies that were previously falsely attributed with optical counterparts. Interestingly, we see that a number of our galaxies are deficient in gas compared to the average population. We note that a significant number of these outliers are classified as AGN.

We note that a significant number of the outliers with low gas fraction are classified as AGN. We note that the presence of an AGN can influence the measurement of the stellar mass of the galaxy and artificially lower the calculated gas fraction of the galaxies. One of these galaxies has a low gas fraction (14%) and does not show any sign of an AGN. This galaxy is a particularly striking example of interacting galaxies, with strong tidal tails. This galaxy does not have a high star formation rate, it lies on the MS, but it does display a starburst-like behavior since it exhibits a short gas depletion time. This galaxy could, therefore, be a member of the population of galaxies described in Elbaz et al. (2018), a starburst galaxy hidden in the main sequence.

We find a negative correlation between the stellar mass and the gas fraction (see Fig. 8.7, right panel). The following equation characterizes this relationship:

$$f_{gas} = (-0.55 \pm 0.07) \times \log_{10}(M_*) + 6.58 \pm 0.78 \quad (8.26)$$

A similar relationship has been found in other studies (e.g. Popping et al., 2012; Magdis et al., 2012; Sargent et al., 2014; Schinnerer et al., 2016). Those galaxies hosting an AGN do not seem

to occupy a particular position in Fig. 8.7. We also indicate in the left panel the distance to the main sequence as a function of the stellar mass. We can also see a clear negative correlation between the stellar mass and  $R_{SB}$ . On the other hand, it is not possible to say whether selection effects are driving this trend. To be detected, a galaxy of low mass must have a larger  $R_{SB}$  than a massive galaxy. On the other hand, we do not find massive galaxies ( $M_* > 10^{11} M_\odot$  with  $R_{SB} > 6$ ).

We also considered the evolution of depletion time as a function of the stellar mass. We found no correlation. This means that the star-formation efficiency ( $SFE = M_{gas}/SFR = 1/\tau_{dep}$ ) does not change according to the mass of the galaxy. Galaxies transform their gas into stars at a rate independent of the stellar mass of the galaxy.

Galaxies with the lowest gas fractions and shortest depletion times also appear to be the most massive suggesting that are witnessing a slow downfall of the galaxies with the most massive galaxies dropping the first ones from forming stars to becoming elliptical galaxies, in a similar way to what had been shown ?.

### 8.3.2 Towards a reduction in the size of galaxies

#### Size

Several studies have reported the observation of massive star-forming galaxies, compact in the  $H$ -band (e.g., blue nuggets; Dekel and Burkert 2014). It has been proposed that these galaxies are the progenitors of massive, compact and passive galaxies at  $z = 2$  (e.g., Barro et al., 2013; Williams et al., 2014; Toft et al., 2014; van der Wel et al., 2014; Barro et al., 2016; Kocevski et al., 2017).

We have, thanks to the GOODS-ALMA survey, selected a sample of massive star-forming galaxies. These galaxies are among the most massive among the UVJ active galaxies (Williams et al. 2009, using the same definition as in F18) listed in the ZFOURGE catalog (see Fig. 12 in Franco et al., in prep). For example, with ALMA we have detected the most massive ZFOURGE galaxy in the redshift range  $1 < z < 2$ , the most massive galaxy at  $2 < z < 3$ , the second most massive galaxy at  $3 < z < 4$  and finally the most massive galaxy in the redshift range  $4 < z < 5$  (this galaxy is extremely faint in UV, so the determination of the mass may suffer from significant uncertainties). These galaxies cannot continue to form stars for long periods. If this were the case, they would become much more massive than the most massive galaxies we have observed at  $z = 1$ , or in the local universe.

These galaxies have not been selected as compact galaxies in the  $H$ -band. They are flux-selected. Due to the low dispersion of the main sequence, this selection is equivalent to a mass selection. The compact  $H$ -band galaxies studied at  $z \sim 2-3$  have been proposed to be the progenitors of passive galaxies that are known to be compact at  $z \sim 2$ .

We aim to study here whether galaxies that have not been selected to be compact in the  $H$ -band can also be the progenitors of compact galaxies at  $z = 2$ . To do this, we have compared the  $H$ -band sizes of the galaxies detected by ALMA with the  $H$ -band sizes of the galaxies present in GOODS-ALMA.

The majority of the galaxies studied in this thesis have a redshift between 2 and 4. We report in Fig. 8.9, left panel,  $H$ -band sizes of all galaxies with  $2 < z < 4$  located in the area defined by the GOODS-ALMA survey, as a function of stellar mass, in blue. We also show the  $H$ -band size of the ALMA-detected galaxies with black open markers. Galaxy sizes and Sérsic indices are obtained from van der Wel et al. (2014). These values have been computed by fitting a single-component Sérsic profile using GALFIT Peng et al. (2010), at both 1.4 and 1.6  $\mu\text{m}$ . We focus here on the results at 1.6  $\mu\text{m}$ . We also show the trends for the UVJ active and UVJ passive galaxies with blue and red lines respectively. These two relations were parametrized by van der Wel et al. (2014) following:

$$r_{\text{eff}} = A [(M_*/5 \times 10^{10})/1.7]^\alpha \quad (8.27)$$

where  $R_{\text{eff}}$  is the effective radius, in other words, the semi-major axis of the ellipse that contains half of the total flux of the best-fitting Sérsic model, in kpc. We use the following parameters:  $\log_{10}(A) = -0.06 \pm 0.03$ ,  $\alpha = 0.79 \pm 0.07$ , and  $\sigma \log_{10}(R_{\text{eff}}) = 0.14 \pm 0.03$  for the early-type galaxies and  $\log_{10}(A) = 0.51 \pm 0.01$ ,  $\alpha = 0.18 \pm 0.02$ , and  $\sigma \log_{10}(R_{\text{eff}}) = 0.19 \pm 0.01$  for the late-type galaxies. We see that there is a significant difference in size between active and quiescent galaxies. The size of quiescent galaxies is on average larger than passive galaxies. Mosleh et al. (2011) noted, for example, that the UV-bright galaxies with  $10^{10} < M_* < 10^{11}$  and  $0.5 < z < 3.5$  are larger than quiescent galaxies in the same mass and redshift range by a factor  $0.45 \pm 0.09$  dex.

For the vast majority of the ALMA detected galaxies (open black squares), the optical rest-frame sizes of these galaxies are comparable to the sizes of the  $H$ -band selected UVJ active galaxies (blue hexagons). We also over-plot, in Fig. 8.9, the compactness criterion given in Barro et al. (2013) and modified by Barro et al. (2016):

$$\frac{M_*}{r_e^{1.5}} \geq 10^{10.4} M_\odot \text{kpc}^{-1.5} \quad (8.28)$$

Only three GOODS-ALMA galaxies are compact following the compactness criterion. These galaxies lie on the trend for quiescent galaxies. We note that those galaxies that do not follow the trend of star-forming galaxies systematically host an AGN. These galaxies, whose sizes are comparable with those of quenched galaxies, are galaxies that have already begun their quenching process. With the data available to us, it is not possible to distinguish between whether the compaction of the galaxy has triggered the AGN or, on the contrary, it is the presence of the AGN that has caused its compaction.

We also show the ALMA 1.1mm sizes in comparison to the  $H$ -band sizes in Fig. 8.9, right panel. The ALMA sizes for the main and supplementary catalogs are given in Franco et al., in prep. The size distribution differs slightly between the two samples. We showed in F18 that we were biased towards compact sources with our detection limit of  $4.8\sigma$ . By lowering this detection threshold in the supplementary catalog, made possible as a result of basing our detections on priors, we are now detecting galaxies with larger sizes. For the 26 galaxies for which we have both HST  $H$ -band sizes and could measure the size with ALMA, we find that ALMA sizes are generally smaller, with a median  $\text{FWHM}_{\text{HST}}/\text{FWHM}_{\text{ALMA}} = 1.35$ . This ratio is in good agreement with that found by Fujimoto et al. (2017), who find a ratio of 1.4 between the  $H$ -band size and the size from ALMA at 870  $\mu\text{m}$ , for a sample of 1034 ALMA sources. This value is also in good agreement with the studies of Chen et al. (2015); Simpson et al. (2015b); Rujopakarn et al. (2016); Elbaz et al. (2018); Calistro Rivera et al. (2018). Considering that dust emission is a good indicator

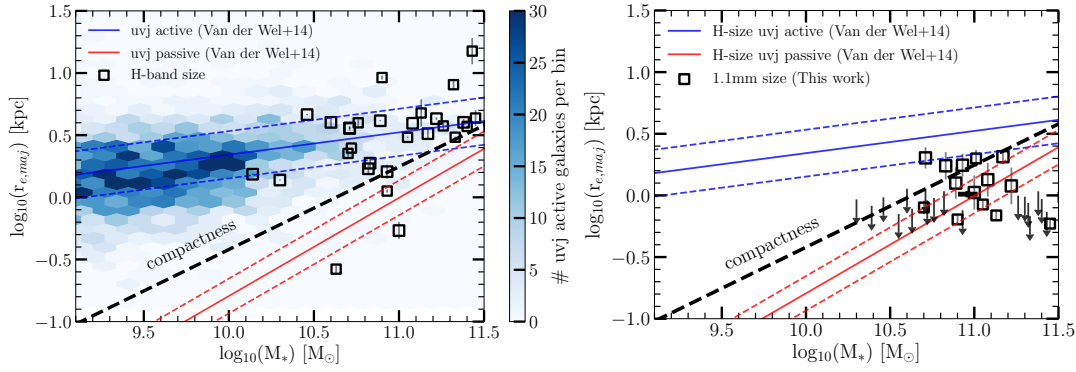


FIGURE 8.9: Left panel:  $H$ -band size-mass plane for the galaxies located in the GOODS-South field for which sizes have been measured in van der Wel et al. (2014). The density of the UVJ active galaxies (with  $2 < z < 4$ ) in the GOODS-ALMA field is represented by the blue hexagons. The blue and red lines represent the trends of active and passive galaxies respectively, while the dashed lines give the scatter on these relations. The ALMA-detected galaxies are shown with black squares and the AGNs are marked with blue stars. Right panel:  $ALMA$  size-mass plane for the ALMA detected galaxies. For comparison, the trends for active and passive galaxies are also shown. We indicate the compactness criterion described in Eq. 8.28 to visualize which galaxies are compact in  $H$ -band.

of dust-obscured star formation, this result indicates compact dust-obscured star formation (at least more compact than optical emission) in the core of the galaxies studied here.

For these galaxies to be the progenitors of compact elliptical galaxies at  $z \simeq 2$ , they need to become more compact than their  $H$ -band size. The observed strong star formation activity concentrated in a small region of the galaxy can morphologically transform a galaxy into a more compact galaxy. Assuming that there is no addition of gas, the majority of these galaxies have gas reservoirs equal to or close to their stellar mass. If this gas is transformed into stars in the compact region of the emission detected by ALMA, these galaxies will become compact and gradually migrate into the location of the mass-size diagram reserved for passive galaxies.

In order for these galaxies to be the progenitors of compact elliptical galaxies at  $z = 2$ , they must also increase the surface brightness at their centers. Indeed, for the population of active UVJ galaxies contained in the region of our survey and measured in van der Wel et al. (2014), the average Sérsic index ( $\langle n_{\text{active}} \rangle = 1.35$ ). The average index for passive galaxies is ( $\langle n_{\text{passive}} \rangle = 2.63$ ), and can reach 4 (Toft et al., 2014). For our galaxies we find  $\langle n_{\text{AGS}} \rangle = 1.08$ . Our resolution and depth are not sufficient to derive a Sérsic index for the dust emission. However, we note that Hodge et al. (2016) and Elbaz et al. (2018) derived Sérsic indices from ALMA emission close to 1, implying that the dust emission is disk-like. This scenario of increasing the surface brightness in the centers of galaxies is compatible with strong star formation activity in the heart of the galaxy, as suggested by the small size of dust emission measured at 1.1mm.

## Morphology

We here aim to look at the mechanisms that may have driven the gas in the center if the ALMA galaxies. This may be violent disc instabilities (Dekel and Burkert, 2014), or other dissipative processes, including mergers (Wellons et al., 2015). To investigate the role of mergers in the compaction process, we now investigate the morphology of the ALMA-detected galaxies.



Increasing numbers of observations have demonstrated that elliptical galaxies at  $z = 2$  are particularly compact (e.g. [Trujillo et al., 2006](#); [van Dokkum et al., 2008](#); [Conselice, 2014](#); [van der Wel et al., 2014](#)). Major merger events can give rise to elliptical galaxies (e.g. [Dekel and Cox, 2006](#); [Hopkins et al., 2006](#)), but can also influence the compactness of the star-formation in galaxies (e.g. [Wuyts et al., 2010](#); [Ceverino et al., 2015](#)). Due to their large stellar mass, which has generated and retained a large amount of metals, hence dust, against outflows (e.g. [Dekel and Silk, 1986](#); [Dekel and Woo, 2003](#); [Tremonti et al., 2004](#)), the galaxies detected in this study are extremely dust-obscured. In addition to this, their redshift makes them particularly faint in UV and optical filters. Some of them are  $Y$ -dropout (e.g., AGS5, AGS18),  $V$ -dropouts (e.g., AGS9, AGS10) or visible only in the K-band (AGS4, AGS11, etc.). The morphology of these galaxies is therefore difficult to obtain, and catalogs such as that of [Huertas-Company et al. \(2015a\)](#) only provide fragmented information on them. We cross-matched our sample with the catalog of [Huertas-Company et al. \(2015a\)](#) that estimates the probability of being a spheroid, disk or irregular using the Convolutional Neural Network technique. In addition to the 6 HST-dark galaxies, which, by definition, cannot be categorized, nine other galaxies have H-band fluxes too faint to be classified ( $F_{160W} > 24.5$  AB mag). This leaves only 20 of our galaxies that are present in this catalog. We use the simplified classification proposed in [Huertas-Company et al. \(2015b\)](#):

- pure bulges:  $f_{sph} > 2/3$  AND  $f_{disk} < 2/3$  AND  $f_{irr} < 1/10$ ;
- pure disks:  $f_{sph} < 2/3$  AND  $f_{disk} > 2/3$  AND  $f_{irr} < 1/10$ ;
- disk+sph:  $f_{sph} > 2/3$  AND  $f_{disk} > 2/3$  AND  $f_{irr} < 1/10$ ;
- irregular disks:  $f_{disk} > 2/3$  AND  $f_{sph} < 2/3$  AND  $f_{irr} > 1/10$ ;
- irregulars/mergers:  $f_{disk} < 2/3$  AND  $f_{sph} < 2/3$  AND  $f_{irr} > 1/10$ .

As a result, 61% (11/18) of our galaxies are classified as irregulars/mergers (two galaxies do not fit into any of the categories presented above). If we also take into account irregular disks, 78% (14/18) have an irregular morphology. Several galaxies show clear morphological characteristics of mergers, for example with large tidal tails. The galaxy AGS31, which exhibits large tidal tails, is an excellent illustration of this (see Fig. 6.14). For other galaxies, the interaction with another galaxy is more discrete or uncertain.

We compared these proportions against a control sample. We have for each one of the 18 galaxies for which we were able to determine a morphology from the [Huertas-Company et al. \(2015a\)](#) catalog, a galaxy closest to it in terms of redshift and stellar mass. This control sample exhibits significantly different morphological proportions. Only 6% (1/18) of these galaxies can be classified as irregulars/mergers, 22% (4/18) if we take into account irregular disks. The galaxy population detected by ALMA, therefore, tends to be on average biased towards irregular galaxies. By more precisely considering the morphological classification, we obtain in the sample galaxies detected by ALMA, on average  $f_{sph} = 0.16$ ,  $f_{disk} = 0.50$ ,  $f_{irr} = 0.34$  while for the control sample  $f_{sph} = 0.40$ ,  $f_{disk} = 0.53$ ,  $f_{irr} = 0.07$ . While the disc fraction is relatively constant between these two samples, we are witnessing an inversion of the fraction between the irregulars and the spheroids.

We are therefore in the presence of a heterogeneous population of both secularly evolving disk and merger-type galaxies. This result is slightly higher with that found by models ([Hayward et al., 2011, 2013](#)), which predict that for a population of SMGs with  $S_{1.1mm} > 0.5$  mJy, star-forming galaxy-pairs account for  $\sim 30-50$  percent of the galaxies.

ID	FWHM arcsec	$\tau_{dep}$ Myr	$\Sigma_{SFR}$ $M_{\odot} \text{yr}^{-1} \text{kpc}^{-2}$
AGS1	$0.21 \pm 0.02$	$174^{+23}_{-22}$	$64^{+11}_{-9}$
AGS3	$0.17 \pm 0.16$	$110^{+14}_{-14}$	$125^{+1002}_{-92}$
AGS4	$0.18 \pm 0.02$	$24^{+3}_{-3}$	$327^{+70}_{-54}$
AGS5	$0.19 \pm 0.02$	$55^{+8}_{-8}$	$137^{+33}_{-25}$
AGS7	$0.20 \pm 0.02$	$110^{+70}_{-44}$	$45^{+17}_{-16}$
AGS8	$0.23 \pm 0.02$	$214^{+23}_{-22}$	$36^{+7}_{-5}$
AGS9	$0.23 \pm 0.03$	$129^{+43}_{-42}$	$56^{+17}_{-12}$
AGS10	$0.21 \pm 0.03$	$104^{+15}_{-15}$	$43^{+14}_{-9}$
AGS12	$0.23 \pm 0.04$	$59^{+5}_{-5}$	$52^{+21}_{-13}$
AGS13	$0.23 \pm 0.03$	$119^{+20}_{-20}$	$24^{+8}_{-5}$
AGS18	$0.50 \pm 0.08$	$248^{+57}_{-57}$	$4^{+2}_{-1}$
AGS20	$0.24 \pm 0.02$	$261^{+218}_{-124}$	$18^{+8}_{-8}$
AGS23	$0.24 \pm 0.04$	$577^{+313}_{-289}$	$9^{+4}_{-2}$
AGS26	$0.30 \pm 0.09$	$233^{+26}_{-25}$	$13^{+1}_{-1}$
AGS28	$0.50 \pm 0.07$	$470^{+144}_{-137}$	$3^{+0}_{-0}$
AGS29	$0.28 \pm 0.00$	$80^{+43}_{-29}$	$0^{+6}_{-3}$
AGS31	$0.27 \pm 0.00$	$101^{+14}_{-14}$	$19^{+3}_{-3}$
AGS33	$0.51 \pm 0.10$	$570^{+605}_{-496}$	$3^{+0}_{-0}$
AGS35	$0.45 \pm 0.12$	$45^{+13}_{-13}$	$13^{+0}_{-0}$
AGS36	$0.28 \pm 0.13$	$22245^{+11659}_{-9912}$	$0^{+0}_{-0}$
AGS37	$0.28 \pm 0.10$	$240^{+22}_{-21}$	$11^{+5}_{-3}$
AGS38	$0.32 \pm 0.10$	$1353^{+1344}_{-1337}$	$1^{+0}_{-0}$
AGS39	$0.28 \pm 0.14$	$93^{+13}_{-12}$	$29^{+4}_{-3}$

TABLE 8.3: Column (1) ALMA ID. Column (2) visual morphology from HST-WFC3 H-band: single/isolated galaxy (S), merger (M) and undefined (U). Column (3) FWHM measured from uvmodelfit in CASA. Column (4)  $\Sigma_{SFR}$ . Column (5)  $\tau_{dep}$  ( $= M_{\text{gas}}/SFR$ ), in Myr.

### 8.3.3 IR surface brightness as a prior for the remaining life-time of a galaxy

The role of compact star-formation in enhancing the efficiency of star-formation is illustrated in Fig. 8.10. Galaxies forming stars with the largest star-formation surface density,  $\Sigma_{SFR}$ , experience the strongest star-formation episodes with the shortest depletion times.

The SFR surface density ( $\Sigma_{SFR}$ ) can be defined as:

$$\Sigma_{SFR} = SFR / (2\pi R_{1.1mm}^2) \quad (8.29)$$

where  $R_{1.1mm}$  the effective radius (see Sect. 8.3.2 for a description of the determination of the millimeter size).

We have found a strong negative correlation between  $\Sigma_{SFR}$  and depletion time (see Fig. 8.10). A similar trend was found in Elbaz et al. (2018). This correlation can be characterized by the following equation:

$$\tau_{dep}[Myr] = 1006^{+584}_{-403} \times \Sigma_{SFR}^{(-0.57 \pm 0.13)}. \quad (8.30)$$

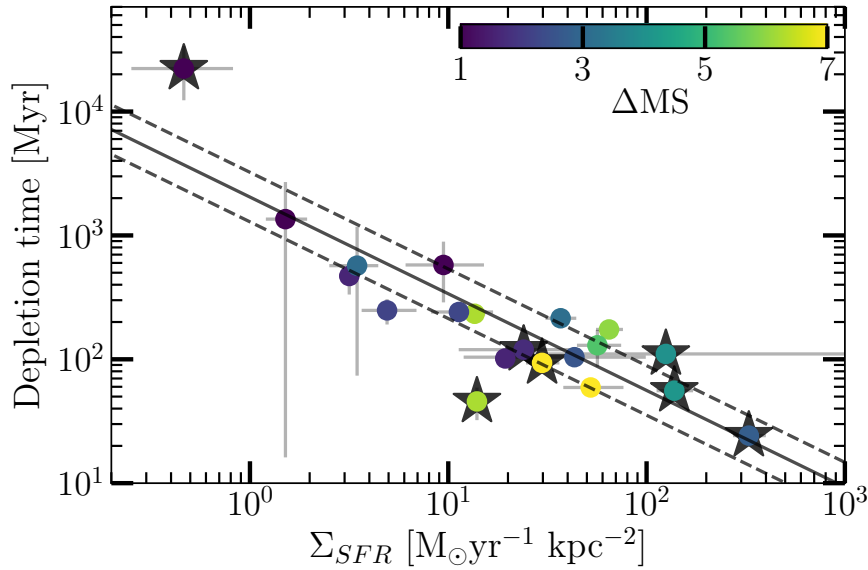


FIGURE 8.10: Depletion time as a function of the  $\Sigma_{SFR}$ , color-coded according to the distance to the main sequence. The solid and dashed lines are the fit to the sliding median and its 68% scatter respectively.

## 8.4 Conclusions

We have taken advantage of the excellent multiwavelength supporting data in the GOODS-South field and the largest contiguous ALMA survey to derive the physical properties of 33 ALMA flux-selected galaxies. This sample of galaxies comes both from purely blind detections (galaxies with a peak flux  $> 4.8\sigma$ , see F18) and from an extension of this catalog that we have built down to the  $3.5\sigma$  limit using IRAC priors to probe fainter millimeter galaxies (see Chapter 6). These galaxies are massive ( $M_{*,med} = 8.5 \times 10^{10} M_{\odot}$ ) and therefore rare, so in order to be able to detect and analyze them, a sufficiently large survey, such as GOODS-ALMA was needed. It is possible for the first time with this survey, covering  $\sim 69$  arcmin<sup>2</sup>. The analysis of the SEDs of these galaxies has made it possible to derive some of the physical properties of these galaxies. We are confronted with a heterogeneous population of galaxies. However, we highlight that about 50% of our galaxy sample exhibits a particularly small gas fraction. We remark that the most massive galaxies in our sample are also the galaxies with the lowest gas fractions. With their high star formation rates (the galaxies are mostly starbursts, or on the upper part of the main sequence) and without a gas refill mechanism, they will consume their gas reservoirs in a typical time of 100 Myr.

We also studied the sizes of these galaxies. The advantage of conducting a blind survey is that it does not impose a priori criteria for selecting the galaxies studied. The ALMA detected galaxies have observed  $H$ -band sizes comparable to the majority of galaxies with the same masses and redshifts, whereas their dust emission regions, i.e., the regions tracing the obscured part of the star formation, are relatively compact and have sizes comparable to passive galaxies at  $z \sim 2$ .

We have investigated the link between depletion time and star formation surface density. We confirm the result showing a tight correlation between these two quantities. The denser the galaxy star-forming region is, the shorter the gas depletion time is. Mechanisms leading to a compaction of the obscured star-forming regions are to be confirmed, but a compact region

massively forming stars at the center of a galaxy can lead to a rapid morphological transition from a spiral to a compact elliptical galaxy such as those observed at  $z \sim 2$ , despite the fact that the ALMA selected galaxies are not yet compact in the  $H$ -band (they are not yet blue nuggets).

All of these different pieces of evidence indicate that our ALMA-detected galaxies are the ideal progenitors of passive galaxies at  $z \sim 2$  and a natural exhaustion of their gas reservoirs (slow downfall) is sufficient for this transition to happen quickly without needed to invoke a quenching mechanism. The large fraction of AGN among galaxies with the shortest depletion times and gas fractions suggest however that they may act by a starvation mechanism in preventing any further growth.

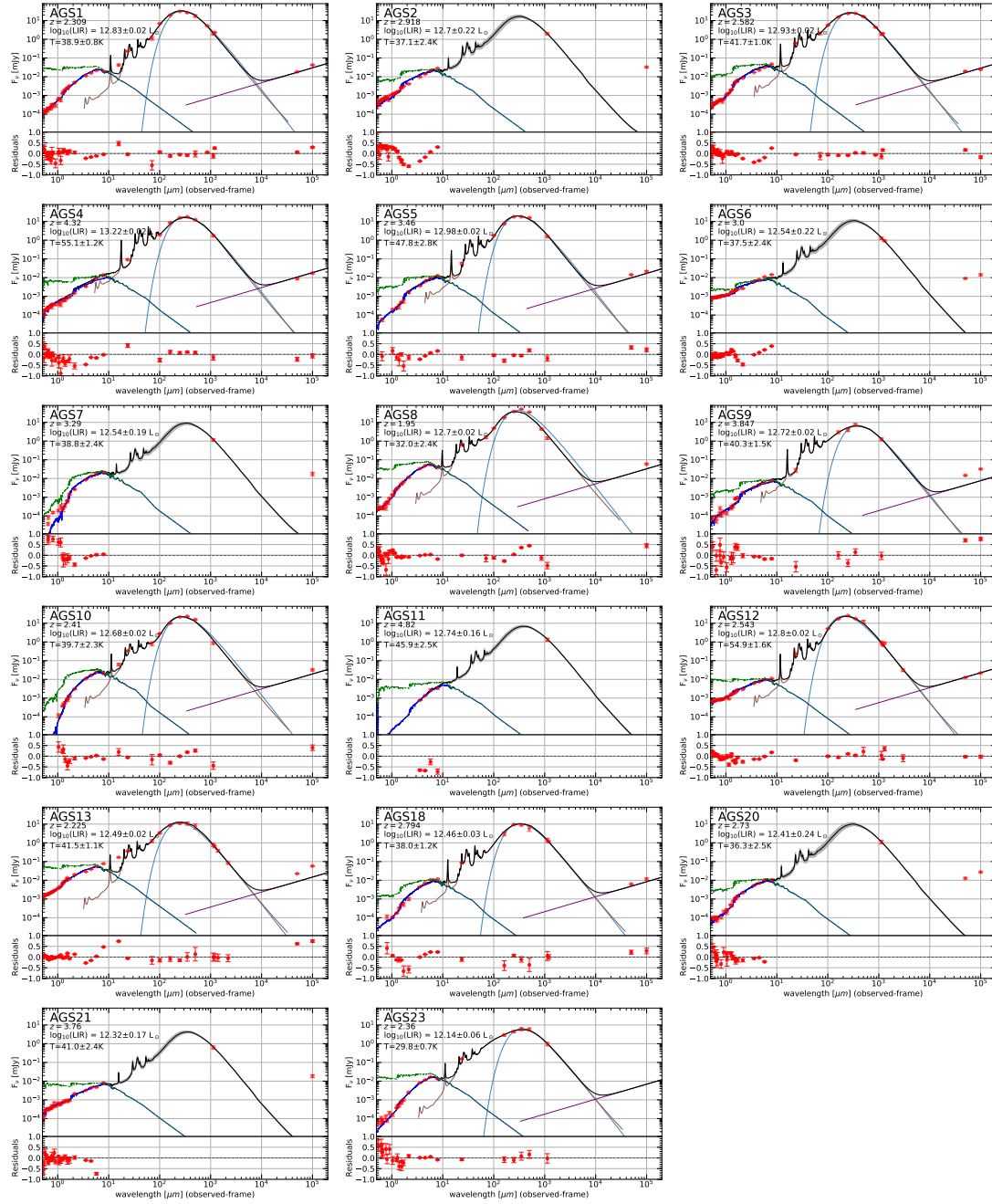


FIGURE 8.11: Optical to radio Spectral Energy Distributions created using the CIGALE code, for the main catalog galaxies. The UV and optical photometry is from the ZFOURGE catalog, the infrared measurements come from the *Herschel* catalog. The radio data at 5 cm is from [Rujopakarn et al. \(2016\)](#). The green (dark blue) lines fit the attenuated (unattenuated) stellar emission. The brown lines fit the dust emission and the purple fits the radio emission. The black is the sum of all emission components. The blue line shows the MBB fit. The lower panel shows the residuals between the observations and the model.

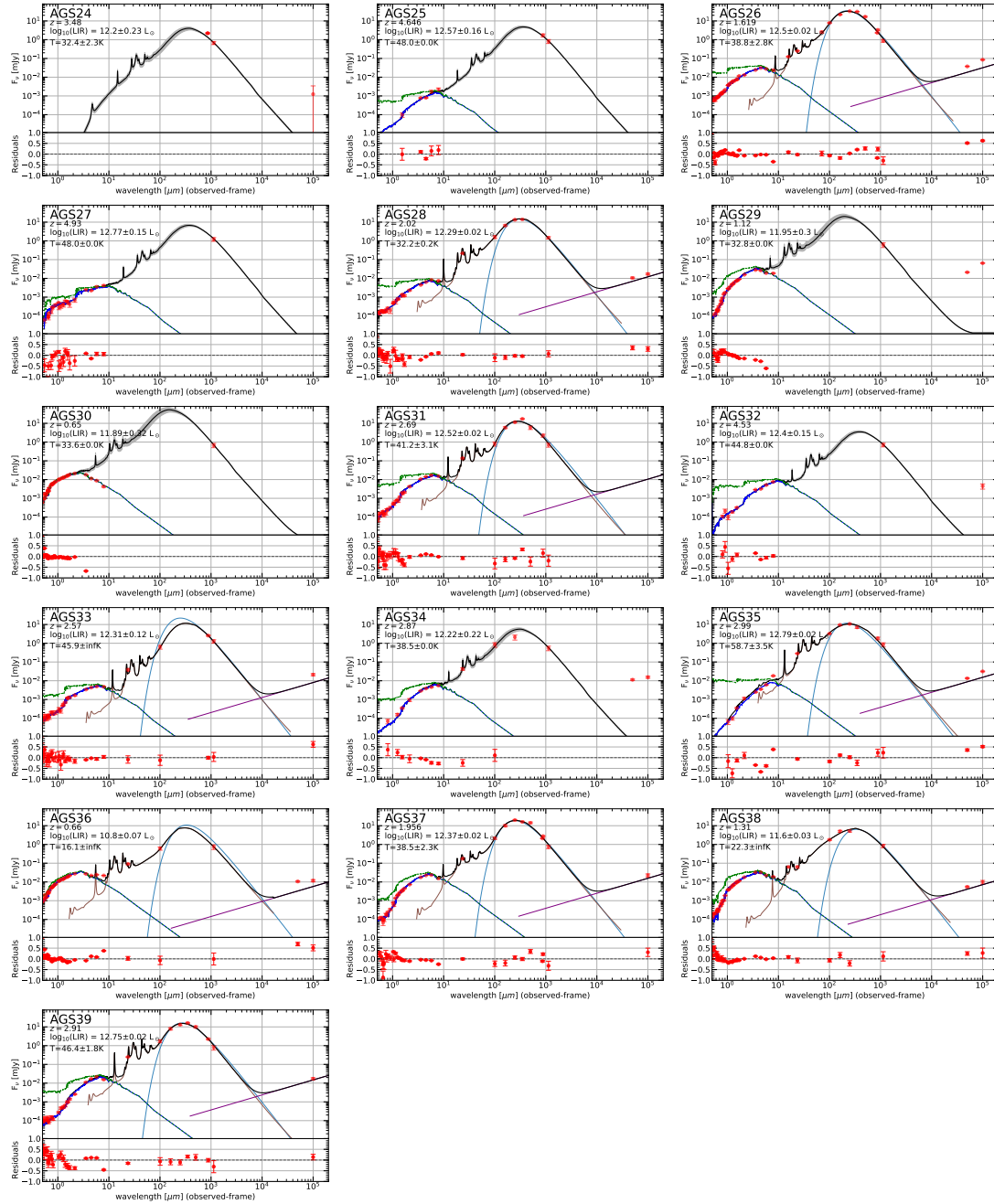


FIGURE 8.12: (continued).





My Ph.D. has focused on the study of galaxy infrared emission from the largest ALMA survey in the GOODS–*South* field. ALMA allows us to overcome the confusion limit that is present with the *Herschel* Space telescope, to reach greater redshifts while having an unprecedented resolution in this wavelength range. These observations are crucial to constrain the star formation history at high redshift, as they provide an unbiased view of star formation after the cosmic noon.

ALMA has been used mostly to observe previously known galaxies with individual pointings. Here we perform a different mode of operation by observing an entire region of the sky, in order to have an unbiased view of this region and to shed new light on these galaxies and their properties. This is not the first blind survey carried out with ALMA, but it is currently the largest in terms of area.

One of the potentially transformational outputs of ALMA is its ability to reveal a new class of galaxies through serendipitous detections. This is also one of the main reasons for performing blind extragalactic surveys. Less efficient than pointed observations using pre-defined priors, blind surveys can provide a complete view on this new parameter space, specific to ALMA.

My thesis was divided into three main steps: the creation of a source catalog, the study of galaxy counts and the determination and analysis of galaxy properties.

### 9.0.1 Catalog creation

In the first part this manuscript we explained the motivations of submillimeter observations, the challenges and of the state of the art in the field, outlined the history of the deep fields in astronomy and in particular explained the genesis of the GOODS–*South* field, and why it was selected to be observed with the large interferometer ALMA. We also presented our survey design and the data reduction, as well as the combination of the six slices of our survey to create an homogeneous image. Although the native resolution of the survey was  $0.2''$ , we note that  $0.2''$  was not the requested resolution. We decided to work almost exclusively in a map tapered at  $0.6''$  to reduce the number of independent beams and thus reduce the number of purely statistical spurious detections, and also prevent the resolution of extended sources.

We analyzed the image to define detectability thresholds and indicators that could quantify the reliability of these detections. After comparing the performance of different source extraction tools, we created a catalog of 23 sources. We also attempted to estimate the size of the galaxies in order to verify whether or not they were resolved, and therefore whether the peak flux was a good estimator of the total flux or if, on the contrary, it was necessary to integrate this flux.

The average rms sensitivity of the  $0''60$ -mosaic is  $\sigma \simeq 0.18 \text{ mJy.beam}^{-1}$  (but varies within the six slices of the survey), and the 1.1mm flux densities of the galaxies range from 0.64 to 2 mJy. The

detection limit was set to  $S/N \geq 4.8$  due to the large number of independent beams that leads to spurious detections that become rapidly more numerous than the number of robust detections below this threshold, despite the tapering at  $0''60$ .

Despite this high detection threshold, we identified three sources that we considered to be spurious detections (indicated by an \* in Table 4.2). Finding 3 spurious detections out of 23 detections matches the expected number of spurious sources obtained from the difference between positive and negative peaks above the  $4.8\sigma$  level ( $4 \pm 2$ ). These three sources are the only ALMA detections we find without any sign of an IRAC counterpart at  $\lambda = 3.6$  or  $4.5 \mu\text{m}$  (Spitzer/IRAC channels 1 and 2), despite the ultra-deep IRAC data in this field (26.5 AB mag, Ashby et al. 2015).

The galaxies detected by ALMA are among the most massive galaxies present in the GOODS-ALMA field of view. All detected galaxies have a stellar mass  $M_* > 5 \times 10^{10} M_\odot$ . The median stellar mass of our catalog is  $M_* = (1.1 \pm 0.4) \times 10^{11} M_\odot$ .

We are pushing the blind detection of massive galaxies with ALMA further in redshift. The sources exhibit flux densities ranging from 0.6 to 2 mJy, and have a median redshift of  $z = 2.92 \pm 0.20$ . By comparison with deeper but smaller ALMA extragalactic surveys (Aravena et al. 2016; Dunlop et al. 2017; González-López et al. 2017; Ueda et al. 2018), our redshift distribution is shifted to higher values even though our survey is shallower. This is due to the low surface density of massive, metal-rich (and hence dust-rich) galaxies at high redshift. We show that the size of the ALMA survey is, therefore, a key parameter to detect high redshift galaxies.

### 9.0.2 Number counts

Due to the limited number of detections and uncertainties on the redshifts, it was not possible to derive luminosity functions. We have therefore carried out counts whose calculation depends only on the flux of galaxies (and detailed insight of the biases related to the image).

The derived differential and cumulative number counts of our 20 primary detections have allowed us to partly alleviate the degeneracy observed above  $1 \text{ mJy.beam}^{-1}$  in previous (sub)millimeter studies. However, we note that due to our low detection rate, our uncertainties on the number counts are relatively high.

This work allowed us to derive the number counts at 1.1 mm using our survey and the main surveys carried out at (sub)-millimeter wavelengths. We modelled them with both a Schechter function and a double power law. We note that the faint-end of the number counts was done using a cluster, taking advantage of lensing. Fujimoto et al. (2016) reached sources down to  $\sim 0.02 \text{ mJy}$  with an ALMA survey at 1.2 mm. Semi-analytical models such as Popping et al. in prep., coupling the UniverseMachine Behroozi et al. (2019) with empirical and theoretical relations on the dust emission, are in good agreement with the trends found for galaxies with fluxes of  $> 0.1 \text{ mJy}$  but present flattening for lower fluxes. This may mean that the faint-end of the number counts over small and lensed regions may not be extrapolated to all number counts.

The number counts show that  $\sim 15\%$  of the extragalactic background light at 1.1 mm is resolved into discrete sources at 0.75 mJy. By extrapolation,  $\sim 50\%$  of the EBL is resolved at 0.1 mJy.

### 9.0.3 HST-dark galaxies

The recent discovery of a population of galaxies previously undetected by the Hubble Space Telescope (e.g., Wang et al., 2016; Elbaz et al., 2018; Schreiber et al., 2018b; Franco et al., 2018; Yamaguchi et al., 2019a; Williams et al., 2019), has improved our understanding of the origin and formation of massive galaxies. These galaxies comprise 20% of the galaxies detected in GOODS-ALMA. Although these galaxies are undetected by the HST (at  $5\sigma$  limiting depth  $H=28$  AB at  $1.6\ \mu\text{m}$ ), they are detectable through their thermal dust emission thanks to the depth and capabilities of ALMA. We were recently able to detect an HST-dark galaxy using data from only 8 ALMA pointings (Elbaz et al., 2018). This serendipitously-detected HST-dark galaxy suggests a blind detection rate of 1 galaxy per 8 pointings, similar to the 20% of HST-dark galaxies found among the galaxies detected by ALMA in Franco et al. (2018).

Among the 6 HST-dark galaxies for which we were able to determine masses and redshifts, there appear to be two distinct trends. Galaxies AGS4 and AGS24 are among the most massive of all active uvj galaxies detected in the region covered by the ALMA survey. AGS4 has a mass  $M_* = 2.81^{+1.65}_{-1.03} \times 10^{11}$ . In other words, it is the most massive galaxy at  $4 < z < 5$  in our catalogs. AGS24 has a stellar mass  $M_* = 1.82^{+0.27}_{-0.50} \times 10^{11}$ . Two HST-dark galaxies are at intermediate mass, but with a redshift greater than 4.5 (see Fig. 6.12) and for the two remaining galaxies, neither the mass nor the redshift have been estimated for the moment.

We have only a relatively poor statistic on these HST-dark galaxies, but they appear to be clustered. Several of these galaxies (AGS11, AGS15, AGS17, and AGS24) may be at the same redshift,  $z \sim 3.5$ . The position of one of these galaxies, AGS24 at the center of the overdensity, as well as its mass, make this galaxy a candidate of a future bright cluster galaxy (BCG) or central dominant (cD) galaxy (Zhou et al., in prep). Several additional observations will be necessary to characterize this structure, and we successfully proposed for ALMA observation time (project ID: 2018.1.01079.S; PI: M. Franco). We have received the first results, and the analysis of these data will be done in the coming months.

These HST-dark galaxies do not appear to be a marginal population of galaxies when considering massive, star-forming galaxies at high redshift. A recent study that systematically analyzed HST-dark galaxies (Wang et al., 2019) shows that the contribution of HST-dark galaxies to the SFRD appears to be dominant for galaxies with  $\log_{10}(M_*) > 10.6$  (Wang et al., 2019).

### 9.0.4 Using IRAC priors to probe fainter millimeter galaxies

We presented a new method for finding sources, involving lowering the detection limit. This method, based on previous detections in Spitzer/IRAC channel 1 (complemented by HST/WFC3  $H$ -band data and an ultra-deep  $K_s$ -band image) made it possible to lower the search threshold from  $4.8$  to  $3.5\ \sigma$ . These detections were reinforced, a posteriori, by a statistical study of the distribution of all detections at  $3.5\sigma$  in our image as well as a control sample. This method gives rise to the detection of 16 supplementary sources. The range of S/N for these sources is  $3.6$ - $4.6\sigma$ . We also note the presence of two low redshift sources at  $z < 1$ , which were not present in F18. The sources presented in this catalog are generally less compact than the sources presented in F18.

We have presented a detailed review of astrometry in the GOODS-South field. In addition to a systematic offset between HST and ALMA ( $\Delta\alpha = -96 \pm 92$  mas and  $\Delta\delta = 253 \pm 107$  mas), we

highlight the presence of a local offset, which can reach  $0.15''$  at the edge of the GOODS-ALMA field.

### 9.0.5 Galaxy properties

Using multiwavelength coverage from the CANDELS program, we derived properties of galaxies detected with ALMA in the GOODS-ALMA field. We explored some of the main parameters driving the star-formation in these galaxies.

After verifying that the galaxies detected by ALMA were not biased towards galaxies with abnormally cold dust (which would have favored their detection), we took advantage of both the new Herschel deblended catalog to derived  $L_{IR}$  as well as the  $L_{UV}$  by modelling the SEDs of the galaxies. This allowed us to derive the star formation rates of the galaxies. We find that the majority of the galaxies detected have an infrared luminosity  $\geq 10^{12} L_{\odot}$ . The majority are starburst galaxies, with a star formation rate greater than 3 times that of the main sequence. The remaining galaxies populate the upper part of the main sequence.

We showed that we are confronted to a heterogeneous population of galaxies, with a significant part of this sample having an abnormally low gas fraction. We see a link between the fraction of gas and the stellar mass of the galaxies. The more massive a galaxy is, the smaller its gas fraction will be.

We have also studied the sizes of galaxies. Unlike other studies that selected the galaxies to be observed with ALMA to be particularly compact in  $H$ -band, and linked these galaxies (blue nuggets) to compact and passive galaxies, we have shown that the galaxies in our sample have standard  $H$ -band sizes (they follow the trend defined by [van der Wel et al. 2014](#)), while they are more compact in ALMA. The ALMA sizes are, for the most part, comparable with the sizes of passive galaxies with the same mass and redshift. Moreover, we have seen that the most massive galaxies in our sample are also the most compact. We confirmed that there is a link between the depletion time ( $\tau_{dep} = M_{gas}/SFR$ ) and the star formation rate ( $\Sigma_{SFR}$ ). This demonstrates that the more compact the star-forming region is, the more efficient the galaxy will be in transforming its gas into stars and the shorter its lifetime (in the absence of replenishment) will be. Looking at the X-ray emission of the galaxies, we found that galaxies with strong X-emission ( $L_X > 10^{43}$  erg.sec $^{-1}$ ) i.e., which most probably host an AGN, are also the most compact galaxies, both in  $H$  and with ALMA, and also have the lowest  $\tau_{dep}$ . All of the conditions are met for these galaxies to be the progenitors of passive galaxies at  $z \sim 2$ . At the same time, their masses are already comparable to the masses typical of passive galaxies. Their high star formation rates can not be sustained over a long period, or the galaxies would reach stellar masses that we have never observed for galaxies at  $z=3$ . Their concentrated star formation is also consistent with a morphological transformation of galaxies, with an increase in the Sérsic index due to increasing the surface brightness at their centers. The questions that now arise are which mechanisms concentrate the gas towards the centre of the galaxies and cause their death, to understand whether this can be explained by hydrodynamic instabilities, to explain more clearly the role of mergers and the environment in this compaction mechanism, to investigate the role of AGN at the end of a galaxy's life by better understanding positive and negative feedback from AGN, and their role in preventing the replenishment of galaxies, as well as studying other scenarios that make galaxies more compact.

## Contents

---

The work of this thesis opens many perspectives. In this thesis, we have presented the results of a survey carried out with ALMA with a native resolution of  $0.24''$ . This resolution was not the resolution originally requested ( $1''$ ), which forced us to adapt our methodology by using techniques such as tapering. Tapering effectively enlarges the size of the beam, which allows us both to reduce the number of independent beams, thus reducing the number of purely statistical spurious detections, and also prevent the resolution of extended sources. Unfortunately, tapering also degrades the sensitivity of the observations.

In the last months of the thesis, the data from the same survey were delivered at the originally requested resolution. In this section, we will present the work we can carry out with this new map, how we can combine it with the high resolution image, and combine it with the different ALMA surveys done in the GOODS-*South* field. We will also see how we can use both of our resolutions to infer the properties of galaxies, and then present two projects. The first is to resolve the dust emission in a clumpy galaxy, and the second is to carry out a complete census in mass in the GOODS-ALMA field. Finally, we will briefly discuss the opportunities that will be offered in the coming years with the new generation of instruments (including the James Webb Space Telescope; JWST) and explain how our work can help prepare for these new fields of exploration.

## 10.1 Lower resolution image

We have recently received data from the same region of the sky as presented in this thesis, but at the originally requested, lower resolution ( $\sim 1.2''$ ). In the rest of this chapter, we will call this image the “low-resolution” image, while the term “high-resolution image” refers to the image we analyzed in this Ph.D.

We have combined the high-resolution and low-resolution images to increase the sensitivity of the image. The theoretical rms of the combination of several images is obtained using the following formula:

$$\sigma^2 = \left( \sum \frac{1}{\sigma^2} \right)^{-1/2} \quad (10.1)$$

The low-resolution map has a beam varying from  $1.2''$  to  $1.5''$ , depending on the slice. To take full advantage of the potential of these two maps, we have tapered them in order to have a circularized beam corresponding to the lowest resolution, i.e.,  $1.5''$ . To analyze this data in

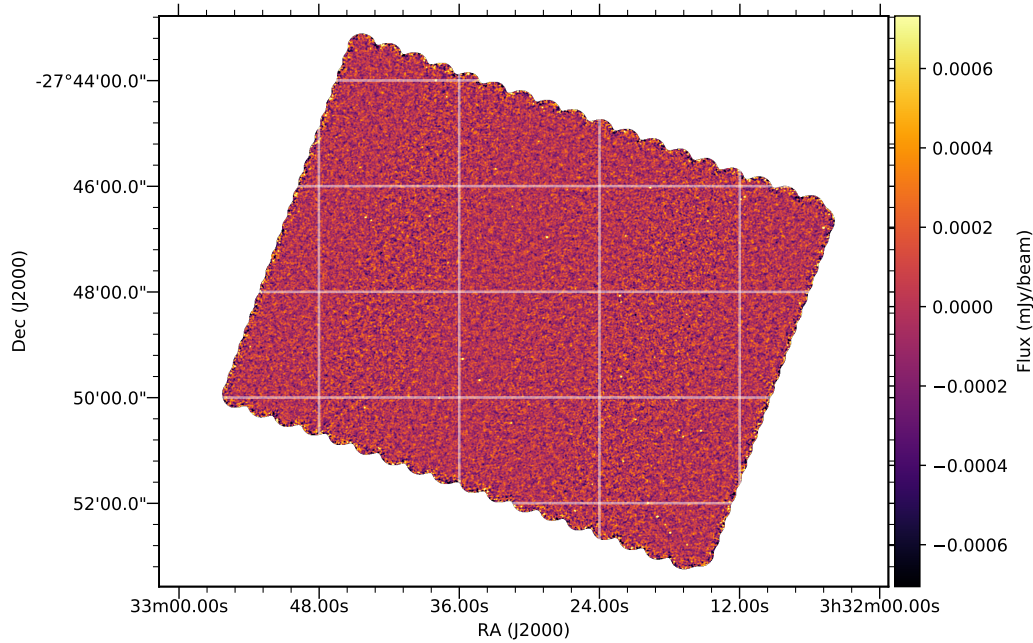


FIGURE 10.1: ALMA 1.1 mm image of the map combined high- and low-resolution images, tapered at 1.5" and cleaned.

the image plane as well as possible, we have cleaned the data using the task *tclean* of CASA, with natural weighting and a cell size of 0.2". We also produced a noise map using the same technique explained in Sect. 3.6 (sigma-clipping). The result of the combination the high and low resolution data is shown in Fig. 10.1. We can see that the difference between the distributions allows us to detect approximately three times more sources, and lowers the detection threshold before the number of negative sources rises drastically.

To get an initial idea of the number of detectable sources in this new image, we compared the detection numbers as a function of the threshold, in both the image and the inverse image (continuum map multiplied by -1). The purity index of 80% is reached at  $\sigma_p = 4.4$  with 57 positive detections against 11 negative ones. In Fig. 10.2, we show the histogram of the two distributions (positive and negative detections) that we put in perspective with the source distribution found in the low-resolution map (0.6").

In addition, high- and low-resolution maps can be used separately to probe the distribution of dust within the galaxy, and also to more easily constrain galaxy sizes.

The analysis of galaxies that have been missed in the high-resolution survey but detected in the low-resolution survey will also give us information both on the bias of our survey, and also on the evolution of the sizes of galaxies with redshift. It will give us information on the proportion of compact galaxies among massive galaxies and will give us a finer insight into the relationships between galaxy size, depletion time, the presence of an AGN and the gas fraction of galaxies.

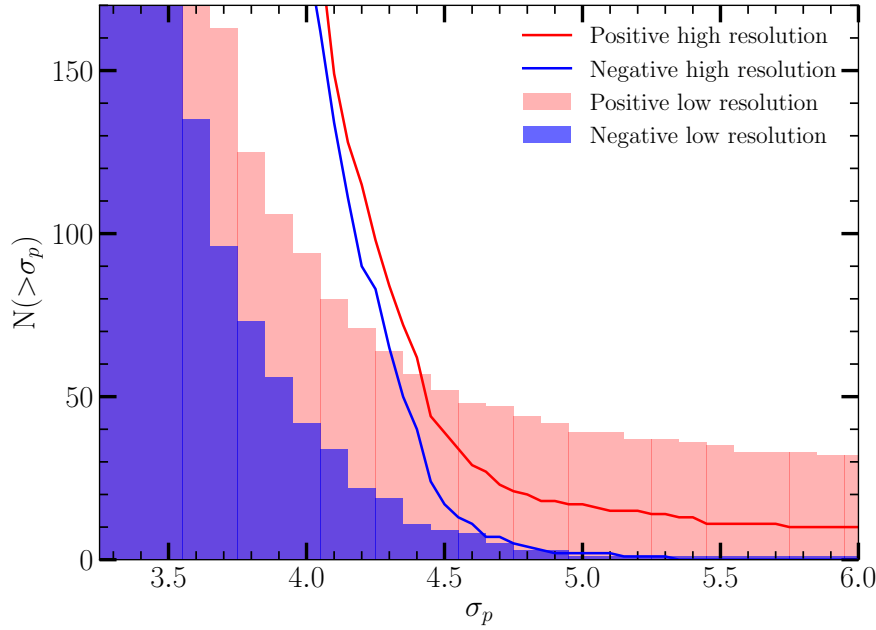


FIGURE 10.2: Cumulative number of positive (red histogram) and negative (blue histogram) detections as a function of  $\sigma_p$  (at fixed  $\sigma_f = 2.7$ ), in units of  $\sigma_f$  in the combined map. For comparison, the distribution of negative and positive sources in the 0.6'' map is also shown with red and blue lines.

These maps, separated into both low and high resolution, will also allow in some cases to understand better the offset that can exist between the IR emission and the UV emission of galaxies.

## 10.2 Combined GOODS–*South* ALMA surveys

In addition, we have combined the different ALMA surveys that have been carried out in the GOODS–*South* field to create the deepest possible ALMA image of this region (see Fig. 10.4 and Fig. 10.3). The image is comprised of 2494 pointings, combining the HUDF (Dunlop et al., 2017), ASAGAO (Hatsukade et al., 2018) and GOODS-ALMA (this work) surveys. This deep image can be used to further develop the analyses presented in this thesis, and in particular to calculate the star formation rate density based on the infrared emission of galaxies, and better constrain the evolution of the SFRD to redshifts greater than 3.

To conclude, the study of IR emission with ALMA of high redshift galaxies has motivated us to investigate two different directions using opposite methods. One is a systematic method to investigate all galaxies within  $2 < z < 6$  with a stellar mass above  $M_* > 5 \times 10^{10} M_\odot$ . We want to avoid selection bias and have a complete picture of this category of galaxy. The second direction is to focus on a single galaxy located at  $z \sim 2.8$  that is partially extended and clumpy, so that the obscured star formation inside the clump of this high redshift galaxy can be analyzed in detail, and the dust distribution can be investigated. It is these two projects that we will present in this last part of this thesis.



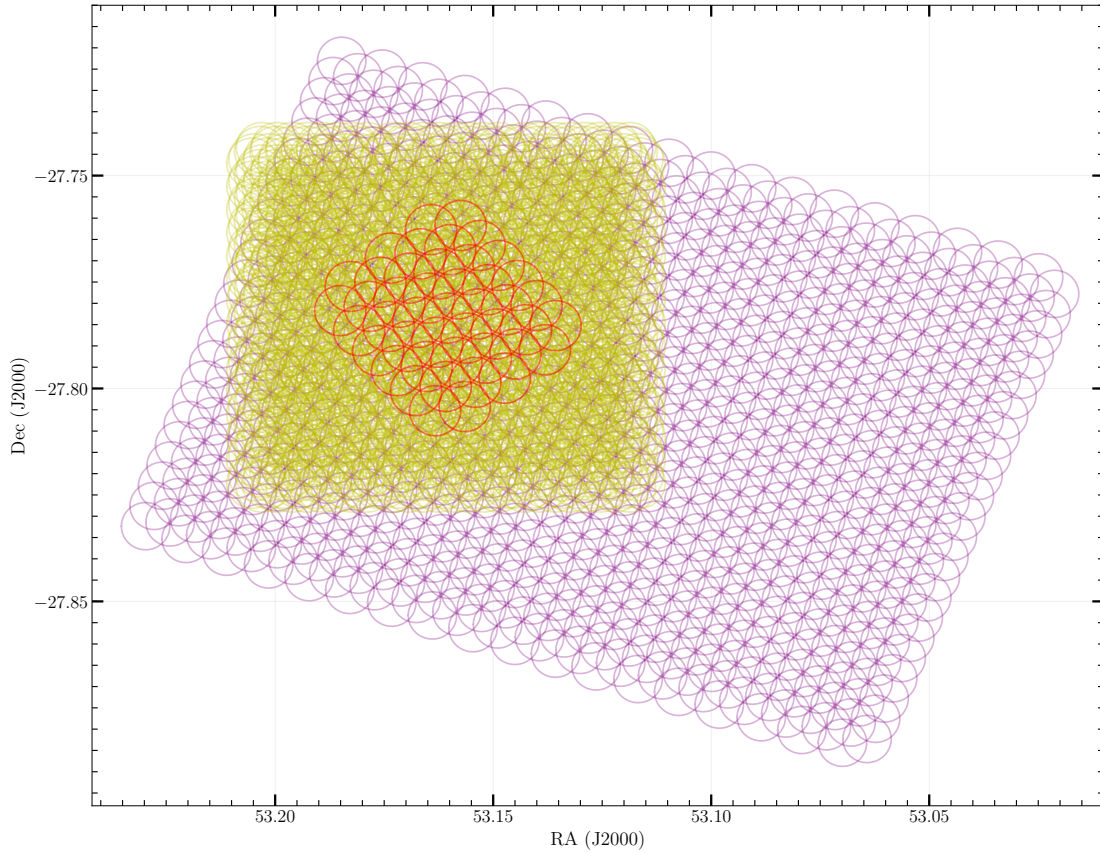


FIGURE 10.3: Visualization of the 2494 pointings comprising the image created by combining the HUDF (Dunlop et al., 2017), ASAGAO Hatsukade et al. (2018) and GOODS-ALMA Franco et al. (2018) surveys. The 45 pointings from the HUDF are shown in red, the 1602 pointings from ASAGAO are shown in yellow and the 847 pointings from GOODS-ALMA are shown in purple.

### 10.3 Resolving the dust emission in a clumpy galaxy

During the exploration of the largest extragalactic blind survey with ALMA in the Great Observatories Origins Deep Survey–*South* (GOODS–*South*) field (2017.1.00755.S; PI: D. Elbaz); we detected and partially resolved the ALMA emission of one particularly extended and clumpy galaxy in the continuum at 1.13mm. We see that the clump emission is extended, as we have a significantly stronger detection when we integrate over the elongated clump region, compared when we consider the clumps as individual sources. The overarching question is now whether the clumps are physically associated, or if there is simply diffuse emission present between them. If there is indeed a physical association between the IR clumps and the UV clumps, this would be the first detection of a galaxy where the majority of the dust-attenuated star formation (and therefore the total SFR) is coming from the clumps. This would mean that a significant part of the mass of galaxies could be generated in clumps, thus contributing to the growth of the galactic bulge without requiring major mergers.

Clumpy galaxies are prominent in the early Universe ( $z > 2$ ; Förster Schreiber et al. 2006; Elmegreen 2007) and the clumpy structures are present for all galaxy types (Elmegreen et al., 2009). One of the questions that arise is whether there is a spatial correlation between UV clumps and gas reservoirs. Although the definition of clumps is still uncertain, the typical stellar mass ( $M_*$ ) of clumps is between  $10^8$  until  $10^9 M_\odot$  (e.g., Elmegreen, 2007; Guo et al., 2012,

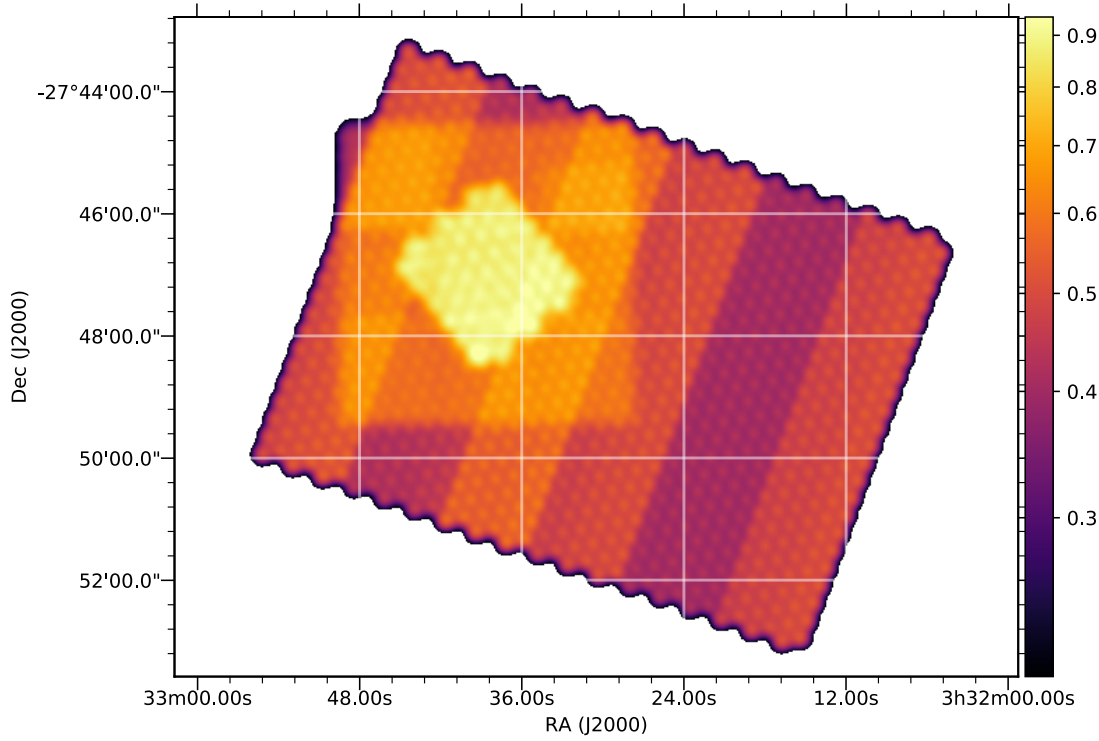


FIGURE 10.4: Primary beam coverage of the combined GOODS-ALMA, ASAGAO and HUDF-ALMA maps.

2015), and with typical sizes from few 100pc to 1kpc (e.g., Elmegreen, 2007; Livermore et al., 2012). Clumps can represent between 20 and 50% of the total star formation rate (SFR) of the galaxy (e.g., Förster Schreiber et al., 2011). The study of clumps is essential to understand the evolution of galaxies, the bulge formation, star formation mechanisms, and the growth of the supermassive black hole.

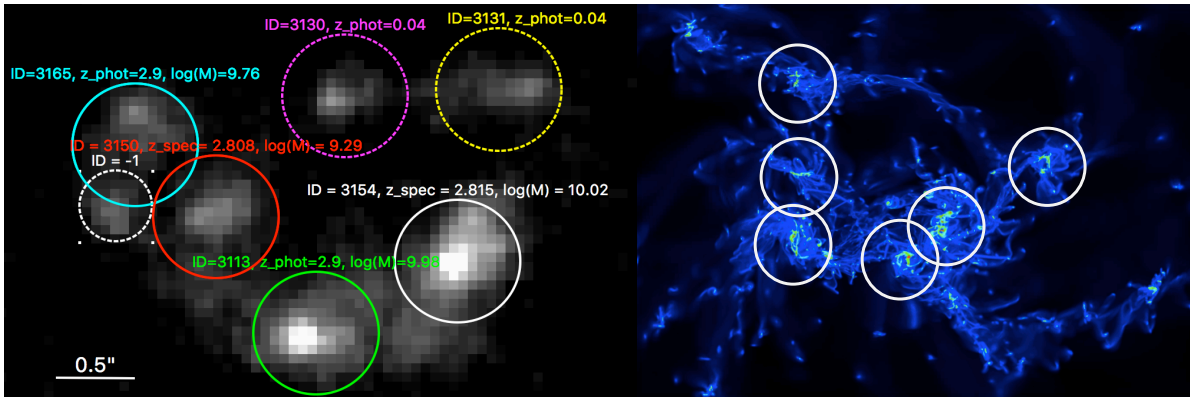


FIGURE 10.5: *Left panel:* HST/*H*-band image of the galaxy. The seven major clumps are shown with (dashed for less certain redshifts, solid for more secure redshifts) color circles. The CANDELS ID Guo et al. (2013), the redshifts (photometric or spectroscopic) and the stellar masses (Chabrier IMF) are shown for each galaxy. *Right panel:* Simulation representing the gas within all the galaxy (~20kpc). Image from Frederic Bournaud.

Until now, the vast majority of clump studies were carried out at UV wavelengths (e.g., Förster Schreiber et al., 2011; Guo et al., 2012). ALMA's sensitivity and resolution now make it possible to explore sub-galactic scales in the (sub)millimeter wavelengths. This new space of observation

parameters reveals contradictory results to previous studies. While Iono et al. (2016), Oteo et al. (2017) or Hodge et al. (2019) show evidence that a part of dust emission ( $\sim 2\text{--}20\%$  of the total continuum emission in Hodge et al. 2019) comes from clump-like structures, others such as Gullberg et al. (2018) or Rujopakarn et al. (2019) find a remarkably smooth distribution of cold dust emission within of a galaxy. Recently, Cibinel et al. (2017) showed for a galaxy at  $z = 1.5$  that the CO(5-4) emission was undetectable down to the 3% level from the UV-bright clumps. We propose to use ALMA to probe the rest-frame emission at  $\sim 240 \mu\text{m}$  of a particularly extended (diameter of  $3''$  in  $H$ -band) and extremely clumpy galaxy. We want to use the accuracy of the ALMA observations to map the dust emission of this galaxy and quantify the infrared luminosity, the gas content ( $M_{\text{gas}}$ ) and the star formation efficiency ( $\text{SFE} = \text{SFR}/M_{\text{gas}}$ ) of the clumpy regions compared to the non-clumpy regions of the galaxy.

### 10.3.1 A galaxy at $z=2.81$ that may be forming the bulk of its stars in well-separated clumps

This galaxy is an ideal observational laboratory to study clumps. Indeed this galaxy is unusually large - its diameter, derived from a Hubble Space Telescope (HST)-WFC3 image at  $1.6 \mu\text{m}$ , was estimated to be  $\sim 3''$ , corresponding to a physical size of  $\sim 25 \text{ kpc}$  at  $z = 2.81$ . The clumps are distant from one another, which excludes any blending (see Fig. 10.6).

This galaxy has a redshift ( $z_{\text{spec}} = 2.81$ ) that is ideal to understand the crucial phase of the bulge formation. In addition, this galaxy presents no AGN contamination from the 7 Ms Source Catalogs (Chandra Deep Field-South Survey; Luo et al. 2017). This means that the star formation rate derived from infrared luminosity is most likely reliable.

This galaxy is located in the deepest part of the CANDELS field, and therefore benefits from excellent multiwavelength support. A first analysis shows that the 5 major clumps of this galaxy have different colors and therefore different dust obscurations. Indeed we can divide these clumps into two categories: the two southernmost clumps of the images are brighter in UV and redder than those present in the northern part. By studying this galaxy, and only one galaxy, we have the opportunity to analyze several types of clump. For 4 of these 5 clumps, redshifts and masses have been determined. Two of these redshifts have been confirmed by the instrument VIMOS as part of the VLT/VIMOS spectroscopy in the GOODS-South field Balestra et al. (2010), at  $z = 2.808$  and  $z = 2.815$  respectively. The photometric redshifts of the other two clumps are compatible with these measurements, at  $z = 2.94$  and  $z = 2.93$ . Finally, neither the redshift nor the mass of the easternmost clump was determined. In addition, in the northern part, we also see two extra blobs, which are either a projection effect (redshifts have been measured at 0.041 and 0.036 respectively), or these redshifts are incorrect, and the two blobs are also part of the structure. Observation with ALMA will give us decisive information to distinguish between these two hypotheses.

The majority of galaxies studied with ALMA at high redshift to reveal clumps have been particularly massive galaxies ( $M_* > 10^{11} M_\odot$ ; e.g., Hodge et al. (2019)) or lensed (e.g., the Cosmic Snake; Cava et al. 2017). The galaxy targeted here, with a smaller mass ( $M_* = 3.6 \times 10^{10} M_\odot$ ; Chabrier 2003 IMF) will allow us to shed new light on less extreme galaxies.

In addition to a first estimation of the flux, thanks to SED fitting (uncertain due to uncertainties on the data near the peak of the SED at  $\sim 300 \mu\text{m}$  (observed-frame); see right panel of Fig. 10.6),

we have also been able to estimate the integrated flux from a new mosaic of the GOODS-ALMA field, observed with a resolution of  $1'' \times 2''$  imaging over  $6.9' \times 10'$  (2017.1.00755.S, PI: D. Elbaz).

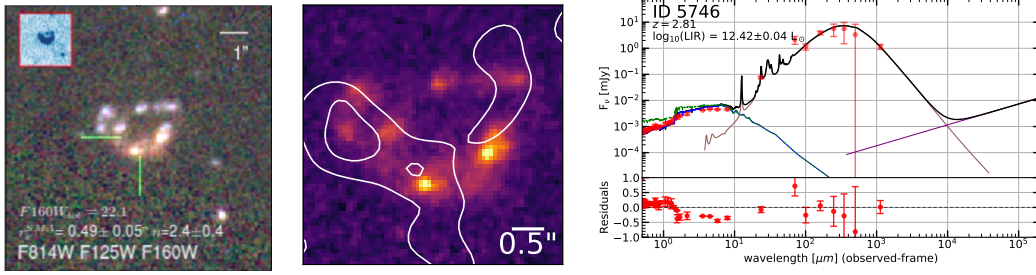


FIGURE 10.6: **Left panel:** RGB (F814W, F125W, F160W) color image of the studied galaxy (image from: <http://zfourge.tamu.edu/>). **Middle panel:** ALMA 1.1mm (white) contours ( $2-3\sigma$ ) overlaid on HST *H*-band images. **Right panel:** Spectral Energy Distribution (SED) of the galaxy using the SED fitting code CIGALE (Noll et al., 2009) and the photometry from the ZFOURGE catalog (Straatman et al., 2016).

Thanks to this object with ideal properties to study the clumps of galaxies, we plan to compare the number of UV clumps to the number of IR clumps. We would also like to derive the percentage of IR luminosity (and therefore the SFR) that comes from clumpy regions in comparison to the total infrared luminosity of the galaxy. We will also be able to determine the mass of dust and therefore the mass of gas. We will then calculate the proportion of gas inside these clumps and compare to simulations (see Fig. 10.7 and Fig. 10.8).

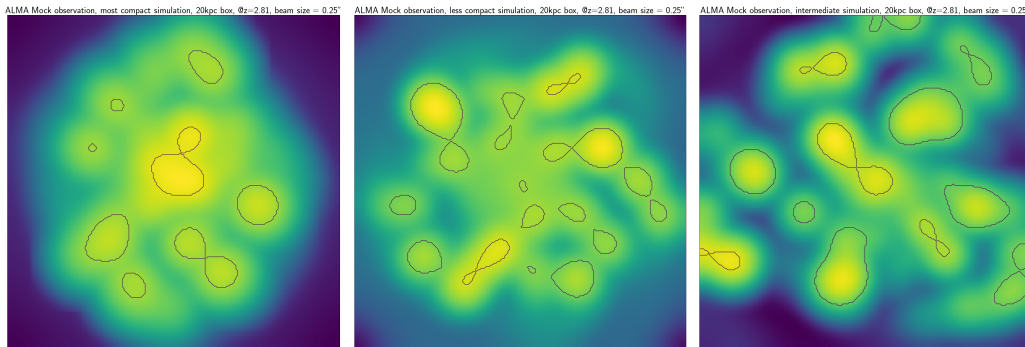


FIGURE 10.7: From **left to right**: Mock observation of three different galaxies of different compactness seen at  $z=2.81$  and with a  $0.25''$  beam. The mock image represents the gas density of the galaxies, realized without any dust emission or absorption, and a face-on view of the galaxy. From left to right: Compact, less compact and intermediate compactness. The galaxies were simulated with the RAMSES hydrodynamical simulation code (Teyssier, 2002). Each box is 20kpc wide. The black contours represent the clumps found by a clump finder algorithm.

We would also like to derive spatially resolved UV ( $\beta$ ) from the HST images and compare the slope of  $\beta$  to the different IR emission regions. We plan to map the excess IR emission in the galaxy and compare it to existing studies (e.g., Gómez-Guijarro et al., 2018) and models (e.g., Meurer et al., 1999). We plan to quantify the star formation efficiency ( $SFE = SFR/M_{gas}$ ) for each clump and compare it to other non-clumpy regions of the galaxy, and measure how the star formation rate within clumps deviates from the Schmidt-Kennicutt relation (Zanella et al., 2015). Simulations predict different signatures and clump shapes seen by ALMA, depending on the formation scenario of the galaxy. If the clumps are made of cold gas, a hierarchical formation of clumps will take place, i.e. the small clumps will gradually grow and form larger clumps in size (e.g., Bournaud et al., 2007; Inoue et al., 2016). On the other hand, if clumps are formed



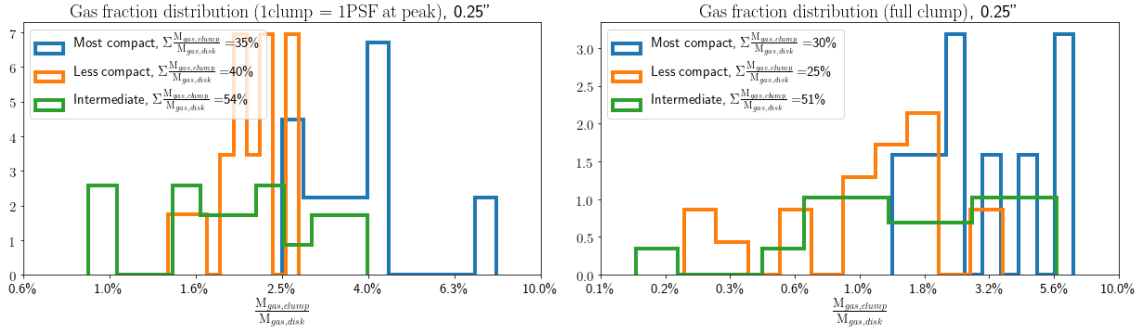


FIGURE 10.8: Distribution of the number of clumps detected by a clump finding algorithm (see Fig. 10.7) as a function of the ratio of the  $M_{\text{gas}}$  contained in a clump (psf size, **left panel**; full clump, **right panel**) over the total  $M_{\text{gas}}$  of the disk. This distribution was performed on a mock catalog of galaxies simulating compact galaxies (blue distribution, less compact, orange distribution, and intermediate, green distribution). The cumulative proportion of the mass of gas contained in all detectable clumps in the galaxy is shown in the insert at the top of the figure.

from hot gas, the opposite scenario is preferred - large structures will fragment and form small clumps. ALMA's resolution is sufficient to favor one hypothesis over another.

## 10.4 Complete census in mass

We propose to reach a complete census on the dusty star formation rate (SFR) of all galaxies within  $2 < z < 6$  with a stellar mass above  $M_* > 5 \times 10^{10} M_\odot$  (red and green dots in Fig. 10.9) in the GOODS-ALMA field. This individual source follow-up will complement the existing ALMA detections that were obtained from the largest extragalactic blind survey covering the deepest part of the CANDELS field (*HST*–WFC3), in the Great Observatories Origins Deep Survey–*South* (GOODS–*South*) field over  $6.9' \times 10'$  (GOODS-ALMA, 2015.1.00543.S, PI: D. Elbaz, [Franco et al. 2018](#)), as well as all existing pointings in the field available in the ALMA archives. All star-forming galaxies in this mass and redshift range were predicted to exhibit flux densities above the  $4\sigma$  survey limit and yet only 13 % of them were detected. This survey is the largest ALMA survey and was obtained with two angular resolutions 0.2'' (Cycle 3) and 1.2'' (Cycle 5). The analysis of the high-angular resolution survey identified massive star-forming galaxies preferentially located in the redshift range  $z = 2 - 4$  with a few galaxies at  $z > 4$  ([Franco et al., 2018](#)). Among the population of galaxies with  $M_* > 5 \times 10^{10} M_\odot$  – where the sensitivity limit of our survey allows us to detect typical SFR- $M_*$  main sequence galaxies at  $z = 2-4$  – we found that only 13% of them were detected even after selecting only the star-forming ones from the UVJ color-color diagram to disentangle passive and star-forming galaxies. We found that nearly all of the detected galaxies experienced extremely compact star-formation. In order to determine whether this was a physical property systematically found in this mass and redshift range, or whether it was related to selection effects (despite tapering at 0.6 arcsec), we analyzed the low-resolution survey of the same area at 1.2''. Thanks to the reduced number of independent beams, we were able to detect sources down to 1.7 times fainter flux limit, and surprisingly most of the newly detected ALMA sources fall below the mass limit of  $5 \times 10^{10} M_\odot$  showing that the missing sources were not missed because they were extended. This suggests that compactness truly is a universal property of the massive star-forming galaxies at these redshifts and that the dispersion of SFR in this mass and epoch range is larger than expected by the extrapolation of the SFR- $M_*$  main sequence. In order to test this hypothesis with strong implications on our understanding of

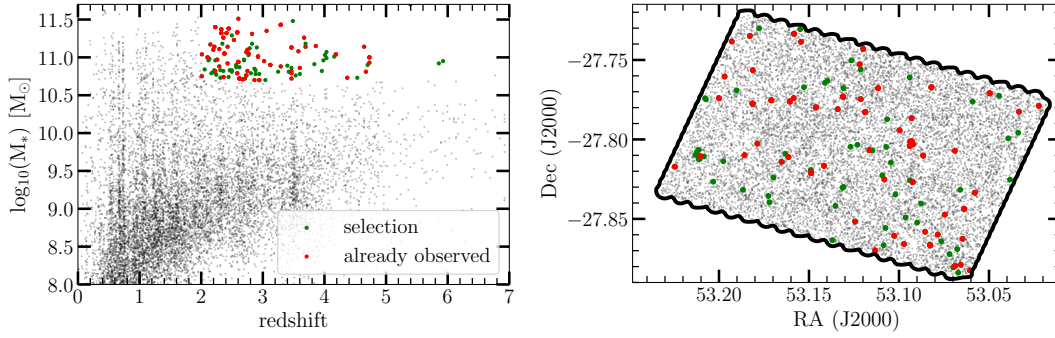


FIGURE 10.9: **Left panel:** Selection of the galaxies with  $M_* > 5 \times 10^{10} M_\odot$  and  $2 < z < 6$ . The black dots represent all of the galaxies in the GOODS-ALMA field. The green dots represent the selected galaxies in the mass and redshift range given above, while the red dots show the galaxies that have already been observed by ALMA (e.g., [Aravena et al., 2016](#); [Dunlop et al., 2017](#); [Franco et al., 2018](#); [Cowie et al., 2018](#); [Hatsukade et al., 2018](#)) and all the archive data. **Right panel:** Spatial position of the GOODS-ALMA survey (solid black line) and of the galaxies, with the same color-coding than the left panel. The black solid line indicates the boundaries of the GOODS-ALMA survey.

the formation of massive ellipticals, we now need to reach a complete census on this parameter space area.

The majority of the galaxies detected in GOODS-ALMA are compact –  $\sim 85\%$  have a size below  $0.25''$ , corresponding to a physical radius of 600 pc at  $z = 3$  ([Franco et al., 2018](#)) suggesting these massive dusty star-forming galaxies could participate to the origin of the massive elliptical galaxies at  $z = 2$ , which are also known to be compact. The analysis of the sizes of the galaxies detected in GOODS-ALMA are in agreement with the results of other recent studies (e.g. [Simpson et al., 2015b](#); [Barro et al., 2016](#); [Rujopakarn et al., 2016](#); [Ikarashi et al., 2017](#); [Fujimoto et al., 2017](#); [Tadaki et al., 2017](#); [Elbaz et al., 2018](#)).

This complete census of star-formation in massive high- $z$  galaxies will allow us to determine the rise of cosmic SFR density during the rise to cosmic noon ( $z \sim 2$ ), quantify the relative amount of obscured star-formation above  $z > 3$  where it is mostly unknown in a complete way, reach a large enough statistical sample to disentangle rapid quenching from slow downfall of star-formation in massive galaxies. The systematic study of massive galaxies ( $M_* > 5 \times 10^{10} M_\odot$ ) during this period of rapid transition between star-forming and quenched galaxies ([Muzzin et al., 2013](#)) is crucial to understanding the mechanism by which star formation ceases in these galaxies. We note that the need for such a wide area survey with ALMA is fundamental as demonstrated by the fact that the HUDF-ALMA survey ([Dunlop et al., 2017](#)) was highly inefficient in detecting distant galaxies most probably because the dusty distant galaxies need to be massive to be dusty, in order to maintain their metals from their deep potential well.

The fact that the majority of the missing galaxies with  $M_* > 5 \times 10^{10} M_\odot$  remain undetected even at the  $3\sigma$  level with the  $1.2''$  resolution suggests that either these galaxies are not as dusty as expected, hence that only a small fraction of the massive galaxies have the expected dust mass, or that they are forming stars with a SFR much below the MS despite being UVJ active. In both cases, this would change in a major way our understanding of star-formation in massive galaxies at  $z=2-4$ . This is the key epoch of the transition to cosmic noon from the higher-redshift side, and of the formation of the massive ellipticals that end up being largely found compact at  $z \sim 2$ . Hence it is truly important to understand whether there is a variety of such galaxies or whether, as suggested by the SFR- $M_*$  sequence, there is a universal star-formation

process in galaxies of a given mass and redshift range. It turns out that we found (papers in prep.) that the majority of the ALMA sources detected in this regime of mass and redshift were highly clustered, could this mean that the missing detections belong to galaxies less or more clustered. The most massive ALMA detection at  $z=3.5$ , AGS24, is an HST-dark source that we found to be located at the very center of an over-density of galaxies at  $z=3.5$ . This galaxy forms stars below the main sequence. The missing massive galaxies could also be those that experienced galaxy harassment, ram pressure stripping, and lost part of their gas reservoirs, in denser environments. They would then be useful tracers of high-density regions in the field. It may also be possible that at these masses and redshifts there is a high proportion of galaxies falling down from the MS, more than expected from the traditional 0.3 dex dispersion. This may be related to the building of what is often called the bending of the MS, in which galaxies at high masses exhibit lower SFR than the extrapolation of the MS slope. If we were able to show that there is a large dispersion of the SFR of galaxies in this mass and redshift range, much wider than expected by the MS, this would allow us to provide a statistical determination of the rapidity with which massive galaxies quench to become ellipticals. The timescale for this passage is fundamental to disentangle various models of massive galaxy formation such as compaction (e.g., Dekel and Burkert, 2014; Tacchella et al., 2015; Barro et al., 2017), major mergers versus minor mergers (Gómez-Guijarro et al., 2018), shock heating of the IGM (Dekel and Cox, 2006) or simply consumption of the internal gas reservoirs (and preventing further infall by eg AGN activity, cf Peng et al. 2010; Maiolino et al. 2004) by quantifying the relative fraction of massive galaxies in the process of secular downfall of star-formation versus rapid quenching through the number density of galaxies in the SFR- $M_*$  plan. This will allow us in the process to determine in a complete manner the cosmic SFR density of  $M_* > 5 \times 10^{10} M_\odot$  galaxies at  $z=2-4$  including galaxies that were HST-dark, found by our two surveys and that could not be followed-up from prior selection techniques. Starting from a systematic blind survey is critical in this analysis.

## 10.5 Preparing the next generation of survey

Several large (sub)millimeter surveys are planned or are currently being observed. For example, the NIKA2 camera at the 30m IRAM telescope is observing the GOODS-South field (160 arcmin<sup>2</sup>) and the COSMOS field (2000 arcmin<sup>2</sup>) for 300h, at two different wavelengths ( $\lambda = 1\text{mm}$  and  $\lambda = 2\text{mm}$ ). This is the “NIKA2 Cosmological Legacy Survey” (PIs: A.Beelen, G.Lagache & N.Ponthieu). Also, in the same way, the Large Millimeter Telescope (LMT), which is optimized for astronomical observations at millimeter wavelengths, has seen its diameter increase to 50m. This instrument is adapted, thanks to its observations mode, to carry out large surveys quickly. A Guaranteed Time Large Program was chosen to observe three of the CANDELS fields: UDS, COSMOS, and GOODS-South.

In the near future, the James Webb Space Telescope will be launched. The population of optically dark galaxies, missed by the HST, will be particularly interesting targets for the first JWST observations. Indeed, one of the objectives of the JWST is to reach more distant and fainter galaxies, including the epoch of reionization. The knowledge gained from the identification of galaxy counterparts and the identification of HST-dark sources in this study can be used to characterize the galaxies in the Extended Groth Strip (EGS), or those in the fields given above. EGS is at the heart of the Cosmic Evolution Early Release Science (CEERS) project, which is an Early Release Science (ERS) project of the James Webb Space Telescope (JWST). The JWST NIRCam



---

instrument will perform a mosaic of 10 pointings covering the majority ( $\sim 100$  arcmin<sup>2</sup>) of the EGS field. Over this region, we expect to find at least 10 HST-dark galaxies.

If other candidates of optically dark galaxies are discovered to be the central dominant galaxy in galaxy (proto-)clusters, this discovery may also change our understanding of these objects, especially in terms of the distribution of the mass within clusters, and the interactions between galaxies.



## BIBLIOGRAPHY

- Abazajian, K. N., Adelman-McCarthy, J. K., Agüeros, M. A., Allam, S. S., Allende Prieto, C., An, D., Anderson, K. S. J., Anderson, S. F., Annis, J., and Bahcall, N. A. (2009). The Seventh Data Release of the Sloan Digital Sky Survey. *ApJS*, 182(2):543–558.
- Abraham, R. G., Tanvir, N. R., Santiago, B. X., Ellis, R. S., Glazebrook, K., and van den Bergh, S. (1996). Galaxy morphology to  $I=25$  mag in the Hubble Deep Field. *MNRAS*, 279:L47–L52.
- Adam, R., Adane, A., Ade, P. A. R., André, P., Andrianasolo, A., Aussel, H., Beelen, A., Benoît, A., Bideaud, A., and Billot, N. (2018). The NIKA2 large-field-of-view millimetre continuum camera for the 30 m IRAM telescope. *A&A*, 609:A115.
- Adelberger, K. L. and Steidel, C. C. (2000). Multiwavelength Observations of Dusty Star Formation at Low and High Redshift. *ApJ*, 544:218–241.
- Akhlaghi, M. and Ichikawa, T. (2015). Noise-based Detection and Segmentation of Nebulous Objects. *ApJS*, 220:1.
- Alexander, D. M., Bauer, F. E., Brandt, W. N., Hornschemeier, A. E., Vignali, C., Garmire, G. P., Schneider, D. P., Chartas, G., and Gallagher, S. C. (2003). The Chandra Deep Field North Survey. XIV. X-Ray-Detected Obscured AGNs and Starburst Galaxies in the Bright Submillimeter Source Population. *AJ*, 125:383–397.
- Alexander, D. M., Brandt, W. N., Smail, I., Swinbank, A. M., Bauer, F. E., Blain, A. W., Chapman, S. C., Coppin, K. E. K., Ivison, R. J., and Menéndez-Delmestre, K. (2008). Weighing the Black Holes in  $z \sim 2$  Submillimeter-Emitting Galaxies Hosting Active Galactic Nuclei. *AJ*, 135:1968–1981.
- Allamandola, L. J., Tielens, A. G. G. M., and Barker, J. R. (1985). Polycyclic aromatic hydrocarbons and the unidentified infrared emission bands: auto exhaust along the milky way. *ApJ*, 290:L25–L28.
- ALMA Partnership et al. (2016). *ALMA Technical Handbook*. ISBN 978-3-923524-66-2.
- Alpher, R. A. and Herman, R. (1948a). Evolution of the Universe. *Nature*, 162:774–775.
- Alpher, R. A. and Herman, R. C. (1948b). On the Relative Abundance of the Elements. *Physical Review*, 74:1737–1742.
- Álvarez-Márquez, J., Burgarella, D., Heinis, S., Buat, V., Lo Faro, B., Béthermin, M., López-Fortín, C. E., Cooray, A., Farrah, D., Hurley, P., Ibar, E., Ilbert, O., Koekemoer, A. M., Lemaux, B. C., Pérez-Fournon, I., Rodighiero, G., Salvato, M., Scott, D., Taniguchi, Y., Vieira, J. D., and Wang, L. (2016). Dust properties of Lyman-break galaxies at  $z \sim 3$ . *A&A*, 587:A122.
- Appleton, P. N., Fadda, D. T., Marleau, F. R., Frayer, D. T., Helou, G., Condon, J. J., Choi, P. I., Yan, L., Lacy, M., Wilson, G., Armus, L., Chapman, S. C., Fang, F., Heinrichson, I., Im, M., Jannuzi, B. T., Storrie-Lombardi, L. J., Shupe, D., Soifer, B. T., Squires, G., and Teplitz, H. I.

- (2004). The Far- and Mid-Infrared/Radio Correlations in the Spitzer Extragalactic First Look Survey. *ApJS*, 154:147–150.
- Aravena, M., Decarli, R., Walter, F., Da Cunha, E., Bauer, F. E., Carilli, C. L., Daddi, E., Elbaz, D., Ivison, R. J., Riechers, D. A., Smail, I., Swinbank, A. M., Weiss, A., Anguita, T., Assef, R. J., Bell, E., Bertoldi, F., Bacon, R., Bouwens, R., Cortes, P., Cox, P., González-López, J., Hodge, J., Ibar, E., Inami, H., Infante, L., Karim, A., Le Le Fèvre, O., Magnelli, B., Ota, K., Popping, G., Sheth, K., van der Werf, P., and Wagg, J. (2016). The ALMA Spectroscopic Survey in the Hubble Ultra Deep Field: Continuum Number Counts, Resolved 1.2 mm Extragalactic Background, and Properties of the Faintest Dusty Star-forming Galaxies. *ApJ*, 833:68.
- Arnouts, S., Cristiani, S., Moscardini, L., Matarrese, S., Lucchin, F., Fontana, A., and Giallongo, E. (1999). Measuring and modelling the redshift evolution of clustering: the Hubble Deep Field North. *MNRAS*, 310:540–556.
- Ashby, M. L. N., Willner, S. P., Fazio, G. G., Dunlop, J. S., Egami, E., Faber, S. M., Ferguson, H. C., Grogin, N. A., Hora, J. L., Huang, J.-S., Koekemoer, A. M., Labbé, I., and Wang, Z. (2015). S-CANDELS: The Spitzer-Cosmic Assembly Near-Infrared Deep Extragalactic Survey. Survey Design, Photometry, and Deep IRAC Source Counts. *ApJS*, 218:33.
- Ashby, M. L. N., Willner, S. P., Fazio, G. G., Huang, J.-S., Arendt, R., Barmby, P., Barro, G., Bell, E. F., Bouwens, R., Cattaneo, A., Croton, D., Davé, R., Dunlop, J. S., Egami, E., Faber, S., Finlator, K., Grogin, N. A., Guhathakurta, P., Hernquist, L., Hora, J. L., Illingworth, G., Kashlinsky, A., Koekemoer, A. M., Koo, D. C., Labbé, I., Li, Y., Lin, L., Moseley, H., Nandra, K., Newman, J., Noeske, K., Ouchi, M., Peth, M., Rigopoulou, D., Robertson, B., Sarajedini, V., Simard, L., Smith, H. A., Wang, Z., Wechsler, R., Weiner, B., Wilson, G., Wuyts, S., Yamada, T., and Yan, H. (2013). SEDS: The Spitzer Extended Deep Survey. Survey Design, Photometry, and Deep IRAC Source Counts. *ApJ*, 769:80.
- Baade, W. (1935). The Globular Cluster NGC 2419. *ApJ*, 82:396.
- Baldry, I. K., Glazebrook, K., Brinkmann, J., Ivezić, Ž., Lupton, R. H., Nichol, R. C., and Szalay, A. S. (2004). Quantifying the Bimodal Color-Magnitude Distribution of Galaxies. *ApJ*, 600(2):681–694.
- Balestra, I., Mainieri, V., Popesso, P., Dickinson, M., Nonino, M., Rosati, P., Teimoorinia, H., Vanzella, E., Cristiani, S., and Cesarsky, C. (2010). The Great Observatories Origins Deep Survey. VLT/VIMOS spectroscopy in the GOODS-south field: Part II. *A&A*, 512:A12.
- Balogh, M. L., Baldry, I. K., Nichol, R., Miller, C., Bower, R., and Glazebrook, K. (2004). The Bimodal Galaxy Color Distribution: Dependence on Luminosity and Environment. *ApJ*, 615(2):L101–L104.
- Barger, A. J., Cowie, L. L., Sanders, D. B., Fulton, E., Taniguchi, Y., Sato, Y., Kawara, K., and Okuda, H. (1998). Submillimetre-wavelength detection of dusty star-forming galaxies at high redshift. *Nature*, 394:248–251.
- Barisic, I., Faisst, A. L., Capak, P. L., Pavesi, R., Riechers, D. A., Scoville, N. Z., Cooke, K., Kartaltepe, J. S., Casey, C. M., and Smolcic, V. (2017). Dust Properties of C II Detected  $z \sim 5.5$  Galaxies: New HST/WFC3 Near-IR Observations. *ApJ*, 845:41.

- Barone, T. M., D'Eugenio, F., Colless, M., Scott, N., van de Sande, J., Bland-Hawthorn, J., Brough, S., Bryant, J. J., Cortese, L., and Croom, S. M. (2018). The SAMI Galaxy Survey: Gravitational Potential and Surface Density Drive Stellar Populations. I. Early-type Galaxies. *ApJ*, 856(1):64.
- Barro, G., Faber, S. M., Pérez-González, P. G., Koo, D. C., Williams, C. C., Kocevski, D. D., Trump, J. R., Mozena, M., McGrath, E., van der Wel, A., Wuyts, S., Bell, E. F., Croton, D. J., Ceverino, D., Dekel, A., Ashby, M. L. N., Cheung, E., Ferguson, H. C., Fontana, A., Fang, J., Giavalisco, M., Grogin, N. A., Guo, Y., Hathi, N. P., Hopkins, P. F., Huang, K.-H., Koekemoer, A. M., Kartaltepe, J. S., Lee, K.-S., Newman, J. A., Porter, L. A., Primack, J. R., Ryan, R. E., Rosario, D., Somerville, R. S., Salvato, M., and Hsu, L.-T. (2013). CANDELS: The Progenitors of Compact Quiescent Galaxies at  $z \sim 2$ . *ApJ*, 765:104.
- Barro, G., Kriek, M., Pérez-González, P. G., Diaz-Santos, T., Price, S. H., Rujopakarn, W., Pandya, V., Koo, D. C., Faber, S. M., Dekel, A., Primack, J. R., and Kocevski, D. D. (2017). Spatially Resolved Kinematics in the Central 1 kpc of a Compact Star-forming Galaxy at  $z \sim 2.3$  from ALMA CO Observations. *ApJ*, 851:L40.
- Barro, G., Kriek, M., Pérez-González, P. G., Trump, J. R., Koo, D. C., Faber, S. M., Dekel, A., Primack, J. R., Guo, Y., Kocevski, D. D., Muñoz-Mateos, J. C., Rujopakarn, W., and Seth, K. (2016). Sub-kiloparsec ALMA Imaging of Compact Star-forming Galaxies at  $z \sim 2.5$ : Revealing the Formation of Dense Galactic Cores in the Progenitors of Compact Quiescent Galaxies. *ApJ*, 827:L32.
- Battersby, C., Armus, L., Bergin, E., Kataria, T., Meixner, M., Pope, A., Stevenson, K. B., Cooray, A., Leisawitz, D., and Scott, D. (2018). The Origins Space Telescope. *Nature Astronomy*, 2:596–599.
- Behroozi, P., Wechsler, R. H., Hearin, A. P., and Conroy, C. (2019). UniverseMachine: The Correlation between Galaxy Growth and Dark Matter Halo Assembly from  $z = 0 - 10$ . *MNRAS*, page 1134.
- Bell, E. F., McIntosh, D. H., Katz, N., and Weinberg, M. D. (2003). The Optical and Near-Infrared Properties of Galaxies. I. Luminosity and Stellar Mass Functions. *ApJS*, 149:289–312.
- Berta, S., Magnelli, B., Lutz, D., Altieri, B., Aussel, H., Andreani, P., Bauer, O., Bongiovanni, A., Cava, A., Cepa, J., Cimatti, A., Daddi, E., Dominguez, H., Elbaz, D., Feuchtgruber, H., Förster Schreiber, N. M., Genzel, R., Gruppioni, C., Katterloher, R., Magdis, G., Maiolino, R., Nordon, R., Pérez García, A. M., Poglitsch, A., Popesso, P., Pozzi, F., Riguccini, L., Rodighiero, G., Saintonge, A., Santini, P., Sanchez-Portal, M., Shao, L., Sturm, E., Tacconi, L. J., Valtchanov, I., Wetzstein, M., and Wierprecht, E. (2010). Dissecting the cosmic infra-red background with Herschel/PEP. *A&A*, 518:L30.
- Bertoldi, F., Carilli, C. L., Menten, K. M., Owen, F., Dey, A., Gueth, F., Graham, J. R., Kreysa, E., Ledlow, M., Liu, M. C., Motte, F., Reichertz, L., Schilke, P., and Zylka, R. (2000). Three high-redshift millimeter sources and their radio and near-infrared identifications. *A&A*, 360:92–98.
- Béthermin, M., De Breuck, C., Sargent, M., and Daddi, E. (2015). The influence of wavelength, flux, and lensing selection effects on the redshift distribution of dusty, star-forming galaxies. *A&A*, 576:L9.

- B  thermin, M., Le Floch, E., Ilbert, O., Conley, A., Lagache, G., Amblard, A., Arumugam, V., Aussel, H., Berta, S., Bock, J., Boselli, A., Buat, V., Casey, C. M., Castro-Rodr  guez, N., Cava, A., Clements, D. L., Cooray, A., Dowell, C. D., Eales, S., Farrah, D., Franceschini, A., Glenn, J., Griffin, M., Hatziminaoglou, E., Heinis, S., Ibar, E., Ivison, R. J., Kartaltepe, J. S., Levenson, L., Magdis, G., Marchetti, L., Marsden, G., Nguyen, H. T., O'Halloran, B., Oliver, S. J., Omont, A., Page, M. J., Panuzzo, P., Papageorgiou, A., Pearson, C. P., P  rez-Fournon, I., Pohlen, M., Rigopoulou, D., Roseboom, I. G., Rowan-Robinson, M., Salvato, M., Schulz, B., Scott, D., Seymour, N., Shupe, D. L., Smith, A. J., Symeonidis, M., Trichas, M., Tugwell, K. E., Vaccari, M., Valtchanov, I., Vieira, J. D., Viero, M., Wang, L., Xu, C. K., and Zemcov, M. (2012). HerMES: deep number counts at 250  $\mu\text{m}$ , 350  $\mu\text{m}$  and 500  $\mu\text{m}$  in the COSMOS and GOODS-N fields and the build-up of the cosmic infrared background. *A&A*, 542:A58.
- B  thermin, M., Wu, H.-Y., Lagache, G., Davidzon, I., Ponthieu, N., Cousin, M., Wang, L., Dor  , O., Daddi, E., and Lapi, A. (2017). The impact of clustering and angular resolution on far-infrared and millimeter continuum observations. *A&A*, 607:A89.
- Bian, F., Fan, X., Jiang, L., McGreer, I., Dey, A., Green, R. F., Maiolino, R., Walter, F., Lee, K.-S., and Dav  , R. (2013). The LBT Bo  tes Field Survey. I. The Rest-frame Ultraviolet and Near-infrared Luminosity Functions and Clustering of Bright Lyman Break Galaxies at  $Z \sim 3$ . *ApJ*, 774:28.
- Bianchi, S. (2013). Vindicating single-T modified blackbody fits to Herschel SEDs. *A&A*, 552:A89.
- Bigiel, F., Leroy, A., Walter, F., Brinks, E., de Blok, W. J. G., Madore, B., and Thornley, M. D. (2008). The Star Formation Law in Nearby Galaxies on Sub-Kpc Scales. *AJ*, 136:2846–2871.
- Blain, A. W. and Longair, M. S. (1993). Submillimetre Cosmology. *MNRAS*, 264:509.
- Blain, A. W., Smail, I., Ivison, R. J., Kneib, J.-P., and Frayer, D. T. (2002). Submillimeter galaxies. *Phys. Rep.*, 369:111–176.
- Blanton, M. R., Eisenstein, D., Hogg, D. W., Schlegel, D. J., and Brinkmann, J. (2005). Relationship between Environment and the Broadband Optical Properties of Galaxies in the Sloan Digital Sky Survey. *ApJ*, 629(1):143–157.
- Blanton, M. R., Eisenstein, D., Hogg, D. W., and Zehavi, I. (2006). The Scale Dependence of Relative Galaxy Bias: Encouragement for the “Halo Model” Description. *ApJ*, 645(2):977–985.
- Boissier, S., Boselli, A., Buat, V., Donas, J., and Milliard, B. (2004). The radial extinction profiles of late-type galaxies. *A&A*, 424:465–476.
- Boogaard, L. A., Decarli, R., Gonz  lez-L  pez, J., van der Werf, P., Walter, F., Bouwens, R., Aravena, M., Carilli, C., Bauer, F. E., Brinchmann, J., Contini, T., Cox, P., da Cunha, E., Daddi, E., D  az-Santos, T., Hodge, J., Inami, H., Ivison, R., Maseda, M., Matthee, J., Oesch, P., Popping, G., Riechers, D., Schaye, J., Schouws, S., Smail, I., Weiss, A., Wisotzki, L., Bacon, R., Cortes, P. C., Rix, H.-W., Somerville, R. S., Swinbank, M., and Wagg, J. (2019). The ALMA Spectroscopic Survey in the HUDF: Nature and physical properties of gas-mass selected galaxies using MUSE spectroscopy. *arXiv e-prints*.
- Boselli, A., Boissier, S., Heinis, S., Cortese, L., Ilbert, O., Hughes, T., Cucciati, O., Davies, J., Ferrarese, L., Giovanelli, R., Haynes, M. P., Baes, M., Balkowski, C., Brosch, N., Chapman, S. C., Charmandaris, V., Clemens, M. S., Dariush, A., De Looze, I., di Serego Alighieri, S., Duc,

- P. A., Durrell, P. R., Emsellem, E., Erben, T., Fritz, J., Garcia-Appadoo, D. A., Gavazzi, G., Grossi, M., Jordán, A., Hess, K. M., Huertas-Company, M., Hunt, L. K., Kent, B. R., Lambas, D. G., Lançon, A., MacArthur, L. A., Madden, S. C., Magrini, L., Mei, S., Momjian, E., Olowin, R. P., Papastergis, E., Smith, M. W. L., Solanes, J. M., Spector, O., Spekkens, K., Taylor, J. E., Valotto, C., van Driel, W., Verstappen, J., Vlahakis, C., Vollmer, B., and Xilouris, E. M. (2011). The GALEX Ultraviolet Virgo Cluster Survey (GUViCS). I. The UV luminosity function of the central 12 sq. deg. *A&A*, 528:A107.
- Boselli, A., Ciesla, L., Cortese, L., Buat, V., Boquien, M., Bendo, G. J., Boissier, S., Eales, S., Gavazzi, G., Hughes, T. M., Pohlen, M., Smith, M. W. L., Baes, M., Bianchi, S., Clements, D. L., Cooray, A., Davies, J., Gear, W., Madden, S., Magrini, L., Panuzzo, P., Remy, A., Spinoglio, L., and Zibetti, S. (2012). Far-infrared colours of nearby late-type galaxies in the Herschel Reference Survey. *A&A*, 540:A54.
- Boughn, S. and Crittenden, R. (2004). A correlation between the cosmic microwave background and large-scale structure in the Universe. *Nature*, 427(6969):45–47.
- Bournaud, F., Elmegreen, B. G., and Elmegreen, D. M. (2007). Rapid Formation of Exponential Disks and Bulges at High Redshift from the Dynamical Evolution of Clump-Cluster and Chain Galaxies. *ApJ*, 670:237–248.
- Bournaud, F., Juneau, S., Le Floch, E., Mullaney, J., Daddi, E., Dekel, A., Duc, P.-A., Elbaz, D., Salmi, F., and Dickinson, M. (2012). An Observed Link between Active Galactic Nuclei and Violent Disk Instabilities in High-redshift Galaxies. *ApJ*, 757:81.
- Bourne, N., Dunlop, J. S., Merlin, E., Parsa, S., Schreiber, C., Castellano, M., Conselice, C. J., Coppin, K. E. K., Farrah, D., Fontana, A., Geach, J. E., Halpern, M., Knudsen, K. K., Michałowski, M. J., Mortlock, A., Santini, P., Scott, D., Shu, X. W., Simpson, C., Simpson, J. M., Smith, D. J. B., and van der Werf, P. P. (2017). Evolution of cosmic star formation in the SCUBA-2 Cosmology Legacy Survey. *MNRAS*, 467:1360–1385.
- Bouwens, R. J., Aravena, M., Decarli, R., Walter, F., da Cunha, E., Labbé, I., Bauer, F. E., Bertoldi, F., Carilli, C., Chapman, S., Daddi, E., Hodge, J., Ivison, R. J., Karim, A., Le Fevre, O., Magnelli, B., Ota, K., Riechers, D., Smail, I. R., van der Werf, P., Weiss, A., Cox, P., Elbaz, D., Gonzalez-Lopez, J., Infante, L., Oesch, P., Wagg, J., and Wilkins, S. (2016). ALMA Spectroscopic Survey in the Hubble Ultra Deep Field: The Infrared Excess of UV-Selected  $z = 2-10$  Galaxies as a Function of UV-Continuum Slope and Stellar Mass. *ApJ*, 833:72.
- Bouwens, R. J., Bradley, L., Zitrin, A., Coe, D., Franx, M., Zheng, W., Smit, R., Host, O., Postman, M., and Moustakas, L. (2014). A Census of Star-forming Galaxies in the  $Z \sim 9-10$  Universe based on HST+Spitzer Observations over 19 Clash Clusters: Three Candidate  $Z \sim 9-10$  Galaxies and Improved Constraints on the Star Formation Rate Density at  $Z \sim 9.2$ . *ApJ*, 795(2):126.
- Bouwens, R. J., Illingworth, G. D., Oesch, P. A., Stiavelli, M., van Dokkum, P., Trenti, M., Magee, D., Labbé, I., Franx, M., and Carollo, C. M. (2010). Discovery of  $z \sim 8$  Galaxies in the Hubble Ultra Deep Field from Ultra-Deep WFC3/IR Observations. *ApJ*, 709(2):L133–L137.
- Bouwens, R. J., Illingworth, G. D., Oesch, P. A., Trenti, M., Labbé, I., Bradley, L., Carollo, M., van Dokkum, P. G., Gonzalez, V., Holwerda, B., Franx, M., Spitler, L., Smit, R., and Magee, D. (2015). UV Luminosity Functions at Redshifts  $z \sim 4$  to  $z \sim 10$ : 10,000 Galaxies from HST Legacy Fields. *ApJ*, 803:34.



- Brammer, G. B., van Dokkum, P. G., and Coppi, P. (2008). EAZY: A Fast, Public Photometric Redshift Code. *ApJ*, 686:1503–1513.
- Brinchmann, J., Charlot, S., White, S. D. M., Tremonti, C., Kauffmann, G., Heckman, T., and Brinkmann, J. (2004). The physical properties of star-forming galaxies in the low-redshift Universe. *MNRAS*, 351:1151–1179.
- Bruzual, G. and Charlot, S. (2003). Stellar population synthesis at the resolution of 2003. *MNRAS*, 344:1000–1028.
- Bryan, S. (2018). The TolTEC Camera for the LMT Telescope. In *Atacama Large-Aperture Submillimeter Telescope (AtLAST)*, page 36.
- Buat, V. and Burgarella, D. (1998). The observation of the nearby universe in UV and in FIR: an evidence for a moderate extinction in present day star forming galaxies. *A&A*, 334:772–782.
- Buat, V., Noll, S., Burgarella, D., Giovannoli, E., Charmandaris, V., Pannella, M., Hwang, H. S., Elbaz, D., Dickinson, M., Magdis, G., Reddy, N., and Murphy, E. J. (2012). GOODS-Herschel: dust attenuation properties of UV selected high redshift galaxies. *A&A*, 545:A141.
- Burgarella, D., Buat, V., and Iglesias-Páramo, J. (2005). Star formation and dust attenuation properties in galaxies from a statistical ultraviolet-to-far-infrared analysis. *MNRAS*, 360:1413–1425.
- Burtscher, L., Orban de Xivry, G., Davies, R. I., Janssen, A., Lutz, D., Rosario, D., Contursi, A., Genzel, R., Graciá-Carpio, J., Lin, M. Y., Schnorr-Müller, A., Sternberg, A., Sturm, E., and Tacconi, L. (2015). Obscuration in active galactic nuclei: near-infrared luminosity relations and dust colors. *A&A*, 578:A47.
- Calistro Rivera, G., Hodge, J. A., Smail, I., Swinbank, A. M., Weiss, A., Wardlow, J. L., Walter, F., Rybak, M., Chen, C.-C., Brandt, W. N., Coppin, K., da Cunha, E., Dannerbauer, H., Greve, T. R., Karim, A., Knudsen, K. K., Schinnerer, E., Simpson, J. M., Venemans, B., and van der Werf, P. P. (2018). Resolving the ISM at the Peak of Cosmic Star Formation with ALMA: The Distribution of CO and Dust Continuum in  $z \sim 2.5$  Submillimeter Galaxies. *ApJ*, 863:56.
- Calzetti, D., Armus, L., Bohlin, R. C., Kinney, A. L., Koornneef, J., and Storchi-Bergmann, T. (2000). The Dust Content and Opacity of Actively Star-forming Galaxies. *ApJ*, 533:682–695.
- Calzetti, D., Kinney, A. L., and Storchi-Bergmann, T. (1994). Dust extinction of the stellar continua in starburst galaxies: The ultraviolet and optical extinction law. *ApJ*, 429:582–601.
- Capak, P. L., Carilli, C., Jones, G., Casey, C. M., Riechers, D., Sheth, K., Carollo, C. M., Ilbert, O., Karim, A., Lefevre, O., Lilly, S., Scoville, N., Smolcic, V., and Yan, L. (2015). Galaxies at redshifts 5 to 6 with systematically low dust content and high [C II] emission. *Nature*, 522:455–458.
- Caputi, K. I., Dunlop, J. S., McLure, R. J., Huang, J.-S., Fazio, G. G., Ashby, M. L. N., Castellano, M., Fontana, A., Cirasuolo, M., Almaini, O., Bell, E. F., Dickinson, M., Donley, J. L., Faber, S. M., Ferguson, H. C., Giavalisco, M., Grogin, N. A., Kocevski, D. D., Koekemoer, A. M., Koo, D. C., Lai, K., Newman, J. A., and Somerville, R. S. (2012). The Nature of Extremely Red H - [4.5]>4 Galaxies Revealed with SEDS and CANDELS. *ApJ*, 750:L20.

- Cardamone, C. N., van Dokkum, P. G., Urry, C. M., Taniguchi, Y., Gawiser, E., Brammer, G., Taylor, E., Damen, M., Treister, E., Cobb, B. E., Bond, N., Schawinski, K., Lira, P., Murayama, T., Saito, T., and Sumikawa, K. (2010). The Multiwavelength Survey by Yale-Chile (MUSYC): Deep Medium-band Optical Imaging and High-quality 32-band Photometric Redshifts in the ECDF-S. *ApJS*, 189:270–285.
- Carlstrom, J. E. and Kronberg, P. P. (1991). H II regions in M82 - High-resolution millimeter continuum observations. *ApJ*, 366:422–431.
- Carniani, S., Maiolino, R., De Zotti, G., Negrello, M., Marconi, A., Bothwell, M. S., Capak, P., Carilli, C., Castellano, M., Cristiani, S., Ferrara, A., Fontana, A., Gallerani, S., Jones, G., Ohta, K., Ota, K., Pentericci, L., Santini, P., Sheth, K., Vallini, L., Vanzella, E., Wagg, J., and Williams, R. J. (2015). ALMA constraints on the faint millimetre source number counts and their contribution to the cosmic infrared background. *A&A*, 584:A78.
- Casertano, S., de Mello, D., Dickinson, M., Ferguson, H. C., Fruchter, A. S., Gonzalez-Lopezlira, R. A., Heyer, I., Hook, R. N., Levay, Z., Lucas, R. A., Mack, J., Makidon, R. B., Mutchler, M., Smith, T. E., Stiavelli, M., Wiggs, M. S., and Williams, R. E. (2000). WFPC2 Observations of the Hubble Deep Field South. *AJ*, 120:2747–2824.
- Casey, C., Capak, P., Staguhn, J., Armus, L., Blain, A., Bethermin, M., Champagne, J., Cooray, A., Coppin, K., and Drew, P. (2019). Taking Census of Massive, Star-Forming Galaxies formed <1 Gyr After the Big Bang. In *BAAS*, volume 51, page 212.
- Casey, C. M., Chen, C.-C., Cowie, L. L., Barger, A. J., Capak, P., Ilbert, O., Koss, M., Lee, N., Le Floch, E., Sanders, D. B., and Williams, J. P. (2013). Characterization of SCUBA-2 450  $\mu$ m and 850  $\mu$ m selected galaxies in the COSMOS field. *MNRAS*, 436:1919–1954.
- Casey, C. M., Narayanan, D., and Cooray, A. (2014). Dusty star-forming galaxies at high redshift. *Phys. Rep.*, 541:45–161.
- Casey, C. M., Zavala, J. A., Spilker, J., da Cunha, E., Hodge, J., Hung, C.-L., Staguhn, J., Finkelstein, S. L., and Drew, P. (2018). The Brightest Galaxies in the Dark Ages: Galaxies’ Dust Continuum Emission during the Reionization Era. *ApJ*, 862(1):77.
- Cassata, P., Giavalisco, M., Williams, C. C., Guo, Y., Lee, B., Renzini, A., Ferguson, H., Faber, S. F., Barro, G., and McIntosh, D. H. (2013). Constraining the Assembly of Normal and Compact Passively Evolving Galaxies from Redshift  $z = 3$  to the Present with CANDELS. *ApJ*, 775(2):106.
- Castellano, M., Salimbeni, S., Trevese, D., Grazian, A., Pentericci, L., Fiore, F., Fontana, A., Giallongo, E., Santini, P., and Cristiani, S. (2007). A Photometrically Detected Forming Cluster of Galaxies at Redshift 1.6 in the GOODS Field. *ApJ*, 671(2):1497–1502.
- Cattaneo, A., Dekel, A., Devriendt, J., Guiderdoni, B., and Blaizot, J. (2006). Modelling the galaxy bimodality: shutdown above a critical halo mass. *MNRAS*, 370(4):1651–1665.
- Cava, A., Biviano, A., Mamon, G. A., Varela, J., Bettoni, D., D’Onofrio, M., Fasano, G., Fritz, J., Moles, M., Moretti, A., and Poggianti, B. (2017). Structural and dynamical modeling of WINGS clusters. I. The distribution of cluster galaxies of different morphological classes within regular and irregular clusters. *A&A*, 606:A108.

- Ceverino, D., Dekel, A., Tweed, D., and Primack, J. (2015). Early formation of massive, compact, spheroidal galaxies with classical profiles by violent disc instability or mergers. *MNRAS*, 447:3291–3310.
- Chabrier, G. (2003). Galactic Stellar and Substellar Initial Mass Function. *PASP*, 115:763–795.
- Chang, Y.-Y., Le Floch, E., Juneau, S., da Cunha, E., Salvato, M., Civano, F., Marchesi, S., Ilbert, O., Toba, Y., Lim, C.-F., Tang, J.-J., Wang, W.-H., Ferraro, N., Urry, M. C., Griffiths, R. E., and Kartaltepe, J. S. (2017). Infrared Selection of Obscured Active Galactic Nuclei in the COSMOS Field. *ApJS*, 233:19.
- Chapman, S. C., Blain, A. W., Ivison, R. J., and Smail, I. R. (2003). A median redshift of 2.4 for galaxies bright at submillimetre wavelengths. *Nature*, 422:695–698.
- Chapman, S. C., Blain, A. W., Smail, I., and Ivison, R. J. (2005). A Redshift Survey of the Submillimeter Galaxy Population. *ApJ*, 622:772–796.
- Chary, R. and Elbaz, D. (2001). Interpreting the Cosmic Infrared Background: Constraints on the Evolution of the Dust-enshrouded Star Formation Rate. *ApJ*, 556(2):562–581.
- Chen, C.-C., Smail, I., Swinbank, A. M., Simpson, J. M., Ma, C.-J., Alexander, D. M., Biggs, A. D., Brandt, W. N., Chapman, S. C., Coppin, K. E. K., Danielson, A. L. R., Dannerbauer, H., Edge, A. C., Greve, T. R., Ivison, R. J., Karim, A., Menten, K. M., Schinnerer, E., Walter, F., Wardlow, J. L., Weiß, A., and van der Werf, P. P. (2015). An ALMA Survey of Submillimeter Galaxies in the Extended Chandra Deep Field South: Near-infrared Morphologies and Stellar Sizes. *ApJ*, 799:194.
- Chiang, Y.-K., Overzier, R. A., Gebhardt, K., and Henriques, B. (2017). Galaxy Protoclusters as Drivers of Cosmic Star Formation History in the First 2 Gyr. *ApJ*, 844(2):L23.
- Cibinel, A., Daddi, E., Bournaud, F., Sargent, M. T., le Floch, E., Magdis, G. E., Pannella, M., Rujopakarn, W., Juneau, S., Zanella, A., Duc, P.-A., Oesch, P. A., Elbaz, D., Jagannathan, P., Nyland, K., and Wang, T. (2017). ALMA constraints on star-forming gas in a prototypical  $z = 1.5$  clumpy galaxy: the dearth of CO(5-4) emission from UV-bright clumps. *MNRAS*, 469:4683–4704.
- Ciesla, L., Elbaz, D., Schreiber, C., Daddi, E., and Wang, T. (2018). Identification of galaxies that experienced a recent major drop of star formation. *A&A*, 615:A61.
- Cimatti, A., Cassata, P., Pozzetti, L., Kurk, J., Mignoli, M., Renzini, A., Daddi, E., Bolzonella, M., Brusa, M., and Rodighiero, G. (2008). GMASS ultradeep spectroscopy of galaxies at  $z \sim 2$ . II. Superdense passive galaxies: how did they form and evolve? *A&A*, 482(1):21–42.
- Cirasuolo, M., McLure, R. J., Dunlop, J. S., Almaini, O., Foucaud, S., Smail, I., Sekiguchi, K., Simpson, C., Eales, S., Dye, S., Watson, M. G., Page, M. J., and Hirst, P. (2007). The evolution of the near-infrared galaxy luminosity function and colour bimodality up to  $z \sim 2$  from the UKIDSS Ultra Deep Survey Early Data Release. *MNRAS*, 380:585–595.
- Colombi, S. and et al. (1999). The cosmic distribution of clustering. In Banday, A. J., Sheth, R. K., and da Costa, L. N., editors, *Evolution of Large Scale Structure : From Recombination to Garching*, page 122.

- Combes, F. (2016). The Evolution of Gas Content and Star Formation from  $z=3$  to  $z=0$ . In Jablonka, P., André, P., and van der Tak, F., editors, *From Interstellar Clouds to Star-Forming Galaxies: Universal Processes?*, volume 315 of *IAU Symposium*, pages 240–246.
- Condon, J. J. (1992). Radio emission from normal galaxies. *ARA&A*, 30:575–611.
- Condon, J. J. (1997). Errors in Elliptical Gaussian FITS. *PASP*, 109:166–172.
- Condon, J. J., Cotton, W. D., Greisen, E. W., Yin, Q. F., Perley, R. A., Taylor, G. B., and Broderick, J. J. (1998). The NRAO VLA Sky Survey. *AJ*, 115:1693–1716.
- Conroy, C., Schiminovich, D., and Blanton, M. R. (2010). Dust Attenuation in Disk-dominated Galaxies: Evidence for the 2175 Å Dust Feature. *ApJ*, 718:184–198.
- Conselice, C. J. (2014). The Evolution of Galaxy Structure Over Cosmic Time. *ARA&A*, 52:291–337.
- Coogan, R. T., Sargent, M. T., Daddi, E., Valentino, F., Strazzullo, V., Béthermin, M., Gobat, R., Liu, D., and Magdis, G. (2019). Suppressed CO emission and high G/D ratios in  $z=2$  galaxies with sub-solar gas-phase metallicity. *MNRAS*.
- Cooper, M. C., Yan, R., Dickinson, M., Juneau, S., Lotz, J. M., Newman, J. A., Papovich, C., Salim, S., Walth, G., Weiner, B. J., and Willmer, C. N. A. (2012). The Arizona CDFS Environment Survey (ACES): A Magellan/IMACS Spectroscopic Survey of the Chandra Deep Field-South. *MNRAS*, 425:2116–2127.
- Coppin, K., Chapin, E. L., Mortier, A. M. J., Scott, S. E., Borys, C., Dunlop, J. S., Halpern, M., Hughes, D. H., Pope, A., and Scott, D. (2006). The SCUBA Half-Degree Extragalactic Survey - II. Submillimetre maps, catalogue and number counts. *MNRAS*, 372(4):1621–1652.
- Coppin, K., Halpern, M., Scott, D., Borys, C., and Chapman, S. (2005). An 850- $\mu\text{m}$  SCUBA map of the Groth Strip and reliable source extraction. *MNRAS*, 357:1022–1028.
- Coppin, K., Halpern, M., Scott, D., Borys, C., Dunlop, J., Dunne, L., Ivison, R., Wagg, J., Aretxaga, I., Battistelli, E., Benson, A., Blain, A., Chapman, S., Clements, D., Dye, S., Farrah, D., Hughes, D., Jenness, T., van Kampen, E., Lacey, C., Mortier, A., Pope, A., Priddey, R., Serjeant, S., Smail, I., Stevens, J., and Vaccari, M. (2008). The SCUBA HALF Degree Extragalactic Survey - VI. 350- $\mu\text{m}$  mapping of submillimetre galaxies. *MNRAS*, 384:1597–1610.
- Coppin, K. E. K., Geach, J. E., Almaini, O., Arumugam, V., Dunlop, J. S., Hartley, W. G., Ivison, R. J., Simpson, C. J., Smith, D. J. B., Swinbank, A. M., Blain, A. W., Bourne, N., Bremer, M., Conselice, C., Harrison, C. M., Mortlock, A., Chapman, S. C., Davies, L. J. M., Farrah, D., Gibb, A., Jenness, T., Karim, A., Knudsen, K. K., Ibar, E., Michałowski, M. J., Peacock, J. A., Rigopoulou, D., Robson, E. I., Scott, D., Stevens, J., and van der Werf, P. P. (2015). The SCUBA-2 Cosmology Legacy Survey: the submillimetre properties of Lyman-break galaxies at  $z = 3-5$ . *MNRAS*, 446:1293–1304.
- Cornwell, T. J. (1988). Radio-interferometric imaging of very large objects. *A&A*, 202:316–321.
- Cortese, L., Boselli, A., Franzetti, P., Decarli, R., Gavazzi, G., Boissier, S., and Buat, V. (2008). Ultraviolet dust attenuation in star-forming galaxies - II. Calibrating the  $A(\text{UV})$  versus  $L_{\text{TIR}}/L_{\text{UV}}$  relation. *MNRAS*, 386(2):1157–1168.

- Cowie, L. L., Barger, A. J., and Kneib, J.-P. (2002). Faint Submillimeter Counts from Deep 850 Micron Observations of the Lensing Clusters A370, A851, and A2390. *AJ*, 123:2197–2205.
- Cowie, L. L., Gonzalez-Lopez, J., Barger, A. J., Bauer, F. E., Hsu, L.-Y., and Wang, W.-H. (2018). A Submillimeter Perspective on the GOODS Fields (SUPER GOODS). III. A Large Sample of ALMA Sources in the GOODS-S. *ArXiv e-prints*.
- Cowie, L. L., Songaila, A., Hu, E. M., and Cohen, J. G. (1996). New Insight on Galaxy Formation and Evolution From Keck Spectroscopy of the Hawaii Deep Fields. *AJ*, 112:839.
- Crawford, A. B., Hogg, D. C., and Hunt, L. E. (1961). A Horn-Reflector Antenna for Space Communication. *Bell System Technical Journal*, 40:1095–1116.
- da Cunha, E., Charlot, S., and Elbaz, D. (2008). A simple model to interpret the ultraviolet, optical and infrared emission from galaxies. *MNRAS*, 388:1595–1617.
- Daddi, E., Bournaud, F., Walter, F., Dannerbauer, H., Carilli, C. L., Dickinson, M., Elbaz, D., Morrison, G. E., Riechers, D., Onodera, M., Salmi, F., Krips, M., and Stern, D. (2010). Very High Gas Fractions and Extended Gas Reservoirs in  $z = 1.5$  Disk Galaxies. *ApJ*, 713:686–707.
- Daddi, E., Cimatti, A., Renzini, A., Fontana, A., Mignoli, M., Pozzetti, L., Tozzi, P., and Zamorani, G. (2004). A New Photometric Technique for the Joint Selection of Star-forming and Passive Galaxies at  $1.4 < z < 2.5$ . *ApJ*, 617(2):746–764.
- Daddi, E., Dickinson, M., Chary, R., Pope, A., Morrison, G., Alexander, D. M., Bauer, F. E., Brandt, W. N., Giavalisco, M., Ferguson, H., Lee, K.-S., Lehmer, B. D., Papovich, C., and Renzini, A. (2005). The Population of BzK-selected ULIRGs at  $z \sim 2$ . *ApJ*, 631:L13–L16.
- Daddi, E., Dickinson, M., Morrison, G., Chary, R., Cimatti, A., Elbaz, D., Frayer, D., Renzini, A., Pope, A., Alexander, D. M., Bauer, F. E., Giavalisco, M., Huynh, M., Kurk, J., and Mignoli, M. (2007). Multiwavelength Study of Massive Galaxies at  $z \sim 2$ . I. Star Formation and Galaxy Growth. *ApJ*, 670:156–172.
- Dale, D. A. and Helou, G. (2002). The Infrared Spectral Energy Distribution of Normal Star-forming Galaxies: Calibration at Far-Infrared and Submillimeter Wavelengths. *ApJ*, 576:159–168.
- Dale, D. A., Helou, G., Contursi, A., Silbermann, N. A., and Kolhatkar, S. (2001). The Infrared Spectral Energy Distribution of Normal Star-forming Galaxies. *ApJ*, 549:215–227.
- Davidzon, I., Ilbert, O., Laigle, C., Coupon, J., McCracken, H. J., Delvecchio, I., Masters, D., Capak, P., Hsieh, B. C., Le Fèvre, O., Tresse, L., Bethermin, M., Chang, Y. Y., Faisst, A. L., Le Floch, E., Steinhardt, C., Toft, S., Aussel, H., Dubois, C., Hasinger, G., Salvato, M., Sanders, D. B., Scoville, N., and Silverman, J. D. (2017). The COSMOS2015 galaxy stellar mass function . Thirteen billion years of stellar mass assembly in ten snapshots. *A&A*, 605:A70.
- Davis, M., Guhathakurta, P., Konidaris, N. P., Newman, J. A., Ashby, M. L. N., Biggs, A. D., Barmby, P., Bundy, K., Chapman, S. C., Coil, A. L., Conselice, C. J., Cooper, M. C., Croton, D. J., Eisenhardt, P. R. M., Ellis, R. S., Faber, S. M., Fang, T., Fazio, G. G., Georgakakis, A., Gerke, B. F., Goss, W. M., Gwyn, S., Harker, J., Hopkins, A. M., Huang, J.-S., Ivison, R. J., Kassin, S. A., Kirby, E. N., Koekemoer, A. M., Koo, D. C., Laird, E. S., Le Floch, E., Lin, L., Lotz, J. M., Marshall, P. J., Martin, D. C., Metevier, A. J., Moustakas, L. A., Nandra, K., Noeske, K. G., Papovich, C., Phillips, A. C., Rich, R. M., Rieke, G. H., Rigopoulou, D., Salim, S., Schiminovich,

- D., Simard, L., Smail, I., Small, T. A., Weiner, B. J., Willmer, C. N. A., Willner, S. P., Wilson, G., Wright, E. L., and Yan, R. (2007). The All-Wavelength Extended Groth Strip International Survey (AEGIS) Data Sets. *ApJ*, 660:L1–L6.
- Dayal, P., Ferrara, A., and Dunlop, J. S. (2013). The physics of the fundamental metallicity relation. *MNRAS*, 430(4):2891–2895.
- de Jong, T., Clegg, P. E., Soifer, B. T., Rowan-Robinson, M., Habing, H. J., Houck, J. R., Aumann, H. H., and Raimond, E. (1984). IRAS observations of Shapley-Ames galaxies. *ApJ*, 278:L67–L70.
- de Vaucouleurs, G. (1959). Classification and Morphology of External Galaxies. *Handbuch der Physik*, 53:275.
- Decarli, R., Walter, F., González-López, J., Aravena, M., Boogaard, L., Carilli, C., Cox, P., Daddi, E., Popping, G., Riechers, D., Uzgil, B., Weiss, A., Assef, R. J., Bacon, R., Bauer, F. E., Bertoldi, F., Bouwens, R., Contini, T., Cortes, P. C., da Cunha, E., Díaz-Santos, T., Elbaz, D., Inami, H., Hodge, J., Ivison, R., Le Fèvre, O., Magnelli, B., Novak, M., Oesch, P., Rix, H.-W., Sargent, M. T., Smail, I. R., Swinbank, A. M., Somerville, R. S., van der Werf, P., Wagg, J., and Wisotzki, L. (2019). The ALMA Spectroscopic Survey in the HUDF: CO luminosity functions and the molecular gas content of galaxies through cosmic history. *arXiv e-prints*.
- Dekel, A. and Birnboim, Y. (2006). Galaxy bimodality due to cold flows and shock heating. *MNRAS*, 368(1):2–20.
- Dekel, A. and Burkert, A. (2014). Wet disc contraction to galactic blue nuggets and quenching to red nuggets. *MNRAS*, 438:1870–1879.
- Dekel, A. and Cox, T. J. (2006). The dissipative merger progenitors of elliptical galaxies. *MNRAS*, 370:1445–1453.
- Dekel, A. and Silk, J. (1986). The origin of dwarf galaxies, cold dark matter, and biased galaxy formation. *ApJ*, 303:39–55.
- Dekel, A. and Woo, J. (2003). Feedback and the fundamental line of low-luminosity low-surface-brightness/dwarf galaxies. *MNRAS*, 344:1131–1144.
- Delhaize, J., Smolčić, V., Delvecchio, I., Novak, M., Sargent, M., Baran, N., Magnelli, B., Zamorani, G., Schinnerer, E., Murphy, E. J., Aravena, M., Berta, S., Bondi, M., Capak, P., Carilli, C., Ciliegi, P., Civano, F., Ilbert, O., Karim, A., Laigle, C., Le Fèvre, O., Marchesi, S., McCracken, H. J., Salvato, M., Seymour, N., and Tasca, L. (2017). The VLA-COSMOS 3 GHz Large Project: The infrared-radio correlation of star-forming galaxies and AGN to  $z \sim 6$ . *A&A*, 602:A4.
- Dicke, R. H., Peebles, P. J. E., Roll, P. G., and Wilkinson, D. T. (1965). Cosmic Black-Body Radiation. *ApJ*, 142:414–419.
- Dickinson, M. and GOODS Legacy Team (2001). The Great Observatories Origins Deep Survey (GOODS). In *American Astronomical Society Meeting Abstracts #198*, volume 33 of *Bulletin of the American Astronomical Society*, page 820.
- Dole, H., Lagache, G., and Puget, J. L. (2003). Predictions for Cosmological Infrared Surveys from Space with the Multiband Imaging Photometer for SIRTf. *ApJ*, 585(2):617–629.

- Dole, H., Lagache, G., Puget, J.-L., Caputi, K. I., Fernández-Conde, N., Le Floch, E., Papovich, C., Pérez-González, P. G., Rieke, G. H., and Blaylock, M. (2006). The cosmic infrared background resolved by Spitzer. Contributions of mid-infrared galaxies to the far-infrared background. *A&A*, 451:417–429.
- Donevski, D., Buat, V., Boone, F., Pappalardo, C., Bethermin, M., Schreiber, C., Mazyed, F., Alvarez-Marquez, J., and Duivenvoorden, S. (2018). Towards a census of high-redshift dusty galaxies with Herschel. A selection of “500  $\mu\text{m}$ -risers”. *A&A*, 614:A33.
- Draine, B. T. (2003). Interstellar Dust Grains. *ARA&A*, 41:241–289.
- Draine, B. T., Aniano, G., Krause, O., Groves, B., Sandstrom, K., Braun, R., Leroy, A., Klaas, U., Linz, H., Rix, H.-W., Schinnerer, E., Schmiedeke, A., and Walter, F. (2014). Andromeda’s Dust. *ApJ*, 780:172.
- Draine, B. T., Dale, D. A., Bendo, G., Gordon, K. D., Smith, J. D. T., Armus, L., Engelbracht, C. W., Helou, G., Kennicutt, Jr., R. C., Li, A., Roussel, H., Walter, F., Calzetti, D., Moustakas, J., Murphy, E. J., Rieke, G. H., Bot, C., Hollenbach, D. J., Sheth, K., and Teplitz, H. I. (2007). Dust Masses, PAH Abundances, and Starlight Intensities in the SINGS Galaxy Sample. *ApJ*, 663:866–894.
- Draine, B. T. and Li, A. (2007). Infrared Emission from Interstellar Dust. IV. The Silicate-Graphite-PAH Model in the Post-Spitzer Era. *ApJ*, 657:810–837.
- Dressler, A. (1980). Galaxy morphology in rich clusters: implications for the formation and evolution of galaxies. *ApJ*, 236:351–365.
- Dunlop, J. S., McLure, R. J., Biggs, A. D., Geach, J. E., Michałowski, M. J., Ivison, R. J., Rujopakarn, W., van Kampen, E., Kirkpatrick, A., Pope, A., Scott, D., Swinbank, A. M., Targett, T. A., Aretxaga, I., Austermann, J. E., Best, P. N., Bruce, V. A., Chapin, E. L., Charlot, S., Cirasuolo, M., Coppin, K., Ellis, R. S., Finkelstein, S. L., Hayward, C. C., Hughes, D. H., Ibar, E., Jagannathan, P., Khochfar, S., Koprowski, M. P., Narayanan, D., Nyland, K., Papovich, C., Peacock, J. A., Rieke, G. H., Robertson, B., Vernstrom, T., Werf, P. P. v. d., Wilson, G. W., and Yun, M. (2017). A deep ALMA image of the Hubble Ultra Deep Field. *MNRAS*, 466:861–883.
- Dyson, Sir, F. (1926). A method for correcting series of parallax observations. *MNRAS*, 86:686.
- Eales, S., Lilly, S., Gear, W., Dunne, L., Bond, J. R., Hammer, F., Le Fèvre, O., and Crampton, D. (1999). The Canada-UK Deep Submillimeter Survey: First Submillimeter Images, the Source Counts, and Resolution of the Background. *ApJ*, 515:518–524.
- Eales, S., Lilly, S., Webb, T., Dunne, L., Gear, W., Clements, D., and Yun, M. (2000). The Canada-UK Deep Submillimeter Survey. IV. The Survey of the 14 Hour Field. *AJ*, 120:2244–2268.
- Eddington, A. S. (1913). On a formula for correcting statistics for the effects of a known error of observation. *MNRAS*, 73:359–360.
- Eddington, Sir, A. S. (1940). The correction of statistics for accidental error. *MNRAS*, 100:354.
- Efstathiou, G., Ma, Y.-Z., and Hanson, D. (2010). Large-angle correlations in the cosmic microwave background. *MNRAS*, 407(4):2530–2542.
- Einstein, A. (1905). Zur Elektrodynamik bewegter Körper. *Annalen der Physik*, 322(10):891–921.



- Einstein, A. (1915). Die Feldgleichungen der Gravitation. *Sitzungsberichte der Königlich Preussischen Akademie der Wissenschaften (Berlin)*, pages 844–847.
- Ekers, R. D. and Rots, A. H. (1979). Short Spacing Synthesis from a Primary Beam Scanned Interferometer. In van Schooneveld, C., editor, *IAU Colloq. 49: Image Formation from Coherence Functions in Astronomy*, volume 76 of *Astrophysics and Space Science Library*, page 61.
- Elbaz, D., Daddi, E., Le Borgne, D., Dickinson, M., Alexander, D. M., Chary, R.-R., Starck, J.-L., Brandt, W. N., Kitzbichler, M., MacDonald, E., Nonino, M., Popesso, P., Stern, D., and Vanzella, E. (2007). The reversal of the star formation-density relation in the distant universe. *A&A*, 468:33–48.
- Elbaz, D., Dickinson, M., Hwang, H. S., Díaz-Santos, T., Magdis, G., Magnelli, B., Le Borgne, D., Galliano, F., Pannella, M., Chanial, P., Armus, L., Charmandaris, V., Daddi, E., Aussel, H., Popesso, P., Kartaltepe, J., Altieri, B., Valtchanov, I., Coia, D., Dannerbauer, H., Dasyra, K., Leiton, R., Mazzarella, J., Alexander, D. M., Buat, V., Burgarella, D., Chary, R.-R., Gilli, R., Ivison, R. J., Juneau, S., Le Floch, E., Lutz, D., Morrison, G. E., Mullaney, J. R., Murphy, E., Pope, A., Scott, D., Brodwin, M., Calzetti, D., Cesarsky, C., Charlot, S., Dole, H., Eisenhardt, P., Ferguson, H. C., Förster Schreiber, N., Frayer, D., Giavalisco, M., Huynh, M., Koekemoer, A. M., Papovich, C., Reddy, N., Surace, C., Teplitz, H., Yun, M. S., and Wilson, G. (2011). GOODS-Herschel: an infrared main sequence for star-forming galaxies. *A&A*, 533:A119.
- Elbaz, D., Leiton, R., Nagar, N., Okumura, K., Franco, M., Schreiber, C., Pannella, M., Wang, T., Dickinson, M., Díaz-Santos, T., Ciesla, L., Daddi, E., Bournaud, F., Magdis, G., Zhou, L., and Rujopakarn, W. (2018). Starbursts in and out of the star-formation main sequence. *A&A*, 616:A110.
- Elmegreen, B. G., Elmegreen, D. M., Fernandez, M. X., and Lemonias, J. J. (2009). Bulge and Clump Evolution in Hubble Ultra Deep Field Clump Clusters, Chains and Spiral Galaxies. *ApJ*, 692:12–31.
- Elmegreen, D. M. (2007). Clumpy Galaxies in the Early Universe. In Combes, F. and Palouš, J., editors, *Galaxy Evolution across the Hubble Time*, volume 235 of *IAU Symposium*, pages 376–380.
- Ezawa, H., Kawabe, R., Kohno, K., and Yamamoto, S. (2004). The Atacama Submillimeter Telescope Experiment (ASTE). In Oschmann, Jr., J. M., editor, *Ground-based Telescopes*, volume 5489 of *Proc. SPIE*, pages 763–772.
- Faber, S. M., Willmer, C. N. A., Wolf, C., Koo, D. C., Weiner, B. J., Newman, J. A., Im, M., Coil, A. L., Conroy, C., and Cooper, M. C. (2007). Galaxy Luminosity Functions to  $z \sim 1$  from DEEP2 and COMBO-17: Implications for Red Galaxy Formation. *ApJ*, 665(1):265–294.
- Fadda, D., Yan, L., Lagache, G., Sajina, A., Lutz, D., Wuyts, S., Frayer, D. T., Marcillac, D., Le Floch, E., Caputi, K., Spoon, H. W. W., Veilleux, S., Blain, A., and Helou, G. (2010). Ultra-deep Mid-infrared Spectroscopy of Luminous Infrared Galaxies at  $z \sim 1$  and  $z \sim 2$ . *ApJ*, 719:425–450.
- Fazio, G. G., Hora, J. L., Allen, L. E., Ashby, M. L. N., Barmby, P., Deutsch, L. K., Huang, J.-S., Kleiner, S., Marengo, M., Megeath, S. T., Melnick, G. J., Pahre, M. A., Patten, B. M., Polizotti, J., Smith, H. A., Taylor, R. S., Wang, Z., Willner, S. P., Hoffmann, W. F., Pipher, J. L., Forrest, W. J., McMurty, C. W., McCreight, C. R., McKelvey, M. E., McMurray, R. E., Koch, D. G., Moseley, S. H., Arendt, R. G., Mentzell, J. E., Marx, C. T., Losch, P., Mayman, P., Eichhorn,

- W., Krebs, D., Jhabvala, M., Gezari, D. Y., Fixsen, D. J., Flores, J., Shakoorzadeh, K., Jungo, R., Hakun, C., Workman, L., Karpati, G., Kichak, R., Whitley, R., Mann, S., Tollestrup, E. V., Eisenhardt, P., Stern, D., Gorjian, V., Bhattacharya, B., Carey, S., Nelson, B. O., Glaccum, W. J., Lacy, M., Lowrance, P. J., Laine, S., Reach, W. T., Stauffer, J. A., Surace, J. A., Wilson, G., Wright, E. L., Hoffman, A., Domingo, G., and Cohen, M. (2004). The Infrared Array Camera (IRAC) for the Spitzer Space Telescope. *ApJS*, 154:10–17.
- Feldmann, R., Carollo, C. M., Porciani, C., Lilly, S. J., Capak, P., Taniguchi, Y., Le Fèvre, O., Renzini, A., Scoville, N., Ajiki, M., Aussel, H., Contini, T., McCracken, H., Mobasher, B., Murayama, T., Sanders, D., Sasaki, S., Scarlata, C., Scoddeggio, M., Shioya, Y., Silverman, J., Takahashi, M., Thompson, D., and Zamorani, G. (2006). The Zurich Extragalactic Bayesian Redshift Analyzer and its first application: COSMOS. *MNRAS*, 372:565–577.
- Felli, M. and Spencer, R. E. (1989). Book-Review - Very Long Baseline Interferometry - Techniques and Applications. *Journal of the British Astronomical Association*, 99:314.
- Ferguson, H. C. (1998). The Hubble Deep Field. *Reviews in Modern Astronomy*, 11:83.
- Ferguson, H. C., Dickinson, M., and Williams, R. (2000). The Hubble Deep Fields. *ARA&A*, 38:667–715.
- Ferreras, I., Pasquali, A., Malhotra, S., Rhoads, J., Cohen, S., Windhorst, R., Pirzkal, N., Grogin, N., Koekemoer, A. M., Lisker, T., Panagia, N., Daddi, E., and Hathi, N. P. (2009). Early-Type Galaxies in the PEARS Survey: Probing the Stellar Populations at Moderate Redshift. *ApJ*, 706:158–169.
- Fixsen, D. J., Dwek, E., Mather, J. C., Bennett, C. L., and Shafer, R. A. (1998). The Spectrum of the Extragalactic Far-Infrared Background from the COBE FIRAS Observations. *ApJ*, 508:123–128.
- Flewelling, H. A., Magnier, E. A., Chambers, K. C., Heasley, J. N., Holmberg, C., Huber, M. E., Sweeney, W., Waters, C. Z., Chen, X., Farrow, D., Hasinger, G., Henderson, R., Long, K. S., Metcalfe, N., Nieto-Santisteban, M. A., Norberg, P., Saglia, R. P., Szalay, A., Rest, A., Thakar, A. R., Tonry, J. L., Valenti, J., Werner, S., White, R., Denneau, L., Draper, P. W., Hodapp, K. W., Jedicke, R., Kaiser, N., Kudritzki, R.-P., Price, P. A., Wainscoat, R. J., Chastel, S., McClean, B., Postman, M., and Shiao, B. (2016). The Pan-STARRS1 Database and Data Products. *ArXiv e-prints*.
- Fontana, A., Dunlop, J. S., Paris, D., Targett, T. A., Boutsia, K., Castellano, M., Galametz, A., Grazian, A., McLure, R., Merlin, E., Pentericci, L., Wuyts, S., Almaini, O., Caputi, K., Chary, R.-R., Cirasuolo, M., Conselice, C. J., Cooray, A., Daddi, E., Dickinson, M., Faber, S. M., Fazio, G., Ferguson, H. C., Giallongo, E., Giavalisco, M., Grogin, N. A., Hathi, N., Koekemoer, A. M., Koo, D. C., Lucas, R. A., Nonino, M., Rix, H. W., Renzini, A., Rosario, D., Santini, P., Scarlata, C., Sommariva, V., Stark, D. P., van der Wel, A., Vanzella, E., Wild, V., Yan, H., and Zibetti, S. (2014). The Hawk-I UDS and GOODS Survey (HUGS): Survey design and deep K-band number counts. *A&A*, 570:A11.
- Fontanot, F., De Lucia, G., Monaco, P., Somerville, R. S., and Santini, P. (2009). The many manifestations of downsizing: hierarchical galaxy formation models confront observations. *MNRAS*, 397:1776–1790.

- Forrest, B., Tran, K.-V. H., Broussard, A., Allen, R. J., Apfel, M., Cowley, M. J., Glazebrook, K., Kacprzak, G. G., Labbé, I., Nanayakkara, T., Papovich, C., Quadri, R. F., Spitler, L. R., Straatman, C. M. S., and Tomczak, A. (2017). Discovery of Extreme [O iii]+H $\beta$  Emitting Galaxies Tracing an Overdensity at  $z \sim 3.5$  in CDF-South. *ApJ*, 838:L12.
- Förster Schreiber, N. M., Genzel, R., Lehnert, M. D., Bouché, N., Verma, A., Erb, D. K., Shapley, A. E., Steidel, C. C., Davies, R., and Lutz, D. (2006). SINFONI Integral Field Spectroscopy of  $z \sim 2$  UV-selected Galaxies: Rotation Curves and Dynamical Evolution. *ApJ*, 645(2):1062–1075.
- Förster Schreiber, N. M., Shapley, A. E., Genzel, R., Bouché, N., Cresci, G., Davies, R., Erb, D. K., Genel, S., Lutz, D., and Newman, S. (2011). Constraints on the Assembly and Dynamics of Galaxies. II. Properties of Kiloparsec-scale Clumps in Rest-frame Optical Emission of  $z \sim 2$  Star-forming Galaxies. *ApJ*, 739(1):45.
- Foster, C., Hopkins, A. M., Gunawardhana, M., Lara-López, M. A., Sharp, R. G., Steele, O., Taylor, E. N., Driver, S. P., Baldry, I. K., and Bamford, S. P. (2012). Galaxy And Mass Assembly (GAMA): the mass-metallicity relationship. *A&A*, 547:A79.
- Franco, M., Elbaz, D., Béthermin, M., Magnelli, B., Schreiber, C., Ciesla, L., Dickinson, M., Nagar, N., Silverman, J., Daddi, E., Alexander, D. M., Wang, T., Pannella, M., Le Floch, E., Pope, A., Giavalisco, M., Maury, A. J., Bournaud, F., Chary, R., Demarco, R., Ferguson, H., Finkelstein, S. L., Inami, H., Iono, D., Juneau, S., Lagache, G., Leiton, R., Lin, L., Magdis, G., Messias, H., Motohara, K., Mullaney, J., Okumura, K., Papovich, C., Pforr, J., Rujopakarn, W., Sargent, M., Shu, X., and Zhou, L. (2018). GOODS-ALMA: 1.1 mm galaxy survey. I. Source catalog and optically dark galaxies. *A&A*, 620:A152.
- Fu, H., Cooray, A., Feruglio, C., Ivison, R. J., Riechers, D. A., Gurwell, M., Bussmann, R. S., Harris, A. I., Altieri, B., Aussel, H., Baker, A. J., Bock, J., Boylan-Kolchin, M., Bridge, C., Calanog, J. A., Casey, C. M., Cava, A., Chapman, S. C., Clements, D. L., Conley, A., Cox, P., Farrah, D., Frayer, D., Hopwood, R., Jia, J., Magdis, G., Marsden, G., Martínez-Navajas, P., Negrello, M., Neri, R., Oliver, S. J., Omont, A., Page, M. J., Pérez-Fournon, I., Schulz, B., Scott, D., Smith, A., Vaccari, M., Valtchanov, I., Vieira, J. D., Viero, M., Wang, L., Wardlow, J. L., and Zemcov, M. (2013). The rapid assembly of an elliptical galaxy of 400 billion solar masses at a redshift of 2.3. *Nature*, 498:338–341.
- Fudamoto, Y., Oesch, P. A., Schinnerer, E., Groves, B., Karim, A., Magnelli, B., Sargent, M. T., Cassata, P., Lang, P., Liu, D., Le Fèvre, O., Leslie, S., Smolčić, V., and Tasca, L. (2017). The dust attenuation of star-forming galaxies at  $z \sim 3$  and beyond: New insights from ALMA observations. *MNRAS*, 472:483–490.
- Fujimoto, S., Ouchi, M., Ono, Y., Shibuya, T., Ishigaki, M., Nagai, H., and Momose, R. (2016). ALMA Census of Faint 1.2 mm Sources Down to  $\sim 0.02$  mJy: Extragalactic Background Light and Dust-poor, High- $z$  Galaxies. *ApJS*, 222:1.
- Fujimoto, S., Ouchi, M., Shibuya, T., and Nagai, H. (2017). Demonstrating a New Census of Infrared Galaxies with ALMA (DANCING-ALMA). I. FIR Size and Luminosity Relation at  $z = 0-6$  Revealed with 1034 ALMA Sources. *ApJ*, 850:83.
- Gabor, D. (1946). Theory of communication. *Journal of the Institute of Electrical Engineering*, 93:429–457.

- Gaia Collaboration, Brown, A. G. A., Vallenari, A., Prusti, T., de Bruijne, J. H. J., Mignard, F., Drimmel, R., Babusiaux, C., Bailer-Jones, C. A. L., Bastian, U., and et al. (2016). Gaia Data Release 1. Summary of the astrometric, photometric, and survey properties. *A&A*, 595:A2.
- Gallazzi, A., Charlot, S., Brinchmann, J., White, S. D. M., and Tremonti, C. A. (2005). The ages and metallicities of galaxies in the local universe. *MNRAS*, 362(1):41–58.
- Galliano, F., Madden, S. C., Tielens, A. G. G. M., Peeters, E., and Jones, A. P. (2008). Variations of the Mid-IR Aromatic Features inside and among Galaxies. *ApJ*, 679(1):310–345.
- Garnett, D. R. (2002). The Luminosity-Metallicity Relation, Effective Yields, and Metal Loss in Spiral and Irregular Galaxies. *ApJ*, 581(2):1019–1031.
- Garrett, M. A. (2002). The FIR/Radio correlation of high redshift galaxies in the region of the HDF-N. *A&A*, 384:L19–L22.
- Gatti, M., Lamastra, A., Menci, N., Bongiorno, A., and Fiore, F. (2015). Physical properties of AGN host galaxies as a probe of supermassive black hole feeding mechanisms. *A&A*, 576:A32.
- Geach, J. E., Dunlop, J. S., Halpern, M., Smail, I., van der Werf, P., Alexander, D. M., Almaini, O., Aretxaga, I., Arumugam, V., Asboth, V., Banerji, M., Beanlands, J., Best, P. N., Blain, A. W., Birkinshaw, M., Chapin, E. L., Chapman, S. C., Chen, C.-C., Chrysostomou, A., Clarke, C., Clements, D. L., Conselice, C., Coppin, K. E. K., Cowley, W. I., Danielson, A. L. R., Eales, S., Edge, A. C., Farrah, D., Gibb, A., Harrison, C. M., Hine, N. K., Hughes, D., Ivison, R. J., Jarvis, M., Jenness, T., Jones, S. F., Karim, A., Koprowski, M., Knudsen, K. K., Lacey, C. G., Mackenzie, T., Marsden, G., McAlpine, K., McMahon, R., Meijerink, R., Michałowski, M. J., Oliver, S. J., Page, M. J., Peacock, J. A., Rigopoulou, D., Robson, E. I., Roseboom, I., Rotermund, K., Scott, D., Serjeant, S., Simpson, C., Simpson, J. M., Smith, D. J. B., Spaans, M., Stanley, F., Stevens, J. A., Swinbank, A. M., Targett, T., Thomson, A. P., Valiante, E., Wake, D. A., Webb, T. M. A., Willott, C., Zavala, J. A., and Zemcov, M. (2017). The SCUBA-2 Cosmology Legacy Survey: 850  $\mu$ m maps, catalogues and number counts. *MNRAS*, 465:1789–1806.
- Genzel, R., Tacconi, L. J., Combes, F., Bolatto, A., Neri, R., Sternberg, A., Cooper, M. C., Bouché, N., Bournaud, F., Burkert, A., Comerford, J., Cox, P., Davis, M., Förster Schreiber, N. M., Garcia-Burillo, S., Gracia-Carpio, J., Lutz, D., Naab, T., Newman, S., Saintonge, A., Shapiro, K., Shapley, A., and Weiner, B. (2012). The Metallicity Dependence of the CO  $\rightarrow$  H<sub>2</sub> Conversion Factor in  $z \sim 1$  Star-forming Galaxies. *ApJ*, 746:69.
- Giacconi, R., Rosati, P., Tozzi, P., Borgani, S., Hasinger, G., Bergeron, J., Gilmozzi, R., Nonino, M., Gilli, R., Zirm, A., Wang, J. X., Zheng, W., Kellermann, K. I., Shaver, P., Schreier, E., Koekemoer, A., Grogin, N., and Norman, C. (2000). The Chandra Deep Field South. In *American Astronomical Society Meeting Abstracts*, volume 32 of *Bulletin of the American Astronomical Society*, page 1562.
- Giacconi, R., Rosati, P., Tozzi, P., Nonino, M., Hasinger, G., Norman, C., Bergeron, J., Borgani, S., Gilli, R., Gilmozzi, R., and Zheng, W. (2001). First Results from the X-Ray and Optical Survey of the Chandra Deep Field South. *ApJ*, 551:624–634.
- Giacconi, R., Zirm, A., Wang, J., Rosati, P., Nonino, M., Tozzi, P., Gilli, R., Mainieri, V., Hasinger, G., Kewley, L., Bergeron, J., Borgani, S., Gilmozzi, R., Grogin, N., Koekemoer, A., Schreier, E., Zheng, W., and Norman, C. (2002). Chandra Deep Field South: The 1 Ms Catalog. *ApJS*, 139:369–410.

- Giavalisco, M., Ferguson, H. C., Koekemoer, A. M., Dickinson, M., Alexander, D. M., Bauer, F. E., Bergeron, J., Biagetti, C., Brandt, W. N., Casertano, S., Cesarsky, C., Chatzichristou, E., Conselice, C., Cristiani, S., Da Costa, L., Dahlen, T., de Mello, D., Eisenhardt, P., Erben, T., Fall, S. M., Fasnacht, C., Fosbury, R., Fruchter, A., Gardner, J. P., Grogin, N., Hook, R. N., Hornschemeier, A. E., Idzi, R., Jogle, S., Kretchmer, C., Laidler, V., Lee, K. S., Livio, M., Lucas, R., Madau, P., Mobasher, B., Moustakas, L. A., Nonino, M., Padovani, P., Papovich, C., Park, Y., Ravindranath, S., Renzini, A., Richardson, M., Riess, A., Rosati, P., Schirmer, M., Schreier, E., Somerville, R. S., Spinrad, H., Stern, D., Stiavelli, M., Strolger, L., Urry, C. M., Vandame, B., Williams, R., and Wolf, C. (2004). The Great Observatories Origins Deep Survey: Initial Results from Optical and Near-Infrared Imaging. *ApJ*, 600:L93–L98.
- Gilmore, G. (2004). The short spectacular life of a superstar. *Science*, 304(5679):1915–1916.
- Ginolfi, M., Maiolino, R., Nagao, T., Carniani, S., Belfiore, F., Cresci, G., Hatsukade, B., Mannucci, F., Marconi, A., and Pallottini, A. (2017). Molecular gas on large circumgalactic scales at  $z = 3.47$ . *MNRAS*, 468(3):3468–3483.
- Glazebrook, K., Abraham, R. G., McCarthy, P. J., Savaglio, S., Chen, H.-W., Crampton, D., Murowinski, R., Jørgensen, I., Roth, K., and Hook, I. (2004). A high abundance of massive galaxies 3-6 billion years after the Big Bang. *Nature*, 430(6996):181–184.
- Glazebrook, K., Schreiber, C., Labbé, I., Nanayakkara, T., Kacprzak, G. G., Oesch, P. A., Papovich, C., Spitler, L. R., Straatman, C. M. S., Tran, K.-V. H., and Yuan, T. (2017). A massive, quiescent galaxy at a redshift of 3.717. *Nature*, 544:71–74.
- Glenn, J., Bock, J. J., Chattopadhyay, G., Edgington, S. F., Lange, A. E., Zmuidzinas, J., Maukopf, P. D., Rownd, B., Yuen, L., and Ade, P. A. (1998). Bolocam: a millimeter-wave bolometric camera. In Phillips, T. G., editor, *Advanced Technology MMW, Radio, and Terahertz Telescopes*, volume 3357 of *Proc. SPIE*, pages 326–334.
- Gobat, R., Daddi, E., Magdis, G., Bournaud, F., Sargent, M., Martig, M., Jin, S., Finoguenov, A., Béthermin, M., and Hwang, H. S. (2018). The unexpectedly large dust and gas content of quiescent galaxies at  $z \gtrsim 1.4$ . *Nature Astronomy*, 2:239–246.
- Golwala, S. (2018). The Chajnantor Sub/Millimeter Survey Telescope. In *Atacama Large-Aperture Submm/mm Telescope (AtLAST)*, page 46.
- Gómez-Guijarro, C., Toft, S., Karim, A., Magnelli, B., Magdis, G. E., Jiménez-Andrade, E. F., Capak, P. L., Fraternali, F., Fujimoto, S., Riechers, D. A., Schinnerer, E., Smolčić, V., Aravena, M., Bertoldi, F., Cortzen, I., Hasinger, G., Hu, E. M., Jones, G. C., Koekemoer, A. M., Lee, N., McCracken, H. J., Michałowski, M. J., Navarrete, F., Pović, M., Puglisi, A., Romano-Díaz, E., Sheth, K., Silverman, J. D., Staguhn, J., Steinhardt, C. L., Stockmann, M., Tanaka, M., Valentino, F., van Kampen, E., and Zirm, A. (2018). Starburst to Quiescent from HST/ALMA: Stars and Dust Unveil Minor Mergers in Submillimeter Galaxies at  $z \sim 4.5$ . *ApJ*, 856:121.
- González-López, J., Bauer, F. E., Romero-Cañizales, C., Kneissl, R., Villard, E., Carvajal, R., Kim, S., Laporte, N., Anguita, T., Aravena, M., Bouwens, R. J., Bradley, L., Carrasco, M., Demarco, R., Ford, H., Ibar, E., Infante, L., Messias, H., Muñoz Arancibia, A. M., Nagar, N., Padilla, N., Treister, E., Troncoso, P., and Zitrin, A. (2017). The ALMA Frontier Fields Survey. I. 1.1 mm continuum detections in Abell 2744, MACS J0416.1-2403 and MACS J1149.5+2223. *A&A*, 597:A41.

- González-López, J., Decarli, R., Pavesi, R., Walter, F., Aravena, M., Carilli, C., Boogaard, L., Pop-ping, G., Weiss, A., Assef, R. J., Bauer, F. E., Bertoldi, F., Bouwens, R., Contini, T., Cortes, P. C., Cox, P., da Cunha, E., Daddi, E., Díaz-Santos, T., Inami, H., Hodge, J., Ivison, R., Le Fèvre, O., Magnelli, B., esch, P., Riechers, D., Rix, H.-W., Smail, I., Swinbank, A. M., Somerville, R. S., Uzgil, B., and van der Werf, P. (2019a). The ALMA Spectroscopic Survey in the HUDF: CO emission lines and 3 mm continuum sources. *arXiv e-prints*, page arXiv:1903.09161.
- González-López, J., Decarli, R., Pavesi, R., Walter, F., Aravena, M., Carilli, C., Boogaard, L., Pop-ping, G., Weiss, A., Assef, R. J., Bauer, F. E., Bertoldi, F., Bouwens, R., Contini, T., Cortes, P. C., Cox, P., da Cunha, E., Daddi, E., Díaz-Santos, T., Inami, H., Hodge, J., Ivison, R., Le Fèvre, O., Magnelli, B., esch, P., Riechers, D., Rix, H.-W., Smail, I., Swinbank, A. M., Somerville, R. S., Uzgil, B., and van der Werf, P. (2019b). The ALMA Spectroscopic Survey in the HUDF: CO emission lines and 3 mm continuum sources. *arXiv e-prints*, page arXiv:1903.09161.
- Goodricke, J. and Englefield, H. C. (1785). Observations of a New Variable Star. By John Goodricke, Esq.; Communicated by Sir H. C. Englefield, Bart. F. R. S. and A. S. *Philosophical Transactions of the Royal Society of London Series I*, 75:153–164.
- Gordon, K. D., Galliano, F., Hony, S., Bernard, J.-P., Bolatto, A., Bot, C., Engelbracht, C., Hughes, A., Israel, F. P., Kemper, F., Kim, S., Li, A., Madden, S. C., Matsuura, M., Meixner, M., Misselt, K., Okumura, K., Panuzzo, P., Rubio, M., Reach, W. T., Roman-Duval, J., Sauvage, M., Skibba, R., and Tielens, A. G. G. M. (2010). Determining dust temperatures and masses in the Herschel era: The importance of observations longward of 200 micron. *A&A*, 518:L89.
- Goto, T. (2005). 266 E+A galaxies selected from the Sloan Digital Sky Survey Data Release 2: the origin of E+A galaxies. *MNRAS*, 357(3):937–944.
- Greve, T. R., Vieira, J. D., Weiß, A., Aguirre, J. E., Aird, K. A., Ashby, M. L. N., Benson, B. A., Bleem, L. E., Bradford, C. M., Brodwin, M., Carlstrom, J. E., Chang, C. L., Chapman, S. C., Crawford, T. M., de Breuck, C., de Haan, T., Dobbs, M. A., Downes, T., Fassnacht, C. D., Fazio, G., George, E. M., Gladders, M., Gonzalez, A. H., Halverson, N. W., Hezaveh, Y., High, F. W., Holder, G. P., Holzapfel, W. L., Hoover, S., Hrubes, J. D., Johnson, M., Keisler, R., Knox, L., Lee, A. T., Leitch, E. M., Lueker, M., Luong-Van, D., Malkan, M., Marrone, D. P., McIntyre, V., McMahon, J. J., Mehl, J., Menten, K. M., Meyer, S. S., Montroy, T., Murphy, E. J., Natoli, T., Padin, S., Plagge, T., Pryke, C., Reichardt, C. L., Rest, A., Rosenman, M., Ruel, J., Ruhl, J. E., Schaffer, K. K., Sharon, K., Shaw, L., Shirokoff, E., Stalder, B., Stanford, S. A., Staniszewski, Z., Stark, A. A., Story, K., Vanderlinde, K., Walsh, W., Welikala, N., and Williamson, R. (2012). Submillimeter Observations of Millimeter Bright Galaxies Discovered by the South Pole Telescope. *ApJ*, 756:101.
- Griffin, M. J., Abergel, A., Abreu, A., Ade, P. A. R., André, P., Augeres, J.-L., Babbedge, T., Bae, Y., Baillie, T., Baluteau, J.-P., Barlow, M. J., Bendo, G., Benielli, D., Bock, J. J., Bonhomme, P., Brisbin, D., Brockley-Blatt, C., Caldwell, M., Cara, C., Castro-Rodriguez, N., Cerulli, R., Charnial, P., Chen, S., Clark, E., Clements, D. L., Clerc, L., Coker, J., Communal, D., Conversi, L., Cox, P., Crumb, D., Cunningham, C., Daly, F., Davis, G. R., de Antoni, P., Delderfield, J., Devin, N., di Giorgio, A., Didschuns, I., Dohlen, K., Donati, M., Dowell, A., Dowell, C. D., Duband, L., Dumaye, L., Emery, R. J., Ferlet, M., Ferrand, D., Fontignie, J., Fox, M., Franceschini, A., Frerking, M., Fulton, T., Garcia, J., Gastaud, R., Gear, W. K., Glenn, J., Goizel, A., Griffin, D. K., Grundy, T., Guest, S., Guillemet, L., Hargrave, P. C., Harwit, M., Hastings, P., Hatziminaoglou, E., Herman, M., Hinde, B., Hristov, V., Huang, M., Imhof, P., Isaak, K. J., Israelsson, U., Ivison,

- R. J., Jennings, D., Kiernan, B., King, K. J., Lange, A. E., Latter, W., Laurent, G., Laurent, P., Leeks, S. J., Lellouch, E., Levenson, L., Li, B., Li, J., Lilienthal, J., Lim, T., Liu, S. J., Lu, N., Madden, S., Mainetti, G., Marliani, P., McKay, D., Mercier, K., Molinari, S., Morris, H., Moseley, H., Mulder, J., Mur, M., Naylor, D. A., Nguyen, H., O'Halloran, B., Oliver, S., Olofsson, G., Olofsson, H.-G., Orfei, R., Page, M. J., Pain, I., Panuzzo, P., Papageorgiou, A., Parks, G., Parr-Burman, P., Pearce, A., Pearson, C., Pérez-Fournon, I., Pinsard, F., Pisano, G., Podosek, J., Pohlen, M., Polehampton, E. T., Pouliquen, D., Rigopoulou, D., Rizzo, D., Roseboom, I. G., Roussel, H., Rowan-Robinson, M., Rownd, B., Saraceno, P., Sauvage, M., Savage, R., Savini, G., Sawyer, E., Scharnberg, C., Schmitt, D., Schneider, N., Schulz, B., Schwartz, A., Shafer, R., Shupe, D. L., Sibthorpe, B., Sidher, S., Smith, A., Smith, A. J., Smith, D., Spencer, L., Stobie, B., Sudiwala, R., Sukhatme, K., Surace, C., Stevens, J. A., Swinyard, B. M., Trichas, M., Tourette, T., Triou, H., Tseng, S., Tucker, C., Turner, A., Vaccari, M., Valtchanov, I., Vigroux, L., Virique, E., Voellmer, G., Walker, H., Ward, R., Waskett, T., Weilert, M., Wesson, R., White, G. J., Whitehouse, N., Wilson, C. D., Winter, B., Woodcraft, A. L., Wright, G. S., Xu, C. K., Zavagno, A., Zemcov, M., Zhang, L., and Zonca, E. (2010). The Herschel-SPIRE instrument and its in-flight performance. *A&A*, 518:L3.
- Grogin, N. A., Kocevski, D. D., Faber, S. M., Ferguson, H. C., Koekemoer, A. M., Riess, A. G., Acquaviva, V., Alexander, D. M., Almaini, O., Ashby, M. L. N., Barden, M., Bell, E. F., Bournaud, F., Brown, T. M., Caputi, K. I., Casertano, S., Cassata, P., Castellano, M., Challis, P., Chary, R.-R., Cheung, E., Cirasuolo, M., Conselice, C. J., Roshan Cooray, A., Croton, D. J., Daddi, E., Dahlen, T., Davé, R., de Mello, D. F., Dekel, A., Dickinson, M., Dolch, T., Donley, J. L., Dunlop, J. S., Dutton, A. A., Elbaz, D., Fazio, G. G., Filippenko, A. V., Finkelstein, S. L., Fontana, A., Gardner, J. P., Garnavich, P. M., Gawiser, E., Giavalisco, M., Grazian, A., Guo, Y., Hathi, N. P., Häussler, B., Hopkins, P. F., Huang, J.-S., Huang, K.-H., Jha, S. W., Kartaltepe, J. S., Kirshner, R. P., Koo, D. C., Lai, K., Lee, K.-S., Li, W., Lotz, J. M., Lucas, R. A., Madau, P., McCarthy, P. J., McGrath, E. J., McIntosh, D. H., McLure, R. J., Mobasher, B., Moustakas, L. A., Mozena, M., Nandra, K., Newman, J. A., Niemi, S.-M., Noeske, K. G., Papovich, C. J., Pentericci, L., Pope, A., Primack, J. R., Rajan, A., Ravindranath, S., Reddy, N. A., Renzini, A., Rix, H.-W., Robaina, A. R., Rodney, S. A., Rosario, D. J., Rosati, P., Salimbeni, S., Scarlata, C., Siana, B., Simard, L., Smidt, J., Somerville, R. S., Spinrad, H., Straughn, A. N., Strolger, L.-G., Telford, O., Teplitz, H. I., Trump, J. R., van der Wel, A., Villforth, C., Wechsler, R. H., Weiner, B. J., Wiklind, T., Wild, V., Wilson, G., Wuyts, S., Yan, H.-J., and Yun, M. S. (2011). CANDELS: The Cosmic Assembly Near-infrared Deep Extragalactic Legacy Survey. *ApJS*, 197:35.
- Gullberg, B., Swinbank, A. M., Smail, I., Biggs, A. D., Bertoldi, F., De Breuck, C., Chapman, S. C., Chen, C. C., Cooke, E. A., and Coppin, K. E. K. (2018). The Dust and [C II] Morphologies of Redshift  $\sim 4.5$  Sub-millimeter Galaxies at  $\sim 200$  pc Resolution: The Absence of Large Clumps in the Interstellar Medium at High-redshift. *ApJ*, 859(1):12.
- Guo, Y., Ferguson, H. C., Bell, E. F., Koo, D. C., Conselice, C. J., Giavalisco, M., Kassin, S., Lu, Y., Lucas, R., Mandelker, N., McIntosh, D. M., Primack, J. R., Ravindranath, S., Barro, G., Ceverino, D., Dekel, A., Faber, S. M., Fang, J. J., Koekemoer, A. M., Noeske, K., Rafelski, M., and Straughn, A. (2015). Clumpy Galaxies in CANDELS. I. The Definition of UV Clumps and the Fraction of Clumpy Galaxies at  $0.5 < z < 3$ . *ApJ*, 800:39.
- Guo, Y., Ferguson, H. C., Giavalisco, M., Barro, G., Willner, S. P., Ashby, M. L. N., Dahlen, T., Donley, J. L., Faber, S. M., Fontana, A., Galametz, A., Grazian, A., Huang, K.-H., Kocevski, D. D., Koekemoer, A. M., Koo, D. C., McGrath, E. J., Peth, M., Salvato, M., Wuyts, S., Castellano, M., Cooray, A. R., Dickinson, M. E., Dunlop, J. S., Fazio, G. G., Gardner, J. P., Gawiser,

- E., Grogin, N. A., Hathi, N. P., Hsu, L.-T., Lee, K.-S., Lucas, R. A., Mobasher, B., Nandra, K., Newman, J. A., and van der Wel, A. (2013). CANDELS Multi-wavelength Catalogs: Source Detection and Photometry in the GOODS-South Field. *ApJS*, 207:24.
- Guo, Y., Giavalisco, M., Ferguson, H. C., Cassata, P., and Koekemoer, A. M. (2012). Multi-wavelength View of Kiloparsec-scale Clumps in Star-forming Galaxies at  $z \sim 2$ . *ApJ*, 757:120.
- Güsten, R., Nyman, L. Å., Schilke, P., Menten, K., Cesarsky, C., and Booth, R. (2006). The Atacama Pathfinder EXperiment (APEX) - a new submillimeter facility for southern skies -. *A&A*, 454:L13–L16.
- Hainline, L. J., Blain, A. W., Smail, I., Alexander, D. M., Armus, L., Chapman, S. C., and Ivison, R. J. (2011). The Stellar Mass Content of Submillimeter-selected Galaxies. *ApJ*, 740:96.
- Hales, C. A., Murphy, T., Curran, J. R., Middelberg, E., Gaensler, B. M., and Norris, R. P. (2012). BLOBCAT: Software to Catalog Blobs. Astrophysics Source Code Library.
- Hao, C. N., Mao, S., Deng, Z. G., Xia, X. Y., and Wu, H. (2006). Isophotal shapes of elliptical/lenticular galaxies from the Sloan Digital Sky Survey. *MNRAS*, 370:1339–1350.
- Hatsukade, B., Kohno, K., Aretxaga, I., Austermann, J. E., Ezawa, H., Hughes, D. H., Ikarashi, S., Iono, D., Kawabe, R., Khan, S., Matsuo, H., Matsuura, S., Nakanishi, K., Oshima, T., Perera, T., Scott, K. S., Shirahata, M., Takeuchi, T. T., Tamura, Y., Tanaka, K., Tosaki, T., Wilson, G. W., and Yun, M. S. (2011). AzTEC/ASTE 1.1-mm survey of the AKARI Deep Field South: source catalogue and number counts. *MNRAS*, 411:102–116.
- Hatsukade, B., Kohno, K., Umehata, H., Aretxaga, I., Caputi, K. I., Dunlop, J. S., Ikarashi, S., Iono, D., Ivison, R. J., Lee, M., Makiya, R., Matsuda, Y., Motohara, K., Nakanishi, K., Ohta, K., Tadaki, K.-i., Tamura, Y., Wang, W.-H., Wilson, G. W., Yamaguchi, Y., and Yun, M. S. (2016). SXDF-ALMA 2-arcmin<sup>2</sup> deep survey: 1.1-mm number counts. *PASJ*, 68:36.
- Hatsukade, B., Kohno, K., Yamaguchi, Y., Umehata, H., Ao, Y., Aretxaga, I., Caputi, K. I., Dunlop, J. S., Egami, E., Espada, D., Fujimoto, S., Hayatsu, N. H., Hughes, D. H., Ikarashi, S., Iono, D., Ivison, R. J., Kawabe, R., Kodama, T., Lee, M., Matsuda, Y., Nakanishi, K., Ohta, K., Ouchi, M., Rujopakarn, W., Suzuki, T., Tamura, Y., Ueda, Y., Wang, T., Wang, W.-H., Wilson, G. W., Yoshimura, Y., and Yun, M. S. (2018). ALMA twenty-six arcmin<sup>2</sup> survey of GOODS-S at one millimeter (ASAGAO): Source catalog and number counts. *PASJ*, 70:105.
- Hatsukade, B., Ohta, K., Seko, A., Yabe, K., and Akiyama, M. (2013). Faint End of 1.3 mm Number Counts Revealed by ALMA. *ApJ*, 769:L27.
- Hayward, C. C., Kereš, D., Jonsson, P., Narayanan, D., Cox, T. J., and Hernquist, L. (2011). What Does a Submillimeter Galaxy Selection Actually Select? The Dependence of Submillimeter Flux Density on Star Formation Rate and Dust Mass. *ApJ*, 743:159.
- Hayward, C. C., Narayanan, D., Kereš, D., Jonsson, P., Hopkins, P. F., Cox, T. J., and Hernquist, L. (2013). Submillimetre galaxies in a hierarchical universe: number counts, redshift distribution and implications for the IMF. *MNRAS*, 428:2529–2547.
- Heckman, T. M., Armus, L., and Miley, G. K. (1990). On the Nature and Implications of Starburst-driven Galactic Superwinds. *ApJS*, 74:833.



- Heckman, T. M., Robert, C., Leitherer, C., Garnett, D. R., and van der Rydt, F. (1998). The Ultraviolet Spectroscopic Properties of Local Starbursts: Implications at High Redshift. *ApJ*, 503(2):646–661.
- Heinis, S., Buat, V., Béthermin, M., Bock, J., Burgarella, D., Conley, A., Cooray, A., Farrah, D., Ilbert, O., Magdis, G., Marsden, G., Oliver, S. J., Rigopoulou, D., Roehlly, Y., Schulz, B., Symeonidis, M., Viero, M., Xu, C. K., and Zemcov, M. (2014). HerMES: dust attenuation and star formation activity in ultraviolet-selected samples from  $z \sim 4$  to  $\sim 1.5$ . *MNRAS*, 437:1268–1283.
- Helou, G., Soifer, B. T., and Rowan-Robinson, M. (1985). Thermal infrared and nonthermal radio - Remarkable correlation in disks of galaxies. *ApJ*, 298:L7–L11.
- Hertzsprung, E. (1913). Über die räumliche Verteilung der Veränderlichen vom  $\delta$  Cephei-Typus. *Astronomische Nachrichten*, 196:201.
- Hezaveh, Y. D. and Holder, G. P. (2011). Effects of Strong Gravitational Lensing on Millimeter-wave Galaxy Number Counts. *ApJ*, 734(1):52.
- Ho, P. T. P., Moran, J. M., and Lo, K. Y. (2004). The Submillimeter Array. *ApJ*, 616(1):L1–L6.
- Hodge, J. A., Karim, A., Smail, I., Swinbank, A. M., Walter, F., Biggs, A. D., Ivison, R. J., Weiss, A., Alexander, D. M., Bertoldi, F., Brandt, W. N., Chapman, S. C., Coppin, K. E. K., Cox, P., Danielson, A. L. R., Dannerbauer, H., De Breuck, C., Decarli, R., Edge, A. C., Greve, T. R., Knudsen, K. K., Menten, K. M., Rix, H.-W., Schinnerer, E., Simpson, J. M., Wardlow, J. L., and van der Werf, P. (2013). An ALMA Survey of Submillimeter Galaxies in the Extended Chandra Deep Field South: Source Catalog and Multiplicity. *ApJ*, 768:91.
- Hodge, J. A., Smail, I., Walter, F., da Cunha, E., Swinbank, A. M., Rybak, M., Venemans, B., Brandt, W. N., Calistro Rivera, G., Chapman, S. C., Chen, C.-C., Cox, P., Dannerbauer, H., Decarli, R., Greve, T. R., Knudsen, K. K., Menten, K. M., Schinnerer, E., Simpson, J. M., van der Werf, P., Wardlow, J. L., and Weiss, A. (2019). ALMA Reveals Potential Evidence for Spiral Arms, Bars, and Rings in High-redshift Submillimeter Galaxies. *ApJ*, 876:130.
- Hodge, J. A., Swinbank, A. M., Simpson, J. M., Smail, I., Walter, F., Alexander, D. M., Bertoldi, F., Biggs, A. D., Brandt, W. N., Chapman, S. C., Chen, C. C., Coppin, K. E. K., Cox, P., Dannerbauer, H., Edge, A. C., Greve, T. R., Ivison, R. J., Karim, A., Knudsen, K. K., Menten, K. M., Rix, H.-W., Schinnerer, E., Wardlow, J. L., Weiss, A., and van der Werf, P. (2016). Kiloparsec-scale Dust Disks in High-redshift Luminous Submillimeter Galaxies. *ApJ*, 833:103.
- Hogg, D. W., Baldry, I. K., Blanton, M. R., and Eisenstein, D. J. (2002). The K correction. *arXiv Astrophysics e-prints*.
- Hogg, D. W., Blanton, M. R., Brinchmann, J., Eisenstein, D. J., Schlegel, D. J., Gunn, J. E., McKay, T. A., Rix, H.-W., Bahcall, N. A., and Brinkmann, J. (2004). The Dependence on Environment of the Color-Magnitude Relation of Galaxies. *ApJ*, 601(1):L29–L32.
- Hogg, D. W., Eisenstein, D. J., Blanton, M. R., Bahcall, N. A., Brinkmann, J., Gunn, J. E., and Schneider, D. P. (2005). Cosmic Homogeneity Demonstrated with Luminous Red Galaxies. *ApJ*, 624(1):54–58.
- Hogg, D. W. and Turner, E. L. (1998). A Maximum Likelihood Method to Improve Faint-Source Flux and Color Estimates. *PASP*, 110:727–731.

- Holland, W. S., Robson, E. I., Gear, W. K., Cunningham, C. R., Lightfoot, J. F., Jenness, T., Ivison, R. J., Stevens, J. A., Ade, P. A. R., Griffin, M. J., Duncan, W. D., Murphy, J. A., and Naylor, D. A. (1999). SCUBA: a common-user submillimetre camera operating on the James Clerk Maxwell Telescope. *MNRAS*, 303:659–672.
- Hopkins, P. F., Hernquist, L., Cox, T. J., Di Matteo, T., Robertson, B., and Springel, V. (2006). A Unified, Merger-driven Model of the Origin of Starbursts, Quasars, the Cosmic X-Ray Background, Supermassive Black Holes, and Galaxy Spheroids. *ApJS*, 163:1–49.
- Hsieh, B.-C., Wang, W.-H., Hsieh, C.-C., Lin, L., Yan, H., Lim, J., and Ho, P. T. P. (2012). The Taiwan ECDFS Near-Infrared Survey: Ultra-deep J and K<sub>S</sub> Imaging in the Extended Chandra Deep Field-South. *ApJS*, 203:23.
- Hsu, L.-T., Salvato, M., Nandra, K., Brusa, M., Bender, R., Buchner, J., Donley, J. L., Kocevski, D. D., Guo, Y., Hathi, N. P., Rangel, C., Willner, S. P., Brightman, M., Georgakakis, A., Budavári, T., Szalay, A. S., Ashby, M. L. N., Barro, G., Dahlen, T., Faber, S. M., Ferguson, H. C., Galametz, A., Grazian, A., Grogin, N. A., Huang, K.-H., Koekemoer, A. M., Lucas, R. A., McGrath, E., Mobasher, B., Peth, M., Rosario, D. J., and Trump, J. R. (2014). CANDELS/GOODS-S, CDFS, and ECDFS: Photometric Redshifts for Normal and X-Ray-Detected Galaxies. *ApJ*, 796:60.
- Huang, J.-S., Zheng, X. Z., Rigopoulou, D., Magdis, G., Fazio, G. G., and Wang, T. (2011). Four IRAC Sources with an Extremely Red H - [3.6] Color: Passive or Dusty Galaxies at  $z > 4.5$ ? *ApJ*, 742:L13.
- Hubble, E. (1929). A Relation between Distance and Radial Velocity among Extra-Galactic Nebulae. *Proceedings of the National Academy of Science*, 15:168–173.
- Hubble, E. (1936a). Effects of Red Shifts on the Distribution of Nebulae. *ApJ*, 84:517.
- Hubble, E. P. (1925). Cepheids in Spiral Nebulae. *Popular Astronomy*, 33.
- Hubble, E. P. (1926). Extragalactic nebulae. *ApJ*, 64.
- Hubble, E. P. (1936b). *Realm of the Nebulae*.
- Huertas-Company, M., Gravet, R., Cabrera-Vives, G., Pérez-González, P. G., Kartaltepe, J. S., Barro, G., Bernardi, M., Mei, S., Shankar, F., Dimauro, P., Bell, E. F., Kocevski, D., Koo, D. C., Faber, S. M., and McIntosh, D. H. (2015a). A Catalog of Visual-like Morphologies in the 5 CANDELS Fields Using Deep Learning. *ApJS*, 221:8.
- Huertas-Company, M., Pérez-González, P. G., Mei, S., Shankar, F., Bernardi, M., Daddi, E., Barro, G., Cabrera-Vives, G., Cattaneo, A., Dimauro, P., and Gravet, R. (2015b). The Morphologies of Massive Galaxies from  $z \sim 3$  - Witnessing the Two Channels of Bulge Growth. *ApJ*, 809:95.
- Hughes, D. H., Serjeant, S., Dunlop, J., Rowan-Robinson, M., Blain, A., Mann, R. G., Ivison, R., Peacock, J., Efstathiou, A., Gear, W., Oliver, S., Lawrence, A., Longair, M., Goldschmidt, P., and Jenness, T. (1998). High-redshift star formation in the Hubble Deep Field revealed by a submillimetre-wavelength survey. *Nature*, 394:241–247.
- Hwang, H. S., Elbaz, D., Magdis, G., Daddi, E., Symeonidis, M., Altieri, B., Amblard, A., Andreani, P., Arumugam, V., Auld, R., Aussel, H., Babbedge, T., Berta, S., Blain, A., Bock, J., Bongiovanni, A., Boselli, A., Buat, V., Burgarella, D., Castro-Rodríguez, N., Cava, A., Cepa, J., Chantal, P., Chapin, E., Chary, R.-R., Cimatti, A., Clements, D. L., Conley, A., Conversi,

- L., Cooray, A., Dannerbauer, H., Dickinson, M., Dominguez, H., Dowell, C. D., Dunlop, J. S., Dwek, E., Eales, S., Farrah, D., Schreiber, N. F., Fox, M., Franceschini, A., Gear, W., Genzel, R., Glenn, J., Griffin, M., Gruppioni, C., Halpern, M., Hatziminaoglou, E., Ibar, E., Isaak, K., Ivison, R. J., Jeong, W.-S., Lagache, G., Le Borgne, D., Le Floch, E., Lee, H. M., Lee, J. C., Lee, M. G., Levenson, L., Lu, N., Lutz, D., Madden, S., Maffei, B., Magnelli, B., Mainetti, G., Maiolino, R., Marchetti, L., Mortier, A. M. J., Nguyen, H. T., Nordon, R., O'Halloran, B., Okumura, K., Oliver, S. J., Omont, A., Page, M. J., Panuzzo, P., Papageorgiou, A., Pearson, C. P., Pérez-Fournon, I., García, A. M. P., Poglitsch, A., Pohlen, M., Popesso, P., Pozzi, F., Rawlings, J. I., Rigopoulou, D., Riguccini, L., Rizzo, D., Rodighiero, G., Roseboom, I. G., Rowan-Robinson, M., Saintonge, A., Portal, M. S., Santini, P., Sauvage, M., Schulz, B., Scott, D., Seymour, N., Shao, L., Shupe, D. L., Smith, A. J., Stevens, J. A., Sturm, E., Tacconi, L., Trichas, M., Tugwell, K. E., Vaccari, M., Valtchanov, I., Vieira, J. D., Vigroux, L., Wang, L., Ward, R., Wright, G., Xu, C. K., and Zemcov, M. (2010). Evolution of dust temperature of galaxies through cosmic time as seen by Herschel. *MNRAS*, 409:75–82.
- Ikarashi, S., Caputi, K., Ohta, K., Ivison, R. J., Lagos, C. D. P., Bisigello, L., Hatsukade, B., Aretxaga, I., Dunlop, J. S., Hughes, D. H., Iono, D., Izumi, T., Kashikawa, N., Koyama, Y., Kawabe, R., Kohno, K., Motohara, K., Nakanishi, K., Tamura, Y., Umehata, H., Wilson, G. W., Yabe, K., and Yun, M. S. (2017). Very compact millimeter sizes for composite star-forming/AGN submillimeter galaxies. *ArXiv e-prints*.
- Ikarashi, S., Ivison, R. J., Caputi, K. I., Aretxaga, I., Dunlop, J. S., Hatsukade, B., Hughes, D. H., Iono, D., Izumi, T., Kawabe, R., Kohno, K., Lagos, C. D. P., Motohara, K., Nakanishi, K., Ohta, K., Tamura, Y., Umehata, H., Wilson, G. W., Yabe, K., and Yun, M. S. (2015). Compact Starbursts in  $z \sim 3-6$  Submillimeter Galaxies Revealed by ALMA. *ApJ*, 810:133.
- Ilbert, O., Arnouts, S., McCracken, H. J., Bolzonella, M., Bertin, E., Le Fèvre, O., Mellier, Y., Zamorani, G., Pellò, R., Iovino, A., Tresse, L., Le Brun, V., Bottini, D., Garilli, B., Maccagni, D., Picat, J. P., Scaramella, R., Scodeggio, M., Vettolani, G., Zanichelli, A., Adami, C., Bardelli, S., Cappi, A., Charlot, S., Ciliegi, P., Contini, T., Cucciati, O., Foucaud, S., Franzetti, P., Gavignaud, I., Guzzo, L., Marano, B., Marinoni, C., Mazure, A., Meneux, B., Merighi, R., Paltani, S., Pollo, A., Pozzetti, L., Radovich, M., Zucca, E., Bondi, M., Bongiorno, A., Busarello, G., de La Torre, S., Gregorini, L., Lamareille, F., Mathez, G., Merluzzi, P., Ripepi, V., Rizzo, D., and Vergani, D. (2006). Accurate photometric redshifts for the CFHT legacy survey calibrated using the VIMOS VLT deep survey. *A&A*, 457:841–856.
- Inami, H., Bacon, R., Brinchmann, J., Richard, J., Contini, T., Conseil, S., Hamer, S., Akhlaghi, M., Bouché, N., Clément, B., Desprez, G., Drake, A. B., Hashimoto, T., Leclercq, F., Maseda, M., Michel-Dansac, L., Paalvast, M., Tresse, L., Ventou, E., Kollatschny, W., Boogaard, L. A., Finley, H., Marino, R. A., Schaye, J., and Wisotzki, L. (2017). The MUSE Hubble Ultra Deep Field Survey. II. Spectroscopic redshifts and comparisons to color selections of high-redshift galaxies. *A&A*, 608:A2.
- Inoue, S., Dekel, A., Mandelker, N., Ceverino, D., Bournaud, F., and Primack, J. (2016). Non-linear violent disc instability with high Toomre's  $Q$  in high-redshift clumpy disc galaxies. *MNRAS*, 456(2):2052–2069.
- Iono, D., Yun, M. S., Aretxaga, I., Hatsukade, B., Hughes, D., Ikarashi, S., Izumi, T., Kawabe, R., Kohno, K., Lee, M., Matsuda, Y., Nakanishi, K., Saito, T., Tamura, Y., Ueda, J., Umehata, H., Wilson, G., Michiyama, T., and Ando, M. (2016). Clumpy and Extended Starbursts in the Brightest Unlensed Submillimeter Galaxies. *ApJ*, 829:L10.

- Iverson, R. J., Greve, T. R., Dunlop, J. S., Peacock, J. A., Egami, E., Smail, I., Ibar, E., van Kampen, E., Aretxaga, I., Babbedge, T., Biggs, A. D., Blain, A. W., Chapman, S. C., Clements, D. L., Coppin, K., Farrah, D., Halpern, M., Hughes, D. H., Jarvis, M. J., Jenness, T., Jones, J. R., Mortier, A. M. J., Oliver, S., Papovich, C., Pérez-González, P. G., Pope, A., Rawlings, S., Rieke, G. H., Rowan-Robinson, M., Savage, R. S., Scott, D., Seigar, M., Serjeant, S., Simpson, C., Stevens, J. A., Vaccari, M., Wagg, J., and Willott, C. J. (2007). The SCUBA HALf Degree Extragalactic Survey - III. Identification of radio and mid-infrared counterparts to submillimetre galaxies. *MNRAS*, 380:199–228.
- Iverson, R. J., Magnelli, B., Ibar, E., Andreani, P., Elbaz, D., Altieri, B., Amblard, A., Arumugam, V., Auld, R., Aussel, H., Babbedge, T., Berta, S., Blain, A., Bock, J., Bongiovanni, A., Boselli, A., Buat, V., Burgarella, D., Castro-Rodríguez, N., Cava, A., Cepa, J., Chantal, P., Cimatti, A., Cirasuolo, M., Clements, D. L., Conley, A., Conversi, L., Cooray, A., Daddi, E., Dominguez, H., Dowell, C. D., Dwek, E., Eales, S., Farrah, D., Förster Schreiber, N., Fox, M., Franceschini, A., Gear, W., Genzel, R., Glenn, J., Griffin, M., Gruppioni, C., Halpern, M., Hatziminaoglou, E., Isaak, K., Lagache, G., Levenson, L., Lu, N., Lutz, D., Madden, S., Maffei, B., Magdis, G., Mainetti, G., Maiolino, R., Marchetti, L., Morrison, G. E., Mortier, A. M. J., Nguyen, H. T., Nordon, R., O'Halloran, B., Oliver, S. J., Omont, A., Owen, F. N., Page, M. J., Panuzzo, P., Papageorgiou, A., Pearson, C. P., Pérez-Fournon, I., Pérez García, A. M., Poglitsch, A., Pohlen, M., Popesso, P., Pozzi, F., Rawlings, J. I., Raymond, G., Rigopoulou, D., Riguccini, L., Rizzo, D., Rodighiero, G., Roseboom, I. G., Rowan-Robinson, M., Saintonge, A., Sanchez Portal, M., Santini, P., Schulz, B., Scott, D., Seymour, N., Shao, L., Shupe, D. L., Smith, A. J., Stevens, J. A., Sturm, E., Symeonidis, M., Tacconi, L., Trichas, M., Tugwell, K. E., Vaccari, M., Valtchanov, I., Vieira, J., Vigroux, L., Wang, L., Ward, R., Wright, G., Xu, C. K., and Zemcov, M. (2010). The far-infrared/radio correlation as probed by Herschel. *A&A*, 518:L31.
- Jackson, J. C. (2012). Ultra-compact radio sources and the isotropy and homogeneity of the Universe. *MNRAS*, 426:779–783.
- James, S. H. G. (1993). DR Isaac Roberts (1829-1904) and his observatories. *Journal of the British Astronomical Association*, 103:120–122.
- Jin, S., Daddi, E., Magdis, G. E., Liu, D., Schinnerer, E., Papadopoulos, P. P., Gu, Q., Gao, Y., and Calabro, A. (2019). Discovery of four cold dusty galaxies at  $z=3.62-5.85$  in the COSMOS field: direct evidence of CMB impact on high-redshift galaxy observables. *arXiv e-prints*, page arXiv:1906.00040.
- Kannappan, S. J. (2004). Linking Gas Fractions to Bimodalities in Galaxy Properties. *ApJ*, 611(2):L89–L92.
- Kannappan, S. J., Guie, J. M., and Baker, A. J. (2009). E/S0 Galaxies on the Blue Color-Stellar Mass Sequence at  $z = 0$ : Fading Mergers or Future Spirals? *AJ*, 138(2):579–597.
- Karim, A., Swinbank, A. M., Hodge, J. A., Smail, I. R., Walter, F., Biggs, A. D., Simpson, J. M., Danielson, A. L. R., Alexander, D. M., Bertoldi, F., de Breuck, C., Chapman, S. C., Coppin, K. E. K., Dannerbauer, H., Edge, A. C., Greve, T. R., Iverson, R. J., Knudsen, K. K., Menten, K. M., Schinnerer, E., Wardlow, J. L., Weiß, A., and van der Werf, P. (2013). An ALMA survey of submillimetre galaxies in the Extended Chandra Deep Field South: high-resolution 870  $\mu\text{m}$  source counts. *MNRAS*, 432:2–9.

- Kauffmann, G., Heckman, T. M., White, S. D. M., Charlot, S., Tremonti, C., Peng, E. W., Seibert, M., Brinkmann, J., Nichol, R. C., and SubbaRao, M. (2003). The dependence of star formation history and internal structure on stellar mass for  $10^5$  low-redshift galaxies. *MNRAS*, 341(1):54–69.
- Kauffmann, G., White, S. D. M., Heckman, T. M., Ménard, B., Brinchmann, J., Charlot, S., Tremonti, C., and Brinkmann, J. (2004). The environmental dependence of the relations between stellar mass, structure, star formation and nuclear activity in galaxies. *MNRAS*, 353(3):713–731.
- Kennicutt, R. C. and Evans, N. J. (2012). Star Formation in the Milky Way and Nearby Galaxies. *ARA&A*, 50:531–608.
- Kennicutt, Jr., R. C. (1983). The rate of star formation in normal disk galaxies. *ApJ*, 272:54–67.
- Kennicutt, Jr., R. C. (1989). The star formation law in galactic disks. *ApJ*, 344:685–703.
- Kennicutt, Jr., R. C. (1998). The Global Schmidt Law in Star-forming Galaxies. *ApJ*, 498:541–552.
- Kewley, L. J., Dopita, M. A., Leitherer, C., Davé, R., Yuan, T., Allen, M., Groves, B., and Sutherland, R. (2013). Theoretical Evolution of Optical Strong Lines across Cosmic Time. *ApJ*, 774(2):100.
- Kinney, A. L., Calzetti, D., Bohlin, R. C., McQuade, K., Storchi-Bergmann, T., and Schmitt, H. R. (1996). Template Ultraviolet to Near-Infrared Spectra of Star-forming Galaxies and Their Application to K-Corrections. *ApJ*, 467:38.
- Kirby, E. N., Cohen, J. G., Guhathakurta, P., Cheng, L., Bullock, J. S., and Gallazzi, A. (2013). The Universal Stellar Mass-Stellar Metallicity Relation for Dwarf Galaxies. *ApJ*, 779(2):102.
- Kirkpatrick, A., Pope, A., Sajina, A., Roebuck, E., Yan, L., Armus, L., Díaz-Santos, T., and Stierwalt, S. (2015). The Role of Star Formation and an AGN in Dust Heating of  $z = 0.3$ – $2.8$  Galaxies. I. Evolution with Redshift and Luminosity. *ApJ*, 814:9.
- Kissler-Patig, M., Pirard, J.-F., Casali, M., Moorwood, A., Ageorges, N., Alves de Oliveira, C., Baksai, P., Bedin, L. R., Bendek, E., Biereichel, P., Delabre, B., Dorn, R., Esteves, R., Finger, G., Gojak, D., Huster, G., Jung, Y., Kiekebush, M., Klein, B., Koch, F., Lizon, J.-L., Mehrgan, L., Petr-Gotzens, M., Pritchard, J., Selman, F., and Stegmeier, J. (2008). HAWK-I: the high-acuity wide-field K-band imager for the ESO Very Large Telescope. *A&A*, 491:941–950.
- Klein, U., Wielebinski, R., and Morsi, H. W. (1988). Radio continuum observations of M82. *A&A*, 190:41–46.
- Knudsen, K. K., van der Werf, P. P., and Kneib, J.-P. (2008). Probing the submillimetre number counts at  $f_{850\mu m} < 2\text{mJy}$ . *MNRAS*, 384:1611–1626.
- Kocevski, D. D., Barro, G., Faber, S. M., Dekel, A., Somerville, R. S., Young, J. A., Williams, C. C., McIntosh, D. H., Georgakakis, A., Hasinger, G., Nandra, K., Civano, F., Alexander, D. M., Almaini, O., Conselice, C. J., Donley, J. L., Ferguson, H. C., Giavalisco, M., Grogin, N. A., Hathi, N., Hawkins, M., Koekemoer, A. M., Koo, D. C., McGrath, E. J., Mobasher, B., Pérez González, P. G., Pforr, J., Primack, J. R., Santini, P., Stefanon, M., Trump, J. R., van der Wel, A., Wuyts, S., and Yan, H. (2017). CANDELS: Elevated Black Hole Growth in the Progenitors of Compact Quiescent Galaxies at  $z \sim 2$ . *ApJ*, 846:112.

- Koekemoer, A. M., Faber, S. M., Ferguson, H. C., Grogin, N. A., Kocevski, D. D., Koo, D. C., Lai, K., Lotz, J. M., Lucas, R. A., McGrath, E. J., Ogaz, S., Rajan, A., Riess, A. G., Rodney, S. A., Strolger, L., Casertano, S., Castellano, M., Dahlen, T., Dickinson, M., Dolch, T., Fontana, A., Giavalisco, M., Grazian, A., Guo, Y., Hathi, N. P., Huang, K.-H., van der Wel, A., Yan, H.-J., Acquaviva, V., Alexander, D. M., Almaini, O., Ashby, M. L. N., Barden, M., Bell, E. F., Bournaud, F., Brown, T. M., Caputi, K. I., Cassata, P., Challis, P. J., Chary, R.-R., Cheung, E., Cirasuolo, M., Conselice, C. J., Roshan Cooray, A., Croton, D. J., Daddi, E., Davé, R., de Mello, D. F., de Ravel, L., Dekel, A., Donley, J. L., Dunlop, J. S., Dutton, A. A., Elbaz, D., Fazio, G. G., Filippenko, A. V., Finkelstein, S. L., Frazer, C., Gardner, J. P., Garnavich, P. M., Gawiser, E., Gruetzbauch, R., Hartley, W. G., Häussler, B., Herrington, J., Hopkins, P. F., Huang, J.-S., Jha, S. W., Johnson, A., Kartaltepe, J. S., Khostovan, A. A., Kirshner, R. P., Lani, C., Lee, K.-S., Li, W., Madau, P., McCarthy, P. J., McIntosh, D. H., McLure, R. J., McPartland, C., Mobasher, B., Moreira, H., Mortlock, A., Moustakas, L. A., Mozena, M., Nandra, K., Newman, J. A., Nielsen, J. L., Niemi, S., Noeske, K. G., Papovich, C. J., Pentericci, L., Pope, A., Primack, J. R., Ravindranath, S., Reddy, N. A., Renzini, A., Rix, H.-W., Robaina, A. R., Rosario, D. J., Rosati, P., Salimbeni, S., Scarlata, C., Siana, B., Simard, L., Smidt, J., Snyder, D., Somerville, R. S., Spinrad, H., Straughn, A. N., Telford, O., Teplitz, H. I., Trump, J. R., Vargas, C., Villforth, C., Wagner, C. R., Wandro, P., Wechsler, R. H., Weiner, B. J., Wiklind, T., Wild, V., Wilson, G., Wuyts, S., and Yun, M. S. (2011). CANDELS: The Cosmic Assembly Near-infrared Deep Extragalactic Legacy Survey - The Hubble Space Telescope Observations, Imaging Data Products, and Mosaics. *ApJS*, 197:36.
- Kong, X., Charlot, S., Brinchmann, J., and Fall, S. M. (2004). Star formation history and dust content of galaxies drawn from ultraviolet surveys. *MNRAS*, 349(3):769–778.
- Koprowski, M. P., Coppin, K. E. K., Geach, J. E., McLure, R. J., Almaini, O., Blain, A. W., Bremer, M., Bourne, N., Chapman, S. C., Conselice, C. J., Dunlop, J. S., Farrah, D., Hartley, W., Karim, A., Knudsen, K. K., Michałowski, M. J., Scott, D., Simpson, C., Smith, D. J. B., and van der Werf, P. P. (2018). A direct calibration of the  $\text{IRX-}\beta$  relation in Lyman-break Galaxies at  $z = 3\text{--}5$ . *MNRAS*, 479:4355–4366.
- Kotel'nikov, V. A. (1933). On the carrying capacity of the ether and wire in telecommunications. *Material for the First All-Union Conference on Questions of Communication*, Izd. Red. Upr. Svyazi RKKA, Moscow.
- Kovács, A., Chapman, S. C., Dowell, C. D., Blain, A. W., Ivison, R. J., Smail, I., and Phillips, T. G. (2006). SHARC-2 350  $\mu\text{m}$  Observations of Distant Submillimeter-selected Galaxies. *ApJ*, 650:592–603.
- Kreysa, E., Gemuend, H.-P., Gromke, J., Haslam, C. G., Reichertz, L., Haller, E. E., Beeman, J. W., Hansen, V., Sievers, A., and Zylka, R. (1998). Bolometer array development at the Max-Planck-Institut fuer Radioastronomie. In Phillips, T. G., editor, *Advanced Technology MMW, Radio, and Terahertz Telescopes*, volume 3357 of *Proc. SPIE*, pages 319–325.
- Kriek, M., Shapley, A. E., Reddy, N. A., Siana, B., Coil, A. L., Mobasher, B., Freeman, W. R., de Groot, L., Price, S. H., and Sanders, R. (2015). The MOSFIRE Deep Evolution Field (MOSDEF) Survey: Rest-frame Optical Spectroscopy for  $\sim 1500$  H-selected Galaxies at  $1.37 < z < 3.8$ . *ApJS*, 218(2):15.
- Kriek, M., van Dokkum, P. G., Franx, M., Illingworth, G. D., Marchesini, D., Quadri, R., Rudnick, G., Taylor, E. N., Förster Schreiber, N. M., Gawiser, E., Labbé, I., Lira, P., and Wuyts, S.

- (2008). A Near-Infrared Spectroscopic Survey of K-Selected Galaxies at  $z \sim 2.3$ : Redshifts and Implications for Broadband Photometric Studies. *ApJ*, 677:219–237.
- Kriek, M., van Dokkum, P. G., Labbé, I., Franx, M., Illingworth, G. D., Marchesini, D., and Quadri, R. F. (2009). An Ultra-Deep Near-Infrared Spectrum of a Compact Quiescent Galaxy at  $z = 2.2$ . *ApJ*, 700:221–231.
- Kurczynski, P., Gawiser, E., Acquaviva, V., Bell, E. F., Dekel, A., de Mello, D. F., Ferguson, H. C., Gardner, J. P., Grogin, N. A., Guo, Y., Hopkins, P. F., Koekemoer, A. M., Koo, D. C., Lee, S.-K., Mobasher, B., Primack, J. R., Rafelski, M., Soto, E., and Teplitz, H. I. (2016). Evolution of Intrinsic Scatter in the SFR-Stellar Mass Correlation at  $0.5 < z < 3$ . *ApJ*, 820:L1.
- Kurk, J., Cimatti, A., Daddi, E., Mignoli, M., Pozzetti, L., Dickinson, M., Bolzonella, M., Zamorani, G., Cassata, P., Rodighiero, G., Franceschini, A., Renzini, A., Rosati, P., Halliday, C., and Berta, S. (2013). GMASS ultradeep spectroscopy of galaxies at  $z \sim 2$ . VII. Sample selection and spectroscopy. *A&A*, 549:A63.
- Labbé, I., Oesch, P. A., Illingworth, G. D., van Dokkum, P. G., Bouwens, R. J., Franx, M., Carollo, C. M., Trenti, M., Holden, B., Smit, R., González, V., Magee, D., Stiavelli, M., and Stefanon, M. (2015). Ultradeep IRAC Imaging Over the HUDF and GOODS-South: Survey Design and Imaging Data Release. *ApJS*, 221:23.
- Lacki, B. C., Thompson, T. A., and Quataert, E. (2010). The Physics of the Far-infrared-Radio Correlation. I. Calorimetry, Conspiracy, and Implications. *ApJ*, 717:1–28.
- Lagache, G., Haffner, L. M., Reynolds, R. J., and Tufte, S. L. (2000). Evidence for dust emission in the Warm Ionised Medium sing WHAM data. *A&A*, 354:247–252.
- Lamastra, A., Menci, N., Fiore, F., Santini, P., Bongiorno, A., and Piconcelli, E. (2013). Probing AGN triggering mechanisms through the starburstiness of the host galaxies. *A&A*, 559:A56.
- Lançon, A. and Rocca-Volmerange, B. (1996). Near-IR spectral evolution of dusty starburst galaxies. *New A*, 1(3):215–234.
- Laporte, N., Bauer, F. E., Troncoso-Iribarren, P., Huang, X., González-López, J., Kim, S., Anguita, T., Aravena, M., Barrientos, L. F., Bouwens, R., Bradley, L., Brammer, G., Carrasco, M., Carvajal, R., Coe, D., Demarco, R., Ellis, R. S., Ford, H., Francke, H., Ibar, E., Infante, L., Kneissl, R., Koekemoer, A. M., Messias, H., Muñoz Arancibia, A., Nagar, N., Padilla, N., Pelló, R., Postman, M., Quénard, D., Romero-Cañizales, C., Treister, E., Villard, E., Zheng, W., and Zitrin, A. (2017). The ALMA Frontier Fields Survey. II. Multiwavelength Photometric analysis of 1.1 mm continuum sources in Abell 2744, MACSJ0416.1-2403 and MACSJ1149.5+2223. *A&A*, 604:A132.
- Lawrence, A., Warren, S. J., Almaini, O., Edge, A. C., Hambly, N. C., Jameson, R. F., Lucas, P., Casali, M., Adamson, A., Dye, S., Emerson, J. P., Foucaud, S., Hewett, P., Hirst, P., Hodgkin, S. T., Irwin, M. J., Lodieu, N., McMahon, R. G., Simpson, C., Smail, I., Mortlock, D., and Folger, M. (2007). The UKIRT Infrared Deep Sky Survey (UKIDSS). *MNRAS*, 379:1599–1617.
- Le Fèvre, O., Cassata, P., Cucciati, O., Garilli, B., Ilbert, O., Le Brun, V., Maccagni, D., Moreau, C., Scodreggio, M., and Tresse, L. (2013). The VIMOS VLT Deep Survey final data release: a spectroscopic sample of 35 016 galaxies and AGN out to  $z \sim 6.7$  selected with  $17.5 \leq i_{AB} \leq 24.75$ . *A&A*, 559:A14.

- Le Fèvre, O., Vettolani, G., Paltani, S., Tresse, L., Zamorani, G., Le Brun, V., Moreau, C., Bottini, D., Maccagni, D., and Picat, J. P. (2004). The VIMOS VLT Deep Survey. Public release of 1599 redshifts to  $I_{AB} \leq 24$  across the Chandra Deep Field South. *A&A*, 428:1043–1049.
- Leavitt, H. S. and Pickering, E. C. (1912). Periods of 25 Variable Stars in the Small Magellanic Cloud. *Harvard College Observatory Circular*, 173:1–3.
- Lee, N., Sanders, D. B., Casey, C. M., Toft, S., Scoville, N. Z., Hung, C.-L., Le Floch, E., Ilbert, O., Zahid, H. J., and Aussel, H. (2015). A Turnover in the Galaxy Main Sequence of Star Formation at  $M_* \sim 10^{10} M_\odot$  for Redshifts  $z > 1.3$ . *ApJ*, 801(2):80.
- Leger, A. and Puget, J. L. (1984). Identification of the “unidentified” IR emission features of interstellar dust ? *A&A*, 500:279–282.
- Lemaître, G. (1927). Un Univers homogène de masse constante et de rayon croissant rendant compte de la vitesse radiale des nébuleuses extra-galactiques. *Annales de la Société Scientifique de Bruxelles*, 47:49–59.
- Lemaître, G. (1931a). Expansion of the universe, A homogeneous universe of constant mass and increasing radius accounting for the radial velocity of extra-galactic nebulae. *MNRAS*, 91:483–490.
- Lemaître, G. (1931b). The Beginning of the World from the Point of View of Quantum Theory. *Nature*, 127(3210):706.
- Leroy, A. K., Bolatto, A., Gordon, K., Sandstrom, K., Gratier, P., Rosolowsky, E., Engelbracht, C. W., Mizuno, N., Corbelli, E., Fukui, Y., and Kawamura, A. (2011). The CO-to-H<sub>2</sub> Conversion Factor from Infrared Dust Emission across the Local Group. *ApJ*, 737:12.
- Leroy, A. K., Walter, F., Brinks, E., Bigiel, F., de Blok, W. J. G., Madore, B., and Thornley, M. D. (2008). The Star Formation Efficiency in Nearby Galaxies: Measuring Where Gas Forms Stars Effectively. *AJ*, 136:2782–2845.
- Li, A. and Draine, B. T. (2001). Infrared Emission from Interstellar Dust. II. The Diffuse Interstellar Medium. *ApJ*, 554:778–802.
- Li, A. and Draine, B. T. (2012). The Carriers of the Interstellar Unidentified Infrared Emission Features: Aromatic or Aliphatic? *ApJ*, 760(2):L35.
- Li, Y., Zheng, X. Z., Gu, Q.-S., Wang, Y.-P., Wen, Z. Z., Guo, K., and An, F. X. (2016). Measuring Structural Parameters Through Stacking Galaxy Images. *AJ*, 152:201.
- Lilly, S. J., Le Fevre, O., Hammer, F., and Crampton, D. (1996). The Canada-France Redshift Survey: The Luminosity Density and Star Formation History of the Universe to  $Z$  approximately 1. *ApJ*, 460:L1.
- Lindner, R. R., Baker, A. J., Omont, A., Beelen, A., Owen, F. N., Bertoldi, F., Dole, H., Fiolet, N., Harris, A. I., Ivison, R. J., Lonsdale, C. J., Lutz, D., and Polletta, M. (2011). A Deep 1.2 mm Map of the Lockman Hole North Field. *ApJ*, 737:83.
- Lintott, C., Schawinski, K., Bamford, S., Slosar, A., Land, K., Thomas, D., Edmondson, E., Masters, K., Nichol, R. C., and Raddick, M. J. (2011). Galaxy Zoo 1: data release of morphological classifications for nearly 900 000 galaxies. *MNRAS*, 410(1):166–178.



- Lintott, C. J., Schawinski, K., Slosar, A., Land, K., Bamford, S., Thomas, D., Raddick, M. J., Nichol, R. C., Szalay, A., and Andreescu, D. (2008). Galaxy Zoo: morphologies derived from visual inspection of galaxies from the Sloan Digital Sky Survey. *MNRAS*, 389(3):1179–1189.
- Livermore, R. C., Jones, T., Richard, J., Bower, R. G., Ellis, R. S., Swinbank, A. M., Rigby, J. R., Smail, I., Arribas, S., Rodriguez Zaurin, J., Colina, L., Ebeling, H., and Crain, R. A. (2012). Hubble Space Telescope H $\alpha$  imaging of star-forming galaxies at  $z \sim 1-1.5$ : evolution in the size and luminosity of giant H II regions. *MNRAS*, 427:688–702.
- Livio, M. (2011). Lost in translation: Mystery of the missing text solved. *Nature*, 479(7372):171–173.
- Luo, B., Brandt, W. N., Xue, Y. Q., Lehmer, B., Alexander, D. M., Bauer, F. E., Vito, F., Yang, G., Basu-Zych, A. R., Comastri, A., Gilli, R., Gu, Q.-S., Hornschemeier, A. E., Koekemoer, A., Liu, T., Mainieri, V., Paolillo, M., Ranalli, P., Rosati, P., Schneider, D. P., Shemmer, O., Smail, I., Sun, M., Tozzi, P., Vignali, C., and Wang, J.-X. (2017). The Chandra Deep Field-South Survey: 7 Ms Source Catalogs. *ApJS*, 228:2.
- Lutz, D., Poglitsch, A., Altieri, B., Andreani, P., Aussel, H., Berta, S., Bongiovanni, A., Brisbin, D., Cava, A., Cepa, J., Cimatti, A., Daddi, E., Dominguez-Sanchez, H., Elbaz, D., Förster Schreiber, N. M., Genzel, R., Grazian, A., Gruppioni, C., Harwit, M., Le Floc’h, E., Magdis, G., Magnelli, B., Maiolino, R., Nordon, R., Pérez García, A. M., Popesso, P., Pozzi, F., Riguccini, L., Rodighiero, G., Saintonge, A., Sanchez Portal, M., Santini, P., Shao, L., Sturm, E., Tacconi, L. J., Valtchanov, I., Wetzstein, M., and Wieprecht, E. (2011). PACS Evolutionary Probe (PEP) - A Herschel key program. *A&A*, 532:A90.
- Madau, P. and Dickinson, M. (2014). Cosmic Star-Formation History. *ARA&A*, 52:415–486.
- Madau, P., Ferguson, H. C., Dickinson, M. E., Giavalisco, M., Steidel, C. C., and Fruchter, A. (1996). High-redshift galaxies in the Hubble Deep Field: colour selection and star formation history to  $z \sim 4$ . *MNRAS*, 283:1388–1404.
- Madgwick, D. S., Somerville, R., Lahav, O., and Ellis, R. (2003). Galaxy spectral parametrization in the 2dF Galaxy Redshift Survey as a diagnostic of star formation history. *MNRAS*, 343(3):871–879.
- Magdis, G. E., Daddi, E., Béthermin, M., Sargent, M., Elbaz, D., Pannella, M., Dickinson, M., Dannerbauer, H., da Cunha, E., Walter, F., Rigopoulou, D., Charmandaris, V., Hwang, H. S., and Kartaltepe, J. (2012). The Evolving Interstellar Medium of Star-forming Galaxies since  $z = 2$  as Probed by Their Infrared Spectral Energy Distributions. *ApJ*, 760:6.
- Magdis, G. E., Rigopoulou, D., Huang, J.-S., and Fazio, G. G. (2010). On the stellar masses of IRAC detected Lyman Break Galaxies at  $z \sim 3$ . *MNRAS*, 401:1521–1531.
- Magnelli, B., Elbaz, D., Chary, R. R., Dickinson, M., Le Borgne, D., Frayer, D. T., and Willmer, C. N. A. (2009). The  $0.4 < z < 1.3$  star formation history of the Universe as viewed in the far-infrared. *A&A*, 496:57–75.
- Magnelli, B., Ivison, R. J., Lutz, D., Valtchanov, I., Farrah, D., Berta, S., Bertoldi, F., Bock, J., Cooray, A., Ibar, E., Karim, A., Le Floc’h, E., Nordon, R., Oliver, S. J., Page, M., Popesso, P., Pozzi, F., Rigopoulou, D., Riguccini, L., Rodighiero, G., Rosario, D., Roseboom, I., Wang, L., and Wuyts, S. (2015). The far-infrared/radio correlation and radio spectral index of galaxies in the SFR- $M_*$  plane up to  $z \sim 2$ . *A&A*, 573:A45.

- Magnelli, B., Karim, A., Staguhn, J., Kovács, A., Jiménez-Andrade, E. F., Casey, C. M., Zavala, J. A., Schinnerer, E., Sargent, M., and Aravena, M. (2019). The IRAM/GISMO 2 mm Survey in the COSMOS Field. *ApJ*, 877(1):45.
- Magnelli, B., Lutz, D., Santini, P., Saintonge, A., Berta, S., Albrecht, M., Altieri, B., Andreani, P., Aussel, H., Bertoldi, F., Béthermin, M., Bongiovanni, A., Capak, P., Chapman, S., Cepa, J., Cimatti, A., Cooray, A., Daddi, E., Danielson, A. L. R., Dannerbauer, H., Dunlop, J. S., Elbaz, D., Farrah, D., Förster Schreiber, N. M., Genzel, R., Hwang, H. S., Ibar, E., Ivison, R. J., Le Floch, E., Magdis, G., Maiolino, R., Nordon, R., Oliver, S. J., Pérez García, A., Poglitsch, A., Popesso, P., Pozzi, F., Riguccini, L., Rodighiero, G., Rosario, D., Roseboom, I., Salvato, M., Sanchez-Portal, M., Scott, D., Smail, I., Sturm, E., Swinbank, A. M., Tacconi, L. J., Valtchanov, I., Wang, L., and Wuyts, S. (2012). A Herschel view of the far-infrared properties of submillimetre galaxies. *A&A*, 539:A155.
- Magnelli, B., Popesso, P., Berta, S., Pozzi, F., Elbaz, D., Lutz, D., Dickinson, M., Altieri, B., Andreani, P., Aussel, H., Béthermin, M., Bongiovanni, A., Cepa, J., Charmandaris, V., Chary, R.-R., Cimatti, A., Daddi, E., Förster Schreiber, N. M., Genzel, R., Gruppioni, C., Harwit, M., Hwang, H. S., Ivison, R. J., Magdis, G., Maiolino, R., Murphy, E., Nordon, R., Pannella, M., Pérez García, A., Poglitsch, A., Rosario, D., Sanchez-Portal, M., Santini, P., Scott, D., Sturm, E., Tacconi, L. J., and Valtchanov, I. (2013). The deepest Herschel-PACS far-infrared survey: number counts and infrared luminosity functions from combined PEP/GOODS-H observations. *A&A*, 553:A132.
- Maiolino, R., Carniani, S., Fontana, A., Vallini, L., Pentericci, L., Ferrara, A., Vanzella, E., Grazian, A., Gallerani, S., Castellano, M., Cristiani, S., Brammer, G., Santini, P., Wagg, J., and Williams, R. (2015). The assembly of ‘normal’ galaxies at  $z \sim 7$  probed by ALMA. *MNRAS*, 452:54–68.
- Maiolino, R., Schneider, R., Oliva, E., Bianchi, S., Ferrara, A., Mannucci, F., Pedani, M., and Roca Sogorb, M. (2004). A supernova origin for dust in a high-redshift quasar. *Nature*, 431(7008):533–535.
- Maltby, D. T., Almaini, O., Wild, V., Hatch, N. A., Hartley, W. G., Simpson, C., Rowlands, K., and Socolovsky, M. (2018). The structure of post-starburst galaxies at  $0.5 < z < 2$ : evidence for two distinct quenching routes at different epochs. *MNRAS*, 480(1):381–401.
- Mannucci, F., Cresci, G., Maiolino, R., Marconi, A., and Gnerucci, A. (2010). A fundamental relation between mass, star formation rate and metallicity in local and high-redshift galaxies. *MNRAS*, 408(4):2115–2127.
- Martí-Vidal, I., Pérez-Torres, M. A., and Lobanov, A. P. (2012). Over-resolution of compact sources in interferometric observations. *A&A*, 541:A135.
- Martin, C. L. and Kennicutt, Robert C., J. (2001). Star Formation Thresholds in Galactic Disks. *ApJ*, 555(1):301–321.
- Martin, D. C., Fanson, J., Schiminovich, D., Morrissey, P., Friedman, P. G., Barlow, T. A., Conrow, T., Grange, R., Jelinsky, P. N., and Milliard, B. (2005). The Galaxy Evolution Explorer: A Space Ultraviolet Survey Mission. *ApJ*, 619(1):L1–L6.
- Martini, P., Persson, S. E., Murphy, D. C., Birk, C., Sheckman, S. A., Gunnels, S. M., and Koch, E. (2004). PANIC: a near-infrared camera for the Magellan telescopes. In Moorwood, A. F. M. and Iye, M., editors, *Ground-based Instrumentation for Astronomy*, volume 5492 of *Proc. SPIE*, pages 1653–1660.

- Masters, K. L., Mosleh, M., Romer, A. K., Nichol, R. C., Bamford, S. P., Schawinski, K., Lintott, C. J., Andreescu, D., Campbell, H. C., and Crowcroft, B. (2010). Galaxy Zoo: passive red spirals. *MNRAS*, 405(2):783–799.
- Mathews, W. G. and Brighenti, F. (2003). Hot Gas in and around Elliptical Galaxies. *ARA&A*, 41:191–239.
- Mathis, J. S., Rumpl, W., and Nordsieck, K. H. (1977). The size distribution of interstellar grains. *ApJ*, 217:425–433.
- McAlpine, S., Smail, I., Bower, R. G., Swinbank, M. A., Trayford, J. W., Theuns, T., Baes, M., Camps, P., Crain, R. A., and Schaye, J. (2019). The nature of sub-millimeter and highly star-forming galaxies in the EAGLE simulation. *arXiv e-prints*.
- McLeod, D. J., McLure, R. J., Dunlop, J. S., Robertson, B. E., Ellis, R. S., and Targett, T. A. (2015). New redshift  $z \sim 9$  galaxies in the Hubble Frontier Fields: implications for early evolution of the UV luminosity density. *MNRAS*, 450:3032–3044.
- McLure, R. J., Pentericci, L., Cimatti, A., Dunlop, J. S., Elbaz, D., Fontana, A., Nandra, K., Amorin, R., Bolzonella, M., and Bongiorno, A. (2018). The VANDELS ESO public spectroscopic survey. *MNRAS*, 479(1):25–42.
- McMullin, J. P., Waters, B., Schiebel, D., Young, W., and Golap, K. (2007). CASA Architecture and Applications. In Shaw, R. A., Hill, F., and Bell, D. J., editors, *Astronomical Data Analysis Software and Systems XVI*, volume 376 of *Astronomical Society of the Pacific Conference Series*, page 127.
- Mei, S., Holden, B. P., Blakeslee, J. P., Rosati, P., Postman, M., Jee, M. J., Rettura, A., Sirianni, M., Demarco, R., and Ford, H. C. (2006). Evolution of the Color-Magnitude Relation in High-Redshift Clusters: Early-Type Galaxies in the Lynx Supercluster at  $z \sim 1.26$ . *ApJ*, 644(2):759–768.
- Mendel, J. T., Simard, L., Ellison, S. L., and Patton, D. R. (2013). Towards a physical picture of star formation quenching: the photometric properties of recently quenched galaxies in the Sloan Digital Sky Survey. *MNRAS*, 429:2212–2227.
- Merlin, E., Fontana, A., Ferguson, H. C., Dunlop, J. S., Elbaz, D., Bourne, N., Bruce, V. A., Buitrago, F., Castellano, M., and Schreiber, C. (2015). T-PHOT: A new code for PSF-matched, prior-based, multiwavelength extragalactic deconvolution photometry. *A&A*, 582:A15.
- Meurer, G. R., Heckman, T. M., and Calzetti, D. (1999). Dust Absorption and the Ultraviolet Luminosity Density at  $z \sim 3$  as Calibrated by Local Starburst Galaxies. *ApJ*, 521:64–80.
- Meurer, G. R., Heckman, T. M., Leitherer, C., Kinney, A., Robert, C., and Garnett, D. R. (1995). Starbursts and Star Clusters in the Ultraviolet. *AJ*, 110:2665.
- Miettinen, O., Delvecchio, I., Smolčić, V., Aravena, M., Brisbin, D., Karim, A., Magnelli, B., Novak, M., Schinnerer, E., Albrecht, M., Aussel, H., Bertoldi, F., Capak, P. L., Casey, C. M., Hayward, C. C., Ilbert, O., Intema, H. T., Jiang, C., Le Fèvre, O., McCracken, H. J., Muñoz Arancibia, A. M., Navarrete, F., Padilla, N. D., Riechers, D. A., Salvato, M., Scott, K. S., Sheth, K., and Tasca, L. A. M. (2017). An ALMA survey of submillimetre galaxies in the COSMOS field: Physical properties derived from energy balance spectral energy distribution modelling. *A&A*, 606:A17.

- Mignoli, M., Cimatti, A., Zamorani, G., Pozzetti, L., Daddi, E., Renzini, A., Broadhurst, T., Cristiani, S., D’Odorico, S., and Fontana, A. (2005). The K20 survey. VII. The spectroscopic catalogue: Spectral properties and evolution of the galaxy population. *A&A*, 437(3):883–897.
- Mohan, N. and Rafferty, D. (2015). PyBDSF: Python Blob Detection and Source Finder. *Astrophysics Source Code Library*.
- Momcheva, I. G., Brammer, G. B., van Dokkum, P. G., Skelton, R. E., Whitaker, K. E., Nelson, E. J., Fumagalli, M., Maseda, M. V., Leja, J., Franx, M., Rix, H.-W., Bezanson, R., Da Cunha, E., Dickey, C., Förster Schreiber, N. M., Illingworth, G., Kriek, M., Labbé, I., Ulf Lange, J., Lundgren, B. F., Magee, D., Marchesini, D., Oesch, P., Pacifci, C., Patel, S. G., Price, S., Tal, T., Wake, D. A., van der Wel, A., and Wuyts, S. (2016). The 3D-HST Survey: Hubble Space Telescope WFC3/G141 Grism Spectra, Redshifts, and Emission Line Measurements for  $\sim 100,000$  Galaxies. *ApJS*, 225:27.
- Moorwood, A., Cuby, J.-G., Ballester, P., Biereichel, P., Brynnel, J., Conzelmann, R., Delabre, B., Devillard, N., van Dijsseldonk, A., Finger, G., Gemperlein, H., Lidman, C., Herlin, T., Huster, G., Knudstrup, J., Lizon, J.-L., Mehrgan, H., Meyer, M., Nicolini, G., Silber, A., Spyromilio, J., and Stegmeier, J. (1999). ISAAC at the VLT. *The Messenger*, 95:1–5.
- Morishita, T., Ichikawa, T., and Kajisawa, M. (2014). The Evolution of Galaxy Size and Morphology at  $z \sim 0.5$ –3.0 in the GOODS-N Region with Hubble Space Telescope/WFC3 Data. *ApJ*, 785(1):18.
- Morris, A. M., Kocevski, D. D., Trump, J. R., Weiner, B. J., Hathi, N. P., Barro, G., Dahlen, T., Faber, S. M., Finkelstein, S. L., and Fontana, A. (2015). A WFC3 Grism Emission Line Redshift Catalog in the GOODS-South Field. *AJ*, 149(6):178.
- Mortier, A. M. J., Serjeant, S., Dunlop, J. S., Scott, S. E., Ade, P., Alexander, D., Almaini, O., Aretxaga, I., Baugh, C., Benson, A. J., Best, P. N., Blain, A., Bock, J., Borys, C., Bressan, A., Carilli, C., Chapin, E. L., Chapman, S., Clements, D. L., Coppin, K., Crawford, M., Devlin, M., Dicker, S., Dunne, L., Eales, S. A., Edge, A. C., Farrah, D., Fox, M., Frenk, C., Gaztañaga, E., Gear, W. K., Gonzales-Solares, E., Granato, G. L., Greve, T. R., Grimes, J. A., Gundersen, J., Halpern, M., Hargrave, P., Hughes, D. H., Ivison, R. J., Jarvis, M. J., Jenness, T., Jimenez, R., van Kampen, E., King, A., Lacey, C., Lawrence, A., Lepage, K., Mann, R. G., Marsden, G., Mauskopf, P., Netterfield, B., Oliver, S., Olmi, L., Page, M. J., Peacock, J. A., Pearson, C. P., Percival, W. J., Pope, A., Priddey, R. S., Rawlings, S., Roche, N., Rowan-Robinson, M., Scott, D., Sekiguchi, K., Seigar, M., Silva, L., Simpson, C., Smail, I., Stevens, J. A., Takagi, T., Tucker, G., Vlahakis, C., Waddington, I., Wagg, J., Watson, M., Willott, C., and Vaccari, M. (2005). The SCUBA Half-Degree Extragalactic Survey - I. Survey motivation, design and data processing. *MNRAS*, 363:563–580.
- Mosleh, M., Williams, R. J., Franx, M., and Kriek, M. (2011). The Evolution of the Mass-Size Relation to  $z = 3.5$  for UV-bright Galaxies and Submillimeter Galaxies in the GOODS-North Field. *ApJ*, 727:5.
- Moster, B. P., Somerville, R. S., Newman, J. A., and Rix, H.-W. (2011). A Cosmic Variance Cookbook. *ApJ*, 731:113.
- Muñoz Arancibia, A. M., González-López, J., Ibar, E., Bauer, F. E., Carrasco, M., Laporte, N., Anguita, T., Aravena, M., Barrientos, F., and Bouwens, R. J. (2018). The ALMA Frontier Fields

- Survey. IV. Lensing-corrected 1.1 mm number counts in Abell 2744, MACS J0416.1-2403 and MACS J1149.5+2223. *A&A*, 620:A125.
- Mullaney, J. R., Alexander, D. M., Goulding, A. D., and Hickox, R. C. (2011). Defining the intrinsic AGN infrared spectral energy distribution and measuring its contribution to the infrared output of composite galaxies. *MNRAS*, 414:1082–1110.
- Murphy, E. J. (2009). The Far-Infrared-Radio Correlation at High Redshifts: Physical Considerations and Prospects for the Square Kilometer Array. *ApJ*, 706:482–496.
- Murphy, E. J., Condon, J. J., Schinnerer, E., Kennicutt, R. C., Calzetti, D., Armus, L., Helou, G., Turner, J. L., Aniano, G., Beirão, P., Bolatto, A. D., Brandl, B. R., Croxall, K. V., Dale, D. A., Donovan Meyer, J. L., Draine, B. T., Engelbracht, C., Hunt, L. K., Hao, C.-N., Koda, J., Roussel, H., Skibba, R., and Smith, J.-D. T. (2011). Calibrating Extinction-free Star Formation Rate Diagnostics with 33 GHz Free-free Emission in NGC 6946. *ApJ*, 737:67.
- Muzzin, A., Marchesini, D., Stefanon, M., Franx, M., McCracken, H. J., Milvang-Jensen, B., Dunlop, J. S., Fynbo, J. P. U., Brammer, G., Labbé, I., and van Dokkum, P. G. (2013). The Evolution of the Stellar Mass Functions of Star-forming and Quiescent Galaxies to  $z = 4$  from the COSMOS/UltraVISTA Survey. *ApJ*, 777:18.
- Narayanan, D., Hayward, C. C., Cox, T. J., Hernquist, L., Jonsson, P., Younger, J. D., and Groves, B. (2010). The formation of high-redshift submillimetre galaxies. *MNRAS*, 401:1613–1619.
- Neugebauer, G., Habing, H. J., van Duinen, R., Aumann, H. H., Baud, B., Beichman, C. A., Beintema, D. A., Boggess, N., Clegg, P. E., de Jong, T., Emerson, J. P., Gautier, T. N., Gillett, F. C., Harris, S., Hauser, M. G., Houck, J. R., Jennings, R. E., Low, F. J., Marsden, P. L., Miley, G., Olton, F. M., Pottasch, S. R., Raimond, E., Rowan-Robinson, M., Soifer, B. T., Walker, R. G., Wesselius, P. R., and Young, E. (1984). The Infrared Astronomical Satellite (IRAS) mission. *ApJ*, 278:L1–L6.
- Newman, A. B., Ellis, R. S., Bundy, K., and Treu, T. (2012). Can Minor Merging Account for the Size Growth of Quiescent Galaxies? New Results from the CANDELS Survey. *ApJ*, 746(2):162.
- Niklas, S., Klein, U., and Wielebinski, R. (1997). A radio continuum survey of Shapley-Ames galaxies at  $\lambda$  2.8cm. II. Separation of thermal and non-thermal radio emission. *A&A*, 322:19–28.
- Noeske, K. G., Weiner, B. J., Faber, S. M., Papovich, C., Koo, D. C., Somerville, R. S., Bundy, K., Conselice, C. J., Newman, J. A., Schiminovich, D., Le Floch, E., Coil, A. L., Rieke, G. H., Lotz, J. M., Primack, J. R., Barmby, P., Cooper, M. C., Davis, M., Ellis, R. S., Fazio, G. G., Guhathakurta, P., Huang, J., Kassin, S. A., Martin, D. C., Phillips, A. C., Rich, R. M., Small, T. A., Willmer, C. N. A., and Wilson, G. (2007). Star Formation in AEGIS Field Galaxies since  $z=1.1$ : The Dominance of Gradually Declining Star Formation, and the Main Sequence of Star-forming Galaxies. *ApJ*, 660:L43–L46.
- Noll, S., Burgarella, D., Giovannoli, E., Buat, V., Marcillac, D., and Muñoz-Mateos, J. C. (2009). Analysis of galaxy spectral energy distributions from far-UV to far-IR with CIGALE: studying a SINGS test sample. *A&A*, 507:1793–1813.
- Nonino, M., Dickinson, M., Rosati, P., Grazian, A., Reddy, N., Cristiani, S., Giavalisco, M., Kuntschner, H., Vanzella, E., Daddi, E., Fosbury, R. A. E., and Cesarsky, C. (2009). Deep

- U Band and R Imaging of Goods-South: Observations, Data Reduction and First Results. *ApJS*, 183:244–260.
- Nyquist, H. (1928). Certain Topics in Telegraph Transmission Theory. *Transactions of the American Institute of Electrical Engineers, Volume 47, Issue 2*, pp. 617–624, 47:617–624.
- Obreschkow, D. and Rawlings, S. (2009). Compactness of cold gas in high-redshift galaxies. *MNRAS*, 400:665–669.
- Oesch, P. A., Bouwens, R. J., Illingworth, G. D., Franx, M., Ammons, S. M., van Dokkum, P. G., Trenti, M., and Labbé, I. (2015). First Frontier Field Constraints on the Cosmic Star Formation Rate Density at  $z \sim 10$  - The Impact of Lensing Shear on Completeness of High-redshift Galaxy Samples. *ApJ*, 808:104.
- Oke, J. B. and Gunn, J. E. (1983). Secondary standard stars for absolute spectrophotometry. *ApJ*, 266:713–717.
- Ono, Y., Ouchi, M., Kurono, Y., and Momose, R. (2014). Faint Submillimeter Galaxies Revealed by Multifield Deep ALMA Observations: Number Counts, Spatial Clustering, and a Dark Submillimeter Line Emitter. *ApJ*, 795:5.
- Osmond, J. P. F. and Ponman, T. J. (2004). The GEMS project: X-ray analysis and statistical properties of the group sample. *MNRAS*, 350(4):1511–1535.
- Oteo, I., Bongiovanni, Á., Magdis, G., Pérez-García, A. M., Cepa, J., Domínguez Sánchez, H., Ederoclite, A., Sánchez-Portal, M., and Pintos-Castro, I. (2014). The ultraviolet to far-infrared spectral energy distribution of star-forming galaxies in the redshift desert. *MNRAS*, 439(2):1337–1363.
- Oteo, I., Cepa, J., Bongiovanni, Á., Pérez-García, A. M., Cedrés, B., Domínguez Sánchez, H., Ederoclite, A., Sánchez-Portal, M., Pintos-Castro, I., and Pérez-Martínez, R. (2013). Far-infrared-detected Lyman-break galaxies at  $z \sim 3$ . Dust attenuation and dust correction factors at high redshift. *A&A*, 554:L3.
- Oteo, I., Zwaan, M. A., Ivison, R. J., Smail, I., and Biggs, A. D. (2016). ALMACAL I: First Dual-band Number Counts from a Deep and Wide ALMA Submillimeter Survey, Free from Cosmic Variance. *ApJ*, 822:36.
- Oteo, I., Zwaan, M. A., Ivison, R. J., Smail, I., and Biggs, A. D. (2017). ALMACAL II: Extreme Star Formation Rate Densities in Dusty Starbursts Revealed by ALMA 20 mas Resolution Imaging. *ApJ*, 837:182.
- Overzier, R. A., Heckman, T. M., Wang, J., Armus, L., Buat, V., Howell, J., Meurer, G., Seibert, M., Siana, B., Basu-Zych, A., Charlot, S., Gonçalves, T. S., Martin, D. C., Neill, J. D., Rich, R. M., Salim, S., and Schiminovich, D. (2011). Dust Attenuation in UV-selected Starbursts at High Redshift and Their Local Counterparts: Implications for the Cosmic Star Formation Rate Density. *ApJ*, 726:L7.
- Padilla, N. D. and Strauss, M. A. (2008). The shapes of galaxies in the Sloan Digital Sky Survey. *MNRAS*, 388:1321–1334.
- Pannella, M., Carilli, C. L., Daddi, E., McCracken, H. J., Owen, F. N., Renzini, A., Strazzullo, V., Civano, F., Koekemoer, A. M., Schinnerer, E., Scoville, N., Smolčić, V., Taniguchi, Y., Aussel,

- H., Kneib, J. P., Ilbert, O., Mellier, Y., Salvato, M., Thompson, D., and Willott, C. J. (2009). Star Formation and Dust Obscuration at  $z \sim 2$ : Galaxies at the Dawn of Downsizing. *ApJ*, 698:L116–L120.
- Pannella, M., Elbaz, D., Daddi, E., Dickinson, M., Hwang, H. S., Schreiber, C., Strazzullo, V., Aussel, H., Bethermin, M., Buat, V., Charmandaris, V., Cibinel, A., Juneau, S., Ivison, R. J., Le Borgne, D., Le Floch, E., Leiton, R., Lin, L., Magdis, G., Morrison, G. E., Mullaney, J., Onodera, M., Renzini, A., Salim, S., Sargent, M. T., Scott, D., Shu, X., and Wang, T. (2015). GOODS-Herschel: Star Formation, Dust Attenuation, and the FIR-radio Correlation on the Main Sequence of Star-forming Galaxies up to  $z \sim 4$ . *ApJ*, 807:141.
- Papovich, C., Labbé, I., Glazebrook, K., Quadri, R., Bekiaris, G., Dickinson, M., Finkelstein, S. L., Fisher, D., Inami, H., Livermore, R. C., Spitler, L., Straatman, C., and Tran, K.-V. (2016). Large molecular gas reservoirs in ancestors of Milky Way-mass galaxies nine billion years ago. *Nature Astronomy*, 1:0003.
- Papovich, C., Momcheva, I., Willmer, C. N. A., Finkelstein, K. D., Finkelstein, S. L., Tran, K.-V., Brodwin, M., Dunlop, J. S., Farrah, D., Khan, S. A., Lotz, J., McCarthy, P., McLure, R. J., Rieke, M., Rudnick, G., Sivanandam, S., Pacaud, F., and Pierre, M. (2010). A Spitzer-selected Galaxy Cluster at  $z = 1.62$ . *ApJ*, 716:1503–1513.
- Pearson, W. J., Wang, L., Hurley, P. D., Małek, K., Buat, V., Burgarella, D., Farrah, D., Oliver, S. J., Smith, D. J. B., and van der Tak, F. F. S. (2018). Main sequence of star forming galaxies beyond the Herschel confusion limit. *A&A*, 615:A146.
- Peebles, P. J. E. (1980). *The large-scale structure of the universe*.
- Peng, C. Y., Ho, L. C., Impey, C. D., and Rix, H.-W. (2010). Detailed Decomposition of Galaxy Images. II. Beyond Axisymmetric Models. *AJ*, 139:2097–2129.
- Penzias, A. A. and Wilson, R. W. (1965). A Measurement of Excess Antenna Temperature at 4080 Mc/s. *ApJ*, 142:419–421.
- Perera, T. A., Chapin, E. L., Austermann, J. E., Scott, K. S., Wilson, G. W., Halpern, M., Pope, A., Scott, D., Yun, M. S., and Lowenthal, J. D. (2008). An AzTEC 1.1mm survey of the GOODS-N field - I. Maps, catalogue and source statistics. *MNRAS*, 391(3):1227–1238.
- Persson, S. E., Murphy, D. C., Smee, S., Birk, C., Monson, A. J., Uomoto, A., Koch, E., Sheckman, S., Barkhouser, R., Orndorff, J., Hammond, R., Harding, A., Scharfstein, G., Kelson, D., Marshall, J., and McCarthy, P. J. (2013). FourStar: The Near-Infrared Imager for the 6.5 m Baade Telescope at Las Campanas Observatory. *PASP*, 125:654.
- Pettini, M., Kellogg, M., Steidel, C. C., Dickinson, M., Adelberger, K. L., and Giavalisco, M. (1998). Infrared Observations of Nebular Emission Lines from Galaxies at  $Z \sim 3$ . *ApJ*, 508:539–550.
- Pety, J. and Rodríguez-Fernández, N. (2010). Revisiting the theory of interferometric wide-field synthesis. *A&A*, 517:A12.
- Pilbratt, G. L., Riedinger, J. R., Passvogel, T., Crone, G., Doyle, D., Gageur, U., Heras, A. M., Jewell, C., Metcalfe, L., and Ott, S. (2010). Herschel Space Observatory. An ESA facility for far-infrared and submillimetre astronomy. *A&A*, 518:L1.

- Piras, D., Joachimi, B., Schäfer, B. M., Bonamigo, M., Hilbert, S., and van Uitert, E. (2018). The mass dependence of dark matter halo alignments with large-scale structure. *MNRAS*, 474(1):1165–1175.
- Poglitsch, A., Waelkens, C., Geis, N., Feuchtgruber, H., Vandenbussche, B., Rodriguez, L., Krause, O., Renotte, E., van Hoof, C., Saraceno, P., Cepa, J., Kerschbaum, F., Agnèse, P., Ali, B., Altieri, B., Andreani, P., Augueres, J.-L., Balog, Z., Barl, L., Bauer, O. H., Belbachir, N., Benedettini, M., Billot, N., Boulade, O., Bischof, H., Blommaert, J., Callut, E., Cara, C., Cerulli, R., Cesarsky, D., Contursi, A., Creten, Y., De Meester, W., Doublier, V., Doumayrou, E., Duband, L., Exter, K., Genzel, R., Gillis, J.-M., Grözinger, U., Henning, T., Herreros, J., Huygen, R., Inguscio, M., Jakob, G., Jamar, C., Jean, C., de Jong, J., Katterloher, R., Kiss, C., Klaas, U., Lemke, D., Lutz, D., Madden, S., Marquet, B., Martignac, J., Mazy, A., Merken, P., Montfort, F., Morbidelli, L., Müller, T., Nielbock, M., Okumura, K., Orfei, R., Ottensamer, R., Pezzuto, S., Popesso, P., Putzeys, J., Regibo, S., Reveret, V., Royer, P., Sauvage, M., Schreiber, J., Stegmaier, J., Schmitt, D., Schubert, J., Sturm, E., Thiel, M., Tofani, G., Vavrek, R., Wetzstein, M., Wieprecht, E., and Wieszorrek, E. (2010). The Photodetector Array Camera and Spectrometer (PACS) on the Herschel Space Observatory. *A&A*, 518:L2.
- Pope, A., Aretxaga, I., Hughes, D., Wilson, G., and Yun, M. (2019). TolTEC/LMT Extragalactic Legacy Surveys: Completing our Census of Dust-Obscured Star Formation. In *American Astronomical Society Meeting Abstracts #233*, volume 233 of *American Astronomical Society Meeting Abstracts*, page 363.20.
- Pope, A., Borys, C., Scott, D., Conselice, C., Dickinson, M., and Mobasher, B. (2005). The Hubble Deep Field North SCUBA Super-map - III. Optical and near-infrared properties of submillimetre galaxies. *MNRAS*, 358:149–167.
- Pope, A., Chary, R.-R., Alexander, D. M., Armus, L., Dickinson, M., Elbaz, D., Frayer, D., Scott, D., and Teplitz, H. (2008). Mid-Infrared Spectral Diagnosis of Submillimeter Galaxies. *ApJ*, 675:1171–1193.
- Pope, A., Montaña, A., Battisti, A., Limousin, M., Marchesini, D., Wilson, G. W., Alberts, S., Aretxaga, I., Avila-Reese, V., Ramón Bermejo-Climent, J., Brammer, G., Bravo-Alfaro, H., Calzetti, D., Chary, R.-R., Cybulski, R., Giavalisco, M., Hughes, D., Kado-Fong, E., Keller, E., Kirkpatrick, A., Labbe, I., Lange-Vagle, D., Lowenthal, J., Murphy, E., Oesch, P., Rosa Gonzalez, D., Sánchez-Argüelles, D., Shipley, H., Stefanon, M., Vega, O., Whitaker, K., Williams, C. C., Yun, M., Zavala, J. A., and Zeballos, M. (2017). Early Science with the Large Millimeter Telescope: Detection of Dust Emission in Multiple Images of a Normal Galaxy at  $z > 4$  Lensed by a Frontier Fields Cluster. *ApJ*, 838:137.
- Popesso, P., Concas, A., Morselli, L., Schreiber, C., Rodighiero, G., Cresci, G., Belli, S., Erfanianfar, G., Mancini, C., and Inami, H. (2019). The main sequence of star-forming galaxies - I. The local relation and its bending. *MNRAS*, 483(3):3213–3226.
- Popesso, P., Dickinson, M., Nonino, M., Vanzella, E., Daddi, E., Fosbury, R. A. E., Kuntschner, H., Mainieri, V., Cristiani, S., and Cesarsky, C. (2009). The great observatories origins deep survey. VLT/VIMOS spectroscopy in the GOODS-south field. *A&A*, 494(2):443–460.
- Popping, G., Caputi, K. I., Somerville, R. S., and Trager, S. C. (2012). An indirect measurement of gas evolution in galaxies at  $0.5 < z < 2.0$ . *MNRAS*, 425:2386–2400.



- Popping, G., Puglisi, A., and Norman, C. A. (2017). Dissecting the IRX- $\beta$  dust attenuation relation: exploring the physical origin of observed variations in galaxies. *MNRAS*, 472:2315–2333.
- Prevot, M. L., Lequeux, J., Maurice, E., Prevot, L., and Rocca-Volmerange, B. (1984). The typical interstellar extinction in the Small Magellanic Cloud. *A&A*, 132:389–392.
- Price, R. and Duric, N. (1992). New results on the radio-far-infrared relation for galaxies. *ApJ*, 401:81–86.
- Puget, J. L., Abergel, A., Bernard, J. P., Boulanger, F., Burton, W. B., Desert, F. X., and Hartmann, D. (1996). Tentative detection of a cosmic far-infrared background with COBE. *A&A*, 308:L5.
- Puget, P., Stadler, E., Doyon, R., Gigan, P., Thibault, S., Luppino, G., Barrick, G., Benedict, T., Forveille, T., Rambold, W., Thomas, J., Vermeulen, T., Ward, J., Beuzit, J.-L., Feautrier, P., Magnard, Y., Mella, G., Preis, O., Vallee, P., Wang, S.-y., Lin, C.-J., Hall, D. N., and Hodapp, K. W. (2004). WIRCam: the infrared wide-field camera for the Canada-France-Hawaii Telescope. In Moorwood, A. F. M. and Iye, M., editors, *Ground-based Instrumentation for Astronomy*, volume 5492 of *Proc. SPIE*, pages 978–987.
- Raabe, H. (1939). Untersuchungen an der wechselzeitigen Mehrfachübertragung (Multiplexübertragung). *Elektr. Nach.tech.*, 16(8):213–228.
- Rafferty, D. A., Brandt, W. N., Alexander, D. M., Xue, Y. Q., Bauer, F. E., Lehmer, B. D., Luo, B., and Papovich, C. (2011). Supermassive Black Hole Growth in Starburst Galaxies over Cosmic Time: Constraints from the Deepest Chandra Fields. *ApJ*, 742:3.
- Ranalli, P., Comastri, A., Vignali, C., Carrera, F. J., Cappelluti, N., Gilli, R., Puccetti, S., Brandt, W. N., Brunner, H., Brusa, M., Georgantopoulos, I., Iwasawa, K., and Mainieri, V. (2013). The XMM deep survey in the CDF-S. III. Point source catalogue and number counts in the hard X-rays. *A&A*, 555:A42.
- Ravikumar, C. D., Puech, M., Flores, H., Proust, D., Hammer, F., Lehnert, M., Rawat, A., Amram, P., Balkowski, C., and Burgarella, D. (2007). New spectroscopic redshifts from the CDFS and a test of the cosmological relevance of the GOODS-South field. *A&A*, 465(3):1099–1108.
- Reddy, N. A. (2006). *A multi-wavelength census of star formation at redshifts  $z$  equals 2*. PhD thesis, California Institute of Technology.
- Reddy, N. A., Erb, D. K., Pettini, M., Steidel, C. C., and Shapley, A. E. (2010). Dust Obscuration and Metallicity at High Redshift: New Inferences from UV,  $H\alpha$ , and  $8\,\mu\text{m}$  Observations of  $z \sim 2$  Star-forming Galaxies. *ApJ*, 712:1070–1091.
- Reddy, N. A., Kriek, M., Shapley, A. E., Freeman, W. R., Siana, B., Coil, A. L., Mobasher, B., Price, S. H., Sanders, R. L., and Shivaiei, I. (2015). The MOSDEF Survey: Measurements of Balmer Decrements and the Dust Attenuation Curve at Redshifts  $z \sim 1.4$ – $2.6$ . *ApJ*, 806:259.
- R  my-Ruyer, A., Madden, S. C., Galliano, F., Hony, S., Sauvage, M., Bendo, G. J., Roussel, H., Pohlen, M., Smith, M. W. L., Galametz, M., Cormier, D., Lebouteiller, V., Wu, R., Baes, M., Barlow, M. J., Boquien, M., Boselli, A., Ciesla, L., De Looze, I., Karczewski, O.   ., Panuzzo, P., Spinoglio, L., Vaccari, M., and Wilson, C. D. (2013). Revealing the cold dust in low-metallicity environments. I. Photometry analysis of the Dwarf Galaxy Survey with Herschel. *A&A*, 557:A95.

- Rettura, A., Rosati, P., and Nonino, M. (2009). Compact Massive Early-type galaxies in the  $z = 1.2$  cluster RDCS1252.9-2927. In Giobbi, G., Tornambe, A., Raimondo, G., Limongi, M., Antonelli, L. A., Menci, N., and Brocato, E., editors, *American Institute of Physics Conference Series*, volume 1111, pages 183–186.
- Retzlaff, J., Rosati, P., Dickinson, M., Vandame, B., Rit , C., Nonino, M., Cesarsky, C., and GOODS Team (2010). The Great Observatories Origins Deep Survey. VLT/ISAAC near-infrared imaging of the GOODS-South field. *A&A*, 511:A50.
- Rieke, G. H., Alonso-Herrero, A., Weiner, B. J., P rez-Gonz lez, P. G., Blaylock, M., Donley, J. L., and Marcillac, D. (2009). Determining Star Formation Rates for Infrared Galaxies. *ApJ*, 692:556–573.
- Rieke, G. H., Young, E. T., Engelbracht, C. W., Kelly, D. M., Low, F. J., Haller, E. E., Beeman, J. W., Gordon, K. D., Stansberry, J. A., Misselt, K. A., Cadien, J., Morrison, J. E., Rivlis, G., Latter, W. B., Noriega-Crespo, A., Padgett, D. L., Stapelfeldt, K. R., Hines, D. C., Egami, E., Muzerolle, J., Alonso-Herrero, A., Blaylock, M., Dole, H., Hinz, J. L., Le Floch, E., Papovich, C., P rez-Gonz lez, P. G., Smith, P. S., Su, K. Y. L., Bennett, L., Frayer, D. T., Henderson, D., Lu, N., Masci, F., Pesenson, M., Rebull, L., Rho, J., Keene, J., Stolovy, S., Wachter, S., Wheaton, W., Werner, M. W., and Richards, P. L. (2004). The Multiband Imaging Photometer for Spitzer (MIPS). *ApJS*, 154:25–29.
- Roberts, I. (1888). the Stellar pantograver. *MNRAS*, 49:5.
- Roberts, I. (1893). *A Selection of Photographs of Stars, Star-Clusters and Nebulae, together with Information concerning the Instruments and the Methods employed in the pursuit of Celestial Photography*.
- Rodighiero, G., Cimatti, A., Gruppioni, C., Popesso, P., Andreani, P., Altieri, B., Aussel, H., Berta, S., Bongiovanni, A., and Brisbin, D. (2010). The first Herschel view of the mass-SFR link in high- $z$  galaxies. *A&A*, 518:L25.
- Rodighiero, G., Daddi, E., Baronchelli, I., Cimatti, A., Renzini, A., Aussel, H., Popesso, P., Lutz, D., Andreani, P., Berta, S., Cava, A., Elbaz, D., Feltre, A., Fontana, A., F rster Schreiber, N. M., Franceschini, A., Genzel, R., Grazian, A., Gruppioni, C., Ilbert, O., Le Floch, E., Magdis, G., Magliocchetti, M., Magnelli, B., Maiolino, R., McCracken, H., Nordon, R., Poglitsch, A., Santini, P., Pozzi, F., Riguccini, L., Tacconi, L. J., Wuyts, S., and Zamorani, G. (2011). The Lesser Role of Starbursts in Star Formation at  $z = 2$ . *ApJ*, 739:L40.
- Rodighiero, G., Renzini, A., Daddi, E., Baronchelli, I., Berta, S., Cresci, G., Franceschini, A., Gruppioni, C., Lutz, D., and Mancini, C. (2014). A multiwavelength consensus on the main sequence of star-forming galaxies at  $z \sim 2$ . *MNRAS*, 443(1):19–30.
- Roseboom, I. G., Ivison, R. J., Greve, T. R., Amblard, A., Arumugam, V., Auld, R., Aussel, H., Bethermin, M., Blain, A., and Bock, J. (2012). The Herschel Multi-tiered Extragalactic Survey: SPIRE-mm photometric redshifts. *MNRAS*, 419(4):2758–2773.
- Rovilos, E., Comastri, A., Gilli, R., Georgantopoulos, I., Ranalli, P., Vignali, C., Lusso, E., Capelluti, N., Zamorani, G., Elbaz, D., Dickinson, M., Hwang, H. S., Charmandaris, V., Ivison, R. J., Merloni, A., Daddi, E., Carrera, F. J., Brandt, W. N., Mullaney, J. R., Scott, D., Alexander, D. M., Del Moro, A., Morrison, G., Murphy, E. J., Altieri, B., Aussel, H., Dannerbauer, H., Kartaltepe, J., Leiton, R., Magdis, G., Magnelli, B., Popesso, P., and Valtchanov, I. (2012).

- GOODS-Herschel: ultra-deep XMM-Newton observations reveal AGN/star-formation connection. *A&A*, 546:A58.
- Rowan-Robinson, M., Oliver, S., Wang, L., Farrah, D., Clements, D. L., Gruppioni, C., Marchetti, L., Rigopoulou, D., and Vaccari, M. (2016). The star formation rate density from  $z = 1$  to 6. *MNRAS*, 461(1):1100–1111.
- Rowan-Robinson, M., Wang, L., Farrah, D., Rigopoulou, D., Gruppioni, C., Vaccari, M., Marchetti, L., and Clements, D. L. (2017). Extreme submillimetre starburst galaxies. *ArXiv e-prints*.
- Rujopakarn, W., Daddi, E., Rieke, G. H., Puglisi, A., Schramm, M., Pérez-González, P. G., Magdis, G. E., Alberts, S., Bournaud, F., Elbaz, D., Franco, M., Ivison, R. J., Kawinwanichakij, L., Kohno, K., Narayanan, D., Silverman, J. D., Wang, T., and Williams, C. C. (2019). ALMA 200-parsec Resolution Imaging of Smooth Cold Dusty Disks in Typical  $z \sim 3$  Star-Forming Galaxies. *arXiv e-prints*.
- Rujopakarn, W., Dunlop, J. S., Rieke, G. H., Ivison, R. J., Cibinel, A., Nyland, K., Jagannathan, P., Silverman, J. D., Alexander, D. M., Biggs, A. D., Bhatnagar, S., Ballantyne, D. R., Dickinson, M., Elbaz, D., Geach, J. E., Hayward, C. C., Kirkpatrick, A., McLure, R. J., Michałowski, M. J., Miller, N. A., Narayanan, D., Owen, F. N., Pannella, M., Papovich, C., Pope, A., Rau, U., Robertson, B. E., Scott, D., Swinbank, A. M., van der Werf, P., van Kampen, E., Weiner, B. J., and Windhorst, R. A. (2016). VLA and ALMA Imaging of Intense Galaxy-wide Star Formation in  $z \sim 2$  Galaxies. *ApJ*, 833:12.
- Salim, S., Rich, R. M., Charlot, S., Brinchmann, J., Johnson, B. D., Schiminovich, D., Seibert, M., Mallery, R., Heckman, T. M., Forster, K., Friedman, P. G., Martin, D. C., Morrissey, P., Neff, S. G., Small, T., Wyder, T. K., Bianchi, L., Donas, J., Lee, Y.-W., Madore, B. F., Milliard, B., Szalay, A. S., Welsh, B. Y., and Yi, S. K. (2007). UV Star Formation Rates in the Local Universe. *ApJS*, 173:267–292.
- Salimbeni, S., Castellano, M., Pentericci, L., Trevese, D., Fiore, F., Grazian, A., Fontana, A., Giallongo, E., Boutsia, K., and Cristiani, S. (2009). A comprehensive study of large-scale structures in the GOODS-SOUTH field up to  $z \sim 2.5$ . *A&A*, 501(3):865–877.
- Salmon, B., Papovich, C., Finkelstein, S. L., Tilvi, V., Finlator, K., Behroozi, P., Dahlen, T., Davé, R., Dekel, A., Dickinson, M., Ferguson, H. C., Giavalisco, M., Long, J., Lu, Y., Mobasher, B., Reddy, N., Somerville, R. S., and Wechsler, R. H. (2015). The Relation between Star Formation Rate and Stellar Mass for Galaxies at  $3.5 < z \leq 6.5$  in CANDELS. *ApJ*, 799:183.
- Salpeter, E. E. (1955). The Luminosity Function and Stellar Evolution. *ApJ*, 121:161.
- Sandage, A. (1961). *The Hubble Atlas of Galaxies*.
- Sandage, A. (1975). *Classification and Stellar Content of Galaxies Obtained from Direct Photography*, page 1. the University of Chicago Press.
- Sandage, A. and Tammann, G. A. (1981). *A Revised Shapley-Ames Catalog of Bright Galaxies*.
- Santini, P., Ferguson, H. C., Fontana, A., Mobasher, B., Barro, G., Castellano, M., Finkelstein, S. L., Grazian, A., Hsu, L. T., Lee, B., Lee, S.-K., Pforr, J., Salvato, M., Wiklind, T., Wuyts, S., Almaini, O., Cooper, M. C., Galametz, A., Weiner, B., Amorin, R., Boutsia, K., Conselice, C. J., Dahlen, T., Dickinson, M. E., Giavalisco, M., Grogin, N. A., Guo, Y., Hathi, N. P., Kocevski, D., Koekemoer, A. M., Kurczynski, P., Merlin, E., Mortlock, A., Newman, J. A., Paris, D., Pentericci,

- L., Simons, R., and Willner, S. P. (2015). Stellar Masses from the CANDELS Survey: The GOODS-South and UDS Fields. *ApJ*, 801:97.
- Santini, P., Fontana, A., Grazian, A., Salimbeni, S., Fiore, F., Fontanot, F., Boutsia, K., Castellano, M., Cristiani, S., de Santis, C., Gallozzi, S., Giallongo, E., Menci, N., Nonino, M., Paris, D., Pentericci, L., and Vanzella, E. (2009). Star formation and mass assembly in high redshift galaxies. *A&A*, 504:751–767.
- Sargent, M. T., Béthermin, M., Daddi, E., and Elbaz, D. (2012). The Contribution of Starbursts and Normal Galaxies to Infrared Luminosity Functions at  $z < 2$ . *ApJ*, 747:L31.
- Sargent, M. T., Daddi, E., Béthermin, M., Aussel, H., Magdis, G., Hwang, H. S., Juneau, S., Elbaz, D., and da Cunha, E. (2014). Regularity Underlying Complexity: A Redshift-independent Description of the Continuous Variation of Galaxy-scale Molecular Gas Properties in the Mass-star Formation Rate Plane. *ApJ*, 793:19.
- Sargent, M. T., Schinnerer, E., Murphy, E., Aussel, H., Le Floch, E., Frayer, D. T., Martínez-Sansigre, A., Oesch, P., Salvato, M., Smolčić, V., Zamorani, G., Brusa, M., Cappelluti, N., Carilli, C. L., Carollo, C. M., Ilbert, O., Kartaltepe, J., Koekemoer, A. M., Lilly, S. J., Sanders, D. B., and Scoville, N. Z. (2010a). The VLA-COSMOS Perspective on the Infrared-Radio Relation. I. New Constraints on Selection Biases and the Non-Evolution of the Infrared/Radio Properties of Star-Forming and Active Galactic Nucleus Galaxies at Intermediate and High Redshift. *ApJS*, 186:341–377.
- Sargent, M. T., Schinnerer, E., Murphy, E., Carilli, C. L., Helou, G., Aussel, H., Le Floch, E., Frayer, D. T., Ilbert, O., Oesch, P., Salvato, M., Smolčić, V., Kartaltepe, J., and Sanders, D. B. (2010b). No Evolution in the IR-Radio Relation for IR-luminous Galaxies at  $z < 2$  in the COSMOS Field. *ApJ*, 714:L190–L195.
- Schawinski, K., Lintott, C., Thomas, D., Sarzi, M., Andreescu, D., Bamford, S. P., Kaviraj, S., Khochfar, S., Land, K., and Murray, P. (2009). Galaxy Zoo: a sample of blue early-type galaxies at low redshift\*. *MNRAS*, 396(2):818–829.
- Schawinski, K., Urry, C. M., Simmons, B. D., Fortson, L., Kaviraj, S., Keel, W. C., Lintott, C. J., Masters, K. L., Nichol, R. C., and Sarzi, M. (2014). The green valley is a red herring: Galaxy Zoo reveals two evolutionary pathways towards quenching of star formation in early- and late-type galaxies. *MNRAS*, 440(1):889–907.
- Schaye, J. (2004). Star Formation Thresholds and Galaxy Edges: Why and Where. *ApJ*, 609(2):667–682.
- Schechter, P. (1976). An analytic expression for the luminosity function for galaxies. *ApJ*, 203:297–306.
- Schinnerer, E., Groves, B., Sargent, M. T., Karim, A., Oesch, P. A., Magnelli, B., LeFevre, O., Tasca, L., Civano, F., Cassata, P., and Smolčić, V. (2016). Gas Fraction and Depletion Time of Massive Star-forming Galaxies at  $z \sim 3.2$ : No Change in Global Star Formation Process out to  $z > 3$ . *ApJ*, 833:112.
- Schlafly, E. F. and Finkbeiner, D. P. (2011). Measuring Reddening with Sloan Digital Sky Survey Stellar Spectra and Recalibrating SFD. *ApJ*, 737:103.
- Schleicher, D. R. G. and Beck, R. (2013). A new interpretation of the far-infrared - radio correlation and the expected breakdown at high redshift. *A&A*, 556:A142.

- Schmidt, M. (1959). The Rate of Star Formation. *ApJ*, 129:243.
- Schreiber, C., Elbaz, D., Pannella, M., Ciesla, L., Wang, T., and Franco, M. (2018a). Dust temperature and mid-to-total infrared color distributions for star-forming galaxies at  $0 > z > 4$ . *A&A*, 609:A30.
- Schreiber, C., Glazebrook, K., Nanayakkara, T., Kacprzak, G. G., Labbé, I., Oesch, P., Yuan, T., Tran, K.-V., Papovich, C., Spitler, L., and Straatman, C. (2018b). Near infrared spectroscopy and star-formation histories of  $3 \leq z \leq 4$  quiescent galaxies. *A&A*, 618:A85.
- Schreiber, C., Labbé, I., Glazebrook, K., Bekiaris, G., Papovich, C., Costa, T., Elbaz, D., Kacprzak, G. G., Nanayakkara, T., Oesch, P., Pannella, M., Spitler, L., Straatman, C., Tran, K.-V., and Wang, T. (2018c). Jekyll & Hyde: quiescence and extreme obscuration in a pair of massive galaxies 1.5 Gyr after the Big Bang. *A&A*, 611:A22.
- Schreiber, C., Pannella, M., Elbaz, D., Béthermin, M., Inami, H., Dickinson, M., Magnelli, B., Wang, T., Aussel, H., Daddi, E., Juneau, S., Shu, X., Sargent, M. T., Buat, V., Faber, S. M., Ferguson, H. C., Giavalisco, M., Koekemoer, A. M., Magdis, G., Morrison, G. E., Papovich, C., Santini, P., and Scott, D. (2015). The Herschel view of the dominant mode of galaxy growth from  $z = 4$  to the present day. *A&A*, 575:A74.
- Schreiber, C., Pannella, M., Leiton, R., Elbaz, D., Wang, T., Okumura, K., and Labbé, I. (2017). The ALMA Redshift 4 Survey (AR4S). I. The massive end of the  $z = 4$  main sequence of galaxies. *A&A*, 599:A134.
- Scott, K. S., Wilson, G. W., Aretxaga, I., Austermann, J. E., Chapin, E. L., Dunlop, J. S., Ezawa, H., Halpern, M., Hatsukade, B., Hughes, D. H., Kawabe, R., Kim, S., Kohno, K., Lowenthal, J. D., Montaña, A., Nakanishi, K., Oshima, T., Sanders, D., Scott, D., Scoville, N., Tamura, Y., Welch, D., Yun, M. S., and Zeballos, M. (2012). The source counts of submillimetre galaxies detected at  $\lambda = 1.1$  mm. *MNRAS*, 423:575–589.
- Scott, S. E., Fox, M. J., Dunlop, J. S., Serjeant, S., Peacock, J. A., Ivison, R. J., Oliver, S., Mann, R. G., Lawrence, A., Efstathiou, A., Rowan-Robinson, M., Hughes, D. H., Archibald, E. N., Blain, A., and Longair, M. (2002). The SCUBA 8-mJy survey - I. Submillimetre maps, sources and number counts. *MNRAS*, 331:817–838.
- Scoville, N., Aussel, H., Brusa, M., Capak, P., Carollo, C. M., Elvis, M., Giavalisco, M., Guzzo, L., Hasinger, G., Impey, C., Kneib, J.-P., LeFevre, O., Lilly, S. J., Mobasher, B., Renzini, A., Rich, R. M., Sanders, D. B., Schinnerer, E., Schminovich, D., Shopbell, P., Taniguchi, Y., and Tyson, N. D. (2007). The Cosmic Evolution Survey (COSMOS): Overview. *ApJS*, 172:1–8.
- Scoville, N., Sheth, K., Aussel, H., Vanden Bout, P., Capak, P., Bongiorno, A., Casey, C. M., Murchikova, L., Koda, J., Álvarez-Márquez, J., Lee, N., Laigle, C., McCracken, H. J., Ilbert, O., Pope, A., Sanders, D., Chu, J., Toft, S., Ivison, R. J., and Manohar, S. (2016). ISM Masses and the Star formation Law at  $Z = 1$  to 6: ALMA Observations of Dust Continuum in 145 Galaxies in the COSMOS Survey Field. *ApJ*, 820:83.
- Scudder, J. M., Oliver, S., Hurley, P. D., Griffin, M., Sargent, M. T., Scott, D., Wang, L., and Wardlow, J. L. (2016). The multiplicity of 250- $\mu$ m Herschel sources in the COSMOS field. *MNRAS*, 460:1119–1130.

- Sérsic, J. L. (1963). Influence of the atmospheric and instrumental dispersion on the brightness distribution in a galaxy. *Boletín de la Asociación Argentina de Astronomía La Plata Argentina*, 6:41.
- Shannon, C. E. (1949). Communication in the Presence of Noise. *IEEE Proceedings*, 37:10–21.
- Shapley, H. (1914). On the Nature and Cause of Cepheid Variation. *ApJ*, 40:448.
- Siebenmorgen, R. and Krügel, E. (2007). Dust in starburst nuclei and ULIRGs. SED models for observers. *A&A*, 461:445–453.
- Silverman, J. D., Daddi, E., Rodighiero, G., Rujopakarn, W., Sargent, M., Renzini, A., Liu, D., Feruglio, C., Kashino, D., Sanders, D., Kartaltepe, J., Nagao, T., Arimoto, N., Berta, S., Béthermin, M., Koekemoer, A., Lutz, D., Magdis, G., Mancini, C., Onodera, M., and Zamorani, G. (2015). A Higher Efficiency of Converting Gas to Stars Pushes Galaxies at  $z \sim 1.6$  Well Above the Star-forming Main Sequence. *ApJ*, 812:L23.
- Silverman, J. D., Mainieri, V., Salvato, M., Hasinger, G., Bergeron, J., Capak, P., Szokoly, G., Finoguenov, A., Gilli, R., and Rosati, P. (2010). The Extended Chandra Deep Field-South Survey: Optical Spectroscopy of Faint X-ray Sources with the VLT and Keck. *ApJS*, 191(1):124–142.
- Simpson, J. M., Smail, I., Swinbank, A. M., Almaini, O., Blain, A. W., Bremer, M. N., Chapman, S. C., Chen, C.-C., Conselice, C., Coppin, K. E. K., Danielson, A. L. R., Dunlop, J. S., Edge, A. C., Farrah, D., Geach, J. E., Hartley, W. G., Ivison, R. J., Karim, A., Lani, C., Ma, C.-J., Meijerink, R., Michałowski, M. J., Mortlock, A., Scott, D., Simpson, C. J., Spaans, M., Thomson, A. P., van Kampen, E., and van der Werf, P. P. (2015a). The SCUBA-2 Cosmology Legacy Survey: ALMA Resolves the Rest-frame Far-infrared Emission of Sub-millimeter Galaxies. *ApJ*, 799:81.
- Simpson, J. M., Smail, I., Swinbank, A. M., Chapman, S. C., Geach, J. E., Ivison, R. J., Thomson, A. P., Aretxaga, I., Blain, A. W., Cowley, W. I., Chen, C.-C., Coppin, K. E. K., Dunlop, J. S., Edge, A. C., Farrah, D., Ibar, E., Karim, A., Knudsen, K. K., Meijerink, R., Michałowski, M. J., Scott, D., Spaans, M., and van der Werf, P. P. (2015b). The SCUBA-2 Cosmology Legacy Survey: ALMA Resolves the Bright-end of the Sub-millimeter Number Counts. *ApJ*, 807:128.
- Simpson, J. M., Swinbank, A. M., Smail, I., Alexander, D. M., Brandt, W. N., Bertoldi, F., de Breuck, C., Chapman, S. C., Coppin, K. E. K., da Cunha, E., Danielson, A. L. R., Dannerbauer, H., Greve, T. R., Hodge, J. A., Ivison, R. J., Karim, A., Knudsen, K. K., Poggianti, B. M., Schinnerer, E., Thomson, A. P., Walter, F., Wardlow, J. L., Weiß, A., and van der Werf, P. P. (2014). An ALMA Survey of Submillimeter Galaxies in the Extended Chandra Deep Field South: The Redshift Distribution and Evolution of Submillimeter Galaxies. *ApJ*, 788:125.
- Siringo, G., Kreysa, E., Kovács, A., Schuller, F., Weiß, A., Esch, W., Gemünd, H.-P., Jethava, N., Lundershausen, G., Colin, A., Güsten, R., Menten, K. M., Beelen, A., Bertoldi, F., Beeman, J. W., and Haller, E. E. (2009). The Large APEX BOlometer CAmera LABOCA. *A&A*, 497:945–962.
- Skelton, R. E., Whitaker, K. E., Momcheva, I. G., Brammer, G. B., van Dokkum, P. G., Labbé, I., Franx, M., van der Wel, A., Bezanson, R., Da Cunha, E., Fumagalli, M., Förster Schreiber, N., Kriek, M., Leja, J., Lundgren, B. F., Magee, D., Marchesini, D., Maseda, M. V., Nelson, E. J., Oesch, P., Pacifici, C., Patel, S. G., Price, S., Rix, H.-W., Tal, T., Wake, D. A., and Wuyts, S. (2014). 3D-HST WFC3-selected Photometric Catalogs in the Five CANDELS/3D-HST Fields: Photometry, Photometric Redshifts, and Stellar Masses. *ApJS*, 214:24.

- Slipher, V. M. (1913). The radial velocity of the Andromeda Nebula. *Lowell Observatory Bulletin*, 2:56–57.
- Slipher, V. M. (1915). Spectrographic Observations of Nebulae. *Popular Astronomy*, 23:21–24.
- Slipher, V. M. (1917). Nebulae. *Proceedings of the American Philosophical Society*, 56:403–409.
- Smail, I., Ivison, R. J., and Blain, A. W. (1997). A Deep Sub-millimeter Survey of Lensing Clusters: A New Window on Galaxy Formation and Evolution. *ApJ*, 490:L5–L8.
- Smail, I., Ivison, R. J., Blain, A. W., and Kneib, J.-P. (2002). The nature of faint submillimetre-selected galaxies. *MNRAS*, 331:495–520.
- Smail, I., Ivison, R. J., Kneib, J.-P., Cowie, L. L., Blain, A. W., Barger, A. J., Owen, F. N., and Morrison, G. (1999). The discovery of ERO counterparts to faint submillimetre galaxies. *MNRAS*, 308:1061–1068.
- Smit, R., Bouwens, R. J., Labbé, I., Franx, M., Wilkins, S. M., and Oesch, P. A. (2016). Inferred H#9082 Flux as a Star Formation Rate Indicator at  $z \sim 4-5$ : Implications for Dust Properties, Burstiness, and the  $z = 4-8$  Star Formation Rate Functions. *ApJ*, 833:254.
- Somerville, R. S., Moustakas, L. A., Mobasher, B., Gardner, J. P., Cimatti, A., Conselice, C., Daddi, E., Dahlen, T., Dickinson, M., and Eisenhardt, P. (2004). The Redshift Distribution of Near-Infrared-Selected Galaxies in the Great Observatories Origins Deep Survey as a Test of Galaxy Formation Scenarios. *ApJ*, 600(2):L135–L138.
- Someya, I. (1949). Waveform Transmission.
- Speagle, J. S., Steinhardt, C. L., Capak, P. L., and Silverman, J. D. (2014). A Highly Consistent Framework for the Evolution of the Star-Forming “Main Sequence” from  $z \sim 0-6$ . *ApJS*, 214:15.
- Spitler, L. R., Straatman, C. M. S., Labbé, I., Glazebrook, K., Tran, K.-V. H., Kacprzak, G. G., Quadri, R. F., Papovich, C., Persson, S. E., van Dokkum, P., Allen, R., Kawinwanichakij, L., Kelson, D. D., McCarthy, P. J., Mehrrens, N., Monson, A. J., Nanayakkara, T., Rees, G., Tilvi, V., and Tomczak, A. R. (2014). Exploring the  $z = 3-4$  Massive Galaxy Population with ZFOURGE: The Prevalence of Dusty and Quiescent Galaxies. *ApJ*, 787:L36.
- Springel, V., Wang, J., Vogelsberger, M., Ludlow, A., Jenkins, A., Helmi, A., Navarro, J. F., Frenk, C. S., and White, S. D. M. (2008). The Aquarius Project: the subhaloes of galactic haloes. *MNRAS*, 391(4):1685–1711.
- Stach, S. M., Dudzevičiūtė, U., Smail, I., Swinbank, A. M., Geach, J. E., Simpson, J. M., An, F. X., Almaini, O., Arumugam, V., Blain, A. W., Chapman, S. C., Chen, C.-C., Conselice, C. J., Cooke, E. A., Coppin, K. E. K., da Cunha, E., Dunlop, J. S., Farrah, D., Gullberg, B., Hodge, J. A., Ivison, R. J., Kocevski, D. D., Michałowski, M. J., Miyaji, T., Scott, D., Thomson, A. P., Wardlow, J. L., Weiss, A., and van der Werf, P. (2019). An ALMA survey of the SCUBA-2 Cosmology Legacy Survey UKIDSS/UDS field: Source catalogue and properties. *arXiv e-prints*.
- Staguhn, J. G., Kovács, A., Arendt, R. G., Benford, D. J., Decarli, R., Dwek, E., Fixsen, D. J., Hilton, G. C., Irwin, K. D., and Jhabvala, C. A. (2014). The GISMO Two-millimeter Deep Field in GOODS-N. *ApJ*, 790(1):77.
- Steidel, C. C., Adelberger, K. L., Dickinson, M., Giavalisco, M., Pettini, M., and Kellogg, M. (1998). A Large Structure of Galaxies at Redshift  $Z$  approximately 3 and Its Cosmological Implications. *ApJ*, 492(2):428–438.

- Steidel, C. C., Adelberger, K. L., Shapley, A. E., Pettini, M., Dickinson, M., and Giavalisco, M. (2003). Lyman Break Galaxies at Redshift  $z \sim 3$ : Survey Description and Full Data Set. *ApJ*, 592(2):728–754.
- Steidel, C. C., Giavalisco, M., Pettini, M., Dickinson, M., and Adelberger, K. L. (1996). Spectroscopic Confirmation of a Population of Normal Star-forming Galaxies at Redshifts  $Z \sim 3$ . *ApJ*, 462:L17.
- Steinhardt, C. L., Capak, P., Masters, D., and Speagle, J. S. (2016). The Impossibly Early Galaxy Problem. *ApJ*, 824(1):21.
- Straatman, C. M. S., Labbé, I., Spitler, L. R., Allen, R., Altieri, B., Brammer, G. B., Dickinson, M., van Dokkum, P., Inami, H., Glazebrook, K., Kacprzak, G. G., Kawinwanichakij, L., Kelson, D. D., McCarthy, P. J., Mehrtens, N., Monson, A., Murphy, D., Papovich, C., Persson, S. E., Quadri, R., Rees, G., Tomczak, A., Tran, K.-V. H., and Tilvi, V. (2014). A Substantial Population of Massive Quiescent Galaxies at  $z \sim 4$  from ZFOURGE. *ApJ*, 783:L14.
- Straatman, C. M. S., Labbé, I., Spitler, L. R., Glazebrook, K., Tomczak, A., Allen, R., Brammer, G. B., Cowley, M., van Dokkum, P., and Kacprzak, G. G. (2015). The Sizes of Massive Quiescent and Star-forming Galaxies at  $z \sim 4$  with ZFOURGE and CANDELS. *ApJ*, 808(1):L29.
- Straatman, C. M. S., Spitler, L. R., Quadri, R. F., Labbé, I., Glazebrook, K., Persson, S. E., Papovich, C., Tran, K.-V. H., Brammer, G. B., Cowley, M., Tomczak, A., Nanayakkara, T., Alcorn, L., Allen, R., Broussard, A., van Dokkum, P., Forrest, B., van Houdt, J., Kacprzak, G. G., Kawinwanichakij, L., Kelson, D. D., Lee, J., McCarthy, P. J., Mehrtens, N., Monson, A., Murphy, D., Rees, G., Tilvi, V., and Whitaker, K. E. (2016). The FourStar Galaxy Evolution Survey (ZFOURGE): Ultraviolet to Far-infrared Catalogs, Medium-bandwidth Photometric Redshifts with Improved Accuracy, Stellar Masses, and Confirmation of Quiescent Galaxies to  $z \sim 3.5$ . *ApJ*, 830:51.
- Strateva, I., Ivezić, Ž., Knapp, G. R., Narayanan, V. K., Strauss, M. A., Gunn, J. E., Lupton, R. H., Schlegel, D., Bahcall, N. A., and Brinkmann, J. (2001). Color Separation of Galaxy Types in the Sloan Digital Sky Survey Imaging Data. *AJ*, 122(4):1861–1874.
- Stromberg, G. (1925). Analysis of radial velocities of globular clusters and non-galactic nebulae. *ApJ*, 61.
- Swinbank, A. M., Simpson, J. M., Smail, I., Harrison, C. M., Hodge, J. A., Karim, A., Walter, F., Alexander, D. M., Brandt, W. N., de Breuck, C., da Cunha, E., Chapman, S. C., Coppin, K. E. K., Danielson, A. L. R., Dannerbauer, H., Decarli, R., Greve, T. R., Ivison, R. J., Knudsen, K. K., Lagos, C. D. P., Schinnerer, E., Thomson, A. P., Wardlow, J. L., Weiß, A., and van der Werf, P. (2014). An ALMA survey of sub-millimetre Galaxies in the Extended Chandra Deep Field South: the far-infrared properties of SMGs. *MNRAS*, 438:1267–1287.
- Szapudi, I., Colombi, S., and Bernardeau, F. (1999). Cosmic statistics of statistics. *MNRAS*, 310(2):428–444.
- Szokoly, G. P., Bergeron, J., Hasinger, G., Lehmann, I., Kewley, L., Mainieri, V., Nonino, M., Rosati, P., Giacconi, R., and Gilli, R. (2004). The Chandra Deep Field-South: Optical Spectroscopy. I. *ApJS*, 155(2):271–349.



- Tacchella, S., Carollo, C. M., Renzini, A., Schreiber, N. M. F., Lang, P., Wuyts, S., Cresci, G., Dekel, A., Genzel, R., and Lilly, S. J. (2015). Evidence for mature bulges and an inside-out quenching phase 3 billion years after the Big Bang. *Science*, 348(6232):314–317.
- Tacconi, L. J., Genzel, R., Saintonge, A., Combes, F., García-Burillo, S., Neri, R., Bolatto, A., Contini, T., Förster Schreiber, N. M., Lilly, S., Lutz, D., Wuyts, S., Accurso, G., Boissier, J., Boone, F., Bouché, N., Bournaud, F., Burkert, A., Carollo, M., Cooper, M., Cox, P., Feruglio, C., Freundlich, J., Herrera-Camus, R., Juneau, S., Lippa, M., Naab, T., Renzini, A., Salome, P., Sternberg, A., Tadaki, K., Übler, H., Walter, F., Weiner, B., and Weiss, A. (2018). PHIBSS: Unified Scaling Relations of Gas Depletion Time and Molecular Gas Fractions. *ApJ*, 853:179.
- Tacconi, L. J., Genzel, R., Smail, I., Neri, R., Chapman, S. C., Ivison, R. J., Blain, A., Cox, P., Omont, A., Bertoldi, F., Greve, T., Förster Schreiber, N. M., Genel, S., Lutz, D., Swinbank, A. M., Shapley, A. E., Erb, D. K., Cimatti, A., Daddi, E., and Baker, A. J. (2008). Submillimeter Galaxies at  $z \sim 2$ : Evidence for Major Mergers and Constraints on Lifetimes, IMF, and CO-H<sub>2</sub> Conversion Factor. *ApJ*, 680:246–262.
- Tadaki, K.-i., Genzel, R., Kodama, T., Wuyts, S., Wisnioski, E., Förster Schreiber, N. M., Burkert, A., Lang, P., Tacconi, L. J., Lutz, D., Belli, S., Davies, R. I., Hatsukade, B., Hayashi, M., Herrera-Camus, R., Ikarashi, S., Inoue, S., Kohno, K., Koyama, Y., Mendel, J. T., Nakanishi, K., Shimakawa, R., Suzuki, T. L., Tamura, Y., Tanaka, I., Übler, H., and Wilman, D. J. (2017). Bulge-forming Galaxies with an Extended Rotating Disk at  $z \sim 2$ . *ApJ*, 834:135.
- Takeuchi, T. T., Yuan, F.-T., Ikeyama, A., Murata, K. L., and Inoue, A. K. (2012). Reexamination of the Infrared Excess-Ultraviolet Slope Relation of Local Galaxies. *ApJ*, 755:144.
- Talia, M., Pozzi, F., Vallini, L., Cimatti, A., Cassata, P., Fraternali, F., Brusa, M., Daddi, E., Delvecchio, I., and Ibar, E. (2018). ALMA view of a massive spheroid progenitor: a compact rotating core of molecular gas in an AGN host at  $z = 2.226$ . *MNRAS*, 476(3):3956–3963.
- Tamura, Y., Iono, D., Wilner, D. J., Kajisawa, M., Uchimoto, Y. K., Alexander, D. M., Chung, A., Ezawa, H., Hatsukade, B., and Hayashino, T. (2010). Submillimeter Array Identification of the Millimeter-selected Galaxy SSA22-AzTEC1: A Protoquasar in a Protocluster? *ApJ*, 724(2):1270–1282.
- Tan, Q., Daddi, E., Sargent, M., Magdis, G., Hodge, J., Béthermin, M., Bournaud, F., Carilli, C., Dannerbauer, H., Dickinson, M., Elbaz, D., Gao, Y., Morrison, G., Owen, F., Pannella, M., Riechers, D., and Walter, F. (2013). A Deep Search for Molecular Gas in Two Massive Lyman Break Galaxies at  $z = 3$  and 4: Vanishing CO-emission Due to Low Metallicity? *ApJ*, 776(2):L24.
- Tasca, L. A. M., Le Fèvre, O., Hathi, N. P., Schaerer, D., Ilbert, O., Zamorani, G., Lemaux, B. C., Cassata, P., Garilli, B., Le Brun, V., Maccagni, D., Pentericci, L., Thomas, R., Vanzella, E., Zucca, E., Amorin, R., Bardelli, S., Cassarà, L. P., Castellano, M., Cimatti, A., Cucciati, O., Durkalec, A., Fontana, A., Giavalisco, M., Grazian, A., Paltani, S., Ribeiro, B., Scodeggio, M., Sommariva, V., Talia, M., Tresse, L., Vergani, D., Capak, P., Charlot, S., Contini, T., de la Torre, S., Dunlop, J., Fotopoulou, S., Koekemoer, A., López-Sanjuan, C., Mellier, Y., Pforr, J., Salvato, M., Scoville, N., Taniguchi, Y., and Wang, P. W. (2015). The evolving star formation rate:  $M_*$  relation and sSFR since  $z \sim 5$  from the VUDS spectroscopic survey. *A&A*, 581:A54.
- Taylor, J. E. (2011). Dark Matter Halos from the Inside Out. *Advances in Astronomy*, 2011:604898.

- Teyssier, R. (2002). Cosmological hydrodynamics with adaptive mesh refinement. A new high resolution code called RAMSES. *A&A*, 385:337–364.
- Thompson, L. A. (2011). Vesto Slipher and the First Galaxy Redshifts. *arXiv e-prints*, page arXiv:1108.4864.
- Toft, S., Smolčić, V., Magnelli, B., Karim, A., Zirm, A., Michalowski, M., Capak, P., Sheth, K., Schawinski, K., Krogager, J.-K., Wuyts, S., Sanders, D., Man, A. W. S., Lutz, D., Staguhn, J., Berta, S., Mccracken, H., Krpan, J., and Riechers, D. (2014). Submillimeter Galaxies as Progenitors of Compact Quiescent Galaxies. *ApJ*, 782:68.
- Toft, S., van Dokkum, P., Franx, M., Labbe, I., Förster Schreiber, N. M., Wuyts, S., Webb, T., Rudnick, G., Zirm, A., and Kriek, M. (2007). Hubble Space Telescope and Spitzer Imaging of Red and Blue Galaxies at  $z \sim 2.5$ : A Correlation between Size and Star Formation Activity from Compact Quiescent Galaxies to Extended Star-forming Galaxies. *ApJ*, 671(1):285–302.
- Tokunaga, A. T. and Vacca, W. D. (2005). The Mauna Kea Observatories Near-Infrared Filter Set. III. Isophotal Wavelengths and Absolute Calibration. *PASP*, 117:421–426.
- Tomczak, A. R., Quadri, R. F., Tran, K.-V. H., Labbé, I., Straatman, C. M. S., Papovich, C., Glazebrook, K., Allen, R., Brammer, G. B., Cowley, M., Dickinson, M., Elbaz, D., Inami, H., Kacprzak, G. G., Morrison, G. E., Nanayakkara, T., Persson, S. E., Rees, G. A., Salmon, B., Schreiber, C., Spitler, L. R., and Whitaker, K. E. (2016). The SFR- $M^*$  Relation and Empirical Star-Formation Histories from ZFOURGE\* at  $0.5 < z < 4$ . *ApJ*, 817:118.
- Toomre, A. and Toomre, J. (1972). Galactic Bridges and Tails. *ApJ*, 178:623–666.
- Tran, K.-V. H., Franx, M., Illingworth, G. D., van Dokkum, P., Kelson, D. D., and Magee, D. (2004). Field E+A Galaxies at Intermediate Redshifts ( $0.3 < z < 1$ ). *ApJ*, 609(2):683–691.
- Tremonti, C. A., Heckman, T. M., Kauffmann, G., Brinchmann, J., Charlot, S., White, S. D. M., Seibert, M., Peng, E. W., Schlegel, D. J., Uomoto, A., Fukugita, M., and Brinkmann, J. (2004). The Origin of the Mass-Metallicity Relation: Insights from 53,000 Star-forming Galaxies in the Sloan Digital Sky Survey. *ApJ*, 613:898–913.
- Tress, M., Marmol-Queraltó, E., Ferreras, I., Pérez-González, P. G., Barro, G., Pampliega, B. A., Cava, A., Domínguez-Sánchez, H., Eliche-Moral, C., Espino-Briones, N., Esquej, P., Hernán-Caballero, A., Rodighiero, G., and Rodríguez-Muñoz, L. (2018). SHARDS: constraints on the dust attenuation law of star-forming galaxies at  $z \sim 2$ . *MNRAS*, 475:2363–2374.
- Treu, T., Ellis, R. S., Kneib, J.-P., Dressler, A., Smail, I., Czoske, O., Oemler, A., and Natarajan, P. (2003). A Wide-Field Hubble Space Telescope Study of the Cluster Cl 0024+16 at  $z = 0.4$ . I. Morphological Distributions to 5 Mpc Radius. *ApJ*, 591(1):53–78.
- Trujillo, I., Förster Schreiber, N. M., Rudnick, G., Barden, M., Franx, M., Rix, H.-W., Caldwell, J. A. R., McIntosh, D. H., Toft, S., Häussler, B., Zirm, A., van Dokkum, P. G., Labbé, I., Moorwood, A., Röttgering, H., van der Wel, A., van der Werf, P., and van Starkenburg, L. (2006). The Size Evolution of Galaxies since  $z \sim 3$ : Combining SDSS, GEMS, and FIRES. *ApJ*, 650:18–41.
- Ueda, Y., Hatsukade, B., Kohno, K., Yamaguchi, Y., Tamura, Y., Umehata, H., Akiyama, M., Ao, Y., Aretxaga, I., Caputi, K., Dunlop, J. S., Espada, D., Fujimoto, S., Hayatsu, N. H., Imanishi, M., Inoue, A. K., Ivison, R. J., Kodama, T., Lee, M. M., Matsuoka, K., Miyaji, T., Morokuma-Matsui,

- K., Nagao, T., Nakanishi, K., Nyland, K., Ohta, K., Ouchi, M., Rujopakarn, W., Saito, T., Tadaki, K., Tanaka, I., Taniguchi, Y., Wang, T., Wang, W.-H., Yoshimura, Y., and Yun, M. S. (2018). ALMA 26 arcmin<sup>2</sup> Survey of GOODS-S at One-millimeter (ASAGAO): X-Ray AGN Properties of Millimeter-selected Galaxies. *ApJ*, 853:24.
- Umehata, H., Hatsukade, B., Smail, I., Alexander, D. M., Ivison, R. J., Matsuda, Y., Tamura, Y., Kohno, K., Kato, Y., and Hayatsu, N. H. (2018). ALMA deep field in SSA22: Survey design and source catalog of a 20 arcmin<sup>2</sup> survey at 1.1 mm. *PASJ*, 70(4):65.
- Umehata, H., Tamura, Y., Kohno, K., Ivison, R. J., Smail, I., Hatsukade, B., Nakanishi, K., Kato, Y., Ikarashi, S., Matsuda, Y., Fujimoto, S., Iono, D., Lee, M., Steidel, C. C., Saito, T., Alexander, D. M., Yun, M. S., and Kubo, M. (2017). ALMA Deep Field in SSA22: Source Catalog and Number Counts. *ApJ*, 835:98.
- Urošević, D. (2014). On the radio spectra of supernova remnants. *Ap&SS*, 354:541–552.
- Urrutia, T., Wisotzki, L., Kerutt, J., Schmidt, K. B., Herenz, E. C., Klar, J., Saust, R., Werhahn, M., Diener, C., and Caruana, J. (2019). The MUSE-Wide Survey: survey description and first data release. *A&A*, 624:A141.
- van den Bergh, S. (1957). The Luminosity Function of Population I. *ApJ*, 125:445.
- van den Bergh, S. (1976). A new classification system for galaxies. *ApJ*, 206:883–887.
- van den Bergh, S. (2011). The Curious Case of Lemaître’s Equation No. 24. *JRASC*, 105(4):151.
- van den Bergh, S., Abraham, R. G., Ellis, R. S., Tanvir, N. R., Santiago, B. X., and Glazebrook, K. G. (1996). A Morphological Catalog of Galaxies in the Hubble deep Field. *AJ*, 112:359.
- van der Wel, A., Bell, E. F., Häussler, B., McGrath, E. J., Chang, Y.-Y., Guo, Y., McIntosh, D. H., Rix, H.-W., Barden, M., Cheung, E., Faber, S. M., Ferguson, H. C., Galametz, A., Grogin, N. A., Hartley, W., Kartaltepe, J. S., Kocevski, D. D., Koekemoer, A. M., Lotz, J., Mozena, M., Peth, M. A., and Peng, C. Y. (2012). Structural Parameters of Galaxies in CANDELS. *ApJS*, 203:24.
- van der Wel, A., Franx, M., van Dokkum, P. G., Skelton, R. E., Momcheva, I. G., Whitaker, K. E., Brammer, G. B., Bell, E. F., Rix, H.-W., Wuyts, S., Ferguson, H. C., Holden, B. P., Barro, G., Koekemoer, A. M., Chang, Y.-Y., McGrath, E. J., Häussler, B., Dekel, A., Behroozi, P., Fumagalli, M., Leja, J., Lundgren, B. F., Maseda, M. V., Nelson, E. J., Wake, D. A., Patel, S. G., Labbé, I., Faber, S. M., Grogin, N. A., and Kocevski, D. D. (2014). 3D-HST+CANDELS: The Evolution of the Galaxy Size-Mass Distribution since  $z = 3$ . *ApJ*, 788:28.
- van Dokkum, P. G., Franx, M., Kriek, M., Holden, B., Illingworth, G. D., Magee, D., Bouwens, R., Marchesini, D., Quadri, R., Rudnick, G., Taylor, E. N., and Toft, S. (2008). Confirmation of the Remarkable Compactness of Massive Quiescent Galaxies at  $z \sim 2.3$ : Early-Type Galaxies Did not Form in a Simple Monolithic Collapse. *ApJ*, 677:L5.
- van Dokkum, P. G., Nelson, E. J., Franx, M., Oesch, P., Momcheva, I., Brammer, G., Förster Schreiber, N. M., Skelton, R. E., Whitaker, K. E., van der Wel, A., Bezanson, R., Fumagalli, M., Illingworth, G. D., Kriek, M., Leja, J., and Wuyts, S. (2015). Forming Compact Massive Galaxies. *ApJ*, 813:23.
- van Dokkum, P. G., Quadri, R., Marchesini, D., Rudnick, G., Franx, M., Gawiser, E., Herrera, D., Wuyts, S., Lira, P., Labbé, I., Maza, J., Illingworth, G. D., Förster Schreiber, N. M., Kriek,

- M., Rix, H.-W., Taylor, E. N., Toft, S., Webb, T., and Yi, S. K. (2006). The Space Density and Colors of Massive Galaxies at  $2 < z < 3$ : The Predominance of Distant Red Galaxies. *ApJ*, 638:L59–L62.
- van Dokkum, P. G., Whitaker, K. E., Brammer, G., Franx, M., Kriek, M., Labbé, I., Marchesini, D., Quadri, R., Bezanson, R., Illingworth, G. D., Muzzin, A., Rudnick, G., Tal, T., and Wake, D. (2010). The Growth of Massive Galaxies Since  $z = 2$ . *ApJ*, 709:1018–1041.
- Vanzella, E., Cristiani, S., Dickinson, M., Giavalisco, M., Kuntschner, H., Haase, J., Nonino, M., Rosati, P., Cesarsky, C., and Ferguson, H. C. (2008). The great observatories origins deep survey. VLT/FORS2 spectroscopy in the GOODS-South field: Part III. *A&A*, 478(1):83–92.
- Visvanathan, N. (1981). Colour-absolute magnitude relation for spiral galaxies. *A&A*, 100(2):L20–L22.
- Visvanathan, N. and Sandage, A. (1977). The color - absolute magnitude relation for E and S0 galaxies. I. Calibration and tests for universality using Virgo and eight other nearby clusters. *ApJ*, 216:214–226.
- Walter, F., Decarli, R., Aravena, M., Carilli, C., Bouwens, R., da Cunha, E., Daddi, E., Ivison, R. J., Riechers, D., Smail, I., Swinbank, M., Weiss, A., Anguita, T., Assef, R., Bacon, R., Bauer, F., Bell, E. F., Bertoldi, F., Chapman, S., Colina, L., Cortes, P. C., Cox, P., Dickinson, M., Elbaz, D., González-López, J., Ibar, E., Inami, H., Infante, L., Hodge, J., Karim, A., Le Fevre, O., Magnelli, B., Neri, R., Oesch, P., Ota, K., Popping, G., Rix, H.-W., Sargent, M., Sheth, K., van der Wel, A., van der Werf, P., and Wagg, J. (2016). ALMA Spectroscopic Survey in the Hubble Ultra Deep Field: Survey Description. *ApJ*, 833:67.
- Wang, S. X., Brandt, W. N., Luo, B., Smail, I., Alexander, D. M., Danielson, A. L. R., Hodge, J. A., Karim, A., Lehmer, B. D., Simpson, J. M., Swinbank, A. M., Walter, F., Wardlow, J. L., Xue, Y. Q., Chapman, S. C., Coppin, K. E. K., Dannerbauer, H., De Breuck, C., Menten, K. M., and van der Werf, P. (2013). An ALMA Survey of Submillimeter Galaxies in the Extended Chandra Deep Field-South: The AGN Fraction and X-Ray Properties of Submillimeter Galaxies. *ApJ*, 778:179.
- Wang, T., Elbaz, D., Schreiber, C., Pannella, M., Shu, X., Willner, S. P., Ashby, M. L. N., Huang, J.-S., Fontana, A., Dekel, A., Daddi, E., Ferguson, H. C., Dunlop, J., Ciesla, L., Koekemoer, A. M., Giavalisco, M., Boutsia, K., Finkelstein, S., Juneau, S., Barro, G., Koo, D. C., Michałowski, M. J., Orellana, G., Lu, Y., Castellano, M., Bourne, N., Buitrago, F., Santini, P., Faber, S. M., Hathi, N., Lucas, R. A., and Pérez-González, P. G. (2016). Infrared Color Selection of Massive Galaxies at  $z > 3$ . *ApJ*, 816:84.
- Wang, T., Schreiber, C., Elbaz, D., Yoshimura, Y., Kohn, K., Shu, X., Yamaguchi, Y., Pannella, M., Franco, M., Huang, J., Lim, C. F., and Wang, W. H. (2019). A dominant population of optically invisible massive galaxies in the early Universe. *Nature*, 572(7768):211–214.
- Wang, W., Kassin, S. A., Pacifici, C., Barro, G., de la Vega, A., Simons, R. C., Faber, S. M., Salmon, B., Ferguson, H. C., Perez-Gonzalez, P. G., Snyder, G. F., Gordon, K. D., Chen, Z., and Kodra, D. (2018). Galaxy inclination and the IRX-beta relation: Effects on UV star-formation rate measurements at intermediate to high redshifts. *ArXiv e-prints*.
- Wardlow, J. L., Smail, I., Coppin, K. E. K., Alexander, D. M., Brandt, W. N., Danielson, A. L. R., Luo, B., Swinbank, A. M., Walter, F., Weiß, A., Xue, Y. Q., Zibetti, S., Bertoldi, F., Biggs, A. D.,

- Chapman, S. C., Dannerbauer, H., Dunlop, J. S., Gawiser, E., Ivison, R. J., Knudsen, K. K., Kovács, A., Lacey, C. G., Menten, K. M., Padilla, N., Rix, H.-W., and van der Werf, P. P. (2011). The LABOCA survey of the Extended Chandra Deep Field-South: a photometric redshift survey of submillimetre galaxies. *MNRAS*, 415:1479–1508.
- Webb, T. M., Eales, S. A., Lilly, S. J., Clements, D. L., Dunne, L., Gear, W. K., Ivison, R. J., Flores, H., and Yun, M. (2003). The Canada-UK Deep Submillimeter Survey. VI. The 3 Hour Field. *ApJ*, 587:41–54.
- Weiβ, A., Kovács, A., Coppin, K., Greve, T. R., Walter, F., Smail, I., Dunlop, J. S., Knudsen, K. K., Alexander, D. M., Bertoldi, F., Brandt, W. N., Chapman, S. C., Cox, P., Dannerbauer, H., De Breuck, C., Gawiser, E., Ivison, R. J., Lutz, D., Menten, K. M., Koekemoer, A. M., Kreysa, E., Kurczynski, P., Rix, H.-W., Schinnerer, E., and van der Werf, P. P. (2009). The Large Apex Bolometer Camera Survey of the Extended Chandra Deep Field South. *ApJ*, 707:1201–1216.
- Weisskopf, M. C., O’dell, S. L., and van Speybroeck, L. P. (1996). Advanced X-Ray Astrophysics Facility (AXAF). In Hoover, R. B. and Walker, A. B., editors, *Multilayer and Grazing Incidence X-Ray/EUV Optics III*, volume 2805 of *Proc. SPIE*, pages 2–7.
- Wellons, S., Torrey, P., Ma, C.-P., Rodriguez-Gomez, V., Vogelsberger, M., Kriek, M., van Dokkum, P., Nelson, E., Genel, S., Pillepich, A., Springel, V., Sijacki, D., Snyder, G., Nelson, D., Sales, L., and Hernquist, L. (2015). The formation of massive, compact galaxies at  $z = 2$  in the Illustris simulation. *MNRAS*, 449(1):361–372.
- Werner, M. W., Roellig, T. L., Low, F. J., Rieke, G. H., Rieke, M., Hoffmann, W. F., Young, E., Houck, J. R., Brandl, B., Fazio, G. G., Hora, J. L., Gehrz, R. D., Helou, G., Soifer, B. T., Stauffer, J., Keene, J., Eisenhardt, P., Gallagher, D., Gautier, T. N., Irace, W., Lawrence, C. R., Simmons, L., Van Cleve, J. E., Jura, M., Wright, E. L., and Cruikshank, D. P. (2004). The Spitzer Space Telescope Mission. *ApJS*, 154:1–9.
- Whitaker, K. E., Franx, M., Bezanson, R., Brammer, G. B., van Dokkum, P. G., Kriek, M. T., Labbé, I., Leja, J., Momcheva, I. G., and Nelson, E. J. (2015). Galaxy Structure as a Driver of the Star Formation Sequence Slope and Scatter. *ApJ*, 811(1):L12.
- Whitaker, K. E., Kriek, M., van Dokkum, P. G., Bezanson, R., Brammer, G., Franx, M., and Labbé, I. (2012). A Large Population of Massive Compact Post-starburst Galaxies at  $z \gtrsim 1$ : Implications for the Size Evolution and Quenching Mechanism of Quiescent Galaxies. *ApJ*, 745(2):179.
- Whitaker, K. E., Labbé, I., van Dokkum, P. G., Brammer, G., Kriek, M., Marchesini, D., Quadri, R. F., Franx, M., Muzzin, A., Williams, R. J., Bezanson, R., Illingworth, G. D., Lee, K.-S., Lundgren, B., Nelson, E. J., Rudnick, G., Tal, T., and Wake, D. A. (2011). The NEWFIRM Medium-band Survey: Photometric Catalogs, Redshifts, and the Bimodal Color Distribution of Galaxies out to  $z \sim 3$ . *ApJ*, 735:86.
- Whitaker, K. E., Pope, A., Cybulski, R., Casey, C. M., Popping, G., and Yun, M. S. (2017). The Constant Average Relationship between Dust-obscured Star Formation and Stellar Mass from  $z = 0$  to  $z = 2.5$ . *ApJ*, 850:208.
- White, M. and Scott, D. (1996). The Impact of the CMB on Large-Scale Structure. *Comments on Astrophysics*, 18.

- Whittaker, E. T. (1915). xviii.—on the functions which are represented by the expansions of the interpolation-theory. *Proceedings of the Royal Society of Edinburgh*, 35:181–194.
- Wiklind, T., Conselice, C. J., Dahlen, T., Dickinson, M. E., Ferguson, H. C., Grogin, N. A., Guo, Y., Koekemoer, A. M., Mobasher, B., Mortlock, A., Fontana, A., Davé, R., Yan, H., Acquaviva, V., Ashby, M. L. N., Barro, G., Caputi, K. I., Castellano, M., Dekel, A., Donley, J. L., Fazio, G. G., Giavalisco, M., Grazian, A., Hathi, N. P., Kurczynski, P., Lu, Y., McGrath, E. J., de Mello, D. F., Peth, M., Safarzadeh, M., Stefanon, M., and Targett, T. (2014). Properties of Submillimeter Galaxies in the CANDELS GOODS-South Field. *ApJ*, 785:111.
- Williams, C. C., Giavalisco, M., Cassata, P., Tundo, E., Wiklind, T., Guo, Y., Lee, B., Barro, G., Wuyts, S., Bell, E. F., Conselice, C. J., Dekel, A., Faber, S. M., Ferguson, H. C., Grogin, N., Hathi, N., Huang, K.-H., Kocevski, D., Koekemoer, A., Koo, D. C., Ravindranath, S., and Salimbeni, S. (2014). The Progenitors of the Compact Early-type Galaxies at High Redshift. *ApJ*, 780(1):1.
- Williams, C. C., Labbe, I., Spilker, J., Stefanon, M., Leja, J., Whitaker, K., Bezanson, R., Narayanan, D., Oesch, P., and Weiner, B. (2019). Discovery of a dark, massive, ALMA-only galaxy at  $z \sim 5-6$  in a tiny 3-millimeter survey. *arXiv e-prints*, page arXiv:1905.11996.
- Williams, R. E., Baum, S., Bergeron, L. E., Bernstein, N., Blacker, B. S., Boyle, B. J., Brown, T. M., Carollo, C. M., Casertano, S., Covarrubias, R., de Mello, D. F., Dickinson, M. E., Espey, B. R., Ferguson, H. C., Fruchter, A., Gardner, J. P., Gonnella, A., Hayes, J., Hewett, P. C., Heyer, I., Hook, R., Irwin, M., Jones, D., Kaiser, M. E., Levay, Z., Lubenow, A., Lucas, R. A., Mack, J., MacKenty, J. W., Madau, P., Makidon, R. B., Martin, C. L., Mazzuca, L., Mutchler, M., Norris, R. P., Perriello, B., Phillips, M. M., Postman, M., Royle, P., Sahu, K., Savaglio, S., Sherwin, A., Smith, T. E., Stiavelli, M., Suntzeff, N. B., Teplitz, H. I., van der Marel, R. P., Walker, A. R., Weymann, R. J., Wiggs, M. S., Williger, G. M., Wilson, J., Zacharias, N., and Zurek, D. R. (2000). The Hubble Deep Field South: Formulation of the Observing Campaign. *AJ*, 120:2735–2746.
- Williams, R. E., Blacker, B., Dickinson, M., Dixon, W. V. D., Ferguson, H. C., Fruchter, A. S., Giavalisco, M., Gilliland, R. L., Heyer, I., Katsanis, R., Levay, Z., Lucas, R. A., McElroy, D. B., Petro, L., Postman, M., Adorf, H.-M., and Hook, R. (1996). The Hubble Deep Field: Observations, Data Reduction, and Galaxy Photometry. *AJ*, 112:1335.
- Williams, R. J., Quadri, R. F., Franx, M., van Dokkum, P., and Labbé, I. (2009). Detection of Quiescent Galaxies in a Bicolor Sequence from  $Z = 0-2$ . *ApJ*, 691:1879–1895.
- Wilson, G. W., Austermann, J. E., Perera, T. A., Scott, K. S., Ade, P. A. R., Bock, J. J., Glenn, J., Golwala, S. R., Kim, S., Kang, Y., Lydon, D., Mauskopf, P. D., Predmore, C. R., Roberts, C. M., Souccar, K., and Yun, M. S. (2008). The AzTEC mm-wavelength camera. *MNRAS*, 386:807–818.
- Windhorst, R. A., Cohen, S. H., Hathi, N. P., McCarthy, P. J., Ryan, Jr., R. E., Yan, H., Baldry, I. K., Driver, S. P., Frogel, J. A., Hill, D. T., Kelvin, L. S., Koekemoer, A. M., Mechtley, M., O’Connell, R. W., Robotham, A. S. G., Rutkowski, M. J., Seibert, M., Straughn, A. N., Tuffs, R. J., Balick, B., Bond, H. E., Bushouse, H., Calzetti, D., Crockett, M., Disney, M. J., Dopita, M. A., Hall, D. N. B., Holtzman, J. A., Kaviraj, S., Kimble, R. A., MacKenty, J. W., Mutchler, M., Paresce, F., Saha, A., Silk, J. I., Trauger, J. T., Walker, A. R., Whitmore, B. C., and Young, E. T. (2011). The Hubble Space Telescope Wide Field Camera 3 Early Release Science Data: Panchromatic Faint Object Counts for 0.2-2  $\mu\text{m}$  Wavelength. *ApJS*, 193:27.

- Wirtz, C. (1918). Über die Bewegungen der Nebelflecke. *Astronomische Nachrichten*, 206:109.
- Wolf, M. (1908). Die Klassifizierung der kleinen Nebelflecken. *Publikationen des Astrophysikalischen Instituts Koenigstuhl-Heidelberg*, 3:109–112.
- Wright, A. H., Robotham, A. S. G., Bourne, N., Driver, S. P., Dunne, L., Maddox, S. J., Alpaslan, M., Andrews, S. K., Bauer, A. E., and Bland-Hawthorn, J. (2016). Galaxy And Mass Assembly: accurate panchromatic photometry from optical priors using LAMBDAR. *MNRAS*, 460(1):765–801.
- Wuyts, S., Cox, T. J., Hayward, C. C., Franx, M., Hernquist, L., Hopkins, P. F., Jonsson, P., and van Dokkum, P. G. (2010). On Sizes, Kinematics, M/L Gradients, and Light Profiles of Massive Compact Galaxies at  $z \sim 2$ . *ApJ*, 722:1666–1684.
- Wuyts, S., Förster Schreiber, N. M., van der Wel, A., Magnelli, B., Guo, Y., Genzel, R., Lutz, D., Aussel, H., Barro, G., and Berta, S. (2011). Galaxy Structure and Mode of Star Formation in the SFR-Mass Plane from  $z \sim 2.5$  to  $z \sim 0.1$ . *ApJ*, 742(2):96.
- Wuyts, S., Labbé, I., Förster Schreiber, N. M., Franx, M., Rudnick, G., Brammer, G. B., and van Dokkum, P. G. (2008). FIREWORKS  $U_{38}$ -to- $24 \mu\text{m}$  Photometry of the GOODS Chandra Deep Field-South: Multiwavelength Catalog and Total Infrared Properties of Distant  $K_s$ -selected Galaxies. *ApJ*, 682:985–1003.
- Wuyts, S., Labbé, I., Franx, M., Rudnick, G., van Dokkum, P. G., Fazio, G. G., Förster Schreiber, N. M., Huang, J., Moorwood, A. F. M., Rix, H.-W., Röttgering, H., and van der Werf, P. (2007). What Do We Learn from IRAC Observations of Galaxies at  $2 < z < 3.5$ ? *ApJ*, 655:51–65.
- Wuyts, S., van Dokkum, P. G., Franx, M., Förster Schreiber, N. M., Illingworth, G. D., Labbé, I., and Rudnick, G. (2009). Optical Spectroscopy of Distant Red Galaxies. *ApJ*, 706(1):885–895.
- Xue, Y. Q., Luo, B., Brandt, W. N., Bauer, F. E., Lehmer, B. D., Broos, P. S., Schneider, D. P., Alexander, D. M., Brusa, M., Comastri, A., Fabian, A. C., Gilli, R., Hasinger, G., Hornschemeier, A. E., Koekemoer, A., Liu, T., Mainieri, V., Paolillo, M., Rafferty, D. A., Rosati, P., Shemmer, O., Silverman, J. D., Smail, I., Tozzi, P., and Vignali, C. (2011). The Chandra Deep Field-South Survey: 4 Ms Source Catalogs. *ApJS*, 195:10.
- Yamaguchi, Y., Kohno, K., Hatsukade, B., Wang, T., Yoshimura, Y., Ao, Y., Caputi, K. I., Dunlop, J. S., Egami, E., Espada, D., Fujimoto, S., Hayatsu, N. H., Ivison, R. J., Kodama, T., Kusakabe, H., Nagao, T., Ouchi, M., Rujopakarn, W., Tadaki, K.-i., Tamura, Y., Ueda, Y., Umehata, H., Wang, W.-H., and Yun, M. S. (2019a). ALMA twenty-six arcmin<sup>2</sup> survey of GOODS-S at one-millimeter (ASAGAO): Near-infrared-dark faint ALMA sources. *arXiv e-prints*.
- Yamaguchi, Y., Kohno, K., Hatsukade, B., Wang, T., Yoshimura, Y., Ao, Y., Caputi, K. I., Dunlop, J. S., Egami, E., Espada, D., Fujimoto, S., Hayatsu, N. H., Ivison, R. J., Kodama, T., Kusakabe, H., Nagao, T., Ouchi, M., Rujopakarn, W., Tadaki, K.-i., Tamura, Y., Ueda, Y., Umehata, H., Wang, W.-H., and Yun, M. S. (2019b). ALMA twenty-six arcmin<sup>2</sup> survey of GOODS-S at one-millimeter (ASAGAO): Near-infrared-dark faint ALMA sources. *arXiv e-prints*.
- Yamaguchi, Y., Tamura, Y., Kohno, K., Aretxaga, I., Dunlop, J. S., Hatsukade, B., Hughes, D., Ikarashi, S., Ishii, S., Ivison, R. J., Izumi, T., Kawabe, R., Kodama, T., Lee, M., Makiya, R., Matsuda, Y., Nakanishi, K., Ohta, K., Rujopakarn, W., Tadaki, K.-i., Umehata, H., Wang, W.-H., Wilson, G. W., Yabe, K., and Yun, M. S. (2016). SXDF-ALMA 2 arcmin<sup>2</sup> deep survey: Resolving and characterizing the infrared extragalactic background light down to 0.5 mJy. *PASJ*, 68:82.

- Yates, R. M., Kauffmann, G., and Guo, Q. (2012). The relation between metallicity, stellar mass and star formation in galaxies: an analysis of observational and model data. *MNRAS*, 422(1):215–231.
- Yesuf, H. M., Faber, S. M., Trump, J. R., Koo, D. C., Fang, J. J., Liu, F. S., Wild, V., and Hayward, C. C. (2014). From Starburst to Quiescence: Testing Active Galactic Nucleus feedback in Rapidly Quenching Post-starburst Galaxies. *ApJ*, 792(2):84.
- Yi, S. K., Yoon, S. J., Kaviraj, S., Deharveng, J. M., Rich, R. M., Salim, S., Boselli, A., Lee, Y. W., Ree, C. H., and Sohn, Y. J. (2005). Galaxy Evolution Explorer Ultraviolet Color-Magnitude Relations and Evidence of Recent Star Formation in Early-Type Galaxies. *ApJ*, 619(1):L111–L114.
- York, D. G., Adelman, J., Anderson, John E., J., Anderson, S. F., Annis, J., Bahcall, N. A., Bakken, J. A., Barkhouser, R., Bastian, S., and Berman, E. (2000). The Sloan Digital Sky Survey: Technical Summary. *AJ*, 120(3):1579–1587.
- Yun, M. S., Reddy, N. A., and Condon, J. J. (2001). Radio Properties of Infrared-selected Galaxies in the IRAS 2 Jy Sample. *ApJ*, 554:803–822.
- Yun, M. S., Scott, K. S., Guo, Y., Aretxaga, I., Giavalisco, M., Austermann, J. E., Capak, P., Chen, Y., Ezawa, H., Hatsukade, B., Hughes, D. H., Iono, D., Johnson, S., Kawabe, R., Kohno, K., Lowenthal, J., Miller, N., Morrison, G., Oshima, T., Perera, T. A., Salvato, M., Silverman, J., Tamura, Y., Williams, C. C., and Wilson, G. W. (2012). Deep 1.1 mm-wavelength imaging of the GOODS-S field by AzTEC/ASTE - II. Redshift distribution and nature of the submillimetre galaxy population. *MNRAS*, 420:957–985.
- Zanella, A., Daddi, E., Le Floch, E., Bournaud, F., Gobat, R., Valentino, F., Strazzullo, V., Cibinel, A., Onodera, M., Perret, V., Renaud, F., and Vignali, C. (2015). An extremely young massive clump forming by gravitational collapse in a primordial galaxy. *Nature*, 521:54–56.



# CHAPTER 11

## LIST OF PUBLICATIONS

### 11.1 First author publications

**Franco, M.** et al., “GOODS-ALMA: 1.1 mm galaxy survey - I. Source catalogue and optically dark galaxies”, A&A 620, A152 (2018)

<http://adsabs.harvard.edu/abs/2018A%26A...620A.152F>

**Franco, M.** et al., “GOODS-ALMA: Using IRAC priors to probe fainter millimeter galaxies”. To be submitted

**Franco, M.** et al., “The slow downfall of star-formation in  $z = 2-3$  massive galaxies”. To be submitted

### 11.2 Other publications

Elbaz, D.; Leiton, R; Nagar, N.; Okurama, K; **Franco, M.** et al., “Starbursts in and out of the star-formation main sequence”, A&A 616, A110 (2018)

<http://adsabs.harvard.edu/abs/2018A%26A...616A.110E>

Schreiber, C.; Elbaz, D.; Pannella, M.; Ciesla, L.; Wang, T. and **Franco, M.** , “Dust temperature and mid-to-total infrared color distributions for star-forming galaxies at  $0 < z < 4$ ”, A&A 609, 30 (2018)

<http://adsabs.harvard.edu/abs/2018A%26A...609A..30S>

McLure, R.J.; [...]; **Franco, M.** et al., “The VANDELS ESO public spectroscopic survey”, MNRAS 479, 1 (2018)

<http://adsabs.harvard.edu/abs/2018MNRAS.479...25M>

Pentericci, L.; [...]; **Franco, M.** et al., “The VANDELS ESO public spectroscopic survey: observations and first data release”, A&A 616, 174 (2018)

<http://adsabs.harvard.edu/abs/2018A%26A...616A.174P>

Rujopakarn, W.; [...]; **Franco, M.** et al., “ALMA 200-parsec Resolution Imaging of Smooth Cold Dusty Disks in Typical  $z \sim 3$  Star-Forming Galaxies”, ApJ 882, 107 (2019)

<https://ui.adsabs.harvard.edu/abs/2019ApJ...882..107R>

Wang, T.; [...]; **Franco, M.** et al., “A dominant population of optically-invisible massive galaxies in the early Universe”, *Nature* 572, 7768 (2019)

<https://ui.adsabs.harvard.edu/abs/2019Natur.572..211W>

Popping, G.; [...]; **Franco, M.** et al., “The galaxies responsible for the observed 850  $\mu\text{m}$  and 1.1 millimeter number counts and how to detect them”, submitted

### 11.3 Non-refereed publications

Casey, C.; [...]; **Franco, M.** et al., “Taking Census of Massive, Star-Forming Galaxies formed 11 Gyr After the Big Bang“

<http://adsabs.harvard.edu/abs/2019arXiv190305634C>

Geach, J.; [...]; **Franco, M.** et al., “The case for a ‘sub-millimeter SDSS’: a 3D map of galaxy evolution to  $z \sim 10$ ”

<http://adsabs.harvard.edu/abs/2019arXiv190304779G>

## 12.1 Approved proposals

**M. Franco** et al., HST-Dark galaxies in the GOODS-ALMA field, ALMA, 10h, 2018.1.01079.S, observed.

D. Elbaz; [...]; **M. Franco** et al., Towards a census of star-formation since  $z \sim 6$  with ALMA-1.1mm, 20h, ALMA, 2017.1.00755.S, observed.

T. Wang; [...]; **M. Franco** et al., On the mysterious origin of the large abundance of HST-dark galaxies at  $z \sim 4$ , 19.4h, ALMA, 2018.1.01807.S

T. Wang; [...]; **M. Franco** et al., Unveiling the nature of the most optically-dark galaxies at  $z \sim 6$ , 28h, IRAM, W17EV.

## 12.2 Pending proposals

**M. Franco** et al., A complete census of massive galaxies in GOODS-ALMA, ALMA, 17.1 h, 2019.1.01805.S

**M. Franco** et al., A galaxy at  $z=2.81$  possibly forming the bulk of its stars in well-separated clumps, 3.9 h, ALMA, 2019.1.01840.S

L. Zhou; [...]; **M. Franco** et al., Optically dark ALMA sources shed light on the formation of a large-scale structure at  $z \sim 3.5$ , 10.6 h, ALMA, 2019.1.01019.S

K. Coppin; [...]; **M. Franco** et al., The nature of the scatter of the IRX-Beta relation at 3i2i4: a resolved HST+ALMA view of normal star-forming galaxies, 36.9 h, ALMA, 2019.1.00899.S

T. Wang; [...]; **M. Franco** et al., Towards a systematic redshift determination of HST-dark galaxies, 6.8 h, ALMA, 2019.1.01285.S

T. Garatt; [...]; **M. Franco** et al., Quantifying the Molecular Gas Properties of Optically Faint, Submillimetre detected Lyman-Break Galaxies, 22.3 h, ALMA, 2019.1.01414.S

K. Coppin; [...]; **M. Franco** et al., 0.1" Resolution mm-Interferometry of a Highly Magnified Lyman Break Galaxy at  $z=3.07$ , 8.7h, ALMA, 2019.1.01642.S

K. Coppin; [...]; **M. Franco** et al., The Lyman Break Galaxy ALMA Reference Sample: probing the  $\text{IRX-}\beta$  relation at high-redshift, 37.3h, VLT/FORS2



# HST-Dark galaxies in the GOODS-ALMA field

2018.1.01079.S

## ABSTRACT

One of the most uncertain and potentially transformational outputs of ALMA is its ability to reveal a new class of galaxies through serendipitous detections. This is also one of the main reasons for performing blind extragalactic surveys which can provide a complete view on this new parameter space, specific to ALMA.

The present proposal targets a systematic identification of serendipitously found HST-dark galaxies in the GOODS-ALMA field to obtain or confirm spectroscopic redshifts from their CO lines. With their ultra-faint optical properties, this is the only way to determine whether there is really a 20% population of new, highly obscured galaxies in the distant Universe or whether these galaxies are actually nearby galaxies or regions of their neighbors but with abnormally low dust temperatures.

With this proposal of 10h, we will (i) determine or confirm the redshifts of these sources, (ii) derive their molecular gas content, (iii) deduce their star formation efficiency.

We will determine if these galaxies are observed during a starburst phase, determine whether they possess abnormally large molecular gas reservoirs and compare their CO conversion factor to that of.

PI NAME:	Maximilien Franco			SCIENCE CATEGORY:	Cosmology and the High Redshift Universe
ESTIMATED 12M TIME:	10.0 h	ESTIMATED ACA TIME:	0.0 h	ESTIMATED NON-STANDARD MODE TIME (12-M):	10.0 h
CO-PI NAME(S): (Large & VLBI Proposals only)					
CO-INVESTIGATOR NAME(S):	David Elbaz; Corentin Schreiber; Roger Leiton; Tao Wang; Mark Dickinson; Emanuele Daddi; Laure Ciesla; Luwenjia Zhou; Wiphu Rujopakarn				
DUPLICATE OBSERVATION JUSTIFICATION:					

## REPRESENTATIVE SCIENCE GOALS (UP TO FIRST 30)

SCIENCE GOAL	POSITION	BAND	ANG.RES.('')	LAS.('')	ACA?	NON-STANDARD MODE
Dark-HST band 4	ICRS 03:32:46.8310, -27:51:20.970	4	0.800	1.000	N	Y
Total # Science Goals : 1						
SCHEDULING TIME CONSTRAINTS	NONE		TIME ESTIMATES OVERRIDDEN ?		No	

# 1 Scientific justification

One of the most uncertain and potentially transformational outputs of ALMA is its ability to reveal a new class of galaxies through serendipitous detections. This is also one of the main reasons for performing blind extragalactic surveys. Blind surveys can provide a complete view on this new parameter space, specific to ALMA.

This proposal comes as a result of the observation by ALMA of the deepest part of the CANDELS field (*HST*–WFC3), in the Great Observatories Origins Deep Survey–*South* (GOODS–*South*) field, imaging over  $6.9' \times 10'$  (2015.1.00543.S, PI: D. Elbaz). Thanks to the availability of very deep, panchromatic photometry at rest-frame UV, optical and NIR in this field, which also includes among the deepest available X-ray and radio maps, precise multi-wavelength analysis incorporating this crucial FIR data has been possible (Franco et al, 2018). This unbiased study, without prior selection, has allowed us to realize a flux limited census at 1.1 mm of all the galaxies present in the field.

A key outcome of this study was the uncovering of a population of candidates for high redshift ( $3 < z < 5$ ) galaxies, too faint to be detected in the deepest *HST*–WFC3 images of the GOODS–*South* field, but detectable through their thermal dust emission thanks to the capabilities of ALMA. In total, 20% (4/20) of the sources detected in this survey are optically ‘dark’ galaxies, and strong evidence suggests that they are not spurious detections (Franco et al. 2018). This discovery, if confirmed, could significantly change our understanding of massive galaxy formation. The inferred redshifts of these galaxies place them at the “rising phase” of the cosmic star formation history, before the peak. This has important implications for understanding whether the apparently lower star formation rate densities at  $z \gg 2$ , inferred mainly from UV rest-frame data, may be in part due to HST non-detection of a population of very dusty galaxies. This new population of galaxies, undetected by the *HST* but revealed by ALMA, has been reported in several recent papers (e.g. Wang et al. 2016, Fujimoto et al. 2016, Elbaz et al. 2018, Franco et al. 2018). These galaxies are ultra-faint at optical wavelengths, apparently very distant ( $z > 4$  for the two galaxies for which photometric redshifts have been estimated) and highly obscured. New ALMA observations, and in particular spectral line observations, are therefore needed in order to further characterize and understand these galaxies. Currently, we have only continuum data at 265 GHz for these galaxies. ALMA is the only instrument able to reach the depths required to extract the spectra of these galaxies.

With these observations, we will (i) determine or confirm the redshifts of the *HST*–dark sources using a spectral scan for expected CO transitions, (ii) derive the galaxies’ molecular gas contents, (iii) deduce their star formation efficiencies,  $SFE = SFR/M_{gas}$ . We will compare the molecular gas content derived from these proposed CO observations to the total gas mass derived from the galaxies’ dust continuum, using our previous data. We can therefore investigate whether the *HST*–dark nature of these galaxies has an effect on other physical galaxy properties, such as the  $H_2$ –to–CO conversion factor and gas-to-dust ratio, and explore what this tells us about the underlying nature of the galaxies.

This will allow us to reach the missing properties of galaxies undetected by the *HST* and to have a complete and precise view of all the galaxies, above the detection limit (0.8 mJy at 1.1 mm) in the GOODS–ALMA field.

These observations will allow us to answer the following questions:

- Are these *HST*–dark galaxies a distinct galaxy population, with characteristics (such as SFE, gas fraction...) distinguishable from those of the classical Star Forming Galaxy population?
- Could physical mechanisms other than dust obscuration be making these galaxies optically dark?

To answer these questions, we propose to study 6 galaxies unveiled by our ALMA continuum observations, which we briefly introduce the global properties of these galaxies in the following

section.

## 1.1 A hidden population of distant and massive galaxies

Although these 6 galaxies do not at first seem homogeneous, some common properties emerge from this sample of galaxies. Of these 6 galaxies, 5 were discovered during the ALMA-GOODS blind survey (4 are described in detail in Franco et al. 2018, the 5th in Franco et al. in preparation, and the sixth (described in Elbaz et al. 2018) was present in the ALMA field of view as part of a follow-up of 8  $z \sim 2$  ULIRGs (PI R.Leiton, ALMA Cycle 1).

**Secure identification :** The presence of an ALMA detection alone does not make these galaxies HST-dark, it is the presence of a several pieces of concordant evidence that strongly indicate that there is a galaxy at the position of the ALMA detection. Firstly, for all six galaxies, an IRAC detection is present within a radius of  $<0.2''$  from the ALMA position. The probability of having an ALMA detection at this distance from an IRAC source due to chance alone is  $<1\%$ , giving a very strong argument to the credibility of these sources. In addition, for three of them (AGS4, AGS17 and AGS24), we detect a 1cm and 5cm flux at the position of the ALMA detection. As the radio part of the spectrum does not benefit from the strong negative  $K$ -correction, it is not unexpected that the radio fluxes are not present for all of the most massive, distant galaxies.

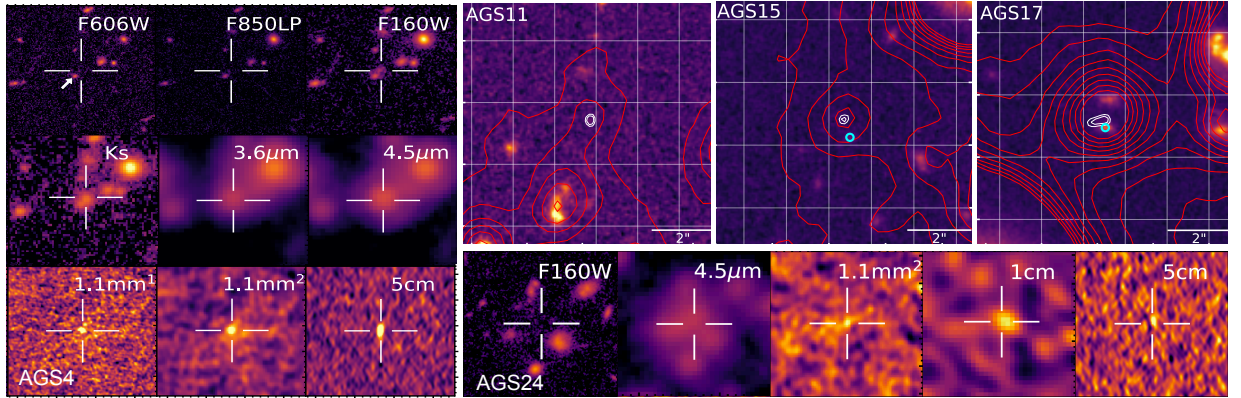


Figure 1: **Left:** Postage stamps of  $10 \times 10$  arcsec from HST-WFC3 at  $0.606 \mu\text{m}$  to VLA at  $5\text{cm}$  for AGS4 **Top right:** IRAC  $3.6 \mu\text{m}$  (red contours) and ALMA  $1.1\text{mm}$  (white contours) overlaid on  $8.3'' \times 8.3''$  HST H-band images. The position of the previously associated HST counterpart is shown by a cyan circle. **Bottom right:** Postage stamps of  $10 \times 10$  arcsec from HST-WFC3 at  $0.606 \mu\text{m}$  to VLA at  $5\text{cm}$  for AGS24

**A population of apparently distant galaxies.** For two of these HST-dark galaxies (GS8 and AGS4), which were located near the line of sight ( $0.3''$  and  $0.4''$  respectively) of a galaxy detected in the optical, a redshift estimation has been determined. In Fig. 1, we clearly see that the ALMA emission is offset from the observed H-band galaxy, indicated by the white arrow. This offset could be explained physically, for example, as a region within the same galaxy extremely obscured by dust, greatly extinguishing the optical rest-frame emission revealed by ALMA. However, many things lead us to believe that they are two different galaxies, with the optical emission originating from the foreground and the infrared emission from the background. Without the high ALMA resolution of our survey, we would have falsely associated the two counterparts. In both cases, the peak of the far-IR emission obtained from the combination of Herschel and ALMA data was found between  $350$  and  $400 \mu\text{m}$ , inconsistent with known SEDs for  $z = 1.616$  ( $z = 0.3$  respectively) galaxies. For GS8

and AGS4, the two sources (optical and submillimeter) were then fit simultaneously using these two light-profile models (using Galfit) on all of the available images, fixing the profile to that observed in the  $H$  band (see Fig. 2). In both cases, the redshifts found for the optical galaxies were coherent with previous values. As the Balmer break is well established in the  $K$ -band for the ALMA galaxy, we also consider the redshift determinations for the ALMA detections to be robust. We find the following redshifts:  $z_{GS8} = 3.24 \pm 0.20$  and  $z_{AGS4} = 4.32^{+0.25}_{-0.21}$ . Additionally, for a third HST-dark galaxy, AGS11, despite the weak flux derived from several stacked images and the limited number of bands available, a redshift has been determined in the ZFOURGE catalogue (Straatman et al. 2016) at  $z = 4.82$ . This makes AGS11 the farthest galaxy detected in our blind survey (Franco et al. 2018). However, we remain cautious regarding this redshift.

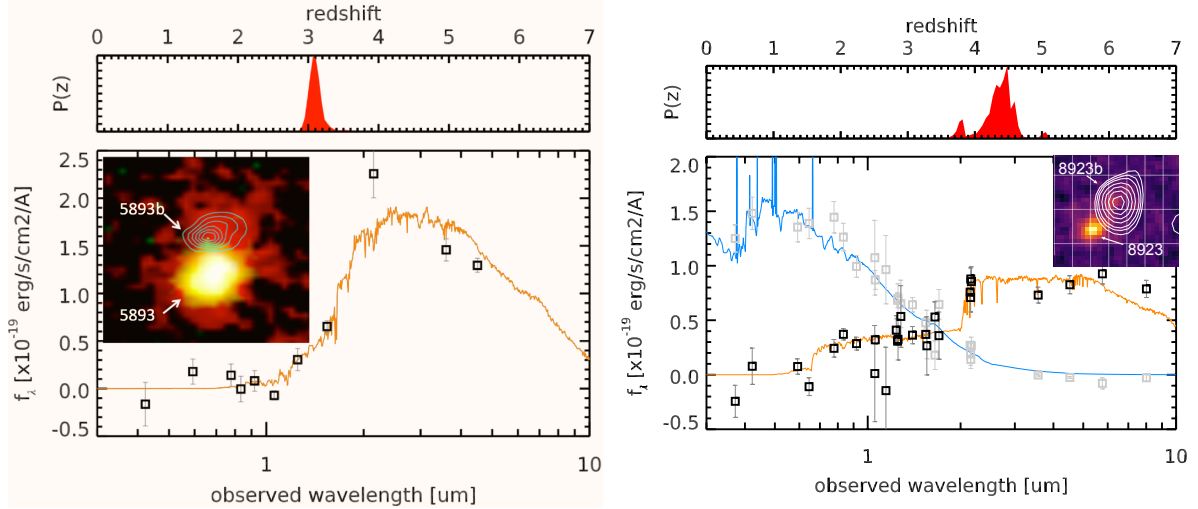


Figure 2: Spectral energy distributions of GS8 (*left panel*) and AGS4 (*right panel*). Aperture photometry allows the separation between the local galaxy detected by the  $HST$  (blue, and indicated by a white arrow in Fig. 1, ID<sub>CANDELS</sub> 8923) and the distant galaxy detected by ALMA (orange). The top panels show the photometric redshift probability distributions for the two ALMA galaxies.

**A population of apparently massive galaxies.** The presence of an IRAC source for these galaxies not detected by the HST indicates a selection towards the most massive galaxies (Wang et al. 2015). ALMA also tends to preferentially detect the most massive galaxies (Franco et al. 2018). This is the third common property of these HST-dark galaxies: they are all very massive galaxies. The two galaxies presented in the previous section both have stellar masses greater than  $10^{11} M_{\odot}$ .

## 2 Description of observations

We propose to follow-up these six galaxies using band-4 spectral scan observations. As shown in Fig.3, band-4 provides excellent line coverage from  $z=1$  to  $z=5$  (with a small gap between  $z=1.6$  and  $z=2$ ).

To estimate the necessary integration time, we base our calculations on the faintest of the six targeted galaxies (0.6 mJy at 1.1mm). Using a standard IR SED (Schreiber et al. 2018), we infer the total LIR from the ALMA 1.1mm flux, use the  $LIR - L'_{CO(5-4)}$  relation (Daddi et al. 2015), and assume the typical SMG spectral line energy distributions from Bothwell et al. (2013) to infer the fluxes of the other CO lines. To optimize the overheads, we use the OT to select the smallest sensitivity for which the scan can be executed in a single SB in band 4. Using the position of the



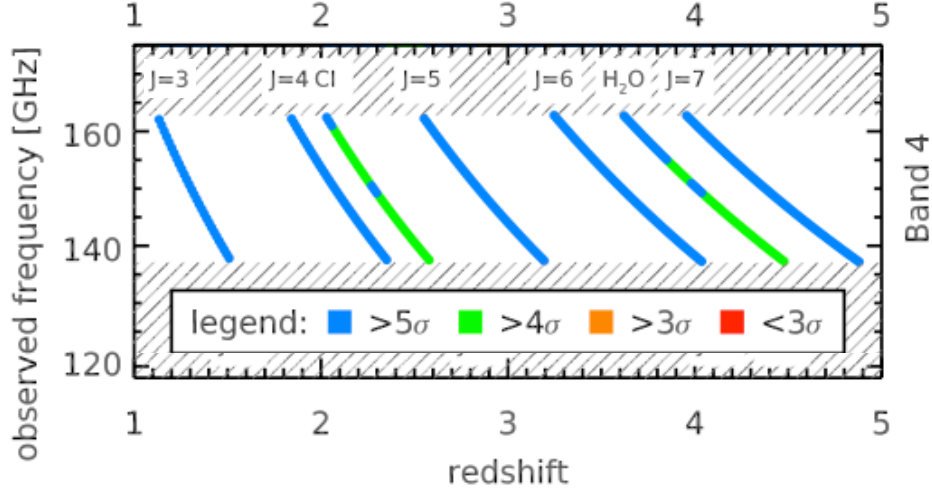


Figure 3: Position of CO transitions and CI lines as a function of  $z$  and observed frequency in band 4, used here for the spectral  $z$  search for the HST–dark galaxies.

1.1mm emission to extract the flux, reaching a  $S/N > 5$  for one line requires a  $400 \text{ km.s}^{-1}$ -averaged RMS of 0.20 mJy in band 4 for a time on source per pointing of less than 10 minutes for **a total of 10.01h including calibration and overheads** for the full proposal. The expected SNRs as a function of redshift are reported in Fig.3. Recent claims have suggested that  $z \sim 4$  galaxies become hard to detect in CO due to their reduced metal content (e.g. Tan et al. 2013). This is not an issue for our particular sample, because of the high attenuation which necessarily implies high metal abundances.

**References:** Bothwell+13 MNRAS 429, 3047 • Daddi+15, A&A 577, 46 • Dunlop+17, MNRAS 466, 861 • Elbaz+18, ArXiv e-prints • Franco+18, ArXiv e-prints • Fujimoto+16, ApJS 222, 1 • Guo+13, ApJS 207, 24 • Grogin+11, ApJS 197, 35 • Rujopakarn+16, ApJ 833, 12 • Schreiber, Elbaz+18, A&A 609, 30 • Skelton+15, ApJS 2414, 24 • Straatman+16, ApJ 830, 51 • Tan+13, ApJ 776, 24 • Wang, Elbaz+16, ApJ 816, 84

2018.1.01079.S

SG : 1 of 1      Dark-HST band 4      Band 4

This science goal contains the scan in band 4, with 4 tunings aligned to the highest frequency observable in the band.

Science Goal Parameters

Ang.Res.	LAS	Requested RMS	RMS Bandwidth	Rep.Freq.	Cont. RMS	Cont. Bandwidth	Poin.Prod.	Non-standard mode
0.8000"	1.0"	200 μJy, 17 mK	399.745 km/s, 200 MHz	149.992000 GHz	17.455 μJy, 1.5 mK	25.797 GHz	XX,YY	Yes

Use of 12m Array (43 antennas)

t_total(all configs)	t_science(C43-3)	t_total()	Imaged area	#12m pointing	12m Mosaic spacing	HPBW	t_per_point	Data Vol	Avg. Data Rate
10.0 h	3.8 h	0.0 h	12.9 "	6	offset	38.8 "	580.0 s	73.6 GB	2.5 MB/s

Use of ACA 7m Array (10 antennas) and TP Array

t_total(ACA)	t_total(7m)	t_total(TP)	Imaged area	#7m pointing	7m Mosaic spacing	HPBW	t_per_point	Data Vol	Avg. Data Rate

Spectral Scan Setup

Start Frequency	END Frequency	Bandwidth	Resolution	Vel. Bandwidth	Vel. Resolution	Res. El. per FWHM	RMS
137.100 GHz	162.800 GHz	1.875 GHz	7.813 MHz	3748 km/s	15.615 km/s	25.6	198.24 μJy, 16.8 mK

6 Targets

No.	Target	Ra,Dec ( ICRS )	V,def.frame --OR--z
1	1-GS8	03:32:46, -27:51:20	929356.62 km/s,lsrk,OPTICAL
2	2-AGS11	03:32:26, -27:52:08	1049273.60 km/s,lsrk,OPTICAL
3	3-AGS4	03:32:34, -27:49:40	629564.16 km/s,lsrk,OPTICAL
4	4-AGS15	03:32:17, -27:52:33	899377.37 km/s,lsrk,OPTICAL
5	5-AGS17	03:32:19, -27:52:14	224844.34 km/s,lsrk,RADIO
6	6-AGS24	03:32:20, -27:50:24	224844.34 km/s,lsrk,RADIO

Expected Source Properties

	Peak Flux	SNR	Linewidth	RMS (over 1/3 linewidth)	linewidth / bandwidth used for sensitivity	Pol.	Pol. SNR
Line	1.10 mJy	3.2	400 km/s	343.25 μJy, 29.1 ...	1.00	80.0%	2.6
Continuum	120.00 uJy	6.9				50.0%	3.4

Dynamic range (cont flux/line rms): 0.6

Spectral scan tunings (frequencies on Sky)

Tuning	Spw1(GHz)	Spw2(GHz)	Spw3(GHz)	Spw4(GHz)
1	138.030625	139.733750	150.030625	151.733750
2	141.436875	143.140000	153.436875	155.140000
3	144.843125	146.546250	156.843125	158.546250
4	148.249375	149.952500	160.249375	161.952500

## CHAPTER 13

PUBLISHED PAPER



# GOODS-ALMA: 1.1 mm galaxy survey

## I. Source catalog and optically dark galaxies

M. Franco<sup>1</sup>, D. Elbaz<sup>1</sup>, M. Béthermin<sup>2</sup>, B. Magnelli<sup>3</sup>, C. Schreiber<sup>4</sup>, L. Ciesla<sup>1,2</sup>, M. Dickinson<sup>5</sup>, N. Nagar<sup>6</sup>, J. Silverman<sup>7</sup>, E. Daddi<sup>1</sup>, D. M. Alexander<sup>8</sup>, T. Wang<sup>1,9</sup>, M. Pannella<sup>10</sup>, E. Le Floch<sup>1</sup>, A. Pope<sup>11</sup>, M. Giavalisco<sup>11</sup>, A. J. Maury<sup>1,12</sup>, F. Bournaud<sup>1</sup>, R. Chary<sup>13</sup>, R. Demarco<sup>6</sup>, H. Ferguson<sup>14</sup>, S. L. Finkelstein<sup>15</sup>, H. Inami<sup>16</sup>, D. Iono<sup>17,18</sup>, S. Juneau<sup>1,5</sup>, G. Lagache<sup>2</sup>, R. Leiton<sup>19,6,1</sup>, L. Lin<sup>20</sup>, G. Magdis<sup>21,22</sup>, H. Messias<sup>23,24</sup>, K. Motohara<sup>25</sup>, J. Mullaney<sup>26</sup>, K. Okumura<sup>1</sup>, C. Papovich<sup>27,28</sup>, J. Pforr<sup>2,29</sup>, W. Rujopakarn<sup>30,31,32</sup>, M. Sargent<sup>33</sup>, X. Shu<sup>34</sup>, and L. Zhou<sup>1,35</sup>

(Affiliations can be found after the references)

Received 1 March 2018 / Accepted 30 July 2018

### ABSTRACT

**Aims.** We present a 69 arcmin<sup>2</sup> ALMA survey at 1.1 mm, GOODS-ALMA, matching the deepest HST-WFC3 *H*-band part of the GOODS-South field.

**Methods.** We tapered the 0''24 original image with a homogeneous and circular synthesized beam of 0''60 to reduce the number of independent beams – thus reducing the number of purely statistical spurious detections – and optimize the sensitivity to point sources. We extracted a catalog of galaxies purely selected by ALMA and identified sources with and without HST counterparts down to a 5 $\sigma$  limiting depth of  $H = 28.2$  AB (HST/WFC3 F160W).

**Results.** ALMA detects 20 sources brighter than 0.7 mJy at 1.1 mm in the 0''60 tapered mosaic (rms sensitivity  $\sigma \simeq 0.18$  mJy beam<sup>-1</sup>) with a purity greater than 80%. Among these detections, we identify three sources with no HST nor *Spitzer*-IRAC counterpart, consistent with the expected number of spurious galaxies from the analysis of the inverted image; their definitive status will require additional investigation. We detect additional three sources with HST counterparts either at high significance in the higher resolution map, or with different detection-algorithm parameters ensuring a purity greater than 80%. Hence we identify in total 20 robust detections.

**Conclusions.** Our wide contiguous survey allows us to push further in redshift the blind detection of massive galaxies with ALMA with a median redshift of  $z = 2.92$  and a median stellar mass of  $M_{\star} = 1.1 \times 10^{11} M_{\odot}$ . Our sample includes 20% HST-dark galaxies (4 out of 20), all detected in the mid-infrared with *Spitzer*-IRAC. The near-infrared based photometric redshifts of two of them ( $z \sim 4.3$  and  $4.8$ ) suggest that these sources have redshifts  $z > 4$ . At least 40% of the ALMA sources host an X-ray AGN, compared to  $\sim 14\%$  for other galaxies of similar mass and redshift. The wide area of our ALMA survey provides lower values at the bright end of number counts than single-dish telescopes affected by confusion.

**Key words.** galaxies: high-redshift – galaxies: evolution – galaxies: star formation – galaxies: active – galaxies: photometry – submillimeter: galaxies

## 1. Introduction

In the late 1990s a population of galaxies was discovered at submillimeter wavelengths using the Submillimeter Common-User Bolometer Array (SCUBA; Holland et al. 1999) on the *James Clerk Maxwell* Telescope (see e.g., Smail et al. 1997; Hughes et al. 1998; Barger et al. 1998; Blain et al. 2002). These “submillimeter galaxies” or SMGs are highly obscured by dust, typically located around  $z \sim 2$ – $2.5$  (e.g., Chapman et al. 2003; Wardlow et al. 2011; Yun et al. 2012), massive ( $M_{\star} > 7 \times 10^{10} M_{\odot}$ ; e.g., Chapman et al. 2005; Hainline et al. 2011; Simpson et al. 2014), gas-rich ( $f_{\text{gas}} > 50\%$ ; e.g., Daddi et al. 2010), with huge star formation rates (SFR) – often greater than  $100 M_{\odot} \text{ yr}^{-1}$  (e.g., Magnelli et al. 2012; Swinbank et al. 2014) – making them significant contributors to the cosmic star formation (e.g., Casey et al. 2013), often driven by mergers (e.g., Tacconi et al. 2008; Narayanan et al. 2010) and often host an active galactic nucleus (AGN; e.g., Alexander et al. 2008; Pope et al. 2008; Wang et al. 2013). These SMGs are plausible progenitors of present-day massive early-type galaxies (e.g., Cimatti et al. 2008; Michałowski et al. 2010).

Recently, thanks to the advent of the Atacama Large Millimeter/submillimeter Array (ALMA) and its capabilities to

perform both high-resolution and high-sensitivity observations, our view of SMGs has become increasingly refined. The high angular resolution compared to single-dish observations reduces drastically the uncertainties of source confusion and blending, and affords new opportunities for robust galaxy identification and flux measurement. The ALMA sensitivity allows for the detection of sources down to 0.1 mJy (e.g., Carniani et al. 2015), the analysis of populations of dust-poor high- $z$  galaxies (Fujimoto et al. 2016) or main sequence (MS; Noeske et al. 2007; Rodighiero et al. 2011; Elbaz et al. 2011) galaxies (e.g., Papovich et al. 2016; Dunlop et al. 2017; Schreiber et al. 2017), and also demonstrates that the extragalactic background light (EBL) can be resolved partially or totally by faint galaxies ( $S < 1$  mJy; e.g., Hatsukade et al. 2013; Ono et al. 2014; Carniani et al. 2015; Fujimoto et al. 2016). Thanks to this new domain of sensitivity, ALMA is able to unveil less extreme objects, bridging the gap between massive starbursts and more normal galaxies: SMGs no longer stand apart from the general galaxy population.

However, many previous ALMA studies have been based on biased samples, with prior selection (pointing) or a posteriori selection (e.g., based on HST detections) of galaxies, or in a relatively limited region. In this study, we present an

unbiased view of a large (69 arcmin<sup>2</sup>) region of the sky, without prior or a posteriori selection based on already known galaxies, in order to improve our understanding of dust-obscured star formation and investigate the main properties of these objects. We take advantage of one of the most uncertain and potentially transformational outputs of ALMA – its ability to reveal a new class of galaxies through serendipitous detections. This is one of the main reasons for performing blind extragalactic surveys.

Thanks to the availability of very deep, panchromatic photometry at rest-frame UV, optical and NIR in legacy fields such as great observatories origins deep survey-South (GOODS-South), which also includes among the deepest available X-ray and radio maps, precise multiwavelength analysis that include the crucial FIR region is now possible with ALMA. In particular, a population of high redshift ( $2 < z < 4$ ) galaxies, too faint to be detected in the deepest HST-WFC3 images of the GOODS-South field has been revealed, thanks to the thermal dust emission seen by ALMA. Sources without an HST counterpart in the *H*-band, the reddest available (so-called HST-dark) have been previously found by color selection (e.g., Huang et al. 2011; Caputi et al. 2012, 2015; Wang et al. 2016), by serendipitous detection of line emitters (e.g., Ono et al. 2014) or in the continuum (e.g., Fujimoto et al. 2016). We will show that ~20% of the sources detected in the survey described in this paper are HST-dark, and strong evidence suggests that they are not spurious detections.

The aim of the work presented in this paper is to exploit a 69 arcmin<sup>2</sup> ALMA image reaching a sensitivity of 0.18 mJy at a resolution of 0''60. We used the leverage of the excellent multiwavelength supporting data in the GOODS-South field: the cosmic assembly near-infrared deep extragalactic legacy survey (Koekemoer et al. 2011; Grogin et al. 2011), the *Spitzer* extended deep survey (Ashby et al. 2013), the GOODS-*Herschel* survey (Elbaz et al. 2011), the *Chandra* deep field-South (Luo et al. 2017) and ultra-deep radio imaging with the VLA (Rujopakarn et al. 2016), to construct a robust catalog and derive physical properties of ALMA-detected galaxies. The region covered by ALMA in this survey corresponds to the region with the deepest HST-WFC3 coverage, and has also been chosen for a guaranteed time observation (GTO) program with the *James Webb* Space Telescope (JWST).

This paper is organized as follows: in Sect. 2 we describe our ALMA survey, the data reduction, and the multiwavelength ancillary data which support our studies. In Sect. 3, we present the methodology and criteria used to detect sources, we also present the procedures used to compute the completeness and the fidelity of our flux measurements. In Sect. 4 we detail the different steps we conducted to construct a catalog of our detections. In Sect. 5 we estimate the differential and cumulative number counts from our detections. We compare these counts with other (sub)millimeter studies. In Sect. 6 we investigate some properties of our galaxies such as redshift and mass distributions. Other properties will be analyzed in Franco et al. (in prep.) and finally in Sect. 8, we summarize the main results of this study. Throughout this paper, we adopt a spatially flat  $\Lambda$ CDM cosmological model with  $H_0 = 70 \text{ km s}^{-1} \text{ Mpc}^{-1}$ ,  $\Omega_m = 0.7$  and  $\Omega_\Lambda = 0.3$ . We assume a Salpeter (Salpeter 1955) initial mass function (IMF). We used the conversion factor of  $M_\star$  (Salpeter 1955, IMF) =  $1.7 \times M_\star$  (Chabrier 2003, IMF). All magnitudes are quoted in the AB system (Oke & Gunn 1983).

## 2. ALMA GOODS-South survey data

### 2.1. Survey description

Our ALMA coverage extends over an effective area of 69 arcmin<sup>2</sup> within the GOODS-South field (Fig. 1), centered at  $\alpha = 3^{\text{h}}32^{\text{m}}30.0^{\text{s}}$ ,  $\delta = -27^\circ48'00''$  (J2000; 2015.1.00543.S; PI: D. Elbaz). To cover this  $\sim 10' \times 7'$  region (comoving scale of 15.1 Mpc  $\times$  10.5 Mpc at  $z = 2$ ), we designed a 846-pointing mosaic, each pointing being separated by 0.8 times the antenna half power beam width (HPBW  $\sim 23''3$ ).

To accommodate such a large number of pointings within the ALMA Cycle 3 observing mode restrictions, we divided this mosaic into six parallel, slightly overlapping, submosaics of 141 pointing each. To get a homogeneous pattern over the 846 pointings, we computed the offsets between the submosaics so that they connected with each other without breaking the hexagonal pattern of the ALMA mosaics.

Each submosaic (or slice) had a length of 6.8 arcmin, a width of 1.5 arcmin and an inclination (PA) of 70 deg (see Fig. 1). This required three execution blocks (EBs), yielding a total on-source integration time of  $\sim 60$  s per pointing (Table 1). We determined that the highest frequencies of the band 6 were the optimal setup for a continuum survey and we thus set the ALMA correlator to Time Division Multiplexing (TDM) mode and optimized the setup for continuum detection at 264.9 GHz ( $\lambda = 1.13$  mm) using four 1875 MHz-wide spectral windows centered at 255.9 GHz, 257.9 GHz, 271.9 GHz and 273.9 GHz, covering a total bandwidth of 7.5 GHz. The TDM mode has 128 channels per spectral window, providing us with  $\sim 37 \text{ km s}^{-1}$  velocity channels.

Observations were taken between the 1st of August and the 2nd of September 2016, using  $\sim 40$  antennae (see Table 1) in configuration C40-5 with a maximum baseline of  $\sim 1500$  m. J0334–4008 and J0348–2749 (VLBA calibrator and hence has a highly precise position) were systematically used as flux and phase calibrators, respectively. In 14 EBs, J0522–3627 was used as bandpass calibrator, while in the remaining 4 EBs J0238+1636 was used. Observations were taken under nominal weather conditions with a typical precipitable water vapor of  $\sim 1$  mm.

### 2.2. Data reduction

All EBs were calibrated with CASA (McMullin et al. 2007) using the scripts provided by the ALMA project. Calibrated visibilities were systematically inspected and few additional flaggings were added to the original calibration scripts. Flux calibrations were validated by verifying the accuracy of our phase and bandpass calibrator flux density estimations. Finally, to reduce computational time for the forthcoming continuum imaging, we time- and frequency-averaged our calibrated EBs over 120 s and 8 channels, respectively.

Imaging was done in CASA using the multifrequency synthesis algorithm implemented within the task CLEAN. Submosaics were produced separately and combined subsequently using a weighted mean based on their noise maps. As each submosaic was observed at different epochs and under different weather conditions, they exhibit different synthesized beams and sensitivities (Table 1). Submosaics were produced and primary beam corrected separately, to finally be combined using a weighted mean based on their noise maps. To obtain a relatively homogeneous and circular synthesized beam across our final mosaic, we applied different  $u, v$  tapers to each submosaic. The best balance between spatial resolution and sensitivity was found with a homogeneous and circular synthesized beam of 0''29 full

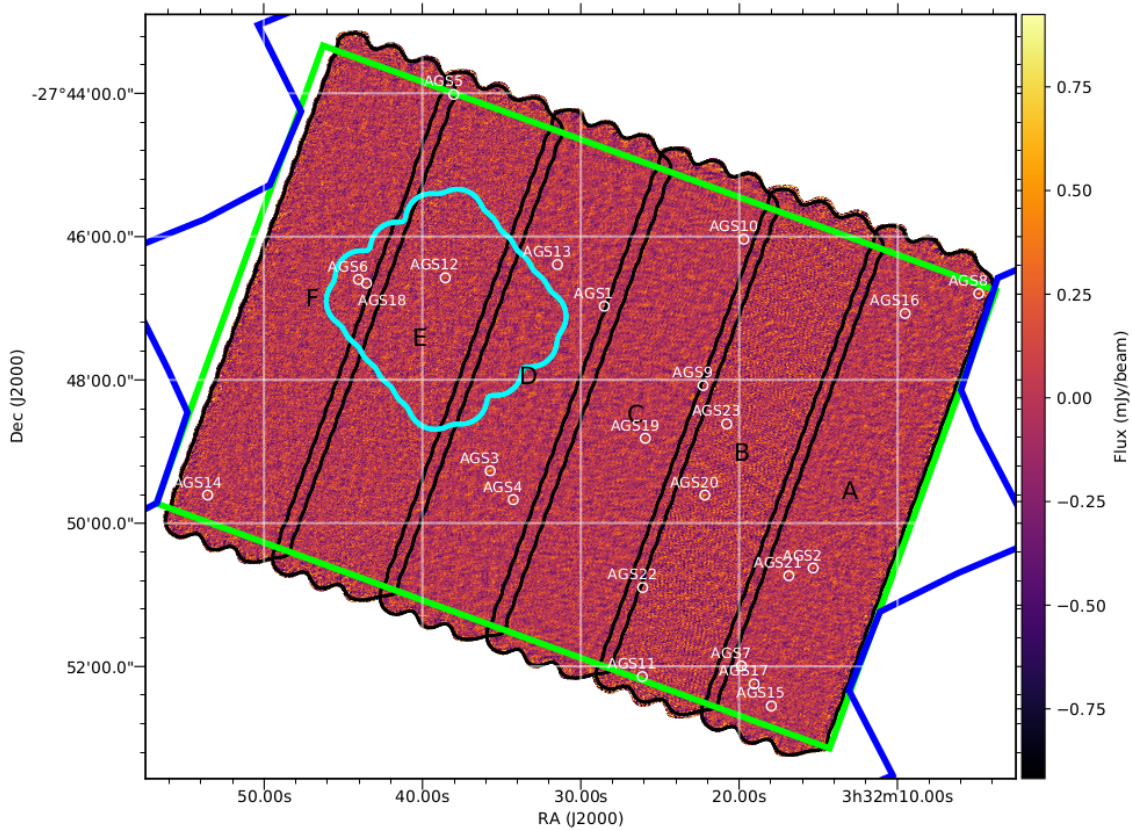


**Fig. 1.** ALMA 1.1 mm image tapered at  $0''.60$ . The white circles have a diameter of 4 arcseconds and indicate the positions of the galaxies listed in Table 3. Black contours show the different slices (labeled A–F) used to compose the homogeneous 1.1 mm coverage, with a median rms-noise of 0.18 mJy per beam. Blue lines show the limits of the HST/ACS field and green lines indicate the HST-WFC3 deep region. The cyan contour represents the limit of the Dunlop et al. (2017) survey covering all the *Hubble* Ultra Deep Field region. All of the ALMA-survey field is encompassed by the *Chandra* deep field-South.

width half maximum (FWHM; hereafter  $0''.29$ -mosaic; Table 1). This resolution corresponds to the highest resolution for which a circular beam can be synthesized for the full mosaic. We also applied this tapering method to create a second mosaic with a homogeneous and circular synthesized beam of  $0''.60$  FWHM (hereafter  $0''.60$ -mosaic; Table 1), in other words, optimized for the detection of extended sources. Mosaics with even coarser spatial resolution could not be created because of drastic sensitivity and synthesized beam shape degradations.

Due to the good coverage in the  $uv$ -plane (see Fig. 2) and the absence of very bright sources (the sources present in our image do not cover a large dynamic range in flux densities; see Sect. 4), we decided to work with the dirty map. This prevents introducing potential biases during the CLEAN process and we noticed that the noise in the clean map is not significantly different ( $<1\%$ ).

### 2.3. Building of the noise map

We built the rms-map of the ALMA survey by a  $k\text{-}\sigma$  clipping method. In steps of four pixels on the image map, the standard deviation was computed in a square of  $100 \times 100$  pixels around the central pixel. The pixels, inside this box, with values greater than three times the standard deviation ( $\sigma$ ) from the median value were masked. This procedure was repeated three times. Finally, we assigned the value of the standard deviation

of the non-masked pixels to the central pixel. This box size corresponds to the smallest size for which the value of the median pixel of the rms map converges to the typical value of the noise in the ALMA map while taking into account the local variation of noise. The step of four pixels corresponds to a subsampling of the beam so, the noise should not vary significantly on this scale. The median value of the standard deviation is  $0.176 \text{ mJy beam}^{-1}$ . In comparison, the Gaussian fit of the unclipped map gave a standard deviation of  $0.182 \text{ mJy beam}^{-1}$ . We adopted a general value of rms sensitivity  $\sigma = 0.18 \text{ mJy beam}^{-1}$ . The average values for the  $0''.29$ -mosaic and the untapered mosaic are given in Table 1.

### 2.4. Ancillary data

The area covered by this survey is ideally located, in that it profits from ancillary data from some of the deepest sky surveys at infrared (IR), optical and X-ray wavelengths. In this section, we describe all of the data that were used in the analysis of the ALMA detected sources in this paper.

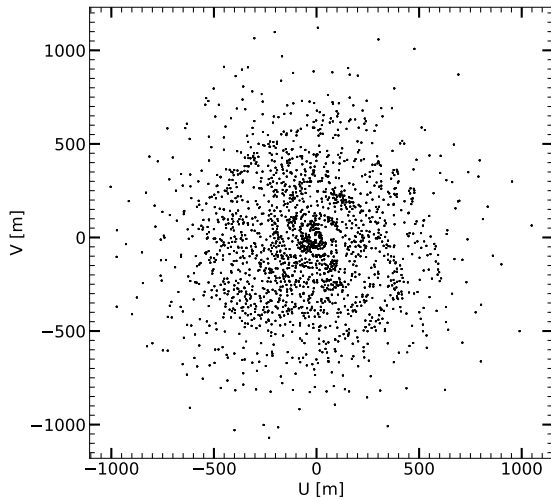
#### 2.4.1. Optical and near-infrared imaging

We have supporting data from the Cosmic Assembly Near-IR Deep Extragalactic Legacy Survey (CANDELS; Grogin et al. 2011) with images obtained with the wide field camera



**Table 1.** Summary of the observations.

Slice	Date	#	$t$ on target min	Total $t$ min	Original Mosaic		0''29-Mosaic		0''60-Mosaic	
					Beam mas $\times$ mas	$\sigma$ $\mu$ Jy beam $^{-1}$	Beam mas $\times$ mas	$\sigma$ $\mu$ Jy beam $^{-1}$	Beam mas $\times$ mas	$\sigma$ $\mu$ Jy beam $^{-1}$
A	August 17	42	46.52	72.12	240 $\times$ 200	98	297 $\times$ 281	108	618 $\times$ 583	171
	August 31	39	50.36	86.76						
	August 31	39	46.61	72.54						
B	September 1	38	46.87	72.08	206 $\times$ 184	113	296 $\times$ 285	134	614 $\times$ 591	224
	September 1	38	48.16	72.48						
	September 2	39	46.66	75.06						
C	August 16	37	46.54	73.94	243 $\times$ 231	102	295 $\times$ 288	107	608 $\times$ 593	166
	August 16	37	46.54	71.58						
	August 27	42	46.52	74.19						
D	August 16	37	46.54	71.69	257 $\times$ 231	107	292 $\times$ 289	111	612 $\times$ 582	164
	August 27	44	46.52	72.00						
	August 27	44	46.52	72.08						
E	August 01	39	46.54	71.84	285 $\times$ 259	123	292 $\times$ 286	124	619 $\times$ 588	186
	August 01	39	46.53	72.20						
	7 August 02	40	46.53	74.46						
F	August 02	40	46.53	72.04	293 $\times$ 256	118	292 $\times$ 284	120	613 $\times$ 582	178
	August 02	41	46.53	71.61						
	August 02	39	46.53	71.55						
Mean		40	46.86	73.35	254 $\times$ 227	110	294 $\times$ 286	117	614 $\times$ 587	182
Total		843.55	1320.22							

**Notes.** The slice ID, the date, the number of antennae, the time on target, the total time (time on target + calibration time), the resolution and the 1- $\sigma$  noise of the slice are given.**Fig. 2.**  $uv$ -coverage of one of the 846 ALMA pointings constituting this survey. This  $uv$ -coverage allows us to perform the source detection in the dirty map.

3/Infrared Channel (WFC3/IR) and UVIS channel, along with the advanced camera for surveys (ACS; Koekemoer et al. 2011). The area covered by this survey lies in the deep region of the CANDELS program (central one-third of the field). The 5- $\sigma$  detection depth for a point-source reaches a magnitude of 28.16 for the  $H_{160}$  filter (measured within a fixed aperture of 0.17'' Guo et al. 2013). The CANDELS/Deep program also provides images in seven other bands: the  $Y_{125}$ ,  $J_{125}$ ,  $B_{435}$ ,  $V_{606}$ ,  $i_{775}$ ,  $i_{814}$  and  $z_{850}$  filters, reaching 5- $\sigma$  detection depths of 28.45, 28.35, 28.95, 29.35, 28.55, 28.84, and 28.77 mag respectively. The Guo et al. (2013) catalog also includes galaxy magnitudes

from the VLT, taken in the  $U$ -band with VIMOS (Nonino et al. 2009), and in the  $K_s$ -band with ISAAC (Retzlaff et al. 2010) and HAWK-I (Fontana et al. 2014).

In addition, we used data coming from the FourStar galaxy evolution survey (ZFOURGE, PI: I. Labbé) on the 6.5 m Magellan Baade telescope. The FourStar instrument (Persson et al. 2013) observed the CDFS (encompassing the GOODS-South field) through five near-IR medium-bandwidth filters ( $J_1$ ,  $J_2$ ,  $J_3$ ,  $H_s$ ,  $H_l$ ) as well as broad-band  $K_s$ . By combination of the FourStar observations in the  $K_s$ -band and previous deep and ultra-deep surveys in the  $K$ -band, VLT/ISAAC/ $K$  (v2.0) from GOODS (Retzlaff et al. 2010), VLT/HAWK-I/ $K$  from HUGS (Fontana et al. 2014), CFHST/WIRCAM/ $K$  from TENIS (Hsieh et al. 2012) and Magellan/PANIC/ $K$  in HUDF (PI: I. Labbé), a super-deep detection image has been produced. The ZFOURGE catalog reaches a completeness greater than 80% to  $K_s < 25.3$ –25.9 (Straatman et al. 2016).

We used the stellar masses and redshifts from the ZFOURGE catalog, except when spectroscopic redshifts were available. Stellar masses have been derived from Bruzual & Charlot (2003) models (Straatman et al. 2016) assuming exponentially declining star formation histories and a dust attenuation law as described by Calzetti et al. (2000).

#### 2.4.2. Mid/far-infrared imaging

Data in the mid and far-IR are provided by the infrared array camera (IRAC; Fazio et al. 2004) at 3.6, 4.5, 5.8, and 8  $\mu$ m, *Spitzer* multiband imaging photometer (MIPS; Rieke et al. 2004) at 24  $\mu$ m, *Herschel* photodetector array camera and spectrometer (PACS; Poglitsch et al. 2010) at 70, 100 and 160  $\mu$ m, and *Herschel* spectral and photometric imaging receiver (SPIRE; Griffin et al. 2010) at 250, 350, and 500  $\mu$ m.

The IRAC observations in the GOODS-South field were taken in February 2004 and August 2004 by the GOODS *Spitzer* legacy project (PI: M. Dickinson). These data have been



supplemented by the *Spitzer* extended deep survey (SEDS; PI: G. Fazio) at 3.6 and 4.5  $\mu\text{m}$  (Ashby et al. 2013) as well as the *Spitzer*-cosmic assembly near-infrared deep extragalactic survey (S-CANDELS; Ashby et al. 2015) and recently by the ultra-deep IRAC imaging at 3.6 and 4.5  $\mu\text{m}$  (Labbé et al. 2015).

The flux extraction and deblending in 24  $\mu\text{m}$  imaging have been provided by Magnelli et al. (2009) to reach a depth of  $S_{24} \sim 30 \mu\text{Jy}$ . *Herschel* images come from a 206.3 h GOODS-South observational program (Elbaz et al. 2011) and combined by Magnelli et al. (2013) with the PACS evolutionary probe (PEP) observations (Lutz et al. 2011). Because the SPIRE confusion limit is very high, we used the catalog of Wang et al. (in prep.), which is built with a state-of-the-art de-blending method using optimal prior sources positions from 24  $\mu\text{m}$  and *Herschel* PACS detections.

#### 2.4.3. Complementary ALMA data

As the GOODS-South field encompasses the *Hubble* Ultra Deep Field (HUDF), we took advantage of deep 1.3-mm ALMA data of the HUDF. The ALMA image of the full HUDF reaches a  $\sigma_{1.3\text{mm}} = 35 \mu\text{Jy}$  (Dunlop et al. 2017), over an area of 4.5  $\text{arcmin}^2$  that was observed using a 45-pointing mosaic at a tapered resolution of 0.7". These observations were taken in two separate periods from July to September 2014. In this region, 16 galaxies were detected by Dunlop et al. (2017), three of them with a high S/N ( $S/N > 14$ ), the other 13 with lower S/Ns ( $3.51 < S/N < 6.63$ ).

#### 2.4.4. Radio imaging

We also used radio imaging at 5 cm from the Karl G. Jansky Very Large Array (VLA). These data were observed during 2014 March–2015 September for a total of 177 h in the A, B, and C configurations (PI: W. Rujopakarn). The images have a  $0''.31 \times 0''.61$  synthesized beam and an rms noise at the pointing center of  $0.32 \mu\text{Jy beam}^{-1}$  (Rujopakarn et al. 2016). Here, 179 galaxies were detected with a significance greater than  $3\sigma$  over an area of 61  $\text{arcmin}^2$  around the HUDF field, with a rms sensitivity better than  $1 \mu\text{Jy beam}^{-1}$ . However, this radio survey does not cover the entire ALMA area presented in this paper.

#### 2.4.5. X-ray

The *Chandra* deep field-South (CDF-S) was observed for 7 Msec between 2014 June and 2016 March. These observations cover a total area of 484.2  $\text{arcmin}^2$ , offset by just 32" from the center of our survey, in three X-ray bands: 0.5–7.0 keV, 0.5–2.0 keV, and 2–7 keV (Luo et al. 2017). The average flux limits over the central region are  $1.9 \times 10^{-17}$ ,  $6.4 \times 10^{-18}$ , and  $2.7 \times 10^{-17} \text{ erg cm}^{-2} \text{ s}^{-1}$  respectively. This survey enhances the previous X-ray catalogs in this field, the 4 Msec *Chandra* exposure (Xue et al. 2011) and the 3 Msec *XMM-Newton* exposure (Ranalli et al. 2013). We will use this X-ray catalog to identify candidate X-ray active galactic nuclei (AGN) among our ALMA detections.

### 3. Source detection

The search for faint sources in high-resolution images with moderate source densities faces a major limitation. At the native resolution ( $0''.25 \times 0''.23$ ), the untapered ALMA mosaic encompasses almost four million independent beams, where the beam

area is  $A_{\text{beam}} = \pi \times FWHM^2 / (4 \ln(2))$ . It results that a search for sources above a detection threshold of  $4\sigma$  would include as many as 130 spurious sources assuming a Gaussian statistics. Identifying the real sources from such catalog is not possible. In order to increase the detection quality to a level that ensures a purity greater than 80% – in other words, the excess of sources in the original mosaic needs to be five times greater than the number of detections in the mosaic multiplied by  $(-1)$  – we have decided to use a tapered image and adapt the detection threshold accordingly.

By reducing the weight of the signal originating from the most peripheral ALMA antennae, the tapering reduces the angular resolution hence the number of independent beams at the expense of collected light. The lower angular resolution presents the advantage of optimizing the sensitivity to point sources – we recall that  $0''.24$  corresponds to a proper size of only 2 kpc at  $z \sim 1-3$  – and therefore will result in an enhancement of the signal-to-noise ratio (S/N) for the sources larger than the resolution.

We chose to taper the image with a homogeneous and circular synthesized beam of  $0''.60$  FWHM – corresponding to a proper size of 5 kpc at  $z \sim 1-3$  – having tested various kernels and finding that this beam was optimized for our mosaic, avoiding both a beam degradation and a too heavy loss of sensitivity. This tapering reduces by nearly an order of magnitude the number of spurious sources expected at a  $4\sigma$  level down to about 19 out of 600 000 independent beams. However, we will check in a second step whether we may have missed in the process some compact sources by also analyzing the  $0''.29$  tapered map.

We also excluded the edges of the mosaic, where the standard deviation is larger than  $0.30 \text{ mJy beam}^{-1}$  in the  $0''.60$ -mosaic. The effective area was thus reduced by 4.9% as compared to the full mosaic (69.46  $\text{arcmin}^2$  out of 72.83  $\text{arcmin}^2$ ).

To identify the galaxies present on the image, we used BLOBCAT (Hales et al. 2012). BLOBCAT is a source extraction software using a “flood fill” algorithm to detect and catalog blobs (see Hales et al. 2012). A blob is defined by two criteria:

- at least one pixel has to be above a threshold ( $\sigma_p$ )
- all the adjacent surrounding pixels must be above a floodclip threshold ( $\sigma_f$ )

where  $\sigma_p$  and  $\sigma_f$  are defined in number of  $\sigma$ , the local rms of the mosaic.

A first guess to determine the detection threshold  $\sigma_p$  is provided by the examination of the pixel distribution of the S/N-map. The S/N-map has been created by dividing the  $0''.60$  tapered map by the noise map. Figure 3 shows that the S/N-map follows an almost perfect Gaussian below  $S/N = 4.2$ . Above this threshold, a significant difference can be observed that is characteristic of the excess of positive signal expected in the presence of real sources in the image. However, this histogram alone cannot be used to estimate a number of sources because the pixels inside one beam are not independent of one another. Hence although the non-Gaussian behavior appears around  $S/N = 4.2$  we performed simulations to determine the optimal values of  $\sigma_p$  and  $\sigma_f$ .

We first conducted positive and negative – on the continuum map multiplied by  $(-1)$  – detection analysis for a range of  $\sigma_p$  and  $\sigma_f$  values ranging from  $\sigma_p = 4$  to 6 and  $\sigma_f = 2.5$  to 4 with intervals of 0.05 and imposing each time  $\sigma_p \geq \sigma_f$ . The difference between positive and negative detections for each pair of  $(\sigma_p, \sigma_f)$  values provides the expected number of real sources.

We then searched for the pair of threshold parameters to find the best compromise between (i) providing the maximum number of detections, and (ii) minimizing the number of spurious

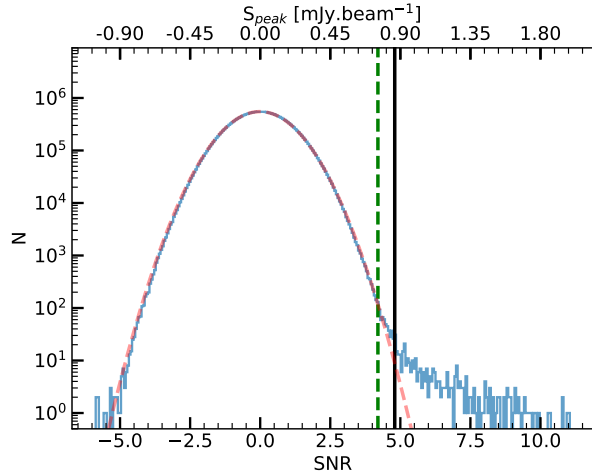


**Fig. 3.** Histogram of pixels of the S/N map, where pixels with noise  $>0.3 \text{ mJy beam}^{-1}$  have been removed. The red dashed line is the best Gaussian fit. The green dashed line is indicative and shows where the pixel brightness distribution moves away from the Gaussian fit. This is also the  $4.2\sigma$  level corresponding to a peak flux of  $0.76 \text{ mJy}$  for a typical noise per beam of  $0.18 \text{ mJy}$ . The solid black line corresponds to our peak threshold of  $4.8\sigma$  ( $0.86 \text{ mJy}$ ).

sources. The later purity criterion,  $p_c$ , is defined as:

$$p_c = \frac{N_p - N_n}{N_p} \quad (1)$$

where  $N_p$  and  $N_n$  are the numbers of positive and negative detections respectively. To ensure a purity of 80% as discussed above, we enforced  $p_c \geq 0.8$ . This led to  $\sigma_p = 4.8\sigma$  when fixing the value of  $\sigma_f = 2.7\sigma$  (see Fig. 4-left). Below  $\sigma_p = 4.8\sigma$ , the purity criterion rapidly drops below 80% whereas above this value it only mildly rises. Fixing  $\sigma_p = 4.8\sigma$ , the purity remains roughly constant at  $\sim 80 \pm 5\%$  when varying  $\sigma_f$ . We did see an increase in the difference between the number of positive and negative detections with increasing  $\sigma_f$ . However, the size of the sources above  $\sigma_f = 2.7\sigma$  drops below the  $0''.60$  FWHM and tends to become pixel-like, hence non physical. This is because an increase of  $\sigma_f$  results in a reduction of the number of pixels above the floodclip threshold ( $\sigma_f$ ) that will be associated with a given source. This parameter can be seen as a percolation criterion that sets the size of the sources in a number of pixels. Reversely reducing  $\sigma_f$  below  $2.7\sigma$  results in adding more noise than signal and a reduction in the number of detections. We therefore decided to set  $\sigma_f$  to  $2.7\sigma$ .

While we did not wish to impose a criterion on the existence of optical counterparts to define our ALMA catalog, we found that high values of  $\sigma_f$  not only generate the problem discussed above, but also generate a rapid drop of the fraction of ALMA detections with an HST counterpart in the Guo et al. (2013) catalog,  $p_{\text{HST}} = N_{\text{HST}}/N_p$ .  $N_{\text{HST}}$  is the number of ALMA sources with an HST counterpart within  $0''.60$  (corresponding to the size of the beam). The fraction falls rapidly from around  $\sim 80\%$  to  $\sim 60\%$ , which we interpreted as being due to a rise of the proportion of spurious sources, since the faintest optical sources, for example, detected by HST-WFC3, are not necessarily associated with the faintest ALMA sources due to the negative  $K$ -correction at  $1.1 \text{ mm}$ . This rapid drop can be seen in the dashed green and dotted pink lines of Fig. 4-right. This confirms that the sources that are added to our catalog with a floodclip threshold greater

than  $2.7\sigma$  are most probably spurious. Similarly, we can see in Fig. 4-left that increasing the number of ALMA detections to fainter flux densities by reducing  $\sigma_p$  below  $4.8\sigma$  leads to a rapid drop of the fraction of ALMA detections with an HST counterpart. Again there is no well-established physical reason to expect the number of ALMA detections with an optical counterpart to decrease with decreasing S/N ratio in the ALMA catalog.

As a result, we decided to set  $\sigma_p = 4.8\sigma$  and  $\sigma_f = 2.7\sigma$  to produce our catalog of ALMA detections. We note that we only discussed the existence of HST counterparts as a complementary test on the definition of the detection thresholds but our approach is not set to limit in any way our ALMA detections to galaxies with HST counterparts.

Indeed, evidence for the existence of ALMA detections with no HST-WFC3 counterparts already exist in the literature. Wang et al. (2016) identified  $H$ -dropouts galaxies, that is galaxies detected above the  $H$ -band with *Spitzer*-IRAC at  $4.5 \mu\text{m}$  but undetected in the  $H$ -band and in the optical. The median flux density of these galaxies is  $F_{870 \mu\text{m}} \approx 1.6 \text{ mJy}$  (Wang et al., in prep.). By scaling this median value to our wavelength of  $1.1 \text{ mm}$  (the details of this computation are given in Sect. 5.4), we obtain a flux density of  $0.9 \text{ mJy}$ , close to the typical flux of our detections (median flux  $\sim 1 \text{ mJy}$ , see Table 3).

## 4. Catalog

### 4.1. Creation of the catalog

Using the optimal parameters of  $\sigma_p = 4.8\sigma$  and  $\sigma_f = 2.7\sigma$  described in Sect. 3, we obtained a total of 20 detections down to a flux density limit of  $S_{1.1 \text{ mm}} \approx 880 \mu\text{Jy}$  that constitute our main catalog. These detections can be seen ranked by their S/N in Fig. 1. The comparison of negative and positive detections suggests the presence of  $4 \pm 2$  (assuming a Poissonian uncertainty on the difference between the number of positive and negative detections) spurious sources in this sample.

In the following, we assume that the galaxies detected in the  $0''.60$ -mosaic are point-like. This hypothesis will later be discussed and justified in Sect. 4.5. In order to check the robustness of our flux density measurements, we compared different flux extraction methods and softwares: PyBDSM (Mohan & Rafferty 2015); Galfit (Peng et al. 2010); Blobcat (Hales et al. 2012). The peak flux value determined by Blobcat refers to the peak of the surface brightness corrected for peak bias (see Hales et al. 2012). The different results were consistent, with a median ratio of  $F_{\text{peak}}^{\text{Blobcat}}/F_{\text{peak}}^{\text{PyBDSM}} = 1.04 \pm 0.20$  and  $F_{\text{peak}}^{\text{Blobcat}}/F_{\text{peak}}^{\text{Galfit}} = 0.93 \pm 0.20$ . The fluxes measured using psf-fitting (Galfit) and peak flux measurement (Blobcat) for each galaxy are listed in Table 3. We also ran CASA fitsky and a simple aperture photometry corrected for the ALMA PSF and also found consistent results. The psf-fitting with Galfit was performed inside a box of  $5 \times 5''$  centered on the source.

The main characteristics of these detections (redshift, flux, S/N, stellar mass, counterpart) are given in Table 3. We used redshifts and stellar masses from the ZFOURGE catalog (see Sect. 2.4.1).

We compared the presence of galaxies between the  $0''.60$ -mosaic and the  $0''.29$ -mosaic. Of the 20 detections found in the  $0''.60$  map, 14 of them are also detected in the  $0''.29$  map. The presence of a detection in both maps reinforces the plausibility of a detection. However, a detection in only one of these two maps may be a consequence of the intrinsic source size. An extended source is more likely to be detected with a larger beam, whereas

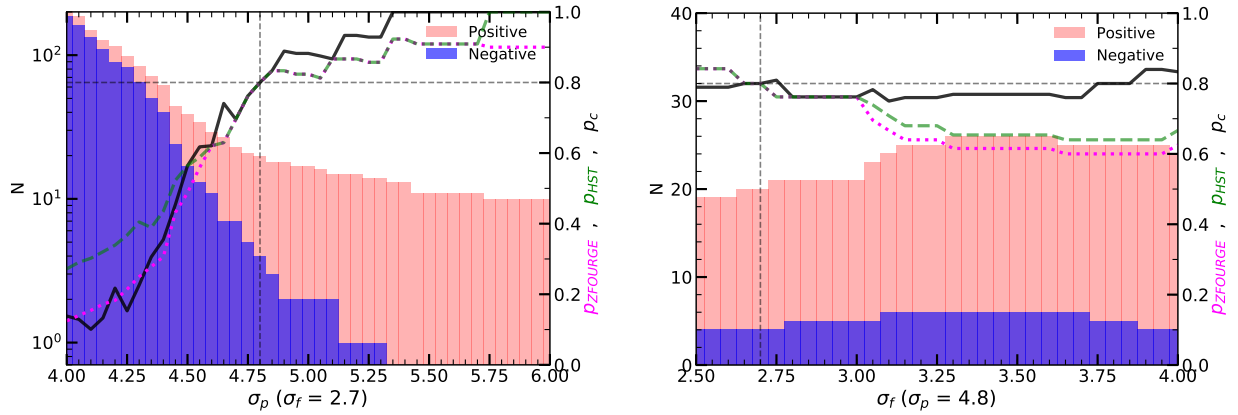


**Fig. 4.** Cumulative number of positive (red histogram) and negative (blue histogram) detections as a function of the  $\sigma_p$  (at a fixed  $\sigma_f$ , left panel) and  $\sigma_f$  (at a fixed  $\sigma_p$ , right panel) in units of  $\sigma$ . Solid black line represents the purity criterion  $p_c$  define by Eq. (1), green dashed-line represents the percentage of positive detection with HST-WFC3 counterpart  $p_{\text{HST}}$  and magenta dashed-line represents the percentage of positive detection with ZFOURGE counterpart  $p_{\text{ZFOURGE}}$ . Gray dashed-lines show the thresholds  $\sigma_p = 4.8\sigma$  and  $\sigma_f = 2.7\sigma$  and the 80% purity limit.

a more compact source is more likely to be missed in the maps with larger tapered sizes and reduced point source sensitivity.

A first method to identify potential false detections was to compare our results with a deeper survey overlapping with our area of the sky. We compared the positions of our catalog sources with the positions of sources found by Dunlop et al. (2017) in the HUDF. This 1.3-mm image is deeper than our survey and reaches a  $\sigma \approx 35 \mu\text{Jy}$  (corresponding to  $\sigma = 52 \mu\text{Jy}$  at 1.1 mm) but overlaps with only  $\sim 6.5\%$  of our survey area. The final sample of Dunlop et al. (2017) was compiled by selecting sources with  $S_{1.3} > 120 \mu\text{Jy}$  to avoid including spurious sources due to the large number of beams in the mosaics and due to their choice of including only ALMA detections with optical counterparts seen with HST.

With our flux density limit of  $S_{1.1\text{ mm}} \approx 880 \mu\text{Jy}$  any non-spurious detection should be associated with a source seen at 1.3 mm in the HUDF 1.3 mm survey, the impact of the wavelength difference being much smaller than this ratio. We detected three galaxies that were also detected by Dunlop et al. (2017), UDF1, UDF2 and UDF3, all of which have  $S_{1.3\text{ mm}} > 0.8 \text{ mJy}$ . The other galaxies detected by Dunlop et al. (2017) have a flux density at 1.3 mm lower than  $320 \mu\text{Jy}$ , which makes them undetectable with our sensitivity.

We note however that we did not impose as a strict criterion the existence of an optical counterpart to our detections, whereas Dunlop et al. (2017) did. Hence if we had detected a source with no optical counterpart within the HUDF, this source may not be included in the Dunlop et al. (2017) catalog. However, as we will see, the projected density of such sources is small and none of our candidate optically dark sources fall within the limited area of the HUDF. We also note that the presence of an HST-WFC3 source within a radius of  $0''.6$  does not necessarily imply that is the correct counterpart. As we will discuss in detail in Sect. 4.4, due to the depth of the HST-WFC3 observations and the large number of galaxies listed in the CANDELS catalog, a match between the HST and ALMA positions may be possible by chance alignment alone (see Sect. 4.4).

#### 4.2. Supplementary catalog

After the completion of the main catalog, three sources that did not satisfy the criteria of the main catalog presented strong

evidence of being robust detections. We therefore enlarged our catalog, in order to incorporate these sources into a supplementary catalog.

These three sources are each detected using a combination of  $\sigma_p$  and  $\sigma_f$  giving a purity factor greater than 80%, whilst also ensuring the existence of an HST counterpart.

The galaxy AGS21 has an  $S/N = 5.83$  in the  $0''.29$  tapered map, but is not detected in the  $0''.60$  tapered map. The non-detection of this source is most likely caused by its size. Due to its dilution in the  $0''.60$ -mosaic, a very compact galaxy detected at  $5\sigma$  in the  $0''.29$ -mosaic map could be below the detection limit in the  $0''.60$ -mosaic. The ratio of the mean rms of the two tapered maps is 1.56, meaning that for a point source of certain flux, a  $5.83\sigma$  measurement in the  $0''.29$ -mosaic becomes  $3.74\sigma$  in the  $0''.60$ -map.

The galaxy AGS22 has been detected with an  $S/N = 4.9$  in the  $0''.60$  tapered map ( $\sigma_p = 4.9$  and  $\sigma_f = 3.1$ ). With  $\sigma_p$  and  $\sigma_f$  values more stringent than the thresholds chosen for the main catalog, it may seem paradoxical that this source does not appear in the main catalog. With a floodclip criterion of  $2.7\sigma$ , this source would have an  $S/N$  just below 4.8, excluding it from the main catalog. This source is associated with a faint galaxy that has been detected by HST-WFC3 (ID<sub>CANDELS</sub> = 28952) at  $1.6 \mu\text{m}$  ( $6.6\sigma$ ) at a position close to the ALMA detection ( $0''.28$ ). Significant flux has also been measured at  $1.25 \mu\text{m}$  ( $3.6\sigma$ ) for this galaxy. In all of the other filters, the flux measurement is not significant ( $<3\sigma$ ). Due to this lack of information, it has not been possible to compute its redshift. AGS22 is not detected in the  $0''.29$ -mosaic map with  $p_c > 0.8$ . The optical counterpart of this source has a low  $H$ -band magnitude ( $26.8 \pm 0.2 \text{ AB}$ ), which corresponds to a range for which the Guo et al. (2013) catalog is no longer complete. This is the only galaxy (except the three galaxies most likely to be spurious: AGS14, AGS16 and AGS19) that has not been detected by IRAC (which could possibly be explained by a low stellar mass). The probability of the ALMA detection being spurious, within the association radius  $0''.6$  of a  $H$ -band source of this magnitude or brighter, is 5.5%. For these reasons, we did not consider it as spurious.

The galaxy AGS23 was detected in the  $0''.60$  map just below our threshold at  $4.8\sigma$ , with a combination  $\sigma_p = 4.6$  and  $\sigma_f = 2.9$  giving a purity criterion greater than 0.9. This detection is associated with an HST-WFC3 counterpart. It is

**Table 2.** Details of the positional differences between ALMA and HST-WFC3 for our catalog of galaxies identified in the 1.1 mm-continuum map.

ID	ID <sub>CLS</sub>	ID <sub>ZF</sub>	RA <sub>ALMA</sub> deg	Dec <sub>ALMA</sub> deg	RA <sub>HST</sub> deg	Dec <sub>HST</sub> deg	$\Delta_{\text{HST}_1}$ arcsec	$\Delta_{\text{HST}_2}$ arcsec	$(\Delta\alpha)_{\text{HST}}$ arcsec	$(\Delta\delta)_{\text{HST}}$ arcsec	$\Delta_{\text{IRAC}}$ arcsec
(1)	(2)	(3)	(4)	(5)	(6)	(7)	(8)	(9)	(10)	(11)	(12)
AGS1	14876	17856	53.118815	-27.782889	53.118790	-27.782818	0.27	0.03	0.091	-0.278	0.16
AGS2	7139	10316	53.063867	-27.843792	53.063831	-27.843655	0.51	0.23	0.163	-0.269	0.04
AGS3	9834	13086	53.148839	-27.821192	53.148827	-27.821121	0.26	0.06	0.099	-0.262	0.10
AGS4	8923b	12333	53.142778	-27.827888	53.142844	-27.827890	0.21	0.40	0.087	-0.264	0.09
AGS5	20765	23898	53.158392	-27.733607	53.158345	-27.733485	0.46	0.13	0.087	-0.329	0.26
AGS6	15669	–	53.183458	-27.776654	53.183449	-27.776584	0.26	0.03	0.054	-0.267	0.40
AGS7	4854	7867	53.082738	-27.866577	53.082705	-27.866567	0.11	0.19	0.124	-0.225	0.03
AGS8	15261	18282	53.020356	-27.779905	53.020297	-27.779829	0.33	0.03	0.159	-0.275	0.20
AGS9	12016	15639	53.092844	-27.801330	53.092807	-27.801208	0.45	0.16	0.100	-0.276	0.18
AGS10	16972	19833	53.082118	-27.767299	53.081957	-27.767202	0.62	0.39	0.128	-0.300	0.40
AGS11	–	7589	53.108818	-27.869055	–	–	–	–	–	–	0.12
AGS12	15876	18701	53.160634	-27.776273	53.160594	-27.776129	0.53	0.28	0.076	-0.242	0.51
AGS13	16274	19033	53.131122	-27.773194	53.131080	-27.773108	0.34	0.05	0.087	-0.291	0.14
AGS14	–	–	53.223156	-27.826771	–	–	–	–	–	–	–
AGS15	3818b	6755	53.074847	-27.875880	53.074755	-27.875976	0.45	0.57	0.125	-0.195	0.12 <sup>1</sup>
AGS16	–	–	53.039724	-27.784557	–	–	–	–	–	–	–
AGS17	4414b	6964	53.079374	-27.870770	53.079327	-27.870781	0.16	0.27	0.122	-0.231	0.06
AGS18	15639	18645	53.181355	-27.777544	53.181364	-27.777501	0.16	0.12	0.043	-0.256	0.10
AGS19	–	–	53.108041	-27.813610	–	–	–	–	–	–	–
AGS20	9089	12416	53.092365	-27.826829	53.092381	-27.826828	0.05	0.29	0.116	-0.247	0.18
AGS21	6905	10152	53.070274	-27.845586	53.070230	-27.845533	0.24	0.06	0.143	-0.249	0.07
AGS22	28952	–	53.108695	-27.848332	53.108576	-27.848242	0.50	0.29	0.106	-0.226	–
AGS23	10954	14543	53.086623	-27.810272	53.086532	-27.810217	0.35	0.19	0.111	-0.263	0.16

**Notes.** Columns: (1) Source ID; (2),(3) IDs of the HST-WFC3 (from the CANDELS catalog) and ZFOURGE counterparts of these detections (the cross correlations between ALMA and HST-WFC3 and between ALMA and ZFOURGE are discussed in Sect. 4.4). b indicates HST-WFC3 galaxies located in a radius of 0''6 around the ALMA detection, although strong evidence presented in Sect. 7 suggests they are not the optical counterparts of our detections; (4), (5) RA and Dec of the sources in the ALMA image (J2000); (6), (7) positions of HST-WFC3 *H*-band counterparts when applicable from Guo et al. (2013); (8), (9) distances between the ALMA and HST source positions before ( $\Delta_{\text{HST}_1}$ ) and after ( $\Delta_{\text{HST}_2}$ ) applying the offset correction derived from the comparison with Pan-STARRS and *Gaia*; (10), (11) offset to be applied to the HST source positions, which includes both the global systematic offset and the local offset; (12) distance from the closest IRAC galaxy. <sup>(1)</sup>For AGS15 we used the distance given in the ZFOURGE catalog (see Sect. 7).

for these two reasons that we include this galaxy in the supplementary catalog. The photometric redshift ( $z = 2.36$ ) and stellar mass ( $10^{11.26} M_{\odot}$ ) both reinforce the plausibility of this detection.

#### 4.3. Astrometric correction

The comparison of our ALMA detections with HST (Sect. 4.1) in the previous section was carried out after correcting for an astrometric offset, which we outline here. In order to perform the most rigorous counterpart identification and take advantage of the accuracy of ALMA, we carefully investigated the astrometry of our images. Before correction, the galaxy positions viewed by HST were systematically offset from the ALMA positions. This offset has already been identified in previous studies (e.g., Maiolino et al. 2015; Rujopakarn et al. 2016; Dunlop et al. 2017).

In order to quantify this effect, we compared the HST source positions with detections from the Panoramic Survey Telescope and Rapid Response System (Pan-STARRS). This survey has the double advantage to cover a large portion of the sky, notably the GOODS-South field, and to observe the sky at a wavelength similar to HST-WFC3. We used the Pan-STARRS DR1 catalog provided by Flewelling et al. (2016) and also included the

corresponding regions issued from the *Gaia* DR1 (Gaia Collaboration 2016).

Cross-matching was done within a radius of 0''5. In order to minimize the number of false identifications, we subtracted the median offset between the two catalogs from the Guo et al. (2013) catalog positions, after the first round of matching. We iterated this process three times. In this way, 629 pairs were found over the GOODS-South field.

To correct for the median offset between the HST and ALMA images, the HST image coordinates needed to be corrected by  $-96 \pm 113$  mas in right ascension,  $\alpha$ , and  $261 \pm 125$  mas in declination,  $\delta$ , where the uncertainties correspond to the standard deviation of the 629 offset measurements. This offset is consistent with that found by Rujopakarn et al. (2016) of  $\Delta\alpha = -80 \pm 110$  mas and  $\Delta\delta = 260 \pm 130$  mas. The latter offsets were calculated by comparing the HST source positions with 2MASS and VLA positions. In all cases, it is the HST image that presents an offset, whereas ALMA, Pan-STARRS, *Gaia*, 2MASS and VLA are all in agreement. We therefore deduced that it is the astrometric solution used to build the HST mosaic that introduced this offset. As discussed in Dickinson et al. (in prep.), the process of building the HST mosaic also introduced less significant local offsets, that can be considered equivalent to a distortion of the HST image. These local offsets are larger in



**Table 3.** Details of the final sample of sources detected in the ALMA GOODS-South continuum map, from the primary catalog in the main part of the table and from the supplementary catalog below the solid line (see Sects. 4.1 and 4.2).

ID	$z$	$S/N$	$S_{\text{peak}}^{\text{Blobcat}}$ mJy	$f_{\text{deboost}}$	$S_{\text{PSF}}^{\text{Galfit}}$ mJy	$\log_{10} M_{\star}$ $M_{\odot}$	0''60	0''29	$S_{6\text{GHz}}$ $\mu\text{Jy}$	$L_X/10^{42}$ $\text{erg s}^{-1}$	ID <sub>sub(mm)</sub>
(1)	(2)	(3)	(4)	(5)	(6)	(7)	(8)	(9)	(10)	(11)	(12)
AGS1	2.309	11.26	$1.90 \pm 0.20$	1.03	$1.99 \pm 0.15$	11.05	1	1	$18.38 \pm 0.71$	1.93	GS6, ASA1
AGS2	2.918	10.47	$1.99 \pm 0.22$	1.03	$2.13 \pm 0.15$	10.90	1	1	—	51.31	
AGS3	2.582	9.68	$1.84 \pm 0.21$	1.03	$2.19 \pm 0.15$	11.33	1	1	$19.84 \pm 0.93$	34.54	GS5, ASA2
AGS4	4.32	9.66	$1.72 \pm 0.20$	1.03	$1.69 \pm 0.18$	11.45	1	1	$8.64 \pm 0.77$	10.39	
AGS5	3.46	8.95	$1.56 \pm 0.19$	1.03	$1.40 \pm 0.18$	11.13	1	1	$14.32 \pm 1.05$	37.40	
AGS6	3.00	7.63	$1.27 \pm 0.18$	1.05	$1.26 \pm 0.16$	10.93	1	1	$9.02 \pm 0.57$	83.30	UDF1, ASA3
AGS7	3.29	7.26	$1.15 \pm 0.17$	1.05	$1.20 \pm 0.13$	11.43	1	1	—	24.00	
AGS8	1.95	7.10	$1.43 \pm 0.22$	1.05	$1.98 \pm 0.20$	11.53	1	1	—	3.46	LESS18
AGS9	3.847	6.19	$1.25 \pm 0.21$	1.05	$1.39 \pm 0.17$	10.70	1	1	$14.65 \pm 1.12$	—	
AGS10	2.41	6.10	$0.88 \pm 0.15$	1.06	$1.04 \pm 0.13$	11.32	1	1	—	2.80	
AGS11	4.82	5.71	$1.34 \pm 0.25$	1.08	$1.58 \pm 0.22$	10.55	1	1	—	—	
AGS12	2.543	5.42	$0.93 \pm 0.18$	1.10	$1.13 \pm 0.15$	10.72	1	1	$12.65 \pm 0.55$	4.53	UDF3, C1, ASA8
AGS13	2.225	5.41	$0.78 \pm 0.15$	1.10	$0.47 \pm 0.14$	11.40	1	0	$22.52 \pm 0.81$	13.88	ASA12
AGS14*	—	5.30	$0.86 \pm 0.17$	1.10	$1.17 \pm 0.15$	—	1	0	—	—	
AGS15	—	5.22	$0.80 \pm 0.16$	1.11	$0.64 \pm 0.15$	—	1	1	—	—	LESS34
AGS16*	—	5.05	$0.82 \pm 0.17$	1.12	$0.99 \pm 0.17$	—	1	0	—	—	
AGS17	—	5.01	$0.93 \pm 0.19^{\dagger}$	1.14	$1.37 \pm 0.18$	—	1	0	—	—	LESS10
AGS18	2.794	4.93	$0.85 \pm 0.18^{\dagger}$	1.15	$0.79 \pm 0.15$	11.01	1	0	$6.21 \pm 0.57$	—	UDF2, ASA6
AGS19*	—	4.83	$0.69 \pm 0.15$	1.16	$0.72 \pm 0.13$	—	1	0	—	—	
AGS20	2.73	4.81	$1.11 \pm 0.24$	1.16	$1.18 \pm 0.23$	10.76	1	1	$12.79 \pm 1.40$	4.02	
AGS21	3.76	5.83	$0.64 \pm 0.11$	1.07	$0.88 \pm 0.19$	10.63	0	1	—	19.68	
AGS22	—	4.90	$1.05 \pm 0.22$	1.15	$1.26 \pm 0.22$	—	1	0	—	—	
AGS23	2.36	4.68	$0.98 \pm 0.21$	1.19	$1.05 \pm 0.20$	11.26	1	0	—	—	

**Notes.** Columns: (1) IDs of the sources as shown in Fig. 1. The sources are sorted by S/N. \* indicates galaxies that are most likely spurious (not detected at any other wavelength); (2) redshifts from the ZFOURGE catalog. Spectroscopic redshifts are shown with three decimal places. As AGS6 is not listed in the ZFOURGE catalog, we used the redshift computed by Dunlop et al. (2017); (3) S/N of the detections in the 0''60 mosaic (except for AGS21). This S/N is computed using the flux from Blobcat and is corrected for peak bias; (4) peak fluxes measured using Blobcat in the 0''60-mosaic image before de-boosting correction; (5) deboosting factor; (6) fluxes measured by PSF-fitting with Galfit in the 0''60-mosaic image before de-boosting correction; (7) stellar masses from the ZFOURGE catalog; (8), (9) flags for detection by Blobcat in the 0''60-mosaic and 0''29-mosaic images, where at least one combination of  $\sigma_p$  and  $\sigma_f$  gives a purity factor (Eq. (1)) greater than 80%; (10) flux for detection greater than  $3\sigma$  by VLA (5 cm). Some of these sources are visible in the VLA image but not detected with a threshold  $>3\sigma$ . AGS8 and AGS16 are not in the field of the VLA survey; (11) absorption-corrected intrinsic 0.5–7.0 keV luminosities. The X-ray luminosities have been corrected to account for the redshift difference between the redshifts provided in the catalog of Luo et al. (2017) and those used in the present table, when necessary. For this correction we used Eq. (1) from Alexander et al. (2003), and assuming a photon index of  $\Gamma = 2$ ; (12) corresponding IDs for detections of the sources in previous (sub)millimeter ancillary data. UDF is for *Hubble* Ultra Deep Field survey (Dunlop et al. 2017) at 1.3 mm, C indicates the ALMA Spectroscopic Survey in the *Hubble* Ultra Deep Field (ASPECS) at 1.2 mm (Aravena et al. 2016), LESS indicates data at 870  $\mu\text{m}$  presented in Hodge et al. (2013), GS indicates data at 870  $\mu\text{m}$  presented in Elbaz et al. (2018), ASA indicates the ALMA 26 arcmin<sup>2</sup> Survey of GOODS-S at One-millimeter (ASAGAO). We also note the pointed observations of AGS1 presented in Barro et al. (2017), and those of AGS13 by Talia et al. (2018). For the two sources marked by a  $\dagger$ , the hypothesis of a point-like source is no longer valid. We therefore apply correction factors of 2.3 and 1.7 to the peak flux values of AGS17 and AGS18 respectively, to take into account the extended flux emission of these sources.

the periphery of GOODS-South than in the center, and close to zero in the HUDF field. The local offsets can be considered as a distortion effect. The offsets listed in Table 2 include both effects, the global and local offsets. The separation between HST and ALMA detections before and after offset correction, and the individual offsets applied for each of the galaxies are indicated in Table 2 and can be visualized in Fig. 5. We applied the same offset corrections to the galaxies listed in the ZFOURGE catalog.

This accurate subtraction of the global systematic offset, as well as the local offset, does not however guarantee a perfect overlap between ALMA and HST emission. The location of the

dust emission may not align perfectly with the starlight from a galaxy, due to the difference in ALMA and HST resolutions, as well as the physical offsets between dust and stellar emission that may exist. In Fig. 6, we show the ALMA contours (4–10 $\sigma$ ) overlaid on the F160W HST-WFC3 images after astrometric correction. In some cases (AGS1, AGS3, AGS6, AGS13, AGS21 for example), the position of the dust radiation matches that of the stellar emission; in other cases, (AGS4, AGS17 for example), a displacement appears between both two wavelengths. Finally, in some cases (AGS11, AGS14, AGS16, and AGS19) there are no optical counterparts. We will discuss the possible explanations for this in Sect. 7.

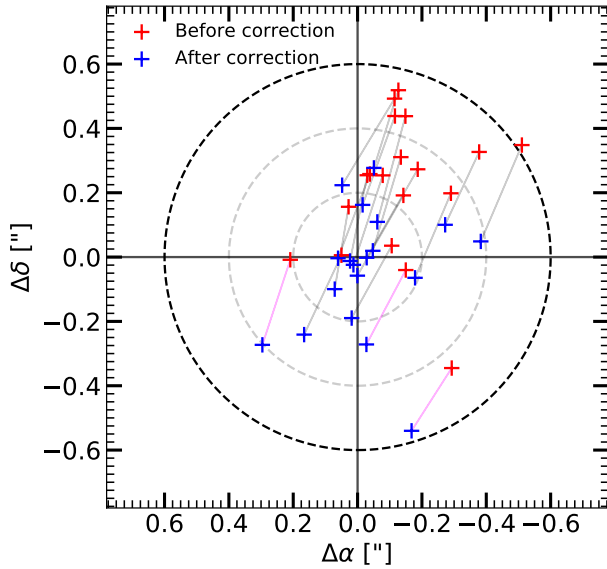


**Fig. 5.** Positional offset ( $\Delta\alpha_{\text{HST}} - \Delta\alpha_{\text{ALMA}}$ ,  $\Delta\delta_{\text{HST}} - \Delta\delta_{\text{ALMA}}$ ) between HST and ALMA before (red crosses) and after (blue crosses) the correction of both a global systematic offset and a local offset. The black dashed circle corresponds to the cross-matching limit radius of  $0''.6$ . The gray dashed circles show a positional offset of  $0''.2$  and  $0''.4$  respectively. The magenta lines indicate the HST galaxies previously falsely associated with ALMA detections.

#### 4.4. Identification of counterparts

We searched for optical counterparts in the CANDELS/GOODS-South catalog, within a radius of  $0''.6$  from the millimeter position after applying the astrometric corrections to the source positions described in Sect. 4.3. The radius of the cross-matching has been chosen to correspond to the synthesized beam ( $0''.60$ ) of the tapered ALMA map used for galaxy detection. Following Condon (1997), the maximal positional accuracy of the detection in the 1.1 mm map is given by  $\theta_{\text{beam}}/(2 \times S/N)$ . In the  $0''.60$ -mosaic, the positional accuracy therefore ranges between 26.5 mas and 62.5 mas for our range of S/N (4.8–11.3), corresponding to physical sizes between 200 and 480 pc at  $z = 3$ .

Despite the high angular resolution of ALMA, the chance of an ALMA-HST coincidence is not negligible, because of the large projected source density of the CANDELS/GOODS-South catalog. Figure 7 shows a Monte Carlo simulation performed to estimate this probability. We separate here the deeper *Hubble* Ultra Deep Field (blue histogram) from the rest of the CANDELS-deep area (orange histogram). We randomly defined a position within GOODS-South and then measured the distance to its closest HST neighbor using the source positions listed in Guo et al. (2013). We repeated this procedure 100 000 times inside and outside the HUDF. The probability for a position randomly selected in the GOODS-South field to fall within  $0.6$  arcsec of an HST source is 9.2% outside the HUDF, and 15.8% inside the HUDF. We repeated this exercise to test the presence of an IRAC counterpart with the Ashby et al. (2015) catalog (green histogram). The probability to randomly fall on an IRAC source is only 2.1%.

With the detection threshold determined in Sect. 3, 80% of the millimeter galaxies detected have an HST-WFC3 counterpart, and four galaxies remain without an optical counter-

part. We cross-matched our detections with the ZFOURGE catalog.

Figure 8 shows  $3''.5 \times 3''.5$  postage stamps of the ALMA-detected galaxies, overlaid with the positions of galaxies from the CANDELS/GOODS-South catalog (magenta double crosses), ZFOURGE catalog (white circles) or both catalogs (sources with an angular separation lower than  $0''.4$ , blue circles). These are all shown after astrometric correction. Based on the ZFOURGE catalog, we found optical counterparts for one galaxy that did not have an HST counterpart: AGS11, a photometric redshift has been computed in the ZFOURGE catalog for this galaxy.

The redshifts of AGS4 and AGS17 as given in the CANDELS catalog are unexpectedly low ( $z = 0.24$  and  $z = 0.03$ , respectively), but the redshifts for these galaxies given in the ZFOURGE catalog ( $z = 3.76$  and  $z = 1.85$ , respectively) are more compatible with the expected redshifts for galaxies detected with ALMA. These galaxies, missed by the HST or incorrectly listed as local galaxies are particularly interesting galaxies (see Sect. 7). AGS6 is not listed in the ZFOURGE catalog, most likely because it is close ( $<0''.7$ ) to another bright galaxy ( $\text{ID}_{\text{CANDELS}} = 15768$ ). These galaxies are blended in the ZFOURGE ground-based  $K_s$ -band images. AGS6 has previously been detected at 1.3 mm in the HUDF, so we adopt the redshift and stellar mass found by Dunlop et al. (2017). The consensus CANDELS zphot from Santini et al. (2015) is  $z = 3.06$  (95% confidence:  $2.92 < z < 3.40$ ), consistent with the value in Dunlop et al. (2017).

#### 4.5. Galaxy sizes

Correctly estimating the size of a source is an essential ingredient for measuring its flux. As a first step, it is imperative to know if the detections are resolved or unresolved. In this section, we discuss our considerations regarding the sizes of our galaxies. The low number of galaxies with measured ALMA sizes in the literature makes it difficult to constrain the size distribution of dust emission in galaxies. Recent studies (e.g., Barro et al. 2016; Rujopakarn et al. 2016; Elbaz et al. 2018; Ikarashi et al. 2017; Fujimoto et al. 2017) with sufficient resolution to measure ALMA sizes of galaxies suggest that dust emission takes place within compact regions of the galaxy.

Two of our galaxies (AGS1 and AGS3) have been observed in individual pointings (ALMA Cycle 1; P.I. R. Leiton, presented in Elbaz et al. 2018) at  $870\mu\text{m}$  with a long integration time (40–50 min on source). These deeper observations give more information on the nature of the galaxies, in particular on their morphology. Due to their high S/N ( $\sim 100$ ) the sizes of the dust emission could be measured accurately:  $R_{1/2\text{maj}} = 120 \pm 4$  and  $139 \pm 6$  mas for AGS1 and AGS3 respectively, revealing extremely compact star-forming regions corresponding to circularized effective radii of  $\sim 1$  kpc at redshift  $z \sim 2$ . The Seric indices are  $1.27 \pm 0.22$  and  $1.15 \pm 0.22$  for AGS1 and AGS3 respectively: the dusty star-forming regions therefore seem to be disk-like. Based on their sizes, their stellar masses ( $>10^{11} M_{\odot}$ ), their SFRs ( $>10^3 M_{\odot} \text{ yr}^{-1}$ ) and their redshifts ( $z \sim 2$ ), these very compact galaxies are ideal candidate progenitors of compact quiescent galaxies at  $z \sim 2$  (Barro et al. 2013; Williams et al. 2014; van der Wel et al. 2014; Kocevski et al. 2017, see also Elbaz et al. 2018).

Size measurements of galaxies at (sub)millimeter wavelengths have previously been made as part of several different studies. Ikarashi et al. (2015) measured sizes for 13 AzTEC-selected SMGs. The Gaussian FWHM range between  $0''.10$  and

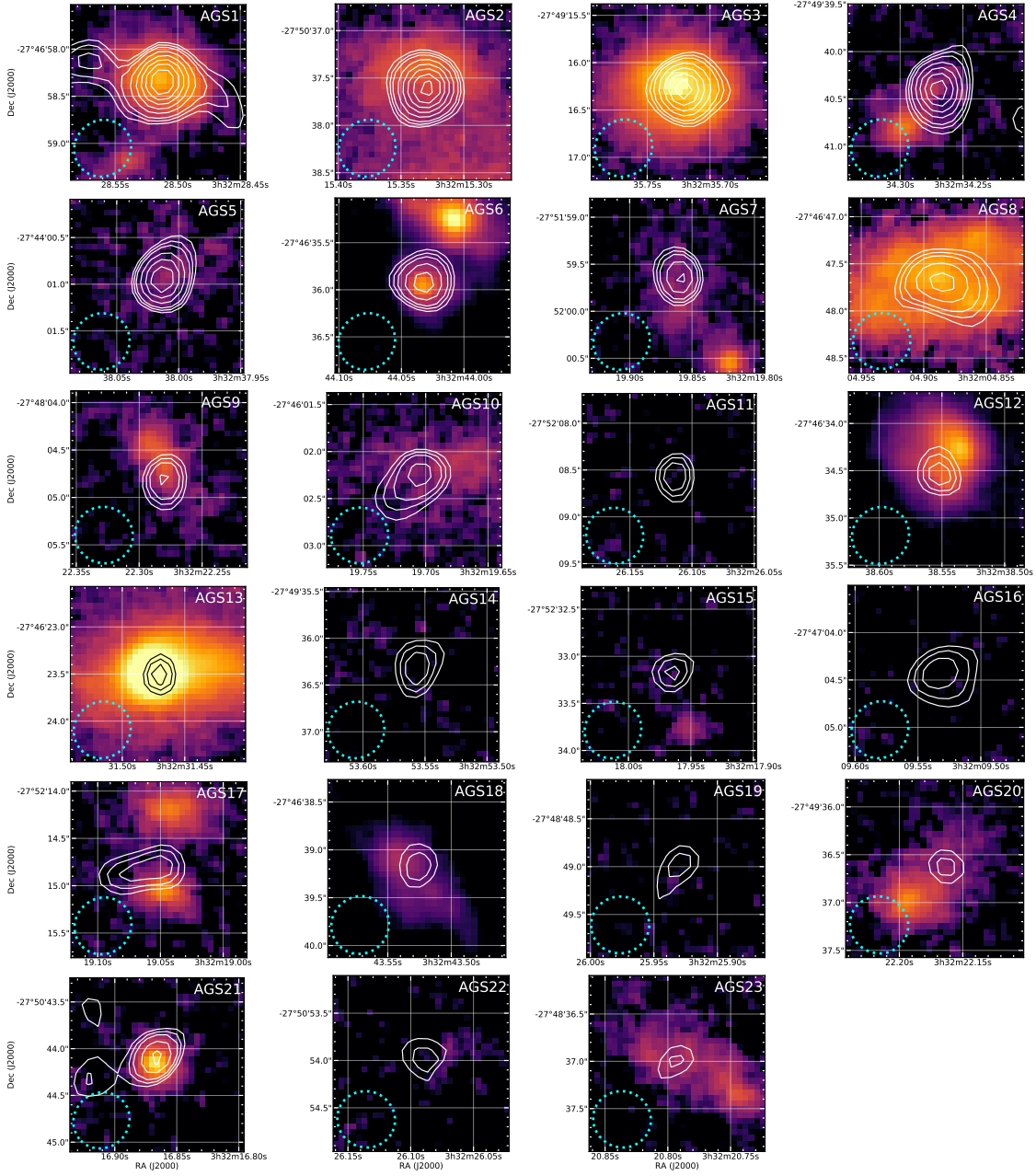


**Fig. 6.** Postage stamps of  $1.8 \times 1.8$  arcsec. ALMA contours (4, 4.5 then 5–10- $\sigma$  with a step of 1- $\sigma$ ) at 1.1 mm (white lines) are overlaid on F160W HST/WFC3 images. The images are centered on the ALMA detections. The shape of the synthesized beam is given in the bottom left corner. Astrometry corrections described in Sect. 4.3 have been applied to the HST images. In some cases (AGS1, AGS3, AGS6, AGS13, AGS21 for example), the position of the dust radiation matches that of the stellar emission; in other cases (AGS4, AGS17 for example), a displacement appears between both two wavelengths. Finally, in some cases (AGS11, AGS14, AGS16, and AGS19) there are no optical counterparts. We will discuss the possible explanations for this in Sect. 7.

$0''.38$  with a median of  $0''.20^{+0''.03}_{-0''.05}$  at 1.1 mm. Simpson et al. (2015a) derived a median intrinsic angular size of  $FWHM = 0''.30 \pm 0''.04$  for their 23 detections with a  $S/N > 10$  in the Ultra Deep Survey (UDS) for a resolution of  $0''.3$  at  $870 \mu\text{m}$ . Tadaki et al. (2017) found a median FWHM of  $0''.11 \pm 0.02$  for 12 sources in a  $0''.2$ -resolution survey at  $870 \mu\text{m}$ . Barro et al. (2016) use a high spatial resolution ( $FWHM \sim 0''.14$ ) to measure a median Gaussian FWHM of  $0''.12$  at  $870 \mu\text{m}$ , with

an average Sersic index of 1.28. For Hodge et al. (2016), the median major axis size of the Gaussian fit is  $FWHM = 0''.42 \pm 0''.04$  with a median axis ratio  $b/a = 0.53 \pm 0.03$  for 16 luminous ALESS SMGs, using high-resolution ( $\sim 0''.16$ ) data at  $870 \mu\text{m}$ . Rujopakarn et al. (2016) found a median circular FWHM at 1.3 mm of  $0''.46$  from the ALMA image of the HUDF (Dunlop et al. 2017). González-López et al. (2017) studied 12 galaxies at  $S/N \geq 5$ , using 3 different beam sizes

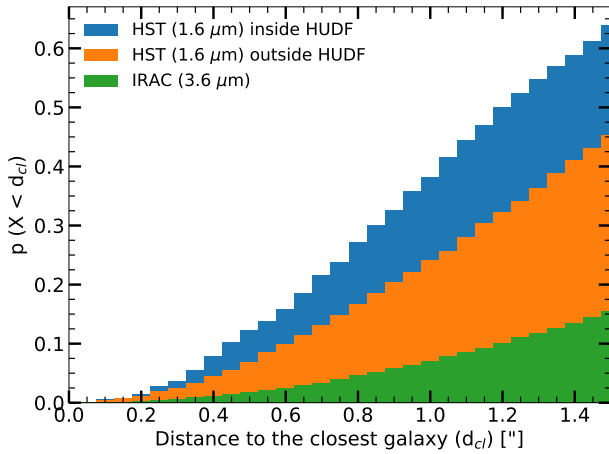


**Fig. 7.** Probability of a randomly selected position in the area defined by this survey to have at least one HST (blue, orange) or IRAC (green) neighbor as a function of distance. We computed this probability by Monte Carlo simulation using the distribution of galaxies listed in the CANDELS/GOODS-South catalog. Due to the presence of the HUDF within the GOODS-South field, we cannot consider that the density of HST galaxies is uniform, and we consider these two fields separately (blue inside and orange outside the HUDF).

( $0''.63 \times 0''.49$ ), ( $1''.52 \times 0''.85$ ) and ( $1''.22 \times 1''.08$ ). They found effective radii spanning  $<0''.05$  to  $0''.37 \pm 0''.21$  in the ALMA Frontier Fields survey at 1.1 mm. Ikarashi et al. (2017) obtained ALMA millimeter-sizes of  $0''.08$ – $0''.68$  (FWHM) for 69 ALMA-identified AzTEC SMGs with an S/N greater than 10. These galaxies have a median size of  $0''.31$ . These studies are all broadly in agreement, revealing compact galaxy sizes in the sub(millimeter) regime of typically  $0''.3 \pm 0''.1$ .

Size measurements require a high S/N detection to ensure a reliable result. The S/N range of our detections is 4.8–11.3. Following Martí-Vidal et al. (2012), the reliable size measurement limit for an interferometer is:

$$\theta_{\min} = \beta \left( \frac{\lambda_c}{2 S/N^2} \right)^{1/4} \times \theta_{\text{beam}} \approx 0.88 \frac{\theta_{\text{beam}}}{\sqrt{S/N}} \quad (2)$$

where  $\lambda_c$  is the value of the log-likelihood, corresponding to the cutoff of a Gaussian distribution to have a false detection and  $\beta$  is a coefficient related to the intensity profile of the source model and the density of the visibilities in Fourier space. This coefficient usually takes values in the range 0.5–1. We assumed  $\lambda_c = 3.84$  corresponding to a  $2\sigma$  cut-off, and  $\beta = 0.75$ . For  $\theta_{\text{beam}} = 0''.60$  and a range of S/N between 4.8 and 11.3, the minimum detectable size (FWHM) therefore varies between  $0''.16$  and  $0''.24$ . Using the  $0''.60$ -mosaic map, the sizes of a large number of detections found in previous studies could therefore not be reliably measured.

To quantitatively test if the millimeter galaxies are resolved in our survey we performed several tests. The first test was to stack the 23 ALMA-detections and compare the obtained flux profile with the profile of the PSF. However, in the mosaic map, each slice has its own PSF. We therefore also needed to stack the PSFs at these 23 positions in order to obtain a global PSF for comparison. Figure 9 shows the different PSFs used in this survey in the  $0''.60$ -mosaic. The FWHM of each PSF is identical, the differences are only in the wings. The stack of the 23 PSFs for the 23 detections and the result of the

source stacking in the  $0''.60$ -mosaic is shown in Fig. 10. The flux of each detection is normalized so that all sources have the same weight, and the stacking is not skewed by the brightest sources.

Size stacking to measure the structural parameters of galaxies is at present a relatively unexplored area. This measurement could suffer from several sources of bias. The uncertainties on the individual ALMA peak positions could increase the measured size in the stacked image, for example. On the other hand, due to the different inclination of each galaxy, the stacked galaxy could appear more compact than the individual galaxies (e.g. Hao et al. 2006; Padilla & Strauss 2008; Li et al. 2016). Alternatively, some studies (e.g. van Dokkum et al. 2010) indicate that size stacking gives reasonably accurate mean galaxy radii. In our case, the result of the size stacking is consistent with unresolved sources or marginally resolved at this resolution which corresponds to a physical diameter of 4.6 kpc at  $z = 3$ .

The second test was to extract the flux for each galaxy using PSF-fitting. We used Galfit (Peng et al. 2010) on the  $0''.60$ -mosaic. The residuals of this PSF-extraction are shown for the 6 brightest galaxies in Fig. 11. The residuals of 21/23 detections do not have a peak greater than  $3\sigma$  in a radius of  $1''$  around the source. Only sources AGS10 and AGS21 present a maximum in the residual map at  $\sim 3.1\sigma$ .

We compared the PSF flux extraction method with Gaussian and Sersic shapes. As our sources are not detected with a particularly high S/N, and in order to limit the number of degrees of freedom, the Sersic index was frozen to  $n = 1$  (exponential disk profile, in good agreement with Hodge et al. 2016 and Elbaz et al. 2018 for example), assuming that the dust emission is disk-like. Figure 11 shows the residuals for the three different extraction profiles. The residuals are very similar between the point source, Gaussian and Sersic profiles, suggesting that the approximation that the sources are not resolved is appropriate, and does not result in significant flux loss. We also note that, for several galaxies, due to large size uncertainties, the Gaussian and Sersic fits give worse residuals than the PSF fit (AGS4 for example).

For the third test, we took advantage of the different tapered maps. We compared the peak flux for each detection between the  $0''.60$ -mosaic map and the  $0''.29$ -mosaic map. The median ratio is  $S_{\text{peak}}^{0''.29}/S_{\text{peak}}^{0''.60} = 0.87 \pm 0.16$ . This small decrease, of only 10% in the peak flux density between the two tapered maps suggests that the flux of the galaxies is only slightly more resolved in the  $0''.29$ -mosaic map.

In order to test the impact of our hypothesis that the sources can be considered as point-like in the mosaic tapered at  $0''.60$ , we fit their light profiles with a circular Gaussian in the  $uv$ -plane using `uvmodelfit` in CASA (we also tested the use of an asymmetric Gaussian but the results remained similar although with a lower precision due to the larger number of free parameters in the fit). The sizes that we obtained confirmed our hypothesis that our galaxies are particularly compact since 85% of the sources (17 out of 20 robust detections) exhibit a FWHM smaller than  $0''.25$  (in other words the half-light radius is twice smaller than this value). The median size of our sample of 20 galaxies is  $0''.18$  (see the distribution of sizes in Fig. 12). This analysis shows that two sources are outliers with sizes of  $0''.41 \pm 0''.03$  and  $0''.50 \pm 0''.08$ , for AGS17 and AGS18 respectively. For these two sources, the assumption of point-like sources is not valid and leads to an underestimate of the actual flux densities by a factor of 2.3 and 1.7 respectively. This correction has been applied to the list of peak flux densities provided in Table 3.



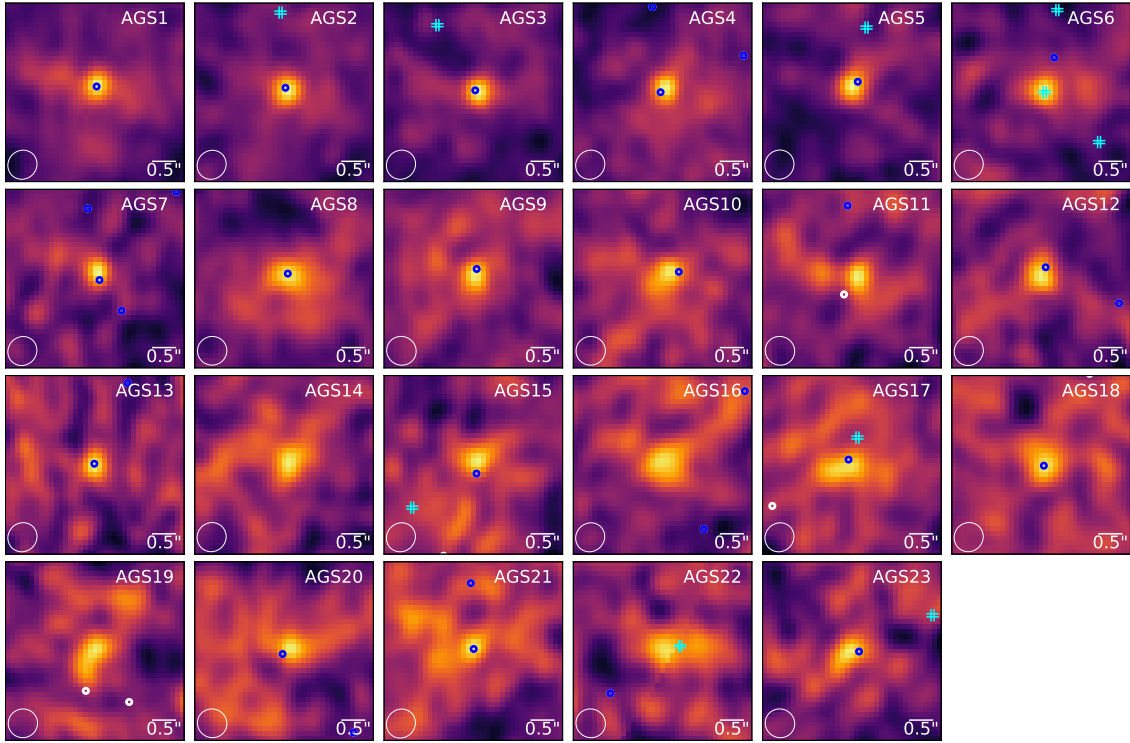


**Fig. 8.** ALMA 1.1 mm continuum maps for the 23 detections tapered at 0.60 arcsec. Each  $3'' \times 3'' \times 3''$  image is centered on the position of the ALMA detection. Cyan double crosses show sources from the GOODS-S CANDELS catalog. White circles show sources from the ZFOURGE catalog. Blue circles show common sources from both optical catalogs (sources with an angular separation lower than  $0''.4$ ). The shape of the synthesized beam is given in the bottom left corner.

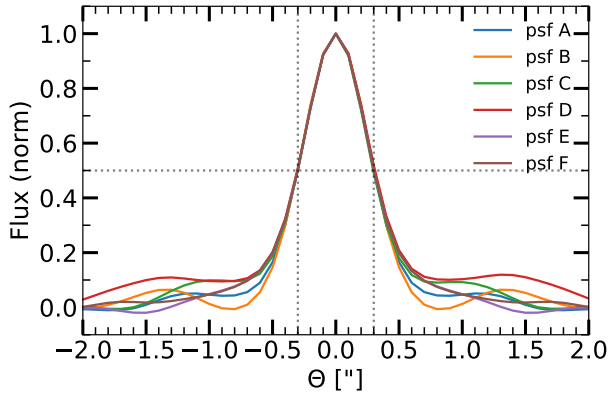


**Fig. 9.** East-west profile of the PSFs corresponding to the six different parallel slices composing the ALMA image in the  $0''.60$ -mosaic (see Fig. 1).

Having performed these tests, we concluded that for all of the detections, except AGS17 and AGS18, the approximation that these sources appear point-like in the  $0''.60$ -mosaic map is justified. For the two remaining sources, we applied a correction given above. Our photometry was therefore performed under this assumption.

## 5. Number counts

### 5.1. Completeness

We assessed the accuracy of our catalog by performing completeness tests. The completeness is the probability for a source

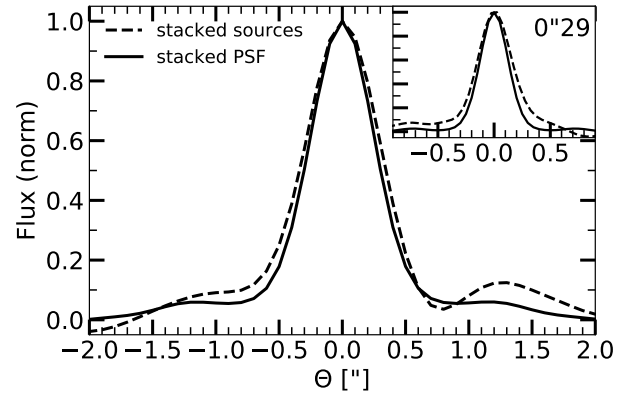


**Fig. 10.** Comparison between the stacked PSF (black solid line) and the stack of the 23 ALMA-detections (black dashed line) in the  $0''.60$ -mosaic. As each slice has a specific PSF, we stack the PSF corresponding to the position of each detection. The fluxes of each detection have been normalized, so that the brightest sources do not skew the results. Fluxes of the PSF and ALMA detections are normalized to 1. Flux profiles are taken across the East-west direction. The result is consistent with unresolved or marginally resolved sources at this resolution. The insert in the top-right corner shows the same procedure for the 15 sources detected in the  $0''.29$ -mosaic (see Table 3).

to be detected in the map given factors such as the depth of the observations. We computed the completeness of our observations using Monte Carlo simulations performed on the  $0''.60$ -mosaic map. We injected 50 artificial sources in each slice. Each



**Fig. 11.**  $10'' \times 10''$  postage stamps, centered on the galaxy detections. Left to right: source in the  $0''60$ -mosaic map, and residuals obtained after PSF, Gaussian and Sersic flux fitting. The residuals are very similar between the three different extraction methods. Only the 6 brightest galaxies are shown.

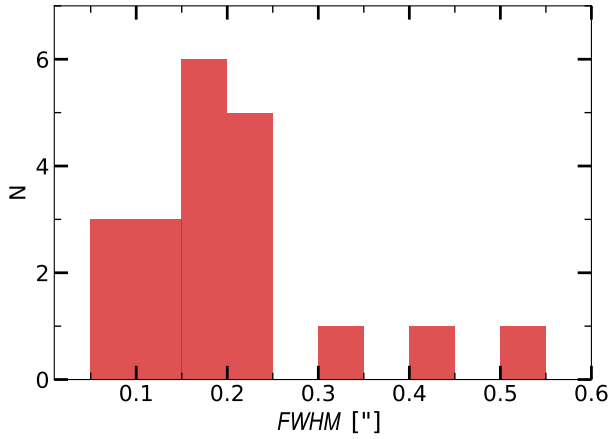


**Fig. 12.** Size distribution histogram for the 20 robust detections. These sizes are computed by fitting the ALMA detections with a circular Gaussian in the  $uv$ -plane using `uvmodel` in CASA. 85% of the sources exhibit a FWHM smaller than  $0''25$ .

source was convolved with the PSF and randomly injected on the dirty map tapered at  $0''60$ . In total, for each simulation run, 300 sources with the same flux were injected into the total map. In view of the size of the map, the number of independent beams and the few number of sources detected in our survey, we can consider, to first order, that our dirty map can be used as a blank map containing only noise, and that the probability to inject a source exactly at the same place as a detected galaxy is negligible. The probability that at least two point sources, randomly injected, are located within the same beam ( $p_b$ ) is:

$$p_b = 1 - \prod_{k=0}^{n-1} \frac{N_b - k}{N_b} \quad (3)$$

where  $N_b$  is the number of beams and  $n$  is the number of injected sources. For each one of the six slices of the survey, we count  $\sim 100\,000$  independent beams. The probability of having source blending for 50 simulated sources in one map is  $\sim 1\%$ .

We then counted the number of injected sources detected with  $\sigma_p = 4.8\sigma$  and  $\sigma_f = 2.7\sigma$ , corresponding to the thresholds of our main catalog. We injected 300 artificial sources of a given flux, and repeated this procedure 100 times for each flux density. Our simulations cover the range  $S_\nu = 0.5$ – $2.4$  mJy in steps of  $0.1$  mJy. Considering the resolution of the survey, it would be reasonable to expect that a non-negligible number of galaxies are not seen as point sources but extended sources (see Sect. 4.5). We simulated different sizes of galaxies with Gaussian FWHM between  $0''2$  and  $0''9$  in steps of  $0''1$ , as well as point-source

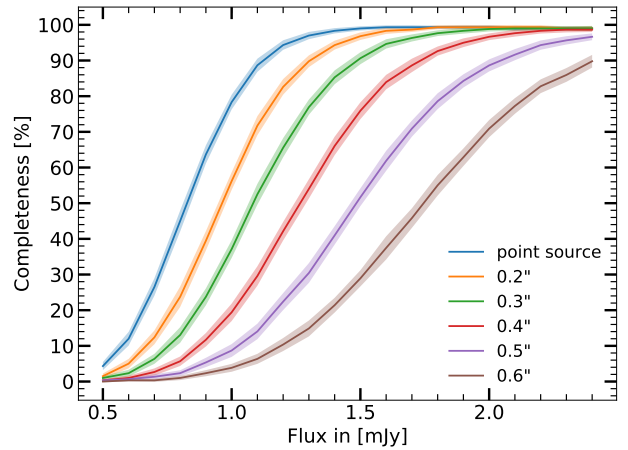


**Fig. 13.** Median source detection completeness for simulated point-like and Gaussian galaxies as a function of integrated flux, for different FWHMs (see figure's legend). The shaded regions correspond to the standard deviation of 100 runs, each containing 300 simulated sources.

galaxies, to better understand the importance of the galaxy size in the detectability process. We matched the recovered source with the input position within a radius of  $0''6$ .

Figure 13 shows the resulting completeness as a function of input flux, for different FWHM Gaussian sizes convolved by the PSF and injected into the map.

As a result of our simulations, we determined that at  $1.2$  mJy, our sample is  $94 \pm 1\%$  complete for point sources. This percentage drastically decreases for larger galaxy sizes. For the same flux density, the median detection rate drops to  $61 \pm 3\%$  for a galaxy with  $FWHM \sim 0''3$ , and to  $9 \pm 1\%$  for a  $FWHM \sim 0''6$  galaxy. This means, that for a galaxy with an intrinsic flux density of  $1.2$  mJy, we are more than ten times more likely to detect a point source galaxy than a galaxy with  $FWHM \sim 0''6$ .

The size of the millimeter emission area plays an essential role in the flux measurement and completeness evaluation. We took the hypothesis that ALMA sizes are  $1.4$  times smaller than the size measured in HST  $H$ -band (as derived by Fujimoto et al. 2017 using 1034 ALMA galaxies). We are aware that this size ratio is poorly constrained at the present time, but such relations have been observed in several studies (see Sect. 4.5). For example, of the 12 galaxies presented by Laporte et al. (2017), with fluxes measured using ALMA at  $1.1$  mm (González-López et al. 2017), seven of them have a size measured by HST F140W/WFC3 similar to the size measured in the ALMA map. On the other hand, for the remaining five galaxies, their sizes are approximately two times more compact

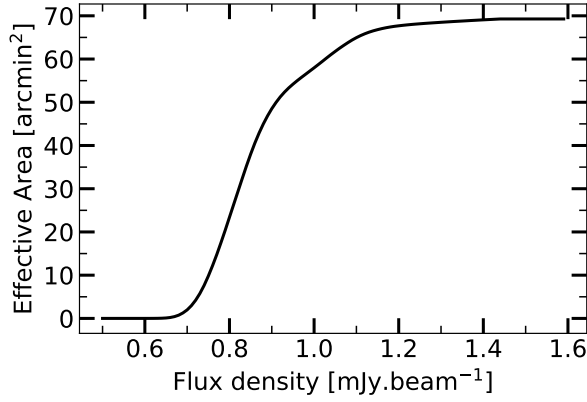


**Fig. 14.** Effective area as a function of flux density, where a source with a given flux can be detected with an  $S/N > 4.8\sigma$ . Ninety percent of the survey area reaches a sensitivity of at least  $1.06 \text{ mJy beam}^{-1}$ .

at millimeter wavelengths than at optical wavelengths. This illustrates the dispersion of this ratio.

### 5.2. Effective area

As the sensitivity of our 1.1 mm ALMA map is not uniform, we defined an effective area where a source with a given flux can be detected with an  $S/N > 4.8\sigma$ , as shown in Fig. 14. Our map is composed of six different slices – one of them, slice B, presents a noise 30% greater than the mean of the other five, whose noise levels are comparable. The total survey area is  $69.46 \text{ arcmin}^2$ , with 90% of the survey area reaching a sensitivity of at least  $1.06 \text{ mJy beam}^{-1}$ . We considered the relevant effective area for each flux density in order to compute the number counts. We considered the total effective area over all slices in the number counts computation.

### 5.3. Flux boosting and Eddington bias

In this section, we evaluate the effect of flux boosting. Galaxies detected with a relatively low  $S/N$  tend to be boosted by noise fluctuations (see Hogg & Turner 1998; Coppin et al. 2005; Scott et al. 2002). To estimate the effect of flux boosting, we used the same set of simulations that we used for completeness estimations.

The results of our simulations are shown in Fig. 15. The boosting effect is shown as the ratio between the input and output flux densities as a function of the measured  $S/N$ . For point sources, we observed the well-known flux boosting effect for the lowest  $S/N$ s. This effect is not negligible for the faintest sources in our survey. At  $4.8\sigma$ , the flux boosting is  $\sim 15\%$ , and drops below 10% for an  $S/N$  greater than 5.2. We estimated the de-boosted flux by dividing the measured flux by the median value of the boosting effect as a function of  $S/N$  (red line in Fig. 15).

We also corrected for the effects of the Eddington bias (Eddington 1913). As sources with lower luminosities are more numerous than bright sources, Gaussian distributed noise gives rise to an overestimation of the number counts in the lowest flux bins. We simulated a realistic number of sources (the slope of the number counts were computed using the coefficients given in Table 5) and added Gaussian noise to each simulated source. The correction factor for each flux bin was therefore the ratio between the flux distribution before and after adding the noise.

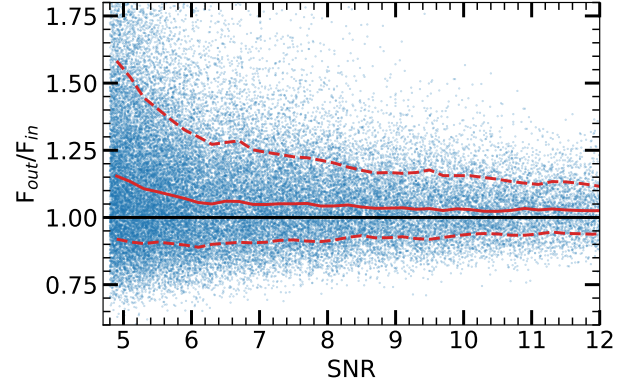


**Fig. 15.** Flux boosting as a function of measured  $S/N$  estimated from simulations. The median of the boosting is shown by a solid red line. The  $1\sigma$  confidence intervals (dashed red lines) are overplotted. The solid black horizontal line corresponds to  $F_{\text{out}} = F_{\text{in}}$  (see text for details). We used the same set of simulations that we used for the completeness analysis.

### 5.4. Cumulative and differential number counts

We used sources with a  $S/N$  greater than 4.8 from the main catalog to create cumulative and differential number counts. We needed to take into account the contamination by spurious sources, completeness effects, and flux boosting in order to compute these number counts.

The contribution of a source with flux density  $S_i \pm dS_i$  to the cumulative number count is given by:

$$\frac{dN(S_i)}{dS_i} = \frac{p_c(S_i)}{A_{\text{eff}}(S_i)C(S_i, R_{\text{ALMA}}^{\text{circ}})} \times \frac{dN_{\text{obs}}(S_i)}{dS_i} \quad (4)$$

where  $p_c(S_i)$  is the purity criterion as defined in Eq. (1) at the flux density  $S_i$ ,  $A_{\text{eff}}(S_i)$  and  $C(S_i, R_{\text{ALMA}}^{\text{circ}})$  are the effective area and the completeness for the flux interval  $dS_i$ , as shown in Figs. 13 and 14. The completeness is strongly correlated with the sizes of the galaxies. To estimate the completeness, galaxies that do not have measured sizes in the  $H$ -band (van der Wel et al. 2012) were considered as point sources, otherwise we used  $R_{\text{ALMA}}^{\text{circ}} = R_H^{\text{circ}}/1.4$  (see Sect. 5.1).

The cumulative number counts are given by the sum over all of the galaxies with a flux density higher than  $S$ :

$$N(>S) = \sum_{S_i > S} \frac{p_c(S_i)}{A_{\text{eff}}(S_i)C(S_i, R_{\text{ALMA}}^{\text{circ}})} \times \frac{dN_{\text{obs}}(S_i)}{dS_i} \times dS_i \quad (5)$$

Errors are computed by Monte-Carlo simulations, added in quadrature to the Poisson uncertainties. The derived number counts are provided in Table 4. AGS19 is located at a position where the noise is artificially low, and has therefore not been taken into account.

In Fig. 16, we compare our results with previous studies (Lindner et al. 2011; Scott et al. 2012; Karim et al. 2013; Hatsukade et al. 2013, 2016; Simpson et al. 2015b; Oteo et al. 2016; Aravena et al. 2016; Fujimoto et al. 2016; Umehata et al. 2017; Geach et al. 2017; Dunlop et al. 2017). To standardize these previous studies, the different flux densities are scaled to 1.1 mm using a Modified Black Body (MBB) model, assuming a dust emissivity index  $\beta = 1.5$  (e.g., Gordon et al. 2010), a dust temperature  $T_d = 35 \text{ K}$  (e.g. Chapman et al. 2005;

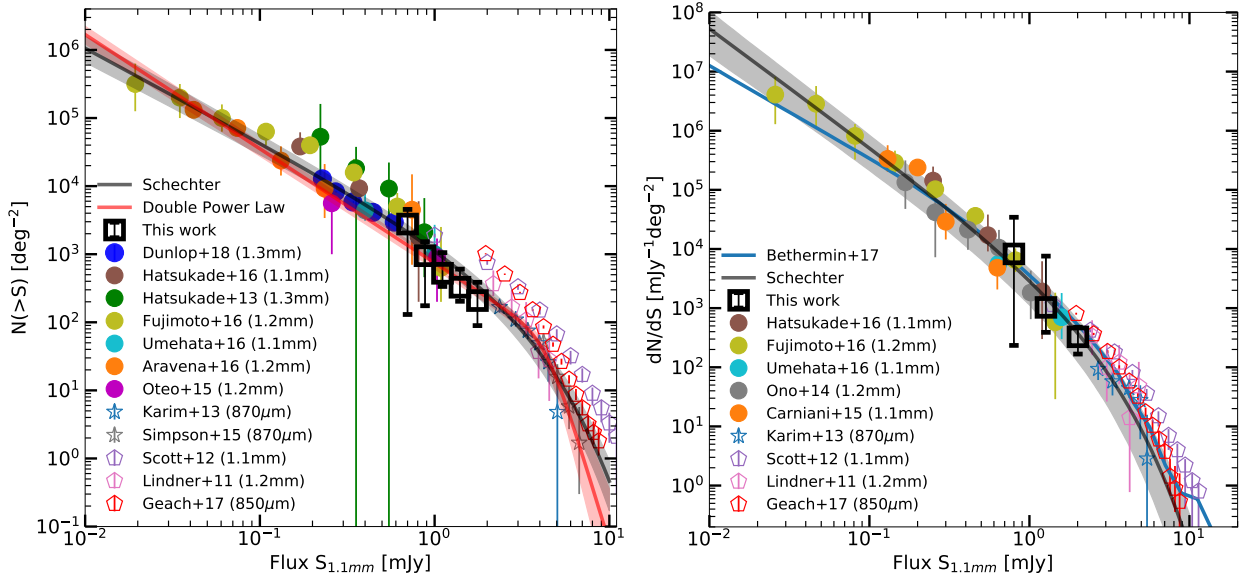


**Fig. 16.** 1.1-mm cumulative (left panel) and differential (right panel) number counts derived using the corrections described in Sect. 5.4, for the sources detected at  $>4.8\sigma$  in the main catalog. AGS19 is located at a position where the noise is artificially low, and has therefore not been taken into account. Previous (sub)millimeter cumulative number counts are also shown (Lindner et al. 2011; Scott et al. 2012; Karim et al. 2013; Hatsukade et al. 2013, 2016; Ono et al. 2014; Simpson et al. 2015b; Oteo et al. 2016; Carniani et al. 2015; Aravena et al. 2016; Fujimoto et al. 2016; Umehata et al. 2017; Geach et al. 2017; Dunlop et al. 2017). The different fluxes are scaled to 1.1 mm flux densities using  $S_{1.1\text{ mm}}/S_{1.3\text{ mm}} = 1.29$ ,  $S_{1.1\text{ mm}}/S_{1.3\text{ mm}} = 1.48$ ,  $S_{1.1\text{ mm}}/S_{870\mu\text{m}} = 0.56$ . From the Umehata et al. (2017) study, we used only sources which do not have  $z = 3.09$ , (which means we are excluding the protocluster members). Results from single-dish surveys are shown with unfilled pentagon markers and are only indicative, they are not considered for model fitting. The gray curve shows the best-fit Schechter function (with  $1-\sigma$ ), the red curve shows the best-fit DPL function (with  $1-\sigma$ ).

**Table 4.** Number counts at 1.1 mm derived from  $>4.8\sigma$  detections (main catalog).

$S_\nu$ mJy	$N(>S_\nu)$ deg $^{-2}$	$N_{\text{cum}}$	$S_\nu$ mJy	$dN/dS_\nu$ mJy $^{-1}$ deg $^{-2}$	$N_{\text{diff}}$
(1)	(2)	(3)	(4)	(5)	(6)
0.70	$2772^{+1776}_{-2641}$	19	0.80	$8257^{+26121}_{-8023}$	7
0.88	$950^{+375}_{-275}$	13	1.27	$1028^{+6547}_{-638}$	6
1.11	$524^{+530}_{-188}$	11	2.01	$327^{+148}_{-160}$	6
1.40	$327^{+277}_{-124}$	7			
1.76	$209^{+178}_{-119}$	4			

**Notes.** Columns: (1) flux density; (2) cumulative number counts; (3) number of entries per bin for cumulative number counts; (4) center of the flux density bin; (5) differential number counts; (6) number of entries per bin for differential number counts. Flux density bins,  $\Delta \log S_\nu = 0.20$  dex wide for differential number counts. The uncertainties are computed by Monte-Carlo simulations, added in quadrature to the Poisson uncertainties.

Kovács et al. 2006; Coppin et al. 2008), and a redshift of  $z = 2.5$  (e.g., Wardlow et al. 2011; Yun et al. 2012). These values have also been chosen to be consistent with Hatsukade et al. (2016). The different fluxes were therefore scaled to 1.1 mm using the relations  $S_{1.1\text{ mm}}/S_{1.3\text{ mm}} = 1.29$ ,  $S_{1.1\text{ mm}}/S_{1.3\text{ mm}} = 1.48$  and  $S_{1.1\text{ mm}}/S_{870\mu\text{m}} = 0.56$ . It is a real challenge to standardize these previous studies because instruments, observational techniques or resolution often vary between studies. Some of these counts have been computed from individual pointings, by brightness selection, or by serendipitous detections. Observations with a

single dish or a low resolution can also overestimate the number counts for the brightest galaxies, because of blending effects (see Ono et al. 2014). Another non-negligible source of error can come from an inhomogeneous distribution of bright galaxies. An underdensity by a factor of two of submillimeter galaxies with far infrared luminosities greater than  $2 \times 10^{12} L_\odot$  in the extended *Chandra* deep field south (ECDFS) compared to other deep fields has been revealed by Weiß et al. (2009).

Despite those potential caveats, the results from our ALMA survey in the GOODS-South field are in good agreement with previous studies for flux densities below 1 mJy. For values above this flux density, two different trends coexist as illustrated in Fig. 16: our counts are similar to those found by Karim et al. (2013), but below the trend characterized by Scott et al. (2012). These two previous studies have been realized under different conditions. The effects of blending, induced by the low resolution of a single dish observation, as with Scott et al. (2012), tend to overestimate the number counts at the bright-end (Ono et al. 2014; Karim et al. 2013; Béthermin et al. 2017). We indicate these points on the Fig. 16 on an indicative basis only.

The differences in wavelength between the different surveys, even after applying the scaling corrections above, can also induce scatter in the results, especially for wavelengths far from 1.1 mm. The cumulative source counts from the 20 detections in this study and the results from other multidish blank surveys are fitted with a Double Power Law (DPL) function (e.g., Scott et al. 2002) given by:

$$N(>S) = \frac{N_0}{S_0} \left[ \left( \frac{S}{S_0} \right)^\alpha + \left( \frac{S}{S_0} \right)^\beta \right]^{-1} \quad (6)$$



**Table 5.** Best-fit parameters for the cumulative and differential number counts for a double power law function (Eq. (6)) and a Schechter function (Eq. (7)).

	$N_0$ $10^2 \text{ deg}^{-2}$	$S_0$ mJy	$\alpha$	$\beta$
Cumulative number counts				
DPL	$2.8 \pm 0.2$	$4.4^{+0.3}_{-0.5}$	$8.45^{+0.28}_{-1.07}$	$1.68 \pm 0.02$
Schechter	$14.3^{+1.4}_{-2.3}$	$2.0 \pm 0.3$	$-1.38 \pm 0.05$	
Differential number counts				
Schechter	$35.2^{+4.6}_{-10.8}$	$1.6^{+0.3}_{-0.4}$	$-1.99 \pm 0.07$	

and a modified Schechter (Schechter 1976) function (e.g., Knudsen et al. 2008):

$$N(>S) = \frac{N_0}{S_0} \left( \frac{S}{S_0} \right)^\alpha \exp\left(-\frac{S}{S_0}\right) d\left(\frac{S}{S_0}\right) \quad (7)$$

where  $N_0$  is the normalization,  $S_0$  the characteristic flux density and  $\alpha$  is the faint-end slope.  $\beta$  is the bright-end slope of the number of counts in Eq. (6). We used a least squares method with the trust region reflective algorithm for these two fitted-functions. The best-fit parameters are given in Table 5.

One of the advantages of using differential number counts compared to cumulative number counts is the absence of correlation of the counts between the different bins. However, the differential number counts are sensitive to the lower number of detections per flux density bin. Here we used  $\Delta \log S_\nu = 0.2$  dex flux density bins.

We compare our results with an empirical model that predicts the number counts at far-IR and millimeter wavelengths, developed by Béthermin et al. (2017). This simulation, called SIDES (Simulated Infrared Dusty Extragalactic Sky), updates the Béthermin et al. (2012) model. These predictions are based on the redshift evolution of the galaxy properties, using a two star-formation mode galaxy evolution model (see also Sargent et al. 2012).

The Béthermin et al. (2017) prediction is in good agreement with the number counts derived in this study, for the two bins with the lowest fluxes. For the highest-flux bin, the model is slightly above the data ( $\sim 1\sigma$  above the best Schechter fit for fluxes greater than 1 mJy). However, both the Béthermin et al. (2017) model and our data points are below the single-dish measurements for fluxes greater than 1 mJy. This disagreement between interferometric and single-dish counts is expected, because the boosting of the flux of single-dish sources by their neighbor in the beam (Karim et al. 2013; Hodge et al. 2013; Scudder et al. 2016). Béthermin et al. (2017) derived numbers counts from a simulated single-dish map based on their model and found a nice agreement with single-dish data, while the intrinsic number counts in the simulation are much lower and compatible with our interferometric study.

Cosmic variance was not taken into account in the calculation of the errors. Above  $z = 1.8$  and up to the redshift of the farthest galaxy in our catalog at  $z = 4.8$ , the strong negative  $K$ -correction at this wavelength ensures that the selection of galaxies is not redshift-biased. The cosmic variance, although significant for massive galaxies in a small solid angle, is counterbalanced by the negative  $K$ -correction, which makes the redshift interval of our sources ( $\Delta z = 3$  in Eq. (12) in Moster et al. 2011) relatively large, spanning a comoving vol-

ume of 1400 Gpc<sup>3</sup>. Based on Moster et al. (2011), the cosmic variance for our sources is  $\sim 15\%$ , which does not significantly affect the calculation of the errors on our number counts.

### 5.5. Contribution to the cosmic infrared background

The extragalactic background light (EBL) is the integrated intensity of all of the light emitted throughout cosmic time. Radiation re-emitted by dust comprises a significant fraction of the EBL, because this re-emitted radiation, peaking around 100  $\mu\text{m}$ , has an intensity comparable to optical background (Dole et al. 2006). The contribution of our ALMA sources to the EBL is derived by integrating the derived number counts down to a certain flux density limit. Using the 20 ( $>4.8\sigma$ ) sources detected, we computed the fraction of the 1.1 mm EBL resolved into discrete sources. The integrated flux density is given by:

$$I(S > S_{\text{lim}}) = \int_{S_{\text{lim}}}^{\text{inf}} \frac{dN(S)}{dS} S \, dS. \quad (8)$$

We used the set of parameters given in Table 5 on the differential number counts. We compared our results with observations from the far infrared absolute spectrophotometer (FIRAS) on the cosmic background explorer (COBE), knowing that uncertainties exist on the COBE measurements (e.g., Yamaguchi et al. 2016). We used the equation given in Fixsen et al. (1998) to compute the total energy of the EBL:

$$I_\nu = (1.3 \pm 0.4) \times 10^{-5} \left( \frac{\nu}{\nu_0} \right)^{0.64 \pm 0.12} P_\nu(18.5 + 1.2 \text{ K}) \quad (9)$$

where  $\nu_0 = 100 \text{ cm}^{-1}$ , and  $P_\nu$  is the familiar Planck function with  $I_\nu$  in  $\text{erg s}^{-1} \text{ cm}^{-1} \text{ Hz}^{-1} \text{ sr}^{-1}$ . From this equation, we found that at 1.1 mm, the energy of the EBL is  $2.87 \text{ nW m}^{-2} \text{ sr}^{-1}$ . From Eq. (8) we can estimate the integrated EBL light. Figure 17 shows this total integrated flux density. For our data, the lowest flux density bin for differential counts  $S_{\text{lim}}$  is 0.8 mJy, and we extrapolate to lower flux densities. We have resolved only  $13.5^{+9.0}_{-8.6}\%$  of the EBL into individual galaxies at 0.8 mJy. This result is in good agreement with studies such as Fujimoto et al. (2016). In order to have the majority of the EBL resolved (e.g., Hatsukade et al. 2013; Ono et al. 2014; Carniani et al. 2015; Fujimoto et al. 2016), we would need to detect galaxies down to 0.1 mJy (about 50 % of the EBL is resolved at this value).

The extrapolation of the integrated flux density below  $S_{\text{lim}}$  suggests a flattening of the number counts. The population of galaxies that dominate this background is composed of the galaxies undetected in our survey, with a flux density below our detection limit.

## 6. Galaxy properties

We now study the physical properties of the ALMA detected sources, taking advantage of the wealth of ancillary data available for the GOODS-South field.

### 6.1. Redshift distribution

Among the 17 ALMA detected sources for which redshifts have been computed, six have a spectroscopic redshift (AGS1, AGS2, AGS3, AGS9, AGS12, AGS13 and AGS18) determined by Kurk et al. (2013), and recently confirmed by Barro et al. (2017), Momcheva et al. (2016), Vanzella et al. (2008), Mobasher (priv. comm.), Inami et al. (2017), Kriek et al. (2008),

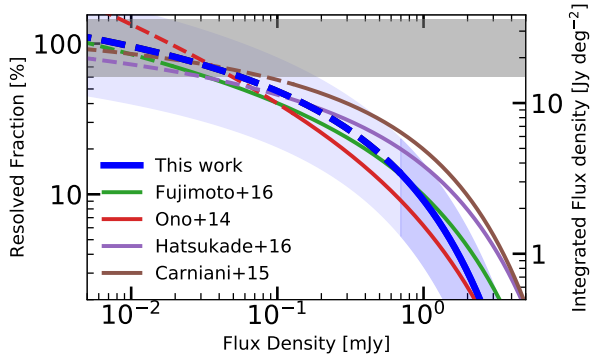


**Fig. 17.** Resolved 1.1 mm EBL computed from the best-fit Schechter function to the differential number counts. The green, red, purple and brown lines are from the number counts estimated by Fujimoto et al. (2016), Ono et al. (2014), Hatsukade et al. (2016), and Carniani et al. (2015) respectively. The blue line and shaded region show the results from this work and the associated uncertainty. The solid lines represent the model above the detection limits, and the dashed lines show the extrapolation below these limits. The gray shaded region shows the 1.1 mm cosmic infrared background measured by COBE (Fixsen et al. 1998).

and Dunlop et al. (2017) – from a private communication of Brammer – respectively. The redshift distribution of these 17 ALMA sources is presented in Fig. 18, compared to the distributions of four other deep ALMA blind surveys (Dunlop et al. 2017; Aravena et al. 2016; González-López et al. 2017; Ueda et al. 2018). Of the 17 sources, 15 are in the redshift range  $z = 1.9$ – $3.8$ . Only two galaxies (AGS4 and AGS11) have a redshift greater than 4 ( $z_{\text{phot}} = 4.32$  and  $4.82$  respectively). We discuss these galaxies further in Sect. 7. The mean redshift of the sample is  $z = 3.03 \pm 0.17$ , where the error is computed by bootstrapping. This mean redshift is significantly higher than those found by Dunlop et al. (2017), Aravena et al. (2016), González-López et al. (2017), and Ueda et al. (2018) who find distributions peaking at 2.13, 1.67, 1.99 and 2.28 respectively. The median redshift of our sample is  $2.92 \pm 0.20$ , which is a little higher than the value expected from the models of Béthermin et al. (2015), which predict a median redshift of 2.5 at 1.1 mm, considering our flux density limit of  $\sim 874 \mu\text{Jy}$  ( $4.8\sigma$ ).

Our limiting sensitivity is shallower than that of previous blind surveys:  $0.184 \text{ mJy}$  here compared with  $13 \mu\text{Jy}$  in Aravena et al. (2016),  $35 \mu\text{Jy}$  in Dunlop et al. (2017),  $(55\text{--}71) \mu\text{Jy}$  in González-López et al. (2017) and  $89 \mu\text{Jy}$  in Ueda et al. (2018). However, our survey covers a larger region on the sky:  $69 \text{ arcmin}^2$  here, compared to  $1 \text{ arcmin}^2$ ,  $4.5 \text{ arcmin}^2$ ,  $13.8 \text{ arcmin}^2$  and  $26 \text{ arcmin}^2$  for these four surveys respectively. The area covered by our survey is therefore a key parameter in the detection of high redshift galaxies due to a tight link between 1.1 mm luminosity and stellar mass as, we will show in the next section. The combination of two effects: a shallower survey allowing us to detect brighter SMGs, which are more biased toward higher redshifts (e.g., Pope et al. 2005), as well as a larger survey allowing us to reach more massive galaxies, enables us to open the parameter space at redshifts greater than 3, as shown in Fig. 18. This redshift space is partly or totally missed in smaller blind surveys.

We emphasize that the two HST-dark galaxies (see Sect. 7) for which the mass and redshift could be determined (AGS4 and AGS11) are the two most distant galaxies in our sample, with redshifts greater than 4.

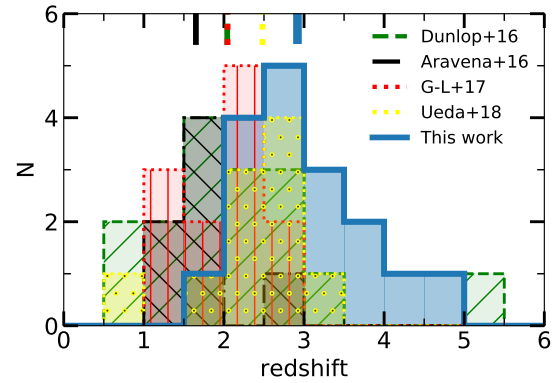


**Fig. 18.** Redshift distributions (photometric or spectroscopic) for millimeter-selected galaxies. The blue solid line shows the redshift distribution of our ALMA GOODS-South blind survey. The green dashed line shows the *Hubble* Ultra Deep Field Survey redshift distribution (Dunlop et al. 2017), the black dash-dotted line shows the ASPECS sample (Aravena et al. 2016), the red dotted line shows the ALMA Frontier Fields survey (González-López et al. 2017) and the yellow dotted line shows the ASAGAO survey (Ueda et al. 2018). Short colored lines at the top of the figure indicate the median redshifts for these four studies.

## 6.2. Stellar masses

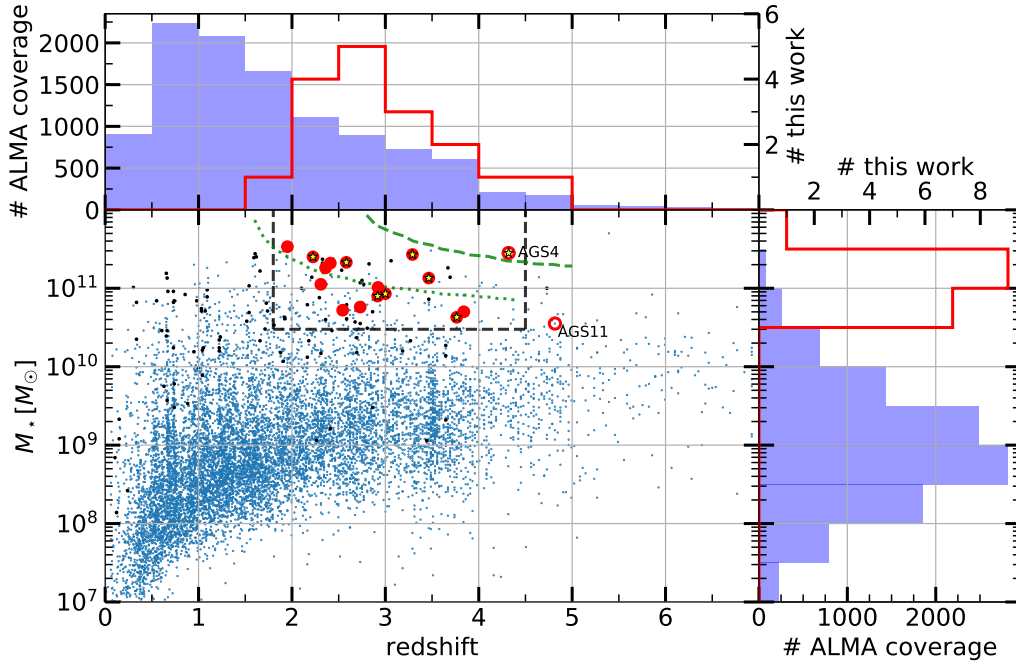
Over half (10/17) of our galaxies have a stellar mass greater than  $10^{11} M_{\odot}$  (median mass of  $M_{\star} = 1.1 \times 10^{11} M_{\odot}$ ). The population of massive and compact star-forming galaxies at  $z \sim 2$  has been documented at length (e.g., Daddi et al. 2005; van Dokkum et al. 2015), but their high redshift progenitors are to-date poorly detected in the UV. Our massive galaxies at redshifts greater than 3 might therefore give us an insight into these progenitors.

Figure 19 shows the stellar mass as a function of redshift for all of the UVJ active galaxies, listed in the ZFOURGE catalog, in our ALMA survey field of view. Star-forming galaxies (SFGs) have been selected by a UVJ color-color criterion as given by Williams et al. (2009) and applied at all redshifts and stellar masses as suggested by Schreiber et al. (2015):

$$\text{SFG} = \begin{cases} U - V < 1.3, \text{ or} \\ V - J > 1.6, \text{ or} \\ U - V < 0.88 \times (V - J) + 0.49 \end{cases} \quad (10)$$

All galaxies not fulfilling these color criteria are considered as quiescent galaxies and are excluded from our comparison sample (9.3% of the original sample). The ALMA detected galaxies in our survey are massive compared to typical SFGs detected in deep optical and near-IR surveys like CANDELS, in the same redshift range ( $2 < z < 4$ ), as shown in Fig. 19.

The high proportion of massive galaxies among the ALMA detected sources suggests that stellar mass can be a strong driver for a source to be detected by ALMA at high redshift (Dunlop et al. 2017). The strong link between detection and stellar mass is related to the underlying relation between stellar mass and star-formation rate of SFGs (e.g., Noeske et al. 2007; Elbaz et al. 2011). Almost one third (7/24) of the galaxies previously cataloged in the field of view of this study with  $M_{\star} > 10^{11}$  and  $2 < z < 3$  are also detected with ALMA. The position of our galaxies along the main sequence of



**Fig. 19.** Stellar mass versus redshift for the galaxies detected in our ALMA GOODS-South blind survey (red points). For comparison, the distribution of all of the galaxies, listed in the ZFOURGE catalog, in the same field of view is given in blue. Only UVJ active galaxies are shown. The two HST-dark galaxies for which we have redshifts (AGS4 and AGS11) are represented by open circles. The redshift of AGS11 is however uncertain. The green dashed line shows the position that would be occupied by a typical star-forming galaxy – lying on the median of the SFR– $M_*$  star-formation main sequence (MS) – that would produce a 1.1 mm flux density equal to our average detection limit of 0.88 mJy ( $4.8\sigma$ ) using the spectral energy distribution (SED) library of Schreiber et al. (2018). The dotted line illustrates the position of galaxies 3 times above the MS using the appropriate SEDs from the same library. Galaxies hosting an AGN that are undetected or detected by ALMA are identified with black dots and yellow stars respectively. Inside the black dashed rectangle, 50% of the galaxies detected by ALMA host an AGN, while only 14% of the UVJ active galaxies undetected by ALMA host an AGN.

star-formation will be studied in a following paper (Franco et al., in prep.).

We observe a lack of detections at redshift  $z < 2$ , driven by both a strong positive  $K$ -correction favoring higher redshifts and a decrease in the star formation activity at low redshift. Indeed, the specific star-formation rate (sSFR), defined as the ratio of galaxy SFR to stellar mass, drops quickly at lower redshifts ( $z < 2$ ), whereas this rate increases continuously at greater redshifts (e.g., Schreiber et al. 2015). In addition, very massive galaxies (stellar mass greater than  $10^{11} M_\odot$ ) are relatively rare objects in the smaller co-moving volumes enclosed by our survey at lower redshift. To detect galaxies with these masses, a survey has to be sufficiently large. The covered area is therefore a critical parameter for blind surveys to find massive high redshift galaxies.

In order to estimate the selection bias relative to the position of our galaxies on the main sequence, we show in Fig. 19 the minimum stellar mass as a function of redshift that our survey can detect, for galaxies on the MS of star-formation (green dashed line), and for those with a SFR three times above the MS (green dotted line).

To determine this limit, we calculated the SFR of a given MS galaxy, based on the galaxy stellar mass and redshift as defined in Schreiber et al. (2015). From this SFR and stellar mass, the galaxy SED can also be calculated using the Schreiber et al. (2018) library. We then integrated the flux of this SED around 1.1 mm.

It can be seen that the stellar mass detection limit corresponding to MS galaxies lies at higher stellar mass than all of the

galaxies detected by our ALMA survey (as well as all but one of the other star-forming galaxies present in the same region). This means that our survey is unable to detect star-forming galaxies below the main sequence. We can quantify the offset of a galaxy from the main sequence, the so-called “starburstiness” (Elbaz et al. 2011), by the ratio  $\text{SFR}/\text{SFR}_{\text{MS}}$ , where  $\text{SFR}_{\text{MS}}$  is the average SFR of “main sequence” galaxies computed from Schreiber et al. (2015). We also indicated our detection limit for galaxies with  $\text{SFR}/\text{SFR}_{\text{MS}} = 3$ . In this case, 7/17 galaxies shown lie above the limit. To have been detected, these galaxies must therefore have SFRs at least larger than the  $\text{SFR}_{\text{MS}}$ , the other ten galaxies must have a SFR at least three times above the MS. This highlights that our survey is biased toward galaxies with high SFRs.

### 6.3. AGN

In this Section, we discuss the presence of AGN within the 20 most robust ALMA detections, in other words, rejecting the three spurious detections with no IRAC counterpart (AGS14, AGS16 and AGS19 marked with a star in Table 3) but including three of the supplementary sources (AGS21, AGS22 and AGS23). We found an X-ray counterpart for 65% of them (13/20) in the 7 Msec X-ray survey of GOODS-South with *Chandra* (Luo et al. 2017). Most of these galaxies were classified as AGN in the catalog of Luo et al. (2017) that identifies as AGN all galaxies with an intrinsic 0.5–7.0 keV luminosity higher than  $L_{\text{X,int}} = 3 \times 10^{42} \text{ erg s}^{-1}$ , among other criteria.

**Table 6.** The probability of an HST or IRAC random association (RaA) between the ALMA detection and the closest HST and IRAC galaxies for the 4 HST-Dark galaxies discussed in Sect. 7

ID	AGS4	AGS11	AGS15	AGS17
HST RaA (%)	4.52	–	9.14	2.12
IRAC RaA (%)	0.06	0.18	0.12	0.05

However, as our ALMA galaxies are biased toward highly star-forming galaxies, we decided to increase the minimum X-ray luminosity to a three times stronger X-ray luminosity threshold to avoid any contamination by star-formation. We also considered as AGN the galaxies exhibiting a hard X-ray spectrum. We therefore adopted here the following criteria to identify AGN: either (i)  $L_{X,\text{int}} > 10^{43} \text{ erg s}^{-1}$  (luminous X-ray sources) or (ii)  $\Gamma < 1.0$  (hard X-ray sources).

As the redshifts adopted by Luo et al. (2017) are not always the same as ours, when necessary we scaled the X-luminosities to our redshifts using Eq. (1) from Alexander et al. (2003), and assuming a photon index of  $\Gamma = 2$ .

Using these conservative criteria, we found that eight ALMA galaxies host an X-ray AGN (marked with a yellow star in Fig. 19). In order to compare the AGN fraction among ALMA detections with galaxies undetected by ALMA with similar masses and redshifts, we restricted our comparison to galaxies with  $M_\star > 3 \times 10^{10} M_\odot$  and  $1.8 < z < 4.5$  (rectangle in black dotted lines in Fig. 19). In this area encompassing 16 ALMA detections, we found that 50% of the ALMA sources host an AGN (8/16) as compared to only 14% (23/160) of the star-forming galaxies undetected by ALMA located in this same area (selected using the UVJ criteria recalled in Eq. (10) in the ZFOURGE catalog).

The presence of a high percentage of AGN among the galaxies detected by ALMA may reflect the fact that the ALMA sources are experiencing a starburst (well above the MS marked with a green dashed line in Fig. 19), possibly triggered by a merger that may dramatically reduce the angular momentum of the gas and drive it towards the center of the galaxies (e.g., Rovilos et al. 2012; Gatti et al. 2015; Lemastra et al. 2013) or violent disk instabilities (Bournaud et al. 2012). In addition, the high AGN fraction may be driven by the link between the presence of an AGN and the compactness of their host galaxy. Elbaz et al. (2018), Chang et al. (2017), and Ueda et al. (2018) suggest that the proportion of galaxies hosting an AGN increases with IR luminosity surface density. As discussed in Sect. 5.1, the size, and therefore the compactness of a galaxy, increases the likelihood of an ALMA detection at our angular resolution. Alternatively, ALMA might preferentially detect galaxies with a high gas, hence also dust, content, more prone to efficiently fuel the central black hole and trigger an AGN.

This fraction of galaxies with a high X-ray luminosity ( $L_{X,\text{int}} > 10^{43} \text{ erg s}^{-1}$ ) seems to be significantly higher than that found in some other ALMA surveys, in particular in Dunlop et al. (2017; 2/16) or Ueda et al. (2018; 4/12).

## 7. HST-dark galaxies

Some galaxies without  $H$ -band HST-WFC3 ( $1.6 \mu\text{m}$ ) counterparts have been discovered. We discuss below the possibility that these detections may be real HST-dark galaxies. Some ALMA detections previously attributed to an HST counterpart seem in fact to be either more distant galaxies, extremely close on the

line of sight to another galaxy, hidden by a foreground galaxy, or too faint at optical rest-frame wavelengths to be detected by HST.

It is already known that some of the most luminous millimeter or submillimeter galaxies can be completely missed at optical wavelengths (Wang et al. 2016), even in the deepest optical surveys, due to dust extinction. Some of these galaxies can also be undetected in the NIR (Wang et al. 2009).

Among the sources that do not have detections in the  $H$ -band of HST-WFC3, we distinguish the sources not detected by HST but detected by other instruments (we will discuss the importance of the IRAC filters), and sources undetected by HST and all of the other available instruments in the GOODS-South field (described in the Sect. 2.4).

Of the 20 galaxies detected in our main catalog, seven (35%) do not present an obvious HST counterpart. This number is slightly higher than the expected number of spurious sources ( $4 \pm 2$ ), predicted by the statistical analysis of our survey. To be more accurate, for three of these seven galaxies (AGS4, AGS15 and AGS17), an HST galaxy is in fact relatively close in the line of sight, but strong evidence, presented below, suggests that the HST galaxies are not the counterpart of the ALMA detections, and without the resolution of ALMA we would falsely associate the counterpart. For the four other ALMA detections without HST-WFC3 counterparts within a radius of  $0''.60$ , one of them (AGS11) has also been detected at other wavelengths. In this section, we will discuss four particularly interesting cases of HST-dark galaxies (AGS4, AGS11, AGS15 and AGS17), and discuss our reasons for classifying the other three as spurious sources.

Our four HST-dark galaxies (AGS4, AGS11, AGS15 and AGS17) have at least one feature in common, the presence of an IRAC detection and the fact that this IRAC detection is closer on the sky than the unrelated HST detection (see Table 6). The IRAC detections come from the Ashby et al. (2015) catalog, except for AGS15 where the position comes from the ZFOURGE catalog, using the Labbé et al. (2015) survey. The offset between the IRAC and HST sources might suggest that they are different sources. Figure 20 shows the IRAC contours at  $3.6 \mu\text{m}$  centered on the ALMA detection, superimposed over the HST  $H$ -band image. The presence of IRAC detections at these distances from the ALMA galaxies is a very strong driver for the identification of sources. The probability of random IRAC association is between one and two orders of magnitude less likely than random HST association for this range of distances, as shown in Fig. 7 and Table 6. The selection of ALMA candidates from galaxies detected in IRAC channels 1 and 2 but missed by HST-WFC3 at  $1.6 \mu\text{m}$  has already been experimented successfully by Wang et al. (in prep.), and seems to be a good indicator to detect HST-dark ALMA galaxies.

As each of our HST-dark galaxies have different features, we will discuss each galaxy individually.

### 7.1. AGS4

AGS4 is a close neighbor of ID<sub>CANDELS</sub> 8923. AGS4 is the fourth brightest detection in our survey with an S/N greater than 9. The center of the ALMA detection is located at only  $0''.38$  from ID<sub>CANDELS</sub> 8923, its closest neighboring galaxy. Before astrometric correction, this distance was only  $0''.21$ . This is therefore an example where the astrometric correction moves the ALMA galaxy away from the supposed counterpart. In Fig. 21, we can clearly see that the ALMA emission is offset from the observed  $H$ -band galaxy shown by the white arrow in Fig. 21. This



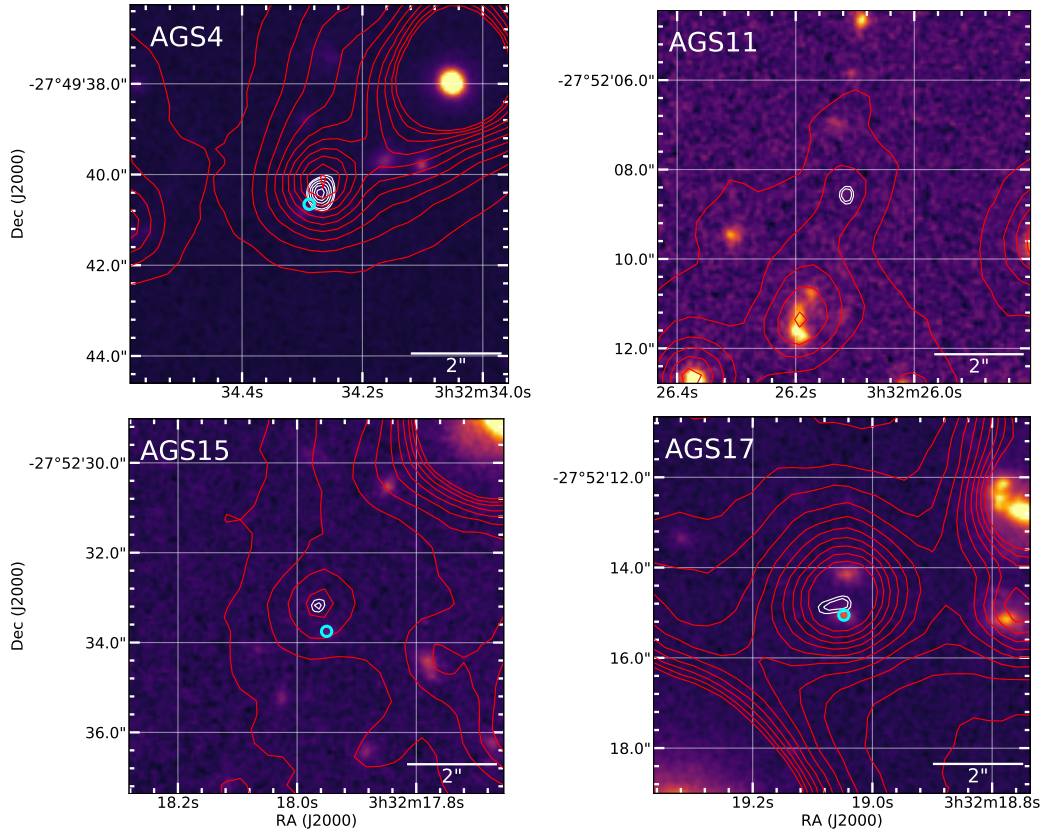


**Fig. 20.** IRAC 3.6  $\mu\text{m}$  (red contours, 3  $\mu\text{Jy}$ –30  $\mu\text{Jy}$  in steps of 3.0  $\mu\text{Jy}$ ) and ALMA 1.1 mm (white contours, 4, 4.5 then 5 to 10- $\sigma$  in steps of 1- $\sigma$ ) overlaid on 8''  $\times$  3'' HST  $H$ -band images. The position of the previously associated HST counterpart is shown by a cyan circle.

offset could be explained physically, for example, as a region extremely obscured by dust, within the same galaxy, greatly extinguishing the optical rest-frame emission that is revealed by ALMA. However, for AGS4, a series of clues suggest another explanation for this offset.

The first piece of evidence is the comparison between the IR SED at the position of the ALMA detection (the SEDs of all of the galaxies detected in this paper will be presented in a future publication, Franco et al., in prep.) and the redshift of the optical galaxy. The redshift of the optical galaxy is  $z = 0.241$ , whereas the far IR SED peaks around 350  $\mu\text{m}$  (see Fig. 22). If AGS4 was a dusty star-forming region on the outskirts of 8923, this infrared SED would suggest an abnormally cold dust temperature. It is therefore more probable that AGS4 is not part of ID<sub>CANDELS</sub> 8923, and is a dusty distant galaxy. The fuzzy emission in the  $H$ -band HST image, exactly centered at the position of the ALMA detection (see Fig. 21) has not led to any detection in the CANDELS catalog. In the  $V$ -band HST images, only ID<sub>CANDELS</sub> 8923 is present, seen to the South-East of the position of the ALMA detection (indicated by a white cross). No emission is visible at the exact position of the ALMA detection. In the  $z$ -band, a barely visible detection appears extremely close to the center of the image.

The second clue is the detection of a galaxy with redshift  $z = 3.76$  in the FourStar galaxy evolution survey, 0''16 from the ALMA detection. This redshift is much more consistent with the peak of the IR SED. The ZFOURGE survey is efficient at detecting galaxies with redshifts between 1 and 4 by using a

$K_s$ -band detection image (instead of  $H$ -band as used for the CANDELS survey), and also due to the high spectral resolution ( $\lambda/\Delta\lambda \approx 10$ ) of the medium-bandwidth filters which provide fine sampling of the Balmer/4000 Å spectral break at these redshifts (Tomczak et al. 2016). Furthermore, the stellar mass derived in the ZFOURGE catalog ( $10^{10.50} M_\odot$  compared with  $10^{7.64} M_\odot$  in the CANDELS catalog) is more consistent with the expected mass of galaxies detected by ALMA. Indeed as shown in this paper, and as already shown by Dunlop et al. (2017), ALMA tends to reveal the most massive dusty galaxies.

The third piece of evidence is the presence, in the *Spitzer*-CANDELS catalog (Ashby et al. 2015), of a galaxy detected with the IRAC filters only 0''1 from our ALMA detection. This IRAC galaxy has a magnitude of 22.51 at 3.6  $\mu\text{m}$ , measured within an aperture of 2''4 radius.

We also note that Rujopakarn et al. (2016) detect a radio galaxy at  $S/N \approx 17$  only 55 mas from the center of the ALMA detection shown in Fig. 21 (the positional accuracy of this VLA image is 40 mas). Additionally, AGS4 is detected in two of the three *Chandra* bands: 0.5–7.0 keV (full band; FB) and 0.5–2.0 keV (soft band; SB), but not at 2–7 keV (hard band; HB) from the 7 Ms *Chandra* observations of the GOODS-South field. The integrated X-ray flux is only  $6.86 \times 10^{40} \text{ erg s}^{-1}$ , but this galaxy is classified as an AGN in the 7 Ms catalog.

The detection of a local galaxy at this position has been largely documented (e.g., Hsu et al. 2014; Skelton et al. 2014; Santini et al. 2015). In contrast, some studies present the galaxy

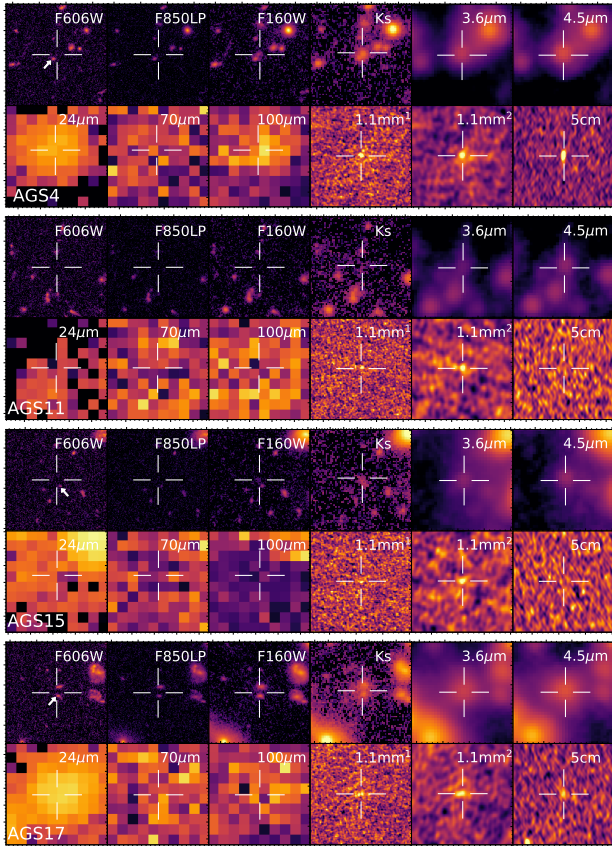


**Fig. 21.** Postage stamps of  $10 \times 10$  arcsec from HST-WFC3 at  $0.606 \mu\text{m}$  to VLA at 5 cm, for the four optically-dark galaxies discussed in Sect. 7. For the two ALMA images at 1.1 mm, those marked by <sup>1</sup> correspond to the non-tapered images, those marked by <sup>2</sup> correspond to the  $0''60$ -mosaic images. The  $K_s$ -band thumbnail comes from the super-deep detection image described in Sect. 2.4.1. All images are centered on the ALMA detection. We indicate with white arrows the position of the previously associated HST counterpart.

located at this location as a distant galaxy. Cardamone et al. (2010) take advantage of the 18-medium-band photometry from the Subaru telescope and the photometric redshift code EAZY (Brammer et al. 2008) to derive a redshift  $z = 3.60$ . Wuyts et al. (2008) find a redshift of  $z = 3.52$  also using EAZY. We can also add a redshift determination by Rafferty et al. (2011) using the Zurich extragalactic bayesian redshift analyzer (ZEBRA; Feldmann et al. 2006), at  $z = 2.92$ . These determinations of high redshift by independent studies support the existence of a distant galaxy at this position.

Although close, the two sources (ID<sub>CANDELS</sub> 8923 and 8923b) were successfully de-blended using two light-profile models, determined by fitting the HST  $H$ -band image with Galfit. The two sources were then fit simultaneously using these two models on all of the available images, fixing the profile to that observed in the  $H$  band. The SEDs of these two galaxies are shown in Fig. 23, in blue for the HST galaxy and in orange for the ALMA galaxy, together with the photometric redshift probability distribution for AGS4. The redshifts were estimated using EAZY. For the blue HST galaxy we found  $z = 0.09^{+0.06}_{-0.07}$ , in good agreement with that found by Skelton et al. (2014). On the other hand, the redshift found for AGS4 is slightly higher than

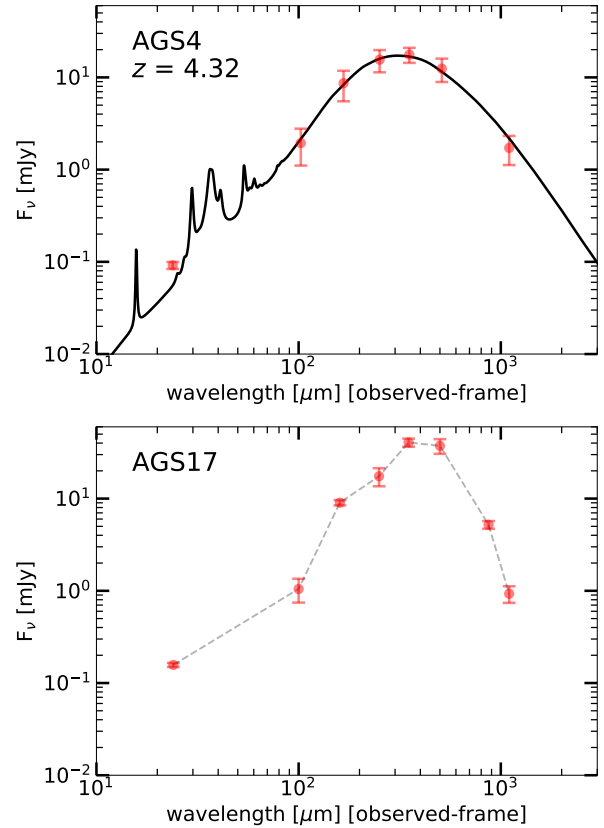


**Fig. 22.** Spectral energy distributions (SED) of the two optically-dark galaxies AGS4 and AGS17. The flux densities from 100 to  $500 \mu\text{m}$  are from GOODS-Herschel Elbaz et al. (2011). AGS4 (top) ( $z = 4.32$ , see Sect. 7) is fitted with the model of Schreiber et al. (2018). The SED of AGS17 (bottom panel), which has no known redshift, is simply presented with an interpolation between the observed flux densities to illustrate that it peaks around  $400 \mu\text{m}$ . This peak is inconsistent with the redshifts of the two optical sources with ID<sub>CANDELS</sub> 4414 ( $z = 1.85$ ) and 4436 ( $z = 0.92$ )

in ZFOURGE, with  $z_{\text{AGS4}} = 4.32^{+0.25}_{-0.21}$ . However, we can also see a secondary peak in the redshift probability distribution, at the position of the ZFOURGE redshift. As the Balmer break is well established in the  $K$ -band, we consider that the redshift determination ( $z_{\text{AGS4}} = 4.32^{+0.25}_{-0.21}$ ) is robust and we adopt this redshift for AGS4. The stellar mass of the ALMA galaxy was then computed with FAST (Kriek et al. 2009), and we found  $10^{11.45 \pm 0.2} M_{\odot}$  (probably slightly overestimated due to the presence of an AGN, suggested by a flux excess in the IRAC bands). The IR SED of this galaxy is shown in Fig. 22. For the first time, thanks to ALMA, we can argue that there exists, at this position, not one but two galaxies, close to each other on the line of sight.

## 7.2. AGS11

AGS11 is detected at 1.1 mm with a flux of 1.4 mJy ( $S/N \sim 8$ ) without any counterpart in the deep HST image. However, the galaxy is also detected by IRAC, confirming the existence of a galaxy at this position. A galaxy was recently found, for the first time, in the ZFOURGE catalog at  $0''18$  from the center of the ALMA position. This galaxy was not detected directly in the

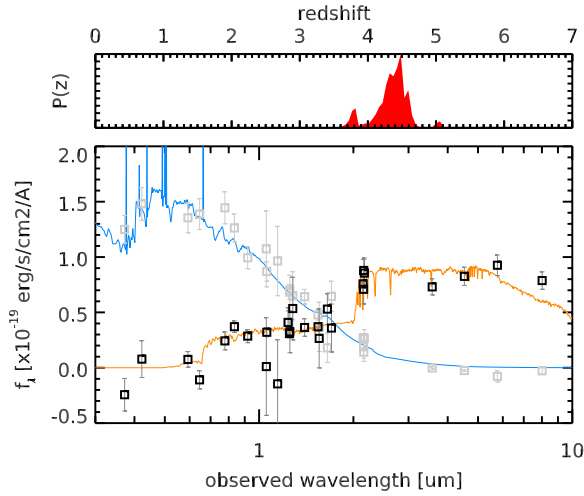


**Fig. 23.** Spectral energy distributions of AGS4 and ID<sub>CANDELS</sub> 8923. Aperture photometry allows the separation between the local galaxy detected by HST (blue, and indicated by a white arrow in Fig. 21, ID<sub>CANDELS</sub> 8923) and the distant galaxy detected by ALMA (orange). The top panel shows the photometric redshift probability distribution of AGS4. As the Balmer break is well established in the *K*-band, we consider that this redshift determination is robust, and we adopt the derived redshift  $z_{\text{AGS4}} = 4.32^{+0.25}_{-0.21}$  and stellar mass ( $10^{11.45 \pm 0.2} M_{\odot}$ ) values for AGS4.

Magellan image but in a super-deep combined *K<sub>s</sub>*-band image at  $4.5\sigma$ . From this position, the flux in the IRAC-bands have been extracted with S/Ns of 26, 34, 8 and 8 at  $3.6 \mu\text{m}$ ,  $4.5 \mu\text{m}$ ,  $5.8 \mu\text{m}$  and  $8.0 \mu\text{m}$  respectively.

This HST-dark galaxy falls in a projected overdensity on the sky, consisting of sources in the redshift range  $3.42 \leq z \leq 3.56$  and brighter than  $K_s < 24.9$  (Forrest et al. 2017). This density has been computed by Forrest et al. (2017) using the 7th nearest-neighbor technique (Papovich et al. 2010). This overdensity, centered at RA =  $53.08^\circ$ , Dec =  $-27.85^\circ$ , extends beyond approximately 1.8 Mpc.

The redshift derived in the ZFOURGE catalog is  $z = 4.82$ , making it the farthest galaxy detected in this blind survey. However, we remain cautious regarding this redshift, as this entry has been flagged in the ZFOURGE catalog (use = 0) due to the S/N of this galaxy (4.7) being below the limit defining galaxies with good photometry ( $S/N \geq 5$ ). This galaxy is the only galaxy in our catalog flagged in the ZFOURGE catalog. For this reason, we represent it with an empty circle Fig. 19. AGS11 has not been detected in the 7 Ms *Chandra* survey.

The stellar mass, derived in the ZFOURGE catalog,  $3.55 \times 10^{10} M_{\odot}$ , is consistent with the masses of all of the other ALMA galaxies found in this survey. What is particularly interesting in the multiwavelength images of this galaxy is that AGS11 is detectable only by ALMA and in the IRAC-bands (in non-stacked images). Outside of these wavelengths, no emission is detectable.

### 7.3. AGS15

AGS15 is at a distance of  $0''.59$  from its possible HST counterpart (ID<sub>CANDELS</sub> 3818) after astrometric correction, corresponding to a physical distance of 4.33 kpc. This is the largest HST-ALMA offset in our entire catalog. The IRAC position, in contrast, matches much more closely with the ALMA posi-

tion, with an offset of only  $0''.14$ . The stellar mass of the optical galaxy, given by the ZFOURGE catalog ( $7.24 \times 10^9 M_{\odot}$ ) would have made AGS15 a galaxy lying far from the median stellar mass ( $1.1 \times 10^{11} M_{\odot}$ ) of our survey. The redshift of ID<sub>CANDELS</sub> 3818 ( $z = 3.46$ ) is nevertheless consistent with the other redshifts found in this study.

### 7.4. AGS17

AGS17 is a close neighbor ( $0''.27$ ) of ID<sub>CANDELS</sub> 4414 ( $z = 1.85$ ). AGS17 is one of the three galaxies detected by Hodge et al. (2013) at  $870 \mu\text{m}$  in the ALMA field of view (along with AGS8 and AGS15 previously discussed). The counterpart of AGS17 was attributed to ID<sub>CANDELS</sub> 4414 by Wiklind et al. (2014) with an offset between the ALMA detection and the corresponding F160W object of  $0''.32$ . Again, there are indications that the identification may be false: the peak of the IR SED is  $\sim 400 \mu\text{m}$  (see Fig. 22), suggesting a more distant galaxy. To be detected with the flux densities reported in Table 4, a galaxy at  $z = 1.85$  would have an extraordinarily high star formation rate ( $\sim 820 \pm 240 M_{\odot} \text{ yr}^{-1}$ ), using the IR SEDs of Schreiber et al. (2018). If truly associated with the CANDELS counterpart, this galaxy would be an extreme starburst with an SFR  $59 \pm 17$  times greater than the  $\text{SFR}_{\text{MS}}$ . Galaxies with these properties cannot be ruled out, as galaxies with much higher star formation rates (and offsets from the main sequence) have already been observed (e.g., Pope et al. 2005; Fu et al. 2013). However, such objects are relatively rare. In addition, the stellar mass of ID<sub>CANDELS</sub> 4414 ( $10^{10} M_{\odot}$ ) is inconsistent with the trend of the other detections (more than one order of magnitude below the median stellar mass of our catalog).

Another galaxy (ID<sub>CANDELS</sub> 4436) is relatively close ( $0''.57$ ) to the ALMA detection. The position of the ALMA detection, which is between ID<sub>CANDELS</sub> 4414 and ID<sub>CANDELS</sub> 4436, could be the signature of a major merger occurring between these two galaxies. The emission observed by ALMA could result in this case from the heating of the dust caused by the interaction of these two galaxies, but the redshift determination of  $0.92^{+0.04}_{-0.18}$  by Le PHARE (Arnouts et al. 1999; Ilbert et al. 2006) dismisses this hypothesis.

After subtraction of the 2 galaxies close on the line of sight (ID<sub>CANDELS</sub> 4414 and 4436) in the HAWK-I image, a diffuse source is revealed (half-light radius =  $1''.55 \pm 0''.12$ , sersic index = 1.0). Lower resolution ALMA observations would be needed in order to correctly measure the total submm flux of this extended source.

We also note the position of the IRAC source, located only  $0''.06$  from the ALMA detection.

### 7.5. Discussion

Of the total 23 detections in this survey, seven do not show an HST *H*-band counterpart. This lack of counterpart could arise from an occultation of the optical counterpart by a foreground galaxy, faint emission at optical wavelengths, or a spurious ALMA detection.

For the four galaxies previously discussed (AGS4, AGS11, AGS15 and AGS17), we observe a signal with IRAC at  $3.6 \mu\text{m}$  and  $4.5 \mu\text{m}$ , despite the limiting sensitivity of IRAC (26 AB mag at  $3\sigma$  for both  $3.6$  and  $4.5 \mu\text{m}$ ; Ashby et al. 2015) being lower than HST-WFC3 (28.16 AB mag at  $5\sigma$  for F160W; Guo et al. 2013) in the respective images. Furthermore, two of the galaxies (AGS15 and AGS17) have already been detected at submillimeter wavelengths ( $870 \mu\text{m}$ ) by Hodge et al. (2013).



The other three galaxies (AGS14, AGS16 and AGS19) are not detected at any other wavelength hence there is a high probability that they are spurious. This number is in good agreement with the expected number of spurious sources for our sample ( $4 \pm 2$ ).

Figure 5 gives us a glimpse into how sources can be falsely associated with an HST galaxy. When the offset correction is applied, the three galaxies shown with magenta lines move further away from the center position ( $\Delta\delta = 0$ ,  $\Delta\alpha = 0$ ), rather than closer to it. Another source also appears to show this behavior: AGS20, seen in the lower left quadrant of Fig. 5. The ALMA detection of AGS20 seems to be clearly offset from an HST galaxy, similar to AGS4. To ensure that there is not a more distant counterpart for AGS20 obscured by the HST source, we performed the same analysis as described in Sect. 7 and illustrated in Fig. 23. The result of the decomposition suggests that the ALMA and HST sources are either two components of the same galaxy or two galaxies merging at this position. A spectroscopic analysis of AGS20 would allow for a distinction between these two possibilities.

The IRAC detections seem to be particularly useful to confirm the existence of a source. In the main catalog, except for the three galaxies that we consider as spurious, all others are also detected in the IRAC filters.

In conclusion, we have detected 20% HST-dark galaxies (4 out of 20 robust detections) with a counterpart confirmed at least by IRAC. This proportion may depend in a manner that we cannot address here on the depth of the optical and millimeter images. Knowing that these HST-dark galaxies are dust, hence metal, rich they are likely progenitors of the most massive galaxies seen at  $z = 0$ , hence potentially hosted by massive groups or clusters of galaxies. Two of these HST-dark galaxies have a tentative redshift of  $z = 4.82$  and  $z = 3.76$ , we therefore expect these galaxies to be located on average within  $z \sim 4-5$ . These two galaxies are already massive ( $10^{10.55} M_\odot$  and  $10^{10.50} M_\odot$  respectively), suggesting that this population of galaxies is particularly interesting for understanding massive galaxy formation during the first billion years after the Big Bang. Spectroscopy with the JWST NIRSpec instrument will permit very sensitive spectroscopic detection of H $\alpha$  emission at  $z < 6.6$ , and hence an important new tool to measure redshifts of these HST-dark galaxies. GOODS-South will undoubtedly be a venue for extensive JWST spectroscopy, including Guaranteed Time Observations. Spectral scan observations with ALMA can also be a powerful tool to determine the distances, and hence physical properties, of this intriguing population of HST-dark galaxies.

## 8. Summary and conclusions

The GOODS-ALMA survey covers an area of 69 arcmin<sup>2</sup> matching the deepest HST-WFC3 coverage of the GOODS-South field at 1.1 mm and at a native resolution of  $\sim 0''.24$ . We used a  $0''.60$  tapered mosaic due to the large number of independent beams at the native resolution. A comparison of the HST source positions with existing catalogs such as Pan-STARRS allowed us to correct the HST astrometry of the GOODS-South field from both a global and local offset (equivalent to a distortion map, see also Dickinson et al., in prep.). We found a median offset between the HST and ALMA images of  $-96 \pm 113$  mas in right ascension,  $\alpha$ , and  $261 \pm 125$  mas in declination,  $\delta$ . The main conclusions from our study are listed below.

1. 20 galaxies brighter than 0.7 mJy at 1.1 mm. We detect in total 20 sources above a detection threshold that guarantees

an 80% purity (less than 20% chance to be spurious). Among these 20 galaxies (with an  $S/N > 4.8$ ), we expect  $4 \pm 2$  spurious galaxies from the analysis of the inverted map and we identify 3 probably spurious detections with no HST nor *Spitzer*-IRAC counterpart, consistent with the expected number of spurious galaxies. An additional three sources with HST counterparts are detected either at high significance in the higher resolution map, or with different detection-algorithm parameters ensuring a purity greater than 80%. Hence we identify in total 20 robust detections.

2. Pushing further in redshift the blind detection of massive galaxies with ALMA. The sources exhibit flux densities ranging from 0.6 to 2 mJy, have a median redshift (and rms) of  $z = 2.92 \pm 0.20$  and stellar mass of  $M_\star = (1.1 \pm 0.4) \times 10^{11} M_\odot$ . By comparison with deeper but smaller ALMA extragalactic surveys (Aravena et al. 2016; Dunlop et al. 2017; González-López et al. 2017; Ueda et al. 2018), our redshift distribution is shifted to higher values even though our survey is shallower. This is due to the low surface density of massive, metal hence dust-rich, galaxies at high redshifts. The size of the ALMA survey is therefore a key parameter to detect high redshift galaxies.
3. 20% HST-dark galaxies. The detection criteria of this main catalog allowed us to identify sources with no HST counterparts. Out of the 20 galaxies listed above, and excluding the three candidate spurious detections, we identified four optically-dark or HST-dark galaxies with the request of 80% purity and with a *Spitzer*-IRAC counterpart at  $3.6 \mu\text{m}$  and  $4.5 \mu\text{m}$ , confirming the existence of a galaxy at the position of the ALMA detection. It is not the first time that such HST-dark sources have been found using e.g., infrared color selections (*H*-dropouts, see e.g., Wang et al. 2016), but their identification in an unbiased survey at the depth of ALMA in the millimeter range allows us to determine that 20% of the ALMA sources detected at 1.1 mm above  $\sim 0.7$  mJy are HST-dark (4/20 sources in the main catalog). Two of these sources are detected in the near-infrared in the ZFOURGE catalog, with a photometric redshift of  $z_{\text{phot}} = 4.32$  (derived in this study; AGS4, also detected in the radio with VLA) and 4.82 (AGS11). The other two sources (AGS15 & AGS17) were detected with the LABOCA ECDFS Submillimeter Survey (LESS) at  $870 \mu\text{m}$  and with ALMA after a follow-up at the same wavelength, confirming that they were not the result of source blending (Hodge et al. 2013).
4. Exceptionally high AGN fraction. We found a high proportion of AGNs in our ALMA 1.1 mm sample with 40% (8 out of 20 robust detections) detected in the 7 Msec *Chandra* X-ray survey of GOODS-South in the 0.5–7.0 keV band with a X-luminosity greater than  $10^{43} \text{ erg s}^{-1}$ . Limiting our analysis to the ALMA sources with a redshift and stellar mass determination, we found that 50% of the ALMA sources located in a well-defined stellar mass ( $M_\star > 3 \times 10^{10} M_\odot$ ) – redshift ( $z \sim 1.8-4.5$ ) range host an AGN as compared to only 14% for the galaxies located within the same zone but undetected by ALMA. This excess AGN contribution may be due to the fact that the ALMA galaxies are preferentially in a starburst mode due to our detection limit – hence possibly experiencing a merger – or/and that the high-resolution of ALMA favors unresolved, hence compact, sources knowing that the mechanism that leads to such compact star-formation may also trigger an AGN.
5. Alleviating the degeneracy of the bright end of the ALMA counts. The differential and cumulative number counts of

our 20 primary detections allowed us to partly alleviate the degeneracy observed above  $1\text{ mJy beam}^{-1}$  in previous (sub)millimeter studies. We show that  $\sim 15\%$  of the extragalactic background light is resolved into individual sources at  $0.75\text{ mJy}$ . By extrapolation,  $\sim 50\%$  of the EBL is resolved at  $0.1\text{ mJy}$ .

**Acknowledgements.** We wish to thank Ivo Labbé for sharing with us the IRAC/GREATS images and Bahram Mobasher for sharing the spectroscopic redshift of AGS4 with us. This paper makes use of the following ALMA data: ADS/JAO.ALMA#2015.1.00543.S. ALMA is a partnership of ESO (representing its member states), NSF (USA) and NINS (Japan), together with NRC (Canada), MOST and ASIAA (Taiwan), and KASI (Republic of Korea), in cooperation with the Republic of Chile. The Joint ALMA Observatory is operated by ESO, AUI/NRAO and NAOJ. RD and NN gratefully acknowledge the support provided by the BASAL Center for Astrophysics and Associated Technologies (CATA) through grant PFB-06 Etapa II. Support for BM was provided by the DFG priority program 1573 “The physics of the interstellar medium”. DMA thanks the Science and Technology Facilities Council (STFC) for support from grant ST/L00075X/1. WR is supported by JSPS KAKENHI Grant Number JP15K17604, Thailand Research Fund/Office of the Higher Education Commission Grant Number MRG6080294, and Chulalongkorn University’s CUniverse. NN acknowledges funding from Fondecyt 1171506.

## References

- Alexander, D. M., Bauer, F. E., Brandt, W. N., et al. 2003, *AJ*, **125**, 383  
 Alexander, D. M., Brandt, W. N., Smail, I., et al. 2008, *AJ*, **135**, 1968  
 Aravena, M., Decarli, R., Walter, F., et al. 2016, *ApJ*, **833**, 68  
 Arnouts, S., Cristiani, S., Moscardini, L., et al. 1999, *MNRAS*, **310**, 540  
 Ashby, M. L. N., Willner, S. P., Fazio, G. G., et al. 2013, *ApJ*, **769**, 80  
 Ashby, M. L. N., Willner, S. P., Fazio, G. G., et al. 2015, *ApJS*, **218**, 33  
 Barger, A. J., Cowie, L. L., Sanders, D. B., et al. 1998, *Nature*, **394**, 248  
 Barro, G., Faber, S. M., Pérez-González, P. G., et al. 2013, *ApJ*, **765**, 104  
 Barro, G., Kriek, M., Pérez-González, P. G., et al. 2016, *ApJ*, **827**, L32  
 Barro, G., Kriek, M., Pérez-González, P. G., et al. 2017, *ApJ*, **851**, L40  
 Béthermin, M., Le Floc’h, E., Ilbert, O., et al. 2012, *A&A*, **542**, A58  
 Béthermin, M., De Breuck, C., Sargent, M., & Daddi, E. 2015, *A&A*, **576**, L9  
 Béthermin, M., Wu, H.-Y., Lagache, G., et al. 2017, *A&A*, **607**, A89  
 Blain, A. W., Smail, I., Ivison, R. J., Kneib, J.-P., & Frayer, D. T. 2002, *Phys. Rep.*, **369**, 111  
 Bournaud, F., Juneau, S., Le Floc’h, E., et al. 2012, *ApJ*, **757**, 81  
 Brammer, G. B., van Dokkum, P. G., & Coppi, P. 2008, *ApJ*, **686**, 1503  
 Bruzual, G., & Charlot, S. 2003, *MNRAS*, **344**, 1000  
 Calzetti, D., Armus, L., Bohlin, R. C., et al. 2000, *ApJ*, **533**, 682  
 Caputi, K. I., Dunlop, J. S., McLure, R. J., et al. 2012, *ApJ*, **750**, L20  
 Caputi, K. I., Ilbert, O., Laigle, C., et al. 2015, *ApJ*, **810**, 73  
 Cardamone, C. N., van Dokkum, P. G., Urry, C. M., et al. 2010, *ApJS*, **189**, 270  
 Carniani, S., Maiolino, R., De Zotti, G., et al. 2015, *A&A*, **584**, A78  
 Casey, C. M., Chen, C.-C., Cowie, L. L., et al. 2013, *MNRAS*, **436**, 1919  
 Chabrier, G. 2003, *PASP*, **115**, 763  
 Chang, Y.-Y., Le Floc’h, E., Juneau, S., et al. 2017, *ApJS*, **233**, 19  
 Chapman, S. C., Blain, A. W., Ivison, R. J., & Smail, I. R. 2003, *Nature*, **422**, 695  
 Chapman, S. C., Blain, A. W., Smail, I., & Ivison, R. J. 2005, *ApJ*, **622**, 772  
 Cimatti, A., Cassata, P., Pozzetti, L., et al. 2015, *A&A*, **482**, 21  
 Condon, J. J. 1997, *PASP*, **109**, 166  
 Coppin, K., Halpern, M., Scott, D., Borys, C., & Chapman, S. 2005, *MNRAS*, **357**, 1022  
 Coppin, K., Halpern, M., Scott, D., et al. 2008, *MNRAS*, **384**, 1597  
 Daddi, E., Dickinson, M., Chary, R., et al. 2005, *ApJ*, **631**, L13  
 Daddi, E., Bournaud, F., Walter, F., et al. 2010, *ApJ*, **713**, 686  
 Dole, H., Lagache, G., Puget, J.-L., et al. 2006, *A&A*, **451**, 417  
 Dunlop, J. S., McLure, R. J., Biggs, A. D., et al. 2017, *MNRAS*, **466**, 861  
 Eddington, A. S. 1913, *MNRAS*, **73**, 359  
 Elbaz, D., Dickinson, M., Hwang, H. S., et al. 2011, *A&A*, **533**, A119  
 Elbaz, D., Leiton, R., Nagar, N., et al. 2018, *A&A*, **616**, A110  
 Fazio, G. G., Hora, J. L., Allen, L. E., et al. 2004, *ApJS*, **154**, 10  
 Feldmann, R., Carollo, C. M., Porciani, C., et al. 2006, *MNRAS*, **372**, 565  
 Fixsen, D. J., Dwek, E., Mather, J. C., Bennett, C. L., & Shafer, R. A. 1998, *ApJ*, **508**, 123  
 Flewelling, H. A., Magnier, E. A., Chambers, K. C., et al. 2016, *ArXiv e-prints* [arXiv:1612.05243]  
 Fontana, A., Dunlop, J. S., Paris, D., et al. 2014, *A&A*, **570**, A11  
 Forrest, B., Tran, K.-V. H., Broussard, A., et al. 2017, *ApJ*, **838**, L12  
 Fu, H., Cooray, A., Feruglio, C., et al. 2013, *Nature*, **498**, 338  
 Fujimoto, S., Ouchi, M., Ono, Y., et al. 2016, *ApJS*, **222**, 1  
 Fujimoto, S., Ouchi, M., Shibuya, T., & Nagai, H. 2017, *ApJ*, **850**, 83  
 Gaia Collaboration (Brown, A. G. A., et al.) 2016, *A&A*, **595**, A2  
 Gatti, M., Lamastra, A., Menci, N., Bongiorno, A., & Fiore, F. 2015, *A&A*, **576**, A32  
 Geach, J. E., Dunlop, J. S., Halpern, M., et al. 2017, *MNRAS*, **465**, 1789  
 González-López, J., Bauer, F. E., Romero-Cañizales, C., et al. 2017, *A&A*, **597**, A41  
 Gordon, K. D., Galliano, F., Hony, S., et al. 2010, *A&A*, **518**, L89  
 Griffin, M. J., Abergel, A., Abreu, A., et al. 2010, *A&A*, **518**, L3  
 Grogin, N. A., Kocevski, D. D., Faber, S. M., et al. 2011, *ApJS*, **197**, 35  
 Guo, Y., Ferguson, H. C., Giavalisco, M., et al. 2013, *ApJS*, **207**, 24  
 Hainline, L. J., Blain, A. W., Smail, I., et al. 2011, *ApJ*, **740**, 96  
 Hales, C. A., Murphy, T., Curran, J. R., et al. 2012, *Astrophysics Source Code Library*, [record ascl:1208.009]  
 Hao, C. N., Mao, S., Deng, Z. G., Xia, X. Y., & Wu, H. 2006, *MNRAS*, **370**, 1339  
 Hatsukade, B., Ohta, K., Seko, A., Yabe, K., & Akiyama, M. 2013, *ApJ*, **769**, L27  
 Hatsukade, B., Kohn, K., Umehata, H., et al. 2016, *PASJ*, **68**, 36  
 Hodge, J. A., Karim, A., Smail, I., et al. 2013, *ApJ*, **768**, 91  
 Hodge, J. A., Swinbank, A. M., Simpson, J. M., et al. 2016, *ApJ*, **833**, 103  
 Hogg, D. W., & Turner, E. L. 1998, *PASP*, **110**, 727  
 Holland, W. S., Robson, E. I., Gear, W. K., et al. 1999, *MNRAS*, **303**, 659  
 Hsieh, B.-C., Wang, W.-H., Hsieh, C.-C., et al. 2012, *ApJS*, **203**, 23  
 Hsu, L.-T., Salvato, M., Nandra, K., et al. 2014, *ApJ*, **796**, 60  
 Huang, J.-S., Zheng, X. Z., Rigopoulou, D., et al. 2011, *ApJ*, **742**, L13  
 Hughes, D. H., Serjeant, S., Dunlop, J., et al. 1998, *Nature*, **394**, 241  
 Ikarashi, S., Ivison, R. J., Caputi, K. I., et al. 2015, *ApJ*, **810**, 133  
 Ikarashi, S., Caputi, K. I., Ohta, K., et al. 2017, *ApJ*, **849**, L36  
 Ilbert, O., Arnouts, S., McCracken, H. J., et al. 2006, *A&A*, **457**, 841  
 Inami, H., Bacon, R., Brinchmann, J., et al. 2017, *A&A*, **608**, A2  
 Karim, A., Swinbank, A. M., Hodge, J. A., et al. 2013, *MNRAS*, **432**, 2  
 Knudsen, K. K., van der Werf, P. P., & Kneib, J.-P. 2008, *MNRAS*, **384**, 1611  
 Kocevski, D. D., Barro, G., Faber, S. M., et al. 2017, *ApJ*, **846**, 112  
 Koekemoer, A. M., Faber, S. M., Ferguson, H. C., et al. 2011, *ApJS*, **197**, 36  
 Kovács, A., Chapman, S. C., Dowell, C. D., et al. 2006, *ApJ*, **650**, 592  
 Kriek, M., van Dokkum, P. G., Franx, M., et al. 2008, *ApJ*, **677**, 219  
 Kriek, M., van Dokkum, P. G., Labbé, I., et al. 2009, *ApJ*, **700**, 221  
 Kurk, J., Cimatti, A., Daddi, E., et al. 2013, *A&A*, **549**, A63  
 Labbé, I., Oesch, P. A., Illingworth, G. D., et al. 2015, *ApJS*, **221**, 23  
 Lamastra, A., Menci, N., Fiore, F., et al. 2013, *A&A*, **559**, A56  
 Laporte, N., Bauer, F. E., Troncoso-Iribarren, P., et al. 2017, *A&A*, **604**, A132  
 Li, Y., Zheng, X. Z., Gu, Q.-S., et al. 2016, *AJ*, **152**, 201  
 Lindner, R. R., Baker, A. J., Omont, A., et al. 2011, *ApJ*, **737**, 83  
 Luo, B., Brandt, W. N., Xue, Y. Q., et al. 2017, *ApJS*, **228**, 2  
 Lutz, D., Poglitsch, A., Altieri, B., et al. 2011, *A&A*, **532**, A90  
 Magnelli, B., Elbaz, D., Chary, R. R., et al. 2009, *A&A*, **496**, 57  
 Magnelli, B., Lutz, D., Santini, P., et al. 2012, *A&A*, **539**, A155  
 Magnelli, B., Popesso, P., Berta, S., et al. 2013, *A&A*, **553**, A132  
 Maiolino, R., Carniani, S., Fontana, A., et al. 2015, *MNRAS*, **452**, 54  
 Martí-Vidal, I., Pérez-Torres, M. A., & Lobanov, A. P. 2012, *A&A*, **541**, A135  
 McMullin, J. P., Waters, B., Schiebel, D., Young, W., & Golap, K. 2007, in *Astronomical Data Analysis Software and Systems XVI* eds. R. A. Shaw, F. Hill, & D. J. Bell, *ASP Conf. Ser.*, **376**, 127  
 Michałowski, M., Hjorth, J., & Watson, D. 2010, *A&A*, **514**, A67  
 Mohan, N., & Rafferty, D. 2015, *Astrophysics Source Code Library* [record ascl:1502.007]  
 Momcheva, I. G., Brammer, G. B., van Dokkum, P. G., et al. 2016, *ApJS*, **225**, 27  
 Moster, B. P., Somerville, R. S., Newman, J. A., & Rix, H.-W. 2011, *ApJ*, **731**, 113  
 Narayanan, D., Hayward, C. C., Cox, T. J., et al. 2010, *MNRAS*, **401**, 1613  
 Noeske, K. G., Weiner, B. J., Faber, S. M., et al. 2007, *ApJ*, **660**, L43  
 Nonino, M., Dickinson, M., Rosati, P., et al. 2009, *ApJS*, **183**, 244  
 Oke, J. B., & Gunn, J. E. 1983, *ApJ*, **266**, 713  
 Ono, Y., Ouchi, M., Kurono, Y., & Momose, R. 2014, *ApJ*, **795**, 5  
 Oteo, I., Zwaan, M. A., Ivison, R. J., Smail, I., & Biggs, A. D. 2016, *ApJ*, **822**, 36  
 Padilla, N. D., & Strauss, M. A. 2008, *MNRAS*, **388**, 1321  
 Papovich, C., Momcheva, I., Willmer, C. N. A., et al. 2010, *ApJ*, **716**, 1503  
 Papovich, C., Labbé, I., Glazebrook, K., et al. 2016, *Nat. Astron.*, **1**, 0003  
 Peng, C. Y., Ho, L. C., Impey, C. D., & Rix, H.-W. 2010, *AJ*, **139**, 2097  
 Persson, S. E., Murphy, D. C., Smee, S., et al. 2013, *PASP*, **125**, 654

- Poglitich, A., Waelkens, C., Geis, N., et al. 2010, *A&A*, **518**, L2
- Pope, A., Borys, C., Scott, D., et al. 2005, *MNRAS*, **358**, 149
- Pope, A., Chary, R.-R., Alexander, D. M., et al. 2008, *ApJ*, **675**, 1171
- Rafferty, D. A., Brandt, W. N., Alexander, D. M., et al. 2011, *ApJ*, **742**, 3
- Ranalli, P., Comastri, A., Vignali, C., et al. 2013, *A&A*, **555**, A42
- Retzlaff, J., Rosati, P., Dickinson, M., et al. 2010, *A&A*, **511**, A50
- Rieke, G. H., Young, E. T., Engelbracht, C. W., et al. 2004, *ApJS*, **154**, 25
- Rodighiero, G., Daddi, E., Baronchelli, I., et al. 2011, *ApJ*, **739**, L40
- Rovilos, E., Comastri, A., Gilli, R., et al. 2012, *A&A*, **546**, A58
- Rujopakarn, W., Dunlop, J. S., Rieke, G. H., et al. 2016, *ApJ*, **833**, 12
- Salpeter, E. E. 1955, *ApJ*, **121**, 161
- Santini, P., Ferguson, H. C., Fontana, A., et al. 2015, *ApJ*, **801**, 97
- Sargent, M. T., Béthermin, M., Daddi, E., & Elbaz, D. 2012, *ApJ*, **747**, L31
- Schechter, P. 1976, *ApJ*, **203**, 297
- Schreiber, C., Pannella, M., Elbaz, D., et al. 2015, *A&A*, **575**, A74
- Schreiber, C., Pannella, M., Leiton, R., et al. 2017, *A&A*, **599**, A134
- Schreiber, C., Elbaz, D., Pannella, M., et al. 2018, *A&A*, **609**, A30
- Scott, S. E., Fox, M. J., Dunlop, J. S., et al. 2002, *MNRAS*, **331**, 817
- Scott, K. S., Wilson, G. W., Aretxaga, I., et al. 2012, *MNRAS*, **423**, 575
- Scudder, J. M., Oliver, S., Hurley, P. D., et al. 2016, *MNRAS*, **460**, 1119
- Simpson, J. M., Swinbank, A. M., Smail, I., et al. 2014, *ApJ*, **788**, 125
- Simpson, J. M., Smail, I., Swinbank, A. M., et al. 2015a, *ApJ*, **799**, 81
- Simpson, J. M., Smail, I., Swinbank, A. M., et al. 2015b, *ApJ*, **807**, 128
- Skelton, R. E., Whitaker, K. E., Momcheva, I. G., et al. 2014, *ApJS*, **214**, 24
- Smail, I., Ivison, R. J., & Blain, A. W. 1997, *ApJ*, **490**, L5
- Straatman, C. M. S., Spitler, L. R., Quadri, R. F., et al. 2016, *ApJ*, **830**, 51
- Swinbank, A. M., Simpson, J. M., Smail, I., et al. 2014, *MNRAS*, **438**, 1267
- Tacconi, L. J., Genzel, R., Smail, I., et al. 2008, *ApJ*, **680**, 246
- Tadaki, K.-I., Genzel, R., Kodama, T., et al. 2017, *ApJ*, **834**, 135
- Talia, M., Pozzi, F., Vallini, L., et al. 2018, *MNRAS*, **476**, 3956
- Tomeczak, A. R., Quadri, R. F., Tran, K.-V. H., et al. 2016, *ApJ*, **817**, 118
- Ueda, Y., Hatsukade, B., Kohno, K., et al. 2018, *ApJ*, **853**, 24
- Umehata, H., Tamura, Y., Kohno, K., et al. 2017, *ApJ*, **835**, 98
- van der Wel, A., Bell, E. F., Häussler, B., et al. 2012, *ApJS*, **203**, 24
- van der Wel, A., Franx, M., van Dokkum, P. G., et al. 2014, *ApJ*, **788**, 28
- van Dokkum, P. G., Whitaker, K. E., Brammer, G., et al. 2010, *ApJ*, **709**, 1018
- van Dokkum, P. G., Nelson, E. J., Franx, M., et al. 2015, *ApJ*, **813**, 23
- Vanzella, E., Cristiani, S., Dickinson, M., et al. 2008, *A&A*, **478**, 83
- Wang, W.-H., Barger, A. J., & Cowie, L. L. 2009, *ApJ*, **690**, 319
- Wang, S. X., Brandt, W. N., Luo, B., et al. 2013, *ApJ*, **778**, 179
- Wang, T., Elbaz, D., Schreiber, C., et al. 2016, *ApJ*, **816**, 84
- Wardlow, J. L., Smail, I., Coppin, K. E. K., et al. 2011, *MNRAS*, **415**, 1479
- Weiß, A., Kovács, A., Coppin, K., et al. 2009, *ApJ*, **707**, 1201
- Wiklind, T., Conselice, C. J., Dahlen, T., et al. 2014, *ApJ*, **785**, 111
- Williams, R. J., Quadri, R. F., Franx, M., van Dokkum, P., & Labbé, I. 2009, *ApJ*, **691**, 1879
- Williams, C. C., Giavalisco, M., Cassata, P., et al. 2014, *ApJ*, **780**, 1
- Wuyts, S., Labbé, I., Förster Schreiber, N. M., et al. 2008, *ApJ*, **682**, 985
- Xue, Y. Q., Luo, B., Brandt, W. N., et al. 2011, *ApJS*, **195**, 10
- Yamaguchi, Y., Tamura, Y., Kohno, K., et al. 2016, *PASJ*, **68**, 82
- Yun, M. S., Scott, K. S., Guo, Y., et al. 2012, *MNRAS*, **420**, 957
- (WPI), The University of Tokyo Institutes for Advanced Study, The University of Tokyo, Kashiwa, Chiba 277-8583, Japan
- <sup>8</sup> Center for Extragalactic Astronomy, Department of Physics, Durham University, Durham DH1 3LE, UK
- <sup>9</sup> Institute of Astronomy, University of Tokyo, 2-21-1 Osawa, Mitaka, Tokyo 181-0015, Japan
- <sup>10</sup> Fakultät für Physik der Ludwig-Maximilians-Universität, 81679 München, Germany
- <sup>11</sup> Astronomy Department, University of Massachusetts, Amherst, MA 01003, USA
- <sup>12</sup> Harvard-Smithsonian Center for Astrophysics, Cambridge, MA 02138, USA
- <sup>13</sup> Infrared Processing and Analysis Center, MS314-6, California Institute of Technology, Pasadena, CA 91125, USA
- <sup>14</sup> Space Telescope Science Institute, 3700 San Martin Drive, Baltimore, MD 21218, USA
- <sup>15</sup> Department of Astronomy, The University of Texas at Austin, Austin, TX 78712, USA
- <sup>16</sup> Univ. Lyon, Univ. Lyon1, ENS de Lyon, CNRS, Center de Recherche Astrophysique de Lyon (CRAL) UMR5574, 69230 Saint-Genis-Laval, France
- <sup>17</sup> National Astronomical Observatory of Japan, National Institutes of Natural Sciences, 2-21-1 Osawa, Mitaka, Tokyo 181-8588, Japan
- <sup>18</sup> SOKENDAI (The Graduate University for Advanced Studies), 2-21-1 Osawa, Mitaka, Tokyo 181-8588, Japan
- <sup>19</sup> Instituto de Física y Astronomía, Universidad de Valparaíso, Avda. Gran Bretaña 1111, Valparaíso, Chile
- <sup>20</sup> Institute of Astronomy & Astrophysics, Academia Sinica, Taipei 10617, Taiwan
- <sup>21</sup> Dark Cosmology Centre, Niels Bohr Institute, University of Copenhagen, Juliane Mariesvej 30, 2100 Copenhagen, Denmark
- <sup>22</sup> Institute for Astronomy, Astrophysics, Space Applications and Remote Sensing, National Observatory of Athens, 15236 Athens, Greece
- <sup>23</sup> Joint ALMA Observatory, Alonso de Córdova 3107, Vitacura 763-0355, Santiago, Chile
- <sup>24</sup> European Southern Observatory, Alonso de Córdova 3107, Vitacura, Casilla 19001 19 Santiago, Chile
- <sup>25</sup> Institute of Astronomy, Graduate School of Science, The University of Tokyo, 2-21-1 Osawa, Mitaka, Tokyo 181-0015, Japan
- <sup>26</sup> Department of Physics and Astronomy, The University of Sheffield, Hounsfield Road, Sheffield S3 7RH, UK
- <sup>27</sup> Department of Physics and Astronomy, Texas A&M University, College Station, TX 77843-4242, USA
- <sup>28</sup> George P. and Cynthia Woods Mitchell Institute for Fundamental Physics and Astronomy, Texas A&M University, College Station, TX 77843-4242, USA
- <sup>29</sup> Scientific Support Office, ESA/ESTEC, Noordwijk, The Netherlands
- <sup>30</sup> Department of Physics, Faculty of Science, Chulalongkorn University, 254 Phayathai Road, Pathumwan, Bangkok 10330, Thailand
- <sup>31</sup> National Astronomical Research Institute of Thailand (Public Organization), Donkaew, Maerim, Chiangmai 50180, Thailand
- <sup>32</sup> Kavli Institute for the Physics and Mathematics of the Universe (WPI), The University of Tokyo Institutes for Advanced Study, The University of Tokyo, Kashiwa, Chiba 277-8583, Japan
- <sup>33</sup> Astronomy Centre, Department of Physics and Astronomy, University of Sussex, Brighton BN1 9QH, UK
- <sup>34</sup> Department of Physics, Anhui Normal University, Wuhu Anhui 241000, PR China
- <sup>35</sup> School of Astronomy and Space Science, Nanjing University, Nanjing 210093, PR China



# GOODS-ALMA: II. Using IRAC priors to probe fainter millimeter galaxies

M. Franco<sup>1</sup>\* et al.

Laboratoire AIM-Paris-Saclay, F-91191 Gif-sur-Yvette, France, e-mail: maximilien.franco@cea.fr

Received –; accepted –

## ABSTRACT

Using prior positional information at 3.6 and 4.5  $\mu\text{m}$  (from *Spitzer*-IRAC), we were able to explore the presence of galaxies detected at 1.1 mm with ALMA below the blind detection limit of  $4.8\text{-}\sigma$  under which the number of spurious sources largely overcome that of real sources. In total we find 16 galaxies in the Supplementary Catalog, including 2 HST-dark galaxies, that bring the total sample of GOODS-ALMA 1.1 mm sources to 35 galaxies. Galaxies in the new sample cover a wider dynamic range in redshift ( $z = 0.65 - 5.36$ ), exhibit twice larger physical sizes (1.3 vs 0.65 kpc) and about half median stellar masses. This increase in the ALMA sizes is not large enough to question the fact that the ALMA emission is particularly compact at 1.1 mm at  $z > 2$ . We show that the astrometry of the HST image does not only struggle from a global astrometric shift, as already discussed in previous papers, but also from local shifts that produced the equivalent of a distortion map that was artificially introduced in the process of building the mosaic of the GOODS-South HST image. We present a solution for this astrometric issue derived from the comparison of the positions of nearly 400 galaxies in common between HST and Pan-STARRS in the GOODS-ALMA field.

## 1. Introduction

The formation and evolution of the most massive galaxies ( $M_\star > 5 \times 10^{10} M_\odot$ ) at redshifts  $z > 2$  is still largely debated. Their observed number density exceeds theoretical expectations assuming typical dark matter to stellar mass ratios (Steinhardt et al. 2016). The downsizing of galaxy formation challenges theoretical models which match either the low or high mass end but are unable to match both ends (e.g., Fontanot et al. 2009). The presence of a population of massive passive galaxies at  $z \sim 2$  with compact stellar surface densities challenges searches for their progenitors (van der Wel et al. 2014).

Since infrared (IR) wavelengths contribute to approximately half of the total Extragalactic Background Light (EBL; e.g., Dole et al. 2006), the study of dust-enshrouded star-formation in distant galaxies is an important tool to progress in our understanding of the evolution of massive galaxies. The first submillimeter extragalactic surveys (Smail et al. 1997; Barger et al. 1998; Hughes et al. 1998) performed with the Submillimetre Common-User Bolometer Array (SCUBA; Holland et al. 1999) on the James Clerk Maxwell Telescope (JCMT) have revealed a population of high redshift galaxies that are massive, highly obscured and have high star formation rates (SFRs). Recent observations using the Atacama Large Millimetre/submillimetre Array (ALMA), which provides a resolution more than an order of magnitude higher than SCUBA, have since refined our understanding of galaxy evolution by securing the identification of optical counterparts and allowing us to detect not only extreme galaxies (galaxies with particularly high star formation rates, e.g., starburst or lensed galaxies), but also “normal” galaxies that are secularly forming stars.

This paper extends our previous analysis (Franco et al. 2018, hereafter F18) of a deep continuum 1.1 mm survey with ALMA over an area of 69 arcmin<sup>2</sup>. This survey is located in the Great Observatories Origins Deep Survey–South (GOODS–South) at

a location covered with the deepest integrations in the H-band with the HST-WFC3 camera. In F18, we limited our analysis to the blind detection of ALMA sources without considering prior information at other wavelengths. Due to the large number of independent beams in the high-resolution ALMA image, we were limited to the  $4.8\text{-}\sigma$  detection limit. Here we extend the detection limit to  $3.5\text{-}\sigma$  by cross-matching the ALMA detections with catalogs in the near and mid-infrared. The need for a good astrometric calibration led us to introduce an improved correction for the astrometry of the HST image of the GOODS–South field (hereafter GOODS–S).

This paper is organized as follows: in §2, we present the data used. In §3, we describe the astrometric correction to be applied to HST positions to align them with those of ALMA. We give the astrometric correction to be applied for all galaxies in the GOODS–South field present in the Guo et al. (2013) catalog, provided as an external link. In §4, we present the criteria and methods used to select the sample of galaxies which constitutes a Supplementary Catalog to the Main Catalog presented in F18. In §5, we present the properties of the galaxies of the Supplementary Catalog, including two optically-dark galaxies. Finally, in §6, we perform a comparative analysis of the distribution of stellar masses, redshifts, and sizes between the sample of galaxies presented in this paper and in F18 and discuss the implications on the nature of the ALMA sources.

Throughout this paper, we adopt a spatially flat  $\Lambda$ CDM cosmological model with  $H_0 = 70 \text{ km s}^{-1} \text{ Mpc}^{-1}$ ,  $\Omega_m = 0.3$  and  $\Omega_\Lambda = 0.7$ . We assume a Salpeter (Salpeter 1955) Initial Mass Function (IMF). We use the conversion factor of  $M_\star$  (Salpeter 1955 IMF) =  $1.7 \times M_\star$  (Chabrier 2003 IMF). All magnitudes are quoted in the AB system (Oke & Gunn 1983).

\* E-mail: maximilien.franco@cea.fr

## 2. Data

### 2.1. ALMA data

This paper uses the 1.1mm photometric survey obtained with the Atacama Large Millimeter/Submillimeter Array (ALMA) between August and September 2016 (Project ID: 2015.1.00543.S; PI: D. Elbaz). The survey performed using band 6 covers an effective area of 69 arcmin<sup>2</sup> matching the deepest HST/WFC3 *H*-band part of the Cosmic Assembly Near-infrared Deep Extragalactic Legacy Survey (CANDELS; Grogin et al. 2011, Koekoemoer et al. 2011, PIs: S. Faber, H. Ferguson), in the Great Observatories Origins Deep Survey–*South* (GOODS–*South*). It is centered at  $\alpha = 3^{\text{h}} 32^{\text{m}} 30.0^{\text{s}}$ ,  $\delta = -27^{\circ} 48' 00''$  (J2000). The original 0''.2 angular resolution was tapered with a homogeneous and circular synthesized beam of 0''.60 Full-Width Half Maximum (FWHM; hereafter 0''.60-mosaic). The sensitivity of the 0''.60-mosaic varies within the six slices of the survey around a median value of RMS  $\approx 0.18$  mJy beam<sup>-1</sup>.

### 2.2. Additional data

#### 2.2.1. IRAC catalog

We use the *Spitzer*-Cosmic Assembly Near-Infrared Deep Extragalactic Survey (S-CANDELS; Ashby et al. 2015) catalog of galaxies detected at 3.6 and 4.5  $\mu\text{m}$  with the Infrared Array Camera (IRAC; Fazio et al. 2004) aboard the *Spitzer* Space Telescope (Werner et al. 2004). The catalog (Ashby et al. 2015) – hereafter S-CANDELS catalog – that reaches a 5- $\sigma$  depth of 26.5 mag (AB) includes 2627 galaxies in the GOODS-ALMA field, i.e. about 38 sources.arcmin<sup>-2</sup>.

#### 2.2.2. HST H-band catalog

The GOODS-ALMA area covers the deepest H-band part of the Cosmic Assembly Near-IR Deep Extragalactic Legacy Survey (CANDELS; Grogin et al. 2011) field (central one-third of the field). The point source catalog reaches a 5- $\sigma$  depth of 28.16 mag (AB) in the  $H_{160}$  filter (measured within a fixed aperture of 0''.17; Guo et al. 2013). The surface density of galaxies detected at 1.6  $\mu\text{m}$  with the Wide Field Camera 3 / infrared channel (WFC3/IR) within the GOODS-ALMA field is about 233 sources.arcmin<sup>-2</sup>.

#### 2.2.3. Near-infrared $K_s$ -band catalog

We use the 2.2  $\mu\text{m}$  catalog described in Straatman et al. (2016) that uses an ultradeep image resulting from the combination of multiple observations in the  $K$  and  $K_s$  bands from: (i) the Very Large Telescope (VLT), which combines the images of GOODS-S done with the Infrared Spectrometer and array camera (ISAAC; Moorwood et al. 1999) in the  $K_s$ -band (Retzlaff et al. 2010) with the High Acuity Wide field  $K$ -band imager (Hawk-I; Kissler-Patig et al. 2008) image in the  $K$ -band (Fontana et al. 2014), (ii) the 6.5m Magellan Baade Telescope combining the  $K_s$ -band image from the FourStar Galaxy Evolution Survey (ZFOURGE, PI: I. Labbé) using the FourStar near-infrared Camera (Persson et al. 2013) with the  $K$ -band image using the Persson's Auxillary Nasmyth infrared camera (PANIC; Martini et al. 2004) in the HUDF (PI: I. Labbé), (iii) the Canada-France-Hawaii Telescope (CFHT), with the  $K$  band image done with the wide-field infrared camera (WIRCam; Puget et al. (2004) as part of the Taiwan ECDIFS Near Infrared Survey (TENIS; Hsieh et al. 2012).

The 5- $\sigma$  point-source detection threshold in this ultra-deep  $K_s$  image reaches a magnitude between 26.2 and 26.5, which leads to an average galaxy surface density of about 168 sources.arcmin<sup>-2</sup>.

### 2.2.4. Radio catalog

A radio image that encompasses the GOODS-ALMA field was observed with the Karl G. Jansky Very Large Array (VLA) at a frequency of 3 GHz (10 cm) and an angular resolution of  $\sim 0''.3$  for a total of 177 hours (configurations A, B, & C; PI: W. Rujopakarn). Down to the average depth of the radio catalog within the GOODS-ALMA region of RMS = 2.1  $\mu\text{Jy.beam}^{-1}$ , the average surface density of radio sources is about 5 sources.arcmin<sup>-2</sup>.

## 3. Astrometric correction of the HST image of GOODS-South

We describe in F18 the presence of a systematic offset of  $\Delta\text{RA} = -96 \pm 113$  mas in right ascension, and  $\Delta\text{Dec} = 261 \pm 25$  mas in declination between the ALMA, and HST images. This offset, interpreted as a positional shift of the HST image with respect to all other reference frames, is in good agreement with the offset previously discussed in Dunlop et al. (2017) and Rujopakarn et al. (2016). For the GOODS-North field, the coordinates were shifted by approximately 0.3 arcsec, primarily in declination, compared to those of other astrometric reference datasets (Dunlop et al. 2017). However, this correction has not been made to the v2.0 release for GOODS-South, in part because no external astrometric reference data with both suitable absolute accuracy and faint source density (such as the SDSS) were available<sup>1</sup>.

The offset used until now only corrects for the bulk global shift in astrometry but it does not account for the relative error in the astrometric calibration that was introduced in the building of the HST mosaic. In the following, we propose to determine this local correction that behaves like a distortion correction. This correction is important in the present study since we aim at using prior knowledge of existing sources from other wavelengths in order to push the ALMA detection limit to deeper levels.

We take advantage of the Panoramic Survey Telescope and Rapid Response System (Pan-STARRS) Data Release 2 (Flewelling et al. 2016). The offset between HST and Pan-STARRS images computed using an ensemble of 375 common detections (see Fig. 1 left panel) is comparable to the one presented in F18:  $\Delta\text{RA} = -96 \pm 83$  mas and  $\Delta\text{Dec} = 252 \pm 107$  mas.

The comparison of the positions of 69 sources in common between our 3 GHz VLA catalog (5 $\sigma$  detections; Rujopakarn et al., in prep.) and Pan-STARRS within a radius of 0''.6 shows that there is no offset between both images (Fig. 1 middle panel). To reduce the risk of misidentification, in all the astrometric analysis, we only retained galaxies that had been observed at least twice in the same filter during the Pan-STARRS survey. The average deviations are found to be  $\Delta\text{RA} = 0 \pm 98$  mas and  $\Delta\text{Dec} = 12 \pm 160$  mas.

Similarly, we find no offset between our ALMA sources (both the Main catalog presented in F18 and the supplementary catalog presented in the following) and their VLA counterparts for the 27 galaxies in common between both catalogs (Fig. 1, right panel). The average offset is  $\Delta\text{RA} = 3 \pm 113$  mas and  $\Delta\text{Dec} = 16 \pm 93$  mas well within the expected uncertainties for S/N  $\sim 4$  sources (Iverson et al. 2007; Hatsukade et al. 2018).

<sup>1</sup> [https://archive.stsci.edu/pub/hlsp/goods/v2/h\\_goods\\_v2.0\\_rdm.html](https://archive.stsci.edu/pub/hlsp/goods/v2/h_goods_v2.0_rdm.html)



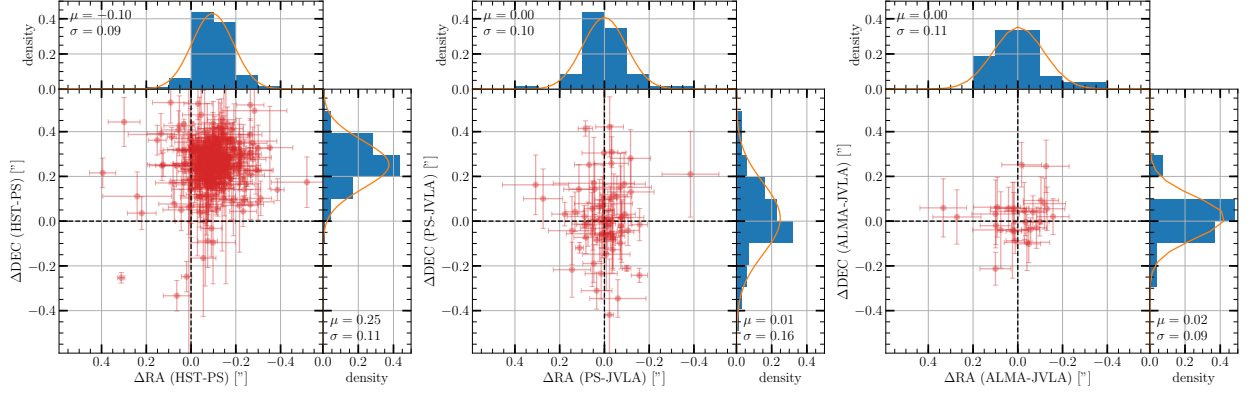


**Fig. 1.** Left: offset between Pan-STARRS and HST; Middle: offset between JVLA and Pan-STARRS; Right: offset between JVLA and ALMA. For each panel, the histogram of the offsets in RA and DEC is shown as well as a fit with a Gaussian function (orange curve). The position of the peak and the standard deviation of the Gaussian is indicated for each curve. The middle and the right panels show that there are no significant astrometric differences between ALMA and JVLA nor between JVLA and PS1, while The left panel shows the clear shift in both RA and DEC between the positions of 375 sources in common between the Pan-STARRS (PS) and HST images. We measure a systematic offset of  $\Delta RA = -96 \pm 83$  mas and  $\Delta Dec = 252 \pm 107$  mas. In addition, a local offset is presented in Fig. 2.

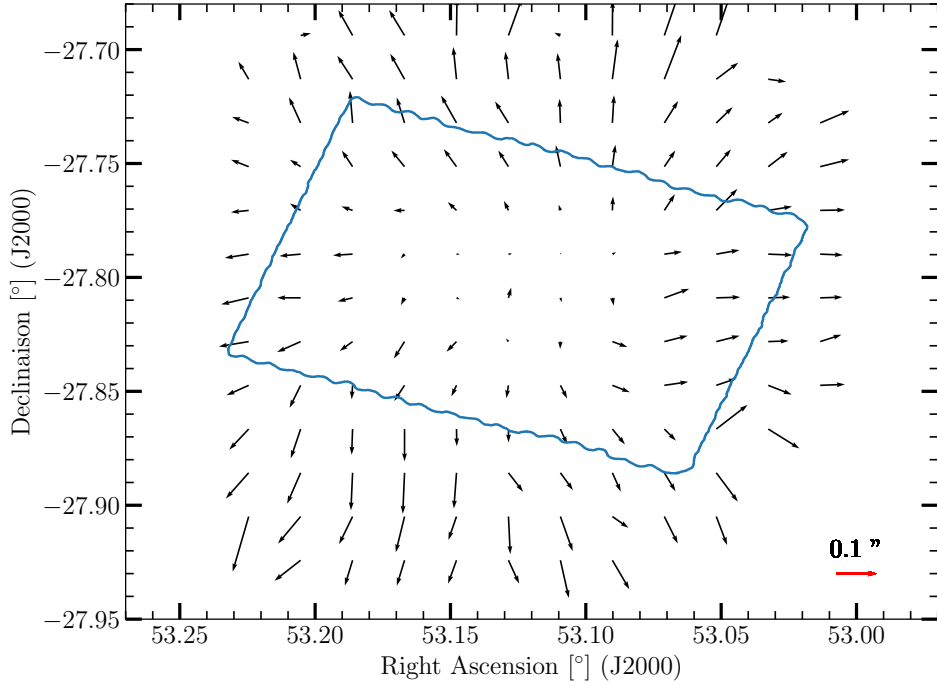


**Fig. 2.** Difference between HST and Pan-STARRS position after subtraction of the median offset value. Each arrow represents a sliding median including on average 15 points, with an overlap of 60 percent between neighboring arrows. The blue line defines the area encompassing the GOODS-ALMA survey.

Some of these sources come from the supplementary list discussed in the following sections of this work, but since we applied this astrometric correction to the HST sources used as priors in the catalog production, we decided to present the astrometric correction upfront and to illustrate the positions of all our ALMA galaxies in this section.

The excellent agreement in the astrometry of VLA, ALMA, and Pan-STARRS implies that it is most likely the HST coordinate system that needs to be corrected.

After subtracting this systematic and global offset from the HST data, the residuals offsets present spatially coherent patterns (see Fig. 2). Each arrow represents the median offset between Pan-STARRS and HST positions, for a sliding median containing on average 30 points. This local offset varies with position in the GOODS-South field, and we refer to this as a distortion offset artificially introduced in the mosaicing of the HST data. The absolute value of the distortion offset is lower than the systematic offset, but it is not negligible, and can reach values higher than  $0''.15$  at the edge of our GOODS-ALMA sur-

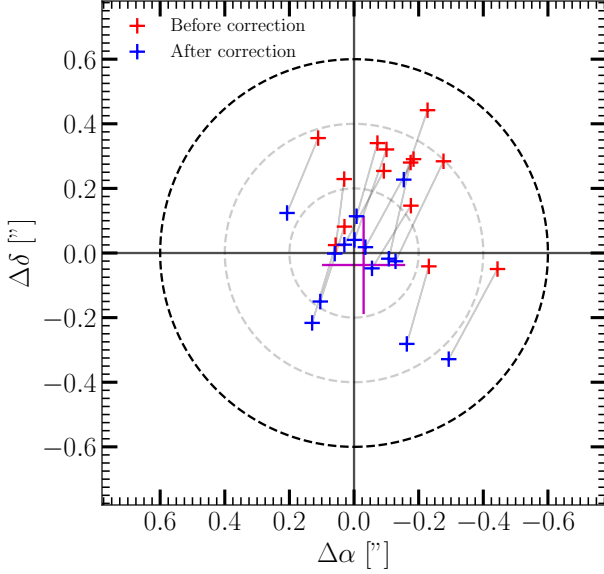


**Fig. 3.** Positional offset ( $\text{RA}_{\text{HST}} - \text{RA}_{\text{ALMA}}$ ,  $\text{DEC}_{\text{HST}} - \text{DEC}_{\text{ALMA}}$ ) between *HST* and ALMA, before (red crosses) and after (blue crosses) the correction of both a global systematic offset and a local distortion offset. The black dashed circle corresponds to the cross-matching limit radius of  $0''.6$ . The grey dashed circles show positional offsets of  $0''.2$  and  $0''.4$  respectively. The mean offset and the standard deviation are shown by the magenta cross.

vey. A possible explanation for this local distortion may come from the process of making the HST maps themselves. Before the projection of the HST image onto the reference grid according to the World Coordinate System (WCS), a geometric distortion was applied using the WFC3 SMOV F606W data alone<sup>2</sup> (Windhorst et al. 2011). This wavelength-independent geometric solution becomes greater for regions near the field edge (Windhorst et al. 2011), where the error on the correction itself also becomes very large. The combined effect of the global offset and distortion offset between the ALMA and HST positions is illustrated in Fig. 3 and listed in Table 1 both before and after applying the global offset of  $\Delta\text{RA} = -96 \pm 83$  mas and  $\Delta\text{Dec} = 252 \pm 107$  mas and the distortion offset. With the exception of two galaxies for which the offset between the ALMA detected position and that of HST is  $\sim 0''.4$  (after correction of both the global offset and the distortion offsets, AGS27 and AGS35), all other galaxies have a difference in the two positions of  $< 0''.27$ . The average deviation after correction is  $-35$  mas in RA and  $47$  mas in DEC for the sample of galaxies selected in this study. (indicated by a magenta cross in Fig. 3). The updated RA and Dec positions derived for all galaxies in the Guo et al. (2013) catalog after the correction of both systematic and local offset are given at <https://github.com/maximilienfranco/astrometry/>.

## 4. ALMA Main and Supplementary catalogs

### 4.1. ALMA Main Catalog

The main ALMA catalog consists of 20 sources detected above  $4.8\sigma$  (F18). This catalog was built without any prior assumption from a blind source extraction down to the  $4.8\sigma$ -limit using BLOBCAT (Hales et al. 2012).

<sup>2</sup> [http://www.stsci.edu/hst/wfc3/idctab\\_lbn](http://www.stsci.edu/hst/wfc3/idctab_lbn)

The detection limit was set to  $\text{S/N} \geq 4.8$  due to the large number of independent beams that leads to spurious detections that become rapidly more numerous than the number of robust detections below this threshold, despite the tapering at  $0''.60$ . Here the  $4.8\sigma$ -limit concerns the central pixel detection threshold ( $\sigma_p = 4.8$ ) and is associated with a constraint on the adjacent surrounding pixels that are included in the source if they pass a detection threshold of  $\sigma_f = 2.7$ . This combination of parameters ensures an 80% purity where the purity criterion  $p_f$  is defined as:

$$p_f = \frac{N_p - N_n}{N_p} > 0.8 \quad (1)$$

where  $N_p$  and  $N_n$  are the number of positive and negative detections. The negative detections refer to the detections in the inverse map (in other words detections in the continuum map multiplied by -1).

The initial catalog coming out of the blind source extraction contains 23 detections including 3 detections that we flagged as spurious in F18 (marked with an asterisk in the Table 2 of F18). Finding three spurious detections out of 23 detections matches the expected number of spurious sources obtained from the difference between positive and negative peaks above the  $4.8\sigma$  level of 4 with a Poissonian uncertainty of  $\pm 2$ . These three sources are the only ALMA detections in the list without any sign of an IRAC counterpart at  $\lambda = 3.6$  or  $4.5 \mu\text{m}$  (Spitzer/IRAC channels 1 and 2) despite the availability of ultra-deep IRAC data in this field ( $26.5$  AB mag, Ashby et al. 2015). The possibility that these sources are most likely spurious was later on confirmed by Cowie et al. (2018) using a  $100 \text{ arcmin}^2$  survey of the field down to an RMS  $\sim 0.56$  mJy at  $850 \mu\text{m}$  with SCUBA-2. While none of the three detections that we listed as spurious were detected by SCUBA-2, 17 out of our 20 brightest ALMA sources were detected by Cowie et al. (2018). The remaining 3 sources were either confirmed with ALMA by Cowie et al. (2018) – AGS21 and AGS23 – or lie outside of the SCUBA-2 field of view – AGS22. We note however, that AGS22 is both at the very limit of our detection threshold and that it is the only galaxy of our list that does not show any IRAC counterpart. In view of the very large number of expected spurious detections at the  $3.5\sigma$  limit that we plan to reach in the present paper, we will adopt the strategy to limit ourselves to the most secure ALMA detections, which exhibit a clear IRAC counterpart. As a result, we will limit the original main sample to 19 galaxies only, leaving aside AGS22 for consistency.

### 4.2. ALMA Supplementary Catalog

#### 4.2.1. Using IRAC counterparts to identify robust ALMA sources down to $3.5\sigma$

In the present paper, we propose to use counterparts at other wavelengths to identify robust ALMA detections below the  $4.8\sigma$  limit of the Main Catalog described in Sect. 4.1. This approach is similar in philosophy to a prior source extraction approach, except that we start from the ALMA blind source extraction at a lower threshold and then only keep sources with counterparts already identified in the near and mid infrared.

We start with the list of sources detected with the same algorithm than the Main Catalog but push it down to the  $\sigma_p = 3.5$  limit. A total of 1077 sources are detected down to this threshold, most of which are spurious simply due to the large number of independent beams (more than one million in the  $0''.60$  tapered map). Indeed the inverse map exhibits an equivalently large, even

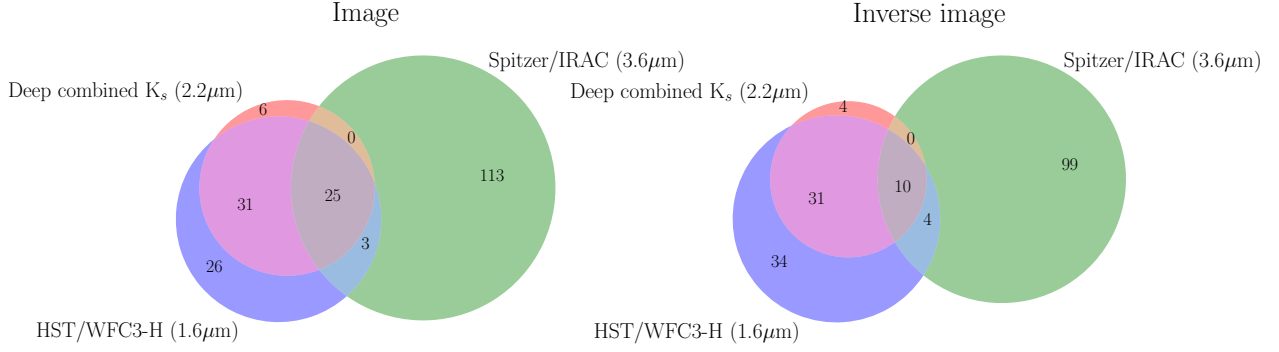


**Fig. 4.** Number of sources cross-matched between the ALMA  $3.5\sigma$  detection and the ZFOURGE (Straatman et al. 2016), CANDELS (Guo et al. 2013) and S-CANDELS (Ashby et al. 2015) catalogs in the image (left panel) and in the inverse image (right panel), within a radius of  $0''.60$  for the ZFOURGE and CANDELS catalogs and  $1''.95$  with the S-CANDELS catalog Ashby et al. (2015). Beforehand, we previously removed from the image the sources that had been detected in F18. For example, in the "direct" image, 6 galaxies are only detected in  $K_s$ -band, 26 only in  $H$ -band, 113 only with IRAC. 31 are detected in the ultra-deep  $K_s$  and  $H$ -band but are not present the S-CANDELS catalog, 3 source are in common between the  $H$ -band image and the Spitzer/IRAC channel 1 image but are not detected in the ultra-deep  $K_s$  image and 25, in addition to being detected at  $3.5\sigma$  with ALMA, are detected in the 3 other wavelengths.

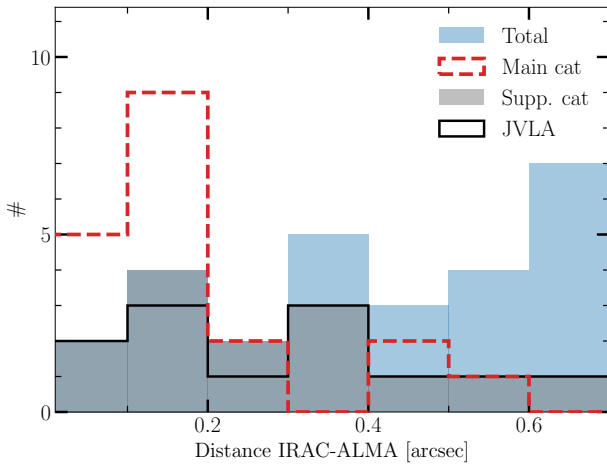


**Fig. 5.** Distance between ALMA positions and the closest IRAC galaxy listed in the S-CANDELS catalog for the sources presented in F18, red-dashed line, for the supplementary catalog, gray and for all the  $3.5\sigma$  detections. We also represented the JVLA counterparts (at 3GHz) with a black solid line and for the all the ALMA  $3.5\sigma$  detections with both IRAC and a JVLA counterpart between  $0''.3$  and  $0''.7$  from the ALMA detections have been selected.

larger, number of detections of 1157. The number of detections at this level obviously depends on noise fluctuations but does not preclude the existence of real positive sources. Hence we cannot rely on Eq. 1 of F18 to calculate the probability that a source is real from a purely blind detection approach.

We observed in F18 that all the ALMA robust detections of the Main Catalog present an IRAC counterpart, hence we start by imposing the requirement that all candidate detections exhibit an IRAC counterpart. We note that this criterion may lead us to reject real ALMA sources without any IRAC counterpart with the possible consequence of biasing our sample towards the most massive galaxies, but this is for the sake of the robustness of the sources. ALMA sources without any IRAC counterpart may well exist (see e.g., Williams et al. 2019) and would be particularly interesting to analyse, but this is out of the scope of the present

paper, since including sources without IRAC counterparts would imply including a significant number of hazardous sources in the sample.

In the process of cross-matching the ALMA and IRAC images, we identified several cases of IRAC sources that were present in the IRAC image but were not listed in the S-CANDELS catalog (see Sect. 2.2.1). These sources were systematically located close to one or several brighter IRAC sources. We therefore implemented a new source extraction for those sources taking care of modeling the neighboring sources to proceed to a clean de-blending of the IRAC sources. This allowed us to determine the S/N ratio of those sources and only keep real detections. In most cases, those sources exhibited a counterpart in either the H and  $K_s$  band catalogs (described in Sect. 2.2.2, 2.2.3). This led us to extend our counterpart search to the H and  $K_s$  bands that we will use as priors to identify candidate IRAC sources that may have been missed in the original S-CANDELS catalog.

We choose the cross-matching radius between the positions of the ALMA detections and the IRAC, H and K band catalogs to be equal to the value of the largest FWHM. It is equal to  $0''.60$ , the FWHM of the tapered 1.1mm ALMA image, for the cross-match with the CANDELS H-band and ZFOURGE K-band catalogs, and equal to  $1''.95$  for the cross-match with the IRAC channel 1 ( $3.6\mu\text{m}$ ) catalog ( $FWHM_{\text{IRAC}} = 1''.95$  at  $3.6\mu\text{m}$ ,  $FWHM_{\text{IRAC}} = 2''.05$  at  $4.5\mu\text{m}$ ). Before performing this cross-matching, we apply the astrometric correction to the CANDELS and ZFOURGE catalogs which use the HST reference frame, as described in Sect. 3.

A total of 204 sources detected with ALMA above  $3.5\sigma$  at 1.1 mm have a counterpart in at least one of the three catalogs (see Fig. 4). In comparison, there are 182 detections above  $3.5\sigma$  that also fulfill these criteria in the inverse image. We recall that we used the H and K-band counterparts as priors to search for IRAC sources that may have been missed in the S-CANDELS catalog due to the presence of a bright neighbor.

We note that 84% (16 out of 19 sources) of the ALMA sources in the Main Catalog described in F18 have an IRAC counterpart closer than  $0''.3$  (red dashed line in Fig. 5). Since our goal is not here to include all possible ALMA sources but to limit the Supplementary Catalog to the most robust candidates,

we decided to impose a more stringent constraint on the association with IRAC counterparts by keeping as robust candidates those within a distance of  $0''.3$ . In total, 8 ALMA sources detected between  $3.5\sigma$  and  $4.8\sigma$  fulfill this criterion. This close association between ALMA and IRAC may be due in part to the fact that the FWHM of the IRAC images is limited by the pixel size rather than the diffraction limit, hence position accuracies may actually be better determined than the  $1''.95$  FWHM of IRAC.

Looking at the remaining three sources in the Main Catalog, we noticed another interesting characteristics. They are all closer than  $0''.7$  from their IRAC counterpart and nearly all exhibit a radio counterpart as well (2 out of 3). In fact, out of the 19 sources in the Main Catalog, 16 hence again 84 % exhibit a radio counterpart. We therefore chose to list in the Supplementary Catalog the sources that have both an IRAC and a radio counterpart closer than  $0''.7$ . This extra condition adds an extra 6 ALMA sources detected between  $3.5\sigma$  and  $4.8\sigma$ .

In total, we end up with a list of 14 sources which fulfill the criteria of having an IRAC counterpart either (i) closer than  $0''.3$  or (ii) closer than  $0''.7$  but associated with a radio counterpart in the 3 GHz catalog.

It is possible that using these criteria does not allow us to detect all "real" ALMA detections with a  $S/N > 3.5$  but these conservative criteria ensure a high purity rate. We performed Monte Carlo simulation to estimate the probability that an ALMA detection lies randomly close to a galaxy listed in the S-CANDELS catalog. We randomly define a position within GOODS-South and then measure the distance to its closest IRAC neighbour using the source positions listed in Ashby et al. (2015) for IRAC sources with  $S/N > 5$ . We repeat this procedure 100 000 times. This method gives results comparable to the one presented in ?. The distance from the nearest IRAC galaxies, within a radius of  $1''.95$  is given Table 1. In our supplementary catalog, for the farthest source of an IRAC source ( $0''.64$ ), the percentage of a random IRAC association is 1.36 %. With the exception of one other source, the other detections have a probability of random IRAC association  $\leq 1\%$ .

We checked whether deeper surveys covering parts of the GOODS-S field could be used to validate or invalidate those ALMA Supplementary Catalog sources. The HUDF (Dunlop et al. 2017) and ASAGAO (Hatsukade et al. 2018) surveys reach a depth of  $RMS \approx 35 \mu Jy$  at 1.3mm and  $RMS \approx 6 \mu Jy$  at 1.2 mm respectively. Using the same scaling factors as those presented in F18, these depths convert to  $RMS \approx 52 \mu Jy$  and  $RMS \approx 79 \mu Jy$  respectively at the wavelength of 1.1mm of the present GOODS-ALMA survey. Only three ALMA 1.1mm sources from the Supplementary Catalog fall in the area covered by these deeper surveys and all of them were detected and listed in the associated catalogs (see Fig. 8). The sources AGS29 and AGS35 from our Supplementary Catalog were both detected within the ASAGAO survey and listed as the sources 18 and 26 respectively (Hatsukade et al. 2018). The source AGS38 falls within the HUDF survey and is listed as UDF16 (Dunlop et al. 2017). Hence our independent identification of sources down to the  $3.5\text{-}\sigma$  level did not bring any spurious source without any counterpart in deeper ALMA surveys, instead all 3 sources in these deeper images are confirmed.

#### 4.2.2. Supplementary catalog: optically dark galaxies

As discussed above, we searched for potential IRAC sources that were present in the IRAC images but missed in the S-CANDELS catalog because of the presence of a bright IRAC neighbor. Start-

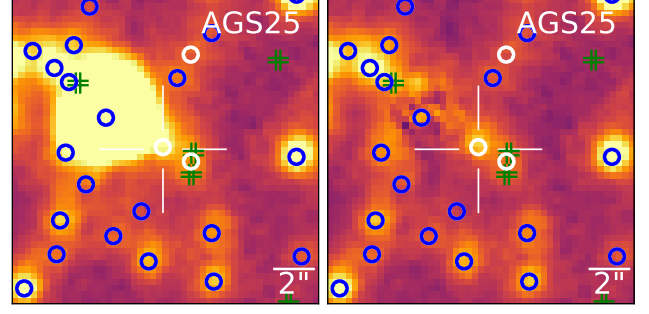


**Fig. 6.** IRAC  $3.6\mu m$  map ( $17'' \times 17''$ ) image centred on the position of the ALMA detection. We show the image before (left panel) and after (right panel) the subtraction with GALFIT of the bright source  $ID_{ZFOURGE} = 11024$  ( $ID_{CANDELS} = 8067$ ) located to the Northeast of the detection and which masks the emission of the source located at the ALMA position. After subtraction we can see emission located in the central position which suggests that the source is not present in Ashby et al. (2015) only because of blending. Green double crosses show sources from the GOODS-S CANDELS catalog. White circles show sources from the ZFOURGE catalog. Blue circles show common sources from both optical catalogs (i.e. sources with an angular separation lower than  $0''.4$ ).

ing from the H and K-band images and catalogs, we identified two such sources, AGS24 and AGS25. Both are detected in the K-band, but neither of these two sources has been detected by the HST even in the  $1.6\mu m$  H-band (down to the  $5\sigma$  limiting depth of  $H = 28$  AB), hence they are HST-dark like 4 sources listed in F18 and as also discussed in Wang et al. e.g., 2016; Elbaz et al. e.g., 2018; Schreiber et al. e.g., 2018; Yamaguchi et al. e.g., 2019.

The source AGS24 exhibits extended IRAC emission that is  $0''.36$  away from the ALMA position. This is slightly larger than the  $0''.3$  criterion but the source is also detected in the radio at 6 GHz ( $3.7\sigma$ ) and 3 GHz ( $5.7\sigma$ ). The  $S/N$  of this source is higher in the  $0''.29$  mosaic than in the  $0''.60$  tapered image, which suggests that it is particularly compact at 1.1 mm. This galaxy will be presented in detail in Zhou et al. (in prep), where a stellar mass and photometric redshift are estimated to be  $z \sim 3.5$  and  $M_{\star} = 1.82^{+0.27}_{-0.50} \times 10^{11} M_{\odot}$ .

The source AGS25 is  $0''.1$  away from its K-band counterpart in the ZFOURGE catalog (after applying the astrometric correction to the position of the ZFOURGE source), the source  $ID_{ZFOURGE} = 11353$  with a magnitude  $K = 25.9$  AB shown by a circle in Fig. 6. This source is not listed in the CANDELS catalog Guo et al. (2013), nor in the S-CANDELS catalog Ashby et al. (2015). It is marginally detected in radio at 5 and 10 cm with a  $S/N$  ratio close to 3. AGS25 is close ( $3''$ ) to a massive galaxy listed in CANDELS,  $ID_{CANDELS} = 8067$  with a stellar mass of  $M_{\star} = 5.6 \times 10^{10} M_{\odot}$  at a redshift of  $z_{spec} = 1.038$ .  $ID_{CANDELS} = 8067$  is the bright neighbor that explains the absence of AGS25 in S-CANDELS. We subtracted it from the IRAC image by modeling a Sérsic profile with GALFIT Peng et al. (2010) and measured an IRAC flux density of  $0.81 \pm 0.19$  mJy (see Fig. 6). The IRAC source is  $0''.28$  away from the ALMA position of AGS25.

Since the ALMA source is only  $0''.1$  away from the ZFOURGE source  $ID_{ZFOURGE} = 11353$ , we use the stellar mass and redshift from the ZFOURGE catalog for this source. The characteristics of this galaxy make it particularly interesting, with  $z_{AGS25} = 4.66^{+0.25}_{-0.26}$  and  $M_{\star, AGS25} = 2.0 \times 10^{10} M_{\odot}$ . These properties are similar to those of the Main Cata-



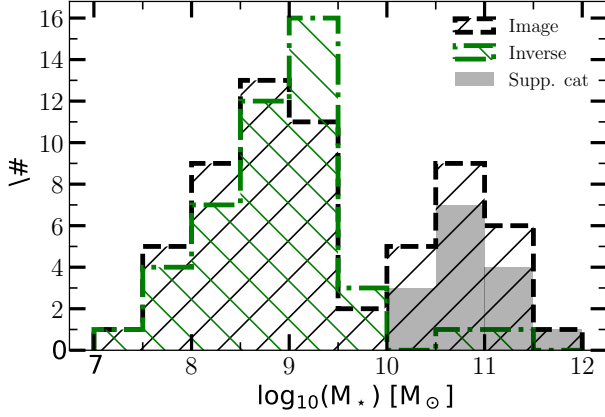


**Fig. 7.** Stellar mass distribution for the sources that were cross-matched between the ZFOURGE catalog and the image (black contours) or the inverse image (green contours). The sample galaxies selected in this study are shown in grey.

log source AGS11, which is also an HST-dark galaxy, with  $z_{\text{AGS11}} = 4.83^{+0.82}_{-0.76}$  and  $M_{\star, \text{AGS11}} = 2.8 \times 10^{10} M_{\odot}$ .

We note that among the 4 HST-dark galaxies for which we were able to determine a mass and redshift, there appear to be two distinct trends. Galaxies (AGS4 and AGS24) are among the most massive of all active UVJ galaxies detected in the region covered by the ALMA survey. AGS4 has a stellar mass  $M_{\star} = 2.81^{+1.65}_{-1.03} \times 10^{11} M_{\odot}$ . In other words, it is the most massive galaxy at  $4 < z < 5$  in our catalogs. AGS24 has a stellar mass  $M_{\star} = 1.82^{+0.27}_{-0.50} \times 10^{11} M_{\odot}$ . The other two HST-dark galaxies are of intermediate stellar mass, but with a redshift higher than 4.5.

In total, we end up with a list of 16 sources in the Supplementary Catalog including the two HST-dark sources AGS24 and AGS25 which exhibit the strongest S/N ratio of the catalog. Their properties are listed in Table 1 and Table 2.

#### 4.3. Consistency test of the Supplementary Catalog: stellar mass distribution

If we compare the nature of the counterparts of ALMA detections above  $3.5\text{-}\sigma$  in the image and the inverse image, we can see a difference that strengthens the solidity of the 16 sources of the Supplementary Catalog. There are 62 and 45 detections above  $3.5\text{-}\sigma$  in the ALMA image that have a counterpart in the K-band of the ZFOURGE catalog in the image and inverse image respectively. The stellar mass distributions of both samples are represented by dashed black and green lines for the image and inverse image respectively in Fig. 7. Both histograms show the same behavior at stellar masses below  $10^{10} M_{\odot}$  but there are nearly no galaxies above this mass threshold in the inverse image while there is a second bump in the histogram of the sources in the real image. Massive galaxies being rarer than low mass ones, the probability to get an association with such galaxy is lower and the fact that there is a second bump at high stellar masses in the real image suggests that these may be real. The Supplementary Catalog histogram shown in filled grey matches very nicely this second bump of massive galaxies. We recall that we did not impose any criterion of brightness or stellar mass in the selection of the Supplementary Catalog but only distances to IRAC, K-band and radio sources. If we limit ourselves to the galaxies above a stellar mass of  $10^{10} M_{\odot}$ , we can see that the number of

sources in the Supplementary Catalog is close to the difference between the image and inverse image.

In the sample of cross-matched galaxies from the positive image, 21/62 galaxies ( $\sim 34\%$ ) have a stellar mass greater than  $10^{10} M_{\odot}$ , compared with only 2/45 galaxies ( $\sim 4\%$ ) in the inverse image (see Fig. 7). A Kolmogorov-Smirnov (KS) test on these data gives a p-value of  $3.9 \times 10^{-3}$  between these two samples, meaning that the likelihood that the two samples were drawn from the same distribution is extremely low. When we remove the sample of 16 galaxies listed in Table 1, the two samples become more similar. The p-value from a KS test then reaches 0.71. This means that once the galaxies in our study have been removed, the detections that remain have as high a probability of originating from the same parent sample as the inverse image detections, so that they are no longer statistically different from noise.

This suggests that not only the Supplementary Catalog is robust but also that there is little margin for an extra population of real sources that we would have missed.

## 5. Catalog

The positions of the ALMA sources listed in the Main and Supplementary catalogs are shown in Fig. 8 where they can be compared to the locations of other ALMA surveys. The postage-stamp images of the sources are shown in Appendix A.1.

### 5.1. Redshifts and stellar masses

Except for the two HST-dark galaxies, AGS24 and AGS25 (discussed in Sect. 4.2.2), all sources listed in the ALMA Supplementary Catalog have been given a photometric redshift by the CANDELS (Guo et al. 2013) and ZFOURGE (Straatman et al. 2016) teams. The two sources of photometric redshifts listed in Col.(5) and Col.(6) of Table 2 are in excellent agreement (see Fig. 9-left). Excluding AGS35 (whose redshift given in the ZFOURGE catalog,  $z = 9.48$  is much higher than that given by the CANDELS catalog,  $z = 2.99$ ), the average of  $|z_{\text{HST}} - z_{\text{ZFOURGE}}| / (1 + (z_{\text{HST}} + z_{\text{ZFOURGE}})/2)$  for the galaxies that have redshifts in both catalogs is 0.03.

A total of 38 % of the galaxies in the Supplementary Catalog (6/16) have been assigned a spectroscopic redshift:

- AGS26:  $z_{\text{spec}} = 1.619$  determined with VLT/FORS2 (Vanzella et al. 2008).
- AGS29:  $z_{\text{spec}} = 1.117$  from the VIMOS VLT Deep Survey (Le Fèvre et al. 2013).
- AGS30:  $z_{\text{spec}} = 0.65$  from the HST/ACS slitless grism spectroscopy of the PEARS program (Ferrerias et al. 2009).
- AGS36:  $z_{\text{spec}} = 0.646$  from the Arizona CDFS Environment Survey (ACES), spectroscopic redshift survey of the Chandra Deep Field South (CDFS) using IMACS on the Magellan-Baade telescope (Cooper et al. 2012) and confirmed by the VIMOS VLT Deep Survey (Le Fèvre et al. 2013).
- AGS37:  $z_{\text{spec}} = 1.956$  determined using the *Spitzer* Infrared Spectrograph (Wuyts et al. 2009; Fadda et al. 2010) and confirmed with the 3D-HST survey (Momcheva et al. 2016).
- AGS38:  $z_{\text{spec}} = 1.314$  determined with VLT/FORS2 (Vanzella et al. 2008).

We note that two additional spectroscopic redshifts have been determined for galaxies in the Main Catalog since the publication of F18.

ID	RA <sub>ALMA</sub>	Dec <sub>ALMA</sub>	RA <sub>HST</sub>	Dec <sub>HST</sub>	$\Delta_{HST1}$	$\Delta_{HST2}$	$(\Delta\alpha)_{HST}$	$(\Delta\delta)_{HST}$	$\Delta_{IRAC}$	%RAa
(1)	deg	deg	deg	deg	arcsec	arcsec	arcsec	arcsec	arcsec	%
AGS24	53.087178	-27.840217	...	...	...	...	...	...	...	...
AGS25	53.183710	-27.836515	...	...	...	...	...	...	...	...
AGS26	53.157229	-27.833468	53.157238	-27.833446	0.09	0.18	0.075	-0.232	0.305	0.33
AGS27	53.069132	-27.807155	53.068992	-27.807169	0.45	0.44	0.151	-0.279	0.643	1.38
AGS28	53.224467	-27.817214	53.224476	-27.817151	0.23	0.06	0.029	-0.231	0.086	0.03
AGS29	53.202362	-27.826284	53.202340	-27.826190	0.35	0.11	0.065	-0.226	0.585	1.14
AGS30	53.168097	-27.832632	53.168025	-27.832509	0.50	0.27	0.074	-0.215	0.261	0.24
AGS31	53.068906	-27.879739	53.068851	-27.879698	0.23	0.07	0.120	-0.194	0.133	0.07
AGS32	53.111595	-27.767860	53.111564	-27.767771	0.34	0.04	0.099	-0.280	0.136	0.07
AGS33	53.049749	-27.771007	53.049662	-27.770929	0.40	0.13	0.148	-0.310	0.206	0.14
AGS34	53.105431	-27.830749	53.105466	-27.830650	0.37	0.24	0.096	-0.232	0.234	0.19
AGS35	53.181971	-27.814127	53.181989	-27.814120	0.06	0.25	0.073	-0.241	0.118	0.05
AGS36	53.153025	-27.735192	53.152971	-27.735114	0.33	0.11	0.068	-0.298	0.370	0.47
AGS37	53.071752	-27.843712	53.071694	-27.843631	0.34	0.04	0.149	-0.273	0.009	0.00
AGS38	53.176650	-27.785435	53.176577	-27.785446	0.24	0.33	0.068	-0.240	0.402	0.55
AGS39	53.091634	-27.853413	53.091606	-27.853342	0.27	0.04	0.122	-0.228	0.114	0.05

**Table 1.** Details of the positional differences between ALMA and *HST*-WFC3 for our catalog of galaxies identified in the 1.1mm-continuum map. Columns: (1) Source ID; (2), (3) Coordinates of the detections in the ALMA image (J2000); (4), (5) Positions of *HST*-WFC3 *H*-band counterparts when applicable from Guo et al. (2013), (6), (7) Distances between the ALMA and *HST* source positions *before* ( $\Delta_{HST1}$ ) and *after* ( $\Delta_{HST2}$ ) applying both the systematic and local offset correction presented in Sect. 3; (8), (9) Offset to be applied to the *HST* source positions, which includes both the global systematic offset and the local offset; (10) Distance from the closest IRAC galaxy; (11) IRAC random association (RaA) between the ALMA detection and the closest IRAC galaxy.

ID ALMA	ID <sub>CLS</sub>	ID <sub>ZF</sub>	ID <sub>S-CLS</sub>	$z_{CLS}$	$z_{ZF}$	$z_{sp}$	S/N	Flux mJy	$\log_{10}(M_*)$ $M_\odot$	$S_{3GHz}$ $\mu Jy$
(1)	(2)	(3)	(4)	(5)	(6)	(7)	(8)	(9)	(10)	(11)
AGS24	...	...	...	...	...	...	3.93	$0.88 \pm 0.22$	$11.26^\dagger$	$12.43 \pm 2.19$
AGS25	...	11353	...	...	4.644	...	4.36	$0.81 \pm 0.19$	10.39	...
AGS26	8409	11442	J033237.75-275000.8	1.711	1.592	$1.619^{sp}$	4.31	$0.97 \pm 0.15$	10.89	$85.09 \pm 2.55$
AGS27	11287	14926	J033216.54-274825.7	4.931	4.729	...	3.76	$1.43 \pm 0.28$	10.93	$5.95 \pm 1.86$
AGS28	10286	13388	J033253.87-274901.9	2.021	2.149	...	4.10	$1.56 \pm 0.21$	11.17	$17.19 \pm 1.85$
AGS29	9242	12438	J033248.53-274934.8	1.346	1.071	$1.117^{sp}$	3.56	$0.61 \pm 0.18$	10.71	$65.01 \pm 2.38$
AGS30	8557	11581	J033240.33-274957.3	0.646	0.672	$0.65^{sp}$	4.00	$0.67 \pm 0.17$	10.30	...
AGS31	3584	6153	J033216.53-275247.0	2.686	2.445	...	3.93	$0.72 \pm 0.19$	11.38	...
AGS32	16822	19964	J033226.78-274604.2	4.526	4.729	...	3.92	$1.23 \pm 0.16$	11.00	$4.47 \pm 1.38$
AGS33	16558	19463	J033211.93-274615.5	2.571	2.676	...	3.85	$1.77 \pm 0.27$	10.71	$21.20 \pm 2.84$
AGS34	14035	17374	J033222.32-274711.9	2.866	2.750	...	3.72	$0.55 \pm 0.15$	10.82	$15.55 \pm 1.98$
AGS35	10497	14146	J033243.67-274851.0	2.986	9.476	...	3.71	$1.16 \pm 0.21$	10.83	$31.49 \pm 1.42$
AGS36	20859	23463	J033236.70-274406.6	0.646	0.663	$0.665^{sp}$	3.66	$0.74 \pm 0.21$	10.46	$11.71 \pm 1.60$
AGS37	7184	10241	J033217.22-275037.3	1.971	1.864	$1.956^{sp}$	3.64	$1.10 \pm 0.16$	11.22	$22.61 \pm 4.39$
AGS38	14638	17465	J033242.37-274707.8	1.346	1.323	$1.314^{sp}$	3.62	$1.00 \pm 0.16$	11.08	$9.92 \pm 2.28$
AGS39	6131	9248	J033222.00-275112.3	2.906	2.360	...	3.62	$0.80 \pm 0.23$	10.60	$17.24 \pm 2.29$

**Table 2.** Columns: (1) Source ID; (2),(3),(4) IDs of the *HST*-WFC3 (from the CANDELS catalog), ZFOURGE and IRAC (SEDs catalog) counterparts of these detections; (5),(6) Photometric redshifts from the CANDELS catalog (Guo et al. 2013),  $z_{CLS}$ , and ZFOURGE catalog (Straatman et al. 2016),  $z_{ZF}$  (note that AGS24 has a photometric redshift of  $z \approx 3.5$  determined by Zhou et al. (in prep., see Sect. 4.2.2); (7) Spectroscopic redshift when available (see Sect. 5.1), flagged with a "sp" exponent to avoid confusion; (8) S/N of the detections in the 0'60 mosaic. This S/N is given for the peak flux; (9) Flux and error on the flux as explained in Sect. 5.2; (10) Stellar mass from the ZFOURGE catalog with the exception of AGS24, marked with a  $\dagger$ , the determination of the stellar mass of this galaxy will be presented in Zhou et al. (in prep.); (11) 3GHz flux density from VLA (PI W.Rujopakarn.)

- AGS6, previously reported at  $z = 3.00$ , has been observed by the ALMA Spectroscopic Survey Large Program (ASPECS-LP; Decarli et al. 2019) in the Hubble Ultra-Deep Field, giving a  $z_{spec} = 2.698$  from the transition of CO(3-2) at 93.51 GHz. This spectroscopic redshift confirms the redshift also found by MUSE, at the same position (Boogaard et al. 2019).
- AGS18, previously reported at  $z = 2.794$ , has also been observed in the ASPECS-LP survey, giving a  $z_{spec} = 2.696$  from the transition of CO(3-2) at 93.51 GHz. This spectroscopic redshift again confirms the one found by MUSE at the same position (Boogaard et al. 2019).

In the following, we will adopt for each source (*i*) the spectroscopic redshift when available, otherwise (*ii*) the photometric redshift from the ZFOURGE catalog (except for AGS35 for which we use the CANDELS redshift). These redshifts are given in Table 2.

We note that the redshift range of the Supplementary Catalog covers a wider dynamic range than the sources of the Main Catalog including two low redshift sources ( $z \sim 0.6$ ), with no equivalent in the Main Catalog. These two sources will be discussed in detail in a following paper.

The stellar masses of the Main and Supplementary catalogs have been chosen from the ZFOURGE catalog (except

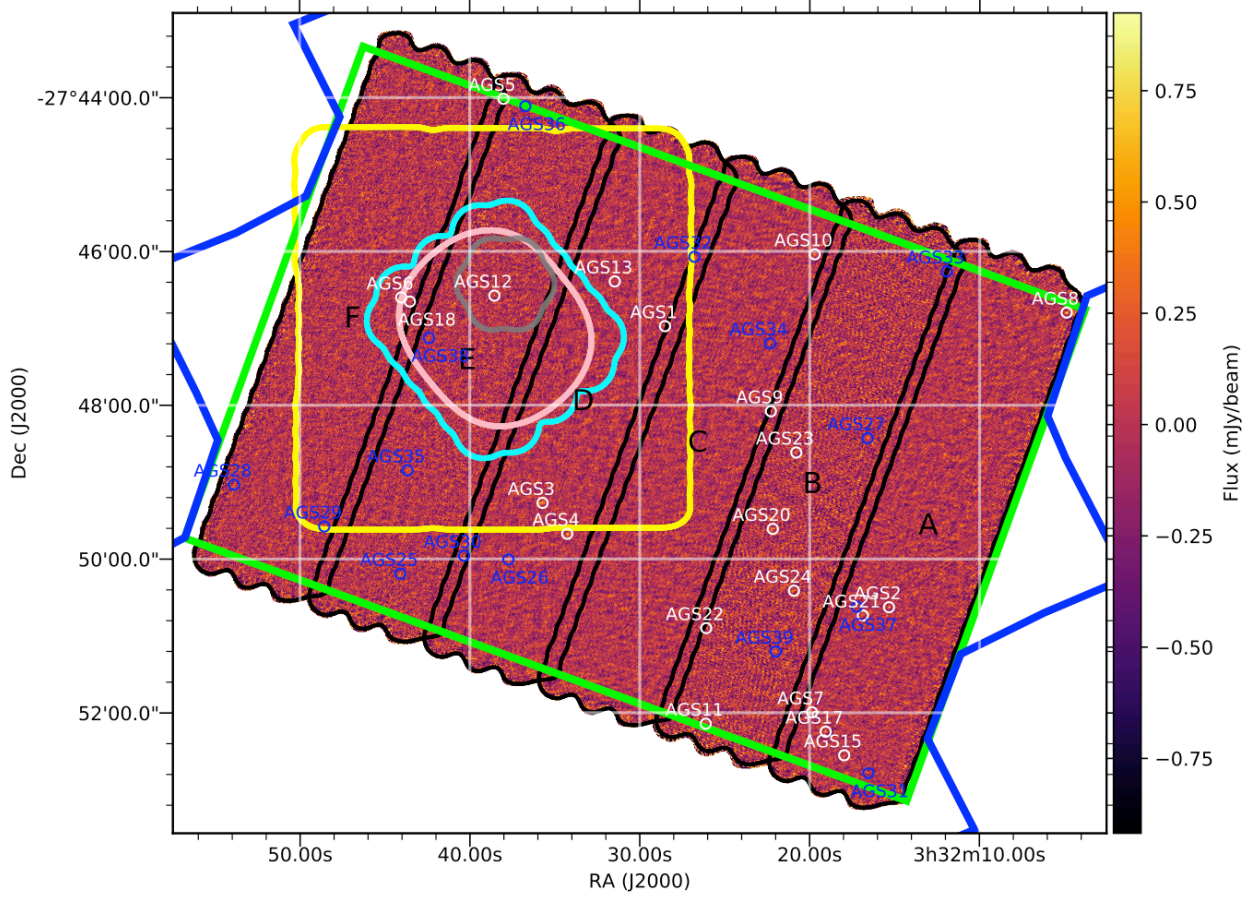


**Fig. 8.** ALMA 1.1 mm image tapered at 0'60. The white circles have a diameter of 4 arcseconds and indicate the positions of the galaxies listed in Table 1. Black contours show the different slices (labeled A to F) used to construct the homogeneous 1.1 mm coverage, with a median RMS = 0.18 mJy.beam<sup>-1</sup>. Blue lines show the limits of the HST/ACS field and green lines indicate the HST-WFC3 deep region. The cyan contours represent the limit of the Dunlop et al. (2017) survey covering all of the Hubble Ultra Deep Field region, the yellow contours show the ASAGAO survey (Hatsukade et al. 2018), while the purple contours show the ASPECS Pilot survey (Walter et al. 2016), the pink contours show the ASPECS Large Program (Decarli et al. 2019). The *Chandra* Deep Field-South encompasses all of the ALMA-survey field.

AGS35, for the reasons mentioned above). They were multiplied by a factor 1.7 to scale them from the Chabrier IMF to a Salpeter IMF. Both catalogs provide globally consistent stellar masses with no systematic offset, the median of the ratio  $M_{\star, \text{CANDELS}}/M_{\star, \text{ZFOURGE}} = 1.06$  (see Fig. 9-right).

## 5.2. Flux and size measurements

Flux densities of the Supplementary Catalog sources were measured by fitting the light profiles with a circular Gaussian in the uv-plane using *uvmodel* in CASA (McMullin et al. 2007). Due to the low S/N ( $3.5 < \text{S/N} < 4.8$ ), we have opted a circular Gaussian rather than an asymmetric Gaussian, in order to limit the number of free parameters. We use the formula given by Martí-Vidal et al. (2012) as in F18 to determine the minimum

size that can be reliably measured in the uv-plane as a function of the S/N ratio of the source for an interferometer :

$$\theta_{\min} \simeq 0.88 \frac{\theta_{\text{beam}}}{\sqrt{\text{S/N}}} \quad (2)$$

We use the S/N of the tapered map at 0'60 and  $\theta_{\text{beam}} = 0'60$ . Galaxies for which the circular Gaussian fit in the uv-plane give a size (FWHM) smaller than  $\theta_{\text{beam}}$ , the size limit given by Eq. 2, we set the size of the galaxy to  $\theta_{\text{beam}}$  and use the peak flux density measured on the direct image. This choice is expected to lead to slightly underestimated flux densities since it implies that sources are assumed to be point-like while the typical size measured for distant ALMA galaxies is on average close to 0'3 (Simpson et al. 2015a; Ikarashi et al. 2017; Elbaz et al. 2018). Assuming a point-like source for a real size extension of 0'3 FWHM would lead to an underestimation of the real flux density by a factor  $F_{\text{real}}/F_{\text{peak}} = 1.2$  (see Fig. 11) but in the absence of a robust size measurement, we decided to keep the peak flux



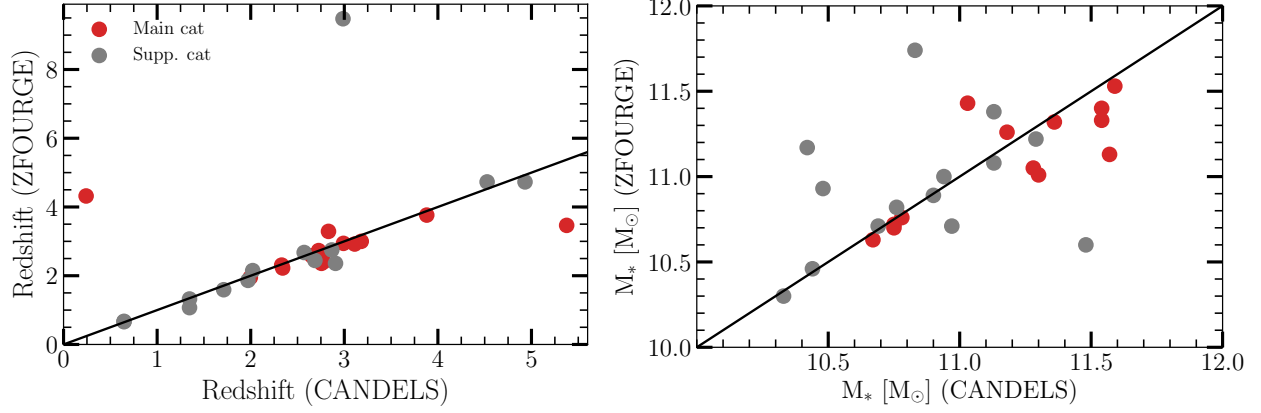


**Fig. 9.** Comparison of redshift (left panel) and stellar mass (right panel) from the CANDELS and the ZFOURGE catalogs. Solid black lines represent  $z_{\text{ZFOURGE}} = z_{\text{CANDELS}}$ . The galaxies presented in F18 (main catalog) are shown in red, while the galaxies presented in this paper are shown in gray. Black squares indicate spectroscopic redshifts. The stellar mass has been scaled from a Chabrier IMF to a Salpeter IMF by applying a factor of 1.7 in the ZFOURGE catalog. In this paper, we will take, with the exception of AGS36 which has an inconsistent redshift ( $z_{\text{AGS37,ZFOURGE}} = 9.47$  and for which we will take the data from the CANDELS catalog), the redshifts and stellar masses by the ZFOURGE catalog.

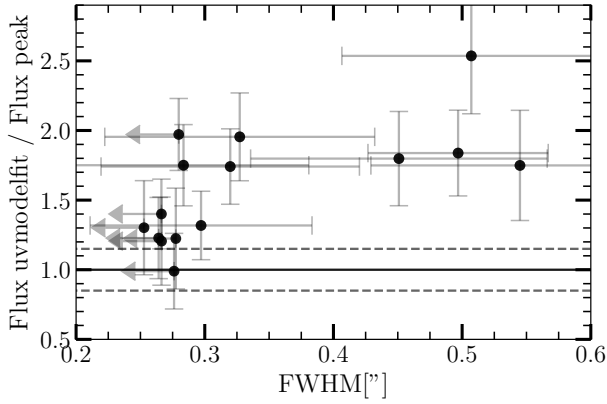


**Fig. 10.** Ratio between the flux extracted using `uvmodelfit` in CASA and the peak flux as a function of the size of the galaxy for the supplementary catalog. When the measured size is below the reliable size measurement limit (see Eq. 2), we consider the size given by Eq. 2 as an upper limit. The horizontal solid line indicates flux `uvmodelfit` = peak flux. The dotted lines show a 15 percent deviation from this equality. For galaxies larger than  $0''.25$  (vertical dotted line), the approximation of a point source is no longer valid, and we assume the flux value derived from `uvmodelfit` for these galaxies.

values having in mind that they may be lower by about 20 %. Using the measurements coming out of `uvmodelfit` would lead to larger uncertainties for those sources with no reliable size measurement.

For galaxies whose sizes measured using `uvmodelfit` are larger than this limit (see Fig. 10), we keep the size given by `uvmodelfit`. For these galaxies, the peak flux approximation is no longer valid and we keep the integrated flux given by `uvmodelfit`. The flux density of each galaxy, as well as its uncertainty, are listed in Table 2. The sizes measured by `uvmodelfit`, the detection limit derived from the Eq. 2 and the size of the galaxies are given Table 3.

In order to check whether our flux density measurements were underestimated by a large factor, we computed the expected ALMA flux density that those sources would have if they had

ID	$\theta_{\text{uvmodelfit}}$	$\theta_{\text{lim}}$	$\theta_{\text{final}}$
AGS24	0.06	0.27	0.27
AGS25	0.12	0.25	0.25
AGS26	0.30	0.25	0.30
AGS27	0.54	0.27	0.54
AGS28	0.50	0.26	0.50
AGS29	...	0.28	0.28
AGS30	...	0.26	0.26
AGS31	...	0.27	0.27
AGS32	0.33	0.27	0.33
AGS33	0.51	0.27	0.51
AGS34	...	0.27	0.27
AGS35	0.45	0.27	0.45
AGS36	0.23	0.28	0.28
AGS37	0.28	0.28	0.28
AGS38	0.32	0.28	0.32
AGS39	0.25	0.28	0.28

**Table 3.** Table of sizes measured with `uvmodelfit` and reliable size measurement limit given by Martí-Vidal et al. (2012). The last column gives the adopted size:  $\theta_{\text{uvmodelfit}}$  if  $\theta_{\text{uvmodelfit}} > \theta_{\text{lim}}$ ,  $\theta_{\text{lim}}$  if  $\theta_{\text{uvmodelfit}} < \theta_{\text{lim}}$ .

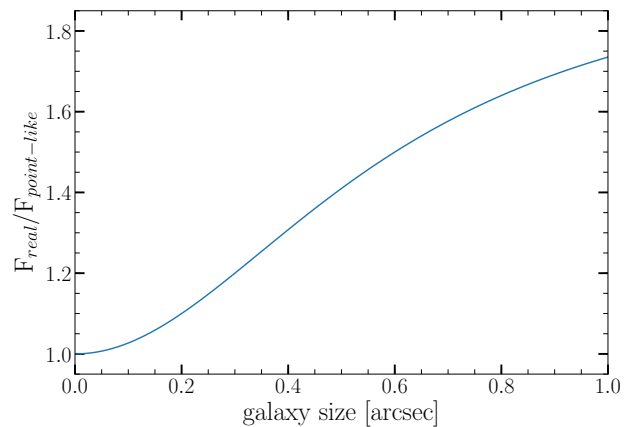


**Fig. 11.** Underestimation of the flux when assuming a point-like source instead of the real size of the galaxy. For example, a source with an intrinsic FWHM of  $0''.3$  will be underestimated by 20%.

been located on the star-formation main sequence (MS; Noeske et al. 2007; Rodighiero et al. 2011; Elbaz et al. 2011). Since a large fraction of the ALMA sources are actually starbursting and above the MS, this assumption only provides a rough estimate of a lower-limit to the ALMA flux densities. We used the infrared spectral energy distributions (IR SED) from the library presented in Schreiber et al. (2018), with the stellar masses and redshifts listed in Table 1 as input parameters. The measured,  $F_{ALMA}$ , and predicted,  $F_{SED}$ , flux densities exhibit a ratio  $F_{ALMA}/F_{SED}$  ranging from 0.73 to 5.2 with a median (average) of 2.4 (2.7) suggesting that about 50 % of the galaxies of the Supplementary Catalog fall within the factor 2 dispersion of the MS, the remaining half being in a starburst phase. None of the measured flux densities fall more than 25 % below the predicted MS ALMA flux density, which suggests that our flux density measurements are probably not largely underestimated.

## 6. Comparison of the properties of the ALMA galaxies from the Main and Supplementary catalogs

### 6.1. Redshifts

The redshifts of the Supplementary Catalog covers a wider range ( $z = 0.65 - 5.36$ ) than the sources of the Main Catalog ( $z = 1.95 - 4.82$ ). Galaxies with a redshift greater than  $z = 4.5$  represented 5 % of the Main Catalog (1/19) and they make 19 % of the Supplementary Catalog (3/16, see Fig. 12). On the other extreme, none of the Main Catalog sources were detected below  $z = 1.9$  whereas 38 % (6/16) of the sources in the Supplementary Catalog are found in this lower redshift range. Despite these differences, the median redshifts of both catalogs are similar,  $z = 2.70$  and 2.56 for the Main and Supplementary catalogs, respectively, showing that there is no systematic shift in redshift between both catalogs but a wider dynamic range for the Supplementary Catalog. This median redshift is also similar to that of Stach et al. (2019), who derive a median redshift of  $2.61 \pm 0.09$ . We found no correlation between redshift and flux density of the Supplementary Catalog sources.

### 6.2. Stellar Masses

All galaxies detected in GOODS-ALMA have a stellar mass greater than  $M_{\star} = 2 \times 10^{10} M_{\odot}$ . The median stellar mass of galaxies from the Supplementary Catalog,  $M_{\star}^{\text{Supp}} = 6.6 \times 10^{10} M_{\odot}$ , is half that from galaxies in the Main Catalog,  $M_{\star}^{\text{Main}} = 1.1 \times 10^{11} M_{\odot}$ . Hence by pushing down the ALMA detection limit using IRAC priors, we have reached more normal galaxies, with less extreme stellar masses, and extended the redshift range of the ALMA sources.

We can now compare the galaxies detected by GOODS-ALMA, combining the Main and Supplementary catalogs, to their parent sample of distant star-forming galaxies taken from the ZFOURGE catalog after selecting only the UVJ active galaxies (Williams et al. 2009, using the same definition as in F18, see Fig. 12).

GOODS-ALMA detects nearly half (46%, 6/13) of the most massive star-forming galaxies with  $\log_{10}(M_{\star}/M_{\odot}) = 11-12$  in the range  $2 < z < 2.5$ . Pushing further in redshift to  $2.5 < z < 3$ , GOODS-ALMA also sees nearly half of the star-forming galaxies with  $\log_{10}(M_{\star}/M_{\odot}) = 10.7-11$  (44%, 7/16). At even further redshifts,  $3 < z < 4$ , GOODS-ALMA detects 38% (3/8) of the most massive galaxies ( $\log_{10}(M_{\star}/M_{\odot}) = 11-12$ ).

In total, GOODS-ALMA detects about 30 % (11/37) of the most massive star-forming galaxies with a redshift  $2 < z < 4$  ( $\log_{10}(M_{\star}/M_{\odot}) = 11 - 12$ ).

### 6.3. Sizes

The sizes of the sources of the Main and Supplementary catalogs were derived by fitting a circular Gaussian in the uv-plane using *uvmodel* in CASA. We find that by pushing down the detection limit to  $3.5\text{-}\sigma$  using IRAC priors, we have been able to identify galaxies with nearly twice larger ALMA sizes. The median ALMA 1.1mm FWHM of the galaxies in the Supplementary Catalog is indeed  $0''.32$  as compared to  $0''.18$  for the galaxies in the Main Catalog. When accounting for the redshift of the sources, we find that the physical circularized half-light radius of the new sources in the present Supplementary Catalog ( $R_{1/2} = \text{FWHM}/2$ ) is 1.3 kpc as compared to only 0.65 kpc for the Main Catalog. If we take into account the fact that the Supplementary sources exhibit stellar masses that are half of those of source in the Main catalog, this implies that by pushing down the ALMA detection limit using priors, we were able to identify lower stellar mass galaxies in which dust-enshrouded star-formation extends over twice larger sizes.

In Fig. 13, we show the cumulative fraction of sources with a major axis below a given size for the Main (red) and Supplementary (grey) catalogs. This figure clearly shows that the galaxies detected in the Main catalog are generally more compact than those in the Supplementary catalog: 80% of the galaxies in the Main Catalog have a FWHM below  $0''.24$ , whereas in the Supplementary Catalog, 80% the sources have a size above  $0''.27$  arcsec. The size below which 80 % of the galaxies in the Supplementary Catalog are found is twice larger with a FWHM of  $0''.49$ .

This shows that while the projected sizes of dust-enshrouded star-formation probed by ALMA are globally small for massive and distant galaxies, the new sources that we present here in the Supplementary Catalog do not extend the sample to much lower flux densities but to sources with a wider extension of the dust emission. This explains in part why these sources were not detected in the Main Catalog. Although their integrated flux densities may be equal (and sometimes higher) than sources in the Main Catalog, this flux is diluted into several beams and therefore drops below the detection limit for the central beam.

We recall that this increase in the ALMA sizes measured in the Supplementary Catalog remains such that globally the ALMA emission extends over much smaller sizes than their H-band sizes, confirming that the ALMA sources are particularly compact at 1.1 mm (e.g., Chen et al. 2015; Simpson et al. 2015b; Rujopakarn et al. 2016; Elbaz et al. 2018; Calistro Rivera et al. 2018, see also Franco et al., in prep).

### 6.4. How complete is the Main plus Supplementary catalog ?

The average noise in the GOODS-ALMA image is  $\text{RMS} = 0.182$  mJy, hence the  $3.5\text{-}\sigma$  limit of the Supplementary Catalog converts into a detection limit of about 0.64 mJy. We note that since the RMS of the noise varies across the image, because it is subdivided in 6 slices taken at different epochs, sources may be detected below 0.64 mJy (a source was detected at 0.55 mJy).

The various studies that have carried out millimetric counts (e.g., Hatsukade et al. 2013; Oteo et al. 2016; Aravena et al. 2016; Umehata et al. 2017; Fujimoto et al. 2017; Dunlop et al. 2017; Franco et al. 2018; Hatsukade et al. 2018) allow us to es-

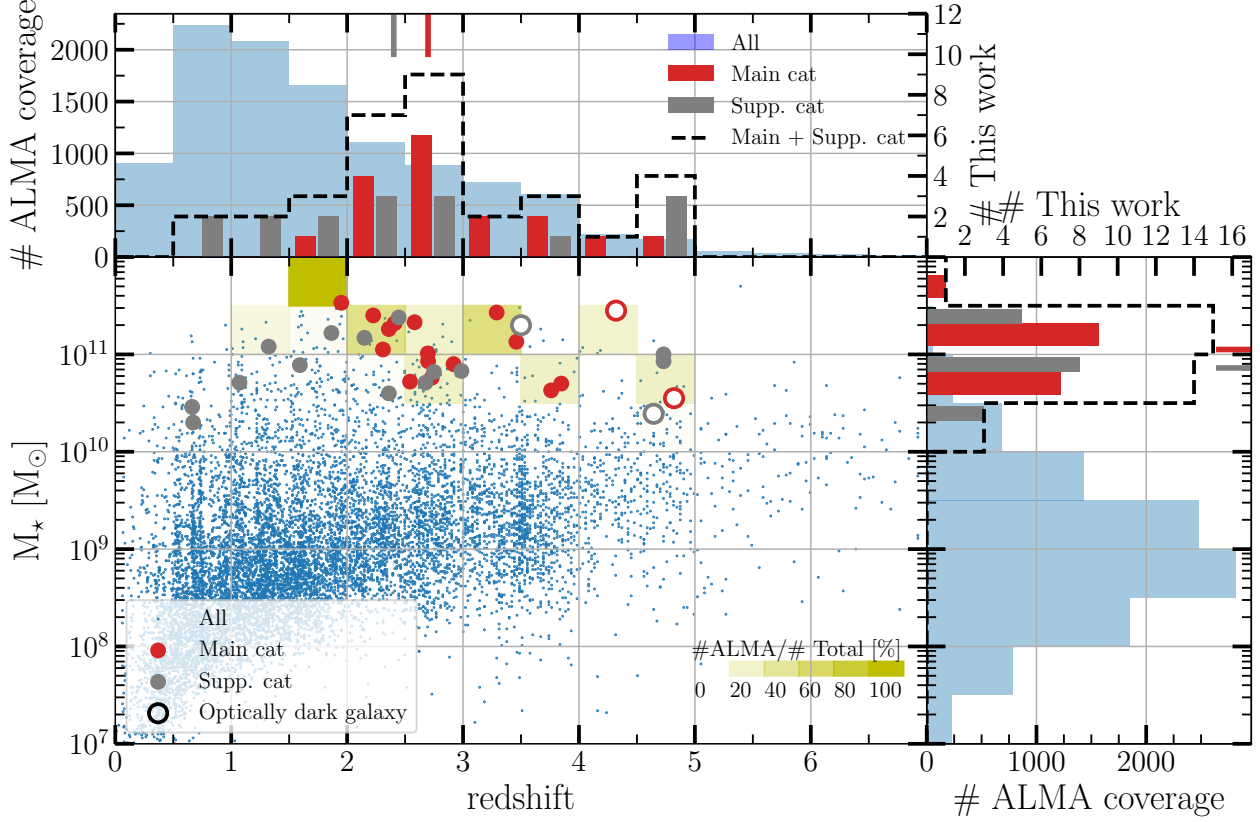


**Fig. 12.** Stellar mass as a function of redshift for the galaxies detected in F18 (red points) and in this work (gray points). For comparison, the distribution of all the galaxies, listed in the ZFOURGE catalog, in the same field of view is given in blue. Only UVJ active galaxies are shown. For each bin of redshift ( $z = 0.5$ ) and stellar mass ( $\log_{10}(M_*/M_\odot) = 0.5$ ), with a yellow shade, the fraction of sources detected by ALMA compares to the UVJ active galaxies in GOODS-ALMA. The optically dark galaxies for which redshifts and masses have been derived are represented by open circles. The upper panel shows the compared distribution of redshift between all the UVJ active galaxies in GOODS-ALMA and the ALMA-detected galaxies while the right panel shows the stellar mass distribution. The median of the redshift and of the stellar mass are shown in these two panels. The median redshift is 2.56 for the galaxies presented in this paper, compared to 2.70 in F18, while the median stellar mass is  $6.7 \times 10^{10} M_\odot$  in this study, compared to  $1.1 \times 10^{11} M_\odot$  in F18.

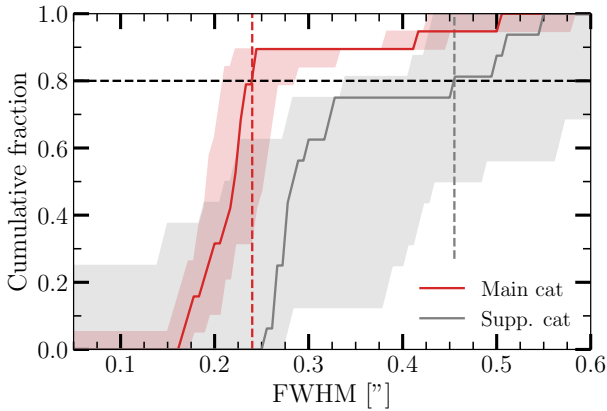


**Fig. 13.** Cumulative fraction of sources with a FWHM below a given size for the main (red) and the supplementary catalog (gray). These sizes are computed by fitting the ALMA detections with a circular Gaussian in the uv-plane using `uvmodelfit` in CASA. The shaded areas correspond to the integration of the individual uncertainties of the sizes of each detection.

estimate an expected galaxy surface density that varies between 2000 and 3500 galaxies. $\text{deg}^2$  above 0.65 mJy at 1.1 mm. Over the size of 69.5 arcmin $^2$  of the GOODS-ALMA survey, this amounts to an estimated number of sources ranging between 39 and 48. In comparison, we have now extended the number of detections in GOODS-ALMA to 35 galaxies. This number is not far from the expected one, especially when one accounts for cosmic variance, and suggests that the present sample may be more than 70 % complete above 0.65 mJy.

## 7. Conclusion

Using prior information at 3.6 and 4.5  $\mu\text{m}$  from IRAC (combined with deep HST *H*-band and ground-based *Ks*-images), we were able to explore the presence of galaxies detected at 1.1mm with ALMA down to the 3.5- $\sigma$  limit. This was done despite the extremely large number of independent beams in the ALMA image even after tapering from 0'29 to 0'6.

In order to avoid introducing spurious associations, we restricted the new sample to ALMA detections with either an IRAC counterpart closer than 0'3 or closer than 0'7 but with a radio counterpart as well. In two cases, we used the K-band

image to deconvolve IRAC sources that were missed by previous studies because of their close proximity to bright IRAC neighbors. These two galaxies do not exhibit any counterpart in the HST images, hence they are HST-dark, but both present a radio counterpart. In total we find 16 galaxies in the Supplementary Catalog that bring the total sample of GOODS-ALMA 1.1mm sources to 35 galaxies. This number is between 70 and 90 % of the predicted number of galaxies expected to be detected at 1.1 mm above 0.65 mJy as derived from existing millimeter number counts. We now detect in GOODS-ALMA between a third and half of the most massive star-forming galaxies ( $\log_{10} (M_{\star}/M_{\odot}) = 11 - 12$ ) depending on the redshift range within  $2 < z < 4$ .

The redshift range of the Supplementary Catalog covers a wider dynamic range ( $z = 0.65 - 5.36$ ) than the sources of the Main Catalog ( $z = 1.95 - 4.82$ ), with no systematic shift in the median redshift of  $z \approx 2.6$ . The typical physical size of the new sources in the present Supplementary Catalog (1.3 kpc) is twice larger than that of the Main Catalog sources (0.65 kpc). The lower surface brightness of these sources explains partly why they were not detected in the Main Catalog. Hence, pushing down the ALMA detection limit using IRAC priors allowed us to reach galaxies with half the stellar mass of the Main Catalog (median stellar mass  $M_{\star} = 6.6 \times 10^{10} M_{\odot}$ ) in which dust-enshrouded star-formation extends over twice larger sizes. However, this increase in the ALMA sizes is not large enough to question the fact that the ALMA emission globally extends over much smaller sizes than the H-band light, confirming that the ALMA sources are particularly compact at 1.1 mm.

Finally, we used a comparison of nearly 400 galaxies in common between HST and Pan-STARRS in the GOODS-ALMA field to show that the astrometry of the HST image does not only suffer from a global astrometric shift, as already discussed in previous papers, but also from local shifts that draw the equivalent of a distortion map that was artificially introduced in the process of building the mosaic of the GOODS-South HST image. We present a solution to correct for this distortion and use this correction in our identification of counterparts. We note that in some cases, the absence of this correction led previous studies to attribute the wrong counterpart to ALMA detections. This will be discussed in more detail in a paper in preparation.

## 8. Acknowledgements

R.D. gratefully acknowledges support from the Chilean Centro de Excelencia en Astrofísica y Tecnologías Afines (CATA) BASAL grant AFB-17000. This paper makes use of the following ALMA data: ADS/JAO.ALMA#2015.1.00543.S. ALMA is a partnership of ESO (representing its member states), NSF (USA) and NINS (Japan), together with NRC (Canada), MOST and ASIAA (Taiwan), and KASI (Republic of Korea), in cooperation with the Republic of Chile. The Joint ALMA Observatory is operated by ESO, AUI/NRAO and NAOJ.

## References

Aravena, M., Decarli, R., Walter, F., et al. 2016, *ApJ*, 833, 68  
 Ashby, M. L. N., Willner, S. P., Fazio, G. G., et al. 2015, *ApJS*, 218, 33  
 Barger, A. J., Cowie, L. L., Sanders, D. B., et al. 1998, *Nature*, 394, 248  
 Boogaard, L. A., Decarli, R., González-López, J., et al. 2019, *arXiv e-prints* [arXiv:1903.09167]  
 Calistro Rivera, G., Hodge, J. A., Smail, I., et al. 2018, *ApJ*, 863, 56  
 Chabrier, G. 2003, *PASP*, 115, 763  
 Chen, C.-C., Smail, I., Swinbank, A. M., et al. 2015, *ApJ*, 799, 194  
 Cooper, M. C., Yan, R., Dickinson, M., et al. 2012, *MNRAS*, 425, 2116

Cowie, L. L., Gonzalez-Lopez, J., Barger, A. J., et al. 2018, *ArXiv e-prints* [arXiv:1805.09424]  
 Decarli, R., Walter, F., González-López, J., et al. 2019, *arXiv e-prints* [arXiv:1903.09164]  
 Dole, H., Lagache, G., Puget, J.-L., et al. 2006, *A&A*, 451, 417  
 Dunlop, J. S., McLure, R. J., Biggs, A. D., et al. 2017, *MNRAS*, 466, 861  
 Elbaz, D., Dickinson, M., Hwang, H. S., et al. 2011, *A&A*, 533, A119  
 Elbaz, D., Leiton, R., Nagar, N., et al. 2018, *A&A*, 616, A110  
 Fadda, D., Yan, L., Lagache, G., et al. 2010, *ApJ*, 719, 425  
 Fazio, G. G., Hora, J. L., Allen, L. E., et al. 2004, *ApJS*, 154, 10  
 Ferreras, I., Pasquali, A., Malhotra, S., et al. 2009, *ApJ*, 706, 158  
 Flewelling, H. A., Magnier, E. A., Chambers, K. C., et al. 2016, *ArXiv e-prints* [arXiv:1612.05243]  
 Fontana, A., Dunlop, J. S., Paris, D., et al. 2014, *A&A*, 570, A11  
 Fontanot, F., De Lucia, G., Monaco, P., Somerville, R. S., & Santini, P. 2009, *MNRAS*, 397, 1776  
 Franco, M., Elbaz, D., Béthermin, M., et al. 2018, *A&A*, 620, A152  
 Fujimoto, S., Ouchi, M., Shibuya, T., & Nagai, H. 2017, *ApJ*, 850, 83  
 Grogin, N. A., Kocevski, D. D., Faber, S. M., et al. 2011, *ApJS*, 197, 35  
 Guo, Y., Ferguson, H. C., Giavalisco, M., et al. 2013, *ApJS*, 207, 24  
 Hales, C. A., Murphy, T., Curran, J. R., et al. 2012, *BLOBCAT: Software to Catalog Blobs, Astrophysics Source Code Library*  
 Hatsukade, B., Kohn, K., Yamaguchi, Y., et al. 2018, *PASJ*, 70, 105  
 Hatsukade, B., Ohta, K., Seko, A., Yabe, K., & Akiyama, M. 2013, *ApJ*, 769, L27  
 Holland, W. S., Robson, E. I., Gear, W. K., et al. 1999, *MNRAS*, 303, 659  
 Hsieh, B.-C., Wang, W.-H., Hsieh, C.-C., et al. 2012, *ApJS*, 203, 23  
 Hughes, D. H., Serjeant, S., Dunlop, J., et al. 1998, *Nature*, 394, 241  
 Ikarashi, S., Caputi, K., Ohta, K., et al. 2017, *ArXiv e-prints* [arXiv:1710.09021]  
 Ivison, R. J., Greve, T. R., Dunlop, J. S., et al. 2007, *MNRAS*, 380, 199  
 Kissler-Patig, M., Pirard, J.-F., Casali, M., et al. 2008, *A&A*, 491, 941  
 Koekemoer, A. M., Faber, S. M., Ferguson, H. C., et al. 2011, *ApJS*, 197, 36  
 Le Fèvre, O., Cassata, P., Cucciati, O., et al. 2013, *A&A*, 559, A14  
 Martí-Vidal, I., Pérez-Torres, M. A., & Lobanov, A. P. 2012, *A&A*, 541, A135  
 Martini, P., Persson, S. E., Murphy, D. C., et al. 2004, in *Proc. SPIE*, Vol. 5492, *Ground-based Instrumentation for Astronomy*, ed. A. F. M. Moorwood & M. Iye, 1653–1660  
 McMullin, J. P., Waters, B., Schiebel, D., Young, W., & Golap, K. 2007, in *Astronomical Society of the Pacific Conference Series*, Vol. 376, *Astronomical Data Analysis Software and Systems XVI*, ed. R. A. Shaw, F. Hill, & D. J. Bell, 127  
 Momcheva, I. G., Brammer, G. B., van Dokkum, P. G., et al. 2016, *ApJS*, 225, 27  
 Moorwood, A., Cuby, J.-G., Ballester, P., et al. 1999, *The Messenger*, 95, 1  
 Noeske, K. G., Weiner, B. J., Faber, S. M., et al. 2007, *ApJ*, 660, L43  
 Oke, J. B., & Gunn, J. E. 1983, *ApJ*, 266, 713  
 Oteo, I., Zwaan, M. A., Ivison, R. J., Smail, I., & Biggs, A. D. 2016, *ApJ*, 822, 36  
 Peng, C. Y., Ho, L. C., Impey, C. D., & Rix, H.-W. 2010, *AJ*, 139, 2097  
 Persson, S. E., Murphy, D. C., Smees, S., et al. 2013, *PASP*, 125, 654  
 Puget, P., Stadler, E., Doyon, R., et al. 2004, in *Proc. SPIE*, Vol. 5492, *Ground-based Instrumentation for Astronomy*, ed. A. F. M. Moorwood & M. Iye, 978–987  
 Retzlaff, J., Rosati, P., Dickinson, M., et al. 2010, *A&A*, 511, A50  
 Rodighiero, G., Daddi, E., Baronchelli, I., et al. 2011, *ApJ*, 739, L40  
 Rujopakarn, W., Dunlop, J. S., Rieke, G. H., et al. 2016, *ApJ*, 833, 12  
 Salpeter, E. E. 1955, *ApJ*, 121, 161  
 Schreiber, C., Labbé, I., Glazebrook, K., et al. 2018, *A&A*, 611, A22  
 Simpson, J. M., Smail, I., Swinbank, A. M., et al. 2015a, *ApJ*, 799, 81  
 Simpson, J. M., Smail, I., Swinbank, A. M., et al. 2015b, *ApJ*, 807, 128  
 Smail, I., Ivison, R. J., & Blain, A. W. 1997, *ApJ*, 490, L5  
 Stach, S. M., Dudzevičiūtė, U., Smail, I., et al. 2019, *arXiv e-prints* [arXiv:1903.02602]  
 Steinhardt, C. L., Capak, P., Masters, D., & Speagle, J. S. 2016, *ApJ*, 824, 21  
 Straatman, C. M. S., Spitler, L. R., Quadri, R. F., et al. 2016, *ApJ*, 830, 51  
 Umehata, H., Tamura, Y., Kohn, K., et al. 2017, *ApJ*, 835, 98  
 van der Wel, A., Franx, M., van Dokkum, P. G., et al. 2014, *ApJ*, 788, 28  
 Vanzella, E., Cristiani, S., Dickinson, M., et al. 2008, *A&A*, 478, 83  
 Walter, F., Decarli, R., Aravena, M., et al. 2016, *ApJ*, 833, 67  
 Wang, T., Elbaz, D., Schreiber, C., et al. 2016, *ApJ*, 816, 84  
 Werner, M. W., Roellig, T. L., Low, F. J., et al. 2004, *ApJS*, 154, 1  
 Williams, C. C., Labbe, I., Spilker, J., et al. 2019, *arXiv e-prints*, arXiv:1905.11996  
 Williams, R. J., Quadri, R. F., Franx, M., van Dokkum, P., & Labbé, I. 2009, *ApJ*, 691, 1879  
 Windhorst, R. A., Cohen, S. H., Hathi, N. P., et al. 2011, *ApJS*, 193, 27  
 Wuyts, S., van Dokkum, P. G., Franx, M., et al. 2009, *ApJ*, 706, 885  
 Yamaguchi, Y., Kohn, K., Hatsukade, B., et al. 2019, *arXiv e-prints* [arXiv:1903.02744]

## Appendix A: Multiwavelength Postage-stamp

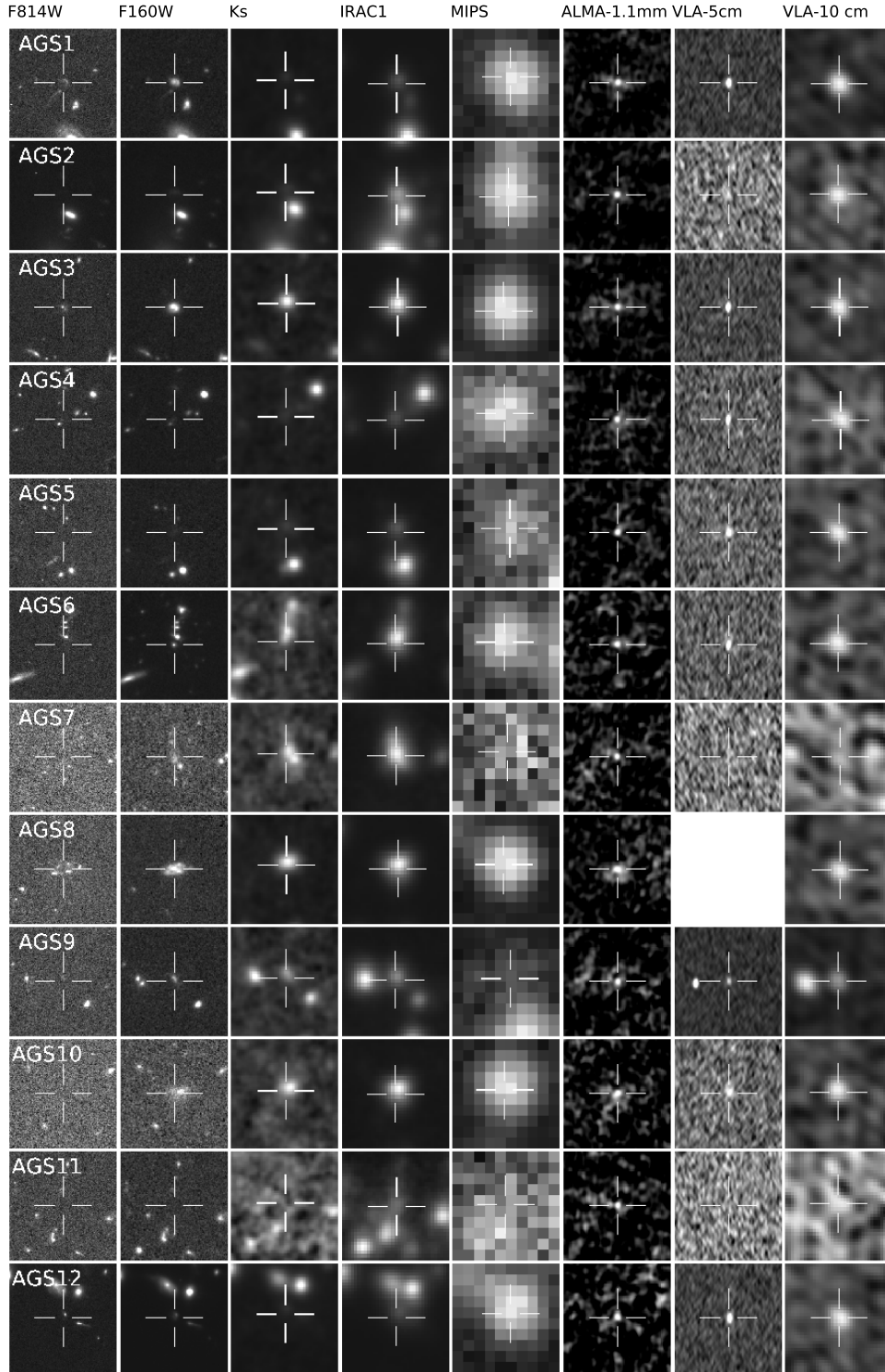


**Fig. A.1.** Postage-stamp ( $10 \times 10$  arcseconds), centred on the position of the ALMA detection at different wavelengths. From left to right : HST-WFC3 (a verifier (F814W, F160W), ZFOURGE ( $K_s$ ), *Spitzer*-IRAC channel 1 ( $3.6 \mu\text{m}$ ), *Spitzer*-MIPS ( $24 \mu\text{m}$ ), ALMA band 6 (1.1mm), VLA (5 and 10 cm). Blank images mean that the source is out of the field of view of the instrument. The white cross indicates the position of the ALMA detection.



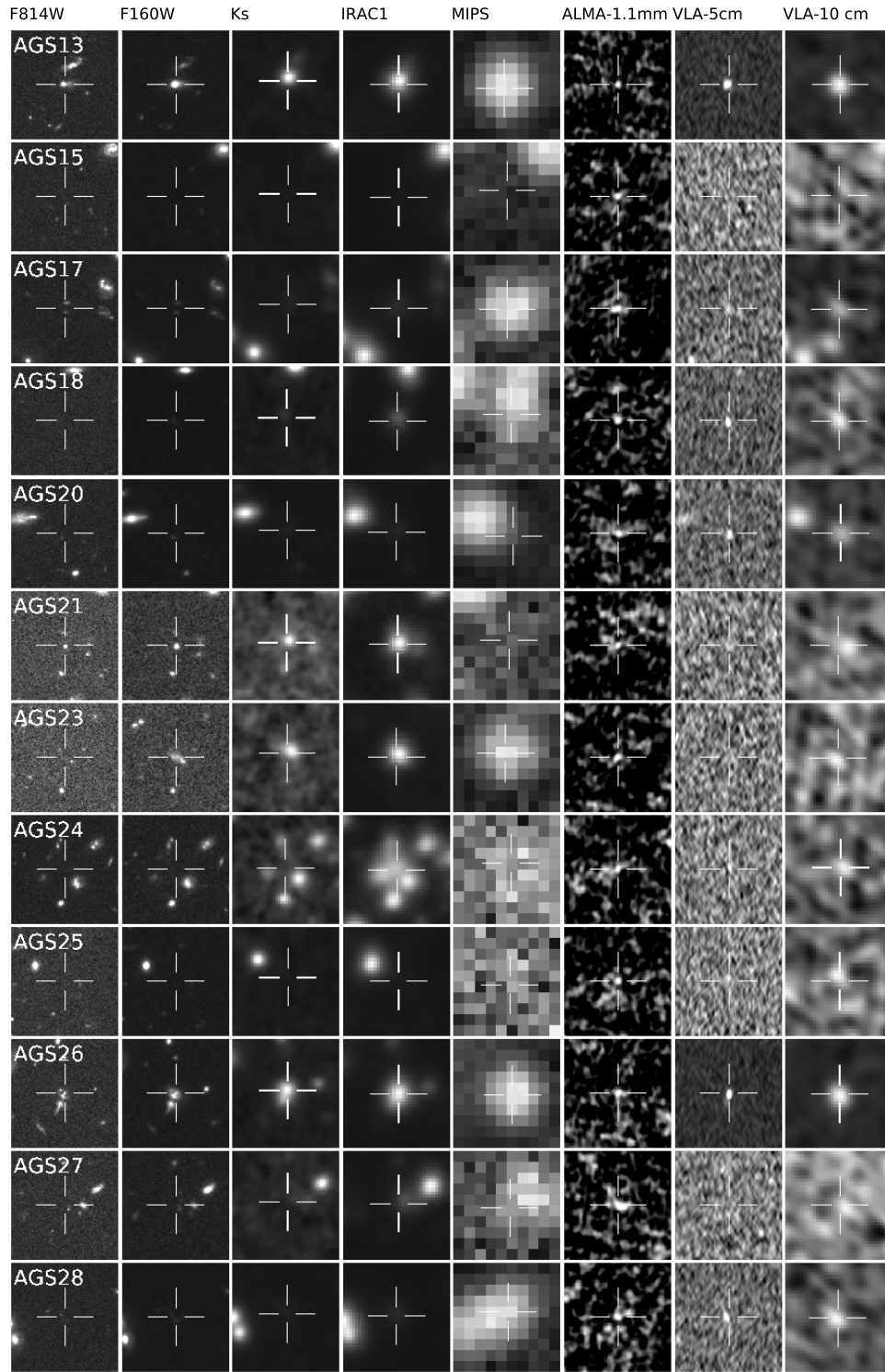


Fig. A.2. (continued)

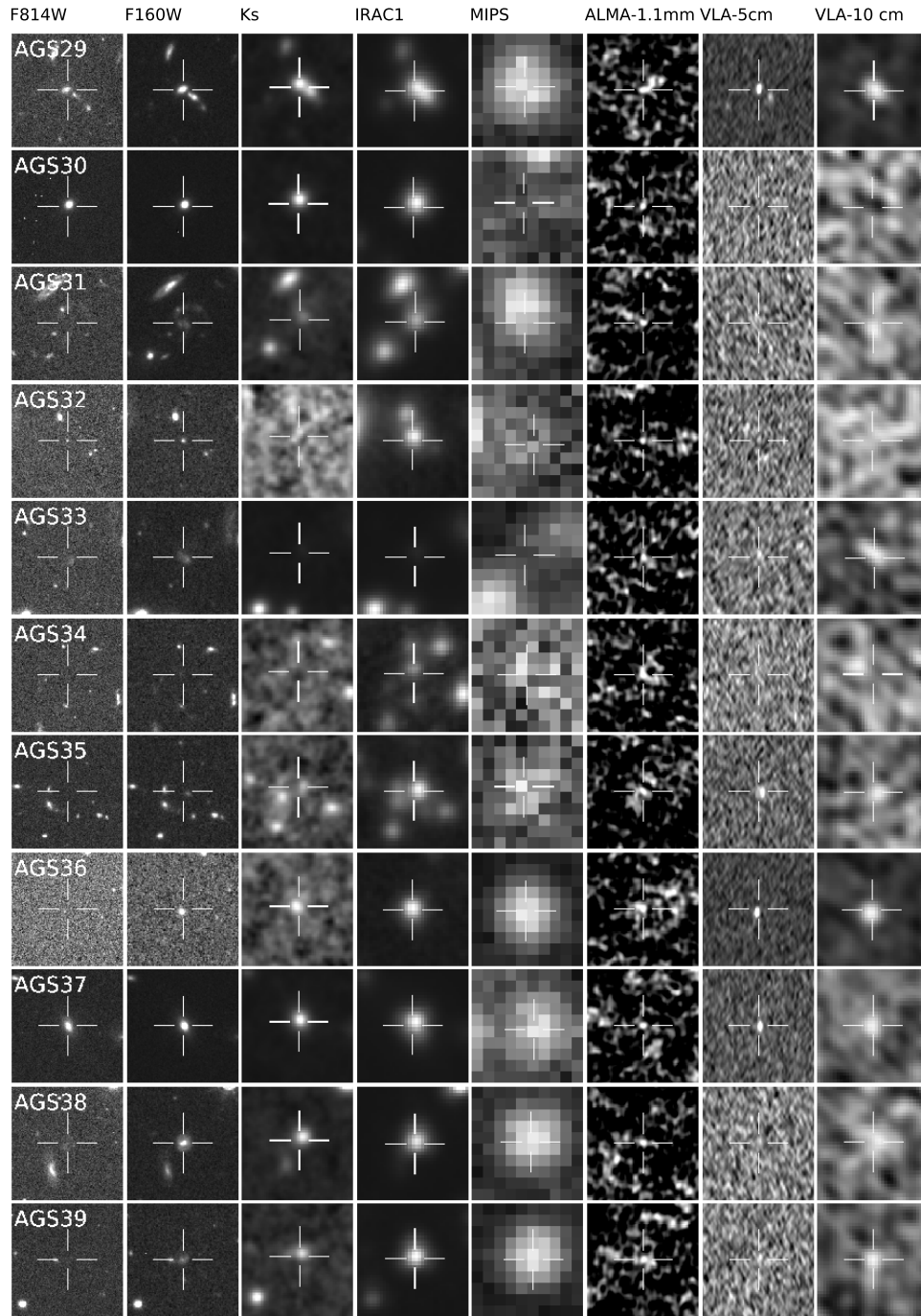


Fig. A.3. (continued)



# A dominant population of optically invisible massive galaxies in the early Universe

T. Wang<sup>1,2,3\*</sup>, C. Schreiber<sup>2,4,5</sup>, D. Elbaz<sup>2</sup>, Y. Yoshimura<sup>1</sup>, K. Kohno<sup>1,6</sup>, X. Shu<sup>7</sup>, Y. Yamaguchi<sup>1</sup>, M. Pannella<sup>8</sup>, M. Franco<sup>2</sup>, J. Huang<sup>9</sup>, C.-F. Lim<sup>10</sup> & W.-H. Wang<sup>10</sup>

**Our current knowledge of cosmic star-formation history during the first two billion years (corresponding to redshift  $z > 3$ ) is mainly based on galaxies identified in rest-frame ultraviolet light<sup>1</sup>. However, this population of galaxies is known to under-represent the most massive galaxies, which have rich dust content and/or old stellar populations. This raises the questions of the true abundance of massive galaxies and the star-formation-rate density in the early Universe. Although several massive galaxies that are invisible in the ultraviolet have recently been confirmed at early epochs<sup>2–4</sup>, most of them are extreme starburst galaxies with star-formation rates exceeding 1,000 solar masses per year, suggesting that they are unlikely to represent the bulk population of massive galaxies. Here we report submillimetre (wavelength 870 micrometres) detections of 39 massive star-forming galaxies at  $z > 3$ , which are unseen in the spectral region from the deepest ultraviolet to the near-infrared. With a space density of about  $2 \times 10^{-5}$  per cubic megaparsec (two orders of magnitude higher than extreme starbursts<sup>5</sup>) and star-formation rates of 200 solar masses per year, these galaxies represent the bulk population of massive galaxies that has been missed from previous surveys. They contribute a total star-formation-rate density ten times larger than that of equivalently massive ultraviolet-bright galaxies at  $z > 3$ . Residing in the most massive dark matter haloes at their redshifts, they are probably the progenitors of the largest present-day galaxies in massive groups and clusters. Such a high abundance of massive and dusty galaxies in the early Universe challenges our understanding of massive-galaxy formation.**

Observations of galaxies across cosmic time have revealed that the more massive galaxies have assembled their stellar masses at earlier epochs, with a substantial population of massive ellipticals already in place at redshifts of about<sup>6–8</sup> 3–4. The early assembly of these massive galaxies has posed serious challenges to current galaxy formation theories. Understanding their formation processes requires studies of their progenitors formed at even higher redshifts. However, most currently known high-redshift galaxies, including mainly Lyman-break galaxies (LBGs) and a few extreme starbursts, are found inadequate to account for the large population of these early formed ellipticals, owing to either low stellar masses and star-formation rates, SFRs (for LBGs<sup>9</sup>), or low space densities (for the extreme starbursts). This suggests that the main progenitors of massive galaxies at  $z > 3$  remain to be found. Identification of these currently missing massive galaxies is key to our understanding of both massive-galaxy formation and the cosmic SFR density in the early Universe.

The main targets of this study are a population of galaxies that are Spitzer/Infrared Array Camera (IRAC)-bright (see below for nomenclature) yet undetected in even the deepest near-infrared (NIR: H-band) imaging with the Hubble Space Telescope (HST), that is, H-dropouts. (Throughout this Letter we use the short form ‘Telescope/Instrument’ to represent usage of a particular instrument on a particular telescope.)

In total, we have identified 63 H-dropouts with IRAC 4.5- $\mu$ m magnitude, [4.5], less than 24 mag, within a total survey area of approximately 600 arcmin<sup>2</sup> in deep CANDELS fields with a typical depth of  $H > 27$  mag ( $5\sigma$ ) (Fig. 1, Extended Data Table 1, Methods). Although previous studies have shown that these bright and red IRAC sources are promising candidates for massive galaxies at<sup>10,11</sup>  $z > 3$ , confirming their nature has been difficult so far owing to the limited sample size, the poor resolution of Spitzer and the lack of multiwavelength information. Here we explore their nature with high-resolution, 870- $\mu$ m continuum imaging with the Atacama Large Millimeter/submillimetre Array (ALMA). With only 1.8 min of integration per object, 39 of them (detection rates of 62%) are detected down to an integrated flux of 0.6 mJy ( $4\sigma$ , Extended Data Fig. 1, Extended Data Table 2). Their 870- $\mu$ m fluxes range from 0.6 mJy to 8 mJy, with a median of  $S_{870\mu\text{m}} = 1.6$  mJy (Extended Data Fig. 2). Hence most of them are fainter than the 2-mJy confusion limit of the single dish instruments that discovered submillimetre galaxies (SMGs) and much fainter than most SMGs studied until now with typical<sup>12</sup>  $S_{870\mu\text{m}} \gtrsim 4$  mJy. The sky density of these ALMA-detected H-dropouts is approximately  $5.3 \times 10^2 \text{ deg}^{-2}$  after correction for incompleteness (Methods), two orders of magnitude higher than Herschel/SPIRE-selected extreme starbursts (with  $\text{SFR} \gtrsim 1,000 M_{\odot} \text{ yr}^{-1}$ ;  $M_{\odot}$ , solar mass)<sup>3,5</sup>.

The ALMA detections confirm unambiguously that most of the H-dropouts are dusty star-forming galaxies at high redshifts, consistent with their admittedly uncertain photometric redshifts—from optical spectral energy distribution (SED) fitting—with median redshift  $z_{\text{median}} = 4$  (Extended Data Fig. 3). Further insights into their properties are obtained from the stacked infrared (IR) SED of the 39 ALMA-detected H-dropouts from MIPS 24  $\mu$ m up to ALMA 870  $\mu$ m. The stacked SED peaks between the observations at 350  $\mu$ m and at 500  $\mu$ m (Extended Data Fig. 3), consistent with being at  $z \approx 4$ . With a median stellar mass of  $M_{*} \approx 10^{10.6} M_{\odot}$  and a characteristic IR luminosity (over 8–1,000  $\mu$ m) of  $L_{\text{IR}} = (2.2 \pm 0.3) \times 10^{12} L_{\odot}$  ( $L_{\odot}$ , solar luminosity) derived from the stacked SED, these ALMA-detected H-dropouts are fully consistent with being normal massive star-forming galaxies at<sup>13</sup>  $z = 4$  (Fig. 2). Moreover, the ALMA detections also provide crucial constraints on the redshift of individual galaxies. Combined with SCUBA-2 450- $\mu$ m and VLA 3-GHz data, the majority of the ALMA-detected H-dropouts exhibit red  $S_{870\mu\text{m}}/S_{450\mu\text{m}}$  and  $S_{1.4\text{GHz}}/S_{870\mu\text{m}}$  colours that are suggestive of redshifts of  $z > 3$  (Extended Data Fig. 4). Similarly, the non-detections at 24  $\mu$ m ( $5\sigma$  detection limit of 20  $\mu$ Jy) for most of the sources implies red  $S_{870\mu\text{m}}/S_{24\mu\text{m}}$  colours that are also consistent with  $z > 3$  assuming typical SED templates<sup>14</sup>. We hence conclude that whereas the estimated redshifts for individual galaxies exhibit a large uncertainty, all the available data point to the ALMA-detected H-dropouts being massive, dusty star-forming galaxies at  $z > 3$ .

For the remaining about 40% of H-dropouts that are not detected with ALMA, photometric redshift estimates based on their optical

<sup>1</sup>Institute of Astronomy, Graduate School of Science, The University of Tokyo, Tokyo, Japan. <sup>2</sup>AIM, CEA, CNRS, Université Paris-Saclay, Université Paris Diderot, Sorbonne Paris Cité, Gif-sur-Yvette, France. <sup>3</sup>National Astronomical Observatory of Japan, Mitaka, Tokyo, Japan. <sup>4</sup>Leiden Observatory, Leiden University, Leiden, The Netherlands. <sup>5</sup>Department of Physics, University of Oxford, Oxford, UK. <sup>6</sup>Research Center for the Early Universe, Graduate School of Science, The University of Tokyo, Tokyo, Japan. <sup>7</sup>Department of Physics, Anhui Normal University, Wuhu, China. <sup>8</sup>Department of Physics, Ludwig-Maximilians-Universität, München, Germany. <sup>9</sup>National Astronomical Observatories of China, Chinese Academy of Sciences, Beijing, China. <sup>10</sup>Academia Sinica Institute of Astronomy and Astrophysics, Taipei, Taiwan. \*e-mail: twang.nju@gmail.com

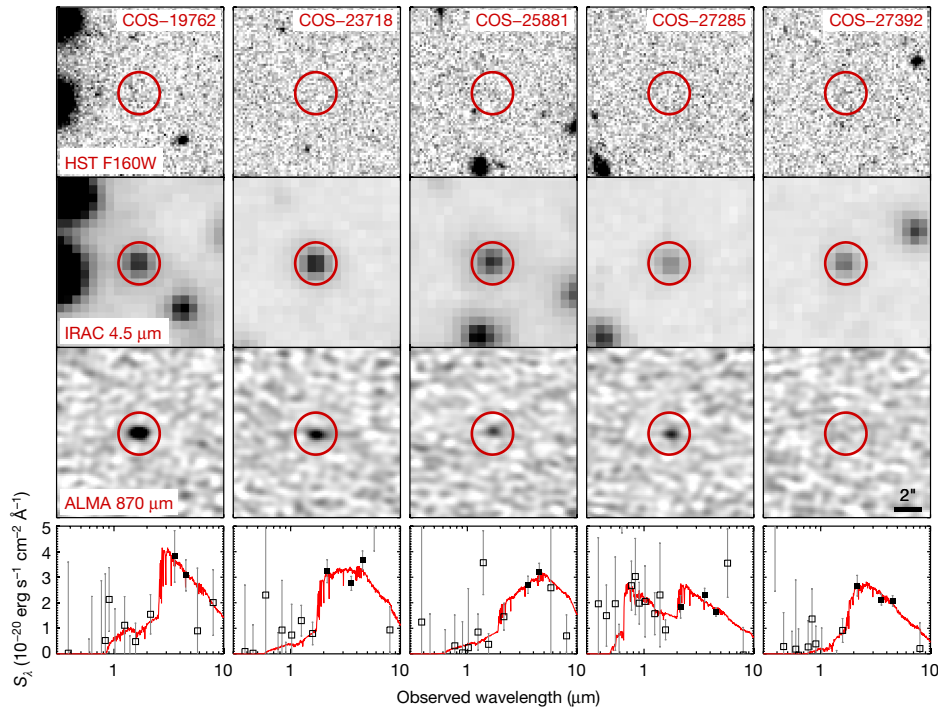


**Fig. 1 | Example images and SEDs of H-dropouts.** Top three rows, images of five H-dropouts obtained in three different spectral bands—HST/F160W (top row), IRAC 4.5  $\mu\text{m}$  (second row) and ALMA 870  $\mu\text{m}$  (third row). The H-dropouts, named in the top row, were selected randomly from the parent sample, with all but the last one (COS-27392) detected with ALMA. Each image is  $12'' \times 12''$ ; see scale bar in bottom right image.

Bottom row, the measured UV-to-NIR SED (squares) and best-fit stellar population synthesis models (red lines).  $S_\lambda$ , differential flux per unit wavelength. The error bars are  $1\sigma$ . The filled and open squares indicate photometric points with measured signal-to-noise ratio (S/N) above and below 3, respectively.

SEDs suggest a similar redshift distribution to that of ALMA-detected ones, with  $z_{\text{median}} = 3.8$  (Extended Data Fig. 2). Their stacked ALMA 870- $\mu\text{m}$  image yields a  $6\sigma$  detection with  $S_{870\mu\text{m}} = 0.24 \pm 0.04$  mJy, approximately 8 times lower than that of ALMA-detected ones, suggesting lower specific SFRs compared to ALMA-detected ones, which is also confirmed by a full fitting of the stacked optical-to-IR SEDs (Extended Data Fig. 5).

Spectroscopic confirmation of H-dropouts has been so far limited to a few sources, which are all found at  $z > 3$ . Most of these confirmed cases are extreme SMGs with  $S_{870\mu\text{m}} \gtrsim 10$  mJy, for example<sup>2</sup>, HDF-850 at  $z = 5.18$ . An H-dropout galaxy with submillimetre flux similar to

that of our sample ( $S_{744\mu\text{m}} = 2.3 \pm 0.1$  mJy) has been recently confirmed<sup>15</sup> to be at  $z = 3.709$ : it was discovered serendipitously near a quiescent galaxy at the same redshift<sup>6</sup>. By targeting three H-dropouts in our sample that show significant excess ( $>4\sigma$ , Methods) in Subaru medium bands in the optical (about 3,500–6,000  $\text{\AA}$ ) with VLT/X-SHOOTER, we have successfully detected Lyman- $\alpha$  for two of them and confirmed their redshifts to be  $z > 3$  ( $z = 3.097$  and  $z = 5.113$ , Extended Data Fig. 6). These spectroscopic redshifts ( $z_{\text{spec}}$ ) are in good agreement with their photometric redshift ( $z_{\text{phot}}$ ) based on optical SED fitting, with  $\sigma_{(z_{\text{phot}} - z_{\text{spec}})/(1+z_{\text{spec}})} \approx 0.1$ .

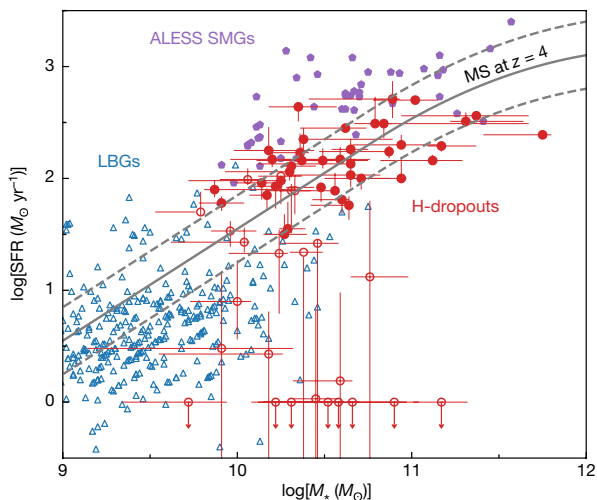


**Fig. 2 | Stellar masses and SFRs of H-dropouts.** The red filled and open circles represent respectively the ALMA-detected and the ALMA-undetected H-dropouts. For comparison, a sample of LBGs at  $z = 4$ – $6$  from the ZFOURGE survey<sup>22</sup> and bright  $z > 3$  SMGs ( $S_{870\mu\text{m}} > 4.2$  mJy) from the ALESS survey are also shown<sup>23</sup>. The stellar masses for the ALESS SMGs are reduced by 0.3 dex to account for the systematic differences caused by the different methods used in mass estimation. The grey solid and dashed lines indicate respectively the star-forming main sequence (MS) at  $z = 4$  and its  $1\sigma$  scatter<sup>24</sup>. The SFRs for ALMA-detected H-dropouts are derived from the 870- $\mu\text{m}$  fluxes assuming their intrinsic far-infrared SED resembles that of the stacked one. Error bars are  $1\sigma$ . The SFRs for ALMA-undetected H-dropouts are derived from optical SED fitting with an additional constraint of  $\text{SFR} > 1 M_\odot \text{ yr}^{-1}$ , for which error bars represent the 16th and 84th percentiles of the distribution obtained in the Monte Carlo simulations (Methods), the same as that for stellar mass estimates.

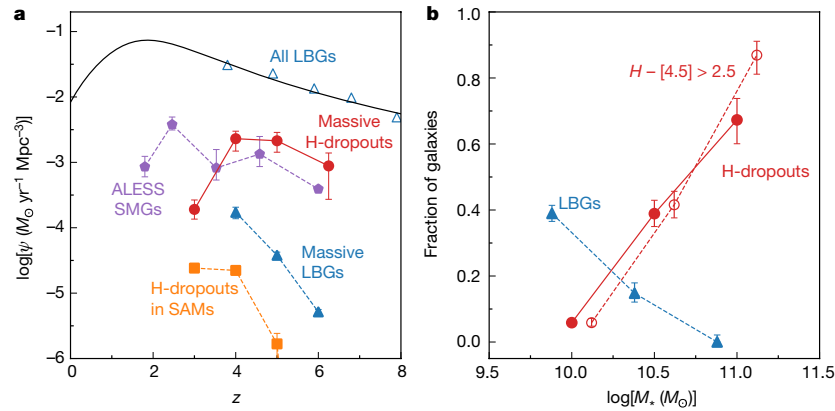


**Fig. 3 | Contribution of H-dropouts to the cosmic SFR density and the stellar mass function.** **a**, Plot of cosmic star-formation-rate density,  $\psi$ , versus redshift  $z$ . The black line indicates the current known total cosmic star-formation history, which is based on LBGs at  $z \gtrsim 4$  ('All LBGs', blue open triangles<sup>17</sup>). Red filled circles ('Massive H-dropouts'), ALMA-detected H-dropouts with  $M_* > 10^{10.3} M_\odot$ . Purple filled pentagons, the ALESS SMGs ( $S_{870\mu\text{m}} > 4.2 \text{ mJy}$ )<sup>12</sup>, whose contribution to the SFR density peaks at  $z \approx 2.5$ . Blue filled triangles ('Massive LBGs'), the SFR density (based on dust-corrected UV) for the brightest/massive LBGs with  $M_* > 10^{10.3} M_\odot$ , based on the latest determination of the UV luminosity

functions<sup>25</sup>. Filled orange squares, the SFR density from H-dropouts ( $[4.5] < 24 \text{ mag}$  and  $H - [4.5] > 2.5 \text{ mag}$ ) in semi-analytical models<sup>19</sup>, which are identified from a K-selected mock catalogue ( $K < 27 \text{ mag}$ ) from a total area of  $75.36 \text{ deg}^2$ . Error bars, s.d. assuming Poisson statistics. **b**, Number fraction of massive galaxies that are detected either as LBGs (blue filled triangles) or as H-dropouts (including both ALMA-detected and ALMA-undetected ones; red filled circles) averaged over  $z = 3.5\text{--}6.5$ . Red open circles, the total contribution of red galaxies, including both H-dropouts and those non-H-dropouts that have similar red colours ( $H - [4.5] > 2.5 \text{ mag}$ ) selected from ZFOURGE at  $3.5 < z < 6.5$ .

Q8

Having established that most of the H-dropouts are massive galaxies at  $z > 3$ , we now derive their contribution to the cosmic SFR density and stellar mass function. Whereas populations of similarly red galaxies are known to exist at lower redshifts<sup>16</sup>, these largely overlap with the stellar-mass-limited sample used to estimate the SFR density

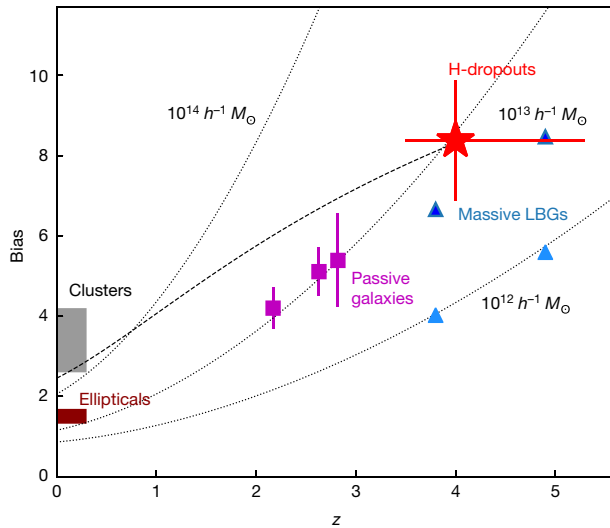


**Fig. 4 | Clustering properties and halo masses of H-dropouts.** Shown is the galaxy bias of ALMA-detected H-dropouts (red star) and its comparison to other populations, including the brightest LBGs ('Massive LBGs', blue triangles) at  $z \approx 4\text{--}5$  (ref. <sup>26</sup>) and massive passive galaxies ('Passive galaxies', purple squares) with  $M_* > 10^{10.5} M_\odot$  at  $z = 2\text{--}3$  (ref. <sup>27</sup>). Error bars,  $1\sigma$  estimated from Poisson statistics. Filled dark-blue and light-blue triangles denote massive and more typical ( $L_*$ ) LBGs with UV magnitudes of  $M_{\text{UV}} \approx -22$  and  $M_{\text{UV}} \approx -20.5$ , respectively. Dotted lines, the corresponding galaxy bias for fixed halo mass (labelled) at different redshifts<sup>28</sup>; dashed line, the evolutionary track<sup>29</sup> for galaxies with the same galaxy bias as H-dropouts. The descendants of H-dropouts are consistent with massive ellipticals at  $z \approx 2\text{--}3$  and today's most massive galaxies residing in massive groups and clusters.

at  $z < 3$ . Assuming that the intrinsic IR SED of the ALMA-detected H-dropouts is the same as the SED derived from stacking, the SFR density of ALMA-detected H-dropouts (in  $M_\odot \text{ yr}^{-1} \text{ Mpc}^{-3}$ ) reaches about 2.9, 2.1 and 0.9 at  $z = 4, 5$  and  $6$ , respectively, or approximately  $1.6 \times 10^{-3} M_\odot \text{ yr}^{-1} \text{ Mpc}^{-3}$  when averaged over the three bins (Fig. 3). This corresponds to about 10% of the SFR density from LBGs at similar redshifts<sup>17</sup>. However, if we focus only on LBGs with masses similar to those of H-dropouts with  $M_* > 10^{10.3} M_\odot$ , the SFR densities of H-dropouts are one to two orders of magnitude higher, demonstrating that H-dropouts dominate the SFR density in massive galaxies. This dominance is further reflected in the stellar mass functions, as shown in Fig. 3. The fraction of H-dropouts becomes progressively higher at higher masses. At  $M_* \gtrsim 10^{10.5} M_\odot$ , the number density of H-dropouts surpasses that of LBGs. Moreover, if we also include galaxies detected in H-band but which show similar red colours ( $H - [4.5] > 2.5 \text{ mag}$ , Extended Data Fig. 7)<sup>8,11</sup>, they make up more than 80% of the most massive galaxies at  $z > 4$ . Taken together, these results suggest that the majority of the most massive galaxies at  $z > 3$  have indeed been missed from the LBG selection, and are optically dark.

To put the H-dropouts in the context of the cosmic evolution of massive galaxies, we probe their clustering properties through their cross-correlation with H-detected galaxies at  $3.5 < z < 5.5$  from the CANDELS survey in the same three fields (Extended Data Fig. 8, Methods). The derived galaxy bias, that is, the relationship between the spatial distribution of galaxies and the underlying dark matter density field, for the H-dropouts is  $b = 8.4 \pm 1.5$ , corresponding to a dark matter halo mass of  $M_h \approx 10^{13 \pm 0.3} h^{-1} M_\odot$  at  $z = 4$  (Fig. 4, Methods). This halo mass of H-dropouts is consistent with them being progenitors of the most massive quiescent galaxies at  $z = 2\text{--}3$ , as well as progenitors of today's ellipticals that reside in the central region of massive groups and clusters.

The discovery and confirmation of these H-dropouts as massive galaxies at  $z \approx 3\text{--}6$  alleviates greatly the tension between the small number of massive LBGs at  $z > 3$  and the rapid emergence of massive (and quiescent) galaxies at  $z \approx 2\text{--}3$ . Assuming an average redshift of  $z \approx 4$  and  $\text{SFR} \approx 220 M_\odot \text{ yr}^{-1}$ , these H-dropouts will grow in stellar mass by  $1.3 \times 10^{11} M_\odot$  before  $z \approx 3$ . Their number density,  $n \approx 2 \times 10^{-5} \text{ Mpc}^{-3}$ , is also comparable to that of the most massive, quiescent galaxies at  $z \approx 3$  with  $M_* > 10^{11} M_\odot$ . The early formation of such a large number of massive, dusty galaxies is unexpected with

current semi-analytical models<sup>19</sup>, which underestimate their density by one to two orders of magnitude (Fig. 3). Similarly, a deficit of such galaxies is also present in hydrodynamic simulations, which contain no such galaxies at  $z > 3$  in mock deep fields (about 23.5 arcmin<sup>2</sup>, from the Illustris Project<sup>20</sup>). Moreover, even considering LBGs alone, the number of massive galaxies already appears too large when compared to the number of massive haloes at  $z > 4$  predicted<sup>21</sup> by our current understanding of galaxy evolution in the Lambda Cold Dark Matter (LCDM) framework. Together, this unexpected large abundance of massive galaxies in the early Universe suggests that our understanding of massive-galaxy formation may require substantial revision. Spectroscopic follow-up of the whole population of H-dropouts would be key to providing further insights into this question, which calls for mid-infrared spectroscopy with James Webb Space Telescope in the near future.

### Online content

Any methods, additional references, Nature Research reporting summaries, source data, extended data, supplementary information, acknowledgements, peer review information; details of author contributions and competing interests; and statements of data and code availability are available at <https://doi.org/10.1038/s41586-019-1452-4>.

Received: 29 June 2018; Accepted: 5 June 2019;

1. Madau, P. & Dickinson, M. Cosmic star-formation history. *Annu. Rev. Astron. Astrophys.* **52**, 415–486 (2014).
2. Walter, F. et al. The intense starburst HDF 850.1 in a galaxy overdensity at  $z \approx 5.2$  in the Hubble Deep Field. *Nature* **486**, 233–236 (2012).
3. Riechers, D. A. et al. A dust-obscured massive maximum-starburst galaxy at redshift of 6.34. *Nature* **496**, 329–333 (2013).
4. Marrone, D. P. et al. Galaxy growth in a massive halo in the first billion years of cosmic history. *Nature* **553**, 51–54 (2018).
5. Dowell, C. D. et al. HerMES: Candidate high-redshift galaxies discovered with Herschel/SPIRE. *Astrophys. J.* **780**, 75 (2013).
6. Glazebrook, K. et al. A massive, quiescent galaxy at a redshift of 3.717. *Nature* **544**, 71–74 (2017).
7. Schreiber, C. et al. Near infrared spectroscopy and star-formation histories of  $3 < z < 4$  quiescent galaxies. *Astron. Astrophys.* **618**, A85 (2018).
8. Spitler, L. R. et al. Exploring the  $z = 3$ –4 massive galaxy population with ZFOURGE: the prevalence of dusty and quiescent galaxies. *Astrophys. J.* **787**, L36 (2014).
9. Williams, C. C. et al. The progenitors of the compact early-type galaxies at high redshift. *Astrophys. J.* **780**, 1 (2014).
10. Huang, J.-S. et al. Four IRAC sources with an extremely red H – [3.6] color: passive or dusty galaxies at  $z > 4.5$ ? *Astrophys. J.* **742**, L13 (2011).
11. Wang (王涛), T. et al. Infrared color selection of massive galaxies at  $z > 3$ . *Astrophys. J.* **816**, 84 (2016).
12. Swinbank, A. M. et al. An ALMA survey of sub-millimetre galaxies in the Extended Chandra Deep Field South: the far-infrared properties of SMGs. *Mon. Not. R. Astron. Soc.* **438**, 1267–1287 (2014).
13. Schreiber, C. et al. Dust temperature and mid-to-total infrared color distributions for star-forming galaxies at  $0 < z < 4$ . *Astron. Astrophys.* **609**, A30 (2018).
14. Daddi, E. et al. Two bright submillimeter galaxies in a  $z = 4.05$  protocluster in GOODS-North, and accurate radio-infrared photometric redshifts. *Astrophys. J.* **694**, 1517 (2009).
15. Schreiber, C. et al. Jekyll & Hyde: quiescence and extreme obscuration in a pair of massive galaxies 1.5 Gyr after the Big Bang. *Astron. Astrophys.* **611**, A22 (2018).
16. Riguccini, L. et al. The composite nature of Dust-Obscured Galaxies (DOGs) at  $z \sim 2$ –3 in the COSMOS field – I. A far-infrared view. *Mon. Not. R. Astron. Soc.* **452**, 470–485 (2015).
17. Bouwens, R. J. et al. UV-continuum slopes at  $z \sim 4$ –7 from the HUDF09+ERS+CANDELS observations: discovery of a well-defined UV color-magnitude relationship for star-forming galaxies. *Astrophys. J.* **754**, 83 (2012).
18. Straatman, C. M. S. et al. A substantial population of massive quiescent galaxies at  $z \sim 4$  from ZFOURGE. *Astrophys. J.* **783**, L14 (2014).
19. Henriques, B. M. B. et al. Galaxy formation in the Planck cosmology – I. Matching the observed evolution of star formation rates, colours and stellar masses. *Mon. Not. R. Astron. Soc.* **451**, 2663–2680 (2015).
20. Snyder, G. F. et al. Massive close pairs measure rapid galaxy assembly in mergers at high redshift. *Mon. Not. R. Astron. Soc.* **468**, 207–216 (2017).
21. Steinhardt, C. L., Capak, P., Masters, D. & Speagle, J. S. The impossibly early galaxy problem. *Astrophys. J.* **824**, 21 (2016).
22. Straatman, C. M. S. et al. The FourStar Galaxy Evolution Survey (ZFOURGE): ultraviolet to far-infrared catalogs, medium-bandwidth photometric redshifts with improved accuracy, stellar masses, and confirmation of quiescent galaxies to  $z \sim 3.5$ . *Astrophys. J.* **830**, 51 (2016).
23. da Cunha, E. et al. An ALMA survey of sub-millimeter galaxies in the Extended Chandra Deep Field South: physical properties derived from ultraviolet-to-radio modeling. *Astrophys. J.* **806**, 110 (2015).
24. Schreiber, C. et al. The Herschel view of the dominant mode of galaxy growth from  $z = 4$  to the present day. *Astron. Astrophys.* **575**, A74 (2015).
25. Ono, Y. et al. Great Optically Luminous Dropout Research Using Subaru HSC (GOLDRUSH). I. UV luminosity functions at  $z \sim 4$ –7 derived with the half-million dropouts on the 100 deg<sup>2</sup> sky. *Publ. Astron. Soc. Jpn* **70**, S10 (2018).
26. Harikane, Y. et al. GOLDRUSH. II. Clustering of galaxies at  $z \sim 4$ –6 revealed with the half-million dropouts over the 100 deg<sup>2</sup> area corresponding to 1 Gpc<sup>3</sup>. *Publ. Astron. Soc. Jpn* **70**, S11 (2018).
27. Hartley, W. G. et al. Studying the emergence of the red sequence through galaxy clustering: host halo masses at  $z > 2$ . *Mon. Not. R. Astron. Soc.* **431**, 3045–3059 (2013).
28. Mo, H. J. & White, S. D. M. The abundance and clustering of dark haloes in the standard  $\Lambda$ CDM cosmogony. *Mon. Not. R. Astron. Soc.* **336**, 112–118 (2002).
29. Fakhouri, O., Ma, C.-P. & Boylan-Kolchin, M. The merger rates and mass assembly histories of dark matter haloes in the two Millennium simulations. *Mon. Not. R. Astron. Soc.* **406**, 2267–2278 (2010).

**Publisher's note:** Springer Nature remains neutral with regard to jurisdictional claims in published maps and institutional affiliations.

© The Author(s), under exclusive licence to Springer Nature Limited 2019



## METHODS

Here we give details of the multi-wavelength observations and the determination of physical properties of sample galaxies. Throughout we adopt a Chabrier initial mass function<sup>30</sup> and the concordance cosmology with matter density parameter  $\Omega_M = 0.3$ , dark energy density parameter  $\Omega_\Lambda = 0.7$  and Hubble constant  $H_0 = 70 \text{ km s}^{-1} \text{ Mpc}^{-1}$ . All magnitudes are in the AB system.

**Observations. Selection of H-dropouts and incompleteness correction.** We have cross-matched the F160W-selected catalogue from the three CANDELS fields (Table 1) with an IRAC 3.6- $\mu\text{m}$  and 4.5- $\mu\text{m}$ -selected catalogue<sup>31</sup> from the SEDS survey. The SEDS survey covers the three fields of H-dropouts to a depth of 26 AB mag ( $3\sigma$ ) at both 3.6  $\mu\text{m}$  and 4.5  $\mu\text{m}$  and is 80% complete down to  $[4.5] \approx 24$  mag. We first matched sources with  $[4.5] < 24$  mag in the SEDS catalogue to the F160W-selected catalogue and identified those without H-band counterparts within a  $2''$  radius (corresponding roughly to the point spread function (PSF) size of IRAC 3.6  $\mu\text{m}$  and 4.5  $\mu\text{m}$  observations). This 4.5- $\mu\text{m}$  magnitude cut was applied to enable sufficient colour range to identify extremely red objects while keeping a complete 4.5- $\mu\text{m}$ -selected sample. We then visually inspected the IRAC images and excluded sources whose flux is contaminated by bright neighbours as well as those falling on the edge of the F160W image. With knowledge of their positions, some of these H-dropouts are marginally detected in the F160W band but exhibit extended profiles and are unidentifiable as real sources without that prior knowledge. This left us 63 sources with 2 of them serendipitously detected in previous band-7 continuum observations with ALMA.

The criterion of no HST counterparts within  $2''$  radius ensures a clean selection of H-dropouts with reliable constraints of IRAC fluxes. However, given the high density of HST sources in these deep fields, the chance probability of an IRAC–HST coincidence (with distance  $< 2''$ ) is non-negligible. This means that we may have missed some H-dropouts simply because of the presence of a random HST source falling within the  $2''$  search radius of the IRAC source. To correct for this effect, we calculate the completeness of this selection approach, which is defined at a given position as the probability of finding zero galaxies in the  $2''$  radius,  $p(n=0) = \exp(-N\pi r^2)$ , with  $N$  representing the surface density of HST sources and  $r$  the searching radius. Averaging over the three CANDELS fields yields  $N = 0.05 \text{ arcsec}^{-2}$ , implying  $p(n=0) = 0.53$ . This suggests that while our approach yields a clean selection of H-dropouts, roughly half of the true H-dropouts have been missed simply due to chance superposition of sources, which needs to be corrected. In fact, this completeness correction is consistent with recent findings from a blind ALMA survey, which reveals four H-dropouts (with  $[4.5] < 24$  mag) that were not picked up by our approach within an area of one-third of the GOODS-South field<sup>32,33</sup>, in comparison to 12 sources selected by our approach in the whole GOODS-South field. Among these four sources, three have at least one HST counterpart within  $2''$  (with the remaining one absent from our IRAC catalogue, which is shallower than the one used in ref. <sup>32</sup>), which is inconsistent with being the right counterpart of the ALMA emission based on the redshift and other physical properties. Albeit with small number statistics, this implies a completeness of our searching approach of about 57%, consistent with our estimated value. In addition to this correction, we also need to correct for the incompleteness of the IRAC imaging from the SEDS survey, which ranges from 93% at  $[4.5] = 22$  mag to 75%–80% at  $[4.5] = 24$  mag in the three fields. Combining the two corrections, a factor of 2 to 2.4 has been applied to the number density (and to the SFR and stellar mass density) of H-dropouts, depending on their IRAC 4.5- $\mu\text{m}$  magnitudes.

**Multiwavelength photometry.** In each field, we gathered mosaics in a large number of bands, including all the images used to build the 3DHST<sup>34</sup> and ZFOURGE<sup>22</sup> catalogues. All our galaxies therefore had rich and deep photometry from the UV to the NIR, reaching typical  $5\sigma$  depths (AB) of 27 in u to i, 26 in z to H, and 25 in Ks. We provide below full details of the mosaics used.

For GOODS-South, we used VLT/VIMOS images in the U and R bands<sup>35</sup>, ESO/WFI images in the U, U38, B, V, R and I bands from GaBoDS<sup>36</sup>, a CTIO/MOSAIC image in the z band from MUSYC<sup>37</sup>, Subaru images in 15 medium bands from MUSYC<sup>38</sup>, Hubble images in the F395W, F606W, F775W, F8514W, F850LP, F105W, F125W and F160W bands from GOODS and CANDELS programmes<sup>39–41</sup>, VLT/ISAAC images in the J, H and Ks bands<sup>42</sup>, CFHT/WIRCam images in the J and Ks bands from TENIS<sup>43</sup>, Magellan/FOURSTAR images in the J1, J2, J3, Hs, Hl and Ks bands from ZFOURGE<sup>22</sup>, a VLT/HawK-I image in the Ks band from HUGS<sup>44</sup>, and Spitzer IRAC images from SEDS<sup>31</sup>.

For UDS, we used a CFHT/Megacam image in the u band produced by the 3DHST team<sup>34</sup>, Subaru images in the B, V, R, i and z bands<sup>45</sup>, Hubble images in the F606W, F814W, F125W, F140W and F160W bands from the CANDELS and 3DHST programmes<sup>41,46</sup>, UKIRT/WFCAM images in the J, H and K bands from UKIDSS<sup>47</sup>, Magellan/FOURSTAR images in the J1, J2, J3, Hs, Hl and Ks bands from ZFOURGE<sup>22</sup>, VLT/HawK-I images in the Y and Ks bands from HUGS<sup>44</sup>, and Spitzer IRAC images from SEDS<sup>31</sup> and SpUDS (PI: J. Dunlop).

For COSMOS, we used CFHT/Megacam images in the u and i bands from CFHTLS<sup>48</sup>, Subaru images in the B, g, V, r, i and z bands as well as 10 medium

bands<sup>49</sup>, Hubble images in the F606W, F814W, F125W, F140W and F160W bands from the CANDELS and 3DHST programmes<sup>41,46</sup>, CFHT/WIRCam images in the H and Ks bands<sup>50</sup>, Magellan/FOURSTAR images in the J1, J2, J3, Hs, Hl and Ks bands from ZFOURGE<sup>22</sup>, VISTA/VIRCAM images in the Y, J, H and Ks bands from UltraVISTA DR3<sup>51</sup>, and Spitzer IRAC images from SEDS<sup>31</sup> and S-COSMOS<sup>52</sup>.

The photometry was obtained with a procedure very similar to that previously used in deep surveys<sup>22,46</sup>, which we summarize here. Fluxes in UV to NIR were extracted on re-gridded and PSF-matched images in fixed apertures of  $2''$  diameter. Because of the broader PSF in Spitzer images, fluxes in the IRAC bands were extracted separately, with a  $3''$  aperture and without PSF matching. The asymmetric IRAC PSF was rotated to match the telescope roll angle for each field. Before extracting the fluxes, all the neighbouring sources within a  $10''$  radius were subtracted from the images. This was done by identifying the sources from a stacked detection image, and using the HST F160W profile of each source as a model. These models were convolved by the PSF of each image, where they were fitted simultaneously using a linear solver. Most often the dropouts were not found in the stacked detection image, and were therefore modelled as point sources at the coordinates of their IRAC centroid during the de-blending stage. Once the flux was extracted, additional ‘sky’ apertures were placed randomly around each dropout. The median flux in these sky apertures was subtracted from the dropout’s flux, to eliminate any remaining background signal, while the standard deviation of these fluxes was used as flux uncertainty. Last, fluxes and uncertainties were aperture-corrected using the matched PSF’s light curve, assuming point-like morphology.

**ALMA observations and data reduction.** Our ALMA band-7 continuum observations of H-dropouts were performed during January and July 2016. The observations were centred on the IRAC positions with a spectral set-up placed around a central frequency of 343.5 GHz. Although we asked for  $0.7''$ -resolution observations for all the three fields, only the CANDELS-COSMOS field was observed as requested, yielding a synthesis beam of  $0.6'' \times 1''$ . The other two fields were observed at  $0.2''$ – $0.3''$  resolution. The integration time was roughly 1.8 min per object with a total observing time of  $\sim 2$  h. We reduced the data using the CASA pipeline (version 4.3.1). To reach an homogeneous angular resolution, we tapered the baselines for these two fields to an angular resolution of  $0.6''$ . This resolution corresponds to  $\sim 4$  kpc at  $z = 4$ , compared to typical sizes of  $\sim 2$  kpc for SMGs<sup>53</sup>.

We measured the total flux of all our targets directly in the  $(u, v)$  plane using the uvmodelfit procedure from the CASA pipeline. The sources were modelled with a circular Gaussian profile of variable total flux, centroid, width, axis ratio and position angle. 39 H-dropouts were detected at  $S/N > 4$  with  $S_{870\mu\text{m}} > 0.6$  mJy, including two galaxies that were serendipitously detected in a previous ALMA programme<sup>54</sup> targeting H-detected  $z \approx 4$  galaxies, which reached a similar depth as this observation. The positions of the 870- $\mu\text{m}$  emission as measured from ALMA are in good agreement with IRAC, with  $\Delta\text{RA} = 0.081'' \pm 0.128''$  and  $\Delta\text{Dec} = -0.13'' \pm 0.16''$ .

**SCUBA-2 450- $\mu\text{m}$  and VLA observations.** One of the three H-dropout fields, CANDELS-COSMOS, is covered by deep SCUBA-2 450- $\mu\text{m}$  and 870- $\mu\text{m}$  observations from the STUDIES survey<sup>55</sup>. Previous observations with JCMT/SCUBA-2 of the same region<sup>56–58</sup> have also been combined to produce an extremely deep 450- $\mu\text{m}$  image and a confusion-limited 850- $\mu\text{m}$  image. The instrumental noise at 450  $\mu\text{m}$  and 850  $\mu\text{m}$  at the deepest regions reach  $\sim 0.65$  mJy and  $\sim 0.1$  mJy, respectively.

The SCUBA-2 450- $\mu\text{m}$  and 850- $\mu\text{m}$  fluxes for H-dropouts are measured at the position of the IRAC 3.6- $\mu\text{m}$  and 4.5- $\mu\text{m}$  emission with the prior-based PSF-fitting code FASTPHOT<sup>59</sup>. We further restrict all the extracted fluxes to be positive with bounded value least-square minimization. During the fit we included all the MIPS 24- $\mu\text{m}$  and VLA detections as priors to perform source extraction. The VLA 3 GHz observation in COSMOS<sup>60</sup> reaches a r.m.s. of  $2.3 \mu\text{Jy}$  per beam at an angular resolution of  $0.75''$ , which is deep enough to put useful constraints on their redshifts. The flux measurement for H-dropouts in the far-infrared suffers minimum source confusion due to our selection criterion (no close neighbours within a  $2''$  radius). A comparison of 870- $\mu\text{m}$  fluxes measured by ALMA and SCUBA-2 yields excellent agreement with a median value of  $S_{\text{ALMA}}/S_{\text{SCUBA-2}} = 1.05$ .

**X-SHOOTER spectra.** In the COSMOS field, deep medium band images in the optical were obtained with the Subaru telescope<sup>49</sup>. We visually inspected these images at the location of each dropout in our sample and found three galaxies with flux excesses in one of these images, with a significance above  $4\sigma$ . Examples are shown in Extended Data Fig. 6. Such flux excess can be interpreted as coming from a bright emission line<sup>61</sup>. For these three dropouts, the line could be identified as  $\text{Ly}\alpha$  at  $z = 5.0, 3.2$  and  $4.1$ , respectively. Even though H-dropouts are typically very obscured,  $\text{Ly}\alpha$  may still be detected through un-obscured sight lines, or by scattering<sup>62</sup>. Judging from the spatial offsets of about  $1''$  we observed between this optical flux excess and the Spitzer–IRAC or ALMA emission, scattering appears to be the most plausible explanation.

We thus followed up these objects with VLT/X-SHOOTER to confirm the presence of an emission line. Each dropout was observed in May 2018 in the UVB and VIS arms for 50 min in stare mode (no nodding), split over three exposures. The 2D spectra were reduced using the standard pipeline, and 1D spectra were produced by fitting a Gaussian profile to each spectral slice. Uncertainties were controlled by computing the standard deviation of spectral elements in regions without sky lines; we found that the 1D uncertainty spectrum had to be rescaled upwards by a factor of 1.27 to match the observed noise.

We then searched for emission lines in the spectra, considering only the wavelength range covered by the Subaru medium band in which the flux excess was previously identified. The result of this search is displayed in Extended Data Fig. 6. We found a  $10\sigma$  detection at  $0.498\ \mu\text{m}$  for dropout 32932, corresponding to  $z_{\text{spec}} = 3.0971 \pm 0.0002$ , and a more marginal but still significant  $4.3\sigma$  detection at  $0.739\ \mu\text{m}$  for dropout 25363, corresponding to  $z_{\text{spec}} = 5.113^{+0.001}_{-0.005}$ . Because our search space is tightly limited by the Subaru passband, the latter only has a 0.4% chance of being spurious, and we therefore consider it a reliable detection. The third dropout showed no significant line emission above  $2\sigma$ .

**Lyman-break galaxy selection.** In order to compare the properties of H-dropouts and LBGs<sup>63</sup>, we have selected LBGs using the ZFOURGE catalogues in the same three CANDELS fields<sup>22</sup>. The advantage of the ZFOURGE catalogue is that it is essentially a K<sub>s</sub>-band-selected catalogue, for which the deep K<sub>s</sub>-band data provide critical constraints on the redshift and stellar mass estimates at  $z > 4$ . We select our  $z = 4$ –6 LBG galaxy sample using the selection criterion in ref. <sup>64</sup>. Owing to the lack of B-band data from HST, the  $z \approx 4$  LBG sample is limited to the GOODS-South field only, while the  $z \approx 5$  and  $z \approx 6$  LBG samples include galaxies from all three fields. To enable a clean selection of galaxies with reliable flux density measurements, we have further limited the selection to galaxies with  $use = 1$  as recommended<sup>22</sup>. This reduces the effective area to  $132.2\ \text{arcmin}^2$ ,  $139.2\ \text{arcmin}^2$  and  $135.6\ \text{arcmin}^2$  for GOODS-South, COSMOS and UDS field, respectively. To identify total SFR density from massive LBGs with  $M_* > 10^{10.3} M_\odot$ , we used the latest determination<sup>25</sup> of the UV luminosity function at  $z \approx 4$ –6. Taking into account variations in the  $M_*$ – $M_{\text{UV}}$  relation, this mass cut corresponds to  $M_{\text{UV}} < [-21.55, -22.04, -22.27]$  at  $z = [4, 5, 6]$ , respectively. We then derive the dust-corrected SFR for these brightest UV-selected galaxies following the approach in ref. <sup>17</sup>.

**Determination of physical properties. Stacked optical SEDs.** To produce the stacked optical SEDs, we took the fluxes of each galaxy in our photometric catalogue and normalized them by their respective IRAC 4.5- $\mu\text{m}$  flux. We then computed the mean flux in each band, using inverse variance weighting, and finally multiplied the resulting stacked fluxes by the average 4.5- $\mu\text{m}$  flux of the stacked sample. In the stack, we combined bands that have similar effective wavelengths, even though the true passbands could be slightly different; for example we stacked together all the K<sub>s</sub> bands from UKIDSS, UltraVISTA, FOURSTAR, WIRCam and ISAAC into a single K<sub>s</sub> band. The uncertainties on the stacked fluxes were derived by formally combining the uncertainties of each stacked galaxy. We note that, since we obtained our photometry using fixed-size apertures, this method is strictly equivalent to stacking the images.

**Photometric redshift and stellar mass determination.** Using the aforementioned multiwavelength photometry, including bands with formal non-detections, photometric redshifts were computed with EAzy<sup>65</sup> using the full set of template SEDs, that is, including the ‘old-and-dusty’ template and the ‘extreme emission line’ template. The prior on the observed magnitudes was not used. Using these redshifts, we then ran FAST<sup>66</sup> to estimate the stellar masses. We assumed a delayed exponentially declining star-formation history, with a range of ages and exponential timescales. Dust attenuation was modelled with the prescription of ref. <sup>67</sup>, allowing  $A_V$  up to 6 mag. Metallicity was fixed to solar during the fitting. We also used the infrared luminosities inferred from the ALMA fluxes to further constrain the fits. This was implemented as follows. From the stacked Herschel SED (see Fig. 3), we measured the mean dust temperature of our sample:  $T_{\text{dust}} = 36.7 \pm 2.1\ \text{K}$ . On the basis of Herschel and ALMA observations of  $z > 2$  galaxies<sup>13</sup>, we expect a typical scatter of 5 K around the average temperature at any given redshift. Assuming this distribution of temperatures holds for the dropouts, we generated probability distributions for  $L_{\text{IR}}$  using a Monte Carlo procedure: the measured ALMA flux was randomly perturbed with Gaussian noise of amplitude set by the flux uncertainty, and the dust temperature was drawn from a Gaussian distribution centred on 36.7 K and with a width of 5 K; the resulting dust SED was then used to extrapolate  $L_{\text{IR}}$  from the ALMA measurement. For galaxies whose ALMA flux has  $S/N < 2$ , the resulting probability distribution of  $L_{\text{IR}}$  was close to Gaussian, while for the detections the probability distribution was close to log-normal. We modelled these two regimes accordingly in the fit, by assuming either Gaussian noise on  $L_{\text{IR}}$  or  $\log_{10}(L_{\text{IR}})$ , respectively. The observed infrared luminosity was then compared to the modelled value, which we computed as the difference of bolometric luminosity before and after applying dust attenuation. This resulted in an additional contribution to the  $\chi^2$ , which was then used for standard model selection.

Uncertainties on the photometric redshifts were derived from the 16th and 84th percentiles of the probability distribution produced by EAzy. This accounts for uncertainty on the photometry as well as on the model galaxy templates. Uncertainties on the derived physical parameters, including the stellar mass, were derived using Monte Carlo simulations, where the observed photometry was randomly perturbed with Gaussian noise of amplitude determined by the estimated photometric uncertainties. This was repeated 200 times. The error bars on physical parameters were then derived from the 16th and 84th percentiles of the distribution of the values obtained in the Monte Carlo simulations. For each fit, the redshift was left free to vary within the 68% confidence interval reported by the photometric redshift code. Therefore the resulting error bars account for uncertainties on the photometry and on the redshift.

**Clustering measurements.** Because the number of H-dropouts is small, we calculate the two-point angular cross-correlation function (CCF,  $\omega$ ) with a much larger population of galaxies sharing the same cosmic volume (redshifts) in order to enhance the statistics. Specifically, we select all the galaxies with  $3.5 < z < 5.5$  from the H-selected catalogue in the same three CANDELS fields (producing the ‘galaxy’ sample), and then calculate the CCF as<sup>68</sup>:

$$\omega(\theta) = \frac{\text{HG}(\theta) - \text{HR}(\theta) - \text{GR}(\theta) + \text{RR}(\theta)}{\text{RR}(\theta)} \quad (1)$$

where  $\theta$ , HG, HR, GR and RR are respectively angular separation, pair counts of H-dropout–galaxy, H-dropout–random, galaxy–random and random–random. The ‘random’ galaxy sample is created within the same CANDELS footprint as the H-dropouts (we exclude HUDF in the GOODS-S field because of its much deeper integration than other regions). The uncertainties of the CCF are estimated as:

$$\Delta\omega(\theta) = \frac{1 + \omega(\theta)}{\sqrt{\text{HG}(\theta)}} \quad (2)$$

We then fit the derived CCF with a power-law model:

$$\omega(\theta) = A_\omega \theta^{-\beta} - \text{IC} \quad (3)$$

where  $A_\omega$  is the correlation amplitude,  $\beta$  is the power-law index fixed to 0.8, and IC is the integral constraint. The integral constraint is an offset due to the clustering measurement over the limited area, and is calculated by:

$$\text{IC} = \frac{\sum \text{RR}(\theta) A_\omega \theta^{-\beta}}{\sum \text{RR}(\theta)} \quad (4)$$

The derived correlation amplitude can be converted to 3D correlation length  $r_0$  by the Limber equation<sup>69</sup> modified by ref. <sup>70</sup> for the cross-correlation.

The correlation length is related to galaxy bias  $b$ , such that

$$\sigma_{8,\text{gal}}^2 = \frac{72}{(3-\gamma)(4-\gamma)(6-\gamma)2^7} \left( \frac{r_0}{8 h^{-1} \text{Mpc}} \right)^\gamma \quad (5)$$

and

$$b = \frac{\sigma_{8,\text{gal}}}{\sigma_8(z)} \quad (6)$$

where  $\sigma_{8,\text{gal}}$  is a galaxy fluctuation,  $\gamma = 1 + \beta$ , and  $\sigma_8(z)$  is the amplitude of the dark matter fluctuation<sup>71</sup> on the scale of  $8 h^{-1} \text{Mpc}$ . The halo mass is then derived from the estimated galaxy bias<sup>28</sup>.

## Data availability

Source data for the ALMA 870- $\mu\text{m}$  imaging are available through the ALMA archive. Optical-to-infrared imaging for all the galaxies in the sample are also publicly available through the HST and Spitzer data archives. The other data that support the plots within this Letter and other findings of this study are available from the corresponding author upon reasonable request.

## Code availability

The codes used to reduce ALMA and X-SHOOTER data are publicly available. The codes used to model the optical-to-infrared SEDs, and to stack the optical and infrared images, are accessible through github (<https://github.com/cschreib>).

30. Chabrier, G. Galactic stellar and substellar initial mass function. *Publ. Astron. Soc. Pacif.* **115**, 763–795 (2003).
31. Ashby, M. L. N. et al. SEDS: the Spitzer Extended Deep Survey. Survey design, photometry, and deep IRAC source counts. *Astrophys. J.* **769**, 80 (2013).
32. Franco, M. et al. GOODS-ALMA: 1.1 mm galaxy survey. I. Source catalog and optically dark galaxies. *Astron. Astrophys.* **620**, A152 (2018).

33. Yamaguchi, Y. et al. ALMA twenty-six arcmin<sup>2</sup> survey of GOODS-S at one-millimeter (ASAGAO): near-infrared-dark faint ALMA sources. Preprint at <https://arxiv.org/abs/1903.02744> (2019).
34. Skelton, R. E. et al. 3D-HST WFC3-selected photometric catalogs in the five CANDELS/3D-HST fields: photometry, photometric redshifts, and stellar masses. *Astrophys. J. Suppl. Ser.* **214**, 24 (2014).
35. Nonino, M. et al. Deep U band and R imaging of GOODS-South: observations, data reduction and first results. *Astrophys. J. Suppl. Ser.* **183**, 244–260 (2009).
36. Hildebrandt, H. et al. GaBoDS: The Garching-Bonn Deep Survey. V. Data release of the ESO deep-public-survey. *Astron. Astrophys.* **452**, 1121–1128 (2006).
37. Gawiser, E. et al. The Multiwavelength Survey by Yale-Chile (MUSYC): survey design and deep public UBV<sub>ri</sub> images and catalogs of the Extended Hubble Deep Field-South. *Astrophys. J. Suppl. Ser.* **162**, 1–19 (2006).
38. Cardamone, C. N. et al. The Multiwavelength Survey by Yale-Chile (MUSYC): deep medium-band optical imaging and high-quality 32-band photometric redshifts in the ECDF-S. *Astrophys. J. Suppl. Ser.* **189**, 270–285 (2010).
39. Giavalisco, M. et al. The Great Observatories Origins Deep Survey: initial results from optical and near-infrared imaging. *Astrophys. J.* **600**, L93–L98 (2004).
40. Grogin, N. A. et al. CANDELS: The Cosmic Assembly Near-infrared Deep Extragalactic Legacy Survey. *Astrophys. J. Suppl. Ser.* **197**, 35 (2011).
41. Koekemoer, A. M. et al. CANDELS: The Cosmic Assembly Near-infrared Deep Extragalactic Legacy Survey — the Hubble Space Telescope observations, imaging data products, and mosaics. *Astrophys. J. Suppl. Ser.* **197**, 36 (2011).
42. Retzlaff, J. et al. The Great Observatories Origins Deep Survey. VLT/ISAAC near-infrared imaging of the GOODS-South field. *Astron. Astrophys.* **511**, A50 (2010).
43. Hsieh, B.-C. et al. The Taiwan ECDFS near-infrared survey: ultra-deep J and K<sub>s</sub> imaging in the Extended Chandra Deep Field-South. *Astrophys. J. Suppl. Ser.* **203**, 23 (2012).
44. Fontana, A. et al. The Hawk-I UDS and GOODS Survey (HUGS): survey design and deep K-band number counts. *Astron. Astrophys.* **570**, A11 (2014).
45. Furusawa, H. et al. The Subaru/XMM-Newton Deep Survey (SXDS). II. Optical imaging and photometric catalogs. *Astrophys. J. Suppl. Ser.* **176**, 1–18 (2008).
46. Momcheva, I. G. et al. The 3D-HST survey: Hubble Space Telescope WFC3/G141 grism spectra, redshifts, and emission line measurements for 100,000 galaxies. *Astrophys. J. Suppl. Ser.* **225**, 27 (2016).
47. Lawrence, A. et al. The UKIRT Infrared Deep Sky Survey (UKIDSS). *Mon. Not. R. Astron. Soc.* **379**, 1599–1617 (2007).
48. Cuillandre, J.-C. J. et al. Introduction to the CFHT Legacy Survey final release (CFHTLS T0007). *Proc. SPIE* **8448**, 84480M (2012).
49. Taniguchi, Y. et al. The Cosmic Evolution Survey (COSMOS): Subaru observations of the HST Cosmos Field. *Astrophys. J. Suppl. Ser.* **172**, 9–28 (2007).
50. McCracken, H. J. et al. The COSMOS-WIRCam near-infrared imaging survey. I. BzK-selected passive and star-forming galaxy candidates at  $z \geq 1.4$ . *Astrophys. J.* **708**, 202–217 (2010).
51. McCracken, H. J. et al. UltraVISTA: a new ultra-deep near-infrared survey in COSMOS. *Astron. Astrophys.* **544**, A156 (2012).
52. Sanders, D. B. et al. S-COSMOS: The Spitzer legacy survey of the Hubble Space Telescope ACS 2 deg<sup>2</sup> COSMOS field I: survey strategy and first analysis. *Astrophys. J. Suppl. Ser.* **172**, 86–98 (2007).
53. Hodge, J. A. et al. Kiloparsec-scale dust disks in high-redshift luminous submillimeter galaxies. *Astrophys. J.* **833**, 103 (2016).
54. Schreiber, C. et al. Observational evidence of a slow downfall of star formation efficiency in massive galaxies during the past 10 Gyr. *Astron. Astrophys.* **589**, A35 (2016).
55. Wang, W.-H. et al. SCUBA-2 Ultra Deep Imaging EAO Survey (STUDIES): faint-end counts at 450  $\mu$ m. *Astrophys. J.* **850**, 37 (2017).
56. Casey, C. M. et al. Characterization of SCUBA-2 450  $\mu$ m and 850  $\mu$ m selected galaxies in the COSMOS field. *Mon. Not. R. Astron. Soc.* **436**, 1919–1954 (2013).
57. Geach, J. E. et al. The SCUBA-2 cosmology legacy survey: blank-field number counts of 450- $\mu$ m-selected galaxies and their contribution to the cosmic infrared background. *Mon. Not. R. Astron. Soc.* **432**, 53–61 (2013).
58. Geach, J. E. et al. The SCUBA-2 cosmology legacy survey: 850  $\mu$ m maps, catalogues and number counts. *Mon. Not. R. Astron. Soc.* **465**, 1789–1806 (2017).
59. Béthermin, M., Dole, H., Cousin, M. & Bavouzet, N. Submillimeter number counts at 250  $\mu$ m, 350  $\mu$ m and 500  $\mu$ m in BLAST data. *Astron. Astrophys.* **516**, A43 (2010).
60. Smolčić, V. et al. The VLA-COSMOS 3 GHz large project: continuum data and source catalog release. *Astron. Astrophys.* **602**, A1 (2017).
61. Sobral, D. et al. Slicing COSMOS with SC4K: the evolution of typical Ly $\alpha$  emitters and the Ly $\alpha$  escape fraction from  $z \sim 2$  to 6. *Mon. Not. R. Astron. Soc.* **476**, 4725–4752 (2018).
62. Finkelstein, S. L., Rhoads, J. E., Malhotra, S., Grogin, N. & Wang, J. Effects of dust geometry in Ly $\alpha$  galaxies at  $z = 4.4$ . *Astrophys. J.* **678**, 655–668 (2008).
63. Steidel, C. C., Giavalisco, M., Pettini, M., Dickinson, M. & Adelberger, K. L. Spectroscopic confirmation of a population of normal star-forming galaxies at redshifts  $z > 3$ . *Astrophys. J.* **462**, L17 (1996).
64. Bouwens, R. J. et al. UV luminosity functions at redshifts  $z \sim 4$  to  $z \sim 10$ : 10,000 galaxies from HST legacy fields. *Astrophys. J.* **803**, 34 (2015).
65. Brammer, G. B., van Dokkum, P. G. & Coppi, P. EAZY: A fast, public photometric redshift code. *Astrophys. J.* **686**, 1503–1513 (2008).
66. Kriek, M. et al. An ultra-deep near-infrared spectrum of a compact quiescent galaxy at  $z = 2.2$ . *Astrophys. J.* **700**, 221–231 (2009).
67. Calzetti, D. The dust opacity of star-forming galaxies. *Publ. Astron. Soc. Pacif.* **113**, 1449–1485 (2001).
68. Landy, S. D. & Szalay, A. S. Bias and variance of angular correlation functions. *Astrophys. J.* **412**, 64–71 (1993).
69. Limber, D. N. The analysis of counts of the extragalactic nebulae in terms of a fluctuating density field. *Astrophys. J.* **117**, 134 (1953).
70. Croom, S. M. & Shanks, T. Radio-quiet QSO environments — I. The correlation of QSOs and  $b_J < 23$  galaxies. *Mon. Not. R. Astron. Soc.* **303**, 411–422 (1999).
71. Peebles, P. J. E. *Principles of Physical Cosmology* (Princeton Univ. Press, 1993).
72. Combes, F. et al. A bright  $z = 5.2$  lensed submillimeter galaxy in the field of Abell 1773. HLSJ091828.6+514223. *Astron. Astrophys.* **538**, L4 (2012).
73. Vieira, J. D. et al. Dusty starburst galaxies in the early Universe as revealed by gravitational lensing. *Nature* **495**, 344–347 (2013).
74. Carilli, C. L. & Yun, M. S. The radio-to-submillimeter spectral index as a redshift indicator. *Astrophys. J.* **513**, L13–L16 (1999).
75. Boquien, M. et al. CIGALE: a python Code Investigating GALaxy Emission. *Astron. Astrophys.* **622**, A103 (2019).
76. Bruzual, G. & Charlot, S. Stellar population synthesis at the resolution of 2003. *Mon. Not. R. Astron. Soc.* **344**, 1000–1028 (2003).
77. Draine, B. T. & Li, A. Infrared emission from interstellar dust. IV. The silicate-graphite-PAH model in the post-Spitzer era. *Astrophys. J.* **657**, 810–837 (2007).
78. Inoue, A. K. Rest-frame ultraviolet-to-optical spectral characteristics of extremely metal-poor and metal-free galaxies. *Mon. Not. R. Astron. Soc.* **415**, 2920–2931 (2011).

**Acknowledgements** This paper makes use of the following ALMA data: ADS/JAO.ALMA 2015.1.01495.S and ADS/JAO.ALMA 2013.1.01292.S. ALMA is a partnership of ESO (representing its member states), NSF (USA) and NINS (Japan), together with NRC (Canada), NSC, ASIAA (Taiwan) and KASI (South Korea), in cooperation with Chile. The Joint ALMA Observatory is operated by ESO, AUI/NRAO and NAOJ. This Letter makes use of JCMT data from programmes M16AL006, MJLSC91, M11BH11A, M12AH11A and M12BH21A. T.W. acknowledges support by NAOJ ALMA scientific research grant no. 2017-06B, JSPS Grant-in-Aid for Scientific Research (S) JP17H06130, and funding from the European Union Seventh Framework Programme (FP7/2007-2013) under grant agreement no. 312725 (ASTRODEEP). X.S. acknowledges support by NSFC 11573001 and National Basic Research Program 2015CB857005. C.-F.L. and W.-H.W. were supported by Ministry of Science and Technology of Taiwan grant 105-2112-M-001-029-MY3.

**Author contributions** T.W., C.S. and D.E. conceived the work, and led the analysis and interpretation. T.W. proposed and carried out ALMA observations, reduced the ALMA data, measured SCUBA-2 fluxes and performed full SED fitting, and authored the majority of the text. C.S. conducted multiwavelength photometry and SED fitting, and carried out VLT/X-SHOOTER observations and data reduction. Y. Yoshimura performed the clustering analysis. C.-F.L., W.-H.W. and X.S. contributed to the 450- $\mu$ m photometry. K.K., Y. Yamaguchi, M.F., M.P. and J.H. contributed to the overall interpretation of the results and various aspects of the analysis.

**Competing interests** The authors declare no competing interests.

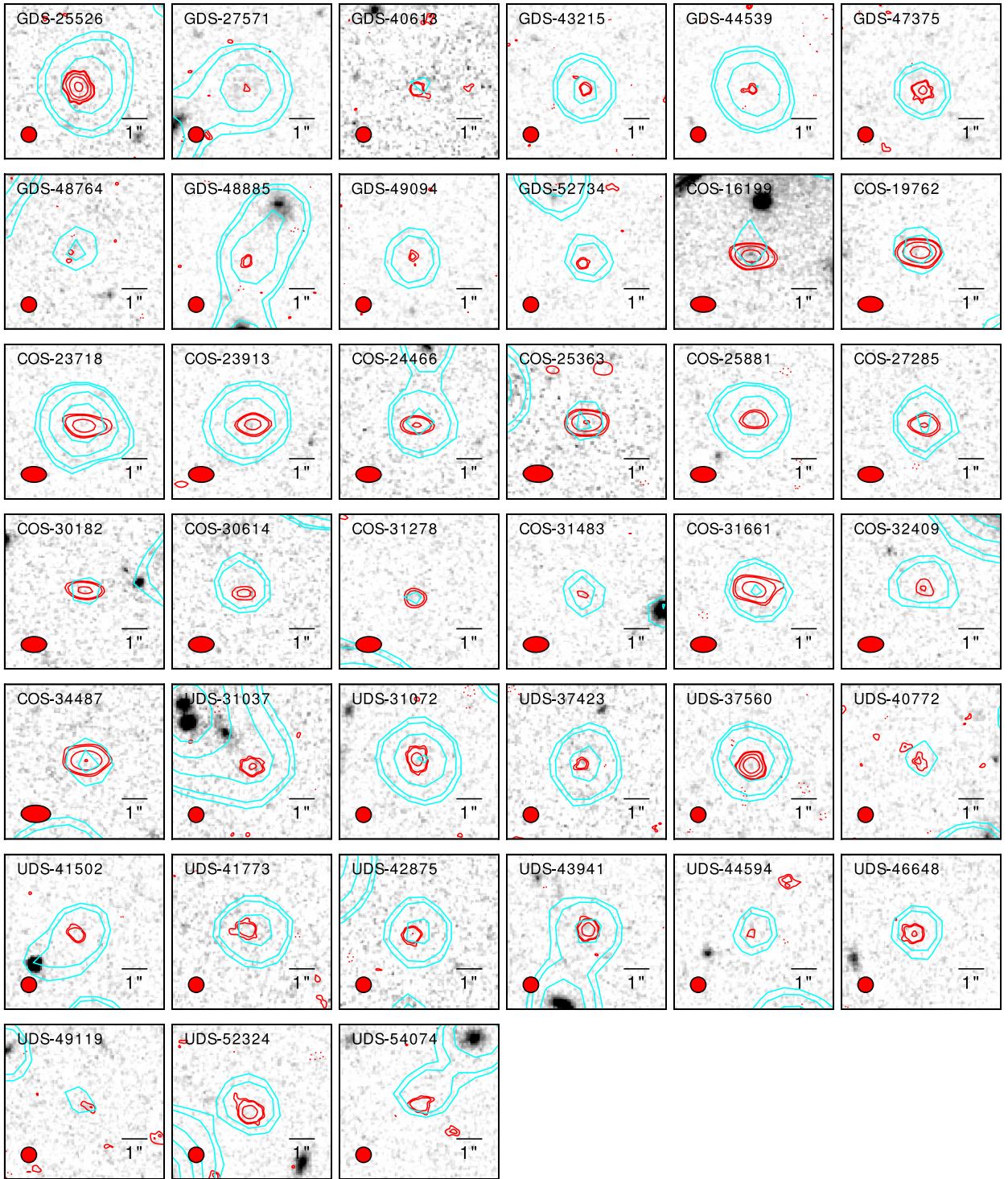
#### Additional information

**Correspondence and requests for materials** should be addressed to T.W.

**Peer review information** Nature thanks Asantha Cooray and Joaquin Vieira for their contribution to the peer review of this work.

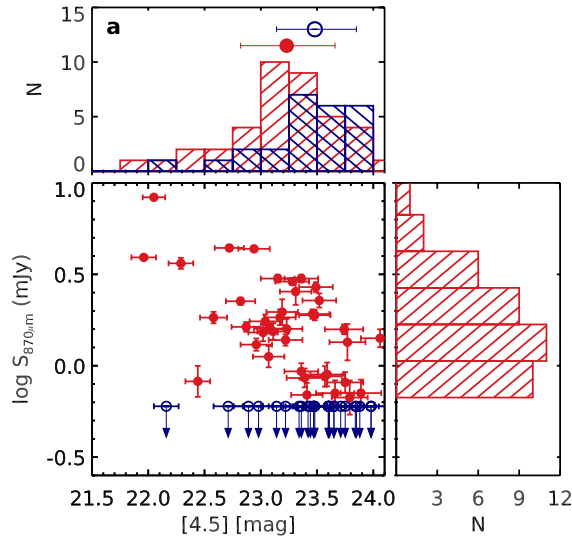
**Reprints and permissions information** is available at <http://www.nature.com/reprints>.



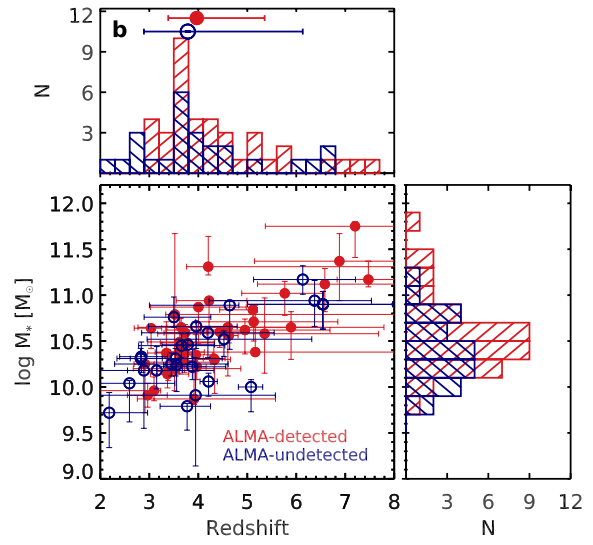


**Extended Data Fig. 1 | NIR and ALMA submillimetre-wavelength images of the ALMA-detected H-dropouts.** Images are  $6'' \times 6''$ , centred at the centroid of the IRAC 4.5- $\mu\text{m}$  emission. The greyscale images are F160W-band (H-band) exposures from the Hubble Space Telescope Wide Field Camera 3 (HST/WFC3). The red solid contours are ALMA 870- $\mu\text{m}$  imaging, with contour levels starting at  $3\sigma$  and increasing as  $3\sigma$ ,  $4\sigma$ ,  $8\sigma$ ,

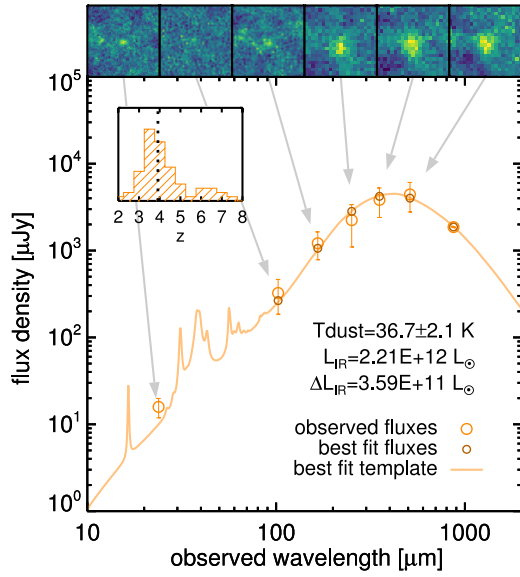
$16\sigma$ ,  $32\sigma$  and  $64\sigma$ . Negative contours at the same significance values are shown with red dashed lines. The exposure times for HST/WFC3 and ALMA imaging are roughly 2 h and 2 min per object, respectively. Although these H-dropouts are not detected in the deep F160W imaging ( $H \gtrsim 27$  mag), they are detected with the indicated significance values by ALMA within a short integration time.



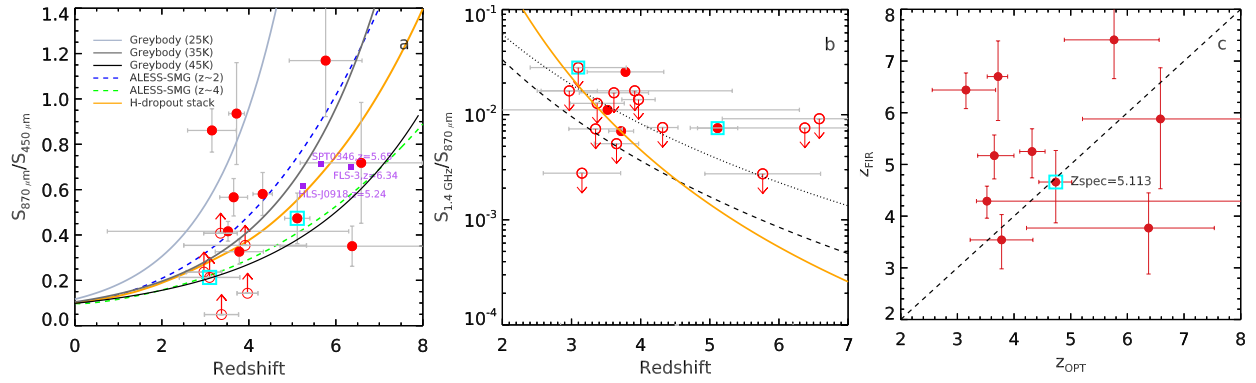
**Extended Data Fig. 2 | Physical properties of ALMA-detected and ALMA-undetected H-dropouts.** The ALMA-detected and ALMA-undetected H-dropouts are shown in blue and red, respectively. **a**, Main panel, the 870- $\mu\text{m}$  fluxes of ALMA-undetected H-dropouts are shown by their upper limits,  $S_{870,\mu\text{m}} < 0.6$  mJy ( $4\sigma$ ). The ALMA-undetected H-dropouts tend to have slightly fainter 4.5- $\mu\text{m}$  magnitudes, with a median value of  $[4.5]_{\text{median}} = 23.5$  mag compared to  $[4.5]_{\text{median}} = 23.2$  mag for ALMA-detected ones. Top panel, histogram showing the distribution of the 4.5- $\mu\text{m}$  magnitudes of H-dropouts. Right panel, histogram showing



the distribution of the 870- $\mu\text{m}$  fluxes. **b**, Main panel, the redshift and stellar masses are derived by template-fitting of their optical-to-NIR photometry, as described in Methods. The ALMA-undetected H-dropouts tend to be at slightly lower redshifts and have lower stellar masses, with a median redshift of  $z_{\text{med}} = 3.8$  and stellar mass of  $M_{*,\text{med}} = 10^{10.31} M_\odot$ , while the ALMA-detected ones have  $z_{\text{med}} = 4.0$  and  $M_{*,\text{med}} = 10^{10.56} M_\odot$ . Top and right panels, histogram of the redshift and the stellar mass distributions of H-dropouts, respectively.



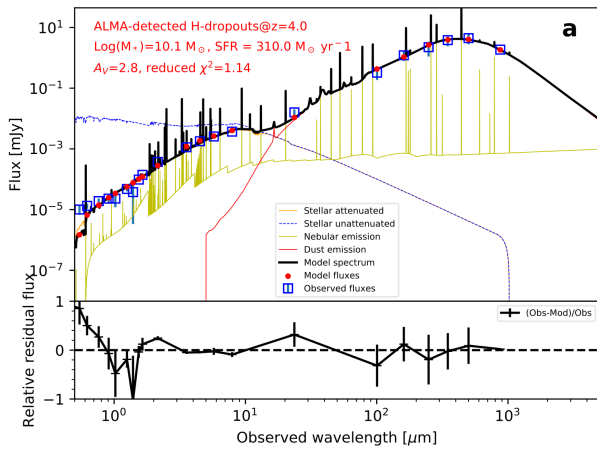
**Extended Data Fig. 3 | Stacked far-infrared SED of ALMA-detected H-dropouts.** The stacked IR SED is derived by median stacking of the Spitzer/24  $\mu\text{m}$ , Herschel/100  $\mu\text{m}$ , 160  $\mu\text{m}$ , 250  $\mu\text{m}$ , 350  $\mu\text{m}$ , 500  $\mu\text{m}$ , and ALMA 870  $\mu\text{m}$  images of the 39 H-dropouts detected with ALMA. The measured fluxes from the stacked images and the predicted fluxes from the best-fit model (solid line) are shown with the large and small open circles, respectively. Error bars ( $1\sigma$ ) on the stacked SED are obtained from either bootstrapping or from the statistics of the residual map (whichever is largest, as described and validated elsewhere<sup>24</sup>). For the ALMA photometry, the error bar is the formal error on the mean ALMA flux, and is smaller than the data point on this figure. The stacked images are shown in the row of insets at the top, which are linked to their corresponding stacked photometric points by grey arrows. The inset histogram shows the photometric redshift distribution of the H-dropouts based on optical-to-NIR SED fitting, which shows a median redshift (dotted line) of  $z \approx 4$ . The infrared luminosity  $L_{\text{IR}}$  and dust temperature  $T_{\text{dust}}$  are derived from the best-fit SED at  $z = 4$ , the average redshift of the sample, using an empirical IR SED library calibrated on galaxies at  $0 < z < 4$  (ref.<sup>13</sup>). The uncertainty on the infrared luminosity ( $\Delta L_{\text{IR}}$ ) accounts for uncertainty on the photometry and on the dust temperature, but not on the mean redshift of the sample.



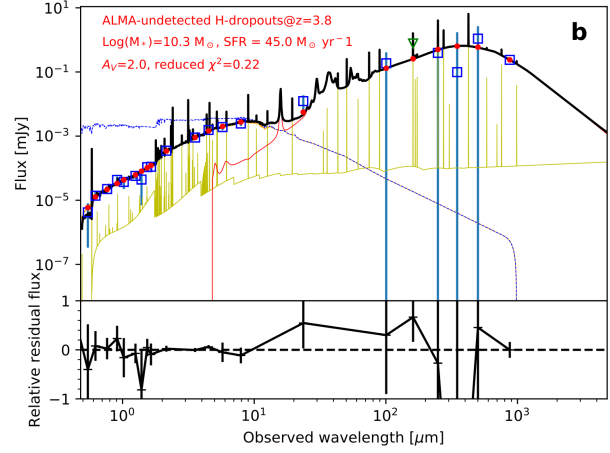
**Extended Data Fig. 4 | Photometric redshifts of H-dropouts.**

**a, b,  $S_{870\mu\text{m}}/S_{450\mu\text{m}}$  (a) and  $S_{1.4\text{GHz}}/S_{870\mu\text{m}}$  (b) colours versus redshift for ALMA-detected H-dropouts in CANDELS-COSMOS; c, comparison between redshifts derived from optical SEDs and from  $S_{870\mu\text{m}}/S_{450\mu\text{m}}$  colours. a, The redshifts are photometric redshifts derived from optical-to-NIR SED fitting except for the two sources denoted in cyan squares, which are spectroscopic redshifts derived from X-SHOOTER spectra. The  $S_{870\mu\text{m}}/S_{450\mu\text{m}}$  colour for galaxies undetected at  $450\mu\text{m}$  ( $S/N < 2$ , open circles) are shown with their lower limits (using the  $4\sigma$  upper limits at  $450\mu\text{m}$ ). One of the spectroscopically confirmed galaxies with  $z_{\text{spec}} = 3.097$  is only marginally detected with  $S_{870\mu\text{m}} = 0.4 \pm 0.1$  mJy, below our conservative detection limit, but we also include it here for illustration. The lines (see key) denote expected colour evolution of different SED templates as a function of redshift, including the stacked IR SED of the H-dropouts. We note that the  $S_{870\mu\text{m}}/S_{450\mu\text{m}}$  colour for both**

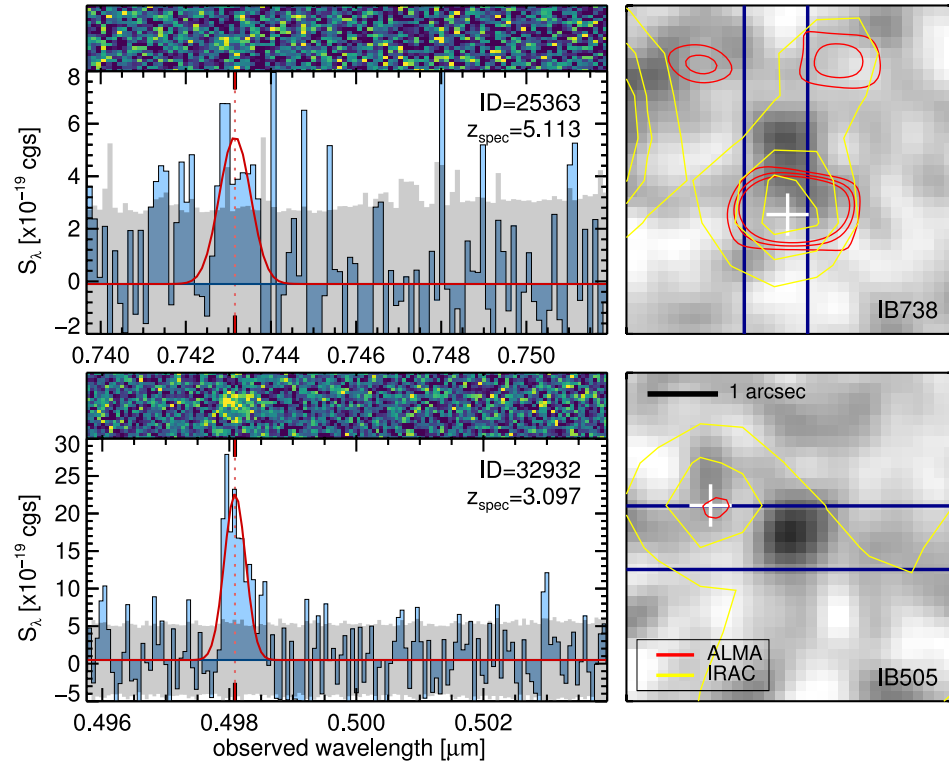
spectroscopically confirmed sources are consistent with the average SED of ALESS  $z = 4$  SMGs. A few previously spectroscopically confirmed bright SMGs at  $z > 5$  are shown by purple squares<sup>3,72,73</sup>. **b, A  $3\sigma$  upper limit of  $7\mu\text{Jy}$  is assigned to non-detections, which are shown with open circles. The dotted and dashed lines denote the relation between  $S_{1.4\text{GHz}}/S_{870\mu\text{m}}$  and redshift for IR SEDs with spectral index in the submillimetre region of 3 (M82-like) and 3.5 (Arp220-like), respectively, as shown in ref.<sup>74</sup>. The same relation for the stacked IR SED of H-dropouts is also shown (orange line). c, Comparison between submillimetre redshifts ( $z_{\text{FIR}}$ ), derived on the basis of their  $S_{870\mu\text{m}}/S_{450\mu\text{m}}$  colour and their stacked IR SED (orange line in the left panel), and redshifts derived from optical SED fitting ( $z_{\text{OPT}}$ ) for sources detected at both  $450\mu\text{m}$  and  $870\mu\text{m}$ . The cyan square denotes the source that is spectroscopically confirmed. Despite their large dispersion, both methods suggest that most of the H-dropouts are indeed at  $z > 3$ .**



**Extended Data Fig. 5 | Full best-fit model of the stacked SEDs of ALMA-detected and ALMA-undetected H-dropouts. a**, ALMA-detected; **b**, ALMA-undetected. Here we show the best-fit SED templates obtained with the SED-fitting tool Cigale<sup>75</sup>. We have adopted the BC03<sup>76</sup> library of single stellar populations and delayed star-formation history model, with

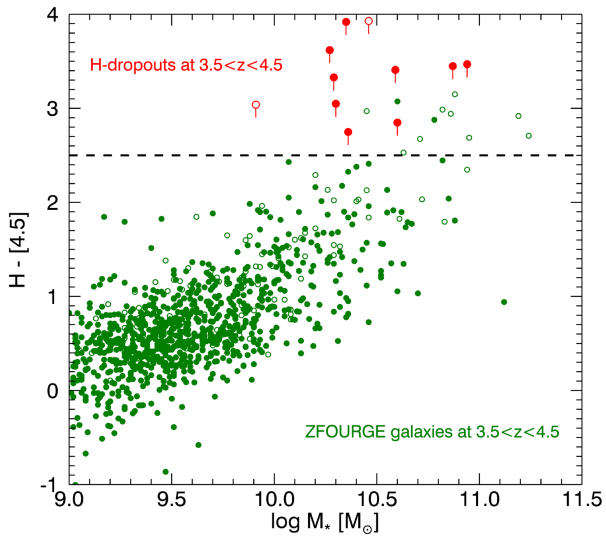


Draine and Li<sup>77</sup> models for the dust emission. Nebular emission based on CLOUDY templates was also included<sup>78</sup>. ALMA-undetected H-dropouts have much lower specific SFR (sSFR) than ALMA-detected ones. Error bars show standard measurement error ( $1\sigma$ ).

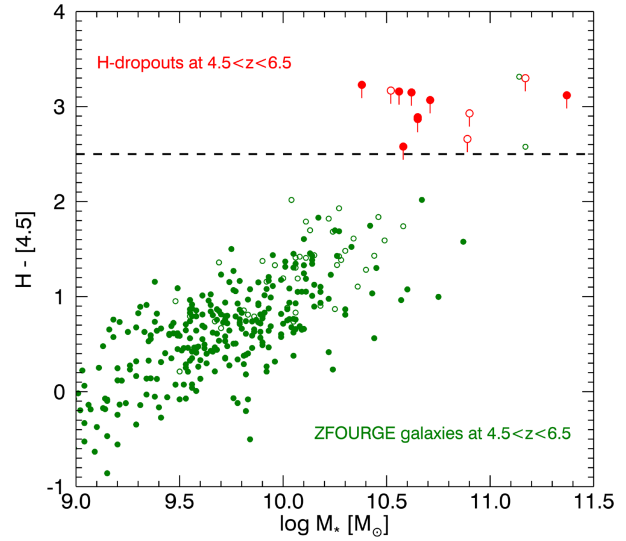


**Extended Data Fig. 6 | X-SHOOTER spectra of two spectroscopically confirmed H-dropouts.** The two galaxies (with IDs 25363 and 32932) are shown on separate rows. Left, main panel, the observed spectra are shown as black solid lines and blue shading, with uncertainties shown in the background as a grey shaded area. The best emission line model for  $\text{Ly}\alpha$  is shown in red, and the centroid of the line is indicated with a vertical dotted line. The 2D spectrum is shown on the top, aligned with the 1D spectrum.

Right, smoothed cutouts of the galaxies as observed in the Subaru medium band (IB738) where  $\text{Ly}\alpha$  was detected. The X-SHOOTER slit is shown in blue, Spitzer-IRAC contours are shown in yellow, and ALMA contours are shown in red. The second galaxy (with ID = 32932) is only marginally detected, with  $S_{870\mu\text{m}} = 0.4 \pm 0.1$  mJy. The centroid of each dropout (determined from the IRAC image) is shown as a white cross.

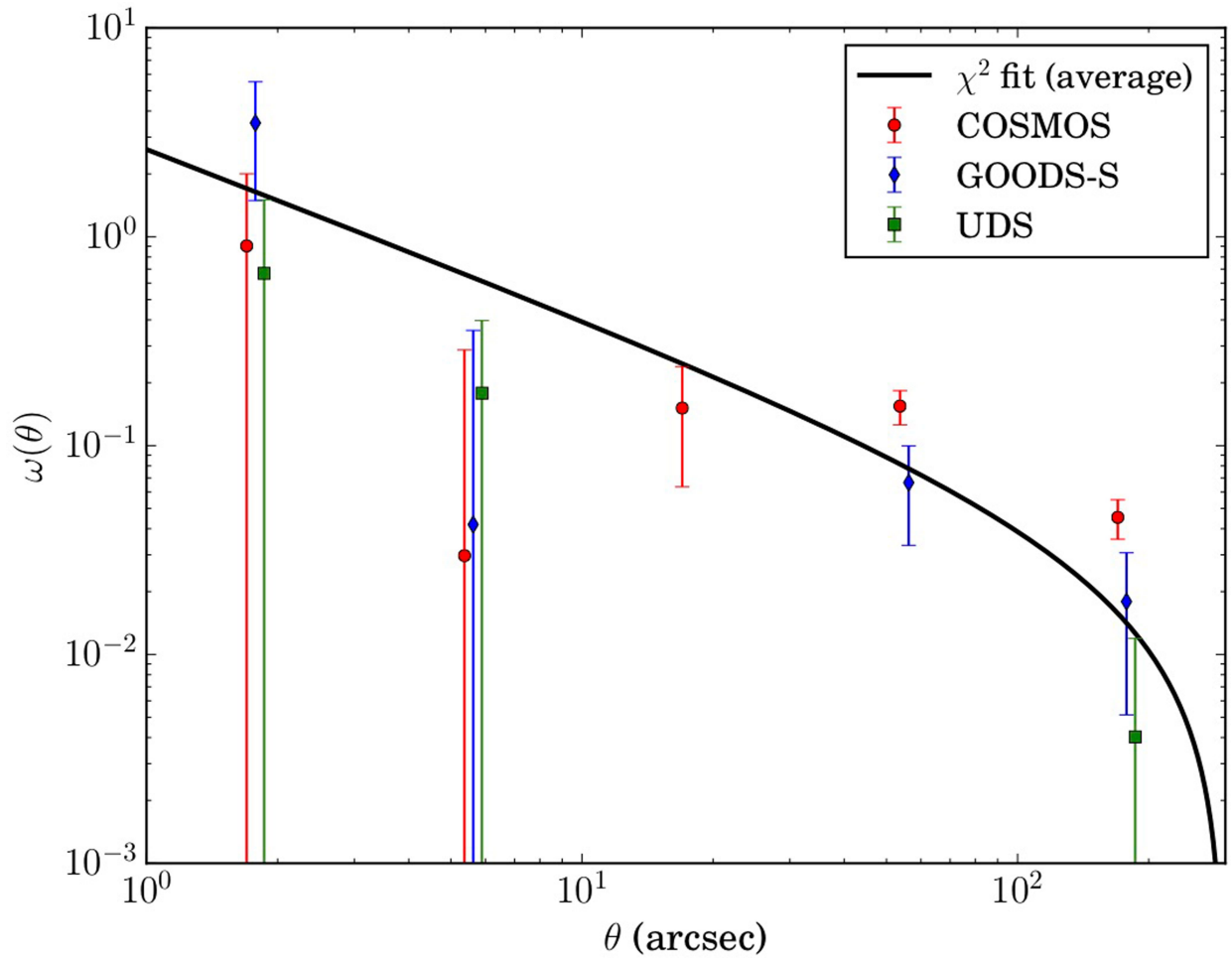


**Extended Data Fig. 7 |  $H - [4.5]$  colour versus stellar mass for massive galaxies at  $3.5 < z < 6.5$ .** Galaxies selected from the ZFOURGE catalogue (left,  $3.5 < z < 4.5$ ; right,  $4.5 < z < 6.5$ ) with HST/F160W detections ( $H > 27$  mag) are shown in green while the H-dropouts selected in the same fields are shown in red. The  $H - [4.5]$  colour of the H-dropouts are



shown by their lower limit assuming  $H > 26.5$  mag ( $5\sigma$ ). Quiescent and star-forming galaxies are shown by open and filled circles, respectively. Quiescent H-dropouts are defined as those undetected with ALMA while quiescent ZFOURGE galaxies are defined by their sSFR (based on SED fitting) with  $\text{sSFR} < 0.3 \text{ Gyr}^{-1}$  and no MIPS 24- $\mu\text{m}$  detections<sup>8</sup>.





**Extended Data Fig. 8 | Angular cross-correlation function between H-dropouts and UV-selected galaxies at  $3.5 < z < 5.5$ .** The two-point angular cross-correlation function shown here,  $\omega(\theta)$ , is computed for the 39 ALMA-detected H-dropouts and approximately 6,000 UV-detected

(H-band) galaxies distributed in the same fields (CANDELS fields COSMOS, GOODS-S and UDS, see key). The solid black line is the best-fit line for the cross-correlation from the two-halo term ( $>10''$  scale). The error bars are estimated from Poisson statistics. See Methods for details.

Extended Data Table 1 | Survey depths for each field

Field	Area arcmin <sup>2</sup>	WFC3/ F160W (5F)	H-dropouts ([4.5] < 24)	ALMA-detected (S <sub>870μm</sub> > 0.6 mJy)	ALMA-undetected (S <sub>870μm</sub> < 0.6 mJy)
CANDELS-GDS	184	H < 27.4–29.7	12	10	2
CANDELS-UDS	202	H < 27.1–27.6	33	14	19
CANDELS-COS	208	H < 27.4–27.8	18	15	3

**Q10** First, second and third lines show data from the three CANDELS fields, GOODS-S, UDS and COSMOS, respectively. WFC3/F160W data are in units of magnitude.

Extended Data Table 2 | Physical properties of H-dropouts

ID	R.A. (J2000)	Decl. (J2000)	[4.5]	$S_{870\ \mu\text{m}}$ (mJy)	$z$	$\text{Log } M_*$ $M_\odot$
GDS-25526	03:32:47.97	-27:54:16.4	22.05	8.34±0.18	4.74 <sup>+0.28</sup> <sub>-0.30</sub>	10.84 <sup>+0.05</sup> <sub>-0.17</sub>
GDS-27571	03:32:30.62	-27:42:24.3	22.44	0.82±0.16	4.64 <sup>+0.19</sup> <sub>-1.64</sub>	10.89 <sup>+0.04</sup> <sub>-0.48</sub>
GDS-40613	03:32:11.44	-27:52:07.1	23.17	1.83±0.18	3.04 <sup>+0.22</sup> <sub>-0.35</sub>	10.64 <sup>+0.02</sup> <sub>-0.22</sub>
GDS-43215	03:32:20.34	-27:42:28.8	23.02	1.52±0.16	2.91 <sup>+0.19</sup> <sub>-0.22</sub>	10.25 <sup>+0.03</sup> <sub>-0.33</sub>
GDS-44539	03:32:28.59	-27:48:50.2	23.41	0.69±0.10	4.22 <sup>+0.67</sup> <sub>-0.77</sub>	10.94 <sup>+0.03</sup> <sub>-0.33</sub>
GDS-47375	03:32:14.62	-27:43:06.0	23.48	1.89±0.12	3.60 <sup>+0.66</sup> <sub>-0.66</sub>	10.27 <sup>+0.13</sup> <sub>-0.12</sub>
GDS-48764	03:32:32.31	-27:54:26.9	23.31	2.54±0.42	5.16 <sup>+0.08</sup> <sub>-1.73</sub>	10.38 <sup>+0.51</sup> <sub>-0.03</sub>
GDS-48885	03:32:47.17	-27:45:25.1	23.57	0.87±0.11	4.62 <sup>+0.19</sup> <sub>-0.17</sub>	10.56 <sup>+0.02</sup> <sub>-0.08</sub>
GDS-49094	03:32:31.85	-27:43:12.7	23.59	0.89±0.13	3.69 <sup>+0.29</sup> <sub>-0.28</sub>	10.29 <sup>+0.10</sup> <sub>-0.05</sub>
GDS-52734	03:32:10.10	-27:50:33.1	24.06	1.41±0.15	5.13 <sup>+1.72</sup> <sub>-1.83</sub>	10.71 <sup>+0.17</sup> <sub>-0.21</sub>
GDS-54513	03:32:04.99	-27:41:56.5	23.71	<0.6	4.33 <sup>+0.32</sup> <sub>-0.37</sub>	10.30 <sup>+0.00</sup> <sub>-0.37</sub>
GDS-58560	03:32:40.11	-27:42:55.3	23.85	<0.6	5.35 <sup>+2.33</sup> <sub>-2.48</sub>	10.58 <sup>+0.39</sup> <sub>-0.43</sub>
COS-16199	10:00:25.41	+02:25:43.9	21.96	3.91±0.09	6.54 <sup>+1.54</sup> <sub>-1.43</sub>	10.90 <sup>+0.14</sup> <sub>-0.27</sub>
COS-19762	10:00:15.89	+02:24:45.9	22.94	4.35±0.10	3.52 <sup>+5.36</sup> <sub>-0.19</sub>	10.79 <sup>+0.88</sup> <sub>-0.08</sub>
COS-23718	10:00:28.95	+02:25:05.3	22.82	2.25±0.10	5.77 <sup>+0.80</sup> <sub>-0.88</sub>	11.02 <sup>+0.13</sup> <sub>-0.24</sub>
COS-23913	10:00:23.03	+02:21:55.0	22.87	1.63±0.09	3.65 <sup>+0.35</sup> <sub>-0.29</sub>	10.65 <sup>+0.10</sup> <sub>-0.11</sub>
COS-24466	10:00:38.07	+02:28:06.2	23.22	1.38±0.09	3.35 <sup>+0.39</sup> <sub>-0.38</sub>	10.37 <sup>+0.34</sup> <sub>-0.26</sub>
COS-25270	10:00:23.62	+02:13:57.4	23.47	<0.6	3.78 <sup>+0.55</sup> <sub>-0.56</sub>	10.48 <sup>+0.04</sup> <sub>-0.20</sub>
COS-25363	10:00:26.68	+02:31:26.2	23.15	3.0 ±0.2	5.113 <sup>+0.001</sup> <sub>-0.005</sub>	10.52 <sup>+0.09</sup> <sub>-0.19</sub>
COS-25881	10:00:27.03	+02:24:24.0	22.96	1.30±0.10	6.58 <sup>+1.38</sup> <sub>-1.43</sub>	11.12 <sup>+0.17</sup> <sub>-0.30</sub>
COS-27285	10:00:27.79	+02:25:52.2	23.74	1.58±0.09	4.32 <sup>+0.23</sup> <sub>-0.22</sub>	10.31 <sup>+0.14</sup> <sub>-0.06</sub>
COS-27392	10:00:27.98	+02:25:29.7	23.42	<0.6	3.61 <sup>+0.51</sup> <sub>-0.49</sub>	10.38 <sup>+0.11</sup> <sub>-0.08</sub>
COS-30182	10:00:14.70	+02:28:01.7	23.08	1.59±0.09	6.37 <sup>+2.15</sup> <sub>-1.16</sub>	10.94 <sup>+0.22</sup> <sub>-0.28</sub>
COS-30614	10:00:14.69	+02:30:04.6	23.39	0.85±0.10	3.97 <sup>+0.19</sup> <sub>-0.29</sub>	10.22 <sup>+0.04</sup> <sub>-0.14</sub>
COS-31278	10:00:26.09	+02:12:31.6	23.36	0.93±0.09	3.37 <sup>+0.43</sup> <sub>-0.35</sub>	10.14 <sup>+0.13</sup> <sub>-0.15</sub>
COS-31483	10:00:46.50	+02:23:09.1	23.89	0.70±0.11	2.97 <sup>+0.40</sup> <sub>-0.41</sub>	9.91 <sup>+0.13</sup> <sub>-0.13</sub>
COS-31661	10:00:41.83	+02:25:47.0	23.28	2.88±0.12	3.72 <sup>+0.17</sup> <sub>-0.19</sub>	10.36 <sup>+0.05</sup> <sub>-0.20</sub>
COS-32409	10:00:15.84	+02:23:04.0	23.66	0.70±0.11	3.91 <sup>+1.66</sup> <sub>-1.16</sub>	9.87 <sup>+0.48</sup> <sub>-0.06</sub>
COS-32932	10:00:22.44	+02:23:41.1	23.22	<0.6	3.0971 <sup>+0.0002</sup> <sub>-0.001</sub>	9.96 <sup>+0.15</sup> <sub>-0.11</sub>
COS-34487	10:00:35.34	+02:28:26.7	23.36	4.3 ±0.15	3.15 <sup>+0.60</sup> <sub>-0.62</sub>	10.18 <sup>+0.26</sup> <sub>-0.20</sub>
UDS-24945	02:16:59.77	-05:11:52.8	22.16	<0.6	3.50 <sup>+0.76</sup> <sub>-0.61</sub>	10.76 <sup>+0.22</sup> <sub>-0.11</sub>
UDS-29006	02:17:05.52	-05:08:45.8	22.71	<0.6	3.79 <sup>+0.61</sup> <sub>-0.53</sub>	10.46 <sup>+0.13</sup> <sub>-0.21</sub>
UDS-31037	02:18:07.67	-05:13:26.8	22.58	1.83±0.13	3.62 <sup>+0.70</sup> <sub>-0.65</sub>	10.49 <sup>+0.26</sup> <sub>-0.07</sub>
UDS-31072	02:17:43.32	-05:11:57.4	22.29	3.63±0.25	4.20 <sup>+4.17</sup> <sub>-0.44</sub>	11.31 <sup>+0.33</sup> <sub>-0.09</sub>
UDS-31959	02:18:11.36	-05:16:23.7	22.98	<0.6	3.88 <sup>+0.68</sup> <sub>-0.73</sub>	10.22 <sup>+0.19</sup> <sub>-0.14</sub>
UDS-34637	02:18:05.80	-05:11:23.1	22.89	1.07±0.37	2.84 <sup>+0.54</sup> <sub>-0.44</sub>	10.33 <sup>+0.16</sup> <sub>-0.17</sub>
UDS-37344	02:18:02.86	-05:15:05.4	23.36	<0.6	2.89 <sup>+0.44</sup> <sub>-1.48</sub>	10.18 <sup>+0.08</sup> <sub>-0.63</sub>
UDS-37423	02:18:10.02	-05:11:31.5	23.07	1.12±0.15	7.47 <sup>+0.63</sup> <sub>-0.64</sub>	11.17 <sup>+0.20</sup> <sub>-0.08</sub>
UDS-37560	02:17:03.44	-05:15:51.3	22.72	4.40±0.14	3.95 <sup>+0.35</sup> <sub>-0.34</sub>	10.35 <sup>+0.22</sup> <sub>-0.17</sub>
UDS-37649	02:17:36.95	-05:16:07.3	23.14	1.25±0.31	2.82 <sup>+0.44</sup> <sub>-0.48</sub>	10.31 <sup>+0.07</sup> <sub>-0.07</sub>
UDS-40772	02:17:36.56	-05:12:52.0	23.19	1.96±0.31	4.00 <sup>+0.98</sup> <sub>-0.44</sub>	10.87 <sup>+0.00</sup> <sub>-0.40</sub>
UDS-41502	02:17:18.03	-05:11:03.9	23.23	1.59±0.20	3.73 <sup>+0.44</sup> <sub>-0.43</sub>	10.59 <sup>+0.09</sup> <sub>-0.33</sub>
UDS-41525	02:16:59.59	-05:14:15.4	23.34	<0.6	6.13 <sup>+1.08</sup> <sub>-1.01</sub>	11.17 <sup>+0.15</sup> <sub>-0.16</sub>
UDS-41773	02:18:07.02	-05:09:18.1	23.11	1.54±0.15	3.52 <sup>+1.35</sup> <sub>-0.84</sub>	10.20 <sup>+0.56</sup> <sub>-0.24</sub>
UDS-42280	02:18:11.16	-05:10:27.1	23.88	1.16±0.37	4.21 <sup>+0.18</sup> <sub>-0.17</sub>	10.06 <sup>+0.09</sup> <sub>-0.16</sub>
UDS-42875	02:18:21.15	-05:09:42.5	23.04	1.74±0.15	7.20 <sup>+1.20</sup> <sub>-1.23</sub>	11.75 <sup>+0.05</sup> <sub>-0.31</sub>
UDS-43941	02:17:43.65	-05:14:23.9	23.46	1.91±0.11	3.39 <sup>+0.53</sup> <sub>-0.23</sub>	10.17 <sup>+0.02</sup> <sub>-0.10</sub>
UDS-44515	02:18:20.89	-05:11:11.1	23.48	<0.6	4.20 <sup>+1.35</sup> <sub>-1.35</sub>	10.59 <sup>+0.07</sup> <sub>-0.27</sub>
UDS-44594	02:17:20.20	-05:11:55.4	23.79	0.66±0.14	4.44 <sup>+0.52</sup> <sub>-0.39</sub>	10.60 <sup>+0.04</sup> <sub>-0.17</sub>
UDS-45868	02:18:15.00	-05:10:02.7	23.61	<0.6	3.66 <sup>+0.88</sup> <sub>-0.88</sub>	10.45 <sup>+0.13</sup> <sub>-0.13</sub>
UDS-46241	02:17:58.31	-05:15:00.3	23.44	<0.6	2.18 <sup>+0.78</sup> <sub>-0.53</sub>	9.72 <sup>+0.22</sup> <sub>-0.38</sub>
UDS-46513	02:18:17.87	-05:11:53.9	23.84	0.58±0.11	3.54 <sup>+0.93</sup> <sub>-0.93</sub>	10.31 <sup>+0.11</sup> <sub>-0.19</sub>
UDS-46648	02:17:08.17	-05:15:37.8	23.52	2.27±0.20	6.88 <sup>+1.67</sup> <sub>-1.74</sub>	11.37 <sup>+0.30</sup> <sub>-0.43</sub>
UDS-46693	02:17:59.07	-05:09:37.5	23.47	<0.6	3.56 <sup>+0.37</sup> <sub>-0.26</sub>	10.24 <sup>+0.03</sup> <sub>-0.23</sub>
UDS-48514	02:17:29.83	-05:14:23.5	23.65	<0.6	2.59 <sup>+0.83</sup> <sub>-0.83</sub>	10.04 <sup>+0.01</sup> <sub>-0.42</sub>
UDS-49119	02:17:07.14	-05:12:54.0	23.77	1.34±0.30	4.60 <sup>+1.94</sup> <sub>-1.83</sub>	10.65 <sup>+0.01</sup> <sub>-0.53</sub>
UDS-49199	02:18:21.40	-05:11:46.3	23.6	<0.6	3.96 <sup>+0.84</sup> <sub>-0.97</sub>	10.66 <sup>+0.04</sup> <sub>-0.24</sub>
UDS-49594	02:18:01.13	-05:13:45.7	23.65	<0.6	3.77 <sup>+0.48</sup> <sub>-0.55</sub>	9.79 <sup>+0.03</sup> <sub>-0.23</sub>
UDS-49784	02:17:37.48	-05:09:47.7	23.6	<0.6	3.95 <sup>+1.63</sup> <sub>-2.21</sub>	9.91 <sup>+0.41</sup> <sub>-0.77</sub>
UDS-51119	02:17:58.29	-05:11:44.7	23.75	<0.6	3.45 <sup>+1.16</sup> <sub>-1.16</sub>	10.25 <sup>+0.12</sup> <sub>-0.13</sub>
UDS-52324	02:17:06.27	-05:09:48.3	23.49	2.69±0.16	4.95 <sup>+1.74</sup> <sub>-1.61</sub>	10.62 <sup>+0.12</sup> <sub>-0.26</sub>
UDS-54074	02:17:09.70	-05:15:11.3	23.75	0.81±0.10	5.89 <sup>+1.90</sup> <sub>-2.37</sub>	10.65 <sup>+0.19</sup> <sub>-0.35</sub>
UDS-63094	02:17:53.06	-05:11:25.5	23.98	<0.6	5.08 <sup>+0.24</sup> <sub>-0.26</sub>	10.00 <sup>+0.08</sup> <sub>-0.27</sub>

In column 4, [4.5] indicates 4.5- $\mu\text{m}$  magnitude.

